

Understanding degradation in lithium-ion and lithium-air batteries

Rory McNulty

School of Chemistry

University of Nottingham

A Thesis submitted for the degree of Doctor of Philosophy

Declaration

I, Rory McNulty, hereby declare that this doctoral thesis, which is approximately 61,400 words in length, is the result of my own investigations and has been written wholly by me. The work presented here has not been submitted in any previous application for a higher education degree.

Signed  .....

31th March 2023

THE FARADAY INSTITUTION

University of Nottingham

UK | CHINA | MALAYSIA

Acknowledgements

A PhD is, by nature, an independent research journey. However, in reality, this journey is undertaken with the help and support of family, friends, and colleagues, some of whom have been there throughout and others that are met along the way.

I would first like to thank my research supervisor, Dr. Lee Johnson, for his guidance and support throughout my PhD – from establishing a battery laboratory in Nottingham to helping me craft my first academic publications. It has been a pleasure to be one of your first PhD students, and I am excited to see your group continue to grow and push the boundaries of battery research.

I would also like to thank the broader Nottingham Applied Materials and Interfaces (NAMI) group, particularly Dr. Graham Newton and Prof. Darren Walsh who, along with Lee, have fostered a collaborative, ambitious, and, most importantly, supportive research environment that challenged me to continually grow from both a personal and an academic perspective.

Within the NAMI group, there are too many people to name that deserve a thank you – the last 4 years would not have been the same without you all. I am particularly grateful to the lithium-air sub-group, within which I completed the latter half of this thesis. Dr. Conrad Holc, Dr. Jack Jordan, and Ganesh Vailaya, it has been a pleasure to work alongside you designing weird and wonderful experiments and frequently discussing mad science.

I am particularly grateful to Dr. Conrad Holc, my assistant supervisor, who has supported me throughout the entirety of my PhD, both as a mentor in the lab and as a good friend outside of it. I wish you all the best in everything that you do, and I look forward to seeing you continue to break barriers in the next-generation battery world.

This section would not be complete without extending my thanks to Konstantinos Dimogiannis. As Lee's first PhD students, we undertook this journey together, from slurry preparation and electrode casting with the help

of online videos to training new students in the ways of battery science. Many good times were had, and many memories were made along the way.

To Matthew Bird, who provided me with electrochemistry wizardry in the lab, sustenance with motivation throughout thesis writing, and true friendship outside of the lab – I appreciate everything that you have done for me.

To Christopher Merrett, who has lived with me throughout the entirety of my PhD, it is certain that I would not have remained sane without your friendship and support. Through bad times and good you have always been there for me – from Dragmar Grove to Jesus Street.

To Lukas Rier who, despite receiving no benefit himself, worked with me to develop GalvAnalyze, an executable for processing battery cycling data, I salute you and your commitment to science – your friendship means a lot to me.

To “the two best friends that anyone could have”, Harry Rogerson, who called me every single week of my thesis writing period, and Alexander Pawley, who paused his life for 3 months to travel the world with me – thank you for everything and never change.

To Ellie Pinkney and the Pinkney family, with whom I have shared countless good times, many triumphant dinners parties, and a good few funk and soul festivals – you have been a home from home. We love you Craig.

A special thank you goes to Rowena Rutherfoord, my wonderful girlfriend, who has offered unwavering support and sacrificed so much to allow me to pursue my passion. You have always offered the perfect advice when I needed it the most and I am excited for the next chapter of our lives together.

The final thank you is reserved for my Mum and Dad, who have given me more than I could ever have asked for. It was a single distinctive phone call with my Dad that started this entire PhD journey, and I would not have made it half this far if it wasn’t for the unconditional love and support I received from both my Mum and Dad.

Publications

Published

1) **McNulty, R. C.**; Penston, K.; Amin, S. S.; Stal, S.; Lee, J. Y.; Samperi, M.; Pérez-García, L.; Cameron, J. M.; Johnson, L. R.; Amabilino, D. B.; Newton, G. N. Self-Assembled Surfactant-Polyoxovanadate Soft Materials as Tuneable Vanadium Oxide Cathode Precursors for Lithium-Ion Batteries. *Angew. Chem. Int. Ed.* ***135***, e202216066 (2023). https://doi.org/10.1002/ange.202216066.
2) **McNulty, R. C.**; Jones, K. D.; Holc, C.; Jordan, J. W.; Bruce, P. G.; Walsh, D. A.; Newton, G. N.; Lam, H. W.; Johnson, L. R. Hydroperoxide-Mediated Degradation of Acetonitrile in the Lithium-Air Battery. *Adv. Energy Mater.* 2300579 (2023) https://doi.org/10.1002/aenm.202300579
3) **McNulty, R. C.**; Rier, L. GalvAnalyze: Streamlining Data Analysis of Galvanostatic Battery Cycling. *Batteries & Supercaps* e202300038 (2023) https://doi.org/10.1002/batt.202300038

Under Review

4) **McNulty, R. C.**; Damian, H. A.; Solé-Daura, A.; Cameron, J. M.; Martin, C.; Johnson, L. R.; Hirst, J. D.; Poblet, J. M.; Carbó J. J.; Mitchell, N. J.; Newton, G. N. Polyoxometalates as Tuneable Probes for Direct Interrogation of Peptide Redox State.
5) **McNulty, R. C.**; Hampson, E.; Cutler, L. N.; Grey, C. P.; Dose, W. M.; Johnson, L. R. Understanding the limits of Li-NMC811 half-cells.

In preparation

6) **McNulty, R. C.**; Hampson, E.; Grey, C. P.; Dose, W. M.; Johnson, L. R. Understanding the Mechanism of Vinylene Carbonate formation in Early-stage Cycling of NMC811 full-cells.
7) Holc, C.; **McNulty, R. C.**; Newton, G. N.; Walsh, D. A.; Bruce. P. G.; Johnson, L. R. Solvation determines whether oxygen is reduced by two

or four electrons and its relation to the rechargeable lithium-oxygen battery operating in air.

8) **McNulty, R. C.**; Holc, C.; Vailaya, G.; Jordan, J. W.; Newton, G. N.; Walsh, D. A.; Rogers, D.; Bruce, P. G.; Johnson, L. R. Employing Acceptor Number Theory for Lithium-air Electrolyte Solvent Selection with High Water Toleration.
9) Jordan, J. W.; Vailaya, G.; Jenkins, M.; **McNulty, R. C.**; Gao, X.; Holc, C.; Walsh, D. A.; Newton, G. N.; Bruce, P. G.; Johnson, L. R. A Lithium-air Battery and Gas Handling System Demonstration.
10) Vailaya, G.; Jordan, J. W., **McNulty, R. C.**; Kibler, A. J.; Holc, C.; Walsh, D. A.; Newton, G. N.; Johnson, L. R. N-ethylphenoxazine as a redox mediator for the oxidation of lithium peroxide in the Li-O_2 battery.

Abstract

With a global transition towards electrification, there is considerable interest in the development of high energy density battery technologies. The current world leading battery chemistries, that are enabling the mass market electrification of transport, are high-nickel positive electrodes. However, as positive electrode nickel-content increases, so too does the reactivity of the positive electrode surface with the electrolyte species, limiting the long-term performance of these cell chemistries. The purpose of the first half of this thesis is to identify failure mechanisms and understand the feasibility of vinylene carbonate formation in cells containing a NMC811 electrode, with the objective of proposing actionable solutions to overcome current inefficiencies hindering research progress.

To enable the electrification of next-generation applications, technologies that far exceed the possible performance of traditional lithium-ion batteries are required. The latter half of this thesis examines the degradation of the lithium-air battery, a technology with a theoretical specific capacity ten times greater than traditional lithium-ion. The purpose of this work was to understand the role of H_2O, and the hydroperoxide species that are introduced by its presence, in chemical and electrochemical degradation reactions. Here hydroperoxide species are directly identified as playing an antagonistic role in the chemical degradation of acetonitrile, and in the electrochemical formation of lithium hydroxide, the mechanism of which is conclusively identified for the first time.

Symbols

A	Electrode area
C	Concentration of species
D_F	Diffusion coefficient
E	Potential
F	Faraday constant
f	Frequency
I	Current
i_L	Limiting current
i_p	Peak current
j	Imaginary number (i.e. $\sqrt{-1}$)
J	Total angular momentum
k_B	Boltzmann constant
L	Orbital angular momentum
n	Number of electrons
R	Resistance
S	Spin angular momentum
t	Time
Z	Impedance
Z_{im}	Imaginary impedance
Z_r	Real impedance
δ_F	Diffusion layer
δ_H	Hydrodynamic boundary layer
η	Dynamic viscosity
λ	Wavelength
ν	Kinematic viscosity
ϕ	Phase shift
ω	Angular rotation rate

Abbreviations

AN	Acceptor number
CEI	Cathode electrolyte interphase
CV	Cyclic voltammetry
CT	Calibration tube
DEMS	Differential electrochemical mass spectrometry
DN	Donor number
DoE	Department of Energy
e^-/O_2	Electrons per molecule of oxygen
EIS	Electrochemical impedance spectroscopy
ESI	Electrospray ionisation
EV	Electric vehicle
Fe-SAC	Iron single atom catalyst
FTIR	Fourier transform Infra-red
Full-cell	Lithium-ion cell with a transition metal cathode and a graphite anode
GC-MS	Gas chromatography mass spectrometry
geom	Geometric area
Gr	Graphite electrode
Half-cell	Lithium-ion cell with a lithium metal counter electrode
HOMO	Highest occupied molecular orbital
HPLC	High performance liquid chromatography
HPLC-MS	High performance liquid chromatography mass spectrometry
IEA	International Economic Association
iR	Voltage/Ohmic drop
IRA	Inflation Reduction Act
kWh	Kilowatt-hour
LCO	Lithium cobalt oxide electrode ($LiCoO_2$)
LFP	Lithium iron phosphate electrode ($LiFePo_4$)
LHS	Left-hand side

Li-air	Lithium-air
LIB	Lithium-ion battery
Li-ion	Lithium-ion
Li-O_2	Lithium-oxygen
Li-S	Lithium-sulfur
LMO	Lithium manganese oxide ($LiMn_2O_4$)
LNO	Lithium nickel oxide ($LiNiO_2$)
LP57	1 M $LiPF_6$ in EC:EMC (3:7 v/v)
LP57-VC	1 M $LiPF_6$ in EC:EMC (3:7 v/v) + 2 wt.% VC
LSV	Linear sweep voltammogram
LTO	Lithium titanium oxide electrode ($Li_4Ti_5O_{12}$)
MO	Molecular orbital
mol%	Percentage by moles
MS	Mass spectrometry
n:p	Ratio of negative (n):(p) positive electrode loading
NIST	National Institute of Standards and Technology
NMC111	Lithium nickel manganese cobalt oxide electrode ($LiNi_{0.33}Mn_{0.33}Co_{0.33}O_2$)
NMC622	Lithium nickel manganese cobalt oxide electrode ($LiNi_{0.6}Mn_{0.2}Co_{0.2}O_2$)
NMC811	Lithium nickel manganese cobalt oxide electrode ($LiNi_{0.8}Mn_{0.1}Co_{0.1}O_2$)
NMR	Nuclear magnetic resonance
OCV	Open circuit voltage
OEMS	On-line electrochemical mass spectrometry
PITT	Potentiostatic intermittent titration
PC	Pressure cell
Pt	Platinum
PTFE	Polytetrafluoroethylene binder
RB	Rose Bengal
R_{CEI}	Cathode electrolyte interphase resistance

R_{CT}	Charge transfer resistance
RDE	Rotating disk electrochemistry
red	Reduction
RHS	Right-hand side
SE	Solid electrolyte
SEI	Solid electrolyte interphase
SS	Stainless steel
TM	Transition metal
UCV	Upper cut-off voltage
vol.%	Percentage by volume
W	Warburg element
Wh kg^{-1}	Watt-hours per kilogram
Wh L^{-1}	Watt-hours per litre
wt.%	Percentage by weight
δ	Chemical shift

Table of Contents

Declaration i

Acknowledgements ii

Publications iv

Abstract vi

Symbols vii

Abbreviations viii

Table of Contents xi

Chapter 1. Introduction 1

1.1 Motivations for the project 1

1.2 The demands of the transport sector 3

1.3 A brief history of lithium-ion battery development 5

1.4 The lithium-ion battery 6

1.5 Single transition metal oxide positive electrodes 7

1.6 Mixed transition metal oxide positive electrodes 12

1.7 Negative electrodes 16

1.8 Electrolyte composition 21

1.9 Degradation of Gr-NMC811 cells 26

1.10 Aims and objectives 31

1.11 References 33

Chapter 2. Experimental 62

2.1 Electrochemical measurements 62

2.1.1 Materials 62

2.1.2 Three electrode electrochemical measurements 63

2.1.3 Linear sweep voltammetry measurements 64

2.1.4 SS flag LSV measurements 65

2.1.5 Rotating disk electrochemistry (RDE) measurements 65
2.1.6 Solution resistance 68
2.1.7 Two-electrode lithium-ion (Li-ion) cell cycling 69
2.1.8 Three-electrode electrochemical impedance spectroscopy 70
2.1.9 Two electrode lithium-air (Li-air) cell cycling 75
2.1.10 SS-free (PFA) two-electrode Li-air cells 78
2.2 Chromatography 79
2.2.1 Gas chromatography (GC) mass spectrometry (MS) 79
2.2.2 High performance liquid chromatography (HPLC) mass spectrometry (MS) 81
2.3 On-line mass spectrometry (OEMS) 82
2.3.1 Li-ion measurements 84
2.3.2 Li-air measurements 85
2.4 Singlet oxygen ($^1O_2$) generation 89
2.5 Li_2O_2 yield measurements 94
2.6 Nuclear magnetic resonance (NMR) spectroscopy 96
2.7 References 98
Chapter 3. Understanding the limits of Li-NMC811 half cells 101
3.1 Introduction 101
3.2 Experimental 103
3.2.1 Materials 103
3.2.2 Electrochemical testing 103
3.2.3 Post-cycling electrolyte analysis 104
3.2.4 Cell reconstitution procedure 104
3.3 Half-cell cycling and the role of VC 105
3.4 Electrolyte degradation and the fate of VC 115

3.5 Understanding the failure mechanism of half-cells based on metallic Li 131

3.6 Lithium titanium oxide as an impartial counter electrode 145

3.7 Conclusions 153

3.8 References 154

Chapter 4. Understanding the mechanism of vinylene carbonate formation in early-stage cycling of Gr-NMC811 full-cells 163

4.1 Introduction 163

4.2 Experimental 164

4.2.1 Materials 164

4.2.2 Catalyst characterisation 166

4.2.3 Electrochemical testing 166

4.2.4 On-line electrochemical mass spectrometry (OEMS) measurements 166

4.2.5 $^1O_2$ generation techniques 167

4.2.6 GC-MS measurements 167

4.2.7 HPLC-MS measurements 169

4.2.8 NMR measurements 169

4.3 Gr-NMC811 full-cell cycling and the role of VC 169

4.4 Investigating gas evolution in Li-NMC811 cells 174

4.5 Detecting the formation of VC in early-stage cycling of Gr-NMC811 cells 182

4.6 Exploring the feasibility of photo-initiated Rose Bengal $^1O_2$-driven VC formation 191

4.7 Synthesis and application of a $^1O_2$ selective single atom catalyst 203

4.8 Conclusions 212

4.9 References 214

Chapter 5. Progress towards a next-generation Li-air battery 220

5.1 Meeting the energy demands of next-generation applications..... 220

5.2 Li-air battery (electro)chemistries 223

5.3 Electrolyte solution degradation 230

5.4 Redox-mediators 234

5.5 H_2O in the Li-air battery 236

5.6 Aims and objectives 244

5.7 References 246

Chapter 6. Hydroperoxide mediated degradation of acetonitrile in the lithium-air battery 262

6.1 Introduction 262

6.2 Experimental 264

6.2.1 Materials 264

6.2.2 Pressure cell measurements 265

6.2.3 Li_2O_2 yield measurements 266

6.2.4 NMR measurements 266

6.2.5 HPLC-MS measurements 266

6.3 Determining the effect of H_2O on O_2 reduction 267

6.4 HPLC-MS study of electrolyte composition 274

6.5 Spectroscopic exploration of model chemical systems 281

6.6 Proposed hydroperoxide mediated MeCN degradation pathway 288

6.7 Conclusions 290

6.8 References 291

Chapter 7. Understanding the requirements for and mechanism of $4e^-$ O_2 reduction in the lithium-air battery 298

7.1 Introduction 298

7.2 Experimental 300
7.2.1 Materials 300
7.2.2 Pressure cell measurements 301
7.2.3 Li_2O_2 yield measurements 302
7.2.4 Characterisation of discharged cathodes 302
7.2.5 Electrochemical measurements 303
7.2.6 Raman spectroscopy measurements 305
7.2.7 SEM imaging 305
7.2.8 OEMS measurements 305
7.2.9 NMR measurements 307
7.3 Understanding the role of solvent AN and DN on the overall AN of H_2O-solvent mixtures 307
7.4 The impact of H_2O concentration on the O_2 reduction pathway in Li-air cells 312
7.5 Exploring the feasibility of chemical LiOH formation 326
7.6 The impact of H_2O on electrochemical O_2 reduction 329
7.7 The fate of hydroperoxide species in Li-air cells 335
7.8 High-performance Li-air batteries with 13% and 100% humidity 343
7.9 Conclusions 362
7.10 References 365
Chapter 8. Perspective and future considerations 371
Appendix 376

Chapter 1. Introduction

1.1 Motivations for the project

It is well established that the global dependency on fossil fuels is unsustainable and a transition to renewable energy sources is critical to reduce man-made impact on the warming global climate and ensure adequate energy supply beyond the exhaustion of fossil fuels.[1,2] The extensive use of fossil fuels, which has enabled widespread accessibility of electricity in the modern era, has facilitated considerable global improvement in the standard of living.[3] This societal progression has been built upon a foundation of energy, particularly electrical energy, that has permitted global connectivity, access to technology, and comprehensive education. Nevertheless, we have a collective responsibility to identify and understand the impact that human activity has on the world and actively transition towards a future built on a foundation of global sustainability.

The Paris Agreement was unanimously supported at the 21st Conference of Parties (COP21) in 2016, wherein 196 parties adopted a legally binding international treaty to limit global warming below 2 °C, preferably 1.5 °C, compared to pre-industrial levels.[4] Despite this, the global consumption of fossil fuels has continued to steadily grow,[5,6] limited briefly by the widespread lockdowns imposed as a result of the COVID-19 pandemic in 2020.[7–10] It is estimated that more than 135,000 TWh of fossil fuels were consumed in 2021 alone (**Figure 1.1**a),[7,8] producing a total of 37 billion tonnes of carbon dioxide (CO_2) emissions (**Figure 1.1**b).[11,12] According to the International Energy Agency, the transportation sector accounted for 37% of CO_2 emissions from end-use sectors in 2021,[13] where petrol- and diesel-powered vehicles exhaust harmful compounds including CO_2, carbon monoxide, hydrocarbons, and nitrogen oxides that contribute to global warming, increase urban pollution, and promote the formation of smog.[14] In population dense areas, transportation is a primary contributor to poor air quality, increasing the risk of respiratory diseases and diminishing public health.[15,16] The reduction of the

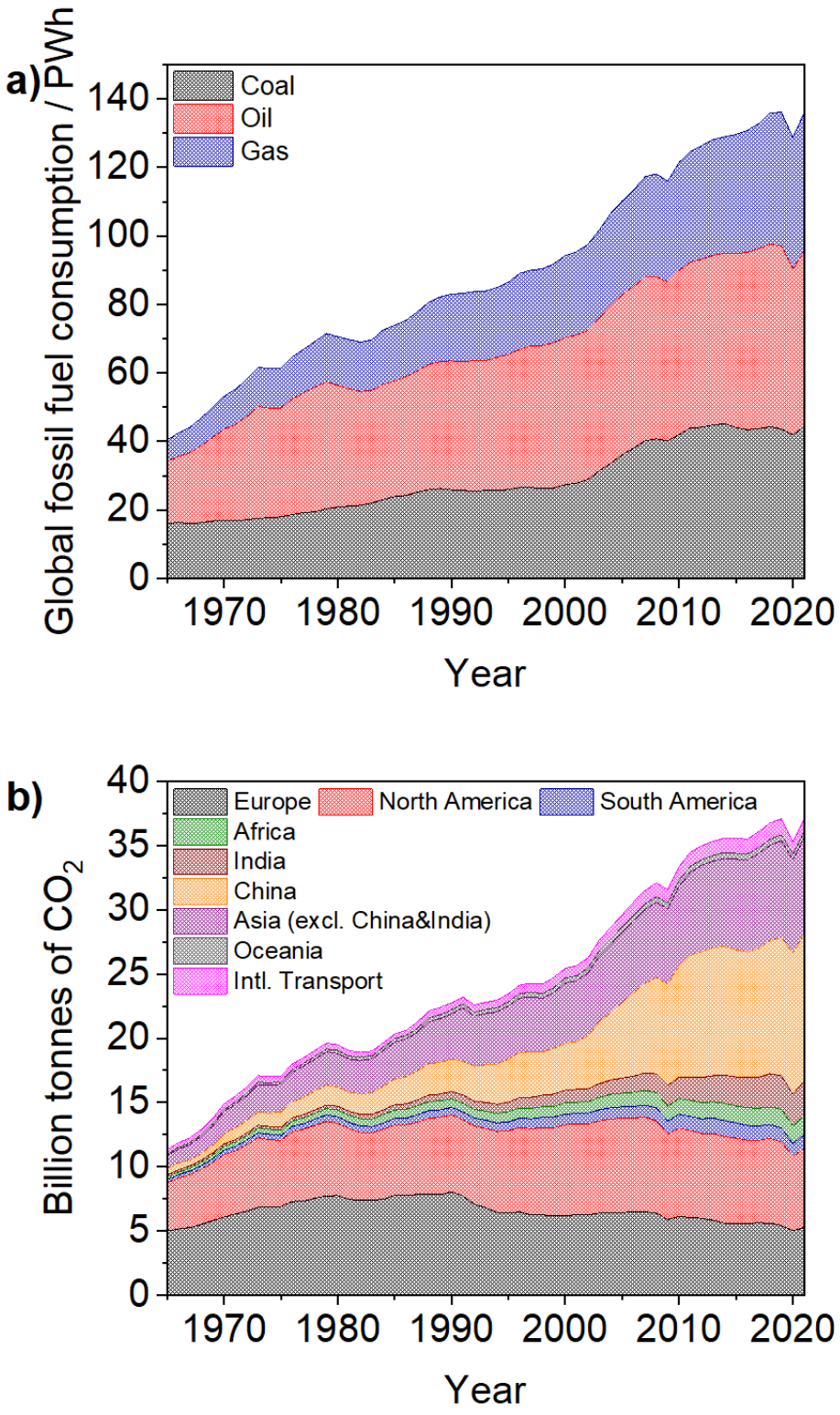


Figure 1.1. *Plots showing the total global annual a) consumption of fossil fuels and b) CO_2 emissions by world region between 1965 and 2021. Reproduced from a) BP Statistical Review of Global Energy,[7,8] and b) Friedlingstein et al.[11,12]*

transport sectors contribution to urban air pollution through electrification is an immediate and essential motivation for the work presented in this thesis. Moreover, broader electrification of industries and the development of energy storage solutions to support these transitions are necessary milestones in the realisation of a renewable energy grid, wherein intermittent renewable energy sources increasingly contribute to global energy supply and fossil fuels are reserved for essential applications.[17]

1.2 The demands of the transport sector

In 2016, the US Department of Energy (DoE) stated that the average lithium-ion battery (LIB) cell cost was $268 per kilowatt-hour ($kWh^{-1}$) and estimated that for mass market electric vehicle (EV) penetration, a required minimum drive range of 300-miles must be achieved at a maximum cost of $125 kWh^{-1}.[18–20] This target corresponds to approximate gravimetric and volumetric energy densities of 235 Wh kg^{-1} and 500 Wh L^{-1} at the system level, which requires a cell level performance of ca. 350 Wh kg^{-1} and 750 Wh L^{-1}, respectively.[18–20] In 2022, Günter and Wassiliadis published a report of cell teardown and characterisation of a 78 Ah cell from a Volkswagen ID.3.[21] Gravimetric and volumetric energy densities of 268 Wh kg^{-1} and 674 Wh L^{-1}, respectively, were reported for this cell, which can be considered representative of state-of-the-art at the time of writing.[21] Although the average price of LIBs has been decreasing steadily over the past decade up to 2021, where it hit a low around $100 kWh^{-1}, the recent volatility of raw materials prices has resulted in an increase in the average LIB cell cost to between $100 – 120 kWh^{-1}, according to Benchmark Minerals Intelligence.[22] Simultaneous improvement in performance while reducing cost has been the result of a combination of technical innovation in active material design and performance, and optimisation in the form of reducing the contribution of inactive material. With state-of-the-art EV specifications now approaching the minimum requirements set by the US DoE for mass market penetration, we are on the precipice of global electrification of transportation.

According to the International Economic Association's (IEA) "Global EV Outlook 2021", there were 10 million EVs on the world's roads at the end of 2020, with EV registrations increasing by 41% in 2020 alone.[23] Approximately 4.6% of global automotive sales were attributed to EVs in 2020, with Europe overtaking China as the world's largest EV market for the first time.[23] Although China has traditionally been the dominant force in the LIB supply chain, Europe and North America are progressively becoming more ambitious with their efforts to secure an increasingly large proportion of this high value industry. In August 2022, the US signed into law the Inflation Reduction Act (IRA),[24] which directs federal spending towards the overall reduction of carbon emissions, reducing healthcare costs, funding the Internal Revenue Service, and improving proper taxpayer compliance, which could represent a much needed catalyst in the development of higher energy density, affordable EV batteries.[24]

An approximate $390 billion in federal funding is pledged to 'clean energy', where a target of reducing carbon emissions by ca. 40% by 2030 (**Figure 1.2**).[24,25] Of this, $47.4 billion is set aside specifically for the development of manufacturing capacity, and a further $23.4 billion in tax credits are allocated to transportation and EVs.[25] However, assigning capital is only one of the challenges that is involved with developing a battery industry, with China's dominance of the critical raw material and specialist chemical



Figure 1.2. *Breakdown of the assignment of federal funding under the 'clean energy' section of the IRA.[24] Reproduced from the Environmental Resources Management "Inflation Reduction Act of 2022: Climate and Energy Provisions" issue briefing.[26]*

supply chains being well-established through governmental foresight and historical investment. To incentivise this, the IRA establishes a required threshold of the market-value of critical minerals that must be sourced domestically (US) or from free-trade partners which increases incrementally, starting at 40% in 2023 and reaching 80% by the start of 2027.[24,27] These ambitious targets not only firmly mark North America's intent on becoming a global leader in the LIB supply chain, and more broadly in the renewable energy transition, but also adeptly highlights the significance of energy storage research. At the time of publication, it stands to be seen if the UK or EU will establish equally ambitious legislation and incentives.

1.3 A brief history of lithium-ion battery development

The 2019 Nobel prize in Chemistry was awarded to John Goodenough, Stanley Whittingham, and Akira Yoshino for their contributions to the development of the LIB.[28–33] In the 1970s, Whittingham paved the foundations of the LIB by developing the first rechargeable lithium intercalation material, titanium disulphide, which he paired with a metallic Li negative electrode,[30] the reactivity of which deemed it too dangerous to enable commercial development.[34,35] In an attempt to increase the voltage of lithium intercalation chemistries, Goodenough used the understanding that the top of the S^{2-} 3p band lies at a higher energy than the top of the O^{2-} 2p band to design oxide-based lithium intercalation cathode chemistries (**Figure 1.3**).[36,37] In 1980, he demonstrated the lithium cobalt oxide (LCO) chemistry, which later gained widespread application in the consumer electronics market.[31] Furthermore, Goodenough not only developed one cathode chemistry, but all three of the leading oxide-based cathode chemistries (layered,[31] spinel,[29,32] and polyanion)[28,33] that are currently in commercial use originated from his research groups at the University of Oxford and the University of Texas at Austin. Akira Yoshino was the first to demonstrate a commercially viable LIB, pairing a LCO positive electrode with a petroleum coke carbonaceous negative electrode, resulting in a lightweight, durable battery that could be reversibly charged hundreds of times.[38] The first commercial rechargeable LIB was

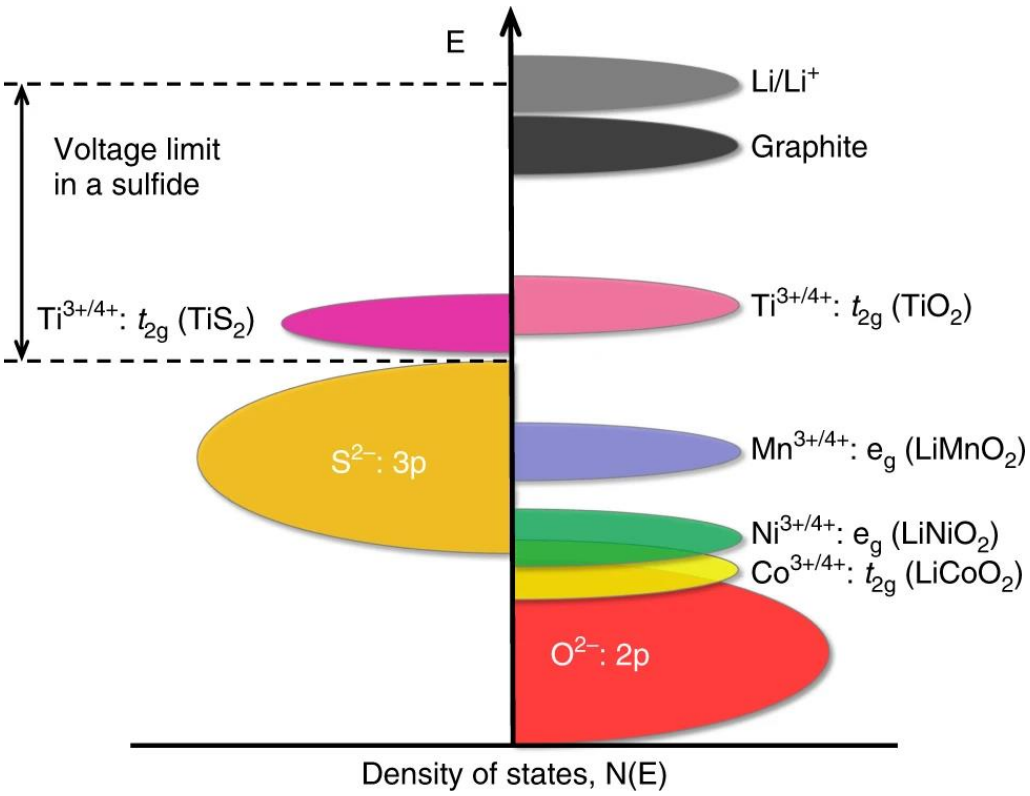


Figure 1.3. *Illustration showing that the top of the S^{2-} 3p band lies at a higher energy than the top of the O^{2-} 2p band which limits the cell voltage of sulfur-based intercalation chemistries compared to oxide-based. Reproduced from Manthiram.*[36]

popularised by Sony and Asahi Kasei in 1991 when they developed mobile phones, kickstarting a global battery revolution.

1.4 The lithium-ion battery

Figure 1.4 shows a schematic illustration of the operation of a traditional LIB. The first charge occurs through the deintercalation of Li^+ from within the layers of a metal oxide positive electrode and the simultaneous intercalation of Li^+ into the layers of a graphitic negative electrode.[39] On discharge the opposite processes occur, deeming the intercalation reversible. The electrode materials are electrically insulated from each other by an ion permeable membrane (i.e. separator) soaked in a non-aqueous electrolyte, which facilitates the transport of Li^+ between the electrodes.[39] Although the substitution of petroleum coke for graphite (Gr) by Yazami and Touzain marked a critical step-increase in the performance of LIBs,[40] the majority of performance enhancements of LIBs since this point have come in the form the development of novel cathode

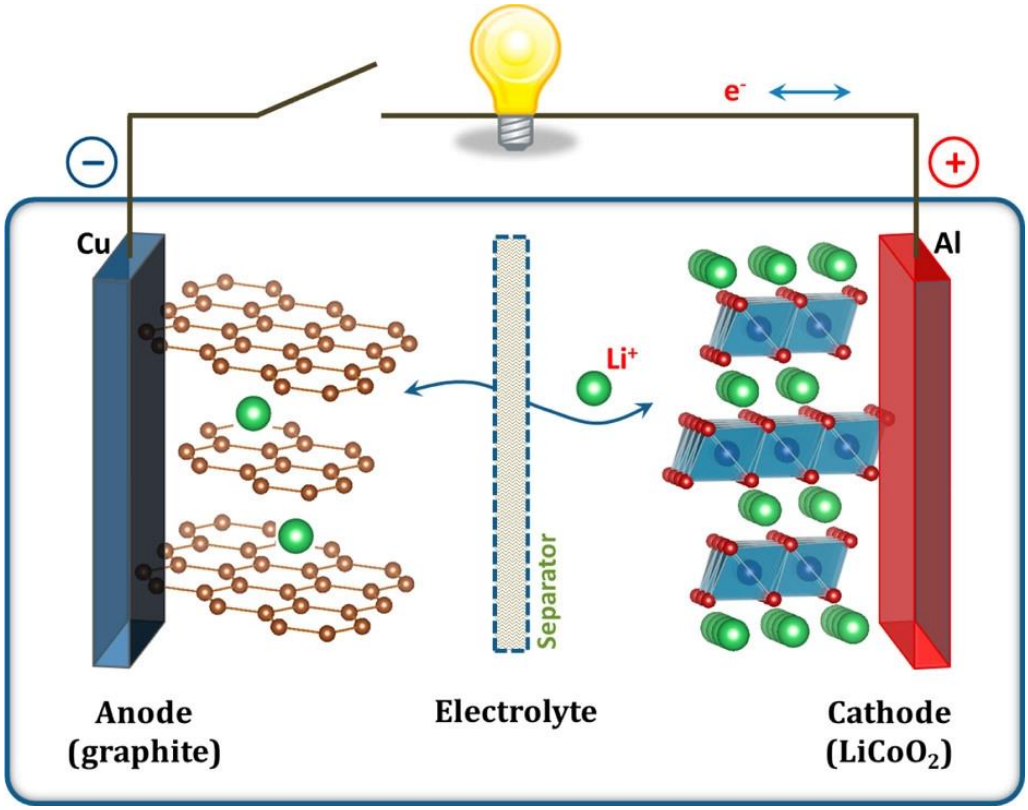


Figure 1.4. *Illustration of an Gr-LCO battery, showing the reversible movement of Li^+ from between the layered positive and negative electrode structures. Reproduced from Goodenough and Kyu-Sung Park.*[39]

chemistries, and the understanding of degradation mechanisms and mitigation strategies brought about by global research efforts.[36,41,42]

1.5 Single transition metal oxide positive electrodes

The cobalt-based LCO was the positive electrode that was used in the first commercial LIB and is still the dominant technology in the consumer electronics market. Monovalent Li^+ and trivalent Co^{3+} ions are ordered on alternate (111) planes of the rock salt structure, with a cubic close-packed array of oxide ions (**Figure 1.5**).[36,43] The large difference in size between Li^+ and Co^{3+} ions results in good cation ordering, supporting fast two-dimensional Li^+ diffusion and conductivity in the lithium plane. Li^+ conduction occurs from one octahedral site to another via neighbouring tetrahedral voids that share faces with three octahedra within the lithium layer. In the fully lithiated state, edge sharing CoO_6 octahedra are linked to form $[CoO_2]^-$ sheets, separated by octahedrally co-ordinated Li^+ in a cubic close-packed O_2^- lattice, resulting in a rhombohedral

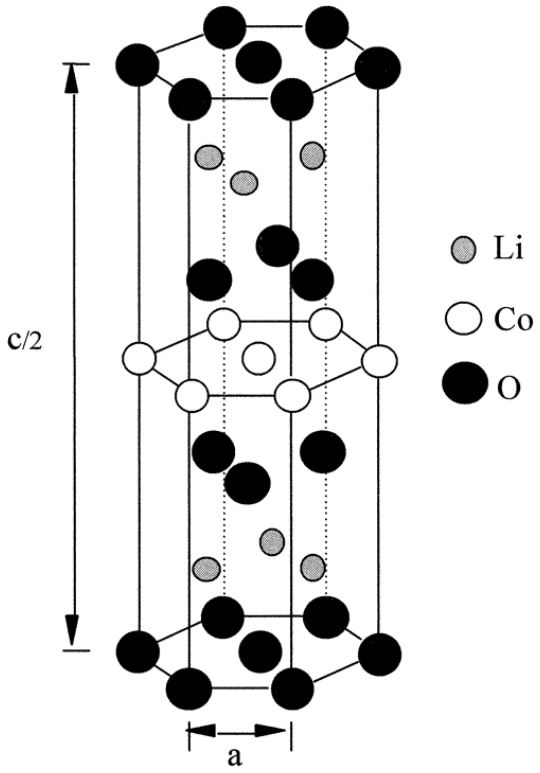


Figure 1.5. *Schematic illustration of the crystal structure of $LiCoO_2$. Reproduced from Chebiam et al.*[43]

structure.[44] On charging, the removal of Li^+ causes in an increase in electrostatic repulsion of the negatively charged CoO_2 sheets, consequently resulting in an expansion of the hexagonal lattice in the *c*-direction. The resultant $Li_{1-x}CoO_2$ ($x \leq 1$) exhibits metallic properties (i.e. high electrical conductivity) due to the introduction of holes into the low-spin $Co^{3+/4+}$ band.[45] These properties result in the chemistry exhibiting high structural stability paired with good ionic and electronic conductivity, marking this chemistry as one of the best positive electrode materials more than 30 years after its initial discovery.[31]

However, of the theoretical specific capacity of 273 mAh g^{-1}, 165 mAh g^{-1} is practically accessible, where delithiation beyond this point results in structural instability that limits long-term cycling performance.[20,46,47] Furthermore, major environmental, social and governance concerns have been raised surrounding the Co supply chain.[48,49] Approximately two thirds of Co is geographically constrained to the Democratic Republic of Congo where historic concerns are still echoed about the immorality of its mining, where in some cases extraction has been performed by children.[48,49] Consequently, exploration of cathode

materials that are able to provide improved capacity performance, while alleviating these supply chain concerns with abundant and sustainably sourced raw materials, were explored.

Various single metal oxide cathode chemistries that are synthesised from abundant precursor minerals including lithium iron phosphate ($LiFePO_4$, LFP), lithium nickel oxide ($LiNiO_2$, LNO) and lithium manganese oxide ($LiMn_2O_4$, LMO), have been developed.[32,50–52] Each of these chemistries has its own benefits and challenges compared to LCO, where high capacity is often achieved at the sacrifice of long-term cycling stability and vice-versa.

LFP was first proposed by John Goodenough in 1996 and has since gained great momentum in the battery market, being one of the leading cathode chemistries for use in stationary energy storage systems and has experienced a recent resurgence in popularity in the EV market.[50,53,54] LFP has an orthorhombic olivine structure consisting of a distorted hexagonal close-packed framework in which Li^+ and $Fe^{2+/3+}$ occupy octahedral sites and P^{5+} occupy one-eighth of the tetrahedral sites (**Figure 1.6**).[55–57] Layers of distorted FeO_6 octahedra are corner shared in the *bc*-plane and linear LiO_6 octahedral chains are edge shared parallel to the *b*-axis.[55,56] These chains are bridged by edge and corner shared phosphate tetrahedra resulting in a stable structure. The distorted FeO_6

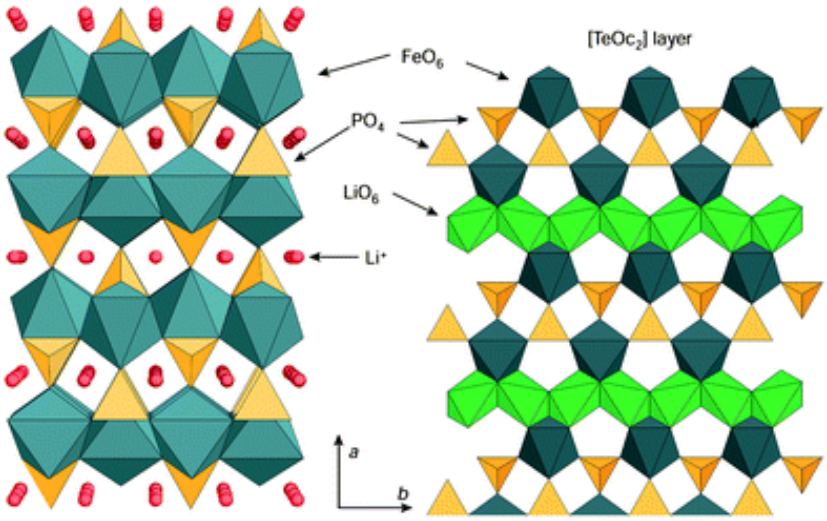


Figure 1.6. *Schematic illustration of the crystal structure of olivine $LiFePO_4$ in projection along [001]. Reproduced from Yuan et al.*[57]

octahedra create channels in which Li^+ can be reversibly intercalated without significant changes the olivine framework.[55,56]

The low-cost, non-toxic nature, and good thermal stability of LFP alleviate many of the concerns associated with LCO, with a comparable practical specific capacity of ca. 160 mAh g^{-1}.[58] However, LFP exhibits poor electric conductivity at all states of lithiation, which prevented the use of large LFP particles, and has a low stable voltage plateau at 3.45 V vs Li^+/Li, which limits the practical energy density and hindered initial commercialisation.[20,48] Conductive carbon additives have since been able to improve the electric conductivity of LFP cathode chemistries and favourable cell to pack energy density retention, enabled by reduced pack safety infrastructure, have led the resurgence in LFP demand in the low-cost EV market.[48]

The high natural abundance of manganese and its well-establish supply chain, as a result of its use in the steel industry, make it an ideal candidate for use as a LIB positive electrode material. LMO was first considered in 1983, where its spinel-type structure results in good structural stability and provides a three-dimensional diffusion pathway for Li^+.[32,52,56,59,60] The cubic spinel structure (SP-LMO) is described with the $Mn^{3+/4+}$ and Li^+ on the 16d and 8a sites, respectively, and the O^{2-} located on the 32e sites, forming a nearly ideal cubic close-packed sublattice (**Figure 1.7**a).[56] The SP-LMO structure is known to undergo transformation into a $CeFe_2O_4$-type $LiMn_2O_4$ (CF-LMO) structure at high pressure, which is referred to as a post-spinel structure (**Figure 1.7**b).[59] CF-LMO possesses distorted edge- or corner-sharing MnO_6 octahedra where the Li^+ ions are co-ordinated by eight O^{2-} ions. This structure modifies the Li^+ migration pathways from three-dimensional in SP-LMO to one-dimension in CF-LMO, improving Li^+ mobility and insertion kinetics.[59]

However, the low theoretical specific capacity of LMO (148 mAh g^{-1}) and even lower practical specific capacity (ca. 100 mAh g^{-1}) make this cathode material largely unsuitable for high-capacity applications, such as EVs. However, the high stability, structural robustness and combination of fast ion insertion kinetics

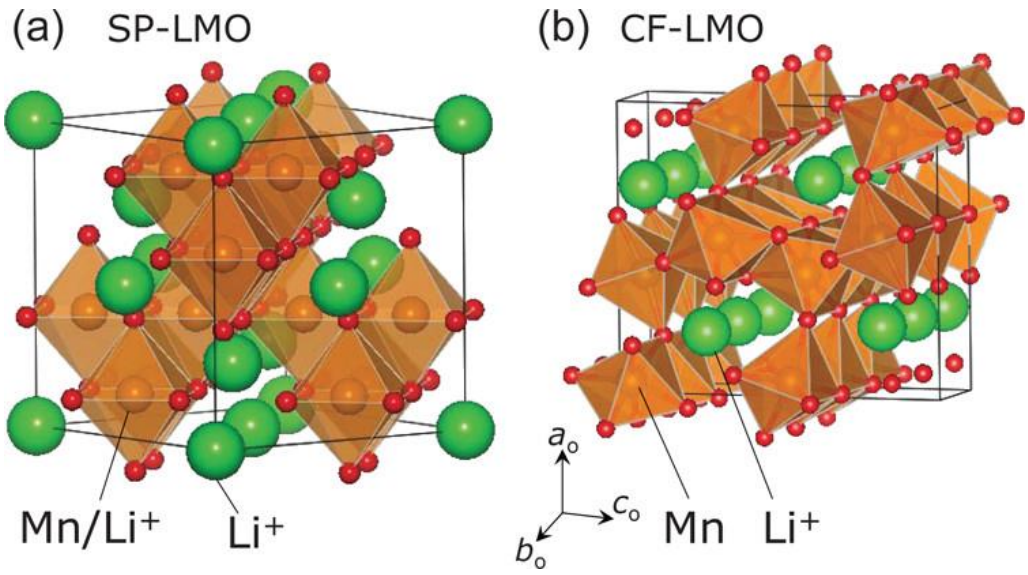


Figure 1.7. *Crystal structures of $Li_{1-x}Mn_2O_4$. a) $0 \leq x \leq 0.33$ (i.e. SP-LMO) and b) $x > 0.33$ (i.e. CF-LMO). Reproduced from Mukai et al.*[59]

and high nominal cell voltage make this material ideal for high power or long-life grid storage applications.[59–62]

The development of the LNO cathode chemistry marked a significant improvement in the capacity performance and cell nominal voltage compared to previous chemistries, while using cheap and abundant raw material inputs.[51] A practical specific capacity of ca. 220 mAh g^{-1} can be reversibly extracted at a nominal cell voltage of ca. 3.8 V vs Li^+/Li, demonstrating opportunity for considerable improvements in gravimetric and volumetric energy density over other single transition metal (TM) oxide cathode chemistries.[63–66] However, increased (electro)chemical reactivity results in interfacial instability and exothermic degradation of electrolyte components which limits long-term cycle life. The collapse of the Li_xNiO_2 ($x \leq 1$) structure during charge results in the oxidation of Ni^{2+} to Ni^{3+} and is accompanied by the irreversible migration of Ni^{3+} to lithium sites, blocking Li^+ insertion and resulting in irreversible capacity loss.[66–68] Moreover, the thermal instability exhibited by this material poses serious safety concerns of use in mass market consumer applications.[65,67] Structural doping,[69] coating/surface modification,[70] core-shell,[71,72] and gradient structures (**Figure 1.8**),[73,74] amongst other methods have been explored

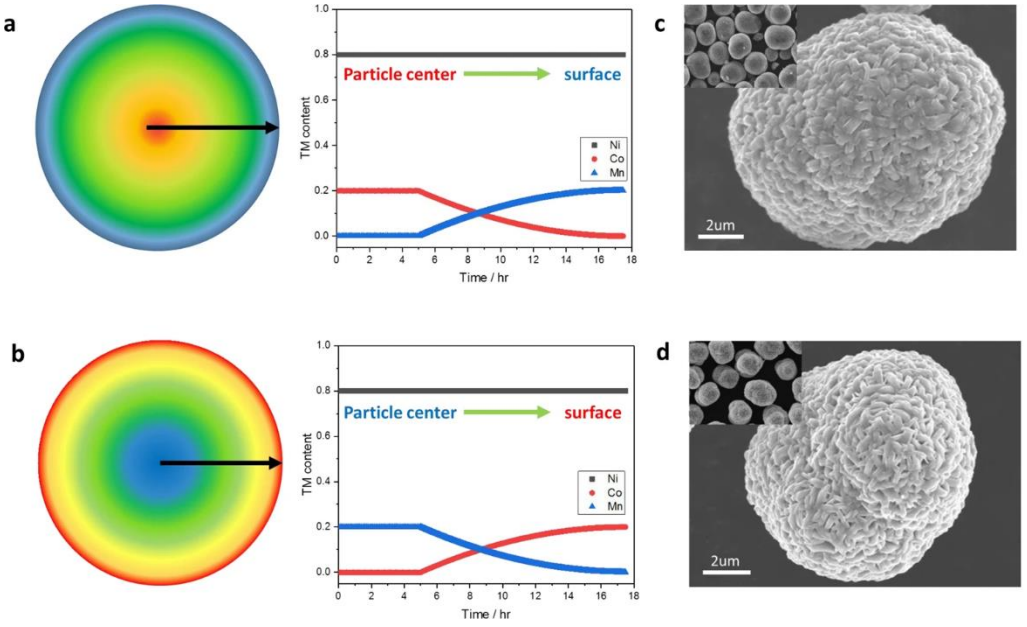


Figure 1.8. *a, b) Schematic illustration and corresponding compositional variation and c,d) SEM images of gradient cathode structures with a high a, c) Co or b, d) Mn outer layer. Reproduced from Liu et al.*[74]

to address these challenges, however, there are still significant barriers that must be overcome today, and formulations of LNO are largely regarded as next-generation cathode materials.

Each of the single TM oxide cathode chemistries possesses bespoke benefits and challenges that limit their application in mass market high-performance industries, such as EVs. In the pursuit of global electrification, higher energy density cathode chemistries with high stability and low raw material costs were required to incentivise the transition.[75–79]

1.6 Mixed transition metal oxide positive electrodes

To this aim, mixed metal oxide cathode chemistries have been developed that combine TM oxide precursors with the aim of identifying optimum molar combinations that improve performance across the board. Of these, nickel-rich positive electrode chemistries have gained commercial application as the dominant materials for the EV market, borne from the high theoretical capacity of LNO (275 mAh g^{-1}) paired with the relatively cheap raw material costs of nickel precursor chemicals.[77,78,80,81] The first automotive cell chemistries

combined Ni, Mn and Co in equimolar proportions, forming the $LiNi_{0.33}Mn_{0.33}Co_{0.33}O_2$ chemistry.[79] These 'NMC' chemistries are named based on the relative molar ratio of the TM components, with this equimolar derivative being commercially termed NMC111 (i.e. Ni:Mn:Co = N:M:C = 1:1:1 molar ratio). This positive electrode chemistry provided a capacity performance comparable to that of the ubiquitous LCO, with improved safety and a significant reduction in raw materials cost.[77,78,80] The current state-of-the-art material classes of nickel-rich positive electrodes typically accommodate a nickel-content of 60 mol% or higher in modern EVs.[79,82,83] The push to high nickel-content was driven by the desire to further increase energy density, while simultaneously limiting raw material cost and reducing cobalt content.[84,85] The high gravimetric and volumetric energy density of subsequent NMC materials, (i.e. NMC622 and NMC811, **Figure 1.9**), have made them the standards for current and future automotive applications, with EV cell manufacturers beginning to implement NMC811+ chemistries in their most recent battery packs.[86–88]

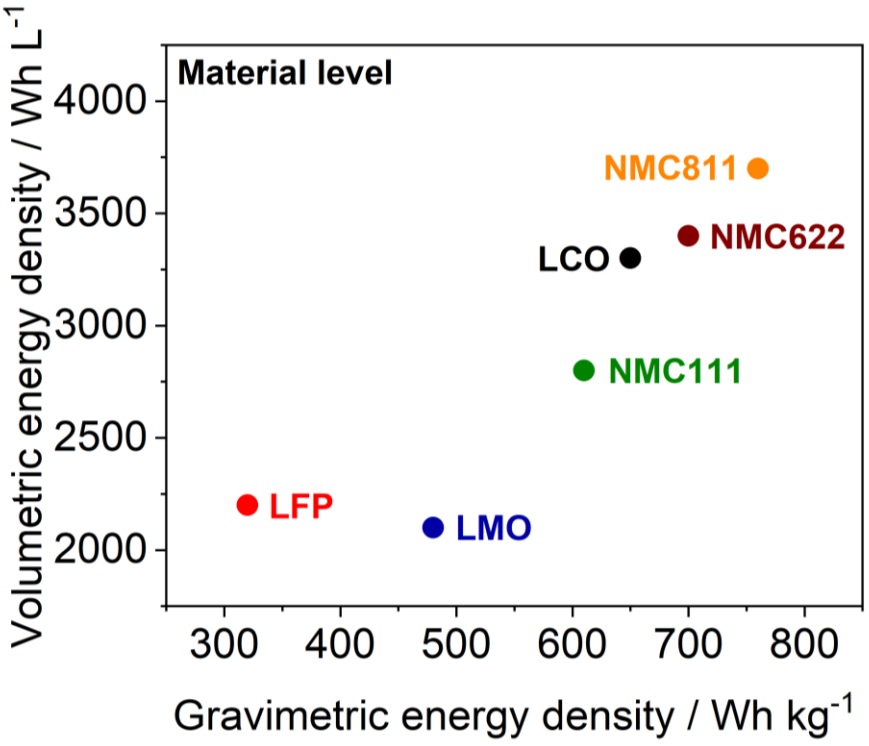


Figure 1.9. *Plot of gravimetric vs volumetric energy density, at the material level, of several cathode chemistries. Reproduced from Dühnen et al.*[89]

NMC811 adopts a layered structure analogous to that of LCO and LNO discussed previously, which is characterised by a close-packed oxygen lattice and alternating layers of lithium and TM ions in octahedral environments.[90,91] A practical specific capacity of ca. 200 mAh g^{-1} can be achieved with NMC811 cathode chemistries paired against a Gr negative electrode which results in an ca. 25% increase over LCO. However, as is the case with LNO, this marked increase in specific capacity comes at the cost of increasing reactivity of the electrode surface. Severe challenges are presented by this interfacial reactivity, which results in premature voltage and capacity fade compared to NMC chemistries with lower Ni-content.[91–93] Li-NMC811 half-cells are commonly cycled between voltage limits of 3.0 – 4.2 V,[87,92,94] with an upper-cut off voltage (UCVs) above 4.2 V being known to push the NMC811 electrode into a region of oxidative stress.[95–97] **Figure 1.10** shows the first cycle of a Li-NMC811 cell where an UCV voltage of 4.4 V is applied, ca. 0.2 V above the standard 4.2 V UCV.[90] A high full-charge capacity of 240 mAh g^{-1} and a reversible capacity of 200 mAh g^{-1} was achieved on discharge, a performance consistent with the state-of-the-art at the time of writing.[90] The voltage profile is relatively featureless, however, differential capacity (d*Q*/d*V*) analysis reveals three major regions that contribute to the extracted capacity below the standard UCV of 4.2 V (**Figure 1.10**b). The maxima of these regions, labelled I, II and III, are found at ca. 3.68, 4.00, and 4.21 V vs Li^+/Li, respectively.[90,91,98,99] Märker *et al.* performed neutron diffraction and synchrotron X-ray diffraction (XRD) studies during these first charge and discharge processes to reveal structural changes within the NMC811 material.[90] These data revealed that, at the start of charge, a two-phase coexistence is observed between the pristine material and a partially delithiated phase, the latter continuing to lose more lithium as the concentration of the pristine phase decreases.[90] Beyond this initial two-phase behaviour, NMC811 undergoes a solid-solution mechanism during charge and discharge, never returning to the two-phase system, demonstrating that this early stage behaviour is irreversible.[90] In region III, a strong decrease in the *c* lattice parameter is observed, resulting in a collapse of the interlayer spacing and reducing the Li^+ mobility.[90,100] As region IV is entered, where ca. 20 mAh g^{-1}

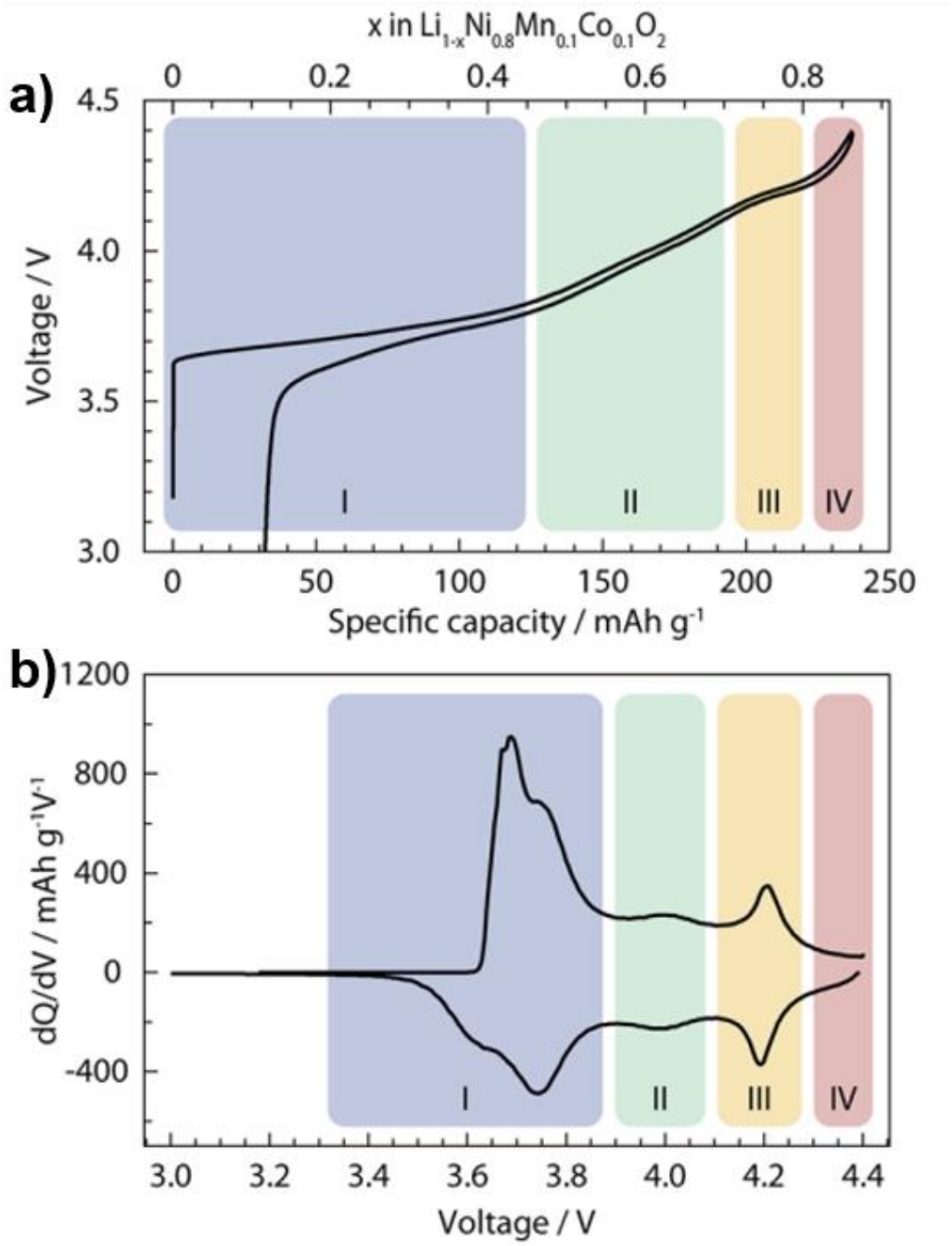


Figure 1.10. *a) First charge and discharge voltage curves of a Li-NMC811 half-cell and b) the corresponding differential capacity (dQ/dV) plot. Reproduced from Märker et al.*[90]

of additional capacity is accessed, approximately 80% of the Li^+ has been deintercalated from the NMC811 electrode and the collapse of the *c* lattice parameter accelerates, dropping below the value when pristine.[90,100] The Ni^{4+} ions that are formed in this region (i.e. upon high delithiation) react aggressively with the electrolyte components, resulting in the release of lattice

oxygen and leaching of TM ions.[101–107] These processes change the surface structure of the NMC811 particles, resulting in a highly resistive cathode electrolyte interphase (CEI).[92,108,109] Furthermore, this electrode-electrolyte interfacial instability results in crosstalk between the positive and negative electrode, where the formation of reactive soluble species, or the products that they form through reaction, can crossover through the cell and catalyse further interphase and electrolyte degradation at the negative electrode that limit the capacity of the cell.[101–107]

Several next-generation classes of cathode materials are being developed that could compete with or exceed the performance of NMC811 (i.e. including nickel aluminium oxides (NCAs),[79,110,111] lithium-rich cathodes,[112–117] O_2-redox cathodes,[118–121] cobalt-free chemistries),[48,122,123] and many more are being developed that, although not competitive with respect to capacity performance, could offer improved cycling stability with lower raw material cost (i.e. manganese-rich chemistries). It is important to note that the development of each these material chemistries is critical to support the global energy transition, where no one chemistry will dominate markets and every successful material chemistry will find an application. However, in line with the aims and objective of the UK Faraday Institution's Degradation Project,[124] under which this thesis was funded, Chapters 3 and 4 assess electrolyte degradation processes in cells containing an NMC811 cathode chemistry. Therefore, noting that several next-generation cathode chemistries exist, and that their development is of critical importance, the remainder of this chapter will focus on defining the current state-of-the-art anode chemistries, electrolyte composition, and degradation processes associated with NMC811 cell chemistries.

1.7 Negative electrodes

Lithium-ion full-cells typically pair a Gr negative electrode with the lithiated TM oxide positive electrode.[36,125,126] **Figure 1.11** shows the voltage profiles of Li-NMC811 and Li-Gr half-cells as a function of the extent of Gr lithiation, where it is assumed that the electrodes are perfectly balanced so that delithiation of

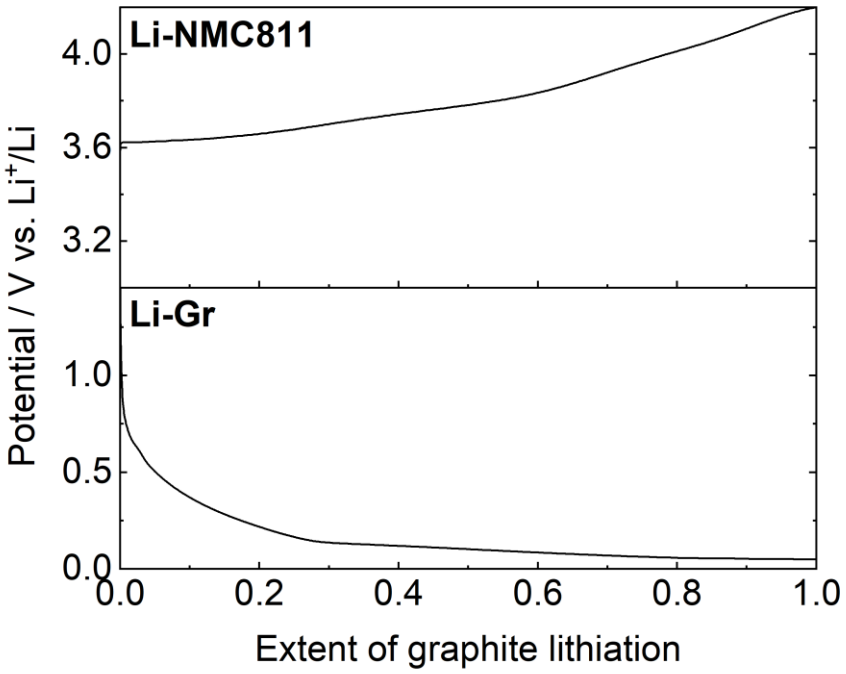


Figure 1.11. *Half-cell study showing the potential window of operation and voltage profiles of NMC811 and Gr electrodes during the first delithiation and lithiation, respectively.*

the NMC811 electrode to 4.2 V is equivalent to full lithiation of the Gr electrode. When fully delithiated, a Gr electrode sits at an open circuit voltage (OCV) of ca. 1.5 V vs Li^+/Li and upon lithiation this potential decreases rapidly, with the majority of Li^+ intercalation occurring between 0.2 – 0.0 V vs Li^+/Li. Gr is considered fully lithiated when the interlayer space is filled with Li^+ to a general formula of LiC_6.[127,128] The intercalation of Li^+ into the layered graphite structure results in an entropic increase, which is managed by a staged intercalation mechanism through a fractional increase in the lithium content, relative to the number of graphite layers between each section being filled with lithium. **Figure 1.12** shows a schematic illustration of the current understanding of the stages of Li^+ intercalation. **Figure 1.12**a shows the mechanism based upon the Daumas-Hérold model,[129] where alternating graphene interlayer spaces are filled sequentially until the structure is filled.[130] However, this simple model of uniform Li^+ intercalation does not depict the intricacies of these processes. In 2018, Lopez *et al.* used *operando* nuclear magnetic resonance (NMR)

spectroscopy to detect phase changes of the Li-Gr intercalation compounds, wherein signatures of stage-VIII LiC_{72} were detected for the first time.[131] Drüe *et al.* built upon this understanding, applying a combination of XRD and metallographic analysis to observe the formation of a series of Li-Gr intercalation compound microstructures which demonstrated that the phase formation and transformation are complex and include superdense, dilute or pseudo-phase structures, where Li^+ uptake and release occur via different mechanisms (**Figure 1.12**b).[130,132]

Although the reversibility of these intercalation processes are the cornerstone of the operation of LIBs, the solid electrolyte interphase (SEI) that is formed on the surface of the graphite electrode upon first lithiation is the critical determining factor of long-term cycling performance.[133,134] To ensure the formation of an optimal SEI, low current densities (ca. C/20 or less i.e. 20 hour (dis)charge) are applied in formation cycles, where electrolyte components are reduced at the surface of the Gr electrode to form a complex interphase between the electrode surface and the electrolyte.[133,135,136] To be effective, this SEI must allow Li^+ transport through its structure into and out of the Gr layers, while simultaneously acting as an electrically insulating and chemically resistant

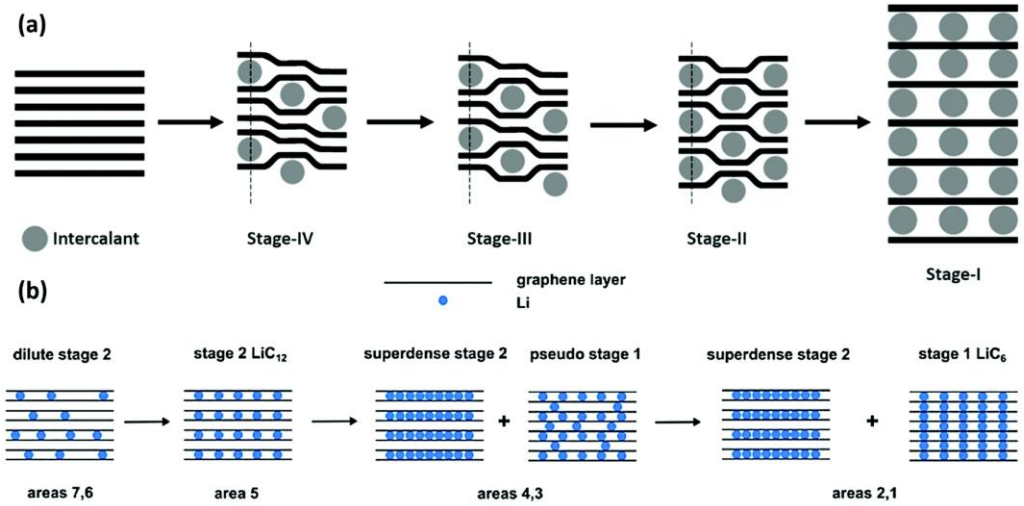


Figure 1.12. *Schematic illustration of the a) Daumas-Hérold model of ion intercalation into graphite and b) microstructures of Li-Gr intercalation compounds observed through a combination of XRD and metallographic analysis. Reproduced from a) Sole et al.[137] and b) Drüe et al.[132]*

interface between the Gr surface and the electrolyte, preventing continuous parasitic degradation. These degradation processes will be discussed further in section 1.8.

Several other anode chemistries have been explored to enhance the performance of LIBs for specific applications. Of these, silicon (Si) and metallic Li are the frontrunners for next-generation high-capacity performance materials, and lithium titanate ($Li_4Ti_5O_{12}$, LTO) possesses outstanding fast-charging and safety characteristics.[138–145] Si is an alloy anode which has gained significant academic and industry attention due to its high theoretical capacity (3572 mAh g^{-1}), almost ten times greater than Gr, borne from each silicon atom being able to bind up to 3.75 lithium atoms in the fully lithiated state ($Li_{15}Si_4$).[143] However, detrimental particle expansion and contraction processes are experienced during the lithium alloying processes, wherein an approximate volumetric expansion of 300% is observed that results in particle cracking and active material isolation through delamination, consequently causing rapid capacity fade.[143,146,147] To combat this instability, Si-Gr composite anodes have been developed that balance capacity improvement relative to pristine Gr with a reduction in the overall volumetric anode expansion, improving long-term cycling performance.[148–152] It has been reported that these Si-Gr composite anodes that use novel material strategies to limit the degradation caused by expansion can achieve capacity performance which far supersedes that of pure Gr anode materials. However, these materials are yet to be proven on mass market commercial scale, with current automotive LIBs containing between 2 – 7% Si as a premium priced range extender.[19,144]

Metallic Li was first used as a negative electrode chemistry when Whittingham and Goodenough developed the first intercalation chemistries. However, it was deemed too reactive with the electrolyte components, where broad degradation and the non-uniform plating and stripping of Li resulted in dendritic lithium growth and caused internal short-circuits, initiating thermal runaway (**Figure 1.13**).[34,35,153] More recent studies exploring the reactivity of metallic Li with the organic carbonates that are used as electrolyte solvents

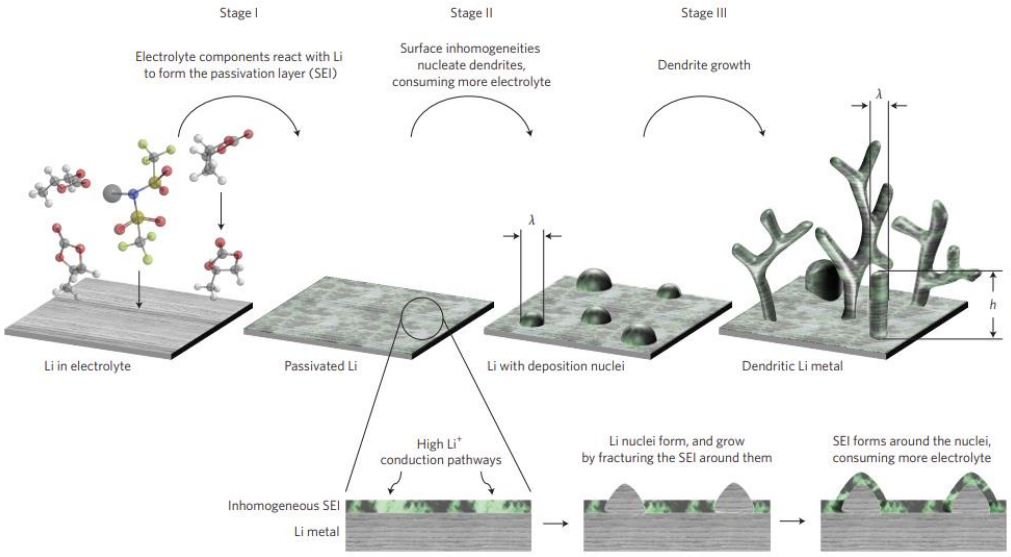


Figure 1.13. *Schematic illustration of the stages of dendrite growth on a planar metallic Li electrode. Reproduced from Tikekar et al.*[153]

today have found that it indiscriminately degrades the organic components that make up lean electrolyte compositions.[154–156] Nevertheless, metallic Li intrinsically possesses the highest possible theoretical capacity (3860 mAh g^{-1}) and the lowest electrochemical potential of any proposed negative electrode candidate for advanced lithium batteries, making it extremely desirable for next-generation applications.[153] Several recent reports have used high loadings of FEC to enable cycling of metallic Li cells, however, these conditions are not representative of normal operating conditions and represent a scenario wherein electrolyte cost would be a significant contributing factor to overall cell cost, deeming this method of protection unsuitable.[157–159] Despite these challenges, metallic Li is often used as a counter electrode to assess the performance of prospective cathode chemistries, where it provides an effectively infinite reservoir of Li^+ with minimal impact on the electrochemical response.[160–162] However, the degradation of electrolyte components brings into question the validity of this application, which is the focus of Chapter 3.

LTO has been proposed as a potential alternative to Gr as a LIB negative electrode material due to its outstanding rate performance and safety characteristics.[138–140] The spinel-type structure allows the reversible

intercalation of Li^+ into the unoccupied octahedral sites with 'zero-strain' on the overall lattice structure and minimal volumetric increase.[138–140] The electrochemical potential for lithium insertion into the LTO lattice lies at ca. 1.55 V vs Li/Li^+, making it benign to reduction of commonly used organic electrolytes. The relatively low practical capacity of 150 mAh g^{-1} limit applicability in high-capacity uses, however, this material has potential in high power applications.[139,140] Although previous reports have indicated that residual H_2O in the electrolyte can reduce on the surface of LTO electrodes, producing hydrogen gas and hydroxide ions that can facilitate gassing degradation reactions, adequate measures to limit H_2O intrusion during cell assembly and choice of appropriate cell format mitigate these effects.[163–165]

1.8 Electrolyte composition

Early studies explored several organic carbonate-based electrolyte solvents and lithium-based electrolytes salts before reaching the state-of-the-art electrolyte composition which is relatively consistent across academia and industry today. Current LIB electrolytes consist of a lithium hexafluorophosphate ($LiPF_6$) salt dissolved in a mixture of linear and cyclic alkyl carbonates. The alkyl carbonates were chosen due to their good electrochemical stability, high polarity (i.e. good conductivity of their solutions), broad temperature of high performance, and low relative toxicity.[166–169] Although several lithium salts were explored (i.e. $LiBF_4$, $LiClO_4$, $LiN(SO_2CF_3)_2$, $LiAsF_6$), these were proven to have too many disadvantages relative to $LiPF_6$, which has gained widespread commercial adoption across all LIB applications.[168–170] An ideal electrolyte salt must dissolve easily in carbonate solvents, have an anion that is relatively (electro)chemically stable, have good thermal stability and be unreactive with the interfacial layer on both electrodes.[133] Many of the prospective electrolyte salts were compatible to these criteria, however, $LiPF_6$ possesses the additional benefit that it protects the aluminium foil current collector from corrosion through the formation of HF which reacts to for an AlF_3 layer that passivates the aluminium in non-aqueous electrolytes.[171,172] The protection of the current collector is

crucial to the overall performance of the battery, resulting in $LiPF_6$ being adopted as the most common electrolyte salt.

The role of the electrolyte is to facilitate low resistance transport of Li^+ between the electrodes while reducing the contribution of degradation reactions to the charge passed.[166–169] Due to the wide voltage range of operation of Gr-NMC811 full-cells (i.e. ca. 0 – 4.2 V vs Li^+/Li), finding electrolyte components that are completely benign under these conditions and possess favourable properties for battery performance is non-trivial. However, electrolyte degradation in the early stages of the first cycle is not necessarily detrimental to the long-term performance of a battery chemistry, as long as the capacity loss is small and the resultant SEI that is formed is highly stable throughout the remainder, or a long-duration, of calendar life.[135,173–175] With this in mind, electrolyte components are design to be largely stable to oxidation at the NMC811 electrode, although not completely benign, and are degraded during formation cycle on the surface of the Gr electrode to form a stable SEI, the characteristic of which ultimately determine cell performance.[95,176]

Where no electrolyte additives are present, each of the common electrolyte solvent components, ethylene carbonate (EC), diethyl carbonate (DEC), dimethyl carbonate (DMC), and ethyl methyl carbonate (EMC), shown in **Figure 1.14**a, all undergo reduction at potentials <1 V vs Li^+/Li.[177–179] Similarly, the $LiPF_6$ electrolyte salt undergoes reduction to form LiF, Li_xPF_y, and $Li_xPO_yF_z$ species at potentials >1 V vs Li^+/Li, providing a pathway for the formation of inorganic SEI components (**Figure 1.14**b).[180,181] The complex combination of electrochemical degradation reactions results in the formation of an intricate SEI made up of a mixture of organic products, including lithium ethylene decarbonate (LEDC), lithium ethyl carbonate, lithium methyl carbonate, lithium methoxide and lithium ethoxide, and inorganic degradation products such as $Li_xPO_yF_z$ species and LiF (**Figure 1.15**).[133,136,178] In most commercial LIB electrolytes, the initial solvent reduction reactions are dominated by the reduction of EC, and therefore the contribution of dialkyl carbonates to the SEI composition is minimal, suggesting that the primary components of the

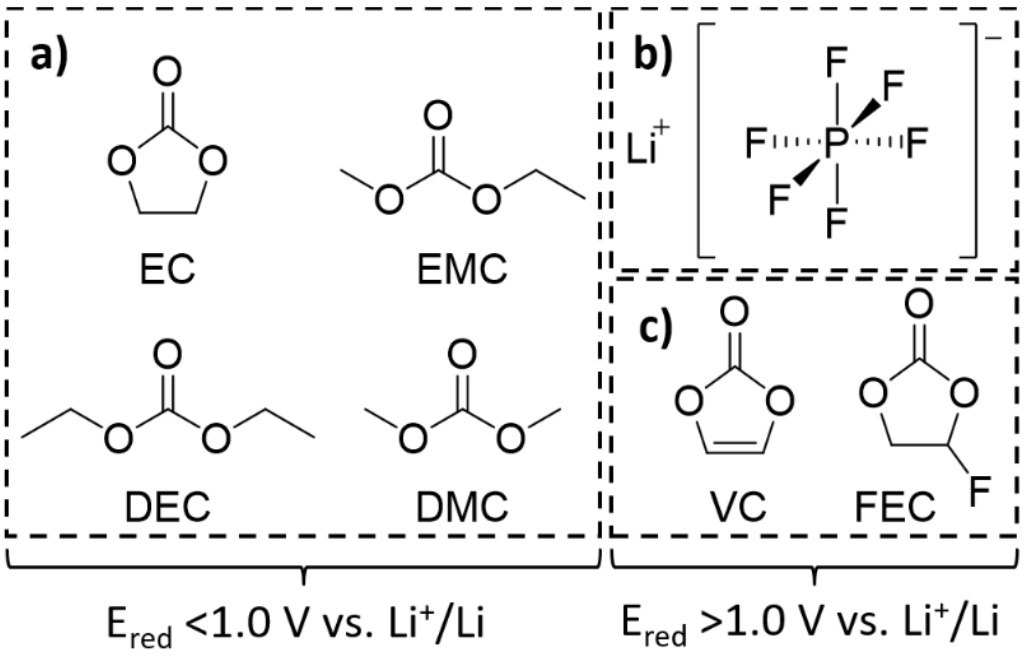


Figure 1.14. *Molecular structures of common electrolyte components categorised by reduction potential. a) bulk carbonate electrolyte solvents, b) $LiPF_6$ electrolyte salt, and c) VC and FEC, two of the most common electrolyte additives.*

Initial SEI in commercial LIBs are LEDC and LiF.[133,182,183] The resultant ca. 50 nm thick SEI is sub-optimal, due to the excessive consumption of Li^+ inventory, resulting in a high first cycle capacity loss and a thick and resistive SEI.[133]

To improve the properties of the SEI produced in formation cycling, electrolyte solvent additives such as vinylene carbonate (VC) and fluoroethylene carbonate (FEC), shown in **Figure 1.14**c, that are reduced at potentials >1 V vs Li^+/Li are doped into electrolyte compositions.[184,185] The thermodynamic driving force for the reduction of these additives results in their preferential degradation on the surface of Gr, optimising the properties of the resultant SEI and improving the long-term cycling performance of Gr-NMC811 full-cells (**Figure 1.16**a).[133] VC is the most commonly used electrolyte additive in commercial LIBs, where its preferential reduction on the surface of the Gr negative electrode initiates a radical polymerisation reaction to form PolyVC on the Gr surface, which improves the thermal and (electro)chemical properties of the resultant SEI compared to an electrolyte composition with no additive (**Figure 1.16**).[184,186–190] Although many decomposition pathways for FEC have

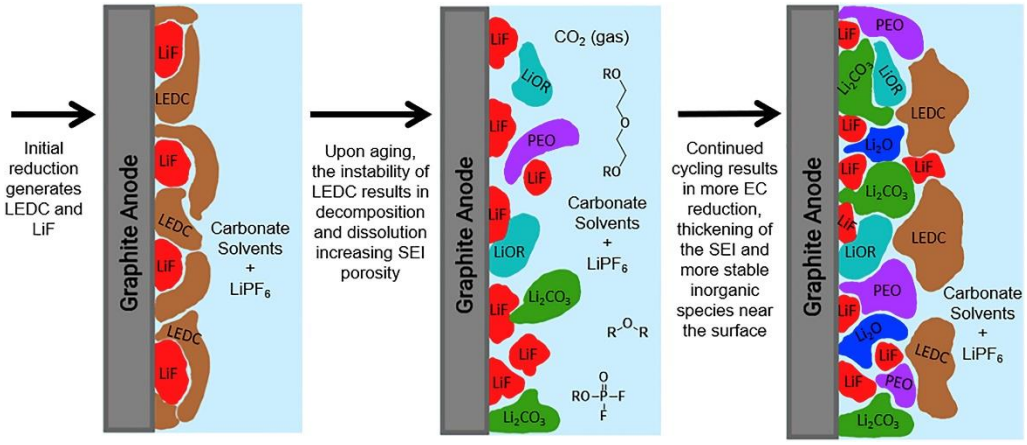


Figure 1.15. *Illustration of the initial SEI formed on a Gr negative electrode, where no additives are present, and the effect of continual electrolyte reduction resulting in a thick SEI. Reproduced from Heiskanen et al.*[133]

been proposed, its stabilising effect is broadly accepted across Gr, Si and metallic Li anode chemistries.[186,191–196] One of the most commonly reported routes of FEC reduction is through $1e^-$ reduction to form LiF and VC, then subsequent VC reduction to form PolyVC.[186,192,197,198] The proposed degradation products of VC and FEC degradation through reduction are shown in **Figure 1.16**b.

It is important to note that oxidation of the electrolyte will simultaneously occur at the surface of the NMC811 electrode, where an operational voltage

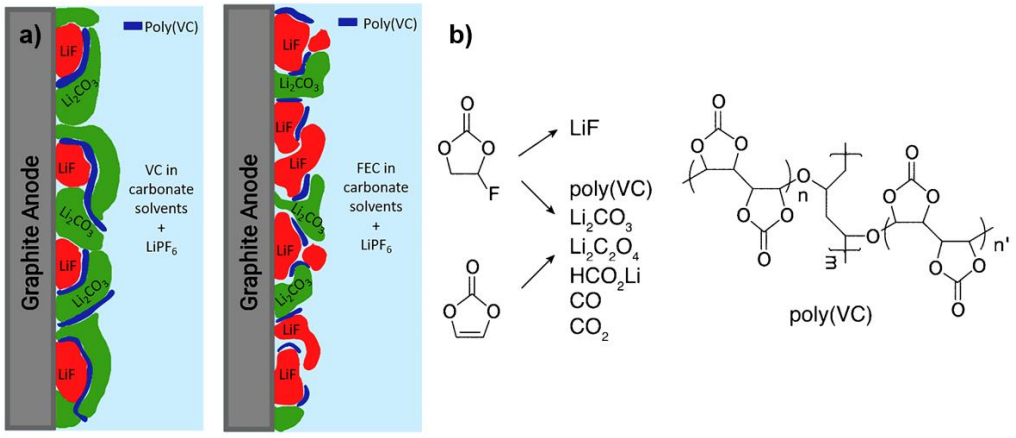


Figure 1.16. *a) Illustration of the thin and stable SEI formed on a Gr negative electrode in electrolytes containing VC (LHS) and FEC (RHS) and b) the proposed degradation products formed from reduction induced degradation mechanism of VC and FEC. Reproduced from a) Heiskanen et al.*[133] *and b) Michan et al.*[186]

range of 3.0 – 4.2 V vs Li^+/Li is accessed in standard operation.[90,126] Although surface confined products such as lithium nickel oxyfluorides, $PF_3=O$, and $Li_xPF_yO_z$ species have been identified through the application of *ex situ* spectroscopic techniques,[199–201] soluble reaction products are not adequately assessed by these techniques. However, these soluble species play a critical role in the long-term performance of lithium-ion full-cells, where they can migrate through the electrolyte and interact with the other electrode in a phenomenon called crosstalk.[202] Identifying the products that are formed, and assessing their impact on the process of SEI formation is both critical to improving the performance of state-of-the-art LIBs and to designing next-generation electrolyte compositions.

The oxidation of electrolyte components at the positive electrode becomes increasingly important as Ni-content increases, where the increased reactivity of the positive electrode surface results in the onset of electrolyte oxidation being pushed to lower voltages.[133,182,183,203–206] As early as 2016, Dahn and co-workers reported that considerable performance benefits can be achieved with lower-nickel oxides by simply removing the EC from the electrolyte mixture,[207–211] a finding which has since been proven effective with high-nickel chemistries.[204,205] Although the oxidation potential of EC is relatively high, it was found that EC molecules dehydrogenate on the surface of layered oxide cathodes due to the catalytic effect of highly oxidised TMs, particularly Ni (**Figure 1.17**).[204,212,213] This process results in both the formation of acidic species, which can further react with $LiPF_6$ to form HF, and changes the surface chemistry of the positive electrode, wherein spinel-like and rock-salt like phases form, establishing a resistive CEI and releasing TM ions into the electrolyte solution.[93,101,212,214–216] Although these processes have a detrimental effect on the performance of the positive electrode, the generated species can migrate through the electrolyte to the surface of the negative electrode where they can catalyse degradation of the Gr SEI, which has been identified as a primary contributor to poor cycle life.[95] It is this phenomenon of crosstalk between the electrodes, and the effect that it has on the interphases that form

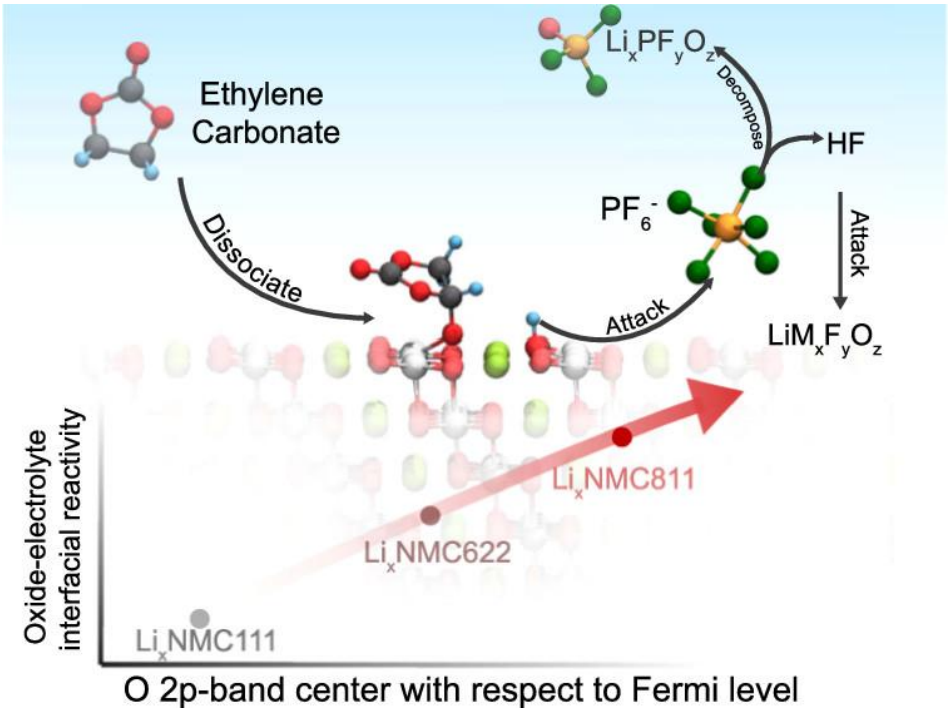


Figure 1.17. *Illustration showing the increasing interfacial reactivity of NMC positive electrode chemistries as Ni-content increases, with respect to the dehydrogenation of EC and subsequent degradation processes. Reproduced from Yu et al.*[201]

and the composition of the electrolyte, that are the focus of Chapters 3 and 4.

1.9 Degradation of Gr-NMC811 cells

Considerable efforts have been made to understand the stability of NMC materials, and the many degradation mechanisms that ultimately determine the performance of Gr-NMC811 cells.[92,93,95,104,217,218] **Figure 1.18** describes several of these processes and displays a number of the analytical techniques that can be used to probe and understand them.[124] As discussed previously, the formation of a stable SEI and CEI are critical to the long-term performance of Gr-NMC811 full-cells, where any decomposition of these interphases results in parasitic side reactions that degrade electrolyte, increase impedance and deplete the finite Li^+ inventory.[93,95,104,126] This section will begin by discussing degradation mechanisms at the surface of NMC811 electrodes, before discussing the phenomenon of crosstalk, wherein species formed at the surface of the NMC electrode pass through the electrolyte and catalyse SEI

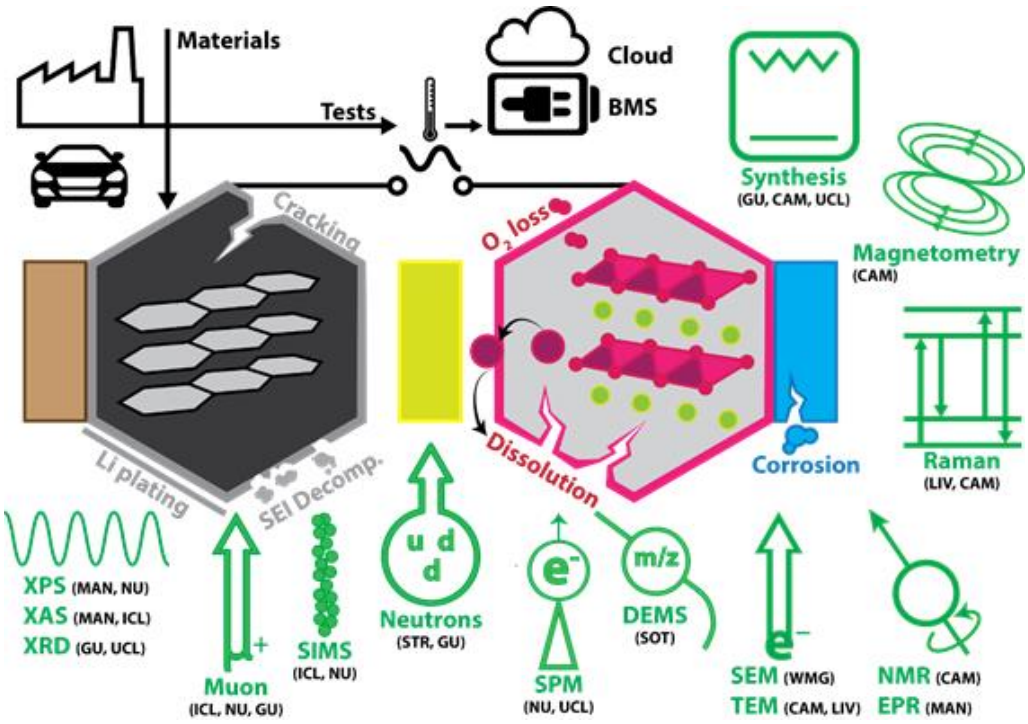


Figure 1.18. *Illustration of several degradation mechanisms in Gr-NMC811 full-cells and techniques that can be used to understand them. Reproduced from The Faraday Institution Degradation Project.*[219]

degradation at the negative electrode. These processes, which become increasingly dominant as Ni-content increases, are the critical determining factors of full-cell degradation and ultimately underpin the long-term cycle life of Gr-NMC chemistries.[93,95,104,126]

As discussed in section 1.6, upon high delithiation of NMC chemistries, parasitic oxidation of electrolyte components occurs in conjunction with loss of lattice oxygen, release of TM ions, and simultaneous surface restructuring.[93,101,212,214–216,220,221] This electrolyte oxidation results in the formation of gaseous species,[177,222–225] detectable by on-line electrochemical mass spectrometry (OEMS). Taken together, these degradation mechanisms generate antagonistic soluble species (i.e. H^+, TM ions, organic degradation products) which can go on to further degrade other components in the cell.[126]

In 2020, Rinkel *et al.* performed a study that identified several electrolyte oxidation pathways through the combination of *in situ* OEMS and post-cycling NMR analysis of electrolytes extracted from Gr-LCO and Gr-NMC811 cells, which identified several species that are formed through oxidation of

electrolyte at the positive electrode (**Figure 1.19**).[104] Although each of these proposed degradation pathways are detrimental to cell performance, as is any degradation process by nature, Freiberg *et al.* proposed the formation of VC, the most common electrolyte additive, as the result of reactive lattice oxygen release in the form of singlet oxygen ($^1O_2$).[225] These data demonstrated that $^1O_2$ is capable of reacting with EC molecules to form VC, generating H_2O_2 as a by-product (**Figure 1.20**).[225] Although no direct spectroscopic evidence for VC formation was presented, this claim was supported by computational calculations and the detection of H_2O_2 through a UV-Visible titration.[225] The detection of VC itself was deemed impractical as a result of its reactivity with both ground-state O_2 and $^1O_2$ that were present in the model system, posing an unfavourable environment for VC accumulation. In 2020, Zhang *et al.* proposed a second, surface confined, pathway for VC formation wherein EC is dehydrogenated through interaction with surface O_2 at the positive electrode and generates soluble VC, leaving protic species on the surface that can initiate further degradation of $LiPF_6$ to form HF (**Figure 1.21**).[199] In this study, VC was

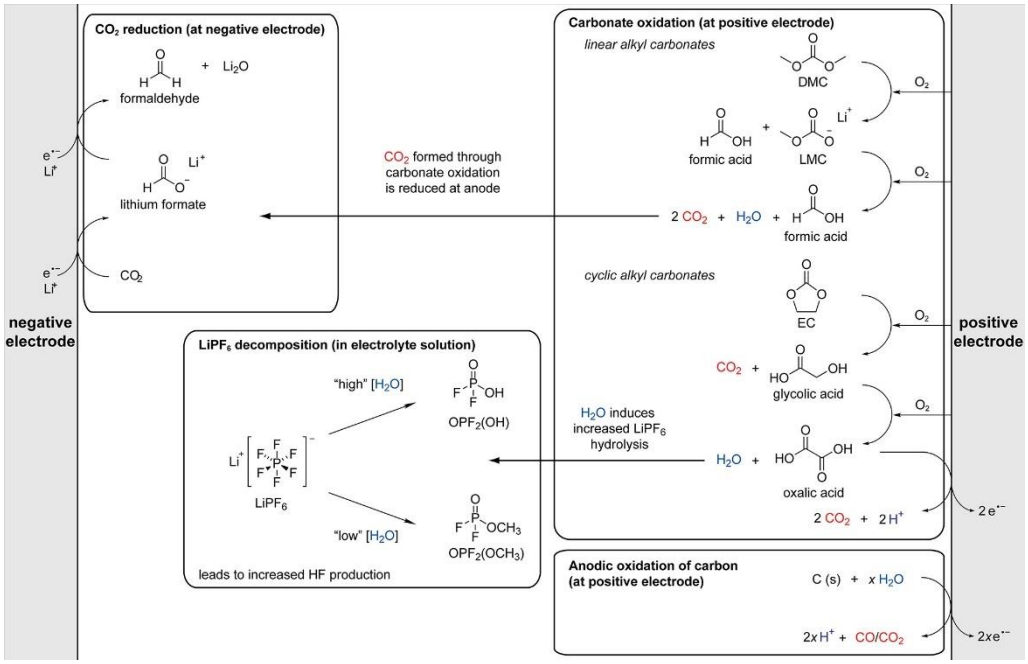


Figure 1.19. *Overview of electrolyte decomposition reactions that occur at high voltages (i.e. high state of charge) initiated at the positive electrode. Reproduced from Rinkel et al.*[226]

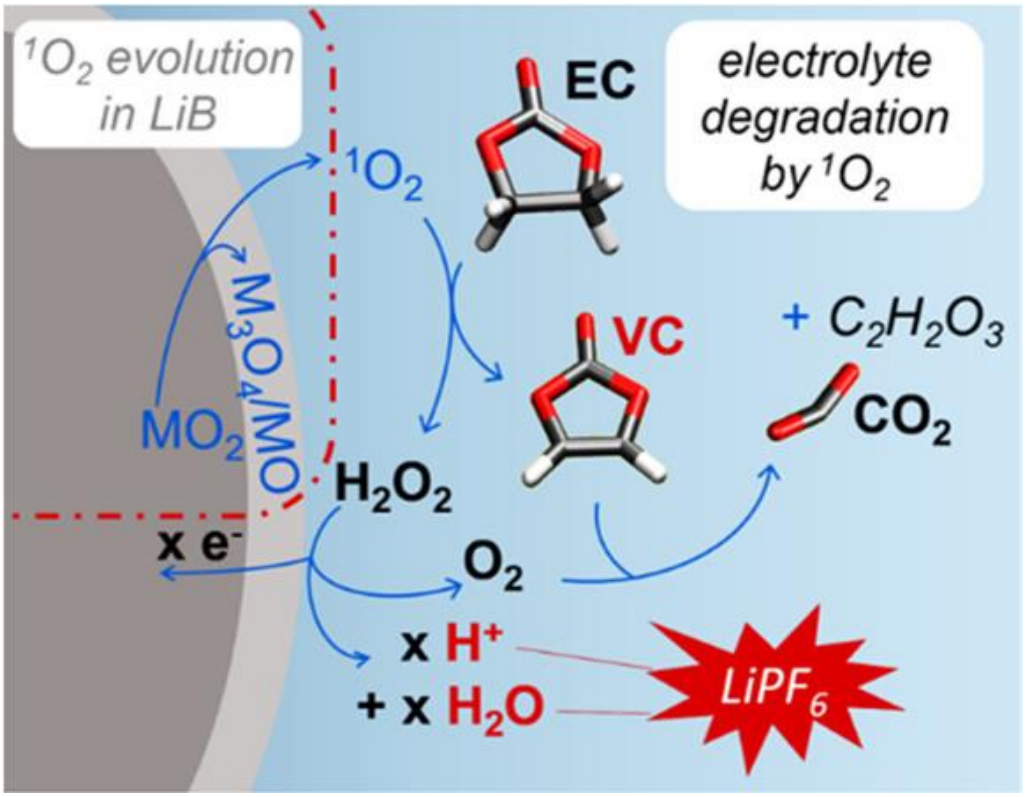


Figure 1.20. *Illustration of the proposed pathway of EC degradation induced by $^1O_2$, which results in the formation of VC and H_2O_2. Reproduced from Freiberg et al.*[225]

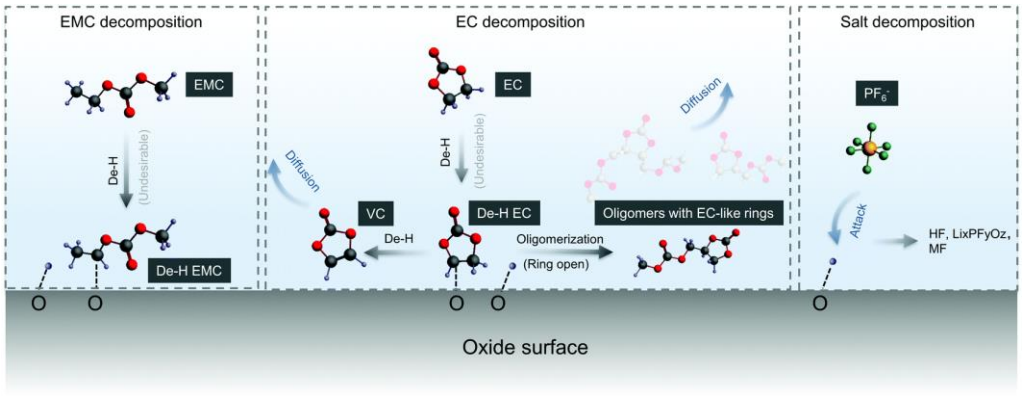


Figure 1.21. *Illustration showing the proposed surface confined degradation of electrolyte solvents through interaction with metal-oxide bonds at high states of charge. The dehydrogenation of EC was proposed to result in the formation of soluble VC species. Reproduced from Zhang et al.*[213]

detected through surface enhanced Fourier transform infra-red (FTIR) spectroscopic measurements, performed in a bespoke spectro-electrochemical cell. Although these studies propose different pathways for VC formation, they draw a common conclusion that the increasing oxidative reactivity of NMC positive electrode materials with increasing Ni-content can provide a pathway for *in situ* VC formation. A recent study by Rinkel *et al.*,[227] published in July 2022, examined this work in detail, applying the same Rose Bengal (RB) photosensitizer used by Freiberg *et al.* with $^{17}O_2$-enriched O_2 and EC to probe the reaction of $^1O_2$ with EC and DMC.[225,227] Surprisingly, this study found that no H_2O_2 was accumulated through the reaction of $^1O_2$ with EC, but instead suggested that EC would be oxidised to form H_2O as its only soluble product, with CO_2 and CO being released as additional gaseous products, bringing into question the validity of the study performed by Freiberg *et al.*[225] Understanding these systems and the feasibility of $^1O_2$ driven VC formation will be explored in detail in Chapter 4.

Concurrent with these electrolyte oxidation processes, changes in the positive electrode surface structure result in the release of TM ions which, along with acidic species can catalyse further cell degradation processes.[93,212,214,215,220,221] The phenomenon of TM leaching is well-reported for lithium manganese spinel-type structures, and has also been reported to occur in NMC materials when they are stressed to high UCVs.[106,220,221,228–230] These TM ions can crossover through the electrolyte to the surface of the Gr SEI, where they exchange rapidly with Li^+, embedding themselves in the interphase.[220,221,231] The accumulation of these ions, especially Mn^{2+}, has been shown to catalyse SEI and electrolyte degradation, resulting in the formation of a thick and resistive SEI (**Figure 1.22**).[220,221,231] In 2018, Solchenbach *et al.* used OEMS to elucidate and quantify the electrolyte reduction on Gr caused by Ni and Mn ions in solution, through the doping of 1.5 µL of Ni- or Mn-trifluoromethanesulfonamide (TFSI) into the electrolyte formulation.[221] The data show that both Ni^{2+} and Mn^{2+} lead to enhanced gas evolution on pristine Gr electrodes once the potential is

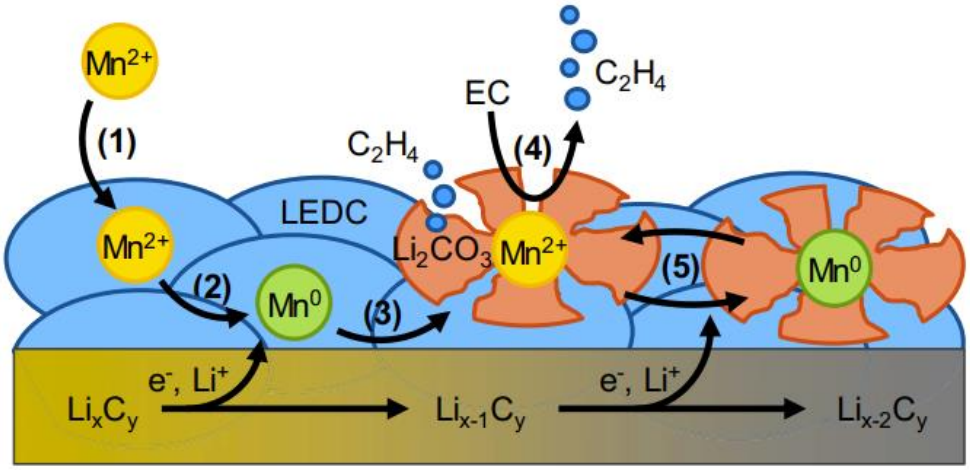


Figure 1.22. *Proposed mechanism for the continuous decomposition of the Gr SEI and electrolyte: (1) Absorption of Mn^{2+} ion into the Gr SEI; (2) reduction of Mn^{2+} ions in the SEI and deintercalation of Li^{+} from Gr; (3) re-oxidation of Mn^{0} to Mn^{2+}; (4) recurrent electrolyte reduction; (5) catalytic cycle of electrolyte decomposition. Reproduced from Solchenbach et al.*[221]

decreased below the reduction potential of these ions, demonstrating that the reduced metals are active towards electrolyte components. Where an SEI was formed on the Gr electrode in a pristine electrolyte (i.e. ideal formation conditions) before doping the electrolyte with Ni- and Mn-$(TFSI)_2$, the activity of Ni towards electrolyte degradation was greatly reduced, whereas the electrolyte with Mn still showed strong gassing, demonstrating that Mn can interact with the Gr SEI, destabilising it regardless of pristine formation conditions.[221] Although Mn-content has decreased in the push for high-Ni cathode chemistries, the increased interfacial reactivity results in greater surface reactivity and earlier onset of TM dissolution, resulting in crosstalk increasingly dominating LIB full-cell performance.[93,126,221,232]

1.10 Aims and objectives

The complexity, and often simultaneous, nature of degradation processes in LIB full-cells necessitate constant and targeted research efforts towards understanding the underlying mechanisms, if adequate mitigation strategies are to be designed. Although it is clear that crosstalk increasingly dominates cell performance as Ni-content increases,[93,126,221,232] the current universal method for the isolated study of the performance of prospective positive and

negative electrode chemistries is the use of half-cells, wherein they are partnered with a metallic Li negative electrode. This solution is sub-optimal for material performance and electrolyte degradation analyses, due to the highly reactive nature of the metallic Li electrode, which is known to degrade the organic carbonate species that constitute the electrolyte solvent.[154–156] Without a method to truly isolate the performance of prospective electrode chemistries, it is extremely difficult to understand the processes which initiate crosstalk and design strategies to mitigate them.

The current best strategies for enabling long-term cycling of metallic Li cells with electrolytes similar to traditional compositions is the use of high concentration FEC electrolytes, which are not representative of the conditions under which commercial LIB full-cells would be cycled and are, as a result of the high production cost, not feasible for real-world application.[157–159] With the aim of developing a cell chemistry that can truly isolate the long-term performance of prospective positive electrode chemistries, Chapter 3 examines the failure mechanism of Li-NMC811 half-cells with commercially relevant electrode loading and electrolyte composition. A variety of electrochemical and spectroscopic techniques are used to understand cell performance and the evolution of electrolyte composition with respect to the extent of cycling. Furthermore, I hope to provide an adequate solution to this problem in the form of a LTO electrode which is relatively benign to the electrolyte composition and is shown to enable a long cycle life, despite the lithium inventory being limited relative to the metallic Li system.

As discussed in section 1.9, previous studies have suggested that as positive electrode Ni-content increases, these materials may be able to form VC through the dehydrogenation of EC. First Freiberg *et al.* used chemical experiments with a RB photosensitizer to propose that $^1O_2$ was the source of VC formation, before Zhang *et al.* proposed a second metal-oxide surface-confined pathway for VC formation through EC dehydrogenation, the activity of which increased with Ni-content (i.e. surface reactivity).[199,225] In 2022, Rinkel *et al.* proposed that the RB photosensitizer used by Freiberg *et al.* did not result in the formation of VC, but

instead caused gaseous degradation of EC with the production of H_2O as the only by-product.[227] These conflicting result bring into question the validity and reproducibility of $^1O_2$ degradation experiments performed with a RB photosensitiser in the organic carbonates used as LIB electrolyte solvents. Chapter 4 aims to understand the performance of Gr-NMC811 full-cells over full cycle life (to below 80% capacity retention) with and without doped VC and understand the effect, if any, of VC formation at the surface of NMC811 electrodes. Given that any stabilisation would have to come in the early-stages of Gr-NMC811 cycling (i.e. when the SEI is formed), a gas chromatography mass spectrometry method is developed for direct VC detection in extracted electrolytes to improve the limit of detection over the previously used NMR and FTIR spectroscopic methods.[213,225,227] Furthermore, with the aim of deconvoluting the disputed claims of Rinkel and Freiberg, a systematic study of $^1O_2$ generation with irradiation of organic carbonate solvents containing the RB photosensitizer is performed. Finally, I hope to propose a heterogeneous selective $^1O_2$ generation single atom catalyst which can reduce the possibility of interference of the photosensitizer molecules in reaction pathways and enable simplification of future research requiring $^1O_2$ generation.

1.11 References

1. Capellán-Pérez, I., Mediavilla, M., de Castro, C., Carpintero, Ó. & Miguel, L. J. Fossil fuel depletion and socio-economic scenarios: An integrated approach. *Energy* **77**, 641–666 (2014).
2. Cook, J. *et al.* Consensus on consensus: a synthesis of consensus estimates on human-caused global warming. *Environ. Res. Lett.* **11**, 048002 (2016).
3. Easterlin, R. A. The Worldwide Standard of Living since 1800. *J. Econ. Perspect.* **14**, 7–26 (2000).

4. *Adoption of the Paris Agreement*. *FCCC/CP/2015/L.9/Rev.1* (2016).

5. Höhne, N. *et al.* Emissions: world has four times the work or one-third of the time. *Nature* **579**, 25–28 (2020).

6. Lamb, W. F. *et al.* A review of trends and drivers of greenhouse gas emissions by sector from 1990 to 2018. *Environ. Res. Lett.* **16**, 073005 (2021).

7. Statistical Review of World Energy | Energy economics | Home. *bp global* https://www.bp.com/en/global/corporate/energy-economics/statistical-review-of-world-energy.html.

8. Ritchie, H., Roser, M. & Rosado, P. Fossil Fuels. *Our World Data* (2022).

9. Liu, Z. *et al.* Near-real-time monitoring of global CO_2 emissions reveals the effects of the COVID-19 pandemic. *Nat. Commun.* **11**, 5172 (2020).

10. Nguyen, X. P., Hoang, A. T., Ölçer, A. I. & Huynh, T. T. Record decline in global CO_2 emissions prompted by COVID-19 pandemic and its implications on future climate change policies. *Energy Sources Part Recovery Util. Environ. Eff.* (2021). https://doi.org/10.1080/15567036.2021.1879969

11. Friedlingstein, P. *et al.* Global Carbon Budget 2022. *Earth Syst. Sci. Data* **14**, 4811–4900 (2022).

12. Ritchie, H., Roser, M. & Rosado, P. CO_2 and Greenhouse Gas Emissions. *Our World Data* (2020).

13. Transport – Topics. *IEA* https://www.iea.org/topics/transport.

14. Fan, Y. V., Perry, S., Klemeš, J. J. & Lee, C. T. A review on air emissions assessment: Transportation. *J. Clean. Prod.* **194**, 673–684 (2018).

15. Jiang, X.-Q., Mei, X.-D. & Feng, D. Air pollution and chronic airway diseases: what should people know and do? *J. Thorac. Dis.* **8**, E31–E40 (2016).

16. Manisalidis, I., Stavropoulou, E., Stavropoulos, A. & Bezirtzoglou, E. Environmental and Health Impacts of Air Pollution: A Review. *Front. Public Health* **8**, (2020).

17. Kebede, A. A., Kalogiannis, T., Van Mierlo, J. & Berecibar, M. A comprehensive review of stationary energy storage devices for large scale renewable energy sources grid integration. *Renew. Sustain. Energy Rev.* **159**, 112213 (2022).

18. Howell, D., Cunningham, B., Duong, T. & Faguy, P. Overview of the DOE VTO Advanced Battery R&D Program. (2016).

19. Ding, Y., Cano, Z. P., Yu, A., Lu, J. & Chen, Z. Automotive Li-Ion Batteries: Current Status and Future Perspectives. *Electrochem. Energy Rev.* **2**, 1–28 (2019).

20. Li, M., Lu, J., Chen, Z. & Amine, K. 30 Years of Lithium-Ion Batteries. *Adv. Mater.* **30**, 1800561 (2018).

21. Günter, F. J. & Wassiliadis, N. State of the Art of Lithium-Ion Pouch Cells in Automotive Applications: Cell Teardown and Characterization. *J. Electrochem. Soc.* **169**, 030515 (2022).

22. Lithium ion battery prices rise for first time in gigafactory era; automakers in negotiations. *Benchmark Source* https://source.benchmarkminerals.com/article/lithium-ion-battery-

prices-rise-for-first-time-in-gigafactory-era-automakers-in-negotiations (2021).

23. Global EV Outlook 2021 – Analysis. *IEA* https://www.iea.org/reports/global-ev-outlook-2021.

24. Yarmuth, John. A. *Inflation Reduction Act of 2022*. *H.R. 5376* (2022).

25. What's in the Inflation Reduction Act (IRA) of 2022 | McKinsey. https://www.mckinsey.com/industries/public-and-social-sector/our-insights/the-inflation-reduction-act-heres-whats-in-it.

26. Environmental Resources Management. Inflation Reduction Act of 2022: Climate and Energy Provisions. (2022).

27. Trost, J. N. & Dunn, J. B. Assessing the feasibility of the Inflation Reduction Act's EV critical mineral targets. *Nat. Sustain.* (2023). https://doi.org/10.1038/s41893-023-01079-8.

28. Manthiram, A. & Goodenough, J. B. Lithium insertion into $Fe_2(SO_4)_3$ frameworks. *J. Power Sources* **26**, 403–408 (1989).

29. Thackeray, M. M., David, W. I. F. & Goodenough, J. B. Structural characterization of the lithiated iron oxides $Li_xFe_3O_4$ and $Li_xFe_2O_3$ (0<x<2). *Mater. Res. Bull.* **17**, 785–793 (1982).

30. Whittingham, M. S. Electrical Energy Storage and Intercalation Chemistry. *Science* **192**, 1126–1127 (1976).

31. Mizushima, K., Jones, P., Wiseman, P. & Goodenough, J. Li_xCoO_2 (0<x<-1): A new cathode material for batteries of high energy density. *Mater. Res. Bull.* **15**, 783–789 (1980).

32. Thackeray, M. M., David, W. I. F., Bruce, P. G. & Goodenough, J. B. Lithium insertion into manganese spinels. *Mater. Res. Bull.* **18**, 461–472 (1983).

33. Manthiram, A. & Goodenough, J. B. Lithium insertion into $Fe_2(MO_4)_3$ frameworks: Comparison of M = W with M = Mo. *J. Solid State Chem.* **71**, 349–360 (1987).

34. Koch, V. R. Status of the secondary lithium electrode. *J. Power Sources* **6**, 357–370 (1981).

35. Brandt, K. Historical development of secondary lithium batteries. *Solid State Ion.* **69**, 173–183 (1994).

36. Manthiram, A. A reflection on lithium-ion battery cathode chemistry. *Nat. Commun.* **11**, 1550 (2020).

37. Goodenough, J. B. Metallic oxides. *Prog. Solid State Chem.* **5**, 145–399 (1971).

38. Yoshino, A., Sanechika, K. & Nakajima, T. Secondary battery. (1987).

39. Goodenough, J. B. & Park, K.-S. The Li-Ion Rechargeable Battery: A Perspective. *J. Am. Chem. Soc.* **135**, 1167–1176 (2013).

40. Yazami, R. & Touzain, Ph. A reversible graphite-lithium negative electrode for electrochemical generators. *J. Power Sources* **9**, 365–371 (1983).

41. Armand, M. *et al.* Lithium-ion batteries – Current state of the art and anticipated developments. *J. Power Sources* **479**, 228708 (2020).

42. Blomgren, G. E. The Development and Future of Lithium Ion Batteries. *J. Electrochem. Soc.* **164**, A5019–A5025 (2017).

43. Chebiam, R. V., Prado, F. & Manthiram, A. Soft Chemistry Synthesis and Characterization of Layered $Li_{1-x}Ni_{1-y}Co_yO_{2-\delta}$ ($0 \leq x \leq 1$ and $0 \leq y \leq 1$). *Chem. Mater.* **13**, 2951–2957 (2001).

44. Saiful Islam, M. & J. Fisher, C. A. Lithium and sodium battery cathode materials: computational insights into voltage, diffusion and nanostructural properties. *Chem. Soc. Rev.* **43**, 185–204 (2014).

45. Nishizawa, M. & Yamamura, S. Irreversible conductivity change of $Li_{1-x}CoO_2$ on electrochemical lithium insertion/extraction, desirable for battery applications. *Chem. Commun.* **16**, 1631–1632 (1998).

46. Ceder, G. *et al.* Identification of cathode materials for lithium batteries guided by first-principles calculations. *Nature* **392**, 694–696 (1998).

47. Liu, Q. *et al.* Approaching the capacity limit of lithium cobalt oxide in lithium ion batteries via lanthanum and aluminium doping. *Nat. Energy* **3**, 936–943 (2018).

48. Zhao, H. *et al.* Cobalt-Free Cathode Materials: Families and their Prospects. *Adv. Energy Mater.* **12**, 2103894 (2022).

49. Democratic Republic of Congo: 'This is what we die for': Human rights abuses in the Democratic Republic of the Congo power the global trade in cobalt. *Amnesty International* https://www.amnesty.org/en/documents/afr62/3183/2016/en/ (2016).

50. Padhi, A. K., Nanjundaswamy, K. S. & Goodenough, J. B. Phospho-olivines as Positive-Electrode Materials for Rechargeable Lithium Batteries. *J. Electrochem. Soc.* **144**, 1188 (1997).

51. Dahn, J. R., Sacken, U. von, Juzkow, M. W. & Al-Janaby, H. Rechargeable $LiNiO_2$ / Carbon Cells. *J. Electrochem. Soc.* **138**, 2207 (1991).

52. Thackeray, M. M., Johnson, P. J., de Picciotto, L. A., Bruce, P. G. & Goodenough, J. B. Electrochemical extraction of lithium from $LiMn_2O_4$. *Mater. Res. Bull.* **19**, 179–187 (1984).

53. LFP's resurgence illustrates the nuances of the electric vehicle supply chain. *Benchmark Source* https://source.benchmarkminerals.com/article/lfps-resurgence-illustrates-the-nuances-of-the-electric-vehicle-supply-chain/ (2020).

54. The rise of LFP batteries outside of China. *Benchmark Source* https://source.benchmarkminerals.com/article/the-rise-of-lfp-batteries-outside-of-china (2023).

55. Satyavani, T. V. S. L., Srinivas Kumar, A. & Subba Rao, P. S. V. Methods of synthesis and performance improvement of lithium iron phosphate for high rate Li-ion batteries: A review. *Eng. Sci. Technol. Int. J.* **19**, 178–188 (2016).

56. Julien, C. M., Mauger, A., Zaghib, K. & Groult, H. Comparative Issues of Cathode Materials for Li-Ion Batteries. *Inorganics* **2**, 132–154 (2014).

57. Yuan, L.-X. *et al.* Development and challenges of $LiFePO_4$ cathode material for lithium-ion batteries. *Energy Environ. Sci.* **4**, 269–284 (2011).

58. Ahsan, Z. *et al.* Recent Progress in Capacity Enhancement of $LiFePO_4$ Cathode for Li-Ion Batteries. *J. Electrochem. Energy Convers. Storage* **18**, (2020).

59. Mukai, K., Uyama, T. & Yamada, I. Structural and Electrochemical Analyses on the Transformation of I_2O_4-Type $LiMn_2O_4$ from Spinel-Type $LiMn_2O_4$. *ACS Omega* **4**, 6459–6467 (2019).

60. Filsø, M. Ø. *et al.* Visualizing Lithium-Ion Migration Pathways in Battery Materials. *Chem. – Eur. J.* **19**, 15535–15544 (2013).

61. Zhu, Y.-F., Xiao, Y., Dou, S.-X., Kang, Y.-M. & Chou, S.-L. Spinel/Post-spinel engineering on layered oxide cathodes for sodium-ion batteries. *eScience* **1**, 13–27 (2021).

62. Kyung Park, O. *et al.* Who will drive electric vehicles, olivine or spinel? *Energy Environ. Sci.* **4**, 1621–1633 (2011).

63. Kim, M. *et al.* Improving $LiNiO_2$ cathode performance through particle design and optimization. *J. Mater. Chem. A* **10**, 12890–12899 (2022).

64. Kaneda, H., Furuichi, Y., Ikezawa, A. & Arai, H. Single-Crystal-like Durable $LiNiO_2$ Positive Electrode Materials for Lithium-Ion Batteries. *ACS Appl. Mater. Interfaces* **14**, 52766–52778 (2022).

65. Su, L., Jo, E. & Manthiram, A. Protection of Cobalt-Free $LiNiO_2$ from Degradation with Localized Saturated Electrolytes in Lithium-Metal Batteries. *ACS Energy Lett.* **7**, 2165–2172 (2022).

66. Li, H., Zhang, N., Li, J. & Dahn, J. R. Updating the Structure and Electrochemistry of Li_xNiO_2 for $0 \leq x \leq 1$. *J. Electrochem. Soc.* **165**, A2985 (2018).

67. Tarascon, J. M. & Armand, M. Issues and challenges facing rechargeable lithium batteries. *Nature* **414**, 359–367 (2001).

68. Rougier, A., Gravereau, P. & Delmas, C. Optimization of the Composition of the $Li_{1-z}Ni_{1+z}O_2$ Electrode Materials: Structural, Magnetic, and Electrochemical Studies. *J. Electrochem. Soc.* **143**, 1168 (1996).

69. Seong, W. M. & Manthiram, A. Complementary Effects of Mg and Cu Incorporation in Stabilizing the Cobalt-Free $LiNiO_2$ Cathode for Lithium-Ion Batteries. *ACS Appl. Mater. Interfaces* **12**, 43653–43664 (2020).

70. Mohan, P. & Kalaignan, G. P. Electrochemical Behaviour of Surface Modified SiO_2-Coated $LiNiO_2$ Cathode Materials for Rechargeable Lithium-Ion Batteries. *J. Nanosci. Nanotechnol.* **13**, 2765–2770 (2013).

71. Sun, Y. *et al.* Influence of core and shell components on the Ni-rich layered oxides with core–shell and dual-shell structures. *Chem. Eng. J.* **400**, 125821 (2020).

72. Noh, J.-K. *et al.* Mechanochemical Synthesis of Li_2MnO_3 Shell/$LiMO_2$ (M = Ni, Co, Mn) Core-Structured Nanocomposites for Lithium-Ion Batteries. *Sci. Rep.* **4**, 4847 (2014).

73. Zhang, Y. *et al.* Enhancing $LiNiO_2$ cathode materials by concentration-gradient yttrium modification for rechargeable lithium-ion batteries. *J. Energy Chem.* **63**, 312–319 (2021).

74. Liu, T. *et al.* Rational design of mechanically robust Ni-rich cathode materials via concentration gradient strategy. *Nat. Commun.* **12**, 6024 (2021).

75. Murdock, B. E., Toghill, K. E. & Tapia-Ruiz, N. A Perspective on the Sustainability of Cathode Materials used in Lithium-Ion Batteries. *Adv. Energy Mater.* **11**, 2102028 (2021).

76. Olivetti, E. A., Ceder, G., Gaustad, G. G. & Fu, X. Lithium-Ion Battery Supply Chain Considerations: Analysis of Potential Bottlenecks in Critical Metals. *Joule* **1**, 229–243 (2017).

77. Manthiram, A. A reflection on lithium-ion battery cathode chemistry. *Nat. Commun.* **11**, 1550 (2020).

78. Duffner, F., Wentker, M., Greenwood, M. & Leker, J. Battery cost modeling: A review and directions for future research. *Renew. Sustain. Energy Rev.* **127**, 109872 (2020).

79. Andre, D. *et al.* Future generations of cathode materials: an automotive industry perspective. *J. Mater. Chem. A* **3**, 6709–6732 (2015).

80. Masias, A., Marcicki, J. & Paxton, W. A. Opportunities and Challenges of Lithium Ion Batteries in Automotive Applications. *ACS Energy Lett.* **6**, 621–630 (2021).

81. Bianchini, M., Roca-Ayats, M., Hartmann, P., Brezesinski, T. & Janek, J. There and Back Again—The Journey of $LiNiO_2$ as a Cathode Active Material. *Angew. Chem. Int. Ed.* **58**, 10434–10458 (2019).

82. Li, W., Erickson, E. M. & Manthiram, A. High-nickel layered oxide cathodes for lithium-based automotive batteries. *Nat. Energy* **5**, 26–34 (2020).

83. Xu, C. *et al.* Future material demand for automotive lithium-based batteries. *Commun. Mater.* **1**, 99 (2020).

84. Olivetti, E. A., Ceder, G., Gaustad, G. G. & Fu, X. Lithium-Ion Battery Supply Chain Considerations: Analysis of Potential Bottlenecks in Critical Metals. *Joule* **1**, 229–243 (2017).

85. Murdock, B. E., Toghill, K. E. & Tapia-Ruiz, N. A Perspective on the Sustainability of Cathode Materials used in Lithium-Ion Batteries. *Adv. Energy Mater.* **11**, 2102028 (2021).

86. Chen, C.-H. *et al.* Development of Experimental Techniques for Parameterization of Multi-scale Lithium-ion Battery Models. *J. Electrochem. Soc.* **167**, 080534 (2020).

87. Günter, F. J. & Wassiliadis, N. State of the Art of Lithium-Ion Pouch Cells in Automotive Applications: Cell Teardown and Characterization. *J. Electrochem. Soc.* **169**, 030515 (2022).

88. Kovachev, G. *et al.* Analytical Dissection of an Automotive Li-Ion Pouch Cell. *Batteries* **5**, 67 (2019).

89. Dühnen, S. *et al.* Toward Green Battery Cells: Perspective on Materials and Technologies. *Small Methods* **4**, 2000039 (2020).

90. Märker, K., Reeves, P. J., Xu, C., Griffith, K. J. & Grey, C. P. Evolution of Structure and Lithium Dynamics in $LiNi_{0.8}Mn_{0.1}Co_{0.1}O_2$ (NMC811) Cathodes during Electrochemical Cycling. *Chem. Mater.* **31**, 2545–2554 (2019).

91. Li, J., Downie, L. E., Ma, L., Qiu, W. & Dahn, J. R. Study of the Failure Mechanisms of $LiNi_{0.8}Mn_{0.1}Co_{0.1}O_2$ Cathode Material for Lithium Ion Batteries. *J. Electrochem. Soc.* **162**, A1401 (2015).

92. Li, T. *et al.* Degradation Mechanisms and Mitigation Strategies of Nickel-Rich NMC-Based Lithium-Ion Batteries. *Electrochem. Energy Rev.* **3**, 43–80 (2020).

93. Jiang, M., Danilov, D. L., Eichel, R.-A. & Notten, P. H. L. A Review of Degradation Mechanisms and Recent Achievements for Ni-Rich Cathode-Based Li-Ion Batteries. *Adv. Energy Mater.* **11**, 2103005 (2021).

94. Märker, K., Reeves, P. J., Xu, C., Griffith, K. J. & Grey, C. P. Evolution of Structure and Lithium Dynamics in $LiNi_{0.8}Mn_{0.1}Co_{0.1}O_2$ (NMC811) Cathodes during Electrochemical Cycling. *Chem. Mater.* **31**, 2545–2554 (2019).

95. Dose, W. M., Xu, C., Grey, C. P. & De Volder, M. F. L. Effect of Anode Slippage on Cathode Cutoff Potential and Degradation Mechanisms in Ni-Rich Li-Ion Batteries. *Cell Rep. Phys. Sci.* **1**, 100253 (2020).

96. Li, J. *et al.* The Impact of Electrolyte Additives and Upper Cut-off Voltage on the Formation of a Rocksalt Surface Layer in $LiNi_{0.8}Mn_{0.1}Co_{0.1}O_2$ Electrodes. *J. Electrochem. Soc.* **164**, A655–A665 (2017).

97. Jung, R., Metzger, M., Maglia, F., Stinner, C. & Gasteiger, H. A. Oxygen release and its effect on the cycling stability of $LiNi_xMn_yCo_zO_2$(NMC) cathode materials for li-ion batteries. *J. Electrochem. Soc.* **164**, A1361–A1377 (2017).

98. Noh, H.-J., Youn, S., Yoon, C. S. & Sun, Y.-K. Comparison of the structural and electrochemical properties of layered $Li[Ni_xCo_yMn_z]O_2$ (x = 1/3, 0.5, 0.6, 0.7, 0.8 and 0.85) cathode material for lithium-ion batteries. *J. Power Sources* **233**, 121–130 (2013).

99. Ryu, H.-H., Park, K.-J., Yoon, C. S. & Sun, Y.-K. Capacity Fading of Ni-Rich $Li[Ni_xCo_yMn_{1-x-y}]O_2$ ($0.6 \leq x \leq 0.95$) Cathodes for High-Energy-Density

Lithium-Ion Batteries: Bulk or Surface Degradation? *Chem. Mater.* **30**, 1155–1163 (2018).

100. Kuo, L.-Y., Guillon, O. & Kaghazchi, P. Origin of Structural Phase Transitions in Ni-Rich $Li_xNi_{0.8}Co_{0.1}Mn_{0.1}O_2$ with Lithiation/Delithiation: A First-Principles Study. *ACS Sustain. Chem. Eng.* **9**, 7437–7446 (2021).

101. Ruff, Z., Xu, C. & Grey, C. P. Transition Metal Dissolution and Degradation in NMC811-Graphite Electrochemical Cells. *J. Electrochem. Soc.* **168**, 060518 (2021).

102. Zheng, H., Sun, Q., Liu, G., Song, X. & Battaglia, V. S. Correlation between dissolution behavior and electrochemical cycling performance for $LiNi_{1/3}Co_{1/3}Mn_{1/3}O_2$-based cells. *J. Power Sources* **207**, 134–140 (2012).

103. Gallus, D. R. *et al.* The influence of different conducting salts on the metal dissolution and capacity fading of NCM cathode material. *Electrochimica Acta* **134**, 393–398 (2014).

104. Rinkel, B. L. D., Hall, D. S., Temprano, I. & Grey, C. P. Electrolyte Oxidation Pathways in Lithium-Ion Batteries. *J. Am. Chem. Soc.* **142**, 15058–15074 (2020).

105. Jayawardana, C., Rodrigo, N. D., Rynearson, L. & Lucht, B. L. Difluorophosphoric Acid Generation and Crossover Reactions in $LiNi_xCo_yMn_zO_2$ Cathodes Operating at High Voltage. *J. Electrochem. Soc.* **169**, 060509 (2022).

106. Gilbert, J. A., Shkrob, I. A. & Abraham, D. P. Transition Metal Dissolution, Ion Migration, Electrocatalytic Reduction and Capacity Loss in Lithium-Ion Full Cells. *J. Electrochem. Soc.* **164**, A389–A399 (2017).

107. Jung, R. *et al.* Nickel, manganese, and cobalt dissolution from Ni-Rich NMC and their effects on NMC622-graphite cells. *J. Electrochem. Soc.* **166**, A378–A389 (2019).

108. Liu, W. *et al.* Nickel-Rich Layered Lithium Transition-Metal Oxide for High-Energy Lithium-Ion Batteries. *Angew. Chem. - Int. Ed.* **54**, 4440–4457 (2015).

109. Yeh, N.-H. *et al.* Controlling Ni^{2+} from the Surface to the Bulk by a New Cathode Electrolyte Interphase Formation on a Ni-Rich Layered Cathode in High-Safe and High-Energy-Density Lithium-Ion Batteries. *ACS Appl. Mater. Interfaces* **13**, 7355–7369 (2021).

110. Placke, T., Schmuch, R., Hörpel, G., Wagner, R. & Winter, M. Performance and cost of materials for lithium-based rechargeable automotive batteries. *Nat. Energy* **3**, 267–278 (2018).

111. Houache, M. S. E., Yim, C.-H., Karkar, Z. & Abu-Lebdeh, Y. On the Current and Future Outlook of Battery Chemistries for Electric Vehicles—Mini Review. *Batteries* **8**, 70 (2022).

112. House, R. A. *et al.* First-cycle voltage hysteresis in Li-rich 3d cathodes associated with molecular O_2 trapped in the bulk. *Nat. Energy* **5**, 777–785 (2020).

113. Liu, J. *et al.* Recent breakthroughs and perspectives of high-energy layered oxide cathode materials for lithium ion batteries. *Mater. Today* **43**, 132–165 (2021).

114. Ji, X. *et al.* A review on progress of lithium-rich manganese-based cathodes for lithium ion batteries. *J. Power Sources* **487**, 229362 (2021).

115. Zhao, S., Yan, K., Zhang, J., Sun, B. & Wang, G. Reaction Mechanisms of Layered Lithium-Rich Cathode Materials for High-Energy Lithium-Ion Batteries. *Angew. Chem. Int. Ed.* **60**, 2208–2220 (2021).

116. Manthiram, A., Knight, J. C., Myung, S.-T., Oh, S.-M. & Sun, Y.-K. Nickel-Rich and Lithium-Rich Layered Oxide Cathodes: Progress and Perspectives. *Adv. Energy Mater.* **6**, 1501010 (2016).

117. Akhilash, M., Salini, P. S., John, B. & Mercy, T. D. A journey through layered cathode materials for lithium ion cells – From lithium cobalt oxide to lithium-rich transition metal oxides. *J. Alloys Compd.* **869**, 159239 (2021).

118. House, R. A. *et al.* The role of O_2 in O-redox cathodes for Li-ion batteries. *Nat. Energy* **6**, 781–789 (2021).

119. House, R. A. *et al.* Superstructure control of first-cycle voltage hysteresis in oxygen-redox cathodes. *Nature* **577**, 502–508 (2020).

120. McColl, K. *et al.* Transition metal migration and O_2 formation underpin voltage hysteresis in oxygen-redox disordered rocksalt cathodes. *Nat. Commun.* **13**, 5275 (2022).

121. Assat, G. & Tarascon, J.-M. Fundamental understanding and practical challenges of anionic redox activity in Li-ion batteries. *Nat. Energy* **3**, 373–386 (2018).

122. Liu, T. *et al.* Understanding Co roles towards developing Co-free Ni-rich cathodes for rechargeable batteries. *Nat. Energy* **6**, 277–286 (2021).

123. Li, W., Lee, S. & Manthiram, A. High-Nickel NMA: A Cobalt-Free Alternative to NMC and NCA Cathodes for Lithium-Ion Batteries. *Adv. Mater.* **32**, 2002718 (2020).

124. Research – Faraday Institution Degradation project. https://degradationproject.com/about/.

125. Chen, W., Liang, J., Yang, Z. & Li, G. A Review of Lithium-Ion Battery for Electric Vehicle Applications and Beyond. *Energy Procedia* **158**, 4363–4368 (2019).

126. Li, T. *et al.* Degradation Mechanisms and Mitigation Strategies of Nickel-Rich NMC-Based Lithium-Ion Batteries. *Electrochem. Energy Rev.* **3**, 43–80 (2020).

127. Guerard, D. & Herold, A. Intercalation of lithium into graphite and other carbons. *Carbon* **13**, 337–345 (1975).

128. Zhang, H., Yang, Y., Ren, D., Wang, L. & He, X. Graphite as anode materials: Fundamental mechanism, recent progress and advances. *Energy Storage Mater.* **36**, 147–170 (2021).

129. Daumas, N. & Herold, A. Relations between phase concept and reaction mechanics in graphite insertion compounds. *C. R. Seances Acad. Sci. Ser. C.* **268**, 373 (1969).

130. Li, Y., Lu, Y., Adelhelm, P., Titirici, M. M. & Hu, Y. S. Intercalation chemistry of graphite: Alkali metal ions and beyond. *Chem. Soc. Rev.* **48,** 4655–4687 (2019).

131. Lopez, J. L. L., J. Grandinetti, P. & C. Co, A. Enhancing the real-time detection of phase changes in lithium–graphite intercalated compounds

through derivative operando (dOp) NMR cyclic voltammetry. *J. Mater. Chem. A* **6**, 231–243 (2018).

132. Drüe, M., Seyring, M. & Rettenmayr, M. Phase formation and microstructure in lithium-carbon intercalation compounds during lithium uptake and release. *J. Power Sources* **353**, 58–66 (2017).

133. Heiskanen, S. K., Kim, J. & Lucht, B. L. Generation and Evolution of the Solid Electrolyte Interphase of Lithium-Ion Batteries. *Joule* **3**, 2322–2333 (2019).

134. Parimalam, B. S., MacIntosh, A. D., Kadam, R. & Lucht, B. L. Decomposition Reactions of Anode Solid Electrolyte Interphase (SEI) Components with $LiPF_6$. *J. Phys. Chem. C* **121**, 22733–22738 (2017).

135. Xu, K. Electrolytes and Interphases in Li-Ion Batteries and Beyond. *Chem. Rev.* **114**, 11503–11618 (2014).

136. Peled, E. & Menkin, S. Review—SEI: Past, Present and Future. *J. Electrochem. Soc.* **164**, A1703 (2017).

137. Sole, C., E. Drewett, N. & J. Hardwick, L. In situ Raman study of lithium-ion intercalation into microcrystalline graphite. *Faraday Discuss.* **172**, 223–237 (2014).

138. Han, C. *et al.* A review of gassing behavior in $Li_4Ti_5O_{12}$-based lithium ion batteries. *J. Mater. Chem. A* **5**, 6368–6381 (2017).

139. Zhang, H. *et al.* $Li_4Ti_5O_{12}$ spinel anode: Fundamentals and advances in rechargeable batteries. *InfoMat* **4**, e12228 (2022).

140. Xu, G. *et al.* $Li_4Ti_5O_{12}$-based energy conversion and storage systems: Status and prospects. *Coord. Chem. Rev.* **343**, 139–184 (2017).

141. Lin, D., Liu, Y. & Cui, Y. Reviving the lithium metal anode for high-energy batteries. *Nat. Nanotechnol.* **12**, 194–206 (2017).

142. Gao, Y., Pan, Z., Sun, J., Liu, Z. & Wang, J. High-Energy Batteries: Beyond Lithium-Ion and Their Long Road to Commercialisation. *Nano-Micro Lett.* **14**, 94 (2022).

143. Dong, H. *et al.* Exploring the practical applications of silicon anodes: a review of silicon-based composites for lithium-ion batteries. *Ionics* **28**, 3057–3077 (2022).

144. Kwade, A. *et al.* Current status and challenges for automotive battery production technologies. *Nat. Energy* **3**, 290–300 (2018).

145. Wang, H., Lu, S.-H., Wang, X., Xia, S. & Chew, H. B. A review of the multiscale mechanics of silicon electrodes in high-capacity lithium-ion batteries. *J. Phys. Appl. Phys.* **55**, 063001 (2021).

146. Xiong, X., Jiao, S. & Ma, H. Improving the electrochemical performance of Si anode by using N-doped carbon materials in lithium-ion batteries. *Ionics* **28**, 683–687 (2022).

147. Pan, J. *et al.* Solid-state batteries designed with high ion conductive composite polymer electrolyte and silicon anode. *Energy Storage Mater.* **43**, 165–171 (2021).

148. Jiang, M. *et al.* An Endotenon Sheath-Inspired Double-Network Binder Enables Superior Cycling Performance of Silicon Electrodes. *Nano-Micro Lett.* **14**, 87 (2022).

149. Ge, M., Rong, J., Fang, X. & Zhou, C. Porous Doped Silicon Nanowires for Lithium Ion Battery Anode with Long Cycle Life. *Nano Lett.* **12**, 2318–2323 (2012).

150. Choi, S. *et al.* Generalized Redox-Responsive Assembly of Carbon-Sheathed Metallic and Semiconducting Nanowire Heterostructures. *Nano Lett.* **16**, 1179–1185 (2016).

151. Wang, L. *et al.* Highly Stretchable Conductive Glue for High-Performance Silicon Anodes in Advanced Lithium-Ion Batteries. *Adv. Funct. Mater.* **28**, 1704858 (2018).

152. Berhaut, C. L. *et al.* Prelithiation of silicon/graphite composite anodes: Benefits and mechanisms for long-lasting Li-Ion batteries. *Energy Storage Mater.* **29**, 190–197 (2020).

153. Tikekar, M. D., Choudhury, S., Tu, Z. & Archer, L. A. Design principles for electrolytes and interfaces for stable lithium-metal batteries. *Nat. Energy* **1**, 16114 (2016).

154. Li, J., Downie, L. E., Ma, L., Qiu, W. & Dahn, J. R. Study of the Failure Mechanisms of $LiNi_{0.8}Mn_{0.1}Co_{0.1}O_2$ Cathode Material for Lithium Ion Batteries. *J. Electrochem. Soc.* **162**, A1401 (2015).

155. Weber, F. M., Kohlhaas, I. & Figgemeier, E. Tuning the Reactivity of Electrolyte Solvents on Lithium Metal by Vinylene Carbonate. *J. Electrochem. Soc.* **167**, 140523 (2020).

156. Zhuang, G., Chen, Y. & Ross, P. N. The Reaction of Lithium with Dimethyl Carbonate and Diethyl Carbonate in Ultrahigh Vacuum Studied by X-ray Photoemission Spectroscopy. *Langmuir* **15**, 1470–1479 (1999).

157. Wang, W. *et al.* Stable Cycling of High-Voltage Lithium-Metal Batteries Enabled by High-Concentration FEC-Based Electrolyte. *ACS Appl. Mater. Interfaces* **12**, 22901–22909 (2020).

158. Dong, L. *et al.* Stabilization of high-voltage lithium metal batteries using a sulfone-based electrolyte with bi-electrode affinity and $LiSO_2F$-rich interphases. *Energy Storage Mater.* **44**, 527–536 (2022).

159. Fu, C. *et al.* A dual-salt coupled fluoroethylene carbonate succinonitrile-based electrolyte enables Li-metal batteries. *J. Mater. Chem. A* **8**, 2066–2073 (2020).

160. Rowden, B. & Garcia-Araez, N. Estimating lithium-ion battery behavior from half-cell data. *Energy Rep.* **7**, 97–103 (2021).

161. Miele, E. *et al.* Hollow-core optical fibre sensors for operando Raman spectroscopy investigation of Li-ion battery liquid electrolytes. *Nat. Commun.* **13**, 1651 (2022).

162. Schulze, M. C. & Neale, N. R. Half-Cell Cumulative Efficiency Forecasts Full-Cell Capacity Retention in Lithium-Ion Batteries. *ACS Energy Lett.* **6**, 1082–1086 (2021).

163. Han, C. *et al.* A review of gassing behavior in $Li_4Ti_5O_{12}$-based lithium ion batteries. *J. Mater. Chem. A* **5**, 6368–6381 (2017).

164. He, Y.-B. *et al.* Gassing in $Li_4Ti_5O_{12}$-based batteries and its remedy. *Sci. Rep.* **2**, 913 (2012).

165. Bernhard, R., Meini, S. & Gasteiger, H. A. On-Line Electrochemical Mass Spectrometry Investigations on the Gassing Behavior of $Li_4Ti_5O_{12}$ Electrodes and Its Origins. *J. Electrochem. Soc.* **161**, A497 (2014).

166. Marcinek, M. *et al.* Electrolytes for Li-ion transport – Review. *Solid State Ion.* **276**, 107–126 (2015).

167. Aurbach, D. *et al.* Design of electrolyte solutions for Li and Li-ion batteries: a review. *Electrochimica Acta* **50**, 247–254 (2004).

168. Xu, K. Li-ion battery electrolytes. *Nat. Energy* **6**, 763–763 (2021).

169. Schipper, F. & Aurbach, D. A brief review: Past, present and future of lithium ion batteries. *Russ. J. Electrochem.* **52**, 1095–1121 (2016).

170. Aravindan, V., Gnanaraj, J., Madhavi, S. & Liu, H.-K. Lithium-Ion Conducting Electrolyte Salts for Lithium Batteries. *Chem. – Eur. J.* **17**, 14326–14346 (2011).

171. Gabryelczyk, A., Ivanov, S., Bund, A. & Lota, G. Corrosion of aluminium current collector in lithium-ion batteries: A review. *J. Energy Storage* **43**, 103226 (2021).

172. Yang, S. *et al.* Corrosion inhibition of aluminum current collector with molybdate conversion coating in commercial $LiPF_6$-esters electrolytes. *Corros. Sci.* **190**, 109632 (2021).

173. Shim, J. & Striebel, K. A. Effect of electrode density on cycle performance and irreversible capacity loss for natural graphite anode in lithium-ion batteries. *J. Power Sources* **119–121**, 934–937 (2003).

174. Ng, S. H. *et al.* Correlations between surface properties of graphite and the first cycle specific charge loss in lithium-ion batteries. *Carbon* **47**, 705–712 (2009).

175. Verma, P., Maire, P. & Novák, P. A review of the features and analyses of the solid electrolyte interphase in Li-ion batteries. *Electrochimica Acta* **55**, 6332–6341 (2010).

176. Tan, J., Matz, J., Dong, P., Shen, J. & Ye, M. A Growing Appreciation for the Role of LiF in the Solid Electrolyte Interphase. *Adv. Energy Mater.* **11**, 2100046 (2021).

177. Metzger, M., Strehle, B., Solchenbach, S. & Gasteiger, H. A. Origin of H_2 Evolution in LIBs: H_2O Reduction vs. Electrolyte Oxidation. *J. Electrochem. Soc.* **163**, A798 (2016).

178. Wang, L. *et al.* Identifying the components of the solid–electrolyte interphase in Li-ion batteries. *Nat. Chem.* **11**, 789–796 (2019).

179. Seo, D. M. *et al.* Reduction Reactions of Carbonate Solvents for Lithium Ion Batteries. *ECS Electrochem. Lett.* **3**, A91 (2014).

180. Parimalam, B. S. & Lucht, B. L. Reduction Reactions of Electrolyte Salts for Lithium Ion Batteries: $LiPF_6$, $LiBF_4$, LiDFOB, LiBOB, and LiTFSI. *J. Electrochem. Soc.* **165**, A251 (2018).

181. Vatamanu, J., Borodin, O. & Smith, G. D. Molecular Dynamics Simulation Studies of the Structure of a Mixed Carbonate/$LiPF_6$ Electrolyte near Graphite Surface as a Function of Electrode Potential. *J. Phys. Chem. C* **116**, 1114–1121 (2012).

182. Liu, T. *et al.* In situ quantification of interphasial chemistry in Li-ion battery. *Nat. Nanotechnol.* **14**, 50–56 (2019).

183. Nie, M. *et al.* Lithium Ion Battery Graphite Solid Electrolyte Interphase Revealed by Microscopy and Spectroscopy. *J. Phys. Chem. C* **117**, 1257–1267 (2013).

184. Haregewoin, A. M., Wotango, A. S. & Hwang, B.-J. Electrolyte additives for lithium ion battery electrodes: progress and perspectives. *Energy Env. Sci* **9**, 1955–1988 (2016).

185. Kitz, P. G., Lacey, M. J., Novák, P. & Berg, E. J. Operando investigation of the solid electrolyte interphase mechanical and transport properties formed from vinylene carbonate and fluoroethylene carbonate. *J. Power Sources* **477**, 228567 (2020).

186. Michan, A. L. *et al.* Fluoroethylene Carbonate and Vinylene Carbonate Reduction: Understanding Lithium-Ion Battery Electrolyte Additives and Solid Electrolyte Interphase Formation. *Chem. Mater.* **28**, 8149–8159 (2016).

187. Madec, L. *et al.* Effect of Sulfate Electrolyte Additives on $LiNi_{1/3}Mn_{1/3}Co_{1/3}O_2$ /Graphite Pouch Cell Lifetime: Correlation between XPS Surface Studies and Electrochemical Test Results. *J. Phys. Chem. C* **118**, 29608–29622 (2014).

188. El Ouatani, L. *et al.* The Effect of Vinylene Carbonate Additive on Surface Film Formation on Both Electrodes in Li-Ion Batteries. *J. Electrochem. Soc.* **156**, A103 (2009).

189. Heiskanen, S. K., Kim, J. & Lucht, B. L. Generation and Evolution of the Solid Electrolyte Interphase of Lithium-Ion Batteries. *Joule* **3**, 2322–2333 (2019).

190. Beltrop, K. *et al.* Triphenylphosphine Oxide as Highly Effective Electrolyte Additive for Graphite/NMC811 Lithium Ion Cells. *Chem. Mater.* **30**, 2726–2741 (2018).

191. Wang, Q., Jiang, L., Yu, Y. & Sun, J. Progress of enhancing the safety of lithium ion battery from the electrolyte aspect. *Nano Energy* **55**, 93–114 (2019).

192. Jin, Y. *et al.* Understanding Fluoroethylene Carbonate and Vinylene Carbonate Based Electrolytes for Si Anodes in Lithium Ion Batteries with NMR Spectroscopy. *J. Am. Chem. Soc.* **140**, 9854–9867 (2018).

193. Chen, X. *et al.* Reduction Mechanism of Fluoroethylene Carbonate for Stable Solid–Electrolyte Interphase Film on Silicon Anode. *ChemSusChem* **7**, 549–554 (2014).

194. Meda, U. S., Lal, L., M, S. & Garg, P. Solid Electrolyte Interphase (SEI), a boon or a bane for lithium batteries: A review on the recent advances. *J. Energy Storage* **47**, 103564 (2022).

195. Jaumann, T. *et al.* Lifetime vs. rate capability: Understanding the role of FEC and VC in high-energy Li-ion batteries with nano-silicon anodes. *Energy Storage Mater.* **6**, 26–35 (2017).

196. Okuno, Y., Ushirogata, K., Sodeyama, K. & Tateyama, Y. Decomposition of the fluoroethylene carbonate additive and the glue effect of lithium fluoride products for the solid electrolyte interphase: an ab initio study. *Phys. Chem. Chem. Phys.* **18**, 8643–8653 (2016).

197. Jung, R. *et al.* Consumption of Fluoroethylene Carbonate (FEC) on Si-C Composite Electrodes for Li-Ion Batteries. *J. Electrochem. Soc.* **163**, A1705 (2016).

198. Jin, Y. *et al.* Identifying the Structural Basis for the Increased Stability of the Solid Electrolyte Interphase Formed on Silicon with the Additive Fluoroethylene Carbonate. *J. Am. Chem. Soc.* **139**, 14992–15004 (2017).

199. Zhang, Y. *et al.* Revealing electrolyte oxidation via carbonate dehydrogenation on Ni-based oxides in Li-ion batteries by in situ Fourier transform infrared spectroscopy. *Energy Environ. Sci.* **13**, 183–199 (2020).

200. Aurbach, D. *et al.* Review on electrode–electrolyte solution interactions, related to cathode materials for Li-ion batteries. *J. Power Sources* **165**, 491–499 (2007).

201. Yu, Y. *et al.* Coupled $LiPF_6$ Decomposition and Carbonate Dehydrogenation Enhanced by Highly Covalent Metal Oxides in High-Energy Li-Ion Batteries. *J. Phys. Chem. C* **122**, 27368–27382 (2018).

202. Harris, O. C., Lee, S. E., Lees, C. & Tang, M. Review: mechanisms and consequences of chemical cross-talk in advanced Li-ion batteries. *J. Phys. Energy* **2**, 032002 (2020).

203. Zhang, T. & Paillard, E. Recent advances toward high voltage, EC-free electrolytes for graphite-based Li-ion battery. *Front. Chem. Sci. Eng.* **12**, 577–591 (2018).

204. Pan, R., Cui, Z., Yi, M., Xie, Q. & Manthiram, A. Ethylene Carbonate-Free Electrolytes for Stable, Safer High-Nickel Lithium-Ion Batteries. *Adv. Energy Mater.* **12**, 2103806 (2022).

205. Li, W., Dolocan, A., Li, J., Xie, Q. & Manthiram, A. Ethylene Carbonate-Free Electrolytes for High-Nickel Layered Oxide Cathodes in Lithium-Ion Batteries. *Adv. Energy Mater.* **9**, 1901152 (2019).

206. Bushkova, O. V., Yaroslavtseva, T. V. & Dobrovolsky, Yu. A. New lithium salts in electrolytes for lithium-ion batteries (Review). *Russ. J. Electrochem.* **53**, 677–699 (2017).

207. Petibon, R. *et al.* Electrolyte System for High Voltage Li-Ion Cells. *J. Electrochem. Soc.* **163**, A2571 (2016).

208. Liu, Q. Q., Xiong, D. J., Petibon, R., Du, C. Y. & Dahn, J. R. Gas Evolution during Unwanted Lithium Plating in Li-Ion Cells with EC-Based or EC-Free Electrolytes. *J. Electrochem. Soc.* **163**, A3010 (2016).

209. Ma, L. *et al.* A Guide to Ethylene Carbonate-Free Electrolyte Making for Li-Ion Cells. *J. Electrochem. Soc.* **164**, A5008 (2016).

210. Logan, E. R. *et al.* A Study of the Transport Properties of Ethylene Carbonate-Free Li Electrolytes. *J. Electrochem. Soc.* **165**, A705 (2018).

211. Xiong, D. J. *et al.* Some physical properties of ethylene carbonate-free electrolytes. *J. Electrochem. Soc.* **165**, A126–A131 (2018).

212. Yu, Y. *et al.* Coupled $LiPF_6$ Decomposition and Carbonate Dehydrogenation Enhanced by Highly Covalent Metal Oxides in High-Energy Li-Ion Batteries. *J. Phys. Chem. C* **122**, 27368–27382 (2018).

213. Zhang, Y. *et al.* Revealing electrolyte oxidation via carbonate dehydrogenation on Ni-based oxides in Li-ion batteries by in situ Fourier transform infrared spectroscopy. *Energy Environ. Sci.* **13**, 183–199 (2020).

214. Lee, H. *et al.* Detrimental Effects of Chemical Crossover from the Lithium Anode to Cathode in Rechargeable Lithium Metal Batteries. *ACS Energy Lett.* **3**, 2921–2930 (2018).

215. Jia, H. *et al.* $LiPF_6$ Stabilizer and Transition-Metal Cation Scavenger: A Bifunctional Bipyridine-Based Ligand for Lithium-Ion Battery Application. *Chem. Mater.* **31**, 4025–4033 (2019).

216. Zhang, X. *et al.* Electrolyte Regulating toward Stabilization of Cobalt-Free Ultrahigh-Nickel Layered Oxide Cathode in Lithium-Ion Batteries. *ACS Energy Lett.* **6**, 1324–1332 (2021).

217. D. Rinkel, B. L., Padmanabhan Vivek, J., Garcia-Araez, N. & P. Grey, C. Two electrolyte decomposition pathways at nickel-rich cathode surfaces in lithium-ion batteries. *Energy Environ. Sci.* **15**, 3416–3438 (2022).

218. Phattharasupakun, N., Bunyanidhi, P., Chiochan, P., Chanlek, N. & Sawangphruk, M. Effect of charging protocols on electrochemical performance and failure mechanism of commercial level Ni-rich NMC811 thick electrode. *Electrochem. Commun.* **139**, 107309 (2022).

219. Research. *Faraday Institution Degradation project* https://degradationproject.com/about/ (2020).

220. Ruff, Z., Xu, C. & Grey, C. P. Transition Metal Dissolution and Degradation in NMC811-Graphite Electrochemical Cells. *J. Electrochem. Soc.* **168**, 060518 (2021).

221. Solchenbach, S., Hong, G., Freiberg, A. T. S., Jung, R. & Gasteiger, H. A. Electrolyte and SEI decomposition reactions of transition metal ions investigated by on-line electrochemical mass spectrometry. *J. Electrochem. Soc.* **165**, A3304–A3312 (2018).

222. Jung, R., Metzger, M., Maglia, F., Stinner, C. & Gasteiger, H. A. Oxygen Release and Its Effect on the Cycling Stability of $LiNi_xMn_yCo_zO_2$ (NMC) Cathode Materials for Li-Ion Batteries. *J. Electrochem. Soc.* **164**, A1361 (2017).

223. Imhof, R. & Novák, P. Oxidative Electrolyte Solvent Degradation in Lithium-Ion Batteries: An In Situ Differential Electrochemical Mass Spectrometry Investigation. *J. Electrochem. Soc.* **146**, 1702 (1999).

224. Jung, R., Metzger, M., Maglia, F., Stinner, C. & Gasteiger, H. A. Chemical versus electrochemical electrolyte oxidation on NMC111, NMC622, NMC811, LNMO, and conductive carbon. *J. Phys. Chem. Lett.* **8**, 4820–4825 (2017).

225. Freiberg, A. T. S., Roos, M. K., Wandt, J., de Vivie-Riedle, R. & Gasteiger, H. A. Singlet Oxygen Reactivity with Carbonate Solvents Used for Li-Ion Battery Electrolytes. *J. Phys. Chem. A* **122**, 8828–8839 (2018).

226. Rinkel, B. L. D., Hall, D. S., Temprano, I. & Grey, C. P. Electrolyte Oxidation Pathways in Lithium-Ion Batteries. *J. Am. Chem. Soc.* **142**, 15058–15074 (2020).

227. D. Rinkel, B. L., Padmanabhan Vivek, J., Garcia-Araez, N. & P. Grey, C. Two electrolyte decomposition pathways at nickel-rich cathode surfaces in lithium-ion batteries. *Energy Environ. Sci.* **15**, 3416–3438 (2022).

228. Terada, Y., Nishiwaki, Y., Nakai, I. & Nishikawa, F. Study of Mn dissolution from $LiMn_2O_4$ spinel electrodes using in situ total reflection X-ray fluorescence analysis and fluorescence XAFS technique. *J. Power Sources* **97–98**, 420–422 (2001).

229. Tsunekawa, H. *et al.* Capacity Fading of Graphite Electrodes Due to the Deposition of Manganese Ions on Them in Li-Ion Batteries. *J. Electrochem. Soc.* **149**, A1326 (2002).

230. Wandt, J. *et al.* Transition metal dissolution and deposition in Li-ion batteries investigated by operando X-ray absorption spectroscopy. *J. Mater. Chem. A* **4**, 18300–18305 (2016).

231. Lee, Y. K., Park, J. & Lu, W. A Comprehensive Study of Manganese Deposition and Side Reactions in Li-Ion Battery Electrodes. *J. Electrochem. Soc.* **164**, A2812 (2017).

232. Dose, W. M., Xu, C., Grey, C. P. & De Volder, M. F. L. Effect of Anode Slippage on Cathode Cutoff Potential and Degradation Mechanisms in Ni-Rich Li-Ion Batteries. *Cell Rep. Phys. Sci.* **1**, 100253 (2020).

Chapter 2. Experimental

2.1 Electrochemical measurements

Battery research is concerned with the movement of ions and electrons with the purpose of storing energy. The research presented in this thesis uses electrochemistry to examine processes that happen at the electrode-electrolyte interface.

2.1.1 Materials

The lithium nickel manganese cobalt oxide (NMC811, $LiNi_{0.8}Mn_{0.1}Co_{0.1}O_2$) and graphite (Gr) electrodes used in Chapter 3 were supplied by LiFun. The lithium titanium oxide (LTO, $Li_4Ti_5O_{12}$) used in Chapter 3 and the NMC811 and Gr electrodes used in Chapter 4 were supplied by the U.S. Department of Energy's CAMP Facility, Argonne National Laboratory. Electrodes were dried under vacuum at 120 °C overnight before being transferred to an Ar-filled glovebox (MBRAUN, <0.1 ppm O_2, <0.1 ppm H_2O) for storage without exposure to air. Metallic Li electrodes used in Chapter 3 and 4 were prepared by roughening the surface of metallic lithium foil (99.9%, Aldrich) to expose pristine lithium, calendared to ensure a uniform surface, and cut into 12 mm or 6 mm diameter disks for use as counter and reference electrodes, respectively.

3 mm glassy carbon (GC) stick electrodes (IJ Cambria) were used for background cyclic voltammetry measurements. A platinum (Pt) counter electrode was used for linear sweep voltammetry reported in Chapter 7, formed through sealing a Pt coiled wire, to ensure a high surface area for charge balancing, in a glass capillary. The reference electrode used in Chapter 7 was partially delithiated lithium iron phosphate (Li_xFePO_4, LFP) soaked in an electrolyte solution of 0.1 M lithium perchlorate ($LiClO_4$, 99.99%, Aldrich) and 1 M tetrabutylammonium perchlorate ($TBAClO_4$, ≥99%, Aldrich) in dimethyl sulfoxide (DMSO, ≥99.5%, Aldrich), which maintains a stable reference potential of 3.45 V vs Li^+/Li in DMSO. To fabricate these electrodes, a LFP putty was made from an 8:1:1 weight ratio of LFP (MTI), conductive carbon additive (Super P, Alfa Aesar), and 10% wt. polytetrafluoroethylene in H_2O (Aldrich), mixed with isopropanol (IPA).

The putty was then spread onto stainless steel (SS) mesh (316 grade, Advent) and allowed to air dry. Delithiation of the LFP is achieved by chemical pre-charging in a solution of 3.6 mL 30% hydrogen peroxide (H_2O_2, 30 wt%. in H_2O, Fisher) and 1.6 mL glacial acetic acid (>99%, Aldrich) in 250 mL deionised H_2O (18.2 MΩ cm, MilliQ) for 15 minutes. The electrodes were twice washed with H_2O before being rinsed with IPA and allowed to air dry. Electrodes were then dried under vacuum at 120 °C overnight before being transferred to a N_2-filled glovebox (MBRAUN, <0.1 ppm O_2, <0.1 ppm H_2O) without exposure to air and soaked in reference electrolyte behind a glass frit. Free-standing LFP electrodes are used as negative electrodes for pressure and rifle cells in Chapters 6 and 7. The LFP putty was made as above before being calendared with no support to a thickness of 350 µm and cut into 12 mm or 24 mm diameter disks. These electrodes were then chemically de-lithiated, dried and stored as previously described.

Electrolyte solutions used in Chapters 3 and 4 were supplied by Solvionic (99.9%, H_2O ≤20 ppm) and used without further purification. Electrolyte solutions used in Chapters 6 and 7 were prepared and stored in an N_2-filled glovebox. Stock solutions were made up of 0.25 M $TBAClO_4$ or $LiClO_4$ in acetonitrile (MeCN, 99.999%, Aldrich), DMSO, dimethoxyethane (DME, ≥99.5%, Aldrich) or tetraethylene glycol dimethyl ether (TEGDME, ≥99%, Aldrich), and doped with deionised H_2O (18.2 MΩ cm, MilliQ) to attain the desired concentration between 0 – 20 M H_2O.

2.1.2 Three electrode electrochemical measurements

All flooded-cell electrochemical measurements performed in Chapter 7 were carried out in a N_2-filled glovebox with a three-electrode configuration consisting of either a 5 mm diameter GC or 5 mm x 5mm (0.5 cm^2) SS mesh working electrode, a Pt coil wire counter electrode, and a LFP reference electrode, prepared as discussed in section 2.1.1. Electrodes were cleaned before each measurement as follows. GC electrodes were mechanically polished by hand using 0.1 µm alumina powder (Buehler) on a neoprene polishing pad, SS mesh electrodes were rinsed with acetone and H_2O, Pt coil

counter electrodes were flame annealed, and the reference housing was rinsed with MeCN, dried, and stored submerged in reference solution.

2.1.3 Linear sweep voltammetry measurements

Linear sweep voltammetry is an electrochemical technique that is commonly used to investigate reduction or oxidation processes of molecular species. The current passed at the working electrode-electrolyte interface is measured as the potential is swept linearly with respect to time. As the potential changes, the fermi level of the electrode is altered and charge-transfer will occur when the energy of the fermi level is sufficiently high or low that it is favourable for the reduction or oxidation, respectively, of a species to occur at the electrode surface through the transfer of an electron.

The linear sweep voltammograms (LSVs) in Chapter 7 were performed in a five-neck heart shaped flask, shown in **Figure 2.1**, to enable the incorporation of a gas inlet and outlet, in addition to the three electrodes, and mitigate O_2 leaks



Figure 2.1. *Photograph of the 5-neck heart-shaped flask used to perform flooded cell LSVs, showing the glass gas inlet (RHS), outlet (LHS), and electrode quick fit joints that mitigate leaks of O_2 into the glovebox atmosphere.*

Into the glovebox atmosphere. The upper and lower limits of electrochemical stability of each electrolyte solution was determined through background cyclic voltammograms that were recorded under N_2. To ensure saturation of the electrolytes with O_2 in Chapter 7, dry electrolytes were bubbled with high-purity O_2 (N5.5, BOC) for periods of 30 seconds, measuring the intensity of the peak current (i_p) with a pristine working electrode after each interval. When further bubbling of the electrolyte did not result in an increase in the intensity of i_p, the electrolyte was considered saturated. The required time for saturation was recorded for each electrolyte studied and used as a minimum requirement for all O_2 redox experiments. 3 minutes of continuous O_2 bubbling was sufficient to saturate all electrolytes studied.

2.1.4 SS flag LSV measurements

The SS flag-shaped electrodes required for the O_2 and H_2O_2 electrochemistry carried out in Chapter 7 were prepared by hand cutting 5 mm × 5 mm (0.5 cm^2) electrodes from SS mesh (316 grade, Advent). A long SS tail was left attached to the electrode to facilitate electrical connection, bearing resemblance to a flag. Care was taken to ensure that the tail was not submerged in the electrolyte solution to allow current to be normalised by geometric surface area. SS flag LSV Measurements were performed in the 5-neck heart shaped flask shown in **Figure 2.1**.

2.1.5 Rotating disk electrochemistry (RDE) measurements

Mass transport in electrochemistry is defined by three processes: 1) diffusion, which occurs in response to a concentration gradient; 2) migration, which occurs in response to a potential gradient; 3) convection, which occurs in response to a pressure gradient. Performing electrochemistry with a rotating electrode generates a laminar flow of material from the bulk solution to the electrode surface. Although the bulk solution is mixed by the rotation of the RDE shaft, a thin layer of solution close to the surface of the electrode rotates with it, remaining effectively stationary relative to the electrode surface. This is called the hydrodynamic boundary layer (δ_H), the thickness of which (typically

100s µm) can be approximated by equation 2.1, where ν is the kinematic viscosity of the solution and ω is the applied angular rotation rate.[1,2]

$$\delta_H = 3.6(\nu/\omega)^{1/2} \quad (2.1)$$

Mass transport of material from the bulk to the hydrodynamic boundary layer is dominated by convection, due to the high rate (e.g. 1000 rpm) of rotation. However, once the material has entered the hydrodynamic boundary layer, its rotation with the electrode renders bulk convection less impactful and the diffusion through this layer to the surface of the electrode becomes the most significant contributor to electrochemical response. Therefore, the electrochemical response measured at a rotating electrode is dominated by the diffusion of analyte across a very thin layer of solution at the electrode surface. The thickness of this diffusion layer (δ_F) can be approximated using equation 2.2, where D_F is the diffusion coefficient of the electrochemically active molecule or ion being studied. δ_F is typically much smaller than the hydrodynamic boundary layer.

$$\delta_F = 1.61 D_F^{1/3} \nu^{1/6} \omega^{-1/2} \quad (2.2)$$

Levich considered the case where only the oxidised form of an analyte is initially present in an electrochemical system and described the limiting current (i_L) observed at a rotating disk electrode when applying a reducing potential with equation 2.3, taking into account the number of electrons transferred in the reduction reaction (n), the concentration of the oxidised species in the bulk (C_O) and its diffusion coefficient (D_O), the electrode area (A), the Faraday constant (F), ν and ω.

$$i_L = 0.620 n F A C_O D_O^{2/3} \nu^{-1/6} \omega^{1/2} \quad (2.3)$$

When i_L is measured experimentally, and all of the other variables are known, equation 2.3 can be applied to calculate the number of electrons transferred in an electrochemical process. This methodology is applied in Chapter 7.

RDE measurements presented in Chapter 7 were recorded using a three-electrode configuration consisting of either a 5 mm diameter GC or SS

ChangeDisk (Pine Instruments) working disk electrode, a fritted LFP reference electrode and a Pt counter electrode. The disk electrodes were polished separately to prevent cross-contamination. The GC and SS disk electrodes were mechanically polished by hand using 0.1 µm alumina powder on a neoprene polishing pad. The electrode was then briefly sonicated in H_2O to remove any residual alumina on the surface, before being dried under vacuum at 70 °C and transferred to a N_2-filled glovebox for cooling. A round bottom five-neck flask was also dried at 70 °C under vacuum and transferred to a N_2-glovebox for cooling. A photograph of the cell setup is shown in **Figure 2.2**. Once the electrodes were cooled, the RDE was assembled and transferred into a N_2-filled glovebox. 10 mL of electrolyte was used for each measurement. As the electrode was rotating, it was not possible to make the five-neck flask gas tight. Saturation was achieved in this system through constant sparging of O_2 in the

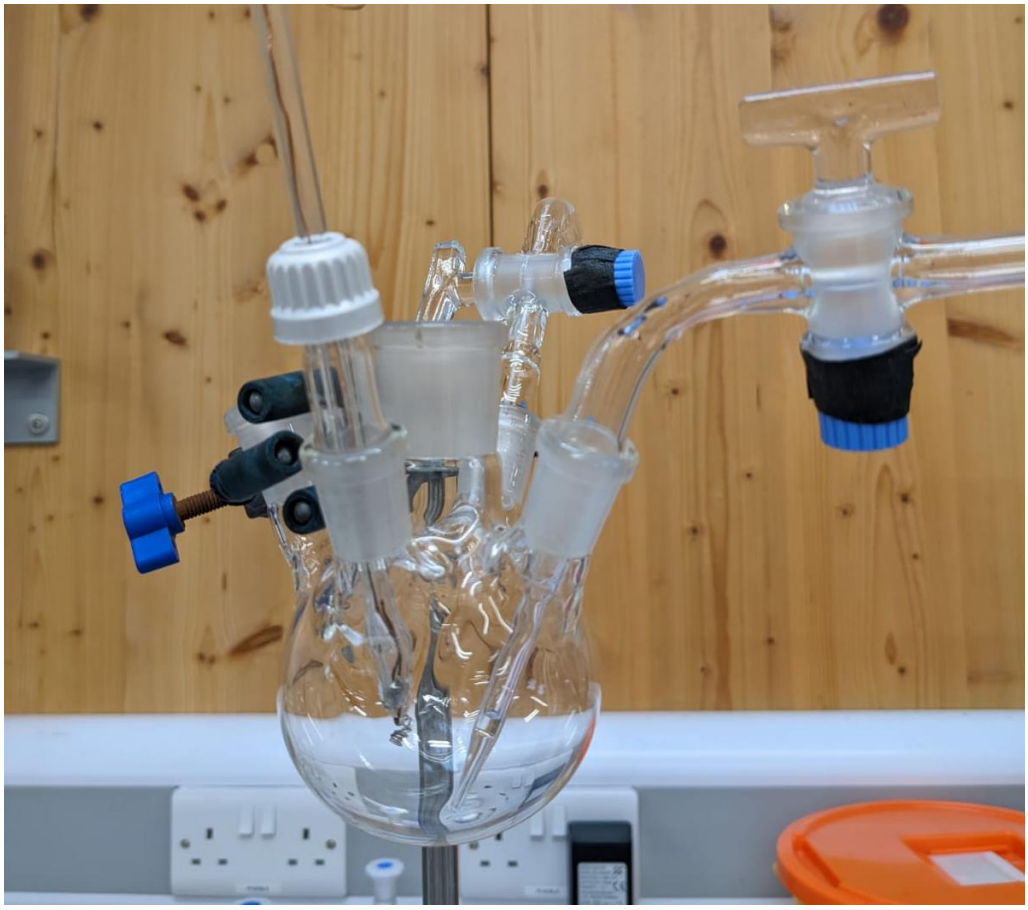


Figure 2.2. *Photograph of the 5-neck flask used to perform three-electrode RDE LSVs, showing the glass gas inlet (RHS), outlet (back), and electrode quick fit joint (front) used to secure the counter electrode. Notably the central fitting, where the RDE sits, cannot be sealed to allow the RDE to rotate.*

cell headspace, while the LSVs were recorded. Between measurements, the RDE electrode and flask were removed from the glovebox and cleaned prior to the next measurement. H_2O_2 measurements were performed under an N_2-atmosphere, with no O_2 sparging of the electrolytes. A 5 mM H_2O_2 concentration was obtained by doping dry electrolyte with a 30 wt.% H_2O_2 solution and deionised H_2O in the required ratio to achieve the desired final H_2O concentration. After addition, the solution was stirred prior to recording a LSV. The RDE electrode and five-neck flask were then removed from the glovebox, cleaned, and dried between measurements.

Following each measurement, the five-neck cell and gas inlet were thoroughly washed with acetone and deionised H_2O and the electrodes were cleaned as previously described. All cell components were dried under vacuum at 70 °C before being transferred into an N_2-filled glovebox whilst hot to mitigate the adsorption of atmospheric moisture.

2.1.6 Solution resistance

When running an electrochemical measurement, it is important to consider that current flow will be affected by the resistivity of the medium that the charge must pass through to facilitate electron transfer. This 'solution resistance' is dependent on both the composition and concentration of the electrolyte solvent and salt and can present a significant contribution to the mass-transfer and charge-transfer properties exhibited in a given system. When examining a specific redox process across a range of electrolyte solutions, understanding and accounting for the effects of solution resistance is essential to allow direct comparison of data. Where solution resistance is significant, a voltage drop (*iR*) is experienced between the reference and working electrodes, which results in deviation from the true value of the potential at the electrode-electrolyte interface. *iR* is a measure of the potential that is required to drive ionic current in solution and can be calculated through electrochemical impedance spectroscopy (EIS) applied in a region where no electrochemical processes occur. *iR* corrections were applied to all LSVs, SS flag, and RDE measurements reported in Chapter 7, through functions built-in to the

relevant potentiostat software. LSV and SS flag measurements were recorded on a BioLogic SP-300 potentiostat and RDE measurements were recorded using a CHI 1140C potentiostat.

2.1.7 Two-electrode lithium-ion (Li-ion) cell cycling

The lithium-ion cell housing used in Chapters 3 and 4 consisted of a ½" inch diameter SS Swagelok union and two ½" diameter SS metal rods used as current collectors. A schematic representation is shown in **Figure 2.3**. The internal surface of the union was lined with 50 µm polytetrafluoroethylene (PTFE, RS Components) film and the rods were secured in place using PTFE ferrules to prevent an internal short circuit. Two Whatman glass fibre separators (GF/F) soaked in electrolyte were used to facilitate Li^+ transport between the electrodes. Cells were half-assembled in air before being dried at 70 °C and transferred whilst hot to an Ar-filled glovebox, where they were stored prior to assembly. Lithium-ion cell cycling was performed on an Ivicycle200 potentiostat. The cell temperature was controlled as required by housing the cells in an oven (40 °C) or incubator (20 °C).

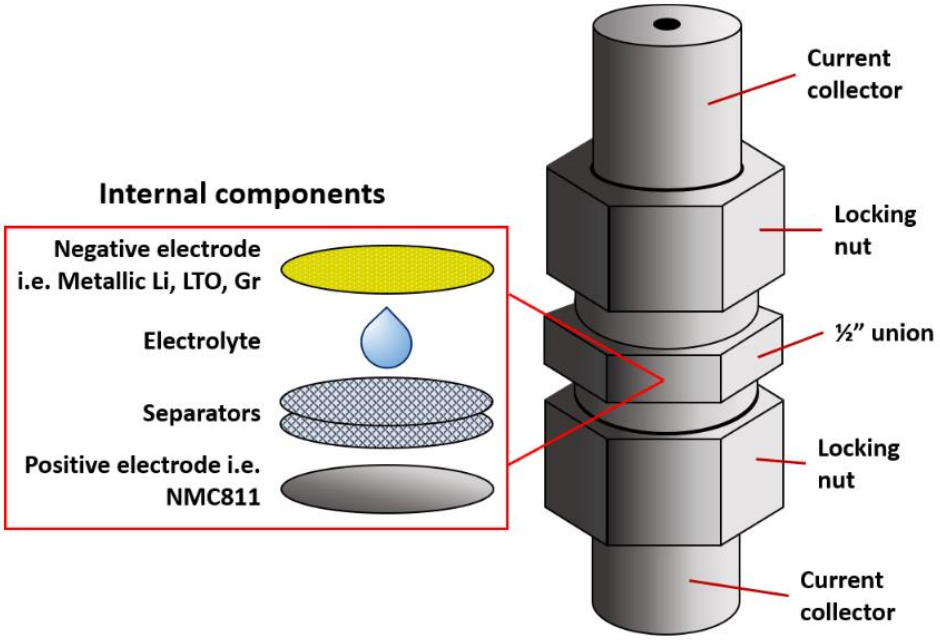


Figure 2.3. *Schematic representation of two-electrode lithium-ion battery cells comprised of a ½" Swagelok union.*

2.1.8 Three-electrode electrochemical impedance spectroscopy

Ohm's law defines electrical resistance as a ratio between potential (E) and current (I) as given in equation 2.4.

$$R = E/I \tag{2.4}$$

However, this relationship is limited to an ideal resistor, wherein resistance values are independent of frequency and alternating current and potential signals through the resistor are in phase with each other (i.e. the response to environmental changes is instantaneous). In reality, circuits are much more complex and can resist the flow of electrical current, which results in a phase shift between the current and potential signals (i.e. delayed response to an applied bias). This imperfect relationship is described by impedance.

Electrochemical impedance is measured by applying a small alternating current or potential to an electrochemical system and tracking the response of the other variable. The alternating nature of the applied bias results in a sinusoidal wave, as described by **Figure 2.4** for the case of an applied potential and the resultant measured current. Given that potential and current are intrinsically linked, as the potential is changed, the current responds to this change, producing a sinusoidal response with a phase shift (ϕ) relative to the response time. Equation 2.5 can be applied to assess the applied potential as a function of time (t), where ω is the radial frequency (radians/s) which is directly proportional to the frequency (*f,* Hz) of the alternating signal (described in equation 2.6).

$$E_t = E_0 \sin(\omega t) \tag{2.5}$$

$$\omega = 2\pi f \tag{2.6}$$

The magnitude of the current response (I_t) at a given time (t) is shifted in phase by a factor of ϕ. Therefore, it will have a different amplitude to E, described by equation 2.7, which accounts for this phase-shift.

$$I_t = I_0 \sin(\omega t + \phi) \tag{2.7}$$

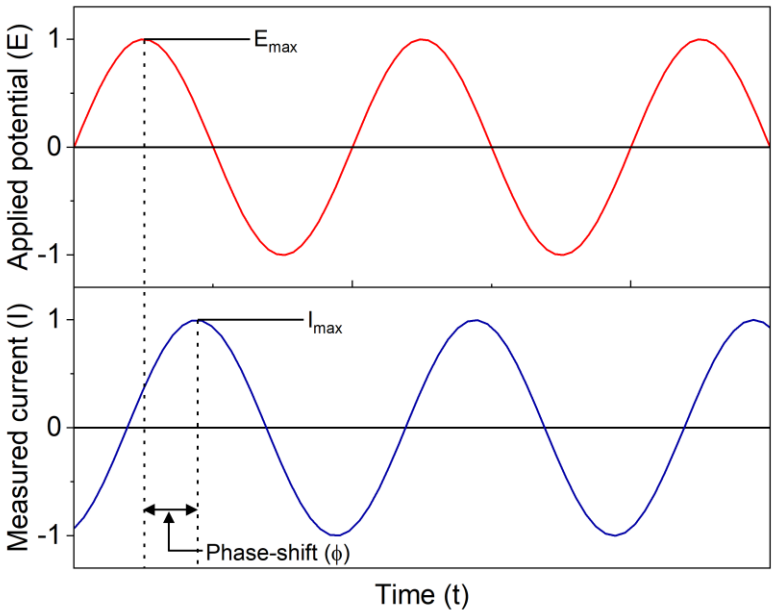


Figure 2.4. *Plot showing the current response (I) of a circuit to an applied potential (E), identifying the phase-shift experienced as a result of electrochemical impedance.*

By substituting equations 2.5 and 2.7 into Ohm's law (equation 2.4) and understanding that R = impedance (Z) in this case, we arrive at equation 2.8 which describes the impedance of a process at a given frequency.

$$Z = \frac{E\sin(\omega t)}{I\sin(\omega t + \phi)} \qquad (2.8)$$

An electrochemical reaction at an electrode-electrolyte interface is comprised of multiple steps (i.e. mass transport, charge transfer, diffusion), each of which can occur at different and distinct rates. Each of these steps is time-dependent and they may occur on different timescales. Put simply, processes that happen at a low rate will not have time to react when a high frequency perturbation is applied to a system, resulting in their contribution to the impedance at high frequencies being negligible. Likewise, at low frequencies, fast processes have time to equilibrate in response to the applied bias, resulting in their contribution to the measured impedance being negligible at low frequencies. Therefore, by scanning across a frequency range from high (100s kHz – MHz) to

low (mHz), the impedance of all processes that take place at an electrode-electrolyte interface can be examined by their rate.[3]

Impedance is made up of two parts: 1) a real contribution (Z_r), which measures the resistance of a process, and 2) an imaginary contribution (Z_{im}), which accounts for the build-up of energy (i.e. capacitive and inductive reactance) through the process. The sum of these contributions generates the impedance of a system at a given ω, as shown in equation 2.9, where j is the imaginary number (i.e. $\sqrt{-1}$).

$$Z(\omega) = Z_r + jZ_{im} \qquad (2.9)$$

Where electrochemical impedance spectroscopy (EIS) is performed in a two-electrode setup, the response contains contributions from both the working electrode (the electrode of interest) and the counter (pseudo reference) electrode. This complicates the interpretation of the impedance response, so a three-electrode design was used in Chapter 3, which enables the positive electrode impedance response to be isolated. The three-electrode EIS cell used in Chapter 3 consisted of a ½" inch diameter PFA T-piece and three ½" diameter SS metal rods used as current collectors. A schematic representation is shown in **Figure 2.5**. The PFA cell housing meant that no insulating PTFE film was

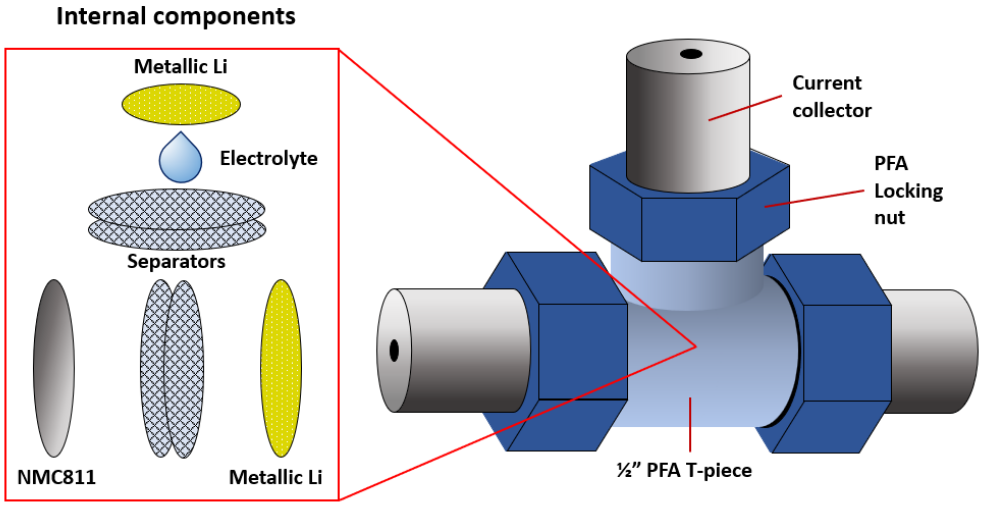


Figure 2.5. *Schematic representation of three-electrode lithium-ion battery cells comprised of a ½" PFA Swagelok T-piece used to perform EIS measurements in Chapter 3.*

required, however, the addition of extra separators and electrolyte were required to enable incorporation of the metallic Li reference electrode. Two glass fibre separators soaked in electrolyte were used between the positive and negative electrodes, with a further two separators and the 6 mm metallic lithium reference electrode being placed perpendicular to the other electrodes. Cells were half assembled outside of the glovebox, before being dried at 70 °C, and transferred hot to an Ar-filled glovebox where they were stored prior to assembly. Cell cycling and EIS measurements were performed on an Ivium Octostat30 potentiostat. The cell temperature was controlled throughout measurements by housing the cells in an oven at 40 °C.

Nyquist plots, which demonstrate the mass transfer and kinetic behaviour of a system, were used in Chapter 3 to understand the impedance growth of an NMC811 positive electrode as a function of extent of cycling. Data was obtained over a range of 10 mHz to 1 MHz, however, due to erroneous values being recorded at frequencies <100 mHz and >2000 Hz, these datapoints were excluded from the presented analysis. Albeit not ideal, the impedance of the cathode electrolyte interphase (CEI) falls within these bounds, enabling assessment of impedance growth within these data restrictions.[3–5]

An equivalent circuit diagram, shown In **Figure 2.6,** was built to fit the impedance data reported in Chapter 3.[6] The equivalent circuit diagram used to fit the impedance data, consisting of a resistor connected to two parallel circuits. The resistor represents the solution resistance (R_S), which describes the physical movement of ions through the solution between the working and reference electrodes. R_S is an intrinsically high frequency process and is influenced by factors such as Li^+ concentration, cell temperature, and electrolyte viscosity. The first parallel circuit relates to the charge transfer resistance (R_{CT}), which considers the movement of electrons into and out of the NMC811 electrode and the complementary diffusion of Li^+ into and out of the surface of the electrode, and the capacitance (Q_1) within this phase. The second parallel circuit concerns Li^+ diffusion through the CEI film (R_{CEI}), the capacitance within this phase (Q_2), and a Warburg element (W), which is a constant phase

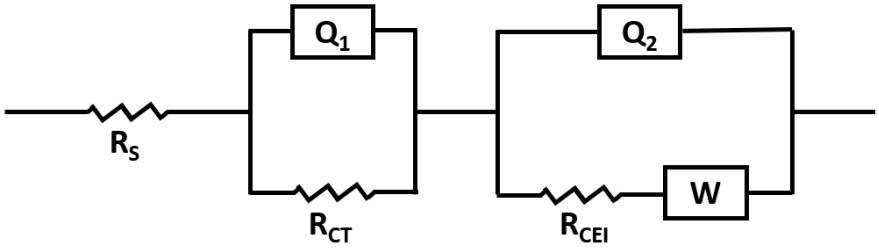


Figure 2.6. *Equivalent circuit diagram used to fit the impedance response of Li-NMC811 half-cells in Chapter 3. The circuit includes contributions from solution resistance (R_S), charge transfer resistance (R_{CT}), Li^+ diffusion resistance of the CEI (R_{CEI}), capacitance (Q_x) and a Warburg element (W).*

element that models Li^+ diffusion through the CEI. **Figure 2.7** shows a Nyquist plot for the isolated response of a NMC811 electrode in a three-electrode Li-NMC811 half-cell after two formation cycles at C/20. Within the region of data collection, two clear processes are observed. The higher frequency process being R_{CEI} and the lower frequency process being R_{CT}. R_S and W are outside of the data collection range, but their anticipated response is shown with dashed grey lines for clarity.

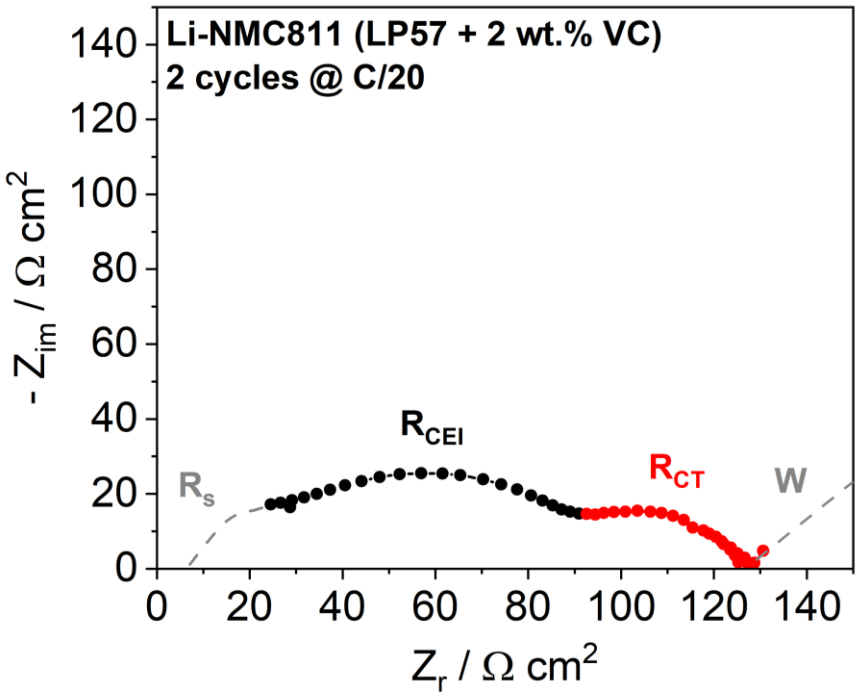


Figure 2.7. *Example Nyquist plot showing the CEI resistance (R_{CEI}, black) and charge-transfer resistance (R_{CT}, red) of an NMC811 electrode measured in a three-electrode Li-NMC811 half-cell after two C/20 formation cycles. Dashed grey lines show the expected trends of the solution resistance (R_S) and Warburg element (W) if the range of data was extended.*

2.1.9 Two electrode lithium-air (Li-air) cell cycling

The pressure cells that were used for *in situ* pressure analysis in Chapters 6 and 7 were built in-house and consisted of a 1" diameter Swagelok fitting, adapted with a port to facilitate electrical connection as the base of the cell housing. On assembly, the base was sealed with a head built in-house containing Swagelok valves, which facilitated the sparging of the cell headspace with O_2, and a pressure transducer (Omega Engineering). A schematic of this cell configuration is shown in **Figure 2.8**. The measured pressure changes are the result of gases in the headspace of the cell being consumed or released throughout cycling. In the Li-air battery, O_2 consumption and evolution are the dominant contributors to pressure change for the discharge and charge processes, respectively. 24 mm free-standing LFP electrodes were used as the negative electrode and two 24 mm carbon paper (H23, QuinTech) disks, topped with a SS mesh current collector, were used as the positive electrode. These electrodes were separated by two glass fibre separators and soaked in 800 µL of electrolyte. The volume of the cell headspace (ca. 12 cm^3) is determined largely by the addition of two SS spacers that were placed on top of the SS mesh current collector. The internal surface of the base was lined with 125 µm PTFE film to prevent an internal short circuit.

Pressure cells were assembled in a N_2-filled glovebox and O_2 (N5.5, BOC) was sparged slowly through the system by opening the valves in the head of the cell. The valve at the centre of the head allows the gas stream to either flow directly through the cell, or bypass through the top valves to enable periodic sparging of the headspace. Cells that used DMSO- or TEGDME-based electrolytes were sparged for >2 minutes with a constant flow of O_2, which was first passed through a drying column to mitigate H_2O intrusion. Cells that used DME- or MeCN-based electrolytes required periodic sparging, where the gas flow was sparged for 4 sets of 15 s open, 15 s bypass to mitigate evaporation of the electrolyte solvent. Once sparged, the valves were sealed and the cell was placed in a bench-top incubator at 20 °C. An Octostat30 potentiostat was used to enable electrochemical and pressure data to be recorded simultaneously.

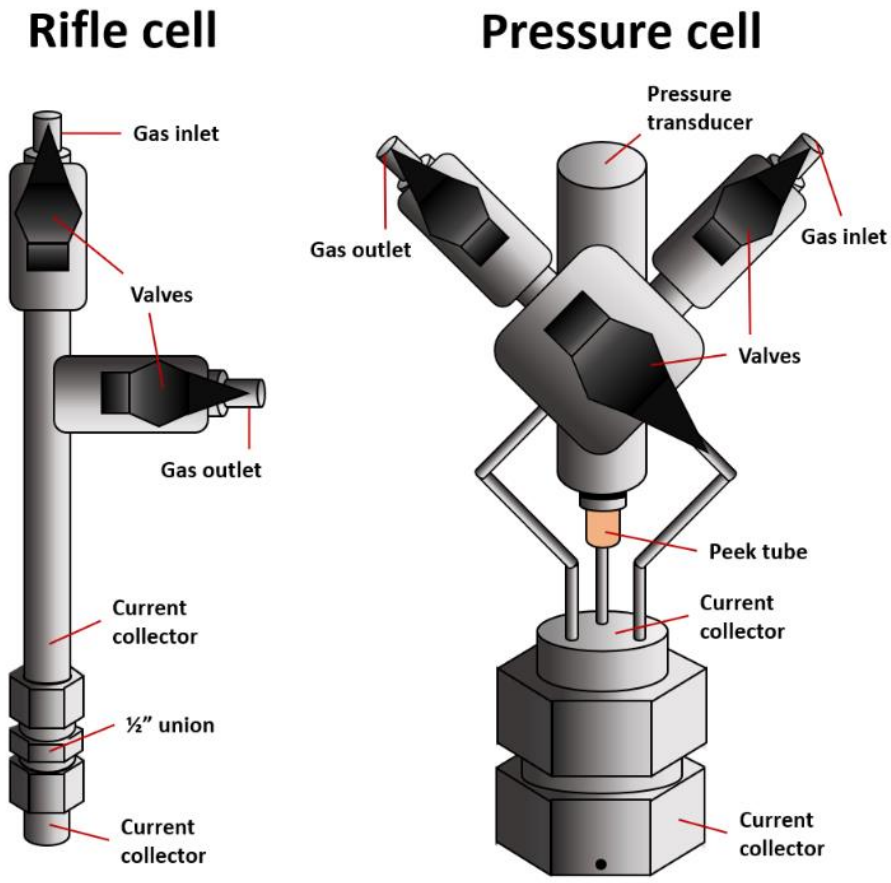


Figure 2.8. *Schematic representation of a Li-air rifle cell (LHS) and pressure cell (RHS) used in Chapters 6 and 7.*

Cells were allowed to thermally equilibrate for several hours before initiating cycling.

Each pressure cell has a bespoke calibration tube that is assigned to one of the valves at the top of the pressure cell. This calibration tube facilitates the calculation of the exact headspace volume for any given experiment through the application of equation 2.10, which is derived from re-arrangement of the ideal gas equation for the sum of the isolated parts (equation 2.11).

$$V_{PC} = \frac{P_{CT}V_{CT} - P_{total}V_{CT}}{P_{total} - P_{PC}} \qquad (2.10)$$

$$P_{total}V_{total} = P_{PC}V_{PC} + P_{CT}V_{CT} \qquad (2.11)$$

The exact volume of the calibration tube and the paired valve (V_{CT}) are calculated by measuring the difference between the weight when empty and

the weight when filled with IPA. The exact volume of the pressure cell (V_{PC}) can then be calculated using equation 2.9 and recording three pressures. The pressure of the calibration tube (P_{CT}) is measured by applying a vacuum to the cell with the calibration tube open and allowing the cell to reach equilibrium before isolating the calibration tube (the pressure when isolated is P_{CT}). A different value for the pressure of the pressure cell (P_{PC}) can then be achieved by opening the main body to atmosphere before closing the valve to isolate it (i.e. P_{PC} = atmospheric pressure). Finally, the calibration tube is opened to the main body of the pressure cell, resulting in a pressure drop, which provides the total combined pressure (P_{total}). The calibration of the absolute headspace volume of the pressure cell allows a ratio of the number of electrons passed per molecule of oxygen (e^-/O_2) to be calculated by comparing the total charge passed and the number of O_2 molecules consumed or released in a given discharge or charge process, respectively.

Where quantitative gas analysis was not required, a simpler cell design was used to facilitate the efficient collection of cycling data and prepare samples for characterisation. These cells, shown in **Figure 2.8**, are referred to here as rifle cells due to the resemblance they bear to a rifle. The long hollow rod provides a large headspace O_2 volume to electrode surface area ratio, which ensures sufficient O_2 availability for cell cycling. The valves at the top of the cell allow the headspace to be sparged with O_2. Cells were filled with the gas line pressurised to 1.4 bar with a constant gas flow for 10 s followed by 10 s with the outlet closed. The cells were then sparged by opening and closing the outlet for 1 s bursts 10 times and then closing the outlet for 10 s. This sparging procedure was repeated 3 times before the cell was sealed, removed from the glovebox, placed in a bench-top incubator at 20 °C and allowed to thermally equilibrate for several hours before initiating cycling. Cell cycling was performed on an Octostat30 potentiostat.

2.1.10 SS-free (PFA) two-electrode Li-air cells

The SS-free Li-air cell housing used in Chapter 7 consisted of a ½" diameter PFA Swagelok union with one ½" peek rod used to seal the bottom half of the cell, and a hollowed out peak cylinder used to hold the stacked cell in place. A schematic representation is shown in **Figure 2.9**. A carbon paper electrode with a long tail was placed below the 12 mm free standing LFP negative electrode to enable electrical connection. Two glass fibre separators were soaked in electrolyte and placed on top of the negative electrode. One 12 mm carbon paper electrode, with a long tail was then placed on top of the separator stack, before a second 12 mm carbon electrode was placed on top and sealed in place with the hollow peak rod, wrapped in 125 µm PTFE. Electrical connection to the negative and positive electrodes was achieved by attaching clips to the tails of the relevant carbon paper electrodes. The PFA cell was stored in sealed containment within a N_2-filled glovebox which was sparged with O_2 through a built-in gas inlet and outlet. A glass bottle containing H_2O was also stored in this containment to ensure 100% relative humidity (20 °C) was maintained throughout analysis. Cycling was performed on an Octostat30 potentiostat in an incubator at 20 °C.

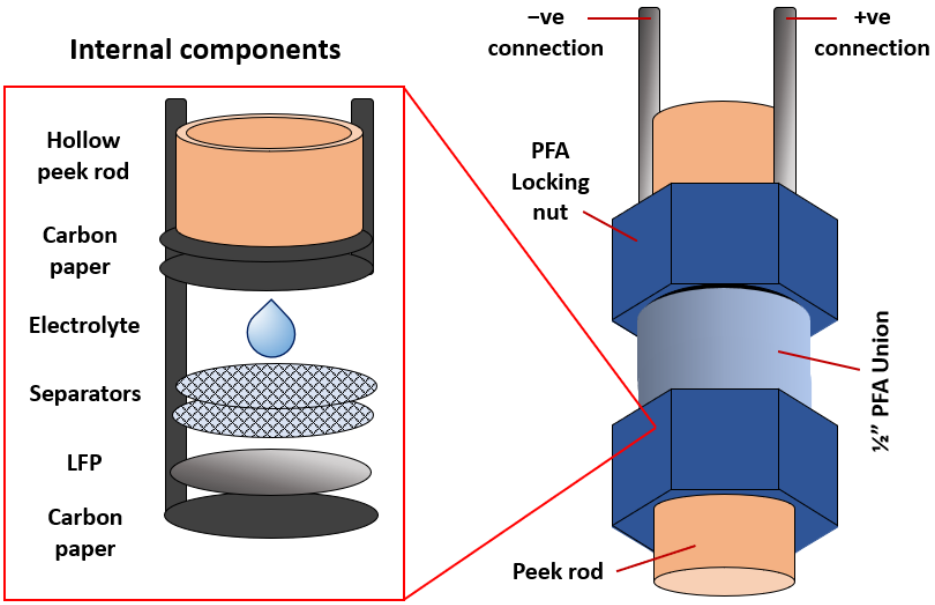


Figure 2.9. *Schematic representation of two-electrode SS-free Li-air battery cells comprised of a ½" PFA Swagelok union.*

2.2 Chromatography

Chromatography, used in Chapters 3, 4, and 6 is a technique that separates molecular species through their relative affinity for a solid immobile interface (stationary phase) and a carrier medium (mobile phase). Analyte is transferred into the column, where it encounters the stationary phase. Where interactions between the analyte and the stationary phase are sufficiently strong, the analyte will adsorb to the stationary phase, resisting the flow of the mobile phase and remaining close to the inlet. On the contrary, where these interactions are weak, the analyte will not bind to the stationary phase and instead travel through the column, carried by the mobile phase until it reaches the outlet.

Consequently, for analytical chromatography it is imperative that the species of interest have adequately different affinities for the selected stationary phase and mobile phase combination, to facilitate separation as they pass through the column. The time taken for a species to pass through the column, termed the retention time, is specific to a species under set conditions and is highly reproducible where conditions are controlled. When the analyte reaches the end of the column, identification can be performed using several analytical techniques. In Chapters 3, 4 and 6 MS is used to identify molecular species and in Chapters 4 and 6 UV-Visible (UV-Vis) spectroscopy is used.

2.2.1 Gas chromatography (GC) mass spectrometry (MS)

GC-MS is a chromatography technique that separates molecular species through their relative affinity with the column coating (stationary phase) and a carrier gas flowing through the column (mobile phase) as a function of temperature. Analyte is vapourised and transferred onto the column, where it condenses onto the column coating. The column is usually held at a relatively low temperature (30 – 50 °C) at the start of a procedure to improve the interaction between the analyte and the stationary phase. As the temperature of the column increases, species that are weakly bound to the coating begin to desorb from the surface and travel through the column, carried by the flow of gas. Where interaction between the analyte and the column is strong, species

will reach close to their boiling point before beginning to desorb from the column. Thus, species are separated by their affinity with the column coating as a function of temperature. The instrument is equipped with a ISQ single quadrupole mass spectrometer which samples the outlet, enabling mass spectral characterisation of species as they exit the column. An example of a temperature ramp procedure, and resultant chromatogram are shown in **Figure 2.10**.

GC-MS samples in Chapters 3 and 4 were prepared by disassembling cells in a Ar-filled glovebox, extracting the separators and soaking them in $CDCl_3$ for at least 30 minutes. This resulted in the precipitation of a large amount of the $LiPF_6$ electrolyte salt, evidenced in Chapter 3. Samples were analysed using a Thermo Fisher TRACE1300/1310 gas chromatograph coupled to an ISQ single quadrupole mass spectrometer. A 30 m Rtx-1701 mid-polarity crossbond phase column with an inner diameter of 0.25 mm and a coating thickness of 0.25 µm was equipped to the inlet. The carrier gas was helium (99.999%) at a constant

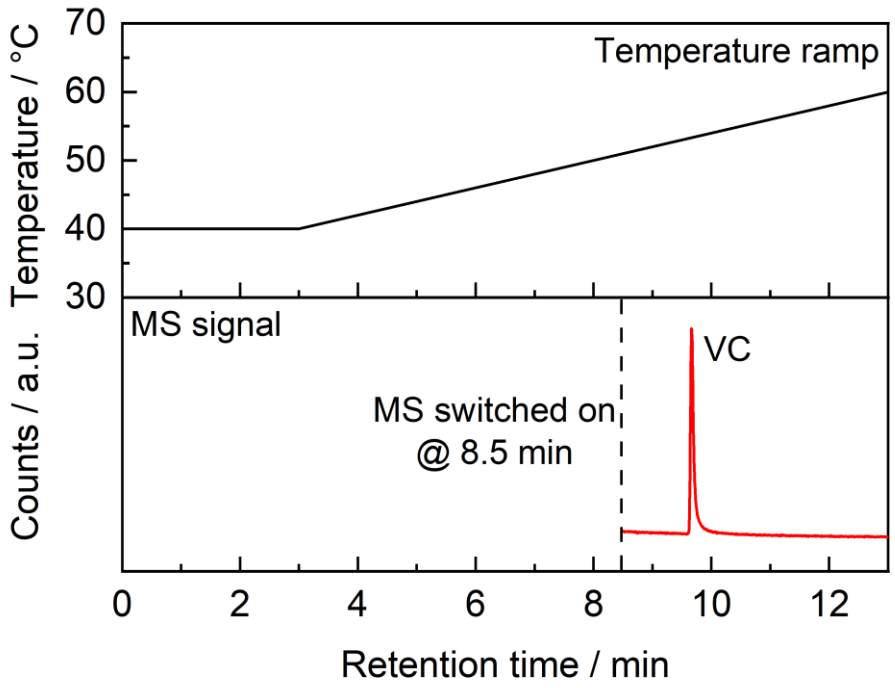


Figure 2.10. *Example GC-MS temperature ramp procedure (black line) and MS signal (red line) from a method developed for vinylene carbonate (VC) detection in Chapters 3 and 4.*

Flow of 1.5 mL min^{-1}. Specific procedures are described in the experimental section of each relevant chapter. A blank injection of methanol (HPLC grade, ≥99.9%, Aldrich) was run between each injection to prevent contamination between sample injections. Data were analysed using Chromeleon software to identify the composition of chromatogram peaks, cross-referencing mass spectra with the National Institute of Standards and Technology (NIST) mass spectral library.[7]

2.2.2 High performance liquid chromatography (HPLC) mass spectrometry (MS)

HPLC is a chromatography technique that separates molecular species through their relative solubility in the eluent (mobile phase) compared to their affinity for the column coating (stationary phase). Analyte is injected into the column, where its solubility is the key determinant of rate of transfer through the column. Where analytes have sufficiently different solubilities in an eluent, an isocratic method can be applied, wherein a single eluent composition is flowed through the column separating the analytes based purely through their solubility in the chosen eluent. Where this is not possible, mixed solvent systems and ramped methods, wherein eluent composition changes throughout the measurement can be used to enhance selectivity and improve analyte separation. An example of a ramped HPLC-MS method, used in Chapter 4, is shown in **Figure 2.11**.

HPLC measurements were carried out on a Thermo Ultimate 3000 HPLC, equipped with a diode array detector capable of recording UV-Vis spectra from 190 – 800 nm. For HPLC-MS measurements, a Bruker microTOF II spectrometer with an electrospray ionisation source was connected to the HPLC outlet. Sample preparation and injection volumes are stated in the experimental section of the relevant chapter.

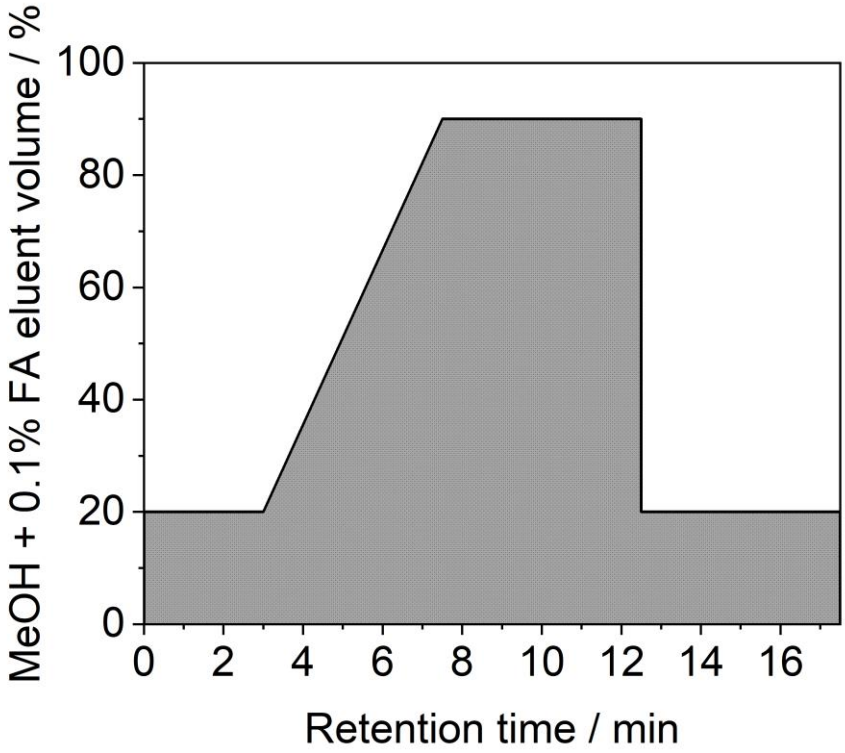


Figure 2.11. *Example ramped eluent HPLC method applied in Chapter 6, wherein the vol.% of MeOH doped with 0.1% formic acid is varied throughout the measurement to facilitate good analyte separation. 0.1% formic acid in H_2O made up the remainder of the eluent composition.*

2.3 On-line mass spectrometry (OEMS)

OEMS is a technique wherein an electrochemical cell is interfaced with a mass spectrometer, facilitating continuous sampling of gaseous species produced during the operation of an electrochemical cell. The OEMS used in Chapter 7, designed and manufactured by the University of Nottingham Mechanical Workshop, was based on the designs published by *Tsiouvaras et al.*[8] and coupled to a quadrupole mass spectrometer (Hiden Analytical), shown in **Figure 2.12**. OEMS measurements, reported in Chapter 4, were performed by Dr Israel Temprano at the University of Cambridge on a similar instrument to the one described here. A connection is made between the sealed headspace of the cell and the mass spectrometer, through which a flow of gas of known composition is diverted. The constant flow of gas through the cell facilitates sampling of the cell headspace, identifying the presence of gases or more broadly volatile species, as they are produced during the measurement.



Figure 2.12. *Photograph of the on-line electrochemical mass spectrometer built in-house by the University of Nottingham Mechanical Workshop.*

It is important to calibrate a given OEMS instrument before performing measurements to ascertain the relative sensitivity factor (RSF) of molecular species. The RSF describes the signal intensity observed for a given molecular species relative to a reference species. Given that in the systems studied in this thesis Ar is used as the balancing gas, if we take Ar has having a RSF of 1, all other species must be calibrated relative to this. The RSF takes into account all of the factors that can affect a molecular species between flowing past the MS transfer capillary to being detected at the MS detector. Many factors including inlet sensitivity (R_I), source sensitivity (R_{SO}), extent of fragmentation (R_F), extent of quadrupole transmission (R_Q) and detection efficiency (R_D) of a given species can affect the total RSF value. These factors are cumulative in nature, with the RSF being comprised by the product of these factors (equation 2.12).

$$RSF = R_I \times R_{SO} \times R_F \times R_Q \times R_D \qquad (2.12)$$

R_I measures the direct selectivity of a species from the flowing gas stream into the MS transfer line relative to the reference species (i.e. Ar). R_{SO} and R_F are

related to the source energy, ionisability, and stability of the species under ionising conditions and describe the sensitivity of the instrument to the generation of species that can travel through the quadrupole relative to the reference species. R_Q and R_D are highly instrument dependent and describe the ability of species, once ionised, to travel through the quadrupole and be detected at the MS detector relative to the reference species. The RSF can be calculated experimentally by flowing a gas of known composition past the MS transfer line and recording the intensity of the MS signal of the target species against that of the reference sample. Taking the referencing of O_2 to Ar as an example, a calibration gas consisting of 1% O_2 and 1% Ar, balanced with N_2, could be flowed through the system. If a RSF of 1 was achieved for O_2 and Ar, then the signal intensities at a mass to charge ratio (m/z) of 32 and 40 would be identical. However, experimentally O_2 has a lower RSF than Ar, which results in a RSF <1, determined by the specifics of the instrument being calibrated. For each OEMS measurement performed in this thesis, the instrument was calibrated as discussed below.

2.3.1 Li-ion measurements

The OEMS measurements reported in Chapter 4 were performed on a Li-NMC811 half-cell through its first charge up to an upper cut-off voltage of 4.6 V, through a 40-hour subsequent voltage hold, before being discharged to 2.5 V vs Li^+/Li. The cells paired an 18 mm NMC811 positive electrode with a 15.6 mm metallic Li electrode and a metallic Li chip reference electrode, separated by two glass fibre separators soaked in 300 µL of electrolyte. This experiment was designed to push the NMC811 electrode into a region of high oxidative reactivity with the organic electrolyte components, wherein it has been previously reported that lattice oxygen release from the transition metal oxide surface would be observed, alongside CO_2 and CO generated through the oxidation of the electrolyte solvent.[9,10] This OEMS system consisted of a SS tube which carried gas through the electrochemical cell, connected through self-sealing quick-connects (Beswick Engineering) to a mass spectrometer, so that the system was never exposed to air. Ar (N6.0, BOC), connected to a gas purifier

before flow control, was used as the carrier gas. A quadrupole mass spectrometer (Pfeiffer) was connected to the cell through a heated capillary (120 °C) to prevent condensation of volatile species and controlled with an Ivium potentiostat.

Calibration was performed by flowing a gas of known composition (1000 ppm of H_2, CO, O_2 and CO_2, balanced with Ar) through the system to establish a correlation between channel ion currents and gas molar flow. The molar flow of CO was established by subtracting the proportional amount of CO_2 measured at a m/z of 44 from the m/z of CO (28) according to the relative intensities of the isotope pattern of CO_2.[11] The CO fragment of CO_2 has a 9.81% relative intensity compared to the CO_2 molecular ion peak.

2.3.2 Li-air measurements

The differential electrochemical mass spectrometry (DEMS) cycling experiments, reported in Chapter 7, were recorded on the in-house built OEMS described above, using an isolated loop which housed a bespoke DEMS cell, shown in **Figure 2.13**, labelled 'DEMS cell'. The cell housed a 24 mm freestanding LFP negative electrode and a porous carbonaceous cathode, electrically isolated by 26 mm glass fibre separators. SS mesh was placed on top of the cathode to ensure good electrical contact. The electrolyte volume used in these measurements was 600 µL. Prior to discharge, the cell was assembled in a N_2-filled glovebox and transferred to the isolated loop with minimal exposure to air. The headspace was then sparged with a 20% O_2, 80% Ar gas mixture (99.999%, CK Isotopes) for at least 24 hours, or until the mass signals had reached equilibrium, ensuring that any air contamination had been purged and the electrolyte has reached equilibrium concentration with the headspace. Where humid gas streams were required, humidifying solutions were attached upstream of the DEMS cell to bubble the carrier gas through. 13% and 100% relative humidities were achieved by diverting the gas through either a saturated LiCl in H_2O or pure H_2O solution, respectively.[12] The cells were cycled

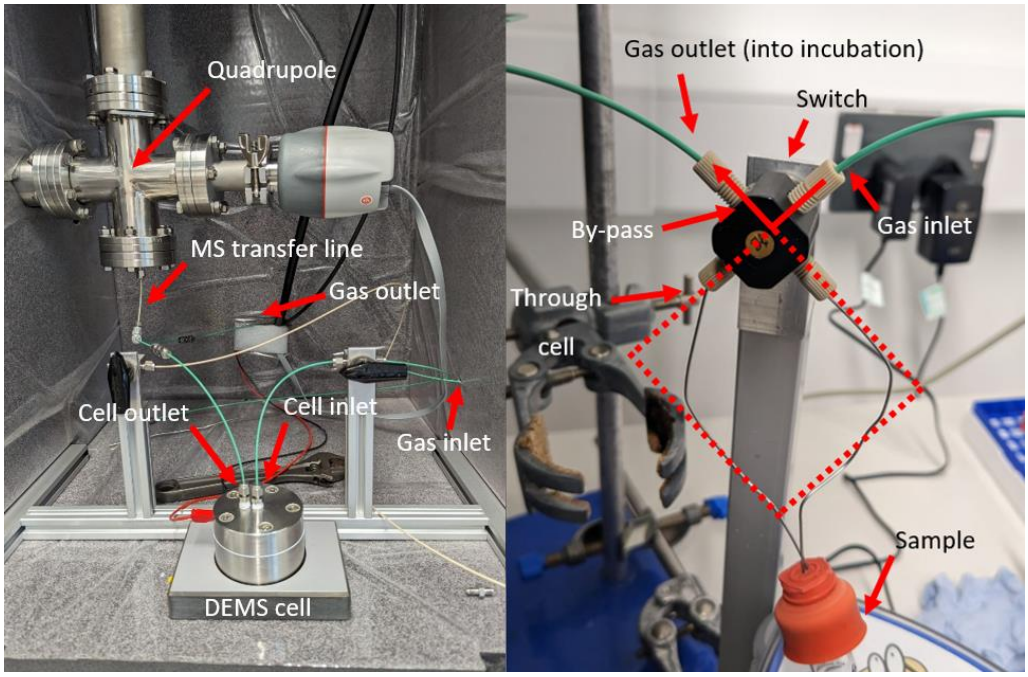


Figure 2.13. *DEMS cell setup (LHS) and OEMS setup (RHS) showing the flow of gas through the respective cell and into the MS transfer line. Valves are used to moderate the path of gas flow to minimise sample exposure to air.*

in insulated containment at 20 °C. An example Li-air DEMS response over the first cycle is shown in **Figure 2.14**. The quantity of O_2 consumed in the discharge process, and produced in the charge process, is calculated by comparing the MS plateau pressure to a calibration fit, created by flowing calibration gases through the gas lines. The calibration fit, shown in **Figure 2.15**, was calculated using two calibration gas compositions: 1) 1% O_2, 1% Ar, balance N_2, which also allowed the relative sensitivities of Ar and O_2 to be calculated, and 2) 17% O_2, balance Ar. These were compared to the signals of the 20% O_2, 80% Ar gas that was used for measurements. All gases were supplied by CK Isotopes (99.999%). A linear relationship between MS response and O_2 concentration is assumed.

For KO_2 chemical disproportionation experiments, performed in Chapter 7, a MS vial was filled with a known quantity of KO_2 (ca. 5 mg) in an Ar-filled glovebox and capped with a rubber bung. The vial was then transferred onto a section of the inlet gas line that is isolated by a 4-way valve, shown in **Figure 2.13**. The carrier gas was then diverted through the vial, allowing Ar (99.999%, CK Isotopes) to flow through the headspace of the vial.

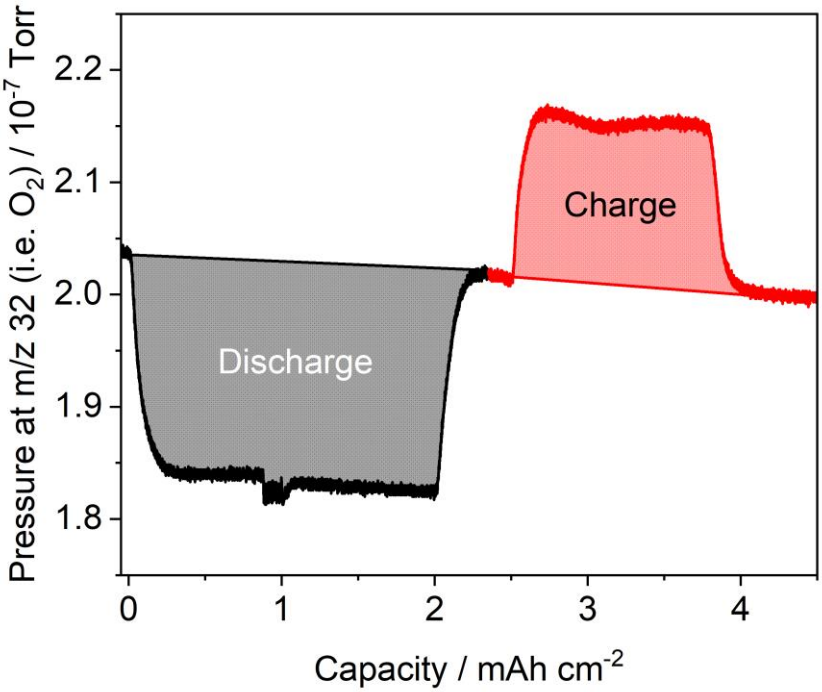


Figure 2.14. *Example MS response showing O_2 consumption (black) and evolution (red) during the first discharge and charge processes, respectively, of a Li-air DEMS cell.*

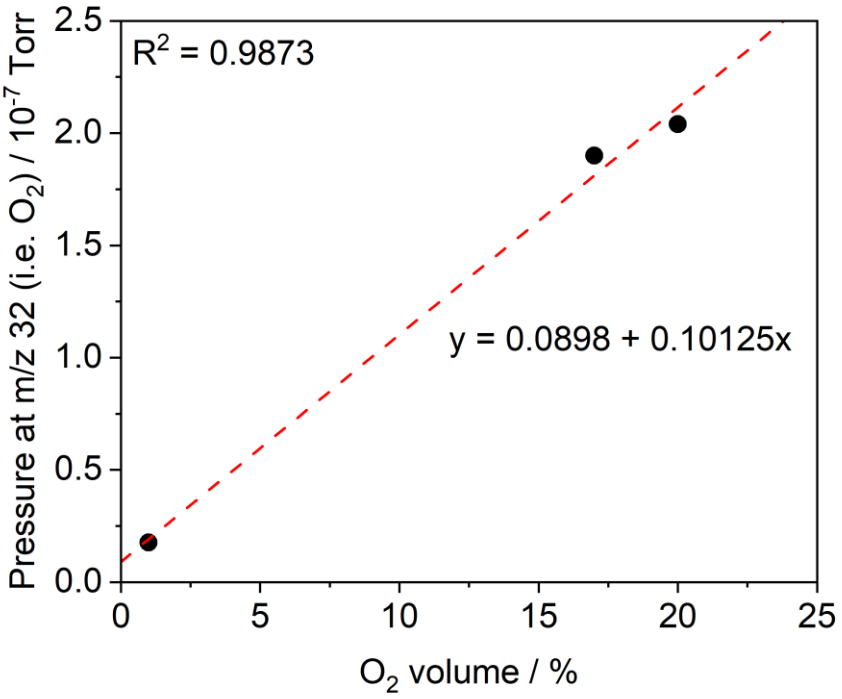


Figure 2.15. *DEMS calibration fit assuming a linear relationship between O_2 volume and MS signal intensity.*

The diversion of the gas stream using the 4-way valve resulted in some air contamination of the sample, due to residual air in the SS needles. However, the MS signals were allowed to reach equilibrium, indicating that any air has been removed from the system, before the disproportionation reaction was initiated by the addition of the desired electrolyte mixture. Electrolyte mixtures were prepared as described in section 2.1.1. The addition of lithiated electrolyte results in disproportionation of KO_2 and the release of O_2 gas, the quantity of which was normalised to the mass of KO_2 to calculate the moles of O_2 evolved per mole of KO_2 consumed. Blank injections, where the vial contained no KO_2, were recorded to ensure that the injection of the electrolyte did not introduce additional O_2 contamination. An example MS response for a KO_2 disproportionation experiment is shown in **Figure 2.16**. Here, the addition of a H_2O-containing TEGDME electrolyte containing a $LiClO_4$ salt results in the rapid conversion of KO_2 to Li_2O_2, generating 0.5 moles of O_2 per mole of KO_2 consumed. Further details on the KO_2 disproportionation reactions can be found in the results and discussion in Chapter 7.

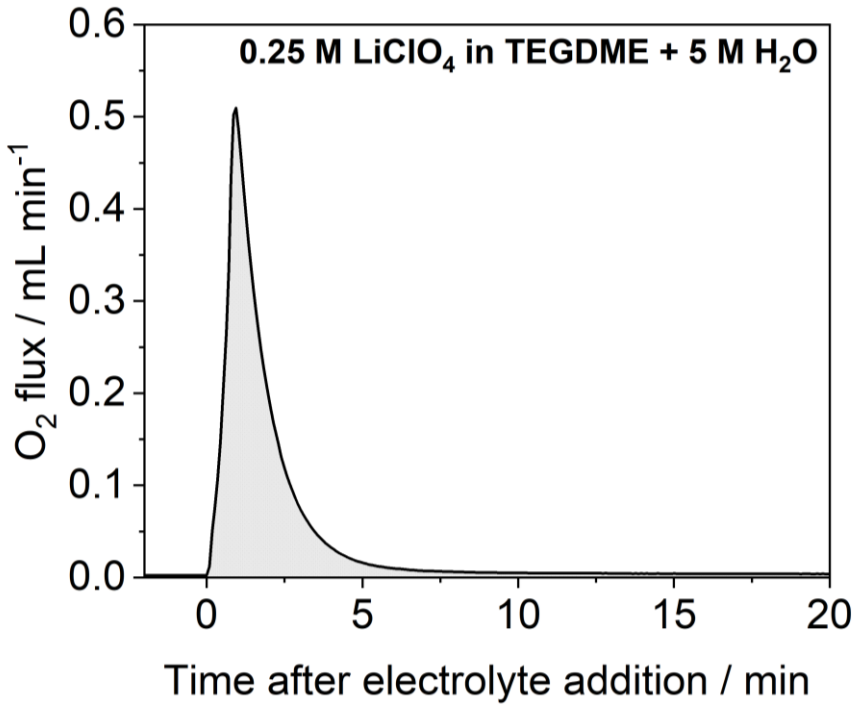


Figure 2.16. *Example MS response during the disproportionation of KO_2 when mixed with a Li^+-containing TEGDME electrolyte doped with 5 M H_2O, tracked through OEMS. The ratio of moles of O_2 evolved to moles of KO_2 consumed can be used to understand the KO_2 disproportionation pathway.*

2.4 Singlet oxygen ($^1O_2$) generation

The reactivity of $^1O_2$ with EC, EMC and VC is explored in detail in Chapter 4. Two methods are used to generate $^1O_2$ *in situ*: 1) the irradiation of a RB photosensitizer as previously used in literature and 2) the application of a Fe-based single atom catalyst (Fe-SAC). Here I will explore $^1O_2$, detailing its characteristics and exploring each of the formation pathways applied. Further details on the synthesis of the Fe-SAC can be found in Chapter 4.

In its ground state O_2 exsists as triplet oxygen ($^3O_2$). This is the lowest energy configuration of the O_2 molecular orbital (MO) diagram, shown in **Figure 2.17**a. Hund's rules states that, for a given electron configuration, the lowest energy term is the one with the greatest value of spin multiplicity.[13] The spin multiplicity of a given state is defined by equation 2.13, where S is the total electronic spin.

$$\text{Spin multiplicity} = 2S + 1 \qquad (2.13)$$

Therefore, the lowest-energy state of a given electronic configuration is usually the one with the highest number of unpaired electrons all with parallel spins. In accordance with this rule, the two electrons in the molecular orbital diagram of $^3O_2$ remain unpaired and spin-paralell, occupying the π_p* antibonding orbital. Term symbols are an abbreviated description of the total spin and orbital angular momentum quantum numbers of a given molecular orbital diagram. The term symbol can be described in the generic form shown in equation 2.14, where *L* describes the orbital and *J* describes the angular momentum, the derivation of which is beyond the scope of this thesis.

$$\text{Term symbol} = {}^{2S+1}L_J \qquad (2.14)$$

When $^3O_2$ is excited to either of its first excited states, a spin-flip process occurs, reducing the spin multiplicity to 1 (i.e. $2S + 1 = 2 \times 0 + 1 = 1$), resulting in these states being classified as singlet states. The MO diagram of the first two excited singlet states of O_2 are shown in **Figure 2.17**b and c, with the lowest singlet state having the term symbol $^1\Delta_g$, where the spin-flip results in electron pairing,

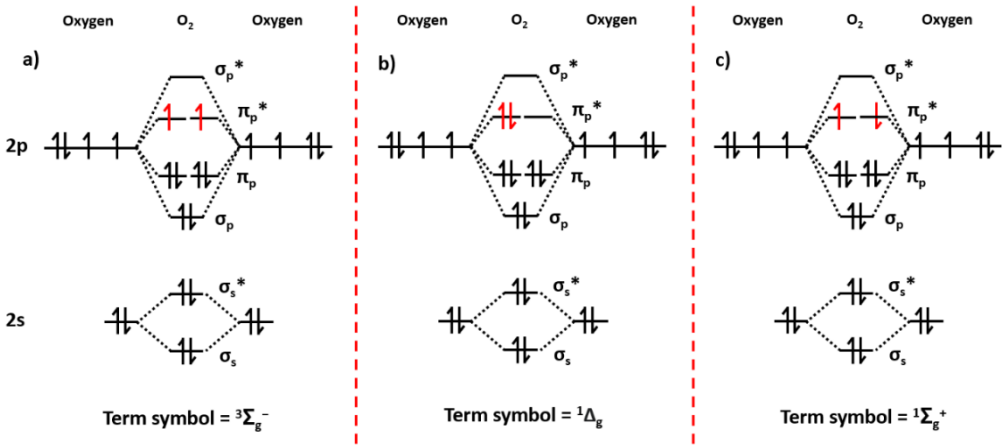


Figure 2.17. *Molecular orbital diagrams showing the electronic arrangements of oxygen in a) ground state ($^3O_2$, $^3\Sigma_g^-$), b) first excited singlet state $^1\Delta_g$, and c) second excited singlet state $^1\Sigma_g^+$.*

being the subject of study in this thesis. It is possible for the $^1\Sigma_g^+$ state to form, however, it is highly unstable and rapidly converts to the $^1\Delta_g$ state where formed, either through non-radiative decay during collision or through a fluorescent transition at ca. 1925 nm.[14]

It is important to note that photosensitizers are selectively chosen for their favourable electronic properties for the targetted activation of a given process. The RB photosensitizer, used in Chapter 4, has been broadly applied for $^1O_2$ generation in organic systems.[15,16] **Figure 2.18** shows the molecular structure of RB, alongside a schematic that describes the generation of $^1O_2$ through the photoexcitation of a RB molecule and subsequent energy transfer to a $^3O_2$ molecule. At rest, both RB and O_2 sit in their ground states, S_0 and T_0 ($^3O_2$, $^3\Sigma_g^-$), respectively. When the solution is irradiated with light of a 525 nm wavelength, a one photon excitation of RB from the ground state to the first excited state (S_1) is achieved.[15,17] The excited RB molecule can then undergo intersystem crossing, a radiationless process which facilitates a transition between two electronic states with different spin multiplicities (i.e. pairing/unpairing of electrons), to the first excited triplet state (T_1). The lifetime of T_1 is much longer than S_1 and allows time for reaction with O_2 through collision, where a RB molecule undergoes radiationless decay back to its S_0 state, exciting $^3O_2$ to its first singlet state (S_1, $^1\Delta_g$) in the process. Once formed, $^1O_2$ can either react

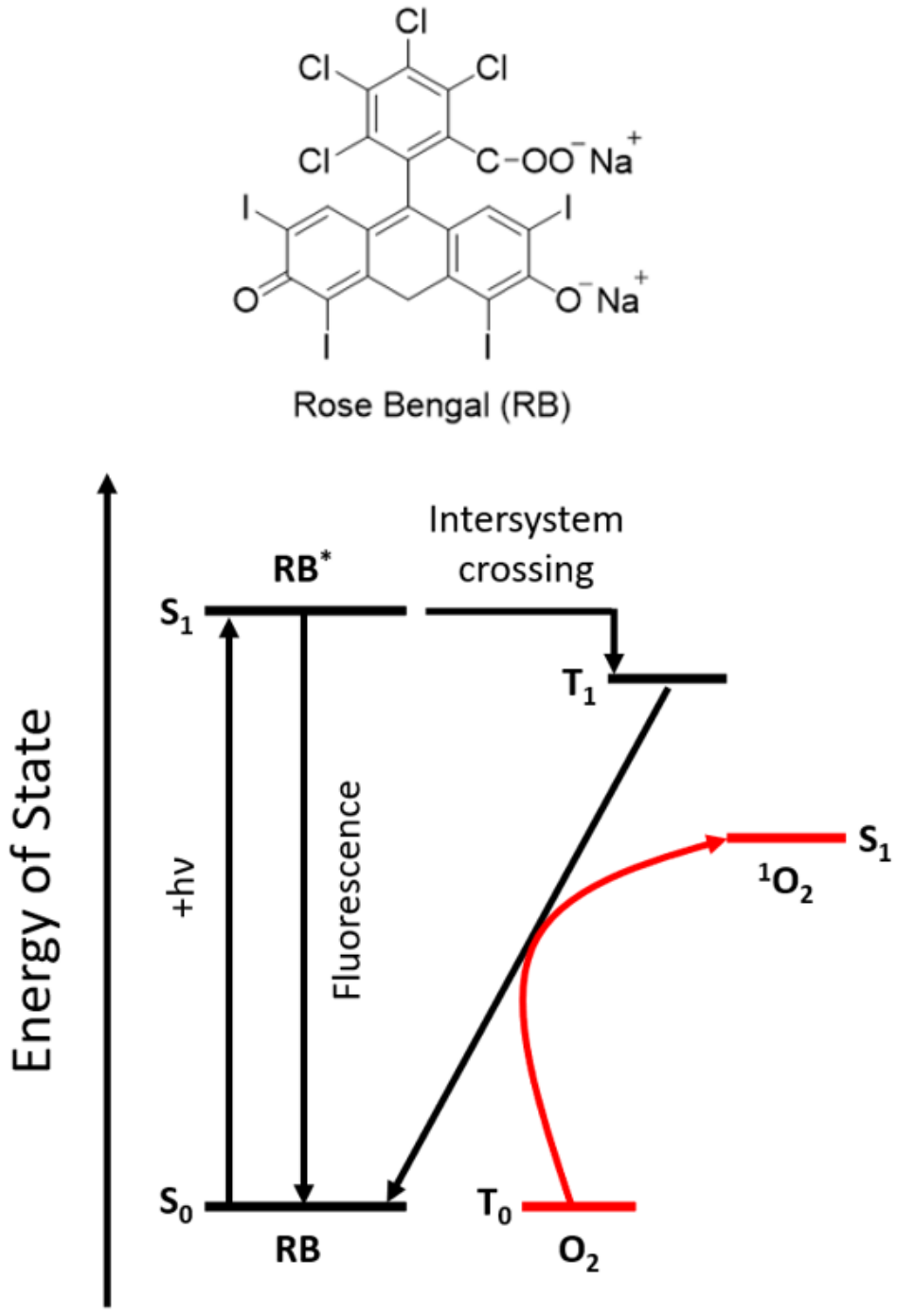


Figure 2.18. *Schematic showing the generation of $^1O_2$ through photoexcitation of a RB photosensitizer (molecular structure shown) to its first excited state (S_1), through intersystem crossing to its first excited triplet state (T_1) where collision with ground state O_2 results in the generation of $^1O_2$.*

chemically or undergo radiative decay back to T_0. Each photosensitizer molecule can typically produce 10^3 – 10^5 molecules of $^1O_2$ before being degraded through photobleaching by $^1O_2$ or by another process.[15]

A second, heterogenous, method of $^1O_2$ generation was explored in Chapter 4, wherein a Fe-SAC, that was proposed by Ma *et al.* as a highly selective method for $^1O_2$ generation, was synthesised and tested in an EC:EMC mixture.[18] In this system, $^1O_2$ is formed through the chemisorption of $^3O_2$ to the single atom Fe-site leading to a spin-flip process, thus generating $^1O_2$ (**Figure 2.17**). Ma *et al.* calculated the adsorption energy of O_2 to an Fe-SAC Fe-site through DFT calculation to be -1.039 eV, and applied Bader charge analysis and charge difference analysis to reveal distinct and significant charge transfer with 0.44 e^- from the Fe-site to O_2, which confirms a strong interaction between the species and elongation of the O-O bond.[18] The transferred electrons will occupy the π*orbital of the O_2 giving rise to a Hirshfeld spin value of 0.25. Given that $^3O_2$ has a Hirshfeld spin of 1 and $^1O_2$ has a Hirshfeld spin of 0, this computation suggests a significant spin-flip process occurs in the O_2 upon chemisorption to an Fe-site.[18]

Although Ma *et al.* proved the generation of $^1O_2$ with the Fe-SAC in aqueous media, the feasibility of $^1O_2$ generation in the organic carbonates used in Chapter 4 needed to be assessed. This was achieved through the use of dimethyl anthracene (DMA), which converts to its endoperoxide (DMA-O_2) through reaction with $^1O_2$.[19,20] DMA reacts selectively with $^1O_2$ through a [4 + 2] cycloaddition mechanism, which can be tracked by the quenching of its distinctive UV-Vis absorbance profile observed between 300 – 450 nm.[21] The molecular structures and UV-Vis absorption profile of DMA are shown in **Figure 2.19**.

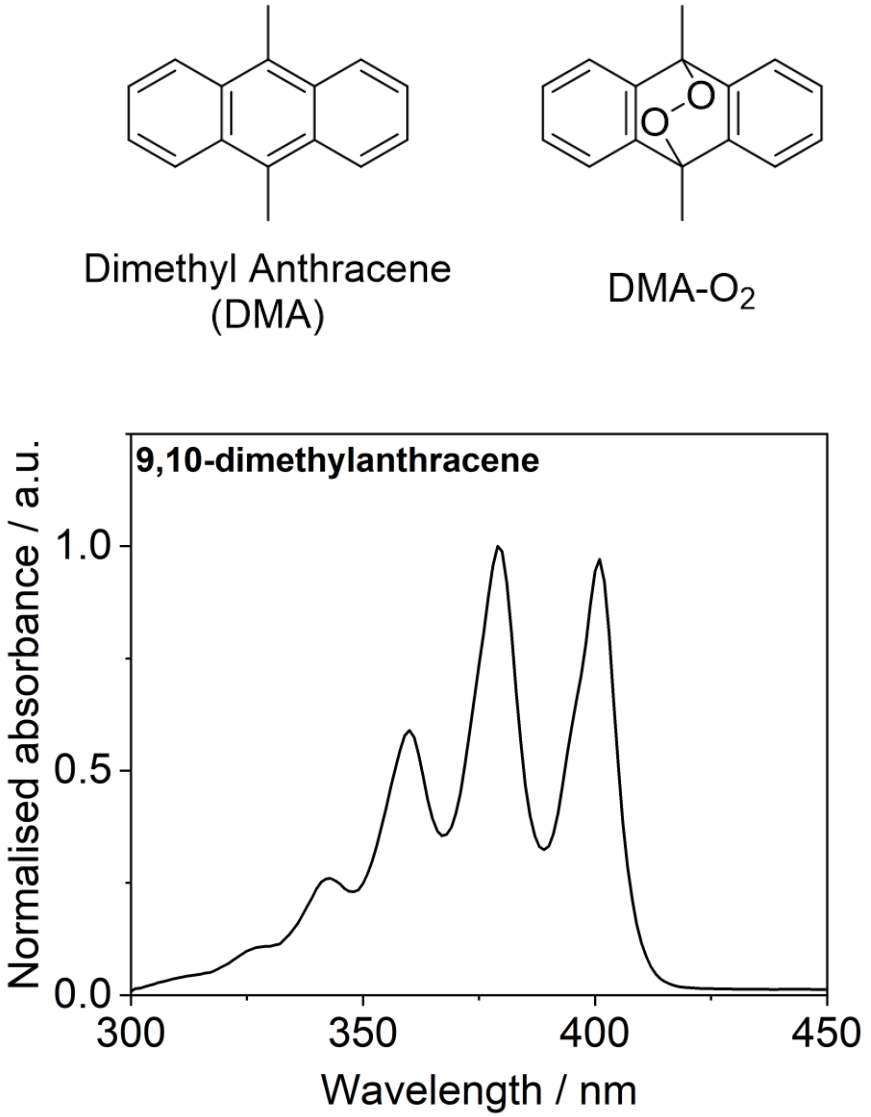


Figure 2.19. *Molecular structure of DMA and its endoperoxide, DMA-O_2, alongside the distinctive UV-Vis absorption profile for DMA dissolved in TEGDME.*

2.5 Li_2O_2 yield measurements

Li_2O_2 is the discharge product of $2e^-$ O_2 reduction in lithiated aprotic solvents and is the basis of the cathode reaction in the rechargeable Li-air battery (equation 2.15).

$$2Li^+_{(sol)} + O_{2\,(sol)} + 2e^- \rightarrow Li_2O_{2\,(s)} \qquad (2.15)$$

The yield of Li_2O_2 produced in the discharge of Li-air pressure cells is reported in Chapters 6 and 7 and used as a metric to assess the performance of a given cell chemistry. When mixed with H_2O, Li_2O_2 chemically converts to H_2O through equation 2.16.

$$Li_2O_{2\,(s)} + 2H_2O_{\,(sol)} \rightarrow H_2O_{2\,(sol)} + 2LiOH_{\,(sol)} \qquad (2.16)$$

In the presence of H_2O_2, titanium(IV) oxysulfate ($TiOSO_4$, Aldrich) reacts to form a titanium-peroxide $[Ti(O_2)]^{2+}$ complex with a distinct yellow colour and a UV-Vis absorbance at ca. 405 nm (**Figure 2.20**). It is therefore possible to measure the quantity of Li_2O_2 formed in the discharge of a Li-air battery through performing UV-Vis analysis of a solution formed through extracting the cathode from a discharged cell and mixing it with an aqueous solution of $TiOSO_4$. In Chapters 6 and 7, the cathode and separator were extracted from a discharged cell and added to a vial containing a known quantity of deionised H_2O. A known volume of this solution was then mixed in a 1:1 ratio with a solution of 2 wt.% $TiOSO_4$ in 1 M H_2SO_4 to achieve an optimum concentration of the coloured complex $[Ti(O_2)]^{2+}$ (λ_{max} = 405 nm) for a predicted UV-Vis absorbance between 0.7 – 1. The UV-Vis absorption at 405 nm was compared to a calibration fit, made through reaction of $TiOSO_4$ with H_2O_2 solutions of known concentration (shown in **Figure 2.21**). Calibration solutions were made through mixing Li_2O_2 with H_2O to make stock solutions, which were then mixed in a 1:1 ratio with an aqueous solution of $TiOSO_4$ (with 1 M H_2SO_4 to aid solubility) and examined through UV-Vis spectroscopy.

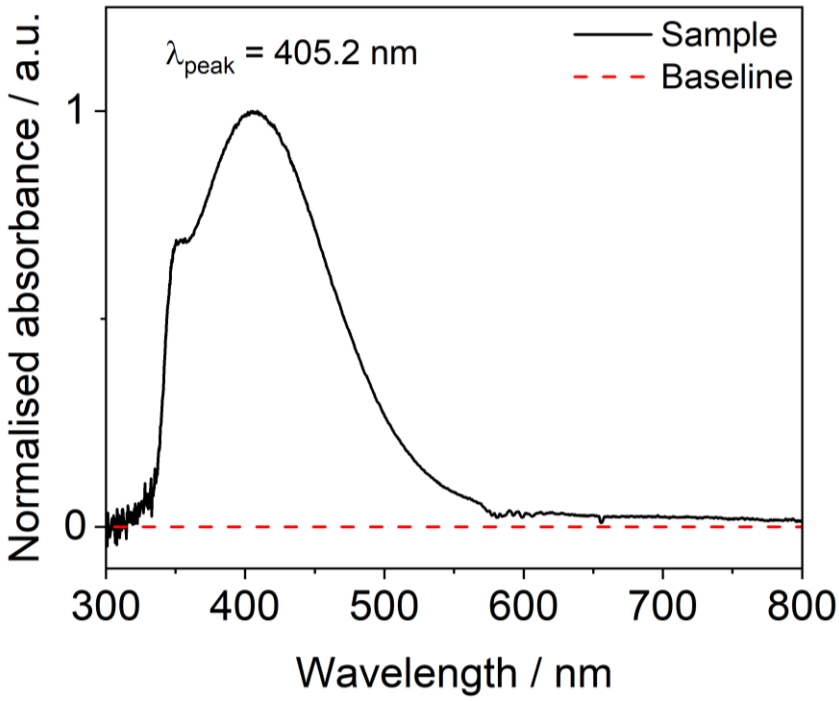


Figure 2.20. *Example UV-Vis spectrum showing the characteristic absorption peak at ca. 405 nm for $[Ti(O_2)]^{2+}$ formed through the reaction of $TiOSO_4$ with H_2O_2. UV-Vis spectra were compared to a calibration to quantitatively assess the yield of Li_2O_2 produced in the discharge of Li-air cells.*

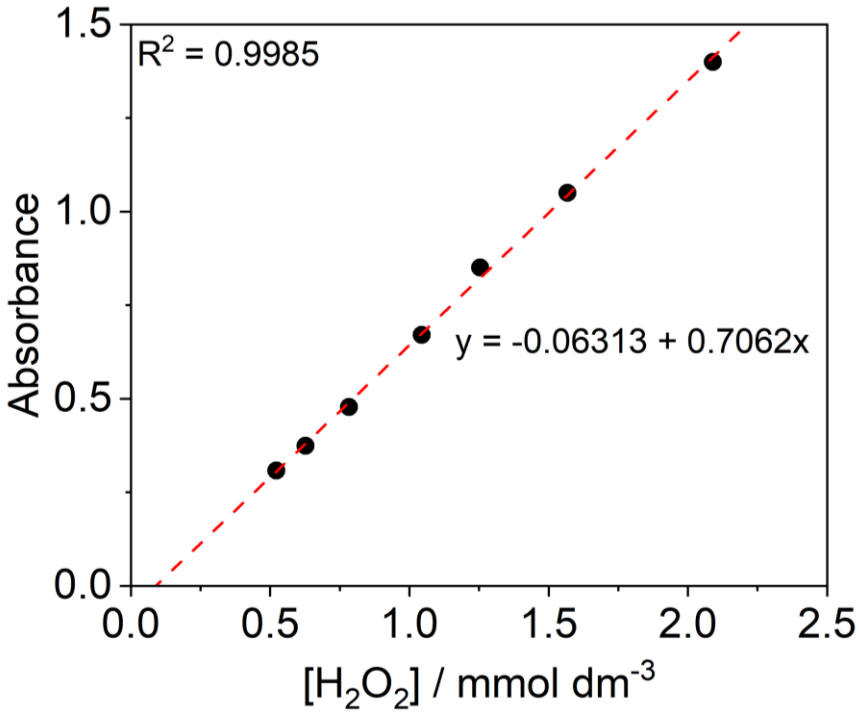


Figure 2.21. *Plot of the UV-Vis peak absorbance of $[Ti(O_2)]^{2+}$ (λ = 405.2 nm) formed when $TiOSO_4$ reacts with H_2O_2 as a function of H_2O_2 concentration. These data were recorded as a calibration to assess Li_2O_2 yield of discharged Li-air cells.*

2.6 Nuclear magnetic resonance (NMR) spectroscopy

The instrumentation and experimental parameters are discussed in the experimental section of each Chapter where appropriate. Broadly, ^{1}H, ^{13}C, ^{19}F and ^{31}P NMR were recorded on a Bruker Ascend 400 MHz spectrometer using 128, 1024, 16, and 128 scans, respectively.

The method used for the determination of H_2O-solvent mixture acceptor numbers (ANs) in Chapter 7 was first described by Mayer *at al.*,[23] wherein diphenylphosphinic chloride (Ph_2POCl) was used as an internal reference. I used triethyl phosphine oxide (Et_3PO) as an internal reference due to its benign nature compared to Ph_2POCl. To enable my samples to be converted to AN in line with Mayer *et al.*, I recorded a ^{31}P NMR spectrum of Ph_2POCl with a deuterated phosphoric acid (D_3PO_4) reference capillary. Reported chemical shift (δ) values are adjusted by – 43.22 to account for this difference. δ was not corrected for magnetic susceptibilities of the solution, as was done by Mayer *et al.* The ^{31}P δ of Et_3PO in several dry solvents (MeCN, DME, DMSO, dimethyl acetamide, TEGDME) and H_2O were determined and the δ was adjusted using the Ph_2POCl reference value. These data were plotted as a function of literature reported AN to produce a calibration fit (**Figure 2.22**). The reported R^2 value close to 1 gives good confidence in this methodology.

For each of the H_2O-solvent mixture ANs determined in Chapter 7, a stock solution of ca. 200 mg Et_3PO_4 in 3 mL of solvent was prepared. Aliquots of the stock solution were diluted with pristine solvent to produce five solutions containing 10, 20, 30, 40, and 50 mg of Et_3PO_4 per mL of solvent. Example data recorded for a 0.5 M H_2O in MeCN solution is shown in **Figure 2.23**. These data were adjusted to the Ph_2POCl reference and compared to the calibration fit to attain the mixture AN.

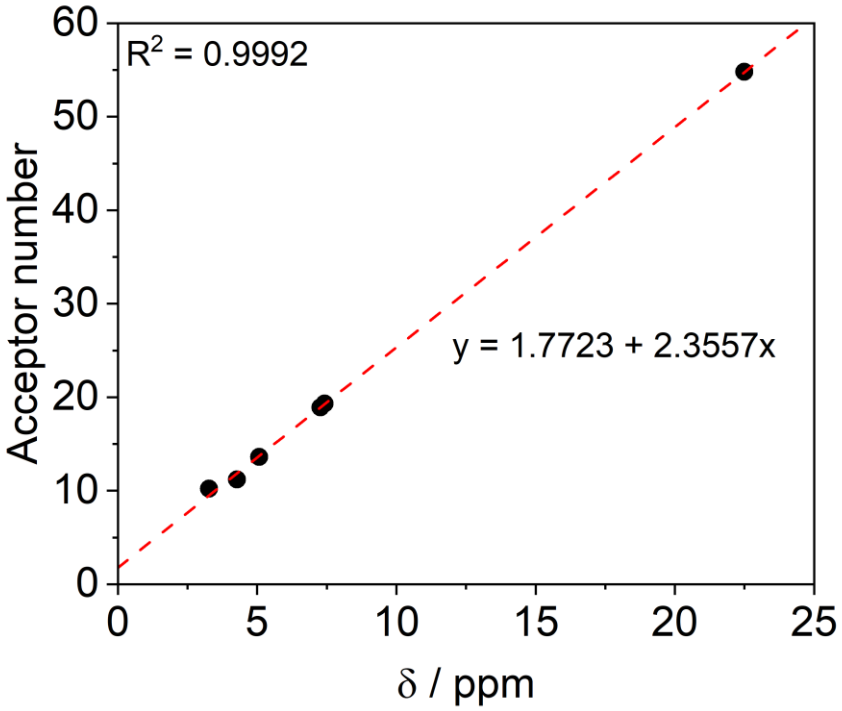


Figure 2.22. *Calibration fit generated through plotting the adjusted ^{31}P δ of Et_3PO in several pure solvents as a function of their literature reported AN values.*

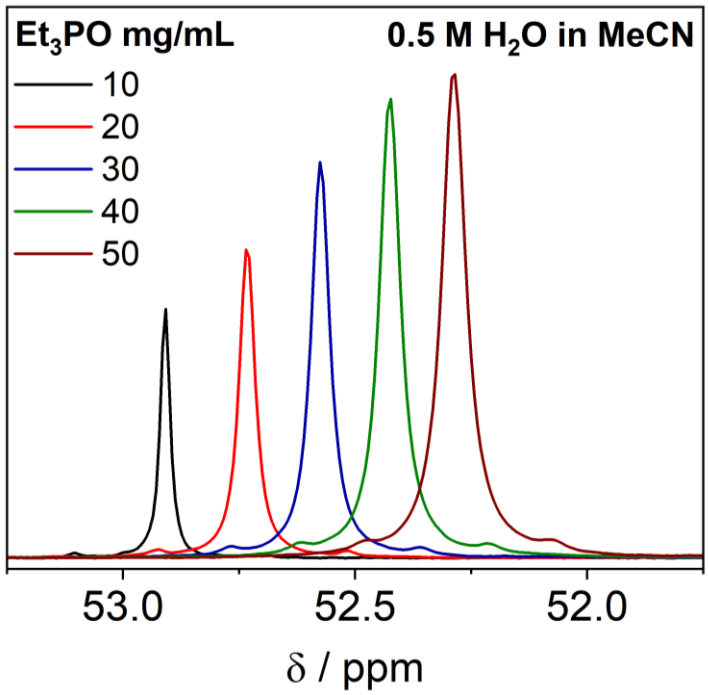


Figure 2.23. *Example ^{31}P NMR spectra showing the change in δ of Et_3PO in a MeCN solution containing 0.5 M H_2O as a function of Et_3PO concentration. The AN of a given solution can be calculated by extrapolating this value to infinite dilution (i.e. Et_3PO = 0 mg/mL).*

2.7 References

1. Rotating Disk Electrode (RDE) Theory. *Pine Research Instrumentation Store* https://pineresearch.com/shop/kb/theory/hydrodynamic-electrochemistry/rotating-disk-electrode-theory/ (2019).
2. Levich, V. G. & Spalding, D. B. *Physicochemical hydrodynamics: V.G. Levich festschrift*. (Advance Publications, 1977).
3. Wang, S. *et al.* Electrochemical impedance spectroscopy. *Nat Rev Methods Primers* **1**, 1–21 (2021).
4. Pritzl, D. *et al.* Identifying Contact Resistances in High-Voltage Cathodes by Impedance Spectroscopy. *J. Electrochem. Soc.* **166**, A582–A590 (2019).
5. Aurbach, D. *et al.* Studies of cycling behavior, ageing, and interfacial reactions of $LiNi_{0.5}Mn_{1.5}O_4$ and carbon electrodes for lithium-ion 5-V cells. *J. Power Sources* **162**, 780–789 (2006).
6. Wang, X. *et al.* High-performance $LiNi_{0.8}Mn_{0.1}Co_{0.1}O_2$ cathode by nanoscale lithium sulfide coating via atomic layer deposition. *J Energy Chem.* **69**, 531–540 (2022).
7. NIST Mass Spectrometry Data Centre. https://chemdata.nist.gov/dokuwiki/doku.php?id=chemdata:start.
8. Tsiouvaras, N., Meini, S., Buchberger, I. & Gasteiger, H. A. A Novel On-Line Mass Spectrometer Design for the Study of Multiple Charging Cycles of a Li-O_2 Battery. *J. Electrochem. Soc.* **160**, A471 (2013).
9. Jiang, M., Danilov, D. L., Eichel, R.-A. & Notten, P. H. L. A Review of Degradation Mechanisms and Recent Achievements for Ni-Rich Cathode-Based Li-Ion Batteries. *Adv. Energy Mater.* **11**, 2103005 (2021).

10. Leanza, D., Mirolo, M., Vaz, C. A. F., Novák, P. & El Kazzi, M. Surface Degradation and Chemical Electrolyte Oxidation Induced by the Oxygen Released from Layered Oxide Cathodes in Li−Ion Batteries. *Batteries & Supercaps* **2**, 482–492 (2019).

11. Dose, W. M. *et al.* Electrolyte Reactivity at the Charged Ni-Rich Cathode Interface and Degradation in Li-Ion Batteries. *ACS Appl. Mater. Interfaces* **14**, 13206–13222 (2022).

12. Greenspan, L. Humidity Fixed Points of Binary Saturated Aqueous Solutions. *J Res Natl Bur Stand A Phys Chem* **81A**, 89–96 (1977).

13. Hund, F. Zur Deutung der Molekelspektren. I. *Z. Physik* **40**, 742–764 (1927).

14. Weldor, D., Poulsen, T. D., Mikkelsen, K. V. & Ogilby, P. R. Singlet Sigma: The "Other" Singlet Oxygen in Solution. *Photochemistry and Photobiology* **70**, 369–379 (1999).

15. DeRosa, M. Photosensitized singlet oxygen and its applications. *Coordination Chemistry Reviews* **233–234**, 351–371 (2002).

16. Li, B., Lin, L., Lin, H. & Wilson, B. C. Photosensitized singlet oxygen generation and detection: Recent advances and future perspectives in cancer photodynamic therapy. *Journal of Biophotonics* **9**, 1314–1325 (2016).

17. Bonnett, R. Photosensitizers of the porphyrin and phthalocyanine series for photodynamic therapy. *Chem. Soc. Rev.* **24**, 19–33 (1995).

18. Ma, W. *et al.* Highly selective generation of singlet oxygen from dioxygen with atomically dispersed catalysts. *Chem. Sci.* **13**, 5606–5615 (2022).

19. Córdoba, D., Rodríguez, H. B. & Calvo, E. J. Singlet Oxygen Formation during the Oxygen Reduction Reaction in DMSO LiTFSI on Lithium Air Battery Carbon Electrodes. *ChemistrySelect* **4**, 12304–12307 (2019).

20. Gross, E., Ehrenberg, B. & Johnson, F. M. Singlet oxygen generation by porphyrins and the kinetics of 9,10-dimethylanthracene photosensitization in liposomes. *Photochem Photobiol* **57**, 808–813 (1993).

21. Steinebrunner, D. *et al.* A versatile heterogeneous photocatalyst: nanoporous gold powder modified with a zinc(II) phthalocyanine derivative for singlet oxygen [4 + 2] cycloadditions. *Photochem Photobiol Sci* **20**, 547–558 (2021).

22. Hartmann, P. *et al.* A comprehensive study on the cell chemistry of the sodium superoxide (NaO_2) battery. *Phys. Chem. Chem. Phys.* **15**, 11661–11672 (2013).

23. Mayer, U., Gutmann, V. & Gerger, W. The acceptor number — A quantitative empirical parameter for the electrophilic properties of solvents. *Monatshefte für Chemie* **106**, 1235–1257 (1975).

Chapter 3. Understanding the limits of Li-NMC811 half cells

3.1 Introduction

The current state-of-the-art material classes of nickel-rich positive electrodes are now the standard in automotive commercial cells, typically accommodating a nickel-content of 60% or higher in modern electric vehicles (EVs).[1–3] Early automotive positive electrodes combined an equimolar ratio of nickel, manganese, and cobalt, creating the NMC111 ($LiNi_{0.33}Mn_{0.33}Co_{0.33}O_2$) chemistry that provides a capacity performance comparable to that of the ubiquitous lithium cobalt oxide, with significant reduction in raw materials cost.[4–6] The subsequent push towards high nickel-content was driven by the desire to further increase energy density, whilst simultaneously limiting raw material cost and reducing cobalt content, the use of which is often tarnished by the environmental, social and governance issues surrounding its mining.[7,8] The volumetric energy density of subsequent NMC materials, NMC622 (ca. 2600 Wh L^{-1}) and NMC811 (ca. 3600 Wh L^{-1}), have made them the standards for current and future automotive applications, with EV cell manufacturers beginning to implement NMC811+ chemistries in their most recent battery packs.[9–11]

This marked increase in capacity performance comes at the cost of increased reactivity of the electrode surface, with Ni^{4+} ions that are formed upon high delithiation of these materials reacting aggressively with the electrolyte components to form a highly resistive cathode electrolyte interphase (CEI).[12–14] Furthermore, this electrode-electrolyte interfacial instability results in crosstalk between the positive and negative electrode, where the formation of acidic species, dissolution of Ni, Mn, and Co ions, and crossover of electrolyte degradation products catalyse further interphase and electrolyte degradation that limit the capacity of the cell.[15–21] This detrimental relationship between increasing Ni-content, solid electrolyte interphase (SEI) and CEI instability, and capacity fade highlights the need to isolate the positive electrode chemistry and its long-term performance.

The use of half-cells – wherein the electrode of interest is paired with a metallic Li counter electrode – is a common approach used in industry and academia for isolated electrochemical analysis of positive electrode materials, with the intrinsically stable reference potential and high specific capacity of metallic Li (3860 mAh g^{-1}) providing an effectively infinite reservoir of Li^+ with minimal impact on the electrochemical response.[22–24] However, the high reactivity of metallic Li with organic carbonates brings into question the reliability of the results obtained in these cells, with indiscriminate degradation of the electrolyte components resulting in premature cell death and increased rate of cell failure compared to a full-cell configuration (i.e. Gr-NMC811).[25–27] Industry standard lithium-ion battery electrolyte solutions are composed of a lithium hexafluorophosphate ($LiPF_6$) salt dissolved in a mixture of cyclic and linear carbonates. Typically these are composed of ethylene carbonate (EC) in combination with one or more linear carbonates: diethyl carbonate (DEC), dimethyl carbonate (DMC), and ethyl methyl carbonate (EMC), all of which undergo reductive decomposition on the surface of metallic Li.[28–30] This base electrolyte composition is often supported by the addition of 2-8 wt.% additives with the specific purpose of improving the composition and characteristics of the SEI at the negative electrode.[31–34] While the field is aware of these difficulties, the specific limits and implications on resulting data sets in Ni-rich cells, where performance is increasingly dominated by electrode cross-talk, is not well quantified and no accepted alternative is available.

In this chapter, I explore the validity of Li-NMC811 half-cell studies using a commercially relevant loading (16.9 mg cm^{-2}, ca. 3.19 mAh cm^{-2}) and electrolyte composition at 40 °C. I determine the limitations of cell cycling and identify the failure mechanisms of these cells. Vinylene carbonate (VC) is examined as the electrolyte additive due to its broad industrial relevance. Time-resolved gas chromatography mass spectrometry (GC-MS), nuclear magnetic resonance (NMR) spectroscopy and electrochemical impedance spectroscopy (EIS) are used to understand the rate of additive consumption and electrolyte degradation. I identify key stages and mechanisms of electrolyte degradation

in Li-NMC811 half-cells, gaining insight into critical cell failure mechanisms. The state of electrode health is explored through cell reconstitution, extracting the cycled electrodes and rebuilding fresh cells that contain a pristine counter electrode and replenished electrolyte. Finally, I demonstrate the use of $Li_4Ti_5O_{12}$ (LTO) as a superior counter electrode which overcomes the shortfalls of metallic Li. I show that the high chemical and electrochemical stability of LTO to traditional electrolyte solutions make it an ideal negative electrode for the long-term isolated study of the electrochemical performance of high nickel electrode chemistries.

3.2 Experimental

3.2.1 Materials

$LiNi_{0.8}Mn_{0.1}Co_{0.1}O_2$ (NMC811, 16.9 mg cm^{-2}, ca. 3.19 mAh cm^{-2}) and graphite (Gr, 11.3 mg cm^{-2}, 3.8 mAh cm^{-2}) electrodes were manufactured by LiFun. NMC811 electrodes comprised of 95.5% active material, 2.5% conductive carbon support, and 2.0% binder coated on aluminium foil. $Li_4Ti_5O_{12}$ (LTO, 25 mg cm^{-2}, 3.7 mAh cm^{-2}) electrodes supplied by the U.S. Department of Energy's CAMP Facility, Argonne National Laboratory. Metallic Li was purchased from Aldrich (99.9%). The base electrolyte (LP57, 1 M $LiPF_6$ in EC:EMC = 3:7 v/v) and the formulated electrolyte with 2 wt.% VC additive were purchased from Solvionic (99.9%, H_2O ≤20 ppm). NMC811, LTO, and Gr electrodes were dried under vacuum at 120 °C for 24 hours before being transferred into an Ar-filled glovebox without exposure to air.

3.2.2 Electrochemical testing

Cells were assembled inside an Ar-filled glovebox (MBRAUN, O_2 and H_2O ≤0.1 ppm). All measurements were carried out at 40 °C with an initial equilibration time of 1-hour to allow for electrode wetting and temperature uniformity. Two Whatman glass microfiber filter paper (GF/F) functioned as the separators, soaked in 120 µL of LP57 either doped with 2 wt.% VC additive or with no additive. Li-, Gr-, and LTO-NMC811 cells were cycled using a two-electrode Swagelok cell, pairing 12 mm electrodes. Further information on cell

design can be found in Chapter 2. C-rates were calculated assuming a nominal NMC811 capacity of 190 mAh g^{-1}. EIS was carried out in a three-electrode Swagelok cell consisting of a 12 mm NMC811 electrode, a 12 mm metallic Li counter electrode, and a 6 mm metallic Li reference electrode. Further information on cell design and methodology can be found in Chapter 2. EIS measurements were taken after a 1-hour voltage hold, once the voltage reached 3.6 V vs Li^+/Li on the desired discharge cycle. Battery cycling and EIS were carried out on an IviCycle200 and Ivium Octostat30 potentiostat, respectively.

3.2.3 Post-cycling electrolyte analysis

After cycling, the cells were disassembled in an Ar-filled glovebox and the glass microfiber filter paper was soaked in deuterated chloroform ($CDCl_3$, 1.5 mL, Aldrich, 99.0%, H_2O <100 ppm) for >30 minutes, adapting the procedure first described by Dahn *et al*.[35] The solutions were split between airtight NMR tubes fitted with Young's taps and GC-MS vials. ^1H, ^{13}C, ^{19}F, and ^{31}P NMR spectra were recorded on a Bruker Ascend 400 MHz spectrometer and analysed using Bruker TopSpin software. GC-MS samples were injected into the inlet with a splitless flow at 200 °C and carried onto the preheated column which was held at 40 °C for 3 minutes. The oven temperature was then ramped at 2 °C min^{-1} for 10 minutes, followed by 10 °C min^{-1} for 3 minutes, then 2 °C min^{-1} for 10 minutes, and finally 10 °C min^{-1} for 13 minutes to a final temperature of 240 °C, where all compounds were evolved from the column. The mass spectrometer transfer line and ion source were held at 250 °C. A blank injection of methanol (HPLC grade, ≥99.9%, Aldrich) was run between each injection to prevent contamination between sample injections. Data were analysed using Chromeleon software to identify the composition of chromatogram peaks, cross-referencing mass spectra with the National Institute of Standards and Technology (NIST) mass spectral library.[36]

3.2.4 Cell reconstitution procedure

Two electrode Li-NMC811 cells were assembled as described above and cycled for two C/20 formation cycles between 3.0 – 4.2 V vs Li^+/Li. The cells were

cycled for a further 100 cycles at C/2 to an upper cut-off voltage (UCV) of either 4.2 or 4.4 V vs Li^+/Li before being reconstituted. The cells were disassembled, taking care to separate the components by exposing the separator-separator interface between the two soaked separators. Each of the cycled electrode-separator pairs were then reassembled in a fresh cell with the addition of a pristine separator, fresh electrolyte, and a pristine partner electrode. The result was two cells, one containing the cycled NMC811 paired with a pristine metallic Li electrode, and the other containing the cycled metallic Li electrode paired with a pristine NMC811 electrode. By separating the components at the separator-separator interface, mechanical disturbance of the SEI and CEI was kept to a minimum. The cells were allowed to rest at 40 °C for 1-hour before the cycling procedure was initiated. To validate the cell reconstitution procedure, 10 C/2 cycles were carried out after formation cycling under standard conditions (3.0 – 4.2 V vs Li^+/Li) before reconstitution.

3.3 Half-cell cycling and the role of VC

Potential limits are applied to battery cycling to balance maximum extraction of reversible capacity from a given battery chemistry while limiting degradation and ensuring safe operation. Standard potential limits for Li-NMC811 half-cells are 3.0 – 4.2 V vs Li^+/Li.[10,12,37] Although extending the UCV beyond 4.2 V enables more Li^+ to deintercalate during charge, it also stresses the positive electrode, increasing interfacial reactivity, the rate of lattice O_2 release, and electrode crosstalk.[38–40] To understand the contribution of positive electrode degradation processes to long-term cycling performance of Li-NMC811 half-cells, cell cycling was carried out under both standard conditions (3.0 – 4.2 V vs Li^+/Li) and stressed conditions (3.0 – 4.4 V vs Li^+/Li), wherein the positive electrode was polarised ca. 0.2 V past the standard UCV.

LP57 (1 M $LiPF_6$ in EC:EMC 3:7 v/v) was chosen as the electrolyte, being employed both in its base composition, where no electrolyte additive is present (VC-free), and with the inclusion of 2 wt.% VC (LP57-VC). These represent standard electrolyte compositions for this battery chemistry.[1,10,41] VC is the most common additive used in commercial lithium-ion batteries,[29,33,42] where

its high reduction potential (>1 V vs Li^+/Li) compared to EC and EMC (<1 V vs Li^+/Li) result in it being sacrificially degraded on the surface of the Gr negative electrode.[43,44] The resultant polymeric species, PolyVC, that is formed during formation cycling improves the thermal and electrochemical properties of the Gr SEI.[45–47] VC is employed in this study to understand its impact on cycling performance when interacting with a metallic Li negative electrode.

All Li-NMC811 cells were initially cycled to an UCV of 4.2 V at a rate of C/20 for two formation cycles before long-term cycling conditions were applied. These formation cycles are essential to the formation of an optimum CEI and SEI and are commonplace in commercial and academic procedures. **Figure 3.1** shows the charge and discharge voltage profiles of the 1st C/20 SEI formation cycle and subsequent 5th, 40th, 50th, 60th and 100th cycles at C/2 of Li-NMC811 cells containing a LP57-VC electrolyte. **Figure 3.1**a shows the voltage profiles of a cell cycled to an UCV of 4.2 V, where characteristics consistent with those previously reported for Li-NMC811 half-cells are observed.[37,48,49] Initial capacity fade is observed upon initiation of C/2 cycling due to increased electrode polarisation, however good retention of voltage profile characteristics and capacity is observed over the first 50 cycles. A significant deviation from the pristine plateau voltages occurs between the 50th and 60th cycle, indicative of increased electrode polarisation. By the 100th cycle, significant capacity loss is observed, and no distinctive voltage profile features can be distinguished.

Figure 3.1b shows the charge and discharge voltage profiles of a cell cycled under analogous conditions, with the extension of the UCV to 4.4 V after formation cycling. On initiation of C/2 cycling, the extension of the UCV allows access to an additional capacity region which enables ca. 40 mAh g^{-1}_{NMC} of additional charge capacity to be attained. A gradual capacity fade and a continual drop in plateau voltages is observed up to the 50th cycle. Between the 50th and 60th cycle these changes accelerate and by the 100th cycle no distinctive features can be identified.

Figure 3.2 shows the capacity performance of representative cells cycled under these conditions containing a LP57-VC electrolyte. An initial discharge capacity

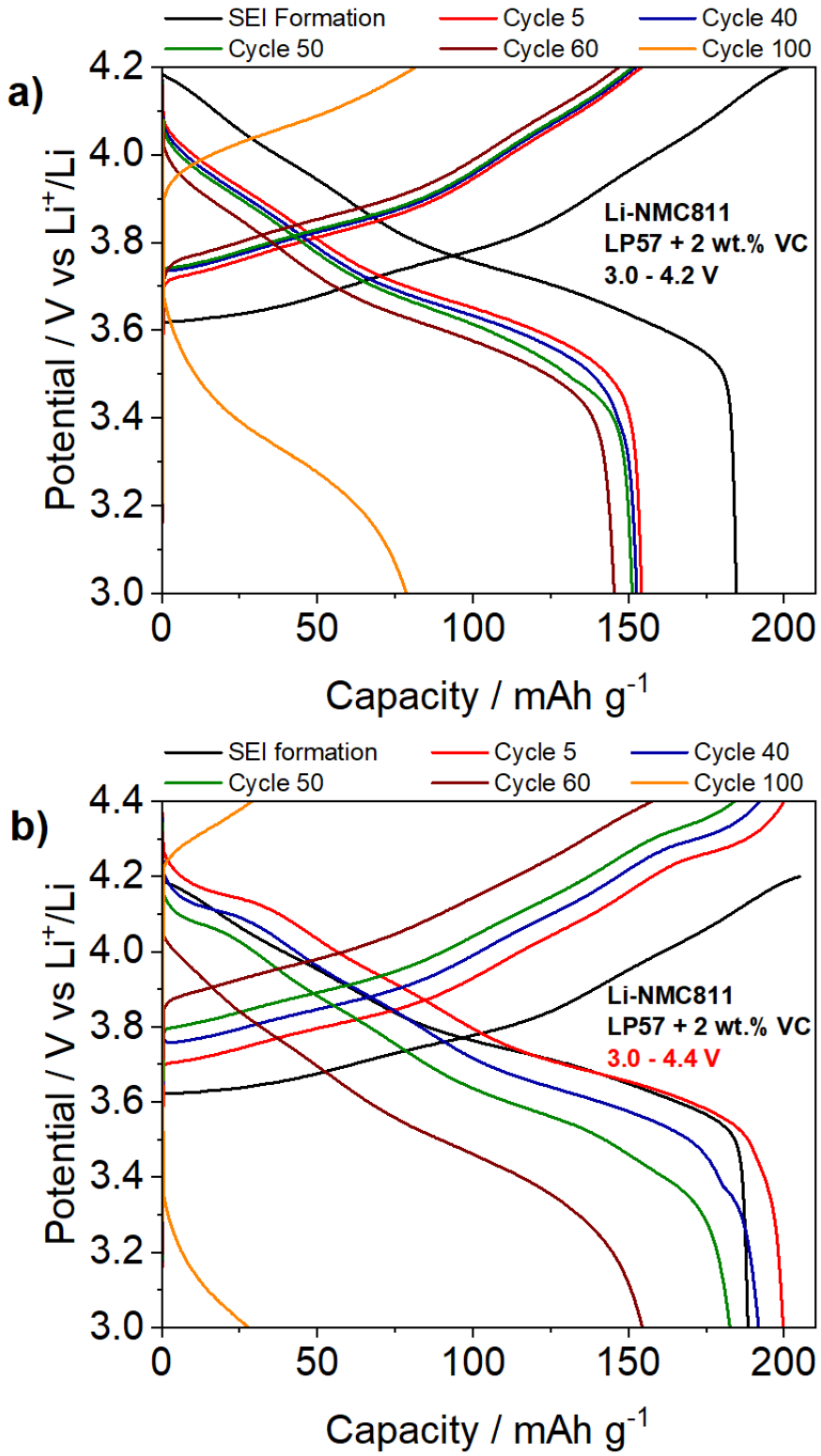


Figure 3.1. *Voltage profiles of Li-NMC811 half-cells cycled to an UCV of a) 4.2 V or b) 4.4 V vs Li^+/Li containing a LP57-VC electrolyte. The 1st C/20 formation cycle and subsequent 5th, 40th, 50th, 60th, and 100th cycles at C/2 are shown.*

of ca. 187 mAh g^{-1}_{NMC} is observed during the C/20 formation cycles in both cells. Upon initiation of C/2 cycling, first discharge capacities of 154.9 and 201.5 mAh g^{-1}_{NMC} were achieved for the cells cycled to an UCV of 4.2 and 4.4 V, respectively. Across the first 50 cycles at C/2, an average coulombic efficiency (CE) of 99.93 and 99.65% were attained for cells cycled to an UCV of 4.2 and 4.4 V, respectively. This performance is consistent with the reversible capacity expected for NMC811 electrodes.[1,50] After 50 cycles, a drop in CE is observed in both cells, which is indicative of deviation from the desired lithium intercalation/de-intercalation reactions and signifies the onset of irreversible side reactions.[51,52] In both cases, the CE continues to decline and significant capacity fade is observed, albeit more pronounced in cells cycled to an UCV of 4.4 V. It is important to note that additional side reactions simultaneously occur at the metallic Li electrolyte interface, forming degradation species that can cross through the electrolyte solution to the positive electrode where they will be oxidised. These reactions may impact CE, however, they will not contribute

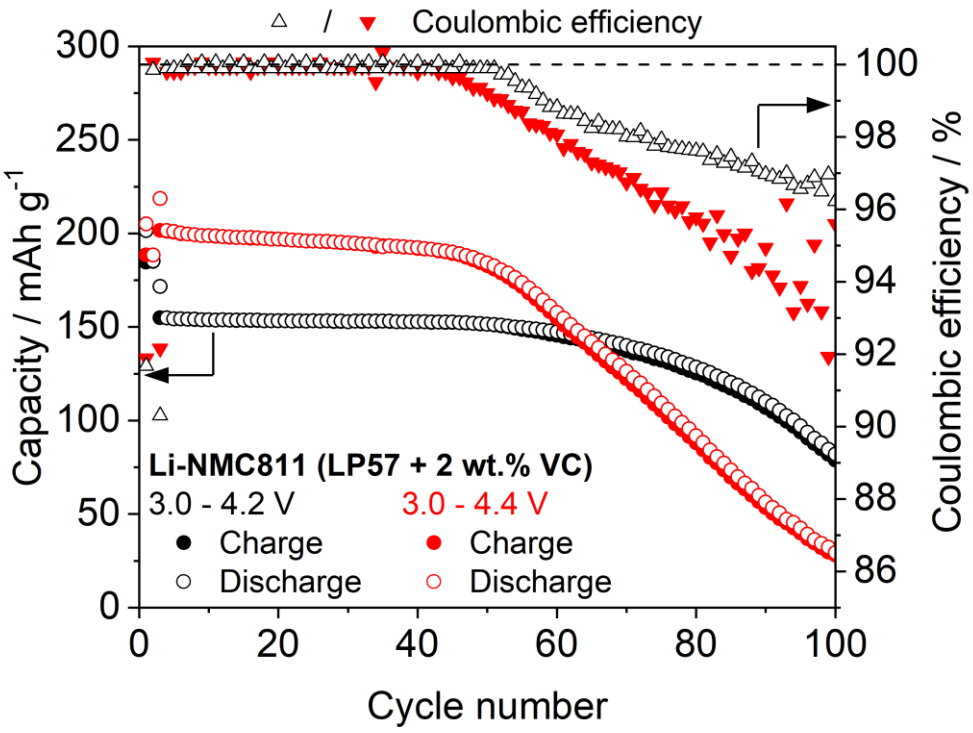


Figure 3.2. *Capacity performance of Li-NMC811 half-cells cycled to an UCV of 4.2 V (black) or 4.4 V (red) vs Li^+/Li containing a LP57-VC electrolyte. Data shows the capacities (circles) and coulombic efficiency (triangles) of two initial C/20 formation cycles and subsequent C/2 cycles.*

to the loss of lithium inventory due to the abundance of Li^+ provided by the metal electrode, which results in these reactions going largely undetected in a half-cell configuration.[53]

To understand the role of VC in the performance of Li-NMC811 half-cells, a comparative cycling study was carried out with cells containing a VC-free LP57 electrolyte (**Figure 3.3** and **Figure 3.4**). **Figure 3.3**a shows the voltage profiles of a cell cycled to an UCV of 4.2 V, where the charge and discharge profile of the 1st C/20 formation cycle are comparable to cells containing a LP57-VC electrolyte. Although capacity fade by the 5th C/2 cycle is more significant, good retention of voltage profile characteristics is observed. However, as the extent of cycling progresses capacity performance decreases dramatically, coincident with intensified deviation from the pristine voltage plateaus. A higher 1st C/2 cycle capacity is observed in the cell cycled to an UCV of 4.4 V (**Figure 3.3**b), with the extended UCV facilitating access of additional intercalation sites. However, aggressive capacity fade and rapid degradation of the voltage profiles is observed throughout cycling.

Figure 3.4 shows the capacity performance of representative cells cycled to UCVs of 4.2 and 4.4 V containing a VC-free LP57 electrolyte. In good agreement with cells cycled containing a LP57-VC electrolyte, initial C/20 formation capacities of ca. 186 mAh g^{-1}_{NMC} are achieved in both cells. Upon initiation of C/2 cycling, initial discharge capacities of 148.2 and 195.0 mAh g^{-1}_{NMC} were attained for cells cycled to an UCV of 4.2 and 4.4 V, respectively, marginally lower than cells containing VC. Contrastingly, immediate capacity fade is observed in these cells, with an average CE of 96.41 and 95.71% being observed over the first 50 cycles of cells cycled to an UCV of 4.2 and 4.4 V, respectively.

To determine the reproducibility of these data, multiple cells were discharged to UCVs of both 4.2 and 4.4 V with both electrolyte compositions (**Figure 3.5**). A total of 10 cells were cycled under each set of conditions, with 4 completing the full 100 cycles at C/2 in all cases. The error bars shown represent the full spread of discharge capacities recorded. **Figure 3.5**a shows the results of cells

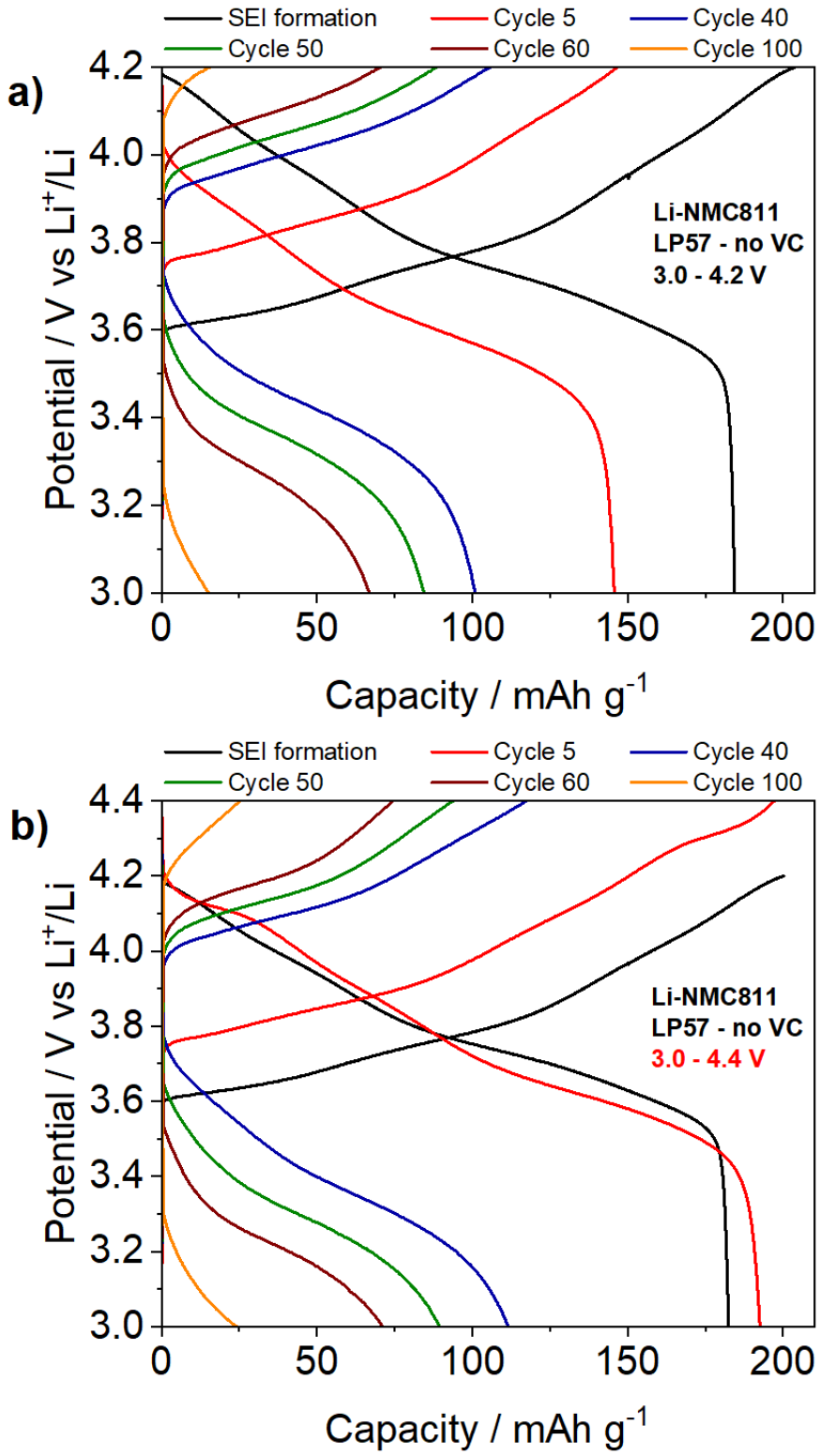


Figure 3.3. *Voltage profiles of Li-NMC811 half-cells cycled to an UCV of a) 4.2 V or b) 4.4 V vs Li^+/Li containing a VC-free LP57 electrolyte. The 1st C/20 formation cycle and subsequent 5th, 40th, 50th, 60th, and 100th cycles at C/2 are shown.*

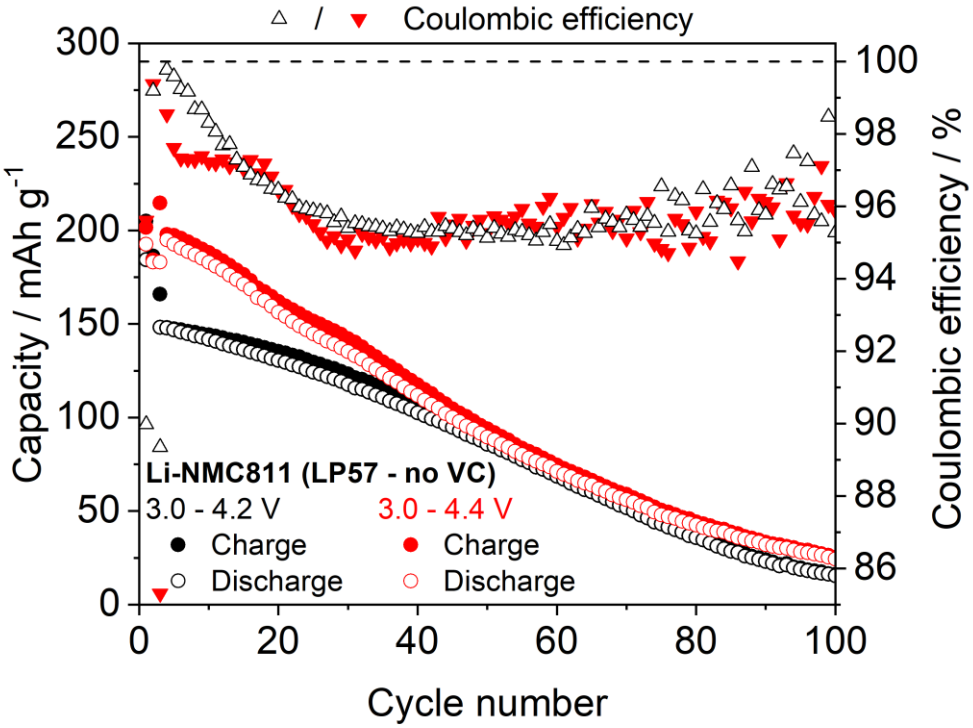


Figure 3.4. *Capacity performance of Li-NMC811 half-cells cycled to an UCV of 4.2 V (black) or 4.4 V (red) vs Li^+/Li containing a VC-free LP57 electrolyte. Data shows the capacities (circles) and coulombic efficiency (triangles) of two initial C/20 formation cycles and subsequent C/2 cycles.*

containing a LP57-VC electrolyte cycled to UCVs of 4.2 and 4.4 V. A high degree of reproducibility is seen in all cells across the first 50 cycles at C/2, after which cells cycled under both conditions begin to experience capacity fade and the spread of recorded capacities increases. After 50 cycles, the rate of the observed capacity fade and the spread of the recorded discharge capacities is considerably higher for the cells cycled to an UCV of 4.4 V, indicating that the degradation processes that onset after 50 cycles are more pronounced in cells where the NMC811 electrode is stressed to high oxidative potentials. **Figure 3.5**b shows the results of analogous cells cycled with a VC-free LP57 electrolyte. All cells showed immediate capacity fade upon initiation of C/2 cycling, with a high reproducibility being evidenced by the tight spread of data. These data confirm that VC plays a critical role in supporting capacity retention in cells that contain a metallic Li negative electrode.

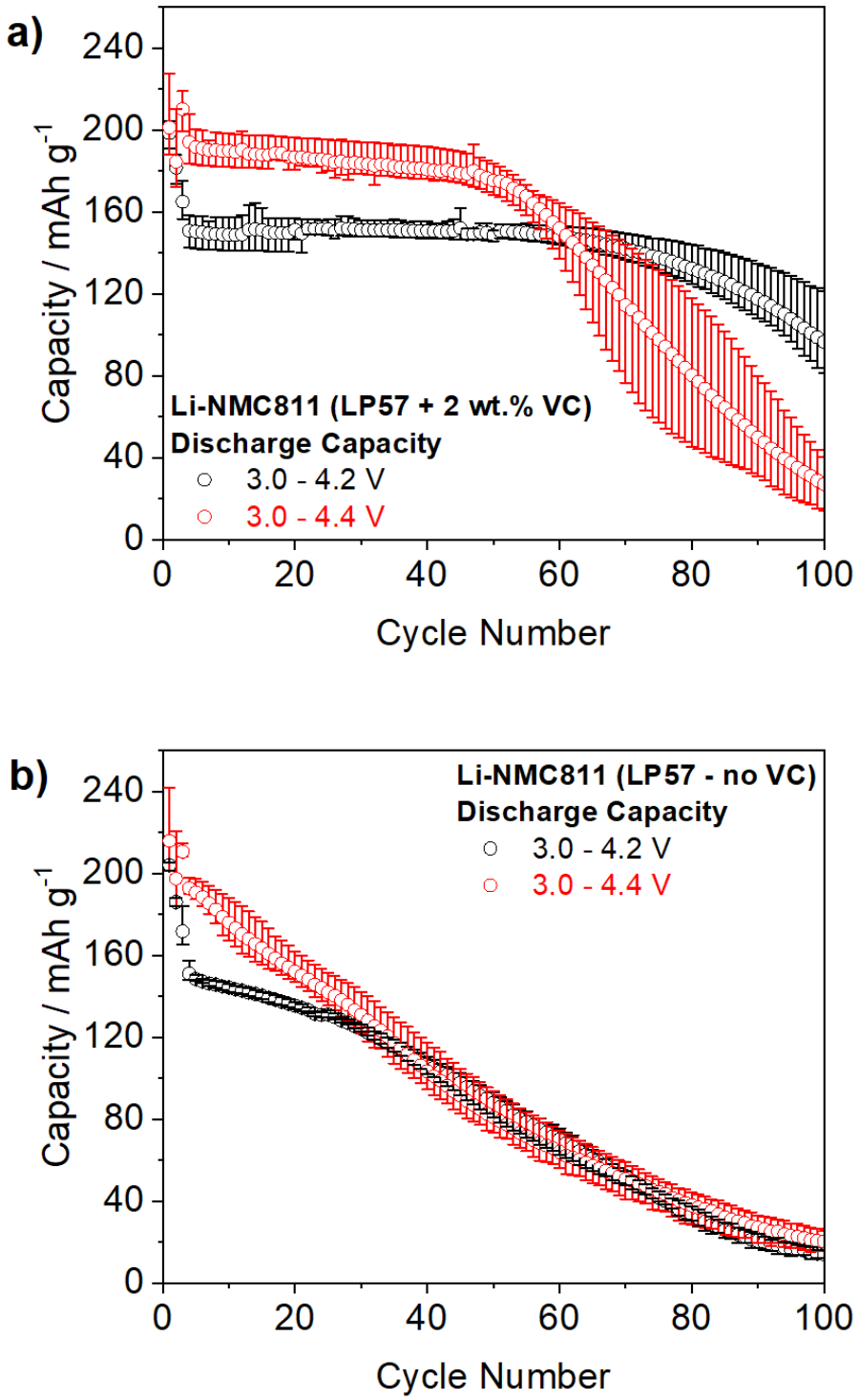


Figure 3.5. *Plots showing mean performance of Li-NMC811 half-cells containing either a a) LP57-VC or b) VC-free electrolyte cycled to a UCV of 4.2 V (black shapes) or 4.4 V (red shapes) vs Li^+/Li. The datapoints represent the mean of the recorded values and the error bars show the true spread of data. A total of 10 cells were cycled under each set of conditions, with 4 cells completing the full 100 cycles.*

Given the high reproducibility of the cycling data, if the dramatic drop in cell performance is an artefact of the NMC811 positive electrode cycling, a similar performance should be observed in full-cells, where the NMC811 positive electrode is paired with a Gr negative electrode (Gr-NMC811). To explore this, Gr-NMC811 cells containing a LP57-VC electrolyte were cycled to UCVs of 4.2 and 4.4 V (**Figure 3.6**). **Figure 3.6**a compares the performance of Li-NMC811 and Gr-NMC811 cells cycled to an UCV of 4.2 V, where an average CE >99.9% is achieved over the first 100 cycles at C/2 for the Gr-NMC811 cell, demonstrating a marked improvement over Li-NMC811 cells. When Gr-NMC811 cells are cycled to an UCV of 4.4 V, considerable capacity fade is observed throughout cycling, with an average CE of 99.42% being attained over the first 100 cycles at C/2 (**Figure 3.6**b). The drop in CE is likely the result of increased electrode crosstalk, with soluble species oxidised at the NMC811-electrolyte interface crossing through the electrolyte and destabilising the Gr SEI during early-stage cycling. The discontinuity between half-cell and full-cell performance demonstrates the importance of isolating and understanding the performance of the positive electrode material and highlights the shortfalls of using metallic Li half-cell data to predict full-cell performance.[41,54,55] Moreover, this observation brings into question the validity of metallic Li as a suitable counter electrode with these electrolyte compositions.

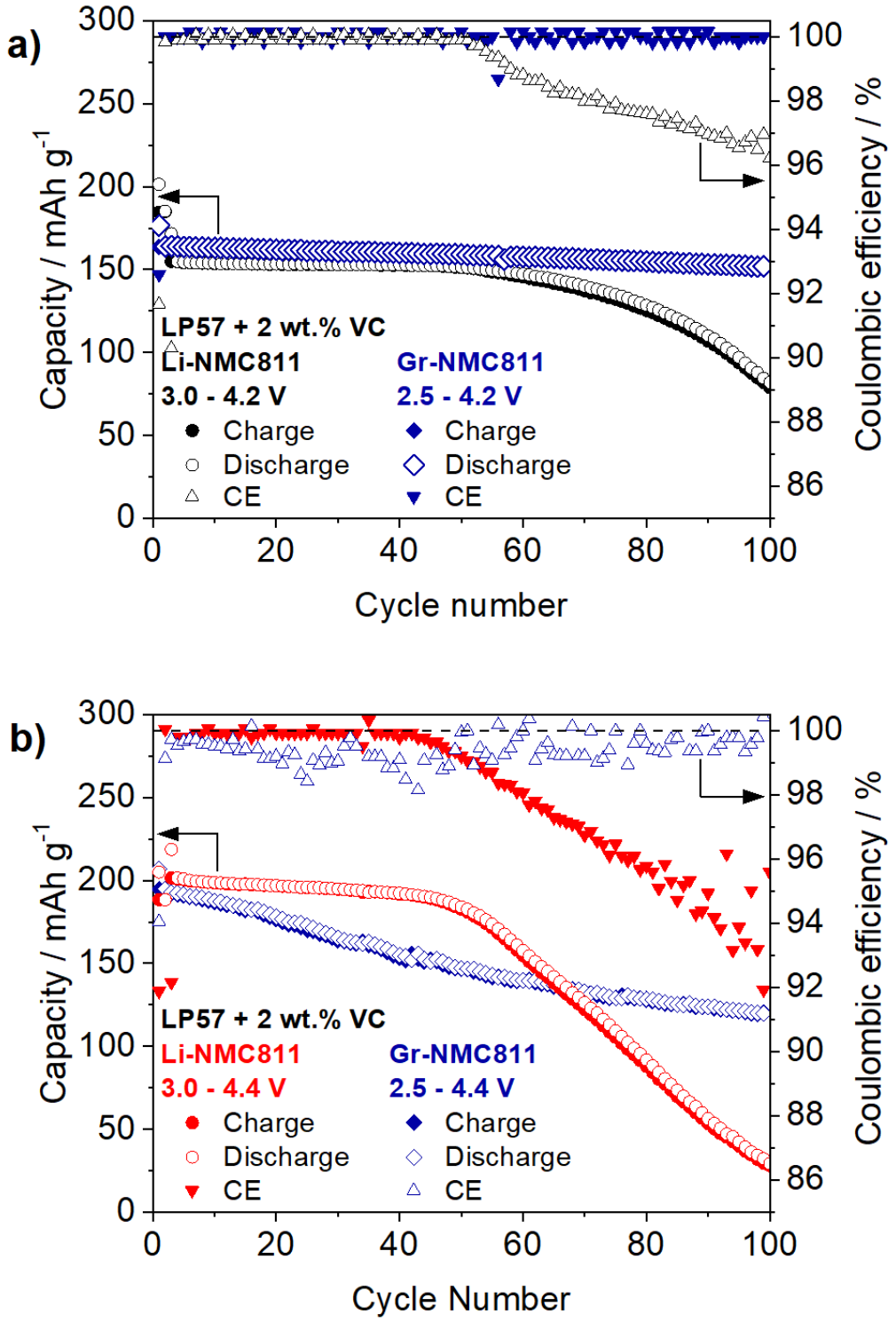


Figure 3.6. *Plots comparing the capacity performance of Li-NMC811 (black, red) and Gr-NMC811 (blue) cells cycled to an UCV of a) 4.2 V or b) 4.4 V vs Li^+/Li containing a LP57-VC electrolyte. Data shows the capacities (circles, diamonds) and coulombic efficiency (triangles) of two initial C/20 formation cycles and subsequent C/2 cycles.*

3.4 Electrolyte degradation and the fate of VC

To understand the role that VC plays in delaying the failure of Li-NMC811 half-cells and identify the formation of soluble degradation products, procedures for GC-MS and NMR analysis of cycled electrolyte were developed. ^{1}H and ^{13}C NMR were run on a pristine LP57 electrolyte which had been extracted from a cell after an 80-hour OCV period at 40 °C, to mirror the formation cycling period, by soaking the separators in $CDCl_3$. **Figure 3.7** shows these spectra, with the characteristic peaks and splitting for the EC, EMC and VC electrolyte solvent molecules evident. Although ^{13}C NMR was collected for all electrolyte samples, and is a useful tool to track the relative ratios of the primary electrolyte species, its low sensitivity compared to ^{1}H NMR preclude analysis of trace degradation products. ^{1}H NMR is approximately 5800 times more sensitive that ^{13}C NMR, providing the most sensitive NMR technique for degradation analysis.

A series of cells were cycled for periodic amounts of C/2 cycles before being disassembled and worked up for spectroscopic analysis. **Figure 3.8** shows the primary regions of activity in the ^{1}H NMR spectra of the extracted electrolyte solution from cells that have undergone 50 and 100 cycles at C/2 to UCVs of either 4.2 or 4.4 V, compared to the pristine electrolyte. **Figure 3.8**a highlights both the VC and EMC/DEC regions of the ^{1}H NMR where, by the 50th cycle at C/2 to both UCVs, a significant reduction in the VC signal is observed and it is no longer detectable at this magnification. Although considerable VC consumption has occurred, the EMC quartet remains well resolved. By the 100th cycle at C/2 the EMC region is convoluted, due to the formation of DEC, which has spectral activity in the same region as a result of the ethyl (CH_2) groups. DEC is commonly reported in literature alongside DMC as the product of the transesterification of EMC through reaction with the negative electrode.[26,56–58] Although DEC is a common electrolyte solvent used in lithium-ion battery cell chemistries and is not intrinsically detrimental to cell performance,[59,60] its formation can be used as an indicator of the onset of broader electrolyte degradation.

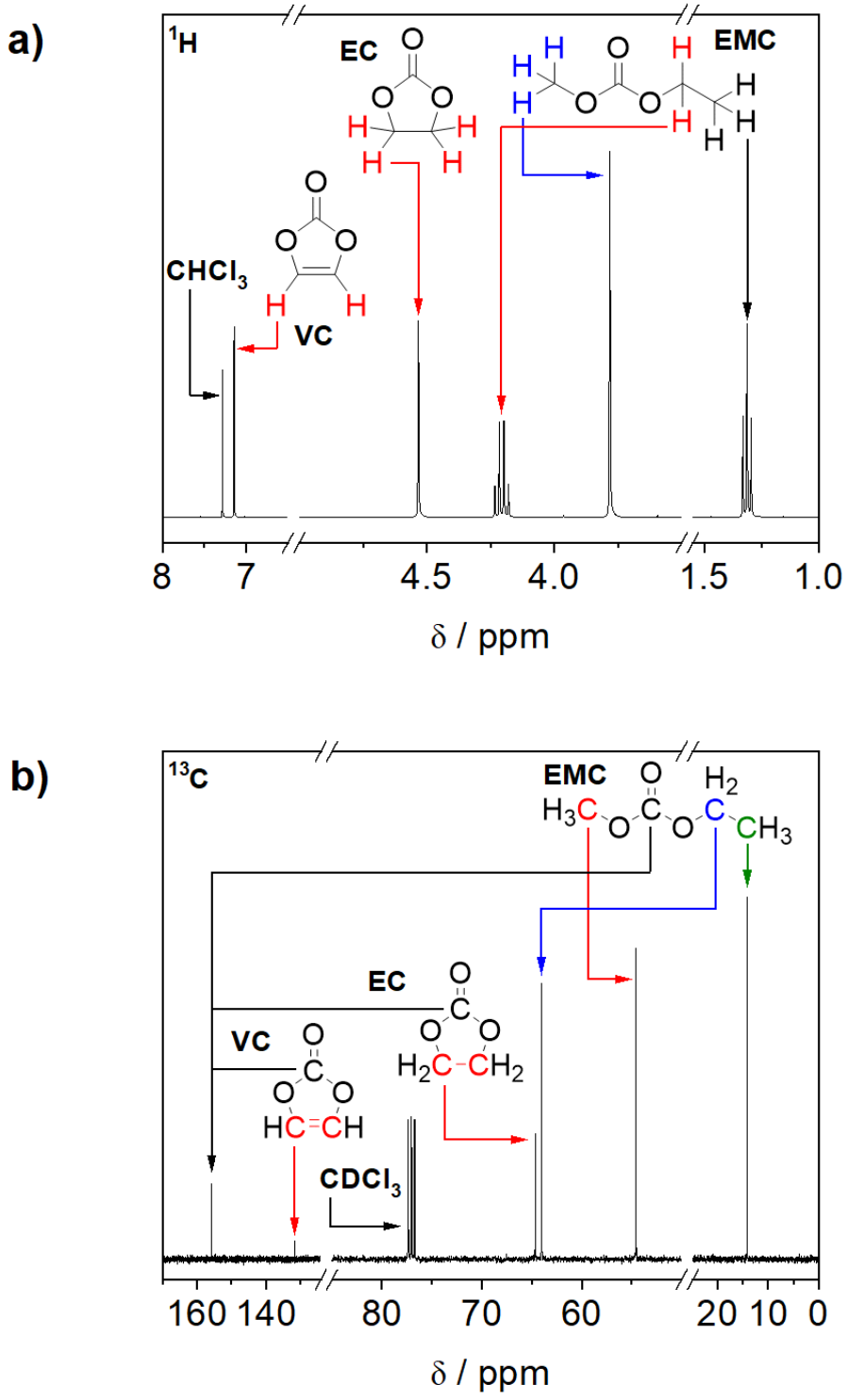


Figure 3.7. *a) ^{1}H and b) ^{13}C NMR spectra of a pristine LP57-VC electrolyte in $CDCl_3$. Peak assignments of the primary electrolyte solvents are shown for clarity, with atomic environments colour coded.*[61]

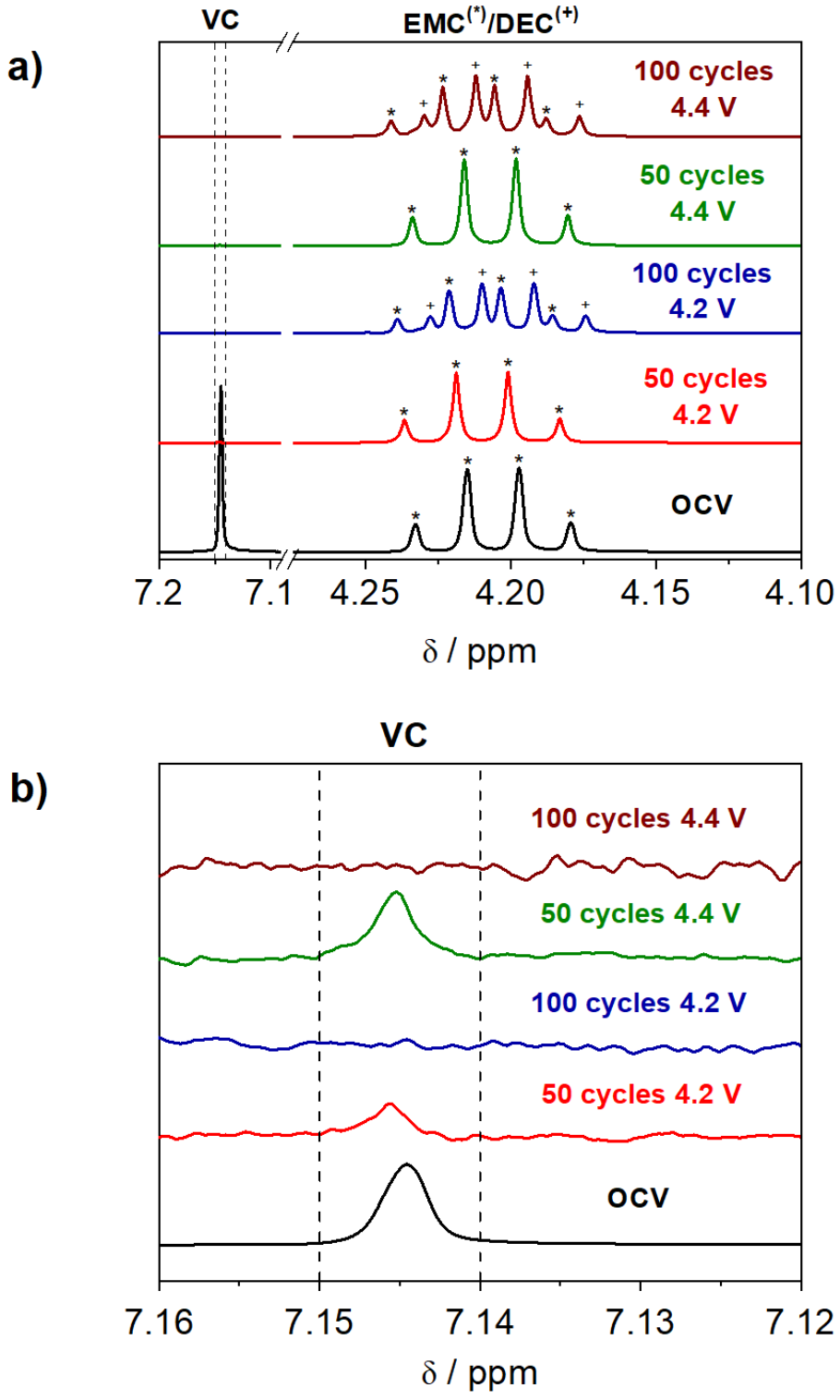


Figure 3.8. *a) EMC/DEC and b) VC regions of ^{1}H NMR spectra showing the formation of DEC and consumption of VC. Pristine LP57-VC electrolyte extracted from Li-NMC811 half-cells after an 80-hour OCV period is shown compared to electrolyte extracted from cells cycled to an UCV of 4.2 V or 4.4 V vs Li^{+}/Li after 50 or 100 cycles at C/2. Cycled electrolyte ^{1}H NMR spectra in b have been scaled 10 times relative to the OCV spectrum.*

VC can also be identified as still present in the extracted electrolyte solution after 50 cycles at C/2 (**Figure 3.8**b). By the 100th cycle no VC is detected in either sample and significant quantities of DEC have been formed. These data match well with the cycling data, indicating that for the first 50 cycles at C/2, while VC is present in the electrolyte, degradation is limited, and cell performance is relatively stable. Shortly after the 50th cycle, all of the VC is consumed and further electrolyte degradation processes will occur.

With the aim of increasing the limit of detection of degradation species and identifying structural compositions, GC-MS was employed to analyse the extracted electrolytes. The GC-MS method development is described in detail in Chapter 2. Analytes containing a high salt concentration are not suitable for GC-MS analysis. When the sample is injected into the inlet and vapourised to facilitate transfer onto the column, any salt will precipitate or degrade, contaminating the inlet. The poor solubility of $LiPF_6$ in deuterated chloroform ($CDCl_3$) enabled precipitation through mixing during sample preparation. To assess the effectiveness of $LiPF_6$ precipitation, ^{19}F and ^{31}P NMR analysis, shown in **Figure 3.9**, were performed on pristine LP57-VC electrolyte extracted in $CDCl_3$, alongside comparative spectra of a LP57-VC electrolyte in d_6-DMSO, in which the $LiPF_6$ salt is soluble. Upon mixing for at least 30 minutes, visible precipitation of salt was observed in the $CDCl_3$ mixture, where no visible changes were apparent in the d_6-DMSO mixture. Although the ^{19}F and ^{31}P NMR indicate that some $LiPF_6$ remains in the sample prepared using $CDCl_3$, the visible precipitation of some $LiPF_6$ makes the samples more suitable for GC-MS analysis than when mixed with d_6-DMSO. **Figure 3.10** shows the chromatogram of 1 µL of the pristine electrolyte. Retention time windows for the organic electrolyte species (EC, EMC, VC) and the most prominent electrolyte degradation species (DEC) are highlighted in the example chromatogram (**Figure 3.10**). The species are separated in good agreement with their relative boiling points, EMC (107 °C) < DEC (126 °C) < VC (162 °C) < EC (244 °C). The polar nature of the analytes results in a polarity mis-match with the mid-polarity crossbond column, which reduces the temperature required for desorption

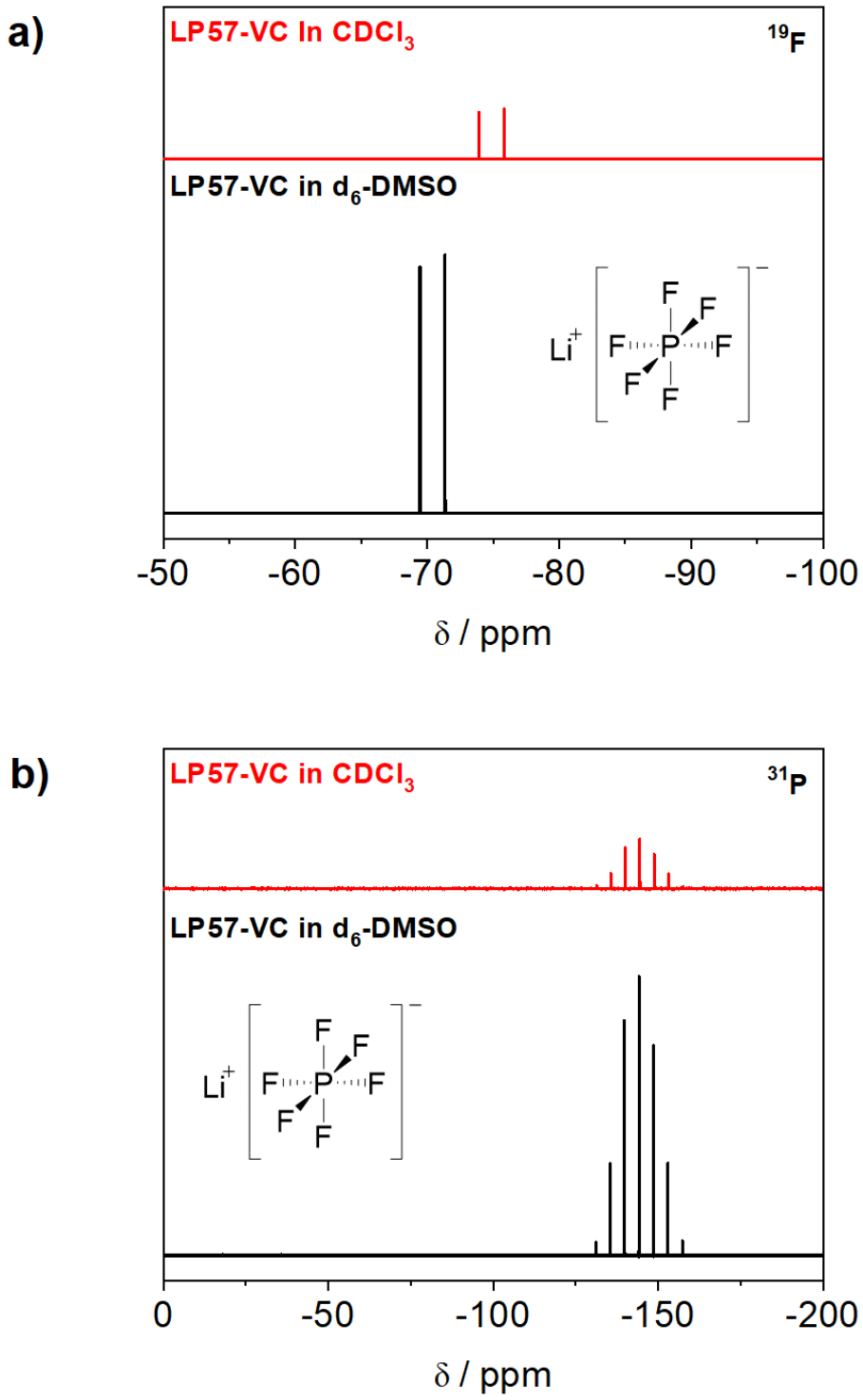


Figure 3.9. *a) ^{19}F and b) ^{31}P NMR spectra of a pristine LP57-VC electrolyte extracted from a Li-NMC811 half-cell after an 80-hour OCV period with either $CDCl_3$ (red lines) or d_6-DMSO (black lines).*

from the column coating. This sub- optimal interaction also results in peak fronting, explaining the non-symmetric nature of the chromatogram peaks. The low relative boiling point of EMC and high concentration in the electrolyte results in a large chromatogram peak at a retention time of 5.6 minutes (**Figure 3.10**). The other primary component of the electrolyte solvent, EC, requires significantly higher temperatures to pass through the column, with a recorded peak retention time of 24.4 minutes. Where present in the analyte, DEC and VC come between these two primary solvent peaks, with peak retention times of 7.5 and 10.3 minutes, respectively.

Chromatogram peak assignments were determined to a high degree of accuracy through comparison of recorded mass spectra to the NIST mass spectral library,[36] which is built-in to the instrument software. Example experimental mass spectra of each component, alongside NIST mass spectral database entries, are shown in the Appendix, displaying good agreement.

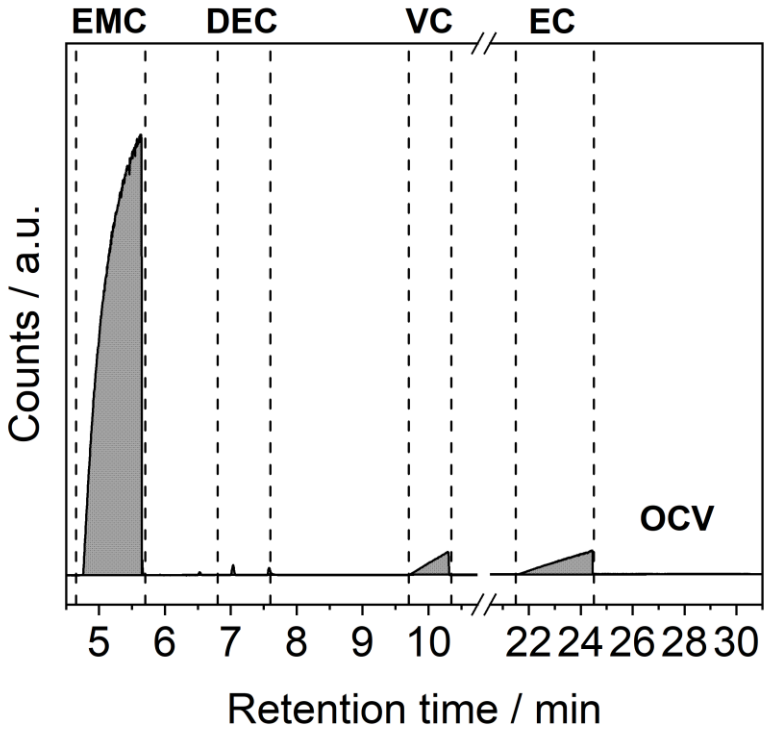


Figure 3.10. *GC-MS chromatogram of a pristine LP57-VC electrolyte extracted from a Li-NMC811 half-cell with $CDCl_3$ after an 80-hour OCV period. The retention time regions of key electrolyte components are highlighted with dashed lines for clarity.*

Figure 3.11 shows the GC-MS chromatograms of the extracted electrolyte solution from cells that have undergone 50 and 100 cycles at C/2 to UCVs of either 4.2 or 4.4 V, compared to the pristine electrolyte. In good agreement with the NMR data, by the 50th cycle at C/2 to both UCVs the majority of VC has been consumed, indicating consumption in early-stage cycling, and no new significant peaks are detected in the chromatograms. After 100 cycles at C/2, both cells cycled to an UCV of 4.2 and 4.4 V contained a considerable peak at a retention time of 7.5 minutes that was identified as DEC through mass spectral assignment. This observation is accompanied by a reduction in the intensity of both the EMC and EC peaks and manifestation of new high retention time peaks, above 26 minutes (see pages 126 – 128).

Figure 3.12 shows the DEC retention time region of the chromatograms produced through analysis of the electrolyte extracted from these cells. Although DMC is also detected in the samples, its low boiling point means that

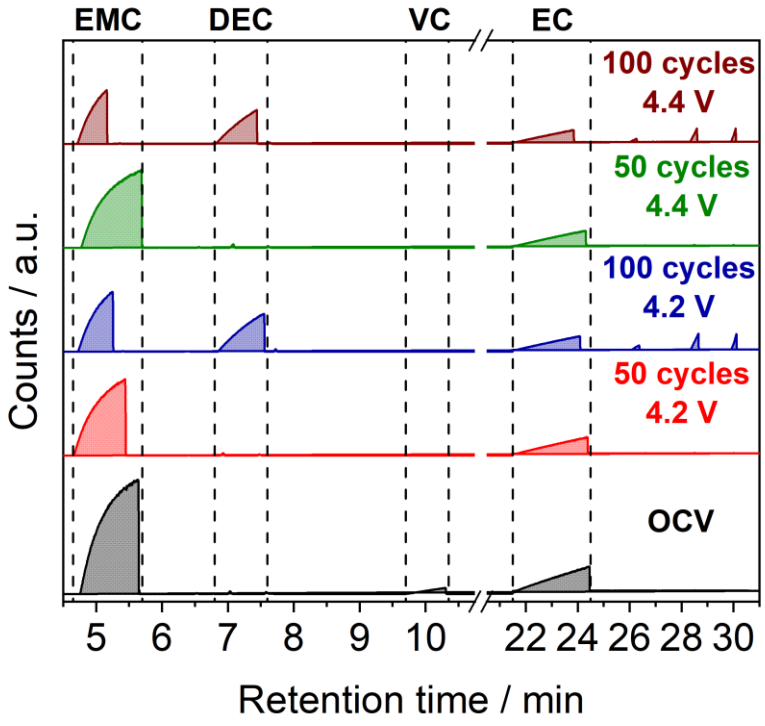


Figure 3.11. *GC-MS chromatograms showing the consumption of VC by the 50th cycle and accumulation of DEC by the 100th cycle of Li-NMC811 half-cells. Pristine LP57 electrolyte doped with 2 wt.% VC extracted after an 80-hour OCV period is shown compared to electrolyte extracted from cells cycled to an UCV of 4.2 V or 4.4 V vs Li$^+$/Li after 50 or 100 cycles at C/2.*

its desorption from the column occurs in conjunction with the majority of the carrier solvent. Some DEC is detected in both the cells cycled to UCVs of 4.2 V (**Figure 3.12**a) and 4.4 V (**Figure 3.12**b), from cell formation through to the 50th cycle at C/2. This indicates that some degradation of the electrolyte has occurred at this point. However, the quantity of DEC detected is small compared to EC and EMC, demonstrating that formation is largely limited at this point, consistent with the stable cycling of these cells up to the 50th cycle.[26,56–58] Between the 50th and 100th cycle, a significant increase in DEC concentration is observed, signalling the onset of EMC transesterification between the 50th and 100th cycle and implying broader electrolyte degradation.

Figure 3.13 highlights the VC retention time region of these chromatograms, where data from the cycled electrolytes are scaled 50 times relative to the chromatogram of the pristine sample. Close inspection reveals that after 50 cycles at C/2, VC is still present in both cells cycled to an UCV of 4.2 and 4.4 V, albeit in low concentration. The relative area of the VC peaks in the cycled electrolytes is <1% of the pristine sample, suggesting that VC will be totally consumed shortly after this observation point. After 100 cycles, no VC is detected in either sample and the DEC peak intensity is now comparable with that of the EMC peak, indicating that the consumption of VC signals the onset of degradation of the other electrolyte components (**Figure 3.11** – **Figure 3.13**).

The formation of DEC is accompanied by additional peaks in the GC–MS chromatograms. **Figure 3.14** shows the baseline of the chromatograms produced by extracted the LP57-VC electrolyte from cells cycled to UCVs of 4.2 and 4.4 V after 10, 20, 50 and 100 cycles at C/2, compared to the pristine electrolyte. Up to the 50th cycle at C/2, good electrolyte stability is observed in the cells cycled to an UCV of 4.2 V. A peak with a retention time of 14.5 minutes is observed in all chromatograms and is assigned to a silicon containing molecular species, likely the result of column degradation. By the 100th cycle, multiple peaks are detected between 14.3 – 19.5 minutes and above 26.0 minutes, indicating the formation of several soluble degradation species. Similar behaviour is observed in the cells cycled to an UCV of 4.4 V, where

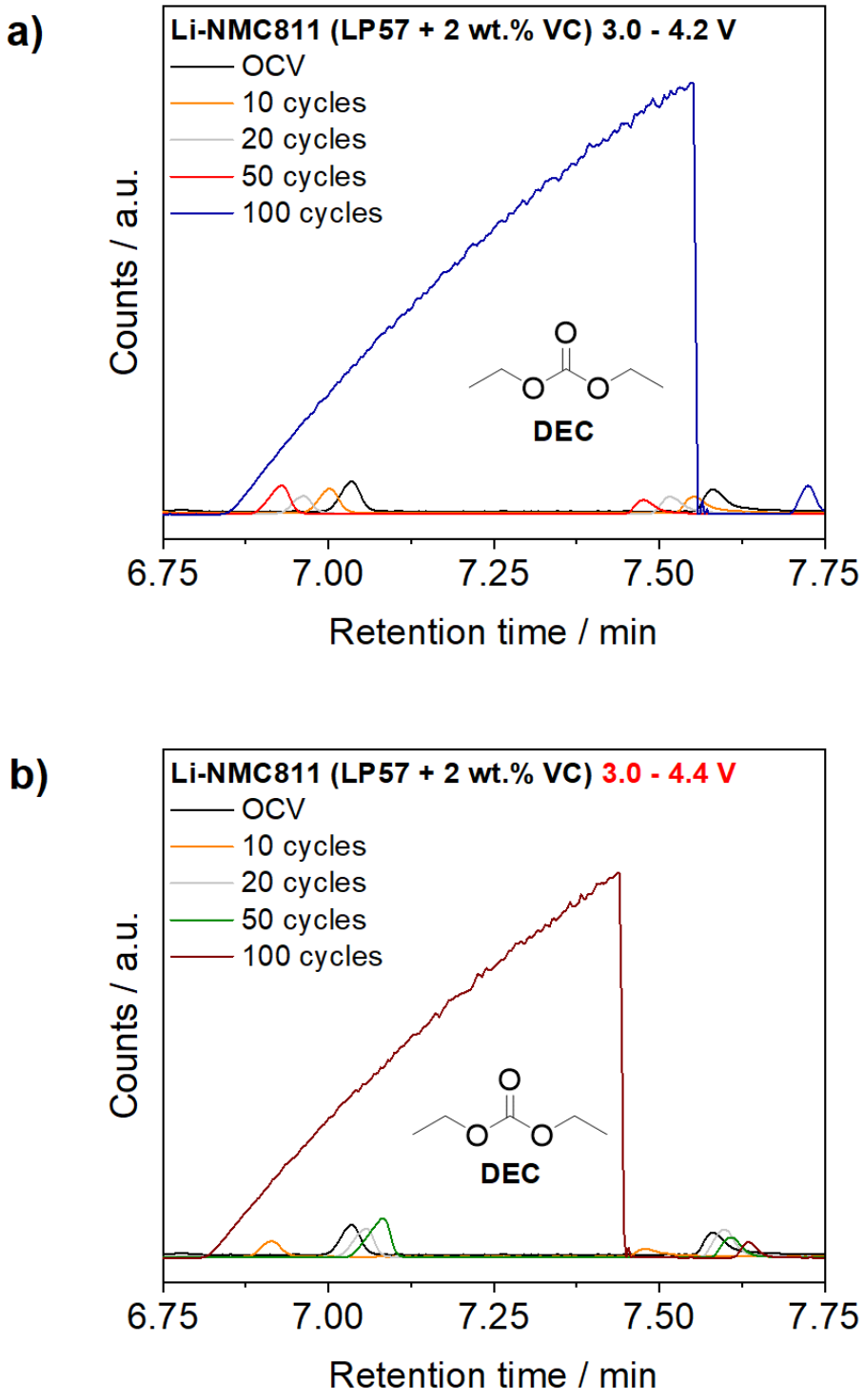


Figure 3.12. *DEC region of GC-MS chromatograms of electrolyte extracted from Li-NMC811 half-cells cycled to an UCV of a) 4.2 V or b) 4.4 V vs Li^+/Li containing LP57-VC. Pristine electrolyte extracted after an 80-hour OCV period is shown compared to electrolyte extracted from cells cycled for two C/20 formation cycles and 10, 20, 50 or 100 subsequent C/2 cycles.*

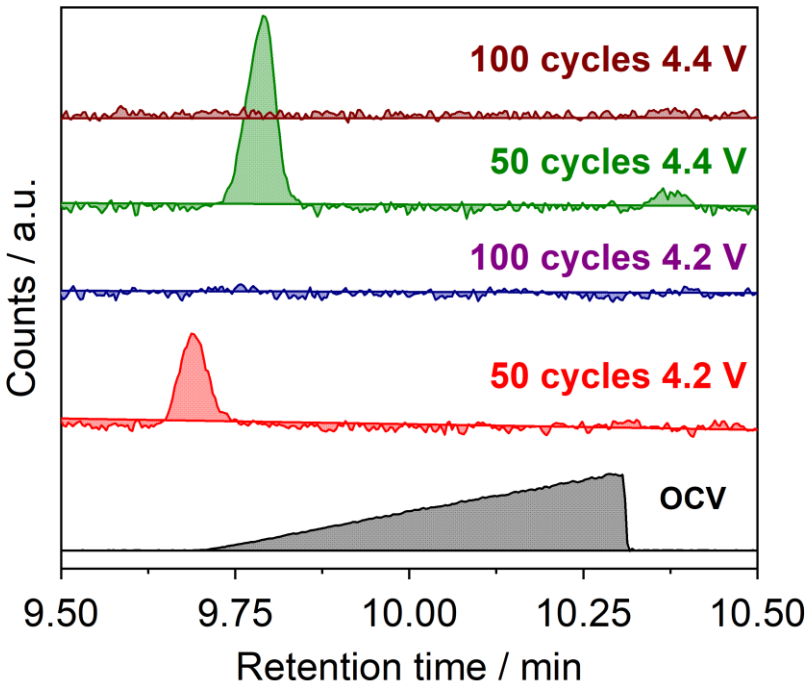


Figure 3.13. *VC region of GC-MS chromatograms showing the presence of trace amounts of VC in electrolytes extracted after the 50th cycle and the absence of a VC peak after the 100th cycle to an UCV of 4.2 V or 4.4 V vs Li^{+}/Li of Li-NMC811 half-cells containing a LP57-VC electrolyte. Electrolyte extracted after an 80-hour OCV period is shown compared to electrolyte extracted from cells cycled to for two C/20 formation cycles and 50 or 100 subsequent C/2 cycles. Cycled electrolyte chromatograms have been scaled 50 times relative to the OCV chromatogram.*

significant new peaks are observed by the 100th cycle at C/2. The degradation species are tentatively identified in **Table 3.1**. These identifications should only be used as a guideline to understand the nature of degradation products, rather than conclusive evidence of their presence. Prospective molecular identifications have been screened and reported only where the MS probability, a measure of agreement with a given NIST mass spectral library entry, is ≥70%. Some of the major new chromatogram peaks above 26 minutes did not meet this confidence threshold, but have been reported due to their high intensity (marked with red text).

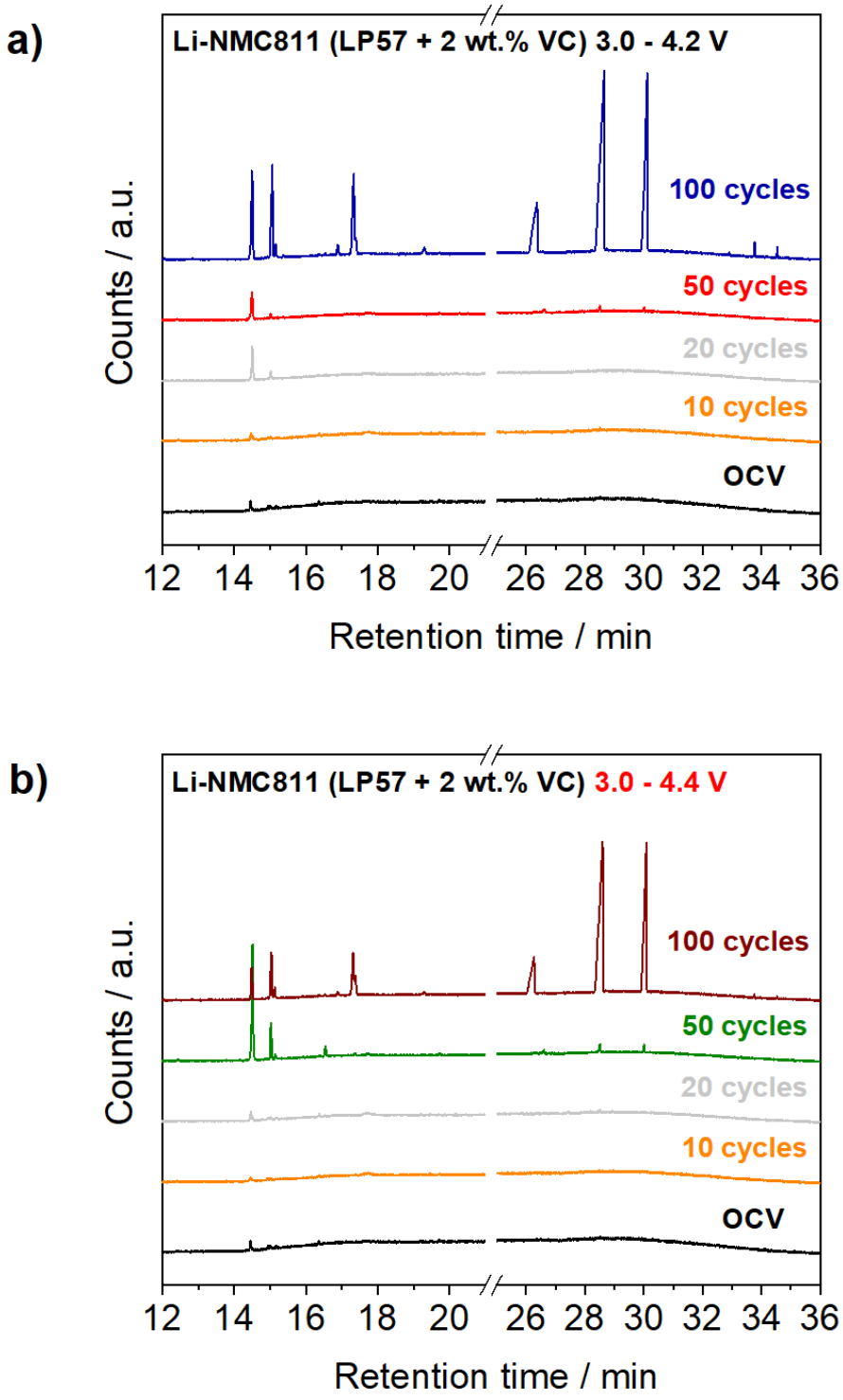
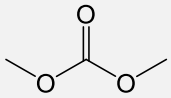
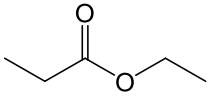
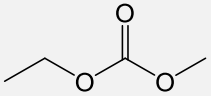
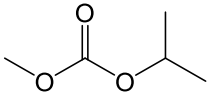
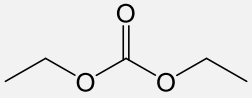
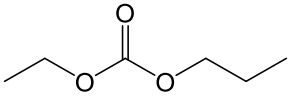
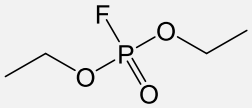
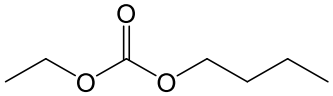
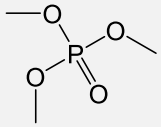
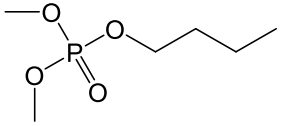
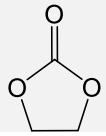
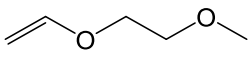
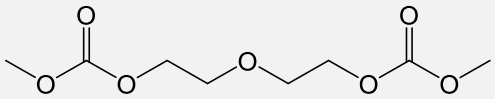
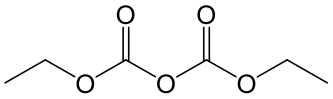
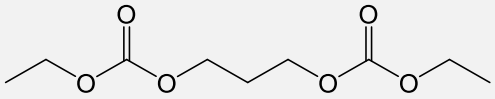
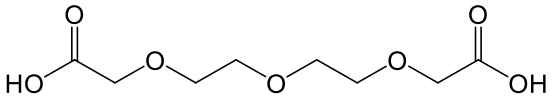
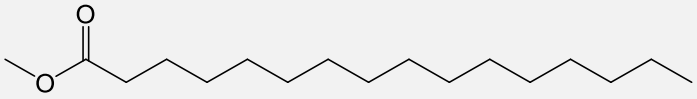


Figure 3.14. *Low intensity degradation product regions of GC-MS chromatograms of electrolyte extracted from Li-NMC811 half-cells cycled to an UCV of a) 4.2 V or b) 4.4 V vs Li^+/Li containing a LP57-VC electrolyte. Pristine electrolyte extracted after an 80-hour OCV period is shown compared to electrolyte extracted from cells cycled for two C/20 formation cycles and 10, 20, 50 or 100 subsequent C/2 cycles.*

Table 3.1. *Proposed identity of chromatogram peaks in the GC trace of the electrolyte extracted from Li-NMC811 half-cells after 100 cycles at C/2 to an UCV of 4.2 or 4.4 V vs Li^+/Li containing a LP57-VC electrolyte. Peaks have been screened for an MS probability ≥70%. Some tentative molecular identifications with a probability below 70% are included where peak intensity is high (highlighted with red text).*

Retention time (mins)	Name	Chemical structure	MS probability (%)
4.33	Dimethyl carbonate		93.1
4.91	Ethyl propionate		66.0
5.17	Ethyl methyl carbonate		97.0
6.14	Methyl isopropyl carbonate		78.1
7.44	Diethyl carbonate		91.8
8.68	Ethyl propyl carbonate		88.1

Retention time (mins)	Name	Chemical structure	MS probability (%)
14.13	Diethyl fluorophosphate		89.5
15.33	Butyl ethyl ester carbonic acid		72.2
16.65	Trimethyl phosphate		84.9
18.69	Butyl dimethyl phosphate		79.3
24.18	Ethylene carbonate		95.68
26.45	2-methoxyethyl vinyl ether		14.74

Retention time (mins)	Name	Chemical structure	MS probability (%)
28.68	Dimethyl diglycolcarbonate		24.25
30.16	Diethyl pyrocarbonate		70.1
31.77	Diethyl propane-1,3-diyl dicarbonate		93.2
36.39	3,6,9-Trioxaundecanedioic acid		21.8
36.45	Methyl palmitate		59.98

With these observations further reinforcing the hypothesis that VC consumption is intrinsically linked to electrolyte degradation in half-cells, analogous cells were assembled with a VC-free LP57 electrolyte and analysed at various extents of cycling. **Figure 3.15** compares the GC-MS chromatograms produced by electrolyte extracted from cells cycled to UCVs of 4.2 and 4.4 V after 10 and 100 cycles at C/2, compared to the pristine electrolyte. These chromatograms clearly show that significant transesterification of EMC to DEC, and further electrolyte degradation processes occur by the 10^{th} cycle under both conditions, confirming that VC is preferentially degraded on the surface of the metallic Li, protecting other electrolyte components from degradation.

The good agreement between the GC-MS, NMR and cell cycling data indicate that VC is preferentially degraded on the surface of the metallic Li electrode, which mitigates bulk electrolyte degradation and results in reproducible capacity performance of half-cell studies when cycle number is limited. The consumption of VC shortly after 50 cycles, and coincident onset of EMC transesterification, demonstrates that the presence of VC mitigates bulk electrolyte degradation.

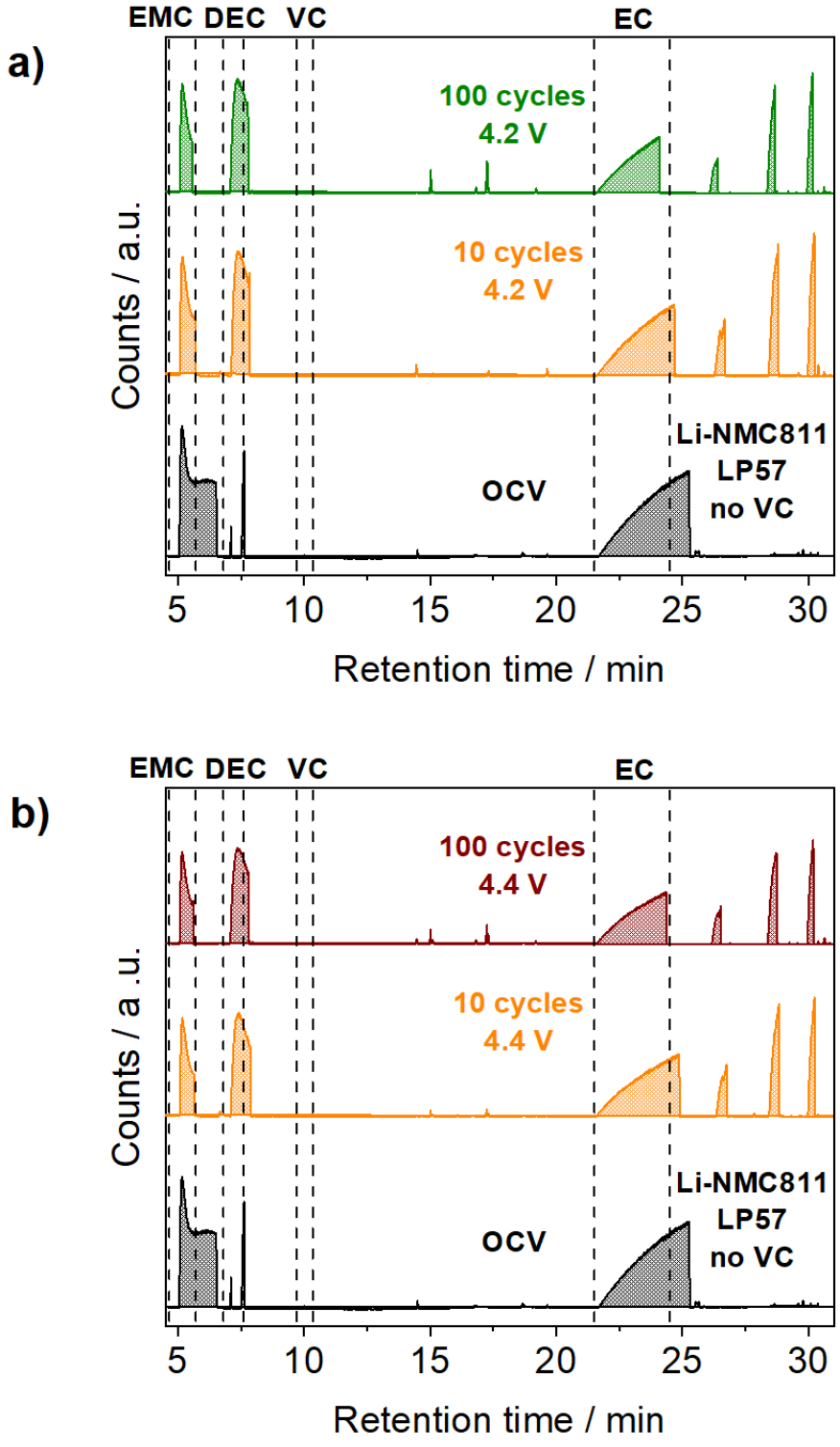


Figure 3.15. *GC-MS chromatograms of electrolyte extracted from Li-NMC811 cells cycled to an UCV of a) 4.2 V or b) 4.4 V vs Li^+/Li containing a VC-free LP57 electrolyte, showing the onset of significant degradation by the 10^{th} cycle. Pristine VC-free LP57 electrolyte extracted after an 80-hour OCV period is shown compared to electrolyte extracted from cells cycled for two C/20 formation cycles and 10 or 100 subsequent C/2 cycles.*

3.5 Understanding the failure mechanism of half-cells based on metallic Li

Although VC has been shown to delay the onset of electrolyte degradation, the exact failure mechanism of these cells is still unclear. To identify the origin of cell failure, Li-NMC811 cells containing a LP57-VC electrolyte were cycled to UCVs of 4.2 and 4.4 V for 100 cycles at C/2, before being reconstituted – disassembled to remove the cycled electrodes and then reassembled in separate cells containing fresh electrolyte and a pristine partner electrode. A schematic of the reconstitution process is shown in **Figure 3.16**. Replenishing the electrolyte acts to simultaneously dilute any remaining contaminants in the cell and re-introduce VC to the system, which can in principle protect the electrolyte solution from further degradation at the surface of the metallic Li electrode. A pristine counter electrode acts to minimise the contribution of the partner electrode to the cell performance, thus elucidating the health of each cycled electrode.

To determine whether the disassembly and reassembly of cycled cells would have detrimental effects on the performance of the electrodes, control cells containing a LP57-VC electrolyte were cycled for two C/20 formation cycles and subsequently 10 cycles at C/2 to an UCV of 4.2 V (**Figure 3.17**). Under these cycling conditions, the capacity performance is stable and minimal

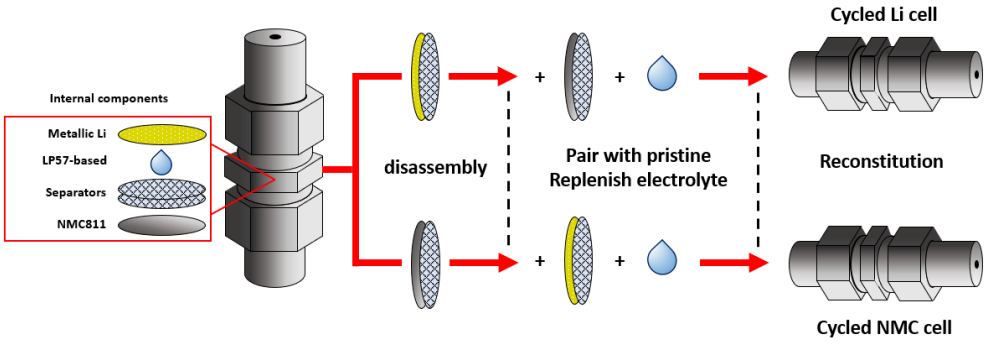


Figure 3.16. *Schematic representation of the cell reconstitution procedure wherein Li-NMC811 half-cells are disassembled and reconstituted. The result is two separate cells, each containing a cycled electrode paired with a pristine partner electrode and fresh electrolyte.*

electrolyte degradation will have occurred. The cell was then reconstituted, pairing the cycled NMC811 electrode with a pristine metallic Li electrode and the cycled metallic Li electrode with a pristine NMC811 electrode, before replenishing the LP57-VC electrolyte. This resulted in two individual cells that could be used to determine the performance of the cycled electrodes, without significant impact from other degraded cell components. **Figure 3.17** shows the results of these cells, where initial pre-reconstitution C/2 cycling achieved a discharge capacity of 151.2 mAh g^{-1}_{NMC} and an average CE >99.9%, excluding the drop due to increasing rate, in good agreement with the average pristine cell performance.

To ensure comparable cycling procedures, after reconstitution two C/20 formation cycles were performed on each cell. This was done to limit the contribution of the pristine NMC811 electrode to the performance of the cycled metallic Li cell. Average C/20 discharge capacities of 171.4 and 196.2 mAh g^{-1}_{NMC} were recorded for the cells containing the cycled NMC811 and cycled metallic Li electrodes, respectively (**Figure 3.17**). The slight drop in the capacity of the cycled NMC811 electrode (blue diamonds) relative to the pre-reconstitution cell (black circles) indicates that even after 10 cycles, the intercalation capacity of the NMC811 electrode is reduced compared to when pristine. However, upon initiation of C/2 cycling, a discharge capacity of 136.1 mAh g^{-1}_{NMC} is recorded, 90.01% of the capacity of the pre-reconstitution cell (**Figure 3.17**a). The disparity in the charge and discharge capacity of the cycled NMC811 cell is seen over the first 10 cycles (cycles 13-22). However, the CE recovers to 99.74% by the 11^{th} cycle and capacity stabilisation is observed up to the 52^{nd} cycle (64 total cycles). Over this stable capacity region, an average CE of 99.82% is achieved, indicating that the electrode is healthy and capable of undergoing cycling similar to the pristine cell.

The cell containing the cycled metallic Li electrode performs similarly to pristine, with an initial C/2 discharge capacity of 151.9 mAh g^{-1}_{NMC}, 100.46% of the capacity of the pre-reconstitution cell (**Figure 3.17**b). This slight increase in capacity relative to the pristine cell is the result of minor differences in the

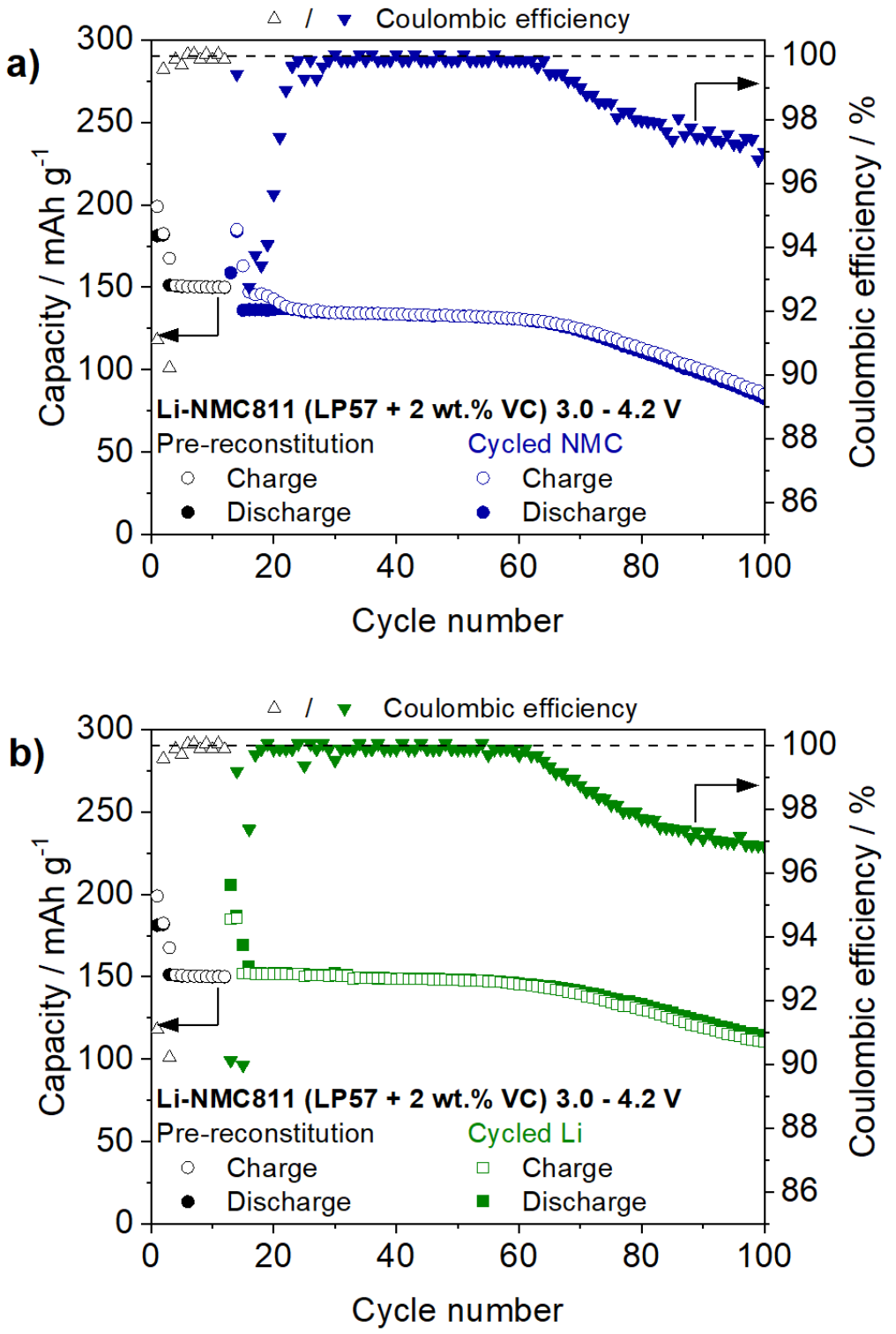


Figure 3.17. *Capacity performance of reconstituted Li-NMC811 half-cells where the cycled a) NMC (blue) and b) Li (green) electrodes are paired with a pristine partner electrode. Two C/20 and 10 C/2 cycles to an UCV of 4.2 V vs Li^+/Li were completed before reconstitution. After reconstitution, cells were cycled for 2 C/20 and 100 C/2 cycles to an UCV of 4.2 V vs Li^+/Li.*

NMC811 electrodes. The near perfect consistency in performance indicates that the metallic Li electrode is largely unaffected by both the previous cycling and reconstitution procedures, supported by an average CE of 99.82% observed over the first 50 cycles (cycles 13-62). The same drop in CE and capacity fade is observed after 50 cycles (64^{th} total cycle) in this cell, indicative of the consumption of VC and the onset of broader electrolyte degradation. These data confirm that the reconstitution procedure does not have a significant impact on the long-term cycling performance or trends observed for the extracted electrodes.

To understand the relative performance of the cycled electrode materials after cell failure, cells containing a LP57-VC electrolyte were cycled for two C/20 formation cycles and 100 cycles at C/2 to an UCV of either 4.2 or 4.4 V before being reconstituted, isolating the cycled electrodes, pairing them with a pristine counter, and replenishing the electrolyte. **Figure 3.18** – **Figure 3.20** show the capacity performance and voltage profiles for the first two C/20 formation cycles and subsequent first C/2 cycle of a pristine cell compared to those for the reconstituted cells. Upon initial C/20 cycling, the cell containing the cycled NMC811 electrode cycled to an UCV of 4.2 V achieved almost complete capacity recovery achieving a discharge capacity of 166.6 mAh g^{-1}_{NMC} (**Figure 3.18**a). This result indicates that the cycled NMC811 electrode is capable of reversibly intercalating 89% of the lithium ions as when pristine, demonstrating that the bulk internal structure is largely intact. However, when the rate was increased to C/2, a large drop in the discharge capacity of the cycled NMC811 electrode to 36.9 mAh g^{-1}_{NMC} was observed, signifying a high positive electrode impedance. The cells containing the cycled NMC811 electrode that was cycled to an UCV of 4.4 V shows the same trend, although at C/20 the capacity recovery was less pronounced, achieving an initial discharge capacity of 137.1 mAh g^{-1}_{NMC} (**Figure 3.18**a). Upon initiation of C/2 cycling, no meaningful capacity could be extracted from the cell, indicating that the extension of the UCV has resulted in a higher positive electrode impedance.

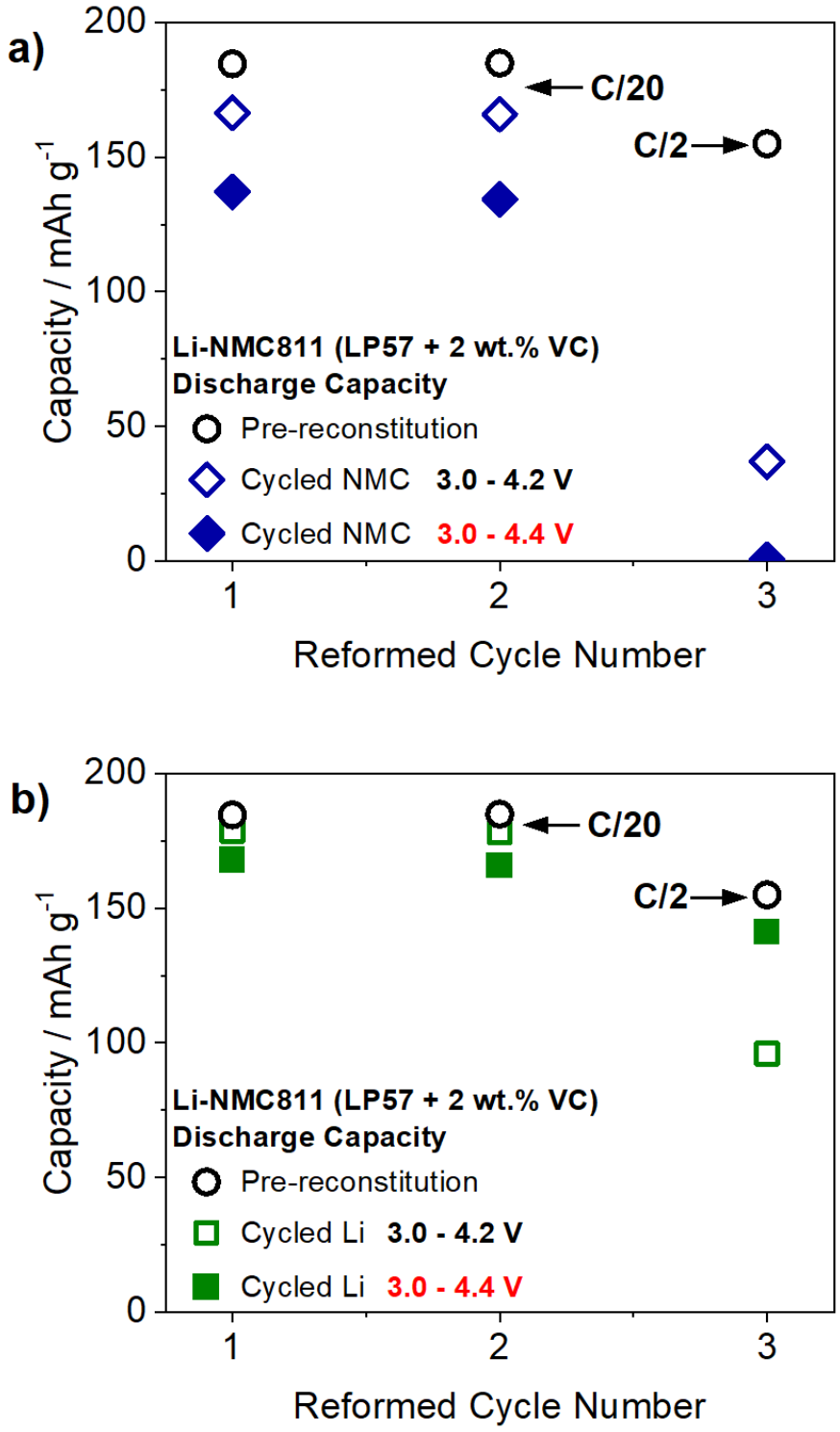


Figure 3.18. *Discharge capacities the first 3 cycles of a cycled a) NMC and b) Li electrodes reconstituted with a pristine partner electrode after two C/20 and 100 C/2 cycles to an UCV of 4.2 V (empty shapes) or 4.4 V (filled shapes) vs Li^+/Li containing a LP57-VC electrolyte. The performance of a pristine Li-NMC811 half-cell cycled to an UCV of 4.2 V vs Li^+/Li containing a LP57-VC electrolyte is shown for comparison (black shapes).*

A similar capacity-current relationship is observed for the cells containing the cycled lithium electrodes, with the cell cycled to an UCV of 4.2 V recording initial C/20 and C/2 discharge capacities of 178.7 and 96.0 mAh g^{-1}_{NMC}, respectively (**Figure 3.18**b). The high initial C/20 capacity, ca. 95% relative to the average pristine cell (**Figure 3.5**a), indicates that although the NMC811 electrode is pristine, performance deviates from the average cell as a result of the presence of a degraded metallic Li electrode. The relatively low first C/2 discharge capacity demonstrates that, although care was taken to allow formation cycling, the performance of the NMC811 electrode has been diminished by the presence of the cycled metallic Li electrode and residual electrolyte degradation products. The cell cycled to an UCV of 4.4 V achieved an initial C/20 capacity of 170.0 mAh g^{-1}_{NMC}, indicating that the metallic Li electrode and electrolyte cause more degradation of the pristine NMC811 electrode when they have undergone cycling in cells with an extended UCV. The high reported initial C/2 capacity of 141.2 mAh g^{-1}_{NMC} is the result of the extended UCV, ca. 70% of the average pristine cell capacity when cycled to an UCV of 4.4 V.

Figure 3.19 and **Figure 3.20** show the cycle profiles of these cells, where good recovery of the charge and discharge voltage profile characteristics is seen in all cells when cycled at C/20. Upon initiation of C/2 cycling, all cells immediately lose these characteristics and considerable capacity loss is observed. These data show that neither the NMC811 electrode nor the metallic Li electrode are exclusively responsible for the failure of these cells and that both the increased impedance of the cycled NMC811 electrode and degradation of the metallic Li electrode, as a result of repeated lithium plating and stripping, contribute to the observed capacity loss.

To understand the origin of the impedance of NMC811 electrodes, and how it develops as a function of cycle number, EIS was employed in a three-electrode configuration to isolate the positive electrode response. Further details regarding cell configuration EIS theory can be found in Chapter 2. In this study, alternating current EIS was utilised to study the resistive properties of processes taking place at the surface of the NMC811 electrode.

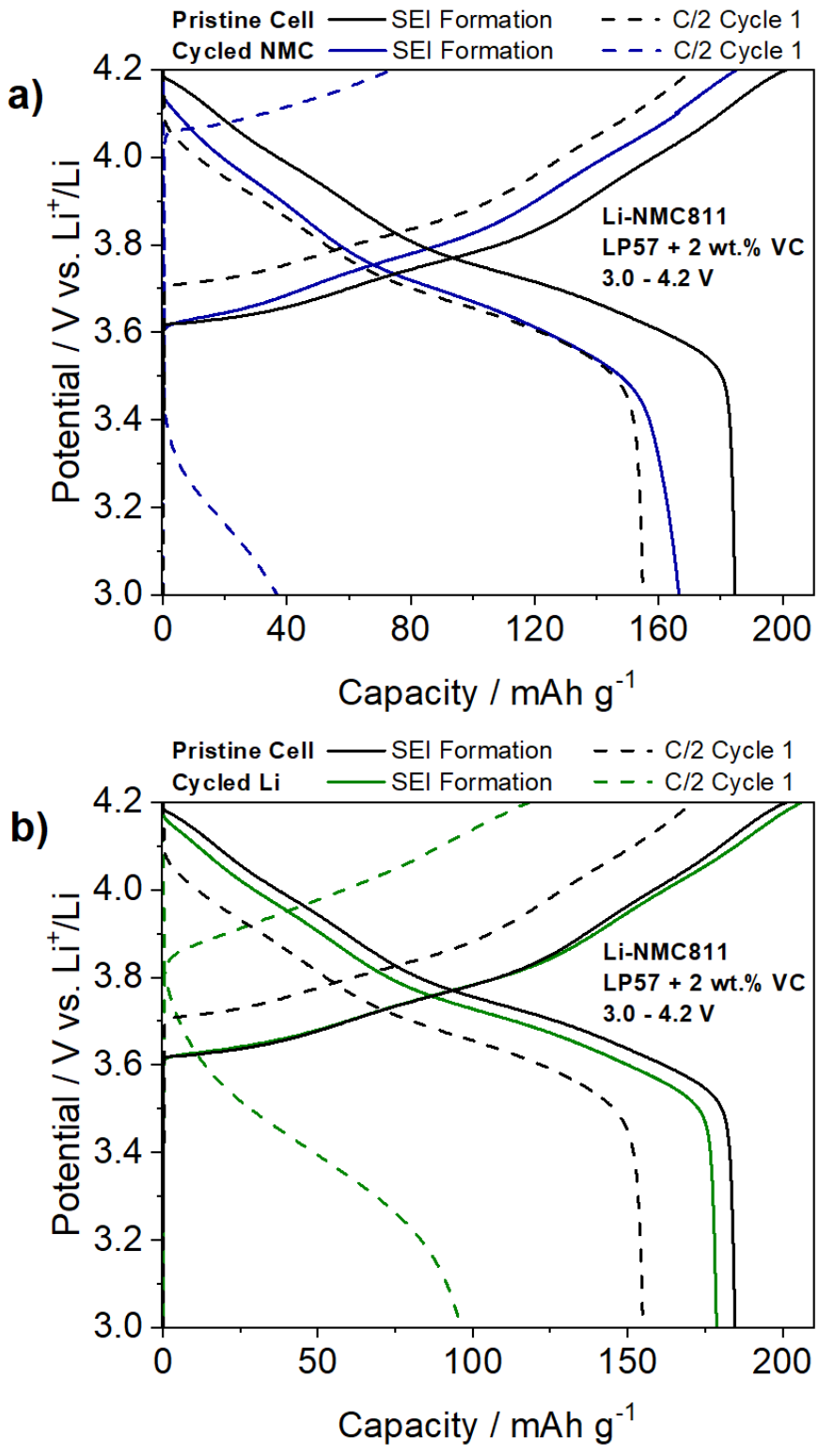


Figure 3.19. *Voltage profiles of the first C/20 and C/2 cycles of reconstituted Li-NMC811 half-cells containing the cycled a) NMC and b) Li electrode paired with a pristine partner electrode cycled to an UCV of 4.2 V. Cells contained a LP57-VC electrolyte and were reconstituted after two C/20 and 100 C/2 cycles to an UCV of 4.2 V vs Li^+/Li, where the electrolyte was replenished. Voltage profiles of a pristine Li-NMC811 half-cell cycled to an UCV of 4.2 V vs Li^+/Li containing a LP57-VC electrolyte are shown for comparison (black lines).*

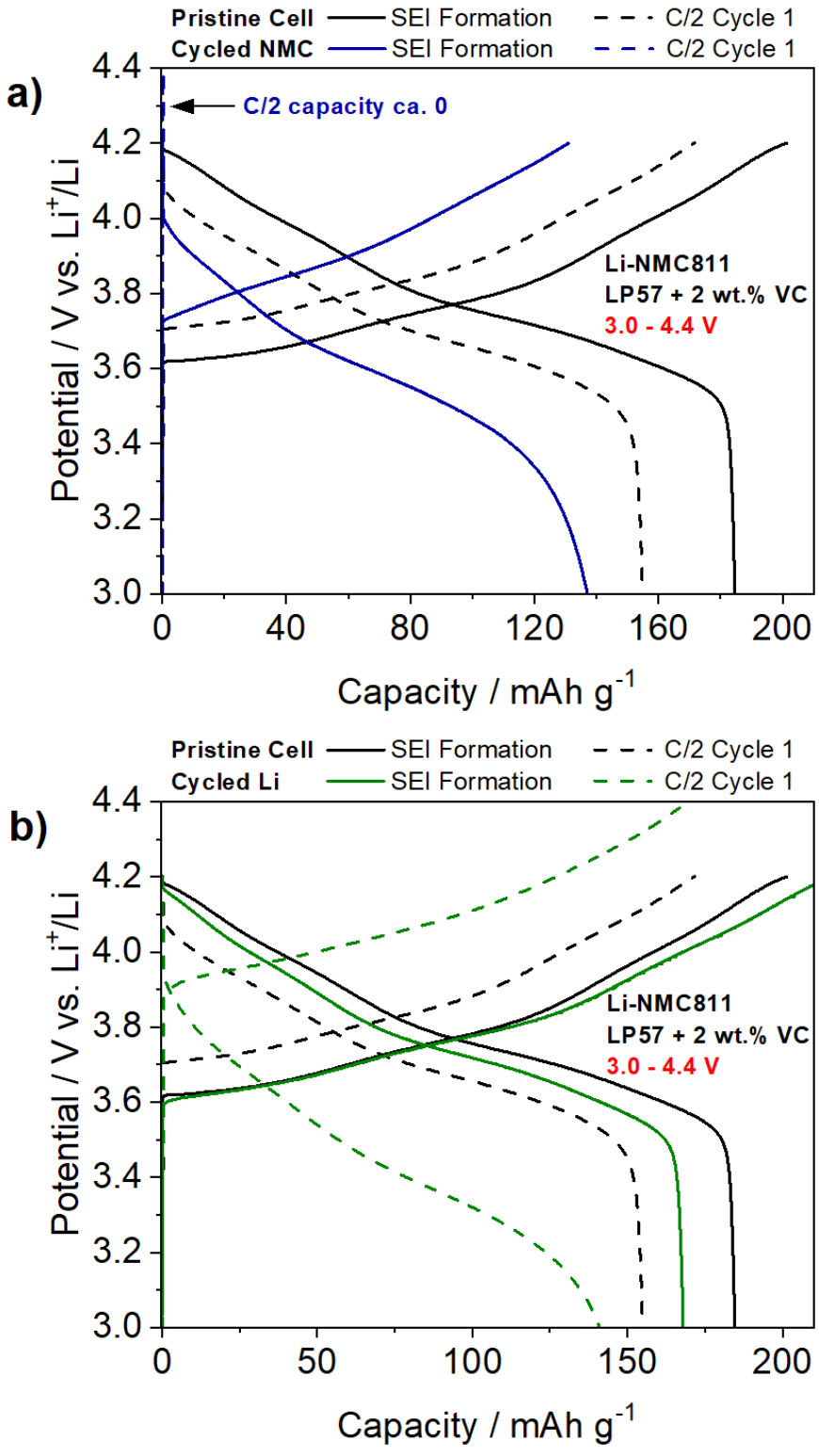


Figure 3.20. *Voltage profiles of the first C/20 and C/2 cycles of reconstituted Li-NMC811 half-cells containing the cycled a) NMC and b) Li electrode paired with a pristine partner electrode cycled to a UCV of 4.4 V. Cells contained a LP57-VC electrolyte and were reconstituted after two C/20 and 100 C/2 cycles to an UCV of 4.4 V vs Li^+/Li, where the electrolyte was replenished. Voltage profiles of a pristine Li-NMC811 half-cell cycled to an UCV of 4.2 V vs Li^+/Li containing a LP57-VC electrolyte are shown for comparison (black lines).*

cells containing either an VC-free or LP57-VC electrolyte were cycled to an UCV of either 4.2 or 4.4 V, for two C/20 formation cycles and 100 subsequent C/2 cycles, with EIS measurements taken at regular intervals. EIS measurements should not be taken near the potential limits of operation, as these represent high resistance boundary conditions, where lithium insertion/de-insertion capacity is near 100%. Cells were cycled to the desired extent of cycling, before being discharged to 3.6 V and held at a constant voltage for 1-hour before EIS measurements were taken.

Figure 3.21 shows the equivalent circuit diagram used to fit the impedance data, consisting of a resistor connected to two parallel circuits. The resistor represents the solution resistance (R_S), which describes the physical movement of ions through the solution between the working and reference electrode. R_S is an intrinsically high frequency process and is influenced by factors such as Li^+ concentration, cell temperature, and electrolyte viscosity. The first parallel circuit relates to the charge transfer resistance (R_{CT}), which considers the movements electrons into and out of the NMC811 electrode and the complementary diffusion of Li^+ into and out of the surface of the electrode, and the capacitance (Q_1) at the interface. The second parallel circuit concerns Li^+ diffusion through the CEI film (R_{CEI}), the capacitance within this phase (Q_2), and a Warburg element (W), which is a constant phase element that models lithium diffusion through the CEI.[62]

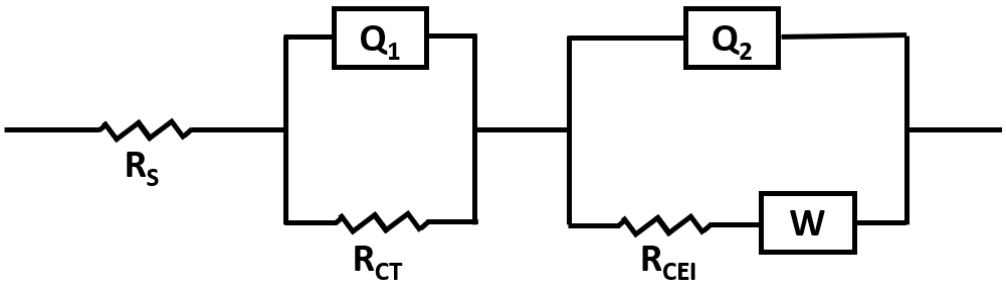


Figure 3.21. *Equivalent circuit diagram used to fit the impedance response of Li-NMC811 half-cells. A three-electrode arrangement with a metallic Li reference electrode was used to isolate the impedance of the NMC811 electrode. Solution resistance (R_s), charge transfer resistance (R_{CT}), Li^+ diffusion resistance of the CEI (R_{CEI}), capacitance (Q_x) and a Warburg element (W) are included.*

All cells were cycled for two C/20 formation cycles to an UCV of 4.2 V before the initiation of C/2 cycling. The impedance response after formation cycling for all cells reveals two distinct semi-circles, attributed to the R_{CEI} (higher frequency) and the R_{CT} (medium frequency) (**Figure 3.22** and **Figure 3.23**).[62] The uptick observed at low frequencies is attributed to a Warburg impedance (W). **Figure 3.22** shows the EIS response recorded in cells containing either an VC-free or LP57-VC electrolyte cycled to an UCV of 4.2 V after CEI formation compared to after the 10th, 20th, 50th, 80th and 100th cycle at C/2. The cell containing LP57-VC demonstrated a significantly lower impedance at each measured cycle than the VC-free cell, confirming that the presence of VC in the electrolyte composition results in reduced positive electrode impedance throughout cycling (**Figure 3.22**). The rate of impedance growth in this cell accelerates after the 50th cycle, in good agreement with the drop in CE, consumption of VC, and onset of broader electrolyte degradation identified previously. In the cell containing VC-free LP57 electrolyte, no stabilisation of the EIS response is observed, with consistent impedance growth being measured as extent of cycling progresses (**Figure 3.22**b), indicating that the absence of VC in the electrolyte results in increased impedance of the positive electrode. **Figure 3.23** shows analogous cells cycled to an UCV of 4.4 V. Pushing the NMC811 electrode into a region of higher stress results in earlier onset and a greater magnitude of impedance growth in both cells, but the overall trends remain the same as the cells cycled to 4.2 V.

To isolate the contribution of CEI resistance to the overall impedance of the cells, the equivalent circuit diagram shown in **Figure 3.21** was used to calculate CEI impedance as a function of cycle number (**Figure 3.24**). **Figure 3.24**a shows the change in CEI resistance of cells containing a LP57-VC electrolyte cycled to UCVs of either 4.2 or 4.4 V. For cells cycled to an UCV of 4.2 V, the CEI resistance remains low across the first 50 cycles, with a measured 10th, 20th and 50th resistance of 111.0, 111.4, and 96.3 Ω cm^2, respectively (**Figure 3.24**a). The low and stable impedance across the first 50 cycles is in good agreement with the stable cycling and compositional analysis of the electrolyte, indicating that the

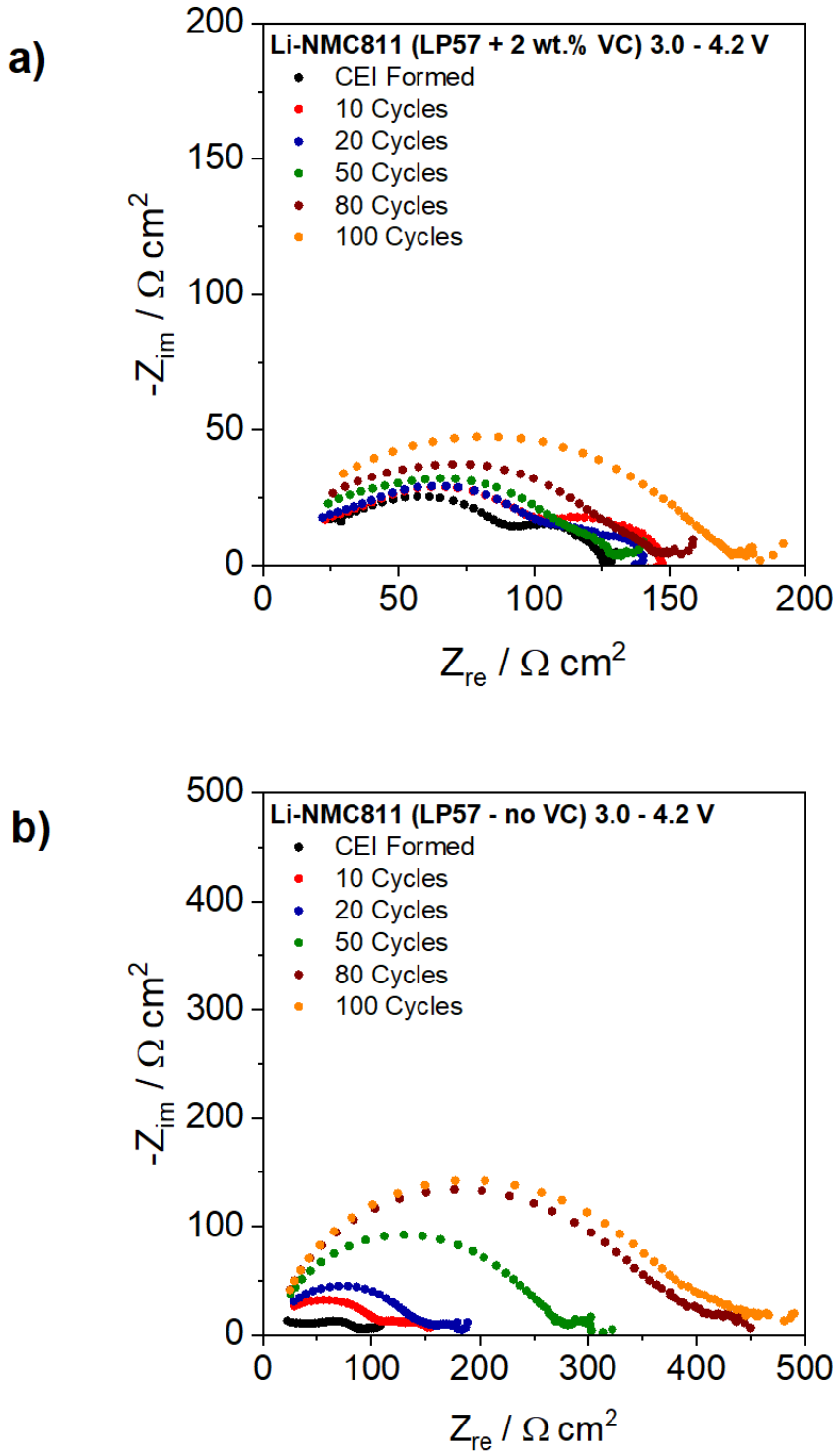


Figure 3.22. *Isolated EIS responses of a NMC811 electrode in a three-electrode Li-NMC811 half-cell containing a a) LP57-VC or b) VC-free electrolyte cycled to an UCV of 4.2 V vs Li^+/Li. EIS was performed after a 1-hour voltage hold at 3.6 V vs Li^+/Li after the 1st C/20 formation cycle and subsequent 10th, 20th, 50th, 80th and 100th cycle, with a metallic Li reference electrode.*

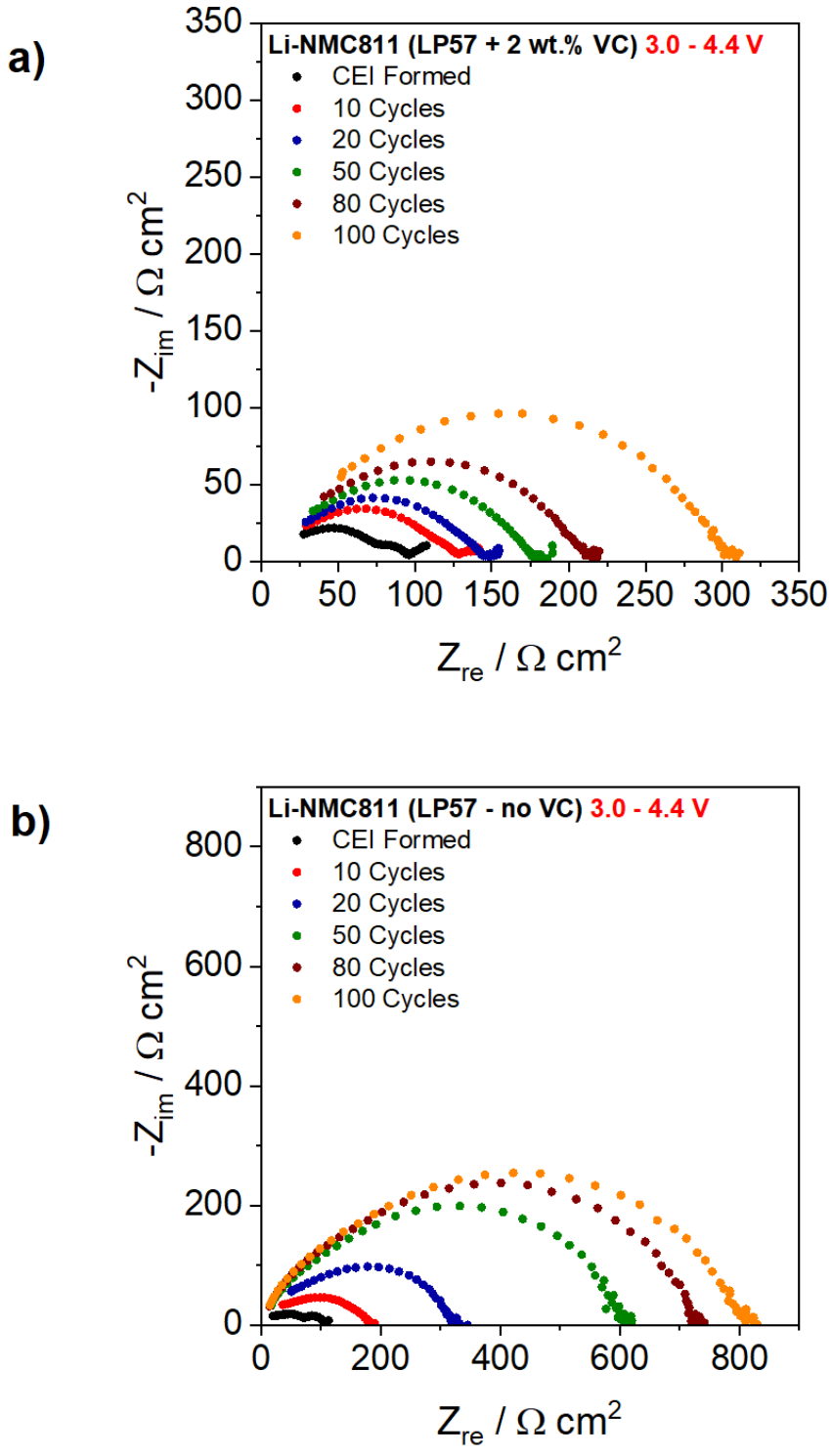


Figure 3.23. *Isolated EIS responses of a NMC811 electrode in a three-electrode Li-NMC811 half-cell containing a a) LP57-VC or b) VC-free electrolyte cycled to an UCV of 4.4 V vs Li^+/Li. EIS was performed after a 1-hour voltage hold at 3.6 V vs Li^+/Li after the 1st C/20 formation cycle and subsequent 10th, 20th, 50th, 80th and 100th cycle, with a metallic Li reference electrode.*

resistance of the CEI is largely unaffected after initial C/2 cycling. A similar CEI resistance is measured in early-stage cycling of the cell cycled to an UCV of 4.4 V, with measured 10th and 20th CEI resistances of 107.2 and 111.0 Ω cm^2, respectively (**Figure 3.24**a). Between the 20th and 50th cycle, the CEI resistance increases by ca. 33% to 148.3 Ω cm^2. Although the increase in CEI resistance for this cell begins before all of the VC has been consumed, this is in good agreement with the marginally lower CE and gentle capacity fade that is observed over the first 50 cycles compared to cells cycled to an UCV of 4.2 V. After the 50th cycle, the CEI resistance of both cells continues to grow, with the 100th cycle impedance of the cell cycled to an UCV of 4.4 V being more than double that of the cell cycled to 4.2 V, indicating a considerably more resistive CEI.

Figure 3.24b shows the change in CEI resistance for analogous cells containing a VC-free LP57 electrolyte. The same overall trend prevails, with the cell cycled to an UCV of 4.2 V having a significantly lower CEI resistance throughout cycling than the cell cycled to an UCV of 4.4 V. In good agreement with the cell cycling and compositional analysis, there is no stability of the CEI resistance, and continual impedance growth is measured under both conditions. By the 10th cycle, the cell cycled to an UCV of 4.4 V has an ca. 50% higher CEI resistance than the cell cycled to an UCV of 4.2 V, with measured values of 99.5 and 148.8 Ω cm^2 for UCVs of 4.2 and 4.4 V, respectively. The CEI resistance of both cells continues to grow throughout cycling, with a 100th cycle CEI impedance of 399.4 and 786.0 Ω cm^2 being recorded for UCVs of 4.2 and 4.4 V, respectively. The early acceleration of CEI impedance growth in these cells confirms that the presence of VC reduces the resistivity of the NMC811 CEI as a function of cycle number. It is important to note that VC is a negative electrode additive, indicating that the processes that result in increased CEI resistance originate at the negative electrode.

Taking these data as a whole, it is likely that the preferential degradation of VC at the surface of metallic Li limits electrolyte degradation on both electrodes and enables stable cycling. However, when VC is removed, either directly or

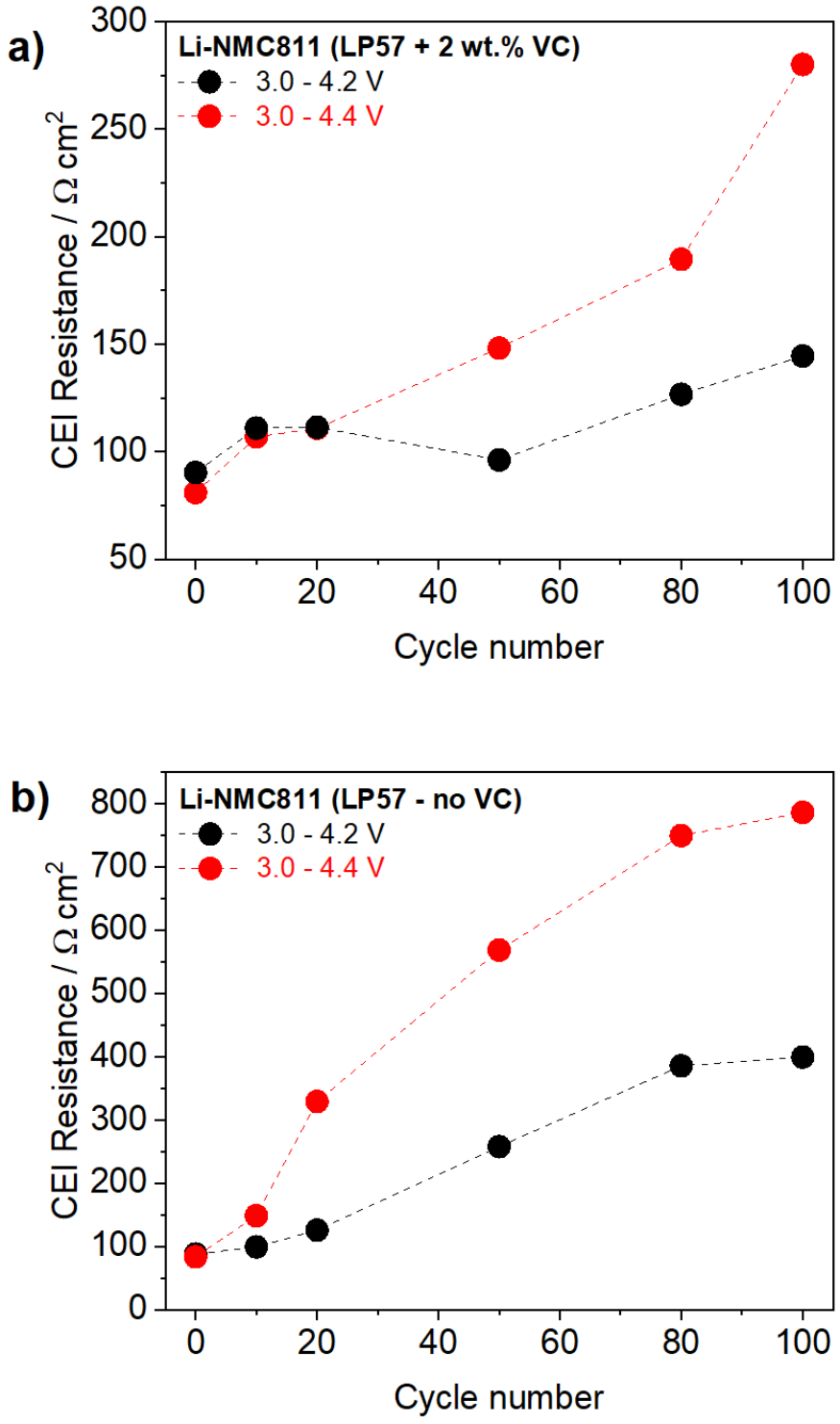


Figure 3.24. *Li^+ diffusion resistance of the CEI of a NMC811 electrode in a three-electrode Li-NMC811 half-cell containing a a) LP57-VC or b) VC-free electrolyte cycled to an UCV of 4.2 V (black circles) or 4.4 V (red circles) vs Li^+/Li. EIS was performed after a 1-hour voltage hold at 3.6 V vs Li^+/Li after the 1^{st} C/20 formation cycle and subsequent 10^{th}, 20^{th}, 50^{th}, 80^{th} and 100^{th} cycle, with a metallic Li reference electrode.*

through reduction, new electrolyte degradation products are formed at the metallic Li electrode which crossover to the NMC811 electrode, inducing parasitic reactions and resulting in the formation of a resistive CEI. Replenishing VC in the electrolyte after cycling does not lead to reduced impedance, or recovery of the capacity (at C/2), indicating that the electrolyte-electrode interfaces of both the NMC811 and metallic Li electrodes are the issue rather than the composition and properties of the electrolyte.

3.6 Lithium titanium oxide as an impartial counter electrode

The findings presented in this chapter clearly show that metallic Li is an unsuitable candidate for examining the performance of prospective intercalation chemistries beyond early stage cycling due to continued reaction with the electrolyte solution. $Li_4Ti_5O_{12}$ (LTO) negative electrodes have a high operational voltage (1.55 V vs Li^+/Li), above the reduction potential of EC, EMC and VC, which results in low reactivity with the electrolyte components, and provides a potential candidate for the isolated study of positive electrode performance.[63,64] Although previous reports have indicated that any residual H_2O present in the electrolyte can be reduced on the surface of LTO electrodes, producing H_2 and OH^- that can enable further gassing degradation reactions, adequate measures to limit H_2O intrusion during cell assembly and choice of appropriate cell format can mitigate these effects.[65–67] To determine the suitability of LTO as an impartial counter electrode, high loading LTO electrodes (25 mg cm^{-2}, ca. 3.7 mAh cm^{-2}), chosen to ensure sufficient counter electrode capacity (n:p = 1.16:1), were paired against the high loading NMC811 electrodes (16.9 mg cm^{-2}, ca. 3.19 mAh cm^{-2}) used throughout this study.

The nominal capacity of LTO electrodes is 150 mAh g^{-1}, ca. 20% lower than the 190 mAh g^{-1} nominal capacity of NMC811 electrodes. To account for this, a high LTO loading was required, which resulted in a thick electrode coating. To mitigate the effects of polarisation due to sluggish lithium insertion kinetics, a rate study was performed on LTO-NMC811 cells containing a VC-free LP57 electrolyte, to determine the rate at which the initial reversible capacity matched that of the Li-NMC811 half-cells. **Figure 3.25** shows the results of a

rate performance study on cells cycled to UCVs of 2.65 and 2.85 V, the equivalent of 4.2 and 4.4 V vs Li^+/Li when the plateau potential of LTO is taken into account. The capacity limits will hereby be referred to as 'standard' (UCV = 2.65 V) and 'stressed' (UCV = 2.85 V) for clarity. Initial C/20 capacities of 187.4 and 213.0 mAh g^{-1}_{NMC} were achieved for standard and stressed conditions, respectively. These capacities are considerably higher than the 148.2 and 195.0 mAh g^{-1}_{NMC} that was recorded for the initial C/2 cycles of the corresponding Li-NMC811 half-cells, and would result in extremely long experimental times and significantly different cycling conditions. When a rate of C/5 was applied, the cell cycled to a stressed UCV (2.85 V) dropped below the initial C/2 capacity of the Li-NMC811 half-cell, achieving an initial capacity of 191.7 mAh g^{-1}_{NMC}. The cell cycled to a standard UCV (2.65 V) achieved 161.6 mAh g^{-1}_{NMC} at this rate, slightly higher than the Li-NMC811 half-cell. To maintain consistency between the LTO-NMC811 datasets, and not push the initial capacity too far below the value achieved for the Li-NMC811

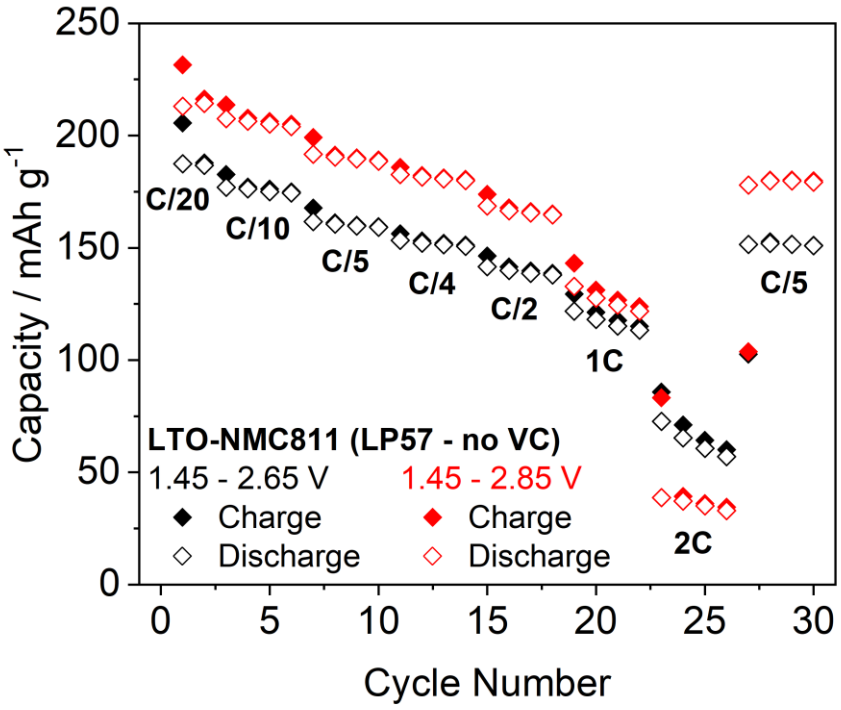


Figure 3.25. *Rate performance of LTO-NMC811 cells containing a VC-free LP57 electrolyte cycled to an UCV of 4.2 V (black diamonds) or 4.4 V (red diamonds) vs Li^+/Li. An adjustment of 1.55 V is applied to convert between LTO and Li reference potentials.*

half-cells, C/5 was chosen as the cycling rate for analysis.

To understand the long-term performance of LTO-NMC811 cells, a cycling protocol consisting of two C/20 formation cycles, followed by 300 C/5 cycles was applied to cells containing a VC-free LP57 electrolyte under standard and stressed conditions. No VC was used in these cells due to the operational potential of both electrode materials being above the reduction potential of VC. To include VC in the electrolyte would introduce an unnecessary species, added to facilitate anode stabilisation, where it is not required. **Figure 3.26** shows the cycling performance of these cells, where initial C/5 discharge capacities of 166.6 and 201.8 mAh g^{-1}_{NMC} were achieved for cells cycled to a standard and stressed UCV, respectively. Under both conditions, CE remained >99.6% for the full 300 cycles, with an average first 100 cycle CE of 99.85 and 99.68% achieved for cells cycled to a standard and stressed UCV, respectively. These results demonstrate the potential of LTO as a negative electrode to isolate the performance of prospective positive electrode intercalation chemistries, outperforming the analogous Li-NMC811 cells by a dramatic margin. In fact, by the 100th cycle, discharge capacities of 144.5 and 177.4 mAh g^{-1}_{NMC} are achieved by the LTO-NMC811 cells cycled to standard and stressed UCVs, respectively. Although in Li-NMC811 half-cells any Li^+ loss to degradation can be replaced by Li^+ supplied by the excess loading of the metallic Li negative electrode, in the LTO-NMC811 cells, there is no excess reservoir of Li^+ and instead these capacities reflect the amount of remaining lithium inventory. Furthermore, the consistently high CE observed in these cells outperforms the stressed Gr-NMC cell which achieved an average CE of 99.42% and a 100th cycle capacity of 120.2 mAh g^{-1}_{NMC}, suggesting that both Gr- and Li-NMC811 half cells suffer from significant crosstalk and parasitic side reactions that are largely to blame for cell capacity fade. **Figure 3.27** shows a direct comparison between the cycling performance of Li-NMC811 half-cells and LTO-NMC811 cells cycled under standard and stressed conditions with a VC-free LP57 electrolyte. These data show that, under both conditions, LTO-NMC811 cells have superior performance which, along with the spectroscopic evidence

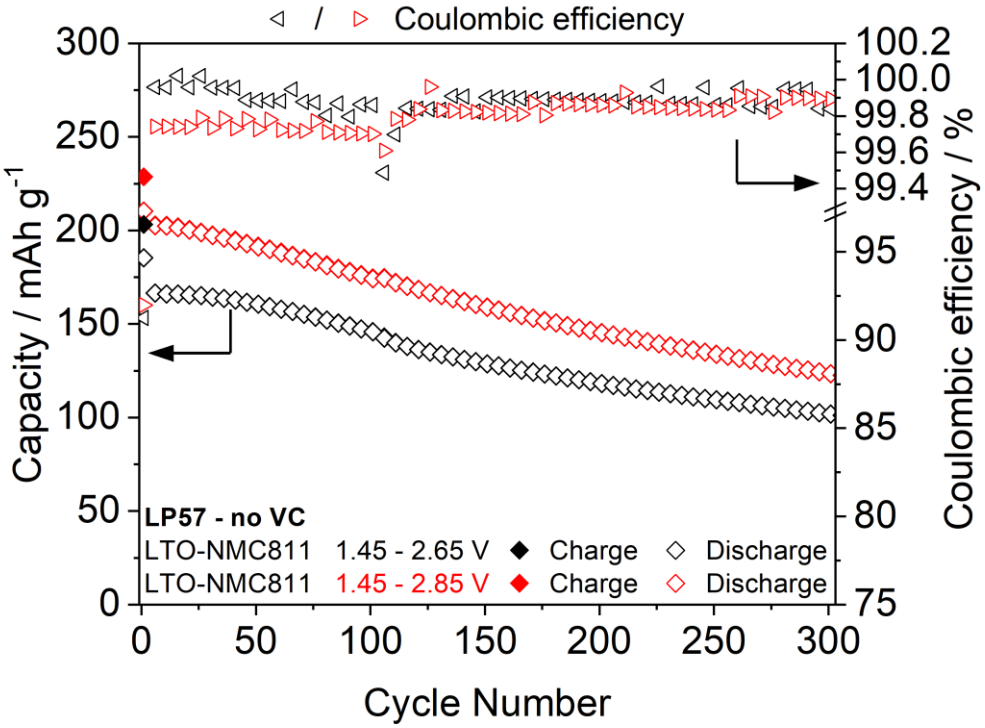


Figure 3.26. *Capacity performance of LTO-NMC811 cells cycled to an UCV of 4.2 V (black diamonds) or 4.4 V (red diamonds) vs Li^+/Li containing a VC-free LP57 electrolyte. Data shows the capacities (diamonds) and coulombic efficiencies (triangles) of two initial C/20 formation cycles and subsequent C/2 cycles. An adjustment of 1.55 V is applied to convert between LTO and Li reference potentials.*

presented in this study, highlights that half-cell failure is not exclusively the due to NMC811 failure, but instead the combination of degradation at the negative electrode and subsequent oxidation of these degradation products at the surface of the positive electrode, which results in significant impedance growth.

To confirm the suitability of the LTO electrode as a benign counter electrode, electrolyte degradation was examined through GC-MS analysis of the cycled electrolyte, which showed little degradation of the electrolyte components after 100 cycles at C/5 (**Figure 3.28**). The only significant additional peak observed in the GC-MS chromatogram was due to the transesterification of EMC to DEC, albeit in much lower intensity than in the Li-NMC811 half-cells. These data confirm the ability of the LTO counter electrode to reflect long-term positive electrode capacity performance more accurately and could offer a testing ground for electrolyte optimisation targeted at positive electrode

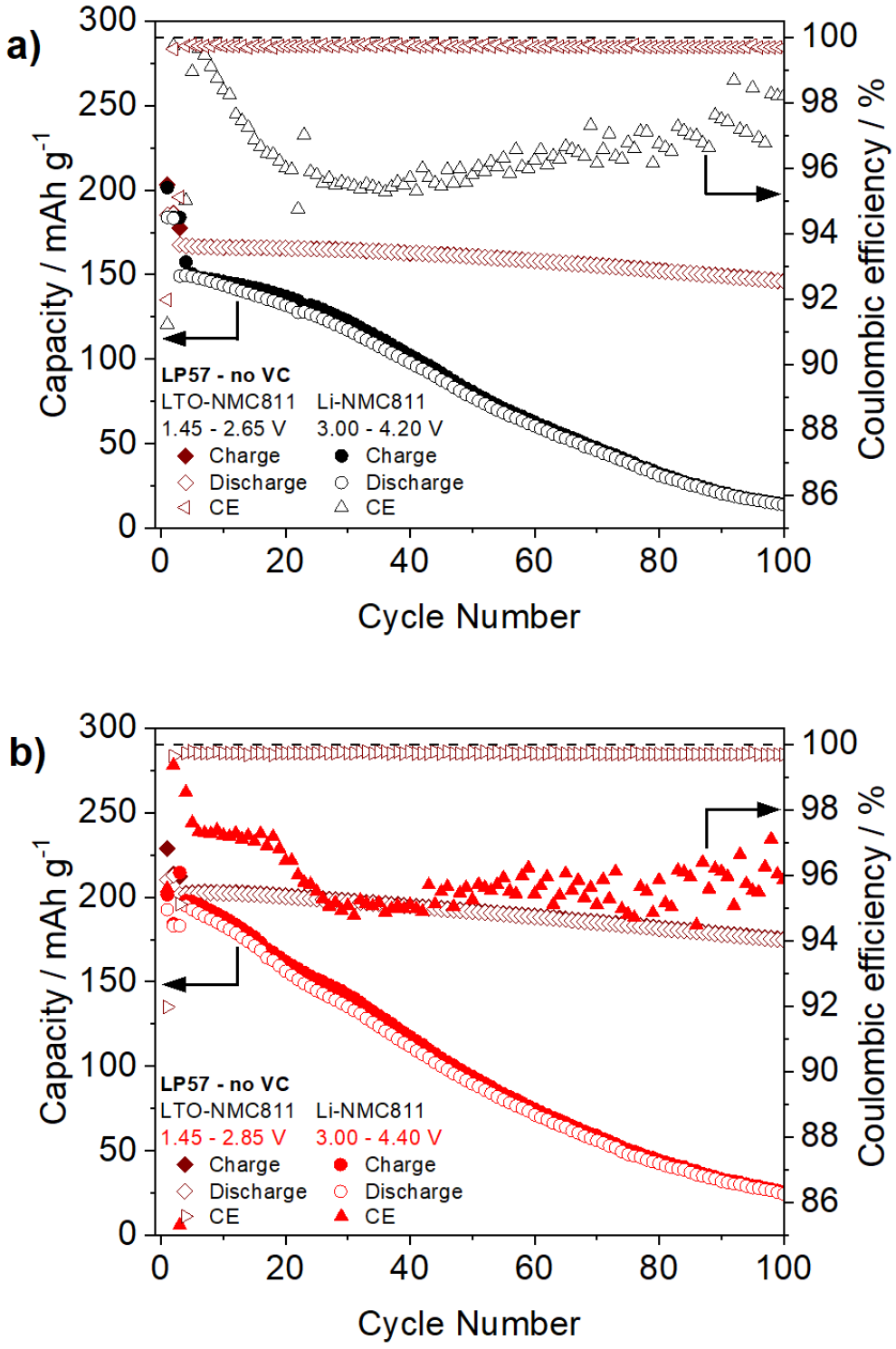


Figure 3.27. *Plots comparing the capacity performance of LTO-NMC811 (diamonds, dark red) and Li-NMC811 (circles, red) cells cycled to an UCV of a) 4.2 V or b) 4.4 V vs Li^+/Li containing a VC-free LP57 electrolyte. Data shows the capacity and coulombic efficiency (triangles) as a function of cycle number. An adjustment of 1.55 V is applied to convert between LTO and Li reference potentials.*

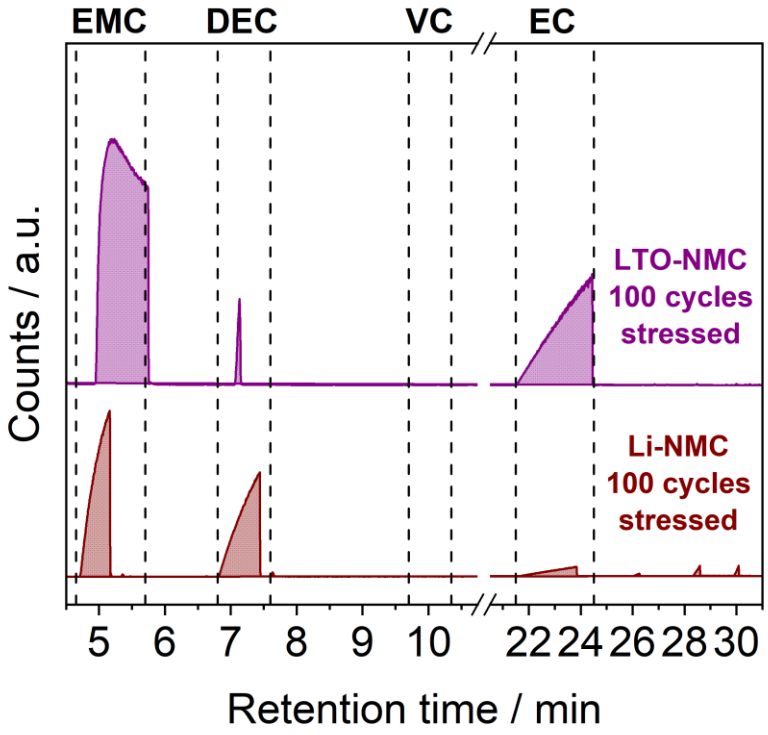


Figure 3.28. *GC-MS chromatograms of electrolyte extracted from Li-NMC811 (dark red) and LTO- NMC811 (purple) cells after 100 cycles to a UCV of 4.4 V vs Li^+/Li containing a VC-free LP57 electrolyte. Data shows the onset of electrolyte degradation in Li-NMC811 cells which is not present in LTO-NMC811 cells.*

stabilisation, without the complexities introduced by traditional full-cell and half-cell formats.

With LTO-NMC811 cell cycling performed at C/5, it is important that the hypotheses are confirmed in Li-NMC811 cells cycled at the same C-rate. **Figure 3.29**a shows the cycling performance of Li-NMC811 half-cells containing a LP57-VC electrolyte cycled to an UCV of 4.2 or 4.4 V. In the cell cycled to an UCV of 4.4 V, good cycle stability is observed for ca. 70 cycles, with an average CE of 99.78%. After this point, rapid capacity fade is observed, with the capacity reaching 27.7 mAh g^{-1}_{NMC} by the 82nd cycle where the rate of capacity fade then slows. Contrastingly, the cell cycled to an UCV of 4.2 V shows extremely good capacity retention and CE across the first 100 cycles at C/5, with an average CE of 99.74% and a 100th cycle capacity of 159.9 mAh g^{-1}_{NMC}. However, a sudden drop in the CE and onset of rapid capacity fade is observed after the 103rd cycle

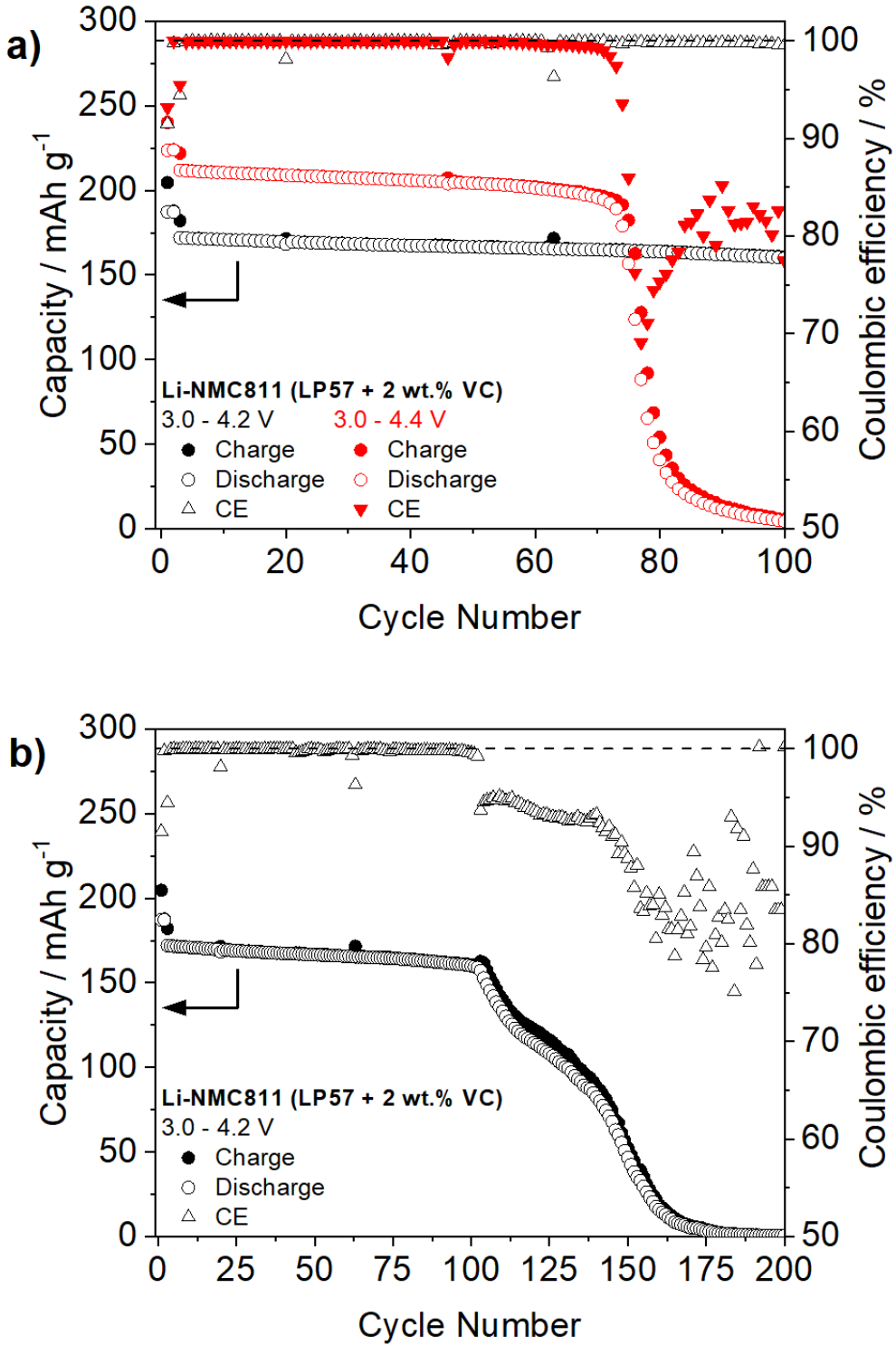


Figure 3.29. *Capacity performance of Li-NMC811 half-cells cycled at C/5 over a) the first 100 cycles to an UCV of 4.2 V (black circles) or 4.4 V (red circles) and b) the first 200 cycles cycled to an UCV of 4.2 V vs Li^+/Li containing a LP57-VC electrolyte. Data shows two C/20 formation cycles and subsequent C/5 cycles.*

at C/5, showing a similar sudden death of the cell cycled to an UCV of 4.4 V (**Figure 3.29**b).Furthermore, when Li-NMC811 cells are cycled with a LP57 electrolyte, where no VC additive is present, the benefits of reduced rate cycling are even less pronounced, and poor CE and rapid capacity fade are observed almost immediately upon initiation of C/5 cycling (**Figure 3.30**). These data confirm that although reducing the cycling rate of Li-NMC811 cells prolongs the stable capacity performance of this cell format, the reliable window of observation is limited and they do not provide a true representation of isolated positive electrode performance.

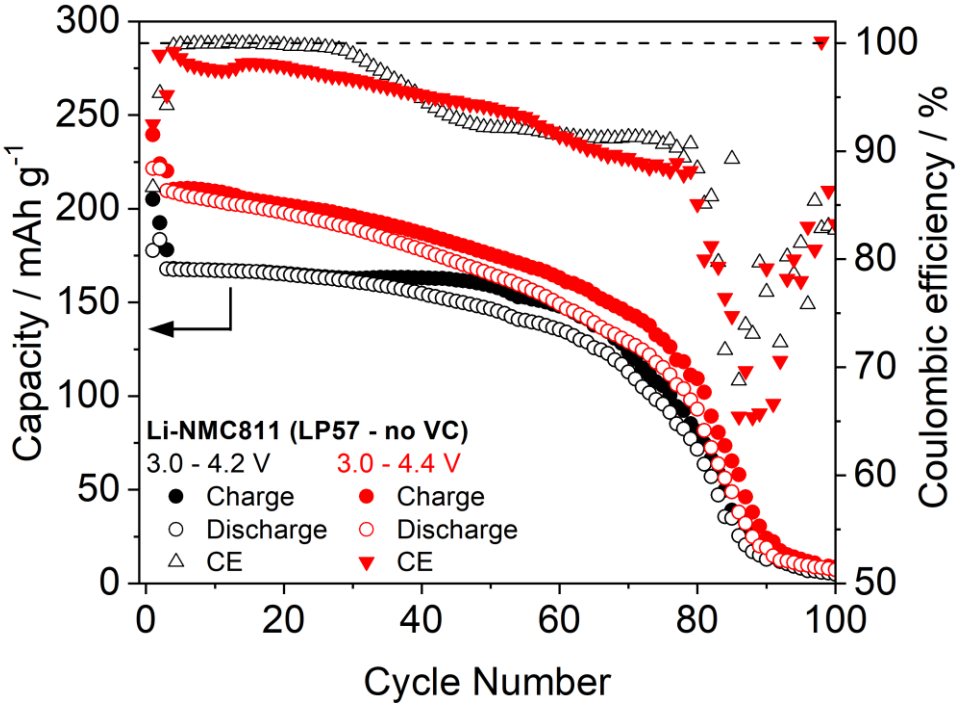


Figure 3.30. *Capacity performance of Li-NMC811 half-cells containing a VC-free LP57 electrolyte cycled at C/5 to an UCV of 4.2 V (black circles) or 4.4 V (red circles) vs Li^+/Li. Data shows two C/20 formation cycles and subsequent C/5 cycles.*

3.7 Conclusions

In this chapter, I evaluated the performance of Li-NMC811 half-cells with a commercially relevant electrode loading (16.9 mg cm^{-2}, ca. 3.19 mAh cm^{-2}) and electrolyte (LP57). I revealed that, despite the prevalence of metallic Li half-cells in literature, this cell configuration offers a limited reliable cycle life and does not accurately portray the performance of prospective positive electrodes, with the additive vinylene carbonate being essential if any region of stable capacity is to be attained.

Following an approximate 50 cycle period of stability, indiscriminate degradation of the electrolyte solution at the surface of the metallic Li electrode produces degradation products that can transport through the electrolyte where they are oxidised at the surface of the positive electrode, resulting in increased interfacial resistance that prematurely limits the capacity and rate performance of the cells. At C/20, cycled NMC811 electrodes show comparable lithium insertion capacity to when pristine, confirming that cell performance is an artifact of the half-cell configuration rather than being specific to the intercalation material under consideration. The need to tailor the electrolyte solution to accommodate the metallic Li electrode, and the significant degradation it causes, precludes informative study of electrolyte additives designed for the positive electrode.

$Li_4Ti_5O_{12}$ is proposed as an alternative counter electrode for the isolated study of positive electrode material performance. LTO-NMC811 cells showed high CE in the commercially relevant electrolyte with no additives, under both standard and stressed conditions, making them ideal for long-term investigation of prospective intercalation chemistries and additives designed to improve their performance. Over 300 cycles with no electrolyte additive, LTO-NMC811 cells cycled to an UCV of 4.4 V vs Li^+/Li outperform both Li-NMC811 and Gr-NMC811 cells, confirming that capacity fade in current half- and full-cell formats cycled to high UCVs is not exclusively the result of positive electrode failure, but also a result of increased electrode crosstalk.

This work highlights the shortfalls of Li-NMC811 half-cells and proposes an alternative cell configuration wherein no negative electrode stabilising additives are required. The LTO-NMC811 cell chemistry not only better portrays the performance of prospective positive electrode chemistries and depletion of lithium inventory, but also enables the testing of prospective positive electrode additives without imposing degradation from metallic Li. I propose that the LTO-NMC811 cell chemistry will find application in the exploration of electrolyte compositions targeted at positive electrode stabilisation, without the significant complications introduced by the chemical and electrochemical activity of the counter electrode.

3.8 References

1. Li, W., Erickson, E. M. & Manthiram, A. High-nickel layered oxide cathodes for lithium-based automotive batteries. *Nat. Energy* **5**, 26–34 (2020).
2. Xu, C. *et al.* Future material demand for automotive lithium-based batteries. *Commun. Mater.* **1**, 99 (2020).
3. Andre, D. *et al.* Future generations of cathode materials: an automotive industry perspective. *J. Mater. Chem. A* **3**, 6709–6732 (2015).
4. Masias, A., Marcicki, J. & Paxton, W. A. Opportunities and Challenges of Lithium Ion Batteries in Automotive Applications. *ACS Energy Lett.* **6**, 621–630 (2021).
5. Duffner, F., Wentker, M., Greenwood, M. & Leker, J. Battery cost modeling: A review and directions for future research. *Renew. Sustain. Energy Rev.* **127**, 109872 (2020).
6. Manthiram, A. A reflection on lithium-ion battery cathode chemistry. *Nat. Commun.* **11**, 1–9 (2020).

7. Olivetti, E. A., Ceder, G., Gaustad, G. G. & Fu, X. Lithium-Ion Battery Supply Chain Considerations: Analysis of Potential Bottlenecks in Critical Metals. *Joule* **1**, 229–243 (2017).

8. Murdock, B. E., Toghill, K. E. & Tapia-Ruiz, N. A Perspective on the Sustainability of Cathode Materials used in Lithium-Ion Batteries. *Adv. Energy Mater.* **11**, 2102028 (2021).

9. Chen, C.-H. *et al.* Development of Experimental Techniques for Parameterization of Multi-scale Lithium-ion Battery Models. *J. Electrochem. Soc.* **167**, 080534 (2020).

10. Günter, F. J. & Wassiliadis, N. State of the Art of Lithium-Ion Pouch Cells in Automotive Applications: Cell Teardown and Characterization. *J. Electrochem. Soc.* **169**, 030515 (2022).

11. Kovachev, G. *et al.* Analytical Dissection of an Automotive Li-Ion Pouch Cell. *Batteries* **5**, 67 (2019).

12. Li, T. *et al.* Degradation Mechanisms and Mitigation Strategies of Nickel-Rich NMC-Based Lithium-Ion Batteries. *Electrochem. Energy Rev.* **3**, 43–80 (2020).

13. Liu, W. *et al.* Nickel-Rich Layered Lithium Transition-Metal Oxide for High-Energy Lithium-Ion Batteries. *Angew. Chem. - Int. Ed.* **54**, 4440–4457 (2015).

14. Yeh, N.-H. *et al.* Controlling Ni^{2+} from the Surface to the Bulk by a New Cathode Electrolyte Interphase Formation on a Ni-Rich Layered Cathode in High-Safe and High-Energy-Density Lithium-Ion Batteries. *ACS Appl. Mater. Interfaces* **13**, 7355–7369 (2021).

15. Ruff, Z., Xu, C. & Grey, C. P. Transition Metal Dissolution and Degradation in NMC811-Graphite Electrochemical Cells. *J. Electrochem. Soc.* **168**, 060518 (2021).

16. Zheng, H., Sun, Q., Liu, G., Song, X. & Battaglia, V. S. Correlation between dissolution behavior and electrochemical cycling performance for $LiNi_{1/3}Co_{1/3}Mn_{1/3}O_2$-based cells. *J. Power Sources* **207**, 134–140 (2012).

17. Gallus, D. R. *et al.* The influence of different conducting salts on the metal dissolution and capacity fading of NCM cathode material. *Electrochimica Acta* **134**, 393–398 (2014).

18. Rinkel, B. L. D., Hall, D. S., Temprano, I. & Grey, C. P. Electrolyte Oxidation Pathways in Lithium-Ion Batteries. *J. Am. Chem. Soc.* **142**, 15058–15074 (2020).

19. Jayawardana, C., Rodrigo, N. D., Rynearson, L. & Lucht, B. L. Difluorophosphoric Acid Generation and Crossover Reactions in $LiNi_xCo_yMn_zO_2$ Cathodes Operating at High Voltage. *J. Electrochem. Soc.* **169**, 060509 (2022).

20. Gilbert, J. A., Shkrob, I. A. & Abraham, D. P. Transition Metal Dissolution, Ion Migration, Electrocatalytic Reduction and Capacity Loss in Lithium-Ion Full Cells. *J. Electrochem. Soc.* **164**, A389–A399 (2017).

21. Jung, R. *et al.* Nickel, manganese, and cobalt dissolution from Ni-Rich NMC and their effects on NMC622-graphite cells. *J. Electrochem. Soc.* **166**, A378–A389 (2019).

22. Rowden, B. & Garcia-Araez, N. Estimating lithium-ion battery behavior from half-cell data. *Energy Rep.* **7**, 97–103 (2021).

23. Miele, E. *et al.* Hollow-core optical fibre sensors for operando Raman spectroscopy investigation of Li-ion battery liquid electrolytes. *Nat. Commun.* **13**, 1651 (2022).

24. Schulze, M. C. & Neale, N. R. Half-Cell Cumulative Efficiency Forecasts Full-Cell Capacity Retention in Lithium-Ion Batteries. *ACS Energy Lett.* **6**, 1082–1086 (2021).

25. Li, J., Downie, L. E., Ma, L., Qiu, W. & Dahn, J. R. Study of the Failure Mechanisms of $LiNi_{0.8}Mn_{0.1}Co_{0.1}O_2$ Cathode Material for Lithium Ion Batteries. *J. Electrochem. Soc.* **162**, A1401 (2015).

26. Weber, F. M., Kohlhaas, I. & Figgemeier, E. Tuning the Reactivity of Electrolyte Solvents on Lithium Metal by Vinylene Carbonate. *J. Electrochem. Soc.* **167**, 140523 (2020).

27. Zhuang, G., Chen, Y. & Ross, P. N. The Reaction of Lithium with Dimethyl Carbonate and Diethyl Carbonate in Ultrahigh Vacuum Studied by X-ray Photoemission Spectroscopy. *Langmuir* **15**, 1470–1479 (1999).

28. Armand, M. *et al.* Lithium-ion batteries – Current state of the art and anticipated developments. *J. Power Sources* **479**, 228708 (2020).

29. Heiskanen, S. K., Kim, J. & Lucht, B. L. Generation and Evolution of the Solid Electrolyte Interphase of Lithium-Ion Batteries. *Joule* **3**, 2322–2333 (2019).

30. Xie, J. & Lu, Y.-C. A retrospective on lithium-ion batteries. *Nat. Commun.* **11**, 2499 (2020).

31. Kitz, P. G., Lacey, M. J., Novák, P. & Berg, E. J. Operando investigation of the solid electrolyte interphase mechanical and transport properties

formed from vinylene carbonate and fluoroethylene carbonate. *J. Power Sources* **477**, 228567 (2020).

32. Nakai, H., Kubota, T., Kita, A. & Kawashima, A. Investigation of the Solid Electrolyte Interphase Formed by Fluoroethylene Carbonate on Si Electrodes. *J. Electrochem. Soc.* **158**, A798 (2011).

33. Haregewoin, A. M., Wotango, A. S. & Hwang, B.-J. Electrolyte additives for lithium ion battery electrodes: progress and perspectives. *Energy Env. Sci* **9**, 1955–1988 (2016).

34. Aurbach, D. *et al.* On the use of vinylene carbonate (VC) as an additive to electrolyte solutions for Li-ion batteries. *Electrochimica Acta* **47**, 1423–1439 (2002).

35. Thompson, L. M. *et al.* Quantifying Changes to the Electrolyte and Negative Electrode in Aged NMC532/Graphite Lithium-Ion Cells. *J. Electrochem. Soc.* **165**, A2732 (2018).

36. NIST Mass Spectrometry Data Centre. https://chemdata.nist.gov/dokuwiki/doku.php?id=chemdata:start.

37. Märker, K., Reeves, P. J., Xu, C., Griffith, K. J. & Grey, C. P. Evolution of Structure and Lithium Dynamics in $LiNi_{0.8}Mn_{0.1}Co_{0.1}O_2$ (NMC811) Cathodes during Electrochemical Cycling. *Chem. Mater.* **31**, 2545–2554 (2019).

38. Dose, W. M., Xu, C., Grey, C. P. & De Volder, M. F. L. Effect of Anode Slippage on Cathode Cutoff Potential and Degradation Mechanisms in Ni-Rich Li-Ion Batteries. *Cell Rep. Phys. Sci.* **1**, 100253 (2020).

39. Li, J. *et al.* The Impact of Electrolyte Additives and Upper Cut-off Voltage on the Formation of a Rocksalt Surface Layer in $LiNi_{0.8}Mn_{0.1}Co_{0.1}O_2$ Electrodes. *J. Electrochem. Soc.* **164**, A655–A665 (2017).

40. Jung, R., Metzger, M., Maglia, F., Stinner, C. & Gasteiger, H. A. Oxygen release and its effect on the cycling stability of $LiNi_xMn_yCo_zO_2$ (NMC) cathode materials for li-ion batteries. *J. Electrochem. Soc.* **164**, A1361–A1377 (2017).

41. Li, W. *et al.* Long-Term Cyclability of NCM-811 at High Voltages in Lithium-Ion Batteries: an In-Depth Diagnostic Study. *Chem. Mater.* **32**, 7796–7804 (2020).

42. Beltrop, K. *et al.* Triphenylphosphine Oxide as Highly Effective Electrolyte Additive for Graphite/NMC811 Lithium Ion Cells. *Chem. Mater.* **30**, 2726–2741 (2018).

43. Zhang, J. *et al.* Exploring the redox decomposition of ethylene carbonate–propylene carbonate in Li-ion batteries. *Mater. Adv.* **2**, 1747–1751 (2021).

44. Borodin, O. *et al.* Modeling Insight into Battery Electrolyte Electrochemical Stability and Interfacial Structure. *Acc. Chem. Res.* **50**, 2886–2894 (2017).

45. Michan, A. L. *et al.* Fluoroethylene Carbonate and Vinylene Carbonate Reduction: Understanding Lithium-Ion Battery Electrolyte Additives and Solid Electrolyte Interphase Formation. *Chem. Mater.* **28**, 8149–8159 (2016).

46. Madec, L. *et al.* Effect of Sulfate Electrolyte Additives on $LiNi_{1/3}Mn_{1/3}Co_{1/3}O_2$ /Graphite Pouch Cell Lifetime: Correlation between XPS Surface Studies and Electrochemical Test Results. *J. Phys. Chem. C* **118**, 29608–29622 (2014).

47. El Ouatani, L. *et al.* The Effect of Vinylene Carbonate Additive on Surface Film Formation on Both Electrodes in Li-Ion Batteries. *J. Electrochem. Soc.* **156**, A103 (2009).

48. Noh, H.-J., Youn, S., Yoon, C. S. & Sun, Y.-K. Comparison of the structural and electrochemical properties of layered $Li[Ni_xCo_yMn_z]O_2$ (x = 1/3, 0.5, 0.6, 0.7, 0.8 and 0.85) cathode material for lithium-ion batteries. *J. Power Sources* **233**, 121–130 (2013).

49. Ryu, H.-H., Park, K.-J., Yoon, C. S. & Sun, Y.-K. Capacity Fading of Ni-Rich $Li[Ni_xCo_yMn_{1-x-y}]O_2$ ($0.6 \leq x \leq 0.95$) Cathodes for High-Energy-Density Lithium-Ion Batteries: Bulk or Surface Degradation? *Chem. Mater.* **30**, 1155–1163 (2018).

50. Jung, R. *et al.* Effect of ambient storage on the degradation of ni-rich positive electrode materials (NMC811) for li-ion batteries. *J. Electrochem. Soc.* **165**, A132–A141 (2018).

51. A. Rulev, A. *et al.* Revising the pathways of the Li reaction with organic carbonates. *Phys. Chem. Chem. Phys.* **22**, 16184–16192 (2020).

52. Dedryvère, R. *et al.* XPS Identification of the Organic and Inorganic Components of the Electrode/Electrolyte Interface Formed on a Metallic Cathode. *J. Electrochem. Soc.* **152**, A689 (2005).

53. Xiao, J. *et al.* Understanding and applying coulombic efficiency in lithium metal batteries. *Nat. Energy* **5**, 561–568 (2020).

54. Harris, O. C., Lee, S. E., Lees, C. & Tang, M. Review: mechanisms and consequences of chemical cross-talk in advanced Li-ion batteries. *J. Phys. Energy* **2**, 032002 (2020).

55. Heenan, T. M. M. *et al.* An Advanced Microstructural and Electrochemical Datasheet on 18650 Li-Ion Batteries with Nickel-Rich NMC811 Cathodes and Graphite-Silicon Anodes. *J. Electrochem. Soc.* **167**, 140530 (2020).

56. Aurbach, D., Markovsky, B., Shechter, A., Ein-Eli, Y. & Cohen, H. A Comparative Study of Synthetic Graphite and Li Electrodes in Electrolyte Solutions Based on Ethylene Carbonate-Dimethyl Carbonate Mixtures. *J. Electrochem. Soc.* **143**, 3809–3820 (1996).

57. Petibon, R. *et al.* Study of Electrolyte Components in Li Ion Cells Using Liquid-Liquid Extraction and Gas Chromatography Coupled with Mass Spectrometry. *J. Electrochem. Soc.* **161**, A1167–A1172 (2014).

58. Strehle, B., Solchenbach, S., Metzger, M., Schwenke, K. U. & Gasteiger, H. A. The Effect of CO_2 on Alkyl Carbonate Trans-Esterification during Formation of Graphite Electrodes in Li-Ion Batteries. *J. Electrochem. Soc.* **164**, A2513 (2017).

59. Quartarone, E. & Mustarelli, P. Review—Emerging Trends in the Design of Electrolytes for Lithium and Post-Lithium Batteries. *J. Electrochem. Soc.* **167**, 050508 (2020).

60. Xu, K. Electrolytes and interphases in Li-ion batteries and beyond. *Chem Rev* **114**, 11503–11618 (2014).

61. Dose, W. M. *et al.* Electrolyte Reactivity at the Charged Ni-Rich Cathode Interface and Degradation in Li-Ion Batteries. *ACS Appl. Mater. Interfaces* **14**, 13206–13222 (2022).

62. Wang, X. *et al.* High-performance $LiNi_{0.8}Mn_{0.1}Co_{0.1}O_2$ cathode by nanoscale lithium sulfide coating via atomic layer deposition. *J. Energy Chem.* **69**, 531–540 (2022).

63. Dose, W. M. *et al.* Onset Potential for Electrolyte Oxidation and Ni-Rich Cathode Degradation in Lithium-Ion Batteries. *ACS Energy Lett.* **7**, 3524–3530 (2022).

64. Tornheim, A., He, M., Su, C.-C. & Zhang, Z. The Role of Additives in Improving Performance in High Voltage Lithium-Ion Batteries with Potentiostatic Holds. *J. Electrochem. Soc.* **164**, A6366 (2017).

65. Han, C. *et al.* A review of gassing behavior in $Li_4Ti_5O_{12}$-based lithium ion batteries. *J. Mater. Chem. A* **5**, 6368–6381 (2017).

66. He, Y.-B. *et al.* Gassing in $Li_4Ti_5O_{12}$-based batteries and its remedy. *Sci. Rep.* **2**, 913 (2012).

67. Bernhard, R., Meini, S. & Gasteiger, H. A. On-Line Electrochemical Mass Spectrometry Investigations on the Gassing Behavior of $Li_4Ti_5O_{12}$ Electrodes and Its Origins. *J. Electrochem. Soc.* **161**, A497 (2014).

Chapter 4. Understanding the mechanism of vinylene carbonate formation in early-stage cycling of Gr-NMC811 full-cells

4.1 Introduction

Electrode crosstalk – wherein species are produced at the surface of one electrode and migrate through the electrolyte to the surface of the other electrode where they can participate in further (electro)chemical reactions – increasingly dominates long-term performance as positive electrode nickel content rises.[1–3] Although all crosstalk reactions are detrimental to cell performance, representing reactions that deviate from the desired Li^+ intercalation/deintercalation processes, recent studies have proposed the formation of vinylene carbonate (VC), the most common commercial electrolyte additive, through the dehydrogenation of ethylene carbonate (EC) at the surface of nickel-rich NMCs, which could be viewed as beneficial to cell performance.[4–8]

In 2018, Freiberg *et al.* proposed that reactive singlet oxygen ($^1O_2$), generated through the energetic release of lattice oxygen, drives VC production.[6] In 2020, Zhang *et al.* proposed a second metal-oxide surface mechanism for the dehydrogenation of EC to form VC, wherein increasing Ni-content reduces the activation energy required for the reaction to proceed.[8] Although spectroscopic evidence was presented that supports VC formation in both studies, the former used the detection of hydrogen peroxide (H_2O_2) to indirectly detect VC, supported by computational calculations, and the latter employed surface enhanced Fourier transform infra-red (FTIR) spectroscopy to study the surface of a drop cast NMC electrode material, stopping short of detecting VC formation in an operational cell. In 2022, Rinkel *et al.* provided the first spectroscopic evidence of VC formation in an operational cell, utilising ^1H NMR to understand electrolyte oxidation reactions initiated by a range of positive electrode materials.[4] Although this study used the same experimental setup as

Freiberg *et al.*,[6] this work claimed to disprove the feasibility of the generation of VC through interaction with $^1O_2$.

In this chapter, I explore the formation of VC in the early-stage cycling of graphite-$LiNi_{0.8}Mn_{0.1}Co_{0.1}O_2$ (Gr-NMC811) full-cells and compare the long-term performance of cells containing an electrolyte doped with 2 wt.% VC to cells where no additive is present. Contrary to previous reports, evidence is presented that shows that the performance of Gr-NMC811 full-cells do not benefit from the inclusion of 2 wt.% VC over a period of 500 cycles at C/2. A variety of spectroscopic techniques are applied to characterise the onset of electrolyte oxidation at NMC811 positive electrodes and explore VC formation in early-stage cycling with a range of applied upper cut-off voltages (UCVs). Conclusive evidence is presented that supports the formation of VC during solid electrolyte interphase (SEI) formation cycling and within the potential limits of standard operation. A Rose Bengal (RB) photosensitizer is applied to assess the feasibility of a $^1O_2$ driven VC formation pathway, as employed by Freiberg *et al.* and Rinkel *et al.*,[4,6] where RB is found to participate in degradation reactions in each of the solvent mixtures explored, bringing into question the validity of these studies. An iron (Fe) based $^1O_2$ selective single atom catalyst (SAC) is synthesised as a non-participating, heterogenous alternative to the RB photosensitizer. The reactivity of $^1O_2$ with the electrolyte solvents is assessed using the Fe-SAC, where no significant reaction products are identified, ruling out VC formation through reaction with $^1O_2$. These data confirm that, although not formed by reaction with $^1O_2$, VC is formed at potentials ≤4.2 V vs Li^+/Li in Gr-NMC811 full-cells throughout the entirety of cycling, which can crossover to the negative electrode and participate in generating a stable Gr SEI.

4.2 Experimental

4.2.1 Materials

NMC811 (8.21 mg cm^{-2}, 1.52 mAh cm^{-2}) and Gr (5.83 mg cm^{-2}, 2.09 mAh cm^{-2}) electrodes were supplied by the U.S. Department of Energy's CAMP Facility, Argonne National Laboratory. NMC811 electrodes comprised of 90% active

material, 5% conductive carbon support, and 5% binder coated on aluminium foil. The base electrolyte (LP57, 1 M $LiPF_6$ in = EC:EMC = 3:7 v/v) and the formulated electrolyte with 2 wt.% VC additive were purchased from Solvionic (99.9%, H_2O ≤20 ppm). NMC811, and Gr electrodes were dried under vacuum at 120 °C for 24 hours before being transferred into an Ar-filled glovebox (MBRAUN, O_2 and H_2O ≤0.1 ppm) without exposure to air. Model electrolyte solutions were prepared by mixing ethylene carbonate (EC, 99%, Aldrich) with ethyl methyl carbonate (EMC, 99%, Aldrich) in a 3:7 v/v ratio in an N_2-filled glovebox (MBRAUN, O_2 and H_2O ≤0.1 ppm). VC (99.5%, acid <200 ppm, H_2O <100 ppm, Aldrich), RB (95%, Aldrich), and 9,10-dimethylanthracene (DMA, 99%, Aldrich) were used without further purification.

The honeycomb-like nitrogen-doped carbon (HNC) Fe-SAC was synthesised according to methods previously reported.[9] Iron acetylacetonate, zinc nitrate hexahydrate, 2-methylimidazole, tannic acid, and methanol were purchased from Aldrich and used without further purification. An Fe zeolitic imidazolate framework (ZIF-8) was synthesised via *in-situ* encapsulation of iron acetylacetonate in the cage of ZIF-8. Typically, both 1.68 g of $Zn(NO_3).6H_2O$ and 3.7 g of 2-methylimidazole were each separately dissolved in 50 mL of methanol. Iron acetylacetonate (200 mg) was dissolved in the methanolic solution of $Zn(NO_3)_2$. The two methanolic solutions were then mixed and stirred for 24 hours at room temperature. The resultant precipitate was collected by centrifugation, washed with methanol several times, and finally dried at 80 °C under vacuum for 12 hours to obtain Fe/ZIF-8. For the preparation of core-shell Fe/ZIF-8@TA, 200 mg of Fe/ZIF-8 was dispersed in 50 mL H_2O. Tannic acid (500 mg) was dissolved in 50 mL H_2O and quickly poured into the Fe/ZIF-8 dispersion. After 5 minutes at rest, the mixture was centrifuged, washed with H_2O several times, and dried at 80 °C under vacuum for 12 hours, yielding the Fe/ZIF-8@TA precursor material. Finally, Fe/ZIF-8@TA was put into a ceramic boat, placed into a tube furnace, and heated to 900 °C for 3 hours under flowing Ar (99.99%). The black powder of Fe_1/HNC (Fe-SAC) was obtained after the carbonisation process.

4.2.2 Catalyst characterisation

X-ray diffraction was used to characterise the Fe-SAC and ensure than no Fe nanoparticles remained on the surface of the HNC. The sample was prepared on a silicon background holder and the surface levelled with a minimal amount of pressure to reduce the introduction of preferred orientation stacking. Data were collected using a Malvern PANalytical Xpert MPD operating in Bragg-Brentano geometry equipped with PIXcel area detector and a sealed tube Cu source operating at 40 kV and 40 mA. A Johansson focussing beam monochromator selected pure $K\alpha_1$ radiation (λ = 1.5406 Å). The incident and diffracted beam path passes through a pair of 0.04 rad Soller slits to reduce axial beam divergence. Programmable Divergence Slits and Programmable anti-scatter slits were used in automatic mode to match the sample length. A fixed mask matching the sample width and a fixed 1° anti-scatter slit were used in the incident beam path. Data were collected with a step size of 0.013° in continuous mode. A total scan time of 1-hour was applied. The sample holder was spun with a duration per spin of 8 seconds.

4.2.3 Electrochemical testing

Cells were assembled inside an Ar-filled. All measurements were carried out at 20 °C with an initial equilibration time of 1-hour allowed for electrode wetting and temperature uniformity. Long-term cycling experiments used a Celgard (2032) separator soaked in 80 µL of electrolyte, and VC detection cells employed Whatman glass microfiber filter paper (GF/F) as the separator, with 120 µL of electrolyte. Cells were cycled using a two-electrode Swagelok cell, pairing 12 mm electrodes. Further information on cell design can be found in Chapter 2. C-rates were calculated assuming a nominal NMC811 capacity of 190 mAh g^{-1}_{NMC}. Battery cycling was carried out on an IviCycle200 potentiostat.

4.2.4 On-line electrochemical mass spectrometry (OEMS) measurements

OEMS measurements were performed on a Li-NMC811 half-cell pairing an 18 mm NMC811 positive electrode with a 15.6 mm metallic Li electrode and a

metallic Li chip reference electrode, separated by glass fibre separators soaked in 300 µL of electrolyte. The cell was charged to an UCV of 4.6 V, where a 40-hour voltage hold period was performed, before being discharged to 2.5 V vs Li^+/Li. The OEMS system consisted of a SS tube which carried gas through the electrochemical cell, connected through self-sealing quick-connects (Beswick Engineering) to a mass spectrometer, so that the system was never exposed to air. Ar (N6.0, BOC), connected to a gas purifier before flow control, was used as the carrier gas. A quadrupole mass spectrometer (Pfeiffer) was connected to the cell through a heated capillary (120 °C) to prevent condensation of volatile species and controlled with an Ivium potentiostat. Further information on the methodology and instrument calibration can be found in Chapter 2.

4.2.5 $^1O_2$ generation techniques

All $^1O_2$ generation experiments were carried out at room temperature in a N_2-filled glovebox. To ensure O_2 saturation of the solutions, dry O_2 (N5.5, BOC) was bubbled through the solutions for at least 10 minutes. The RB salt was dried at 130 °C under vacuum for 60 hours prior to use, where it was dissolved in the desired solvent system at a concentration of 500 µM, chosen to be close to the lowest saturation concentration of the systems studied. Two green lamps (5 W) were used to apply photoexcitation, with the suitability of these light sources for photogeneration of $^1O_2$ being confirmed through DMA endoperoxide (DMA-O_2) formation in tetraethylene glycol dimethyl ether.[10] RB solutions were irradiated in a N_2-filled glovebox with constant stirring.

Heterogenous selective $^1O_2$ generation experiments were performed by adding ca. 5 mg of Fe-SAC into the analyte solution. The generation of $^1O_2$ in EC:EMC mixtures was confirmed through the formation of DMA-O_2 in these systems, tracked using HPLC analysis with a UV-visible detector.

4.2.6 GC-MS measurements

After cycling, cells were disassembled in an Ar-filled glovebox and the glass microfiber filter paper was soaked in deuterated chloroform ($CDCl_3$, 1.5 mL,

Aldrich, 99.0%, H_2O <100 ppm) for at least 30 minutes, adapting the procedure first described by Dahn *et al*.[11] GC-MS samples were injected into the inlet with a splitless flow at 200 °C and carried onto the preheated column which was held at 40 °C for 3 minutes. The oven temperature was then ramped at 2 °C min^{-1} for 10 minutes to a final temperature of 60 °C, by which time any VC in the sample will have passed through the column. The MS transfer line and ion source were held at 250 °C. To avoid overloading the MS detector with EMC, the MS transfer line was opened after 8.5 minutes (see Chapter 3), and to improve instrument sensitivity the detector mass range was limited to between 40 – 100 amu. The limit of detection (LOD) was enhanced further through applying an 86 amu restriction to the data to reduce background noise. A blank injection of methanol (MeOH HPLC grade, ≥99.9%, Aldrich) was run between each injection, to ensure that all components are evolved from the column. The blank samples were injected into the inlet with a splitless flow at 200 °C and carried onto the preheated column which was held at 40 °C for 3 minutes before the oven temperature was ramped at 2 °C min^{-1} for 10 minutes, followed by 10 °C min^{-1} for 3 minutes, then 2 °C min^{-1} for 10 minutes, and finally 10 °C min^{-1} for 13 minutes to a final temperature of 240 °C, where all compounds were evolved from the column. Data were analysed using Chromeleon software to identify the composition of chromatogram peaks, cross-referencing mass spectra with the National Institute of Standards and Technology (NIST) mass spectral library.[12]

Samples for GC-MS LOD and limit of quantification (LOQ) studies were prepared through serial dilutions of VC in $CDCl_3$. A stock solution of 1000 ppm VC in $CDCl_3$ was made up by dispersing 10 mg of VC in 10 mL of $CDCl_3$, measured by weight using the density of $CDCl_3$. Serial dilutions were then used to obtain $CDCl_3$ solutions with VC concentrations between 1 ppm and 40 ppb. A LOD study was run at the start of each set of cycled electrolyte samples, and again at the end, allowing the generation of error bars that show the change in instrument sensitivity over the course of the experiment sequence. To ensure maximum sensitivity, an instrument tune was performed before analysis was initiated.

4.2.7 HPLC-MS measurements

Reference samples were prepared by mixing a small quantity of analyte with MeOH (HPLC grade, ≥99.9%, Aldrich) doped with 0.1% formic acid (FA, HPLC grade, 98-100%, Aldrich). Where the analyte contained a liquid component, 100 µL of analyte was mixed with 900 µL of MeOH-FA. HPLC measurements were carried out on a Thermo Ultimate 3000 HPLC, equipped with a diode array detector capable of recording UV-visible spectra from 190 – 800 nm. For HPLC-MS measurements, a Bruker microTOF II spectrometer with an electrospray ionisation source was connected to the HPLC outlet. 10-40 µL of sample was injected into an Accucore aQ (150 mm x 4.6 mm, 5 µm) column using an initial 80:20 ratio of H_2O doped with 0.1% FA:MeOH doped with 0.1% FA eluent at a constant flow rate of 0.7 mL min^{-1}. The concentration of MeOH doped with 0.1% FA was gradually increased from 20 to 90% between 3.5 and 7.5 minutes, before being held at 90% until a total retention time of 12.5 minutes. The concentration of the MeOH doped with 0.1% FA was then immediately reduced back to 20% for the last 5 minutes of the analysis. MS data was collected in positive mode between 7 – 14 minutes.

HPLC analysis of the conversion of DMA to DMA-O_2 and initial characterisation were performed using MeCN (99.999%, Aldrich). 50 µL of sample was injected into an Accucore aQ column using an 100% MeCN eluent at a constant flow rate of 1.0 mL min^{-1}.

4.2.8 NMR measurements

^{1}H NMR samples were prepared in either a N_2- or Ar-filled glovebox using airtight NMR tubes fitted with Young's taps. ^{1}H spectra were recorded on a Bruker Ascend 400 MHz spectrometer with 128 scans and analysed on Bruker TopSpin software.

4.3 Gr-NMC811 full-cell cycling and the role of VC

To elucidate the effect of VC presence on the efficiency of SEI formation in Gr-NMC811 full-cells, the first C/20 formation cycle of a cell containing a base LP57 electrolyte (1 M $LiPF_6$ in EC:EMC 3:7 v/v) and an analogous cell doped with

2 wt.% VC additive were examined (**Figure 4.1**). LP57 and VC were selected as the electrolyte and additive for this study due to their widespread industrial use, with VC being the most common electrolyte additive used in commercial lithium-ion batteries.[5,7,13–16] **Figure 4.1**a shows a hysteresis voltage plot of the cell containing VC (LP57-VC), where an initial charge capacity and coulombic efficiency (CE) of 217.2 mAh g^{-1}_{NMC} and 91.2% are achieved, respectively. This performance is consistent with the reversible capacity expected for the first formation cycle of Gr-NMC811 cells containing an SEI optimising additive, where some loss of lithium inventory due to SEI formation is expected. **Figure 4.1**b shows the results from an analogous cell cycled with no VC additive (VC-free), in which a marginally higher initial charge capacity of 226.1 mAh g^{-1}_{NMC} but a lower first cycle CE of 86.0% is achieved. The drop in CE can be attributed to the formation of a sub-optimal SEI, where EC will be the primary organic degradation product.

These results, in line with previous literature understanding, would suggest that the long-term performance of the cell containing the VC-free electrolyte should be worse than the cell containing LP57-VC, due to the combinatory effects of a sub-optimal SEI and a greater loss of lithium inventory in the first formation cycle.[17,18] However, my long-term cycling data for Gr-NMC811 cells indicates a deviation from this understanding. **Figure 4.2** compares the capacity performance and CE of the first 500 cycles at C/2 of Gr-NMC811 cells containing either a LP57-VC electrolyte or an analogous VC-free electrolyte, after three C/20 formation cycles have been performed (not shown). Both cells experience capacity fade upon the initiation of C/2 cycling, with average discharge capacities of 183.1 and 185.3 mAh g^{-1}_{NMC} being achieved by cells containing the LP57-VC and VC-free electrolytes, respectively. A high CE is observed throughout cycling of both cells, with an average CE of 99.97 and 99.93% being achieved across the full 500 cycles for the cells containing a LP57-VC and VC-free electrolyte, respectively.

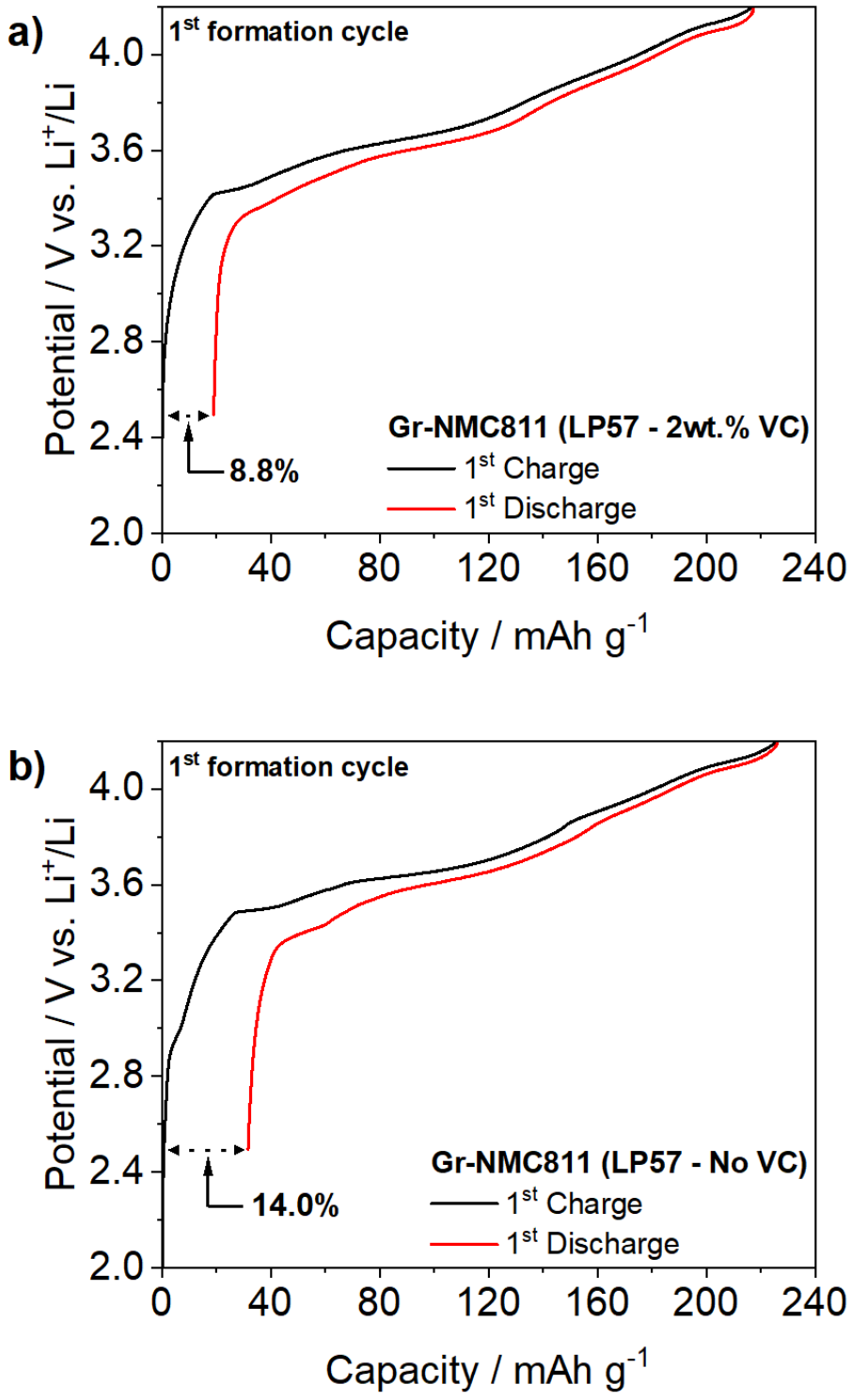


Figure 4.1. *First cycle hysteresis plots of Gr-NMC811 cells containing an a) VC-containing or b) VC-free LP57 electrolyte cycled between 2.5 – 4.2 V vs Li^+/Li, showing the first cycle capacity loss.*

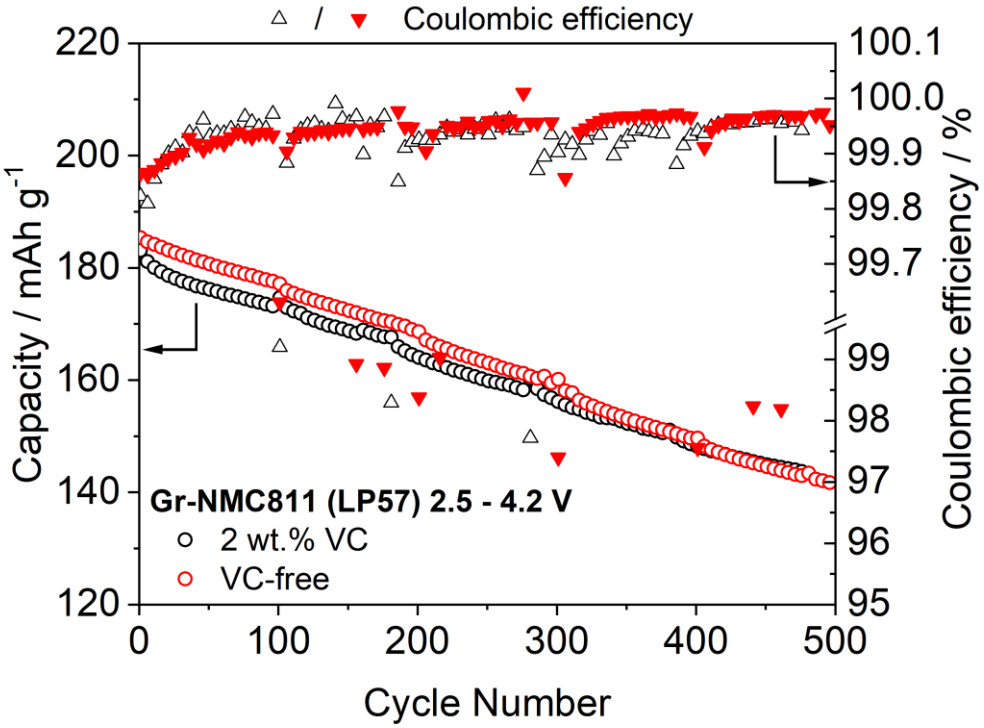


Figure 4.2. *Capacity performance of Gr-NMC811 cells containing either a VC-containing (black shapes) or VC-free (red shapes) LP57 electrolyte cycled between 2.5 – 4.2 V vs Li^+/Li. Three C/20 formation cycles that were performed before C/2 cycling are not shown here. These data were collected by Dr. Wesley Dose at the University of Cambridge and show the average performance of 4 cells.*

Figure 4.3a and b show the capacity performance of the first and last 100 cycles of these cells, respectively, giving greater clarity on cell performance in these regions. The cell containing a VC-free electrolyte clearly outperforms the cell containing a LP57-VC electrolyte across the first 100 cycles, where an average CE of 99.92% is achieved over this range (**Figure 4.3**a). By the 400th cycle, the capacity of the cells containing LP57-VC and a VC-free electrolyte have reached 148.2 and 149.4 mAh g^{-1}_{NMC}, respectively, marking ca. 80% capacity retention compared to the first C/2 cycle, where a commercial cell would be considered end-of-life (**Figure 4.3**b). This observation confirms that Gr-NMC811 cells with no VC additive can perform comparable to, or even exceed, the performance of Gr-NMC811 cells doped with 2 wt.% VC. Between the 400th and 500th cycle,

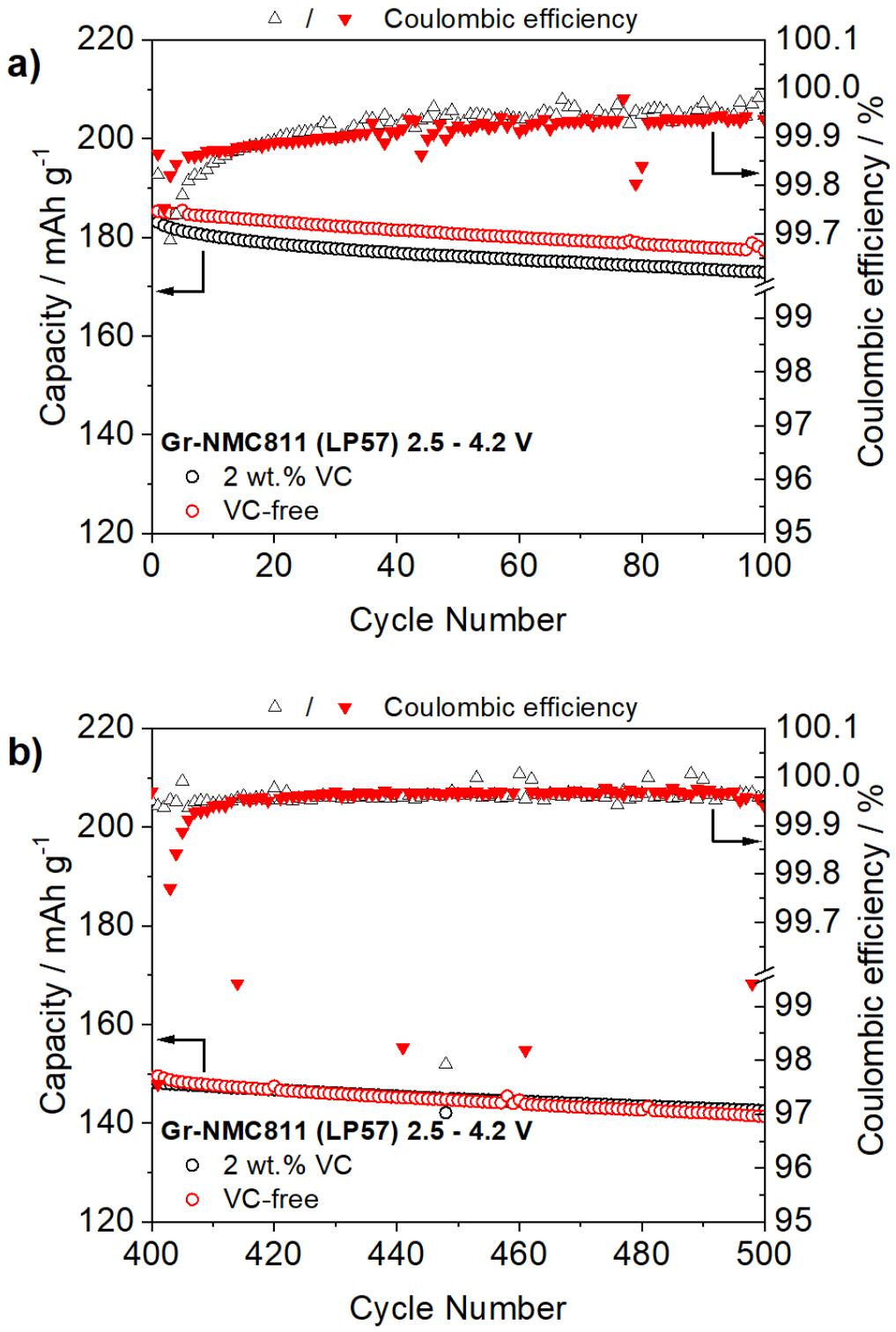


Figure 4.3. *Capacity performance during the a) first 100 and b) 400th – 500th C/2 cycles of Gr-NMC811 cells containing a VC-containing (black shapes) or VC-free (red shapes) LP57 electrolyte cycled between 2.5 – 4.2 V vs Li^{+}/Li. Three C/20 formation cycles that were performed before C/2 cycling are not shown here. These data were collected by Dr. Wesley Dose at the University of Cambridge and show the average performance of 4 cells.*

the cells continue to perform comparably, with 500th cycle capacities of 142.6 and 141.4 mAh g^{-1}_{NMC} being attained in the VC-containing and VC-free cells, respectively.

These data show that, despite the broad acceptance that VC is beneficial to lithium-ion full-cell performance, Gr-NMC811 full-cells cycled with a VC-free electrolyte can outperform those doped with 2 wt.% VC. The beneficial effects of VC for Gr SEI optimisation have been extensively verified and proven in a variety of cell chemistries, thus the efficacy of VC is not challenged here.[13,17–20] Instead a feature of the conditions present when a specific combination of a NMC811 positive electrode with a Gr negative electrode must be responsible for the observed long-term cycling performance in the cell containing a VC-free electrolyte. Given that VC is an additive targeted at stabilisation of the negative electrode and is expected to be comparatively innocent to the positive electrode, it is curious that the inclusion of VC appears to have no significant impact on long-term cell performance.

It has previously been theorised that the trend of increasing surface reactivity with increasing Ni-content could result in the formation of soluble VC through oxidation of EC at the positive electrode, or through reaction with reactive O_2 species that are released from the transition metal oxide surface.[6,8] If VC is generated *in-situ*, this may rationalise the comparable performance of the LP57-VC and VC-free cells (**Figure 4.2**), since the latter could form a SEI comparable to the VC-containing cell, albeit with lower VC electrolyte concentration. Thus, this chapter sets out to explore the formation of VC in early-stage cycling of Gr-NMC811 full-cells, seeking to identify both its presence in electrolyte extracted from cells cycled under operational conditions and understand the feasibility of the proposed $^1O_2$ and surface oxygen driven formation pathways.

4.4 Investigating gas evolution in Li-NMC811 cells

The oxidation of electrolyte components at the surface of Ni-rich positive electrode materials is known to result in the evolution of gaseous products,

either through the direct oxidation of species at the positive electrode surface, or through subsequent chemical or electrochemical reaction of oxidation products with electrolyte components or the negative electrode, respectively.[4,6,8,21–25] To understand the relationship between positive electrode potential and the onset of gas evolution at NMC811 electrodes, OEMS was performed with a Li-NMC811 half-cell, containing a LP57-VC electrolyte, tracking the signal intensity of the mass to charge ratio (m/z) values of O_2, CO_2, CO and H_2. Metallic Li was chosen as the counter-electrode for these experiments to achieve a stable reference potential. However, its high reactivity with organic carbonates, as explored in detail in Chapter 3, necessitates the inclusion of VC in the electrolyte composition to limit the contribution of gas evolution as a result of the direct reduction of EC and EMC on the surface of metallic Li.[26,27]

Figure 4.4a shows the cycling protocol of the OEMS experiment, where the cell was held at 20 °C and a current density of C/20 was applied until it had reached an UCV of 4.6 V vs Li^+/Li, chosen to ensure that the NMC811 electrode was cycled into a region of stress, where high interfacial reactivity with the electrolyte components and gas release is known to occur.[25,28,29] A subsequent voltage hold at 4.6 V was performed for a total of 40 hours, allowing passivation of the positive electrode surface to the extent that gas evolution has fallen back to baseline levels. The cell was then discharged at C/20 to a lower potential limit of 2.5 V vs Li^+/Li, completing the cycle. A total charge capacity of 252.2 mAh g^{-1}_{NMC} was attained, close to the theoretical capacity of NMC811 electrodes (ca. 275 mAh g^{-1}_{NMC}). Upon discharge, a capacity of 229.8 mAh g^{-1}_{NMC} was recovered, demonstrating a CE of 91.1%. Although impressive (given that this is a formation cycle), a considerable amount of both the capacity passed on charge and discharge will likely be the result of parasitic degradation reactions at the surface of the NMC811 electrode and would be accompanied by loss of lithium inventory through SEI formation at the Gr negative electrode in a full-cell configuration. Here, the metallic Li counter electrode acts to suppress the observed loss of lithium inventory, artificially

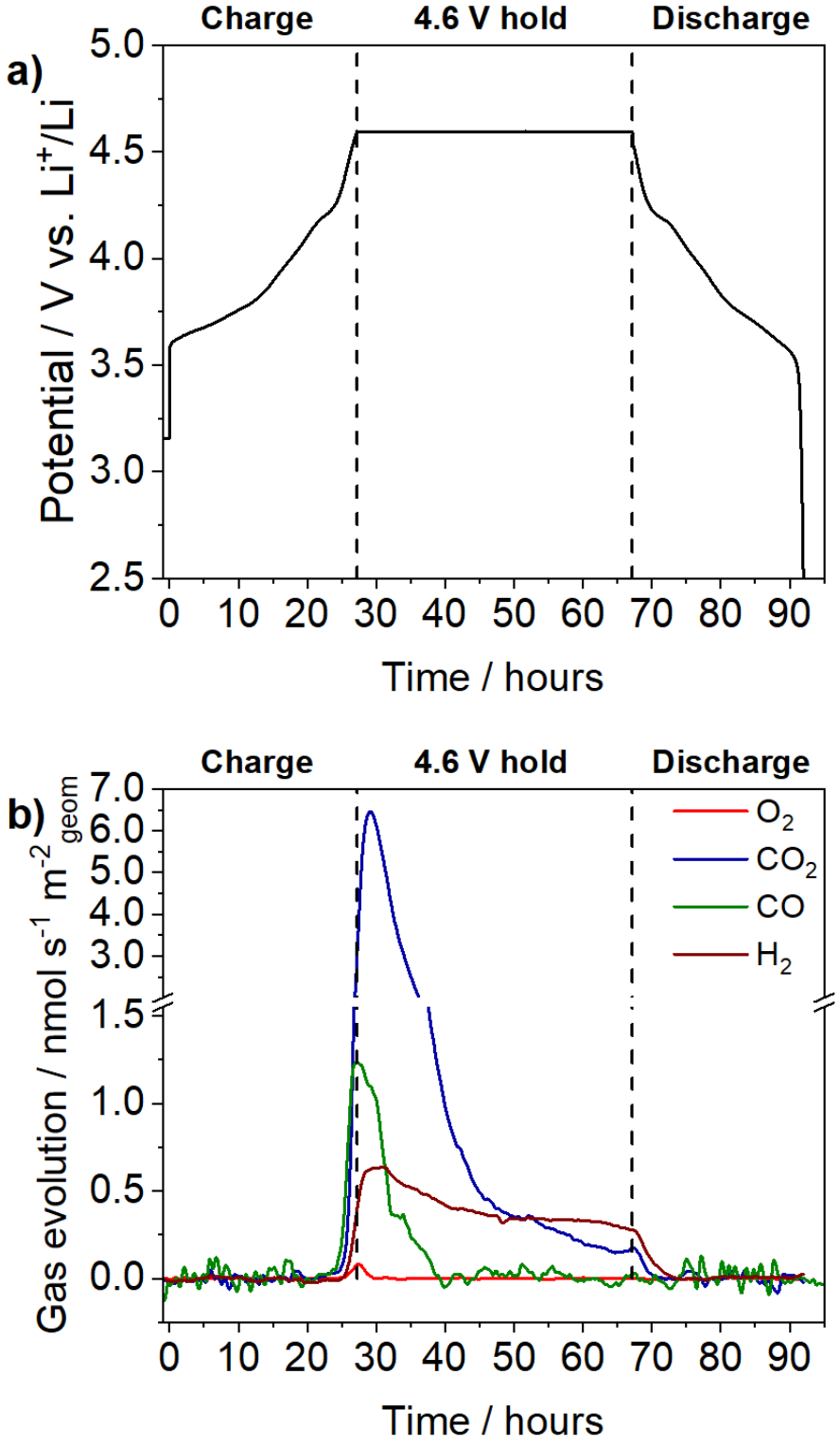


Figure 4.4. *a) Potential profile and b) rate of O_2, CO_2, CO and H_2 evolution as a function of time during an OEMS experiment performed on a Li-NMC811 half-cell, containing a LP57 electrolyte doped with 2 wt.% VC, to study the release of gaseous products through electrolyte oxidation at high UCVs. These data were collected by Dr. Israel Temprano at the University of Cambridge.*

inflating the observed reversibility.

Figure 4.4b shows the quantity of O_2, CO_2, CO and H_2, evolved throughout the application of this cycle protocol, calculated by recording the intensity of the signal at the relevant m/z ratio values (32, 44, 28, and 2, respectively) as a function of time. The raw intensity values are converted to the rate of gas evolution through fitting to a calibration plot, created by flowing a calibration gas with known analyte concentrations through the instrument, and further normalised to the geometric (geom) area of the positive electrode. More details on calibration of on-line mass spectrometers can be found in Chapter 2.

Figure 4.5 shows the rate of O_2 evolution throughout the cycle protocol, where a steady baseline is observed up to ca. 4.32 V vs Li^+/Li. At this potential, the rate of O_2 evolution begins to deviate from the baseline and a rapid increase in the rate of O_2 evolution is observed, which continues to steadily increase up to the

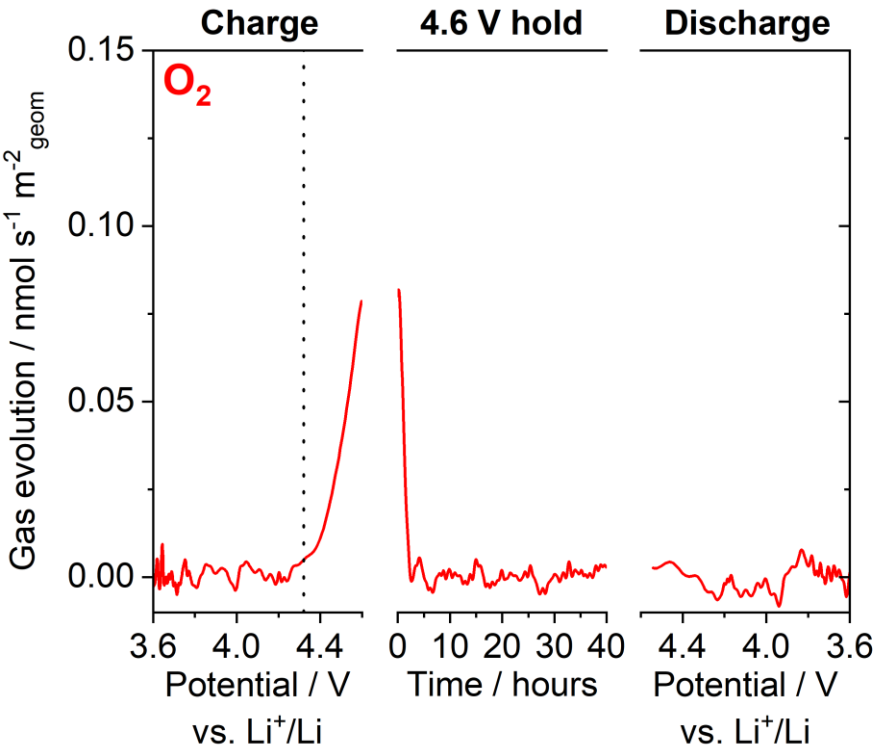


Figure 4.5. *Rate of O_2 evolution from a Li-NMC811 half-cell cycled to an UCV of 4.6 V vs Li^+/Li containing a LP57 electrolyte doped with 2 wt.% VC. The cell was cycled at C/20, with a 40-hour voltage hold at 4.6 V between charge and discharge. The onset of O_2 evolution is marked by the dotted line. These data were collected by Dr. Israel Temprano at the University of Cambridge.*

4.6 V UCV, reaching ca. 0.08 nmol s^{-1} m^{-2}_{geom} at its peak. Upon initiation of the voltage hold period, the rate of O_2 evolution sharply decreases, indicating that the degradation reactions which are responsible for O_2 release are being limited by changes in the environment at the electrode surface. Within the first 2 hours of the voltage hold, the signal drops back to the baseline level, where it remains for the entirety of this period and the subsequent discharge step.

At high degrees of delithiation NMC811 electrodes are known to release lattice oxygen and undergo structural changes.[1,24,25,30] This phase change has been shown to be reversible if surface metal-oxygen bonds are not broken. However, as the potential is pushed to higher UCVs, the thermodynamic driving force for lattice oxygen release becomes increasingly strong.[24] Therefore, the onset of O_2 evolution at ca. 4.32 V vs Li^+/Li is likely the result of irreversible lattice oxygen release, indicating degradation of the NMC811 surface structure. Moreover, this lattice oxygen can be released either in the form of molecular O_2, detected here, or as reactive oxygen species (i.e. $^1O_2$, O^{2-}) where release is highly energetic, which can go on to initiate further degradation reactions.[23,24] Lattice oxygen release causes irreversible changes in the NMC811 surface structure where, once surface oxygen has been released, further O_2 evolution is limited by the rate of O_2 diffusivity from the bulk.[25] The sluggish kinetics of bulk O_2 diffusion describe the observed drop in the rate of O_2 evolution upon initiation of the voltage hold period.

Figure 4.6a and b show the corresponding results recorded at the molecular ion m/z values of CO_2 and CO, respectively. The onset of CO_2 evolution is coincident with the onset of O_2 evolution, where deviation from the baseline is observed at a positive electrode potential of ca. 4.32 V vs Li^+/Li (**Figure 4.6**a). The coincident evolution of O_2 and CO_2 raises the question of whether the two are intrinsically linked. CO_2 has been previously reported as one of the oxidation products of EC, however, this oxidation could be either surface confined or initiated by the release of lattice oxygen in the form of reactive oxygen species (i.e $^1O_2$, O^{2-}) which undergo subsequent chemical reaction with the electrolyte solvents.[4,22,25] The similarities in response continue throughout the charge

process, where a clear relationship between increasing the rate of CO_2 evolution and overpotential is established. However, unlike the O_2 signal, the rate of CO_2 evolution continues to increase through the early stages of the voltage hold period, indicating that the pathway of CO_2 production is not wholly tied to O_2 production. Moreover, it is also important to note the rate of CO_2 evolution is considerably higher than that observed for O_2, with a maximum rate of ca. 6.5 nmol s^{-1} m^{-2}_{geom} being observed at the peak of CO_2 evolution (**Figure 4.6**a). This occurs ca. 6.5 hours into the voltage hold step, at which point O_2 evolution has already returned to baseline levels (**Figure 4.5**). CO_2 continues to be evolved for more than 30 hours of the voltage hold, at which point the signal then falls back to within the range of the baseline signal, indicating that the local environment at the positive electrode has changed sufficiently that the CO_2 producing reactions can no longer proceed (i.e. the electrode surface is passivated).

The observed onset of CO evolution, marked by the deviation from the baseline noise, occurs at ca. 4.42 V vs Li^+/Li, a greater positive electrode potential than for O_2 or CO_2 (**Figure 4.6**b). The intensity of the CO signal has been adjusted for the contribution of CO_2 through molecular fragmentation. Further information regarding this can be found in Chapter 2. The delayed onset of CO release suggests that this oxidation pathway may not be dependent on the O_2 and CO_2 forming reactions, with higher positive electrode potentials being required to initiate this reaction pathway. Nevertheless, the rate of CO evolution increases in-line with positive electrode potential above 4.42 V and continues to be evolved into the voltage hold step. A maximum rate of CO evolution of ca. 1.1 nmol s^{-1} m^{-2}_{geom} is achieved ca. 1 hour into the voltage hold, with the signal falling back to within the baseline noise region after 12 hours at 4.6 V. The longevity and intensity of CO evolution indicates that this degradation pathway is a significant contributor to electrolyte degradation, with the delayed onset suggesting that a greater thermodynamic driving force is required for initiation of this degradation pathway which, once overcome, results in aggressive electrolyte degradation.

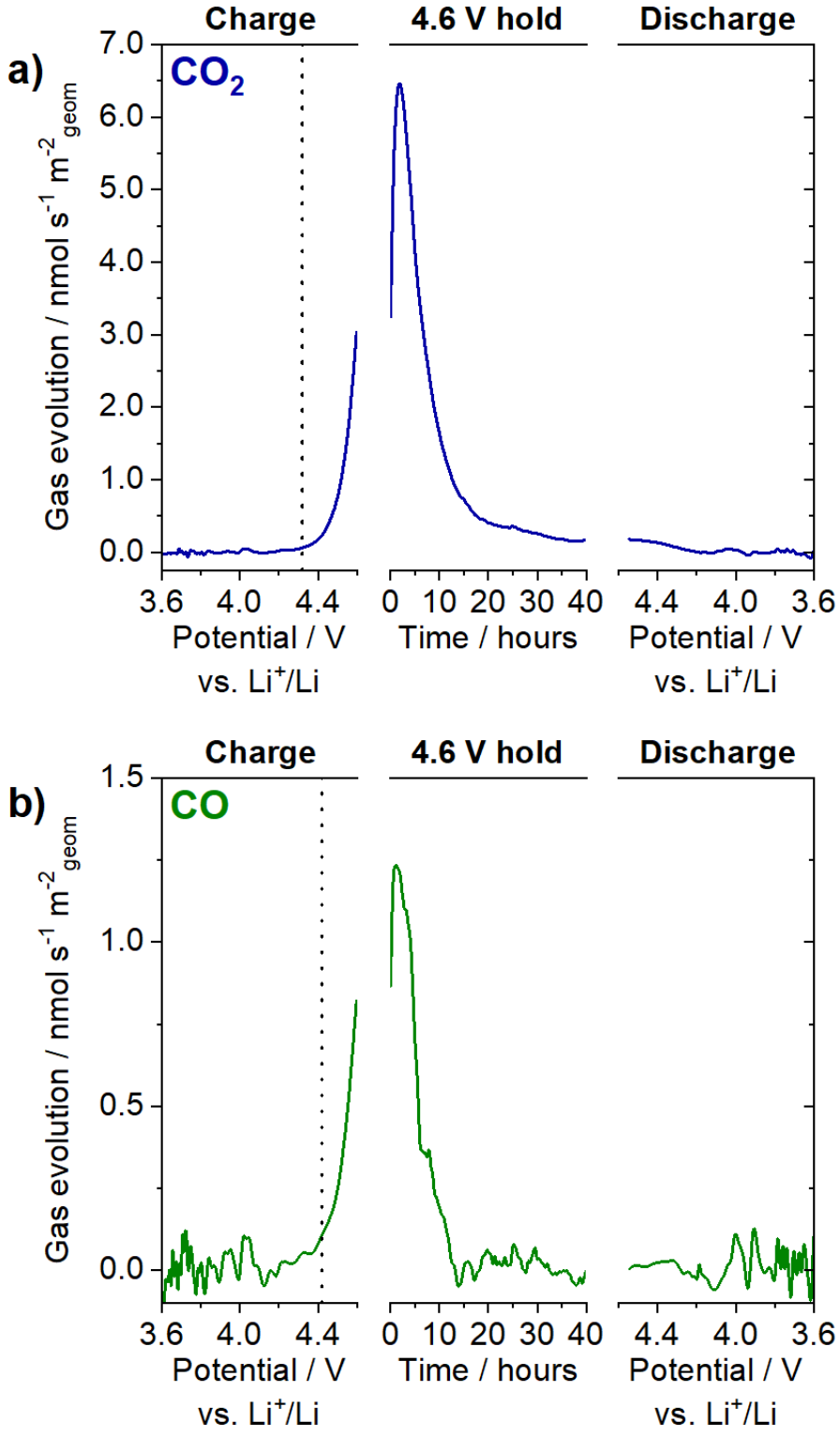


***Figure 4.6**. Rate of a) CO_2 and b) CO evolution from a Li-NMC811 half-cell cycled to an UCV of 4.6 V vs Li^+/Li containing a LP57 electrolyte doped with 2 wt.% VC. The cell was cycled at C/20, with a 40-hour voltage hold at 4.6 V between charge and discharge. The onset of gas evolution is marked by the dotted lines. These data were collected by Dr. Israel Temprano at the University of Cambridge.*

The onset of H_2 evolution is coincident with the release of O_2 and CO_2 (**Figure 4.7**). However, unlike the other gases, H_2 evolution remains at an elevated rate across the entirety of the voltage hold step and continues to be evolved far into the discharge step. This disparity is the result of the evolved H_2 not being generated through electrolyte oxidation, but rather generated by soluble species that are formed through electrolyte oxidation at the surface of the NMC811 electrode crossing over to the metallic Li counter electrode where they are reduced to generate H_2.[21,25] This rationalises both the maintenance of gas release in the hold period, where the rate of O_2, CO_2 and CO evolution returns to baseline levels, and the continuation of H_2 evolution into the discharge process, where these soluble species may still be present in the electrolyte. Nevertheless, the rate of H_2 evolution eventually falls back to baseline levels, indicating that these degradation products are effectively reduced at the metallic Li electrode until their concentration is negligible. This

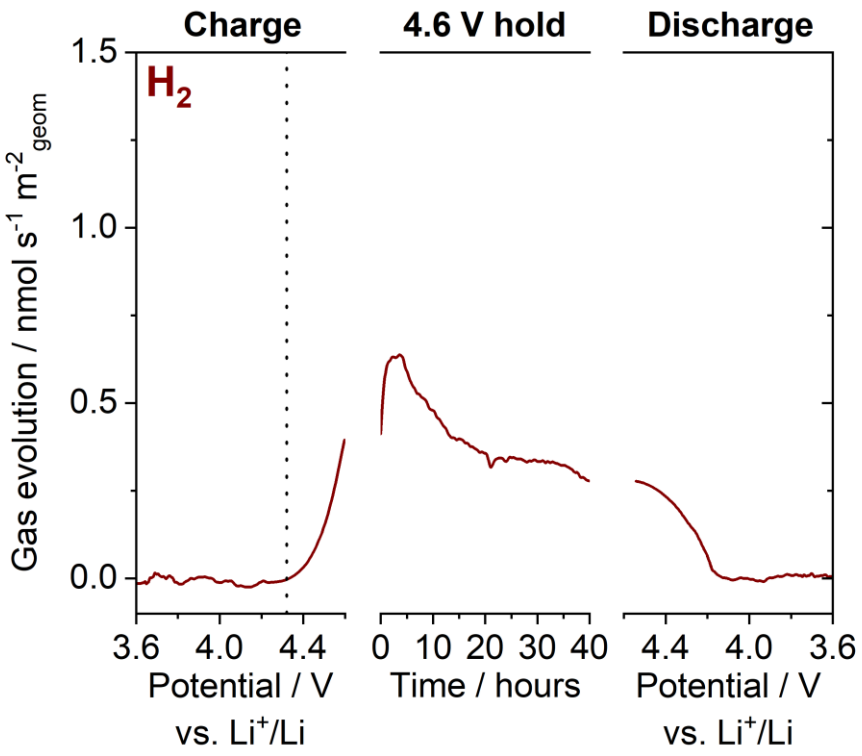


Figure 4.7. *Rate of H_2 evolution from a Li-NMC811 half-cell cycled to an UCV of 4.6 V vs Li^+/Li containing a LP57 electrolyte doped with 2 wt.% VC. The cell was cycled at C/20, with a 40-hour voltage hold at 4.6 V between charge and discharge. The onset of H_2 evolution is marked by the dotted line. These data were collected by Dr. Israel Temprano at the University of Cambridge.*

demonstrates the importance of understanding the crossover of electrolyte degradation products, where products that are formed at the surface of the positive electrode can diffuse through the electrolyte and interact with the negative electrode and vice versa.

These data reveal that CO_2 and CO are the primary gases detected from electrolyte oxidation at the positive electrode in Li-NMC811 half-cells. Lattice oxygen is released above 4.3 V vs Li^+/Li, either in the form of molecular O_2, or as reactive O_2 species (i.e. $^1O_2$, O^{2-}) that can initiate further chemical electrolyte degradation, limiting the quantity of O_2 observed in gas analysis of the cell. Furthermore, these data indicate that soluble oxidation products are formed at the surface of NMC811 electrodes which can diffuse through the electrolyte and interact with the negative electrode. Therefore, it is possible that if VC is formed, through oxidation of EC by Ni-rich positive electrode chemistries, it may crossover through the electrolyte and interact with the surface of a Gr negative electrode, improving the qualities of the SEI and rationalising the deviation from the expected performance of Gr-NMC811 cells with no VC additive (**Figure 4.2**).

4.5 Detecting the formation of VC in early-stage cycling of Gr-NMC811 cells

If VC is formed through the oxidation of EC at the surface of Ni-rich NMC chemistries, its concentration will be low compared to the bulk electrolyte solvent. Furthermore, crossover through the cell and reduction on the surface of the negative electrode will act to simultaneously consume VC, inhibiting accumulation until SEI stabilisation is achieved. To offer the best opportunity to detect VC formed in the operation of a Gr-NMC811 full-cell, a technique is required that can identify trace quantities of the analyte. Mass spectrometry (MS) is one of the most widely used techniques in analytical chemistry for the detection of low-abundance analytes, due to its unparalleled sensitivity and specificity, in the most optimised cases achieving detection of analytes at the low ppt levels.[31,32] However, both the high salt concentration and the presence

of high concentrations of solvent species with activity in the same region as VC (i.e. EC), mean that direct MS of electrolyte solutions is not practical.

A GC-MS method was developed and applied in Chapter 3 which effectively separated and identified VC at a retention time of 9.75 minutes to a high degree of confidence through comparison of experimental MS data to the NIST mass spectral library,[12] indicating that GC-MS detection of trace VC may be possible. LOD studies were carried out to assess the minimum quantity of VC statistically identifiable through GC-MS analysis. The LOD for analytical procedures is the point at which analysis becomes feasible and can be determined by an empirical approach, consisting of measuring progressively more dilute analytes, where the LOD is defined as the mean value of the noise of a blank sample plus 3× the standard deviation of the noise.[33] To understand the LOD of VC, samples of known VC concentration were prepared by performing serial dilutions in $CDCl_3$, chosen to mirror the workup procedure of the cycled electrolyte, and analysed using a targeted GC-MS method. **Figure 4.8** shows the results of this study, where an R^2 value of 0.999 is achieved over a range of 40 – 1000 ppb VC in $CDCl_3$, demonstrating the accuracy of the dilutions and confirming high sensitivity for the detection of trace quantities of VC.

Figure 4.8b examines the plot of VC concentration vs counts at low ppb concentrations, where greater clarity is presented for samples close to the LOD. A statistical LOD of ca. 40 ppb was calculated by taking the mean value of the baseline noise and adding 3× the standard deviation of the noise, giving good agreement with the empirically measured LOD, described by the intersection of the best fit line with the x-axis (**Figure 4.8**b). Furthermore, the LOQ, defined as the concentration at which quantitative analysis can be reported with a high degree of confidence, can be determined by recording the mean value of the noise of a blank sample plus 10× the standard deviation of the noise, resulting in LOQ of ca. 135 ppb.[33] These data demonstrate that extremely low (10s - 100s ppb) concentrations of VC can be detected in samples diluted with $CDCl_3$, confirming GC-MS as a suitable method for the detection of trace VC formed in the early stage cycling of Gr-NMC811 cells.

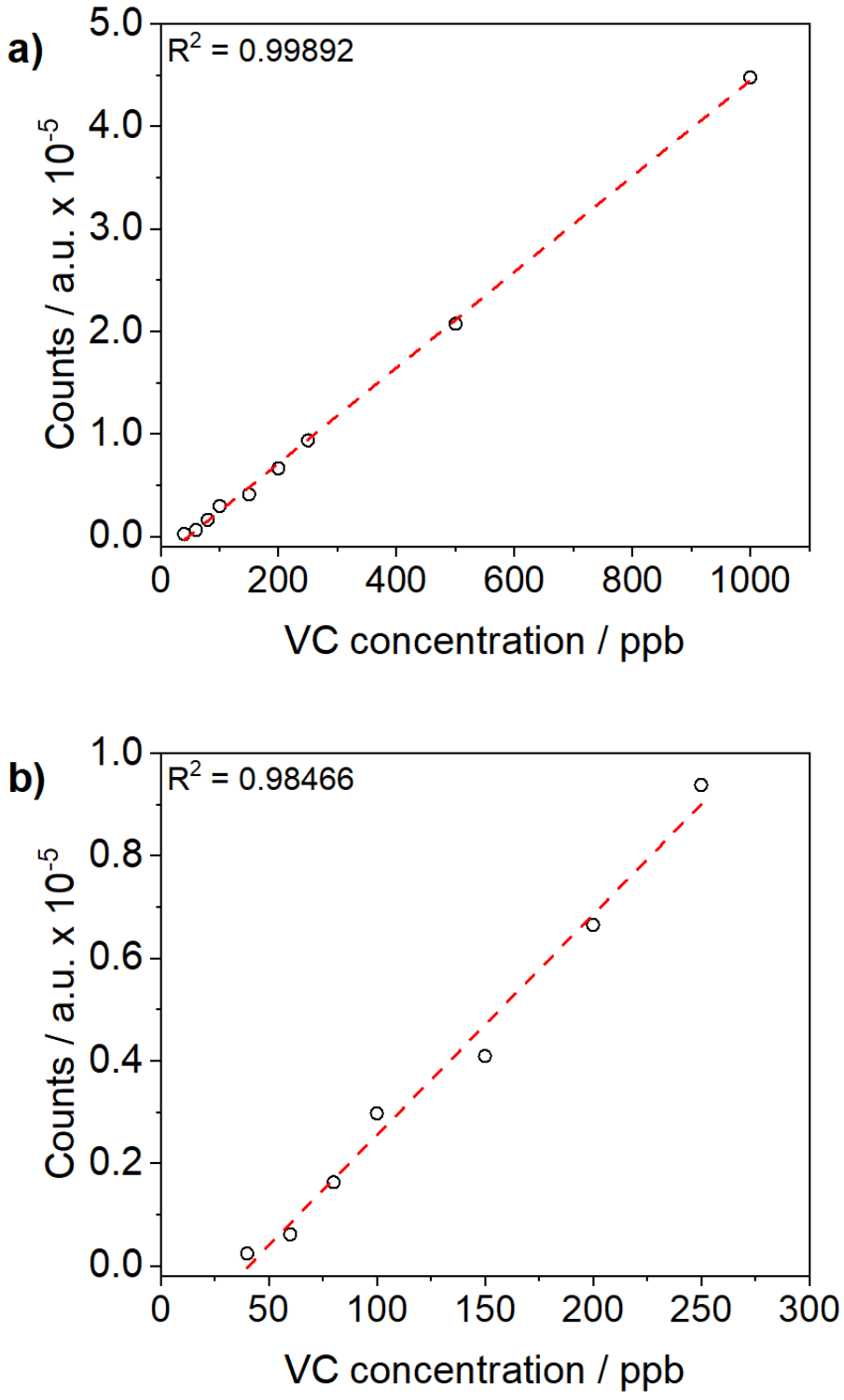


Figure 4.8. *Plots showing the results of a LOD study across a) the full range and b) concentrations ≤250 ppb for GC-MS detection of VC. Samples were prepared through serial dilutions of a 1000 ppm solution to a minimum concentration of 40 ppb. A LOD of ca. 40 ppb is identified.*

If the formation of VC at the surface of NMC811 positive electrodes was the reason for the performance of Gr-NMC811 full-cells containing a VC-free electrolyte being comparable to cells containing VC, it stands to reason that VC must be formed in the early stages of cycling, so that it can be involved with the formation and stabilisation of the Gr SEI. With a clear relationship having been established between UCV and reactivity of the NMC811 electrodes, where no detectable gas-producing oxidation reactions occur below 4.3 V vs Li^+/Li, a range of UCVs were explored for cell cycling experiments. Two protocols were employed: the first where three C/20 formation cycles to the desired UCV were performed; the second where an additional ten cycles at C/2 were performed. All cells were cycled at 20 °C with a VC-free LP57 electrolyte, and a consistent UCV was applied throughout formation cycling and subsequent C/2 cycling. After cycling, the electrolyte was extracted by soaking the separators in $CDCl_3$ to precipitate the majority of the $LiPF_6$ salt. This procedure is explored in detail in Chapter 3, confirming sample compatibility with GC-MS analyses.

Figure 4.9 shows the capacity performance of the cells cycled for three C/20 formation cycles before electrolyte extraction, alongside a plot of the retention time region of the chromatograms associated with VC. A clear relationship between UCV and capacity performance is observed due to increasing UCV facilitating access to a greater extent of NMC811 delithiation (**Figure 4.9**a). As the NMC811 electrode is delithiated, pushing its potential to higher voltages, its electrochemical reactivity with electrolyte components increases, thus more VC formation is expected at higher UCVs. **Figure 4.9**b shows the VC region of the chromatograms recorded of the electrolytes extracted from each of these cells. No deviation from the baseline is observed in the cell cycled to an UCV of 3.9 V, indicating that if any VC is present in the electrolyte, it is below the LOD of the instrument method. As low as 4.0 V, a shallow peak is observed in the chromatogram of the extracted electrolyte, which continues to increase in intensity as a function of UCV. In the electrolyte extracted from the cell cycled to an UCV of 4.2 V, the intensity of the peak is now more than 3× the standard deviation of the baseline noise, demonstrating statistically relevant detection

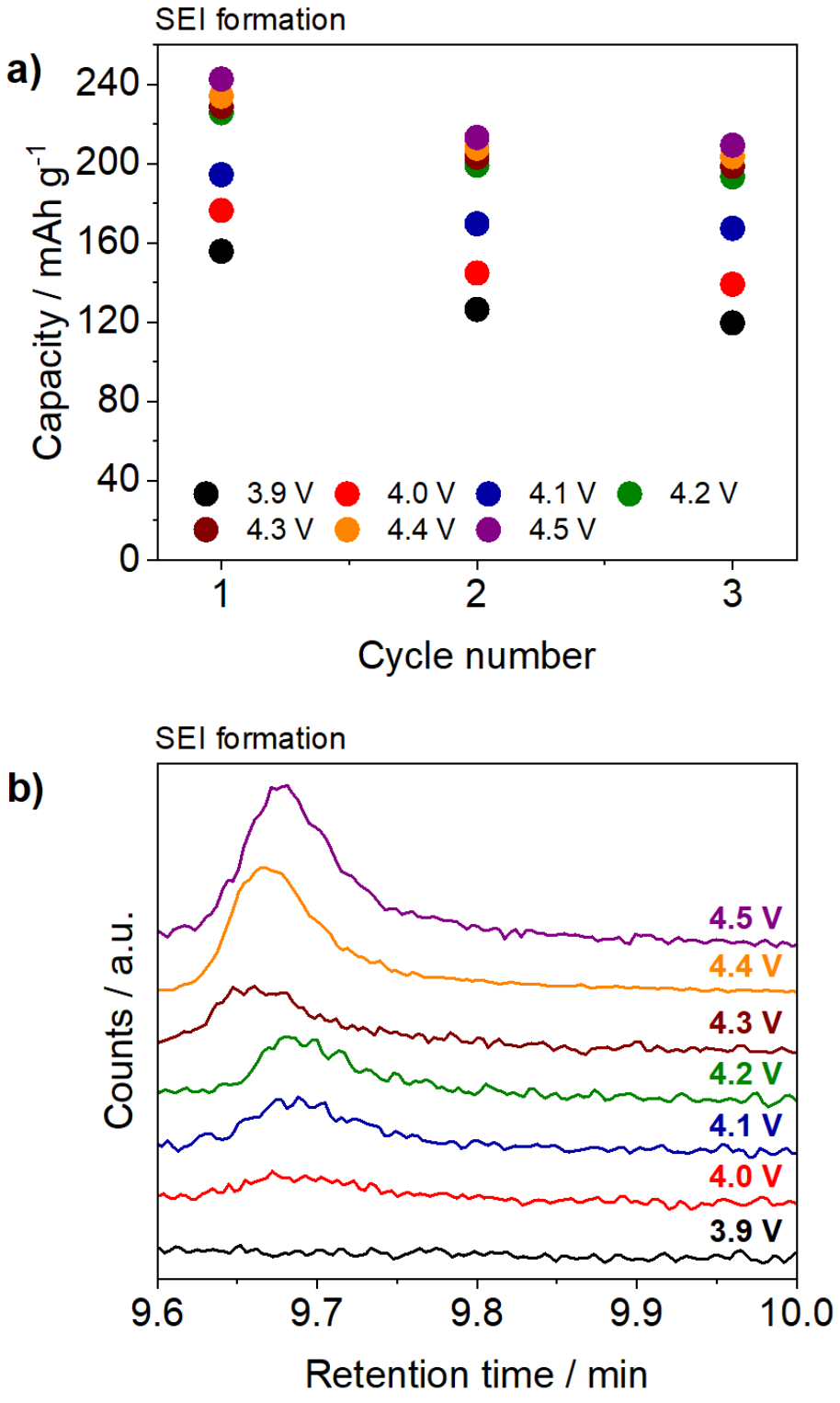


Figure 4.9. *Plots showing the effect of UCV on the a) capacity performance and b) VC region of the GC-MS chromatograms of electrolytes extracted from Gr-NMC811 cells cycled for three C/20 cycles containing a VC-free LP57 electrolyte.*

of VC in early-stage cycling of Gr-NMC811 full-cells within standard operational voltage limits. The intensity of this peak continues to grow as UCV is increased further, illustrating a relationship between UCV and VC accumulation. It is important to note that the detection of VC is a direct measure of formation and, more importantly, accumulation in the electrolyte. Where initially formed, VC will be reduced at the surface of the Gr negative electrode, mitigating accumulation until the point that a stable negative electrode SEI is formed.

To explore how VC concentration develops as a function of cycling, analogous experiments were performed on electrolyte extracted from cells cycled for three C/20 formation cycles and ten C/2 cycles to UCVs between 3.9 – 4.5 V vs Li^+/Li. **Figure 4.10** shows the capacity performance of these cells, alongside the region of the chromatogram associated with the retention time of VC. The highest initial C/2 capacity of 169.4 mAh g^{-1}_{NMC} is achieved by the cell cycled to an UCV of 4.2 V vs Li^+/Li, indicating that formation cycling with an UCV >4.2V results in poor capacity retention (**Figure 4.10**a). This cell continues to outperform the others, in good agreement with the high performance observed in **Figure 4.2**.

Figure 4.10b shows the VC region of the chromatograms recorded of the electrolytes extracted from each of these cells after the ten C/2 cycles, where a peak is observed in the electrolyte extracted from a cell cycled to an UCV of 3.9 V, indicating that some VC is formed at positive electrode potentials well within standard operational voltages. In good agreement with the data presented for the electrolyte extracted after C/20 cycling (**Figure 4.9**), peak intensity continues to grow in line with UCV. A considerable increase in peak intensity is observed between the chromatogram of the electrolyte extracted from cells cycled to an UCV of 4.2 V and 4.3 V, highlighting this potential window as a region where VC accumulation becomes more pronounced.

Figure 4.11 shows quantitative analysis of these VC detection experiments, for all extracted electrolytes, where a clear relationship between UCV and VC concentration is observed. Although some activity is seen in the electrolyte cycled to an UCV of 3.9 V for three C/20 and ten C/2 cycles, enough to

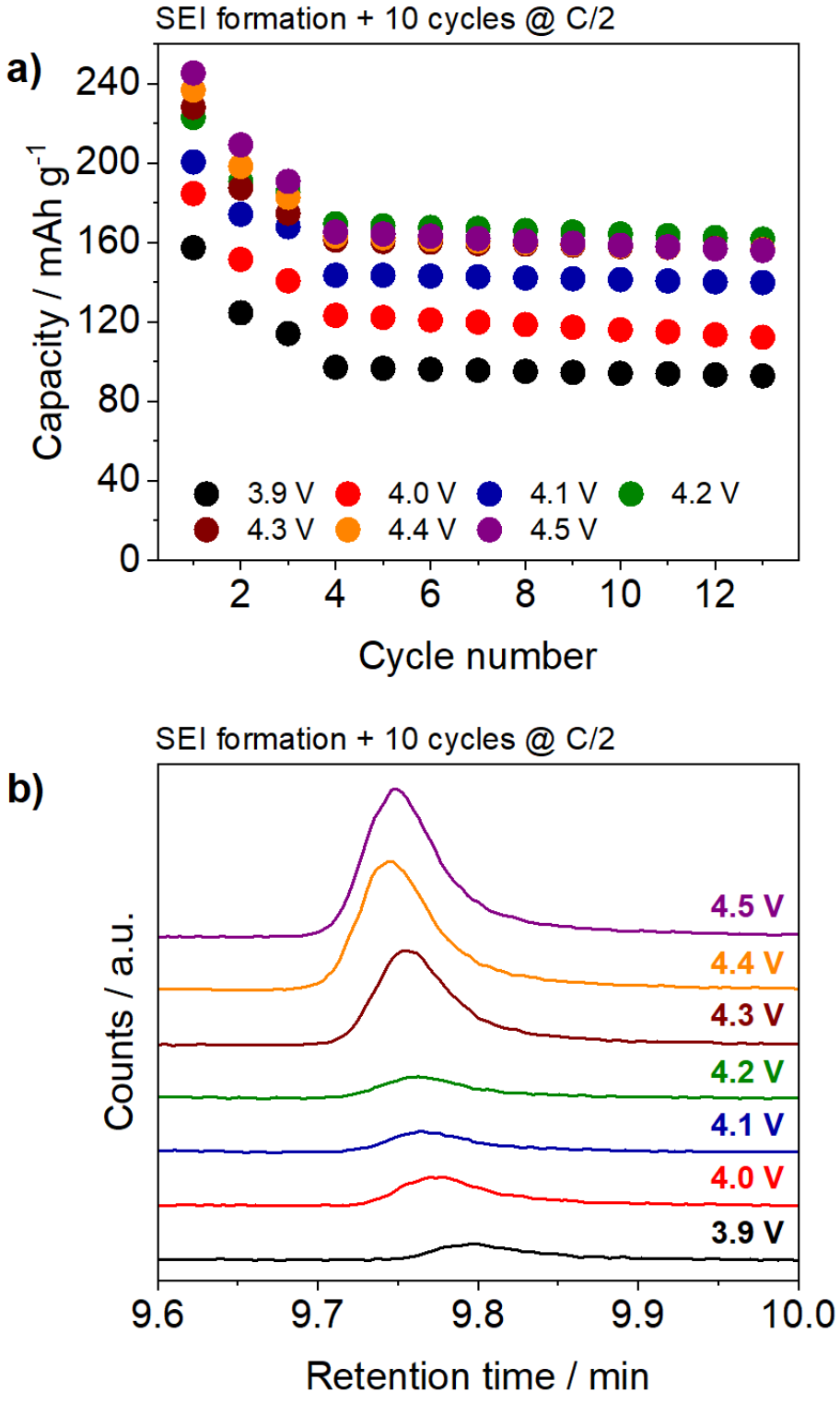


Figure 4.10. *Plots showing the effect of UCV on the a) capacity performance and b) VC region of the GC-MS chromatograms of electrolytes extracted from Gr-NMC811 cells cycled for three C/20 cycles and 10 C/2 cycles containing a VC-free LP57 electrolyte.*

qualitatively identify a peak, the peak intensity is below the LOD and so cannot be identified with sufficient confidence. This too is the case for the electrolyte extracted from the cell cycled for three C/20 formation cycles to an UCV of 4.0 V where, although a peak is observed, its intensity lies below the LOD. Surprisingly, ca. 75 ppb of VC was detected in the analogous cell cycled for an additional ten C/2 cycles to 4.0 V, exceeding the LOD and deeming VC accumulation statistically relevant. Both electrolytes extracted from cells cycled to an UCV of 4.2 V contained enough VC to exceed the LOD, demonstrating that VC is formed in statistically significant quantities within standard operational potential limits, and before the onset of gas evolution.

In electrolytes extracted from cells undergoing three C/20 formation cycles to UCVs above 4.2 V, the quantity of VC detected steadily increases with UCV until it reaches the LOQ (ca. 135 ppb) when the UCV is set to 4.5 V. The analogous

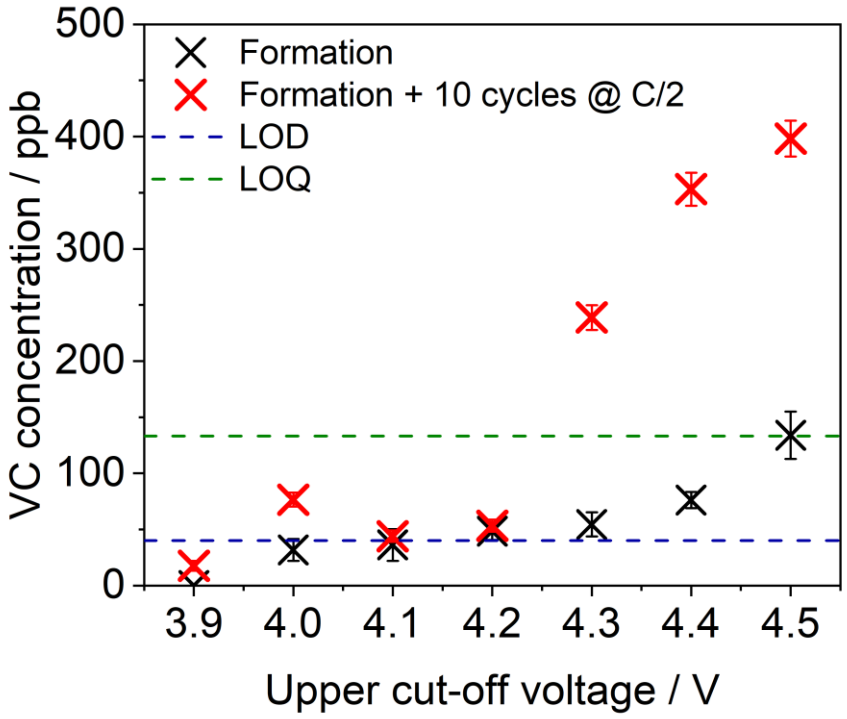


Figure 4.11. *Plot of the concentration of VC formed in Gr-NMC811 cells with a VC-free electrolyte assessed through GC-MS analysis of electrolytes extracted from cells cycled to a range of UCVs. Critically, VC concentrations above the LOD are detected within standard operational voltages (≤4.2 V vs Li^+/Li) confirming formation in early-stage cycling.*

cells cycled for an additional ten C/2 cycles experience the same, but much more pronounced, relationship where ca. 240 ppb of VC is detected in the electrolyte extracted from a cell cycled to an UCV of 4.3 V, above the LOQ. This is below the onset of gas release, indicating that statistically quantifiable amounts of VC are produced prior to gas release from oxidation of species at NMC811 positive electrodes. Furthermore, the rapid increase in accumulation with cycling indicates that both VC production continues past formation cycling, allowing accumulation in the electrolyte, and that the rate of VC consumption at the Gr negative electrode has decreased so that accumulation can occur, indicating the formation of a stable SEI and rationalising the high performance of Gr-NMC811 cells cycled with a VC-free LP57 electrolyte.

Figure 4.12 shows the experimental MS trace of the chromatogram peak at 9.75 minutes from the cell cycled for three C/20 cycles and ten C/2 cycles to an UCV of 4.5 V, compared to the NIST MS library entry for VC. Although additional

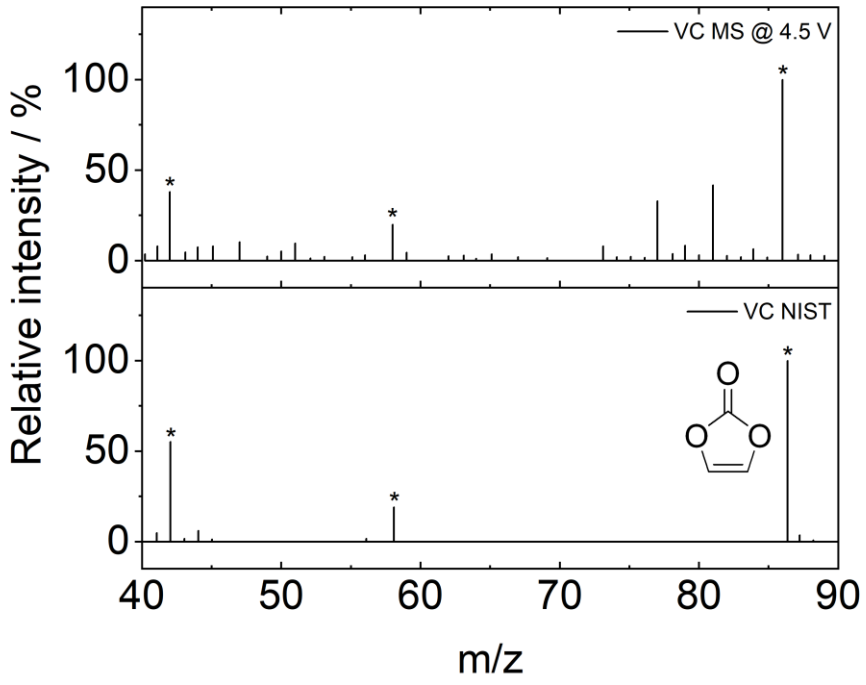


Figure 4.12. *Comparison of the MS recorded during GC-MS analysis of electrolyte extracted from a Gr-NMC811 cell containing a VC-free LP57 electrolyte cycled to an UCV of 4.5 V vs Li^+/Li at a retention time of 9.75 minutes to the NIST mass spectral library entry for VC, confirming the identity of this peak as VC.[12] * is used to highlight the molecular ion and fragment peaks of VC.*

peaks are observed in the baseline, it is clear that the molecular ion mass peak and the two major mass fragment peaks of VC (labelled *) are identified in the spectrum, confirming the identity of the detected species as VC.

These data prove that not only is VC formed at the surface of NMC811 positive electrodes below the onset of significant gas evolution, but also that the onset and rate of production are sufficient to accumulate VC in the electrolyte in statistically relevant quantities. These data explain the comparable performance of Gr-NMC811 full-cells when VC-free LP57 or LP57-VC electrolytes are used, where stabilisation of the Gr electrode can be supported by the *in-situ* formation of VC at the positive electrode in early-stage cycling. With a considerable increase in VC detection being observed in cells cycled to UCVs of ≥4.3 V, the route of VC formation is still unclear. At these potentials, lattice oxygen, possibly in the form of reactive O_2 species (i.e. $^1O_2$, O^{2-}), is introduced into the electrolyte. However, it is also possible that this potential limit marks a significant barrier in activation energy for electrolyte oxidation reactions at the surface of NMC811 positive electrodes which, once overcome, results in the onset of gas-producing oxidation reactions. The remainder of this chapter will focus on understanding the feasibility of $^1O_2$-driven VC formation to bring clarity to the pathway of VC formation.

4.6 Exploring the feasibility of photo-initiated Rose Bengal $^1O_2$-driven VC formation

VC formation through the oxidation of EC by $^1O_2$ was first proposed by Freiberg *et al*. in 2018.[6] There, RB was employed as a photosensitizer to generate $^1O_2$ in a ground state O_2 ($^3O_2$) saturated solution of either EC, DMC, or a mixture of both heated to 45 °C. The generation of $^1O_2$ was proven by on-line MS with a 10% O_2 gas stream, where a drop in the O_2 concentration was observed when the solutions were irradiated, demonstrating that O_2 was being removed from the electrolyte as $^1O_2$ was generated and subsequently reacts with the solvent. Although NMR spectroscopy was employed to search for VC, it was claimed that, once formed from EC, the VC reacts rapidly with $^3O_2$ and $^1O_2$ preventing

its accumulation and therefore detection. Instead, the authors detect H_2O_2, a molecule that they claim is the by-product of VC formation.

A recent study by Rinkel *et al.*,[4] published in July 2022, examined this work in detail, applying the same RB photosensitizer with $^{17}O_2$-enriched O_2 and EC to probe the reaction of $^1O_2$ with EC and DMC. Surprisingly, this study found that no H_2O_2 was accumulated through the reaction of $^1O_2$ with EC, but instead suggested that EC would be oxidised to form H_2O as its only soluble product, with CO_2 and CO being released as additional gaseous products through the mechanism shown in **Figure 4.13**. Despite the proposol of a reaction mechanism that generates considerable amounts of gaseous products, no on-line MS was reported for the reaction with photogenerated $^1O_2$, and the formation of H_2O is the only evidence that is given to support this reaction pathway. Interestingly, a change in ^1H environment of the RB is also reported, with the chemical shift initially observed at 7.32 ppm no longer being present after irradiation and a new low intensity peak at 6.52 ppm instead being

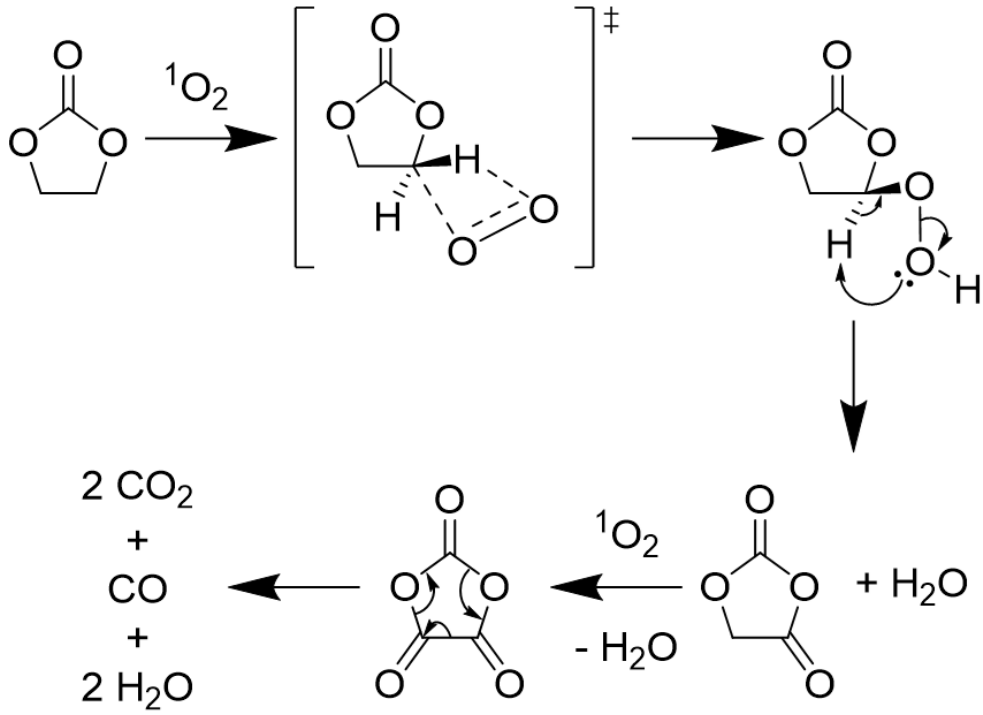


Figure 4.13. *Reaction scheme for the gaseous decomposition of EC in the presence of $^1O_2$ proposed by Rinkel et al.[4]*

observed. Although this is briefly mentioned, it is not addressed in detail in the manuscript and indicates that, despite the sample only being irradiated for 2 hours, the RB photosensitizer may not be a spectator to the reactions that are occuring and may instead be participating in degradation processes. This discrepancy in the reported analysis rationalises further exploration of the reactivity of $^1O_2$ with EC when generated through photoexcitation of a RB photosensitizer.

Before exploring the potential chemistry of our system, it is first important to understand the generation of $^1O_2$ through the use of a photosensitizer. **Figure 4.14** shows the molecular structure of RB, alongside a schematic that describes the generation of $^1O_2$ through the photoexcitation of a RB molecule and subsequent energy transfer to a ground state O_2 molecule. At rest, both RB and O_2 sit in their ground states, S_0 and T_0, respectively. When the solution is irradiated with light of a 525 nm wavelength, a one photon excitation between the ground state and first excited state (S_1) is achieved.[34,35] The excited RB molecule can then undergo intersystem crossing, an isoenergetic radiationless process wherein a molecule transitions between two electronic states with different spin multiplicities, to the first excited triplet state (T_1). The lifetime of T_1 is much longer than S_1 and allows reaction with O_2 through collision, where a RB molecule undergoes radiationless decay back to its S_0 state, exciting $^3O_2$ to its singlet state in the process. Once formed, $^1O_2$ can either react chemically or undergo radiative decay back to T_0. Each photosensitizer molecule can typically produce 10^3 – 10^5 molecules of $^1O_2$ before being degraded through photobleaching by $^1O_2$ or by another process.[34] More information on $^1O_2$ production and classification can be found in Chapter 2.

To understand the interaction of $^1O_2$ with the common electrolyte solvents employed in this study, four solutions containing 500 µM RB were made up for analysis: 1) EC:EMC 3:7 v/v to represent the VC-free LP57 electrolyte; 2) EC:EMC 3:7 v/v + 20 µL VC to represent a scenario where trace VC has formed; 3) EC:EMC 3:7 v/v with 2 wt.% VC additive to represent the doped electrolyte; and 4) VC to explore how $^1O_2$ reacts in the presence of only VC. When initially

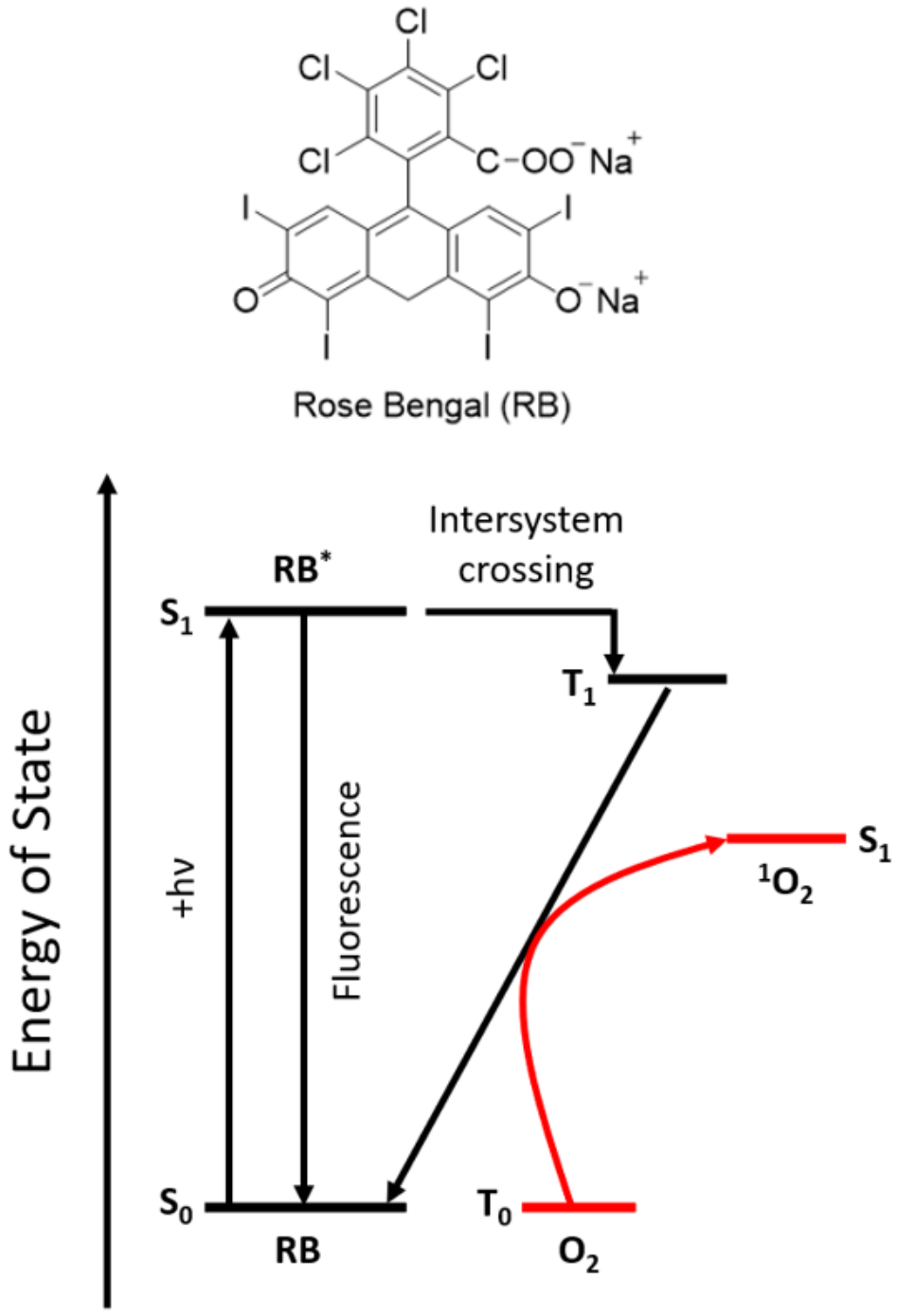


Figure 4.14. *Schematic showing the generation of $^1O_2$ through photoexcitation of a RB photosensitizer (molecular structure shown) to its first excited state (S_1), through intersystem crossing to its first excited triplet state (T_1) where collision with ground state O_2 results in the generation of $^1O_2$.*

mixed, each of these solutions was a vibrant pink colour. However, upon irradiation of these samples with green light for 12 hours, a range of different responses were observed. **Figure 4.15** shows a photograph taken of these mixtures after 12 hours of irradiation saturated with $^3O_2$. No significant difference was observed in the VC-free sample after 12 hours of irradiation (**Figure 4.15**a), providing a baseline of the original solution appearance. The sample doped with 20 µL VC experiences a colour change indicating that, unlike in the VC-free system, a reaction has occurred that has resulted in a change in the optical properties of the solution (**Figure 4.15**b). Furthermore, both the solution doped with 2 wt.% VC (**Figure 4.15**c) and the VC solution (**Figure 4.15**d) turned orange after 12 hours of irradiation. The VC-free solution retained its colour for approximately 120 hours of constant irradiation while saturated with $^3O_2$, indicating a higher stability of the photosensitizer in the absence of VC. These observations raise two questions: 1) Is the colour change representative of degradation of the RB photosensitizer or due to the contribution of new species to the mixture? and 2) why the loss of the characteristic RB photosensitizer colour was not reported by Rinkel *et al.* if it was observed coincident with the observed loss of the RB ^{1}H NMR peak.[4]

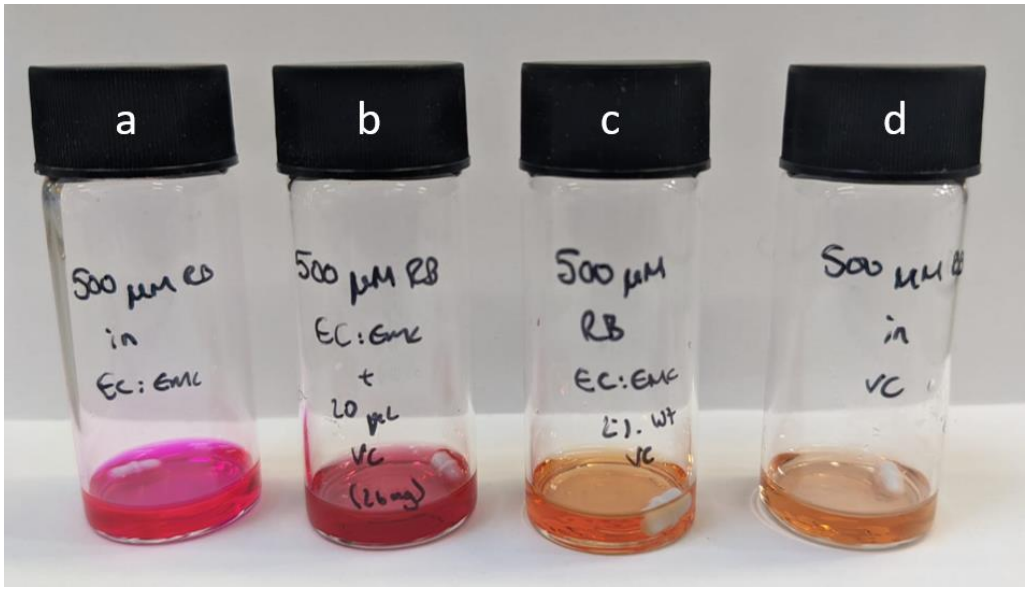


Figure 4.15. *A photograph of solutions containing 500 µM RB dissolved in a) EC:EMC, b) EC:EMC + 20 µL VC, c) EC:EMC + 2 wt.% VC, and d) VC after 12 hours of irradiation. Initial appearance of all samples were comparable to a.*

To understand the composition and characteristics of the RB photosensitizer in these systems, a technique was required that both revealed changes in the UV-visible (UV-Vis) absorption profile and was able to provide information on the composition of the solution.

HPLC, described in detail in Chapter 2, is an analytical technique that facilitates separation of molecular species and identification through UV-Vis absorbance profile and/or MS. **Figure 4.16** shows chromatograms of pristine analytes, recorded to understand the separation and characteristics of each of the base components. MeOH was chosen as the carrier solvent due the good solubility/miscibility of each of the analytes and its application as one of the eluent solvents. **Figure 4.16**a shows the raw chromatogram produced from the injection of pristine MeOH, where the peak at a retention time of ca. 2 minutes is the result of a change in the column solvent composition. To ensure adequate separation, a ramped method was applied, described in detail in the experimental section, which resulted in a gradient in the chromatogram trace. This is due to the UV-Vis baseline, taken at the start of the measurement, no longer being representative of the UV-Vis absorption profile of the pristine eluent (**Figure 4.16**a). As a result of this, a MeOH background chromatogram was used to baseline all other HPLC chromatograms reported.

Figure 4.16b shows the chromatogram produced when RB is doped into a solution of MeOH, where a new peak at ca. 13.6 minutes is observed, representative of the RB molecule eluting from the column. Injection of a MeOH solution doped with RB and VC results in an additional chromatogram peak at a retention time of ca. 2.4 minutes, attributed to VC (**Figure 4.16**c). The chromatogram of the equivalent RB in EC:EMC mixture contained no new significant activity compared to the RB in MeOH blank (**Figure 4.16**d), demonstrating that EC and EMC are not detectable by this method. The identity of the peak at 13.6 minutes was confirmed to be RB through analysis of both the UV-Vis absorption profile, which matches literature reports (**Figure 4.17**a),[36] and through HPLC-MS, wherein a primary mass peak of 972.57

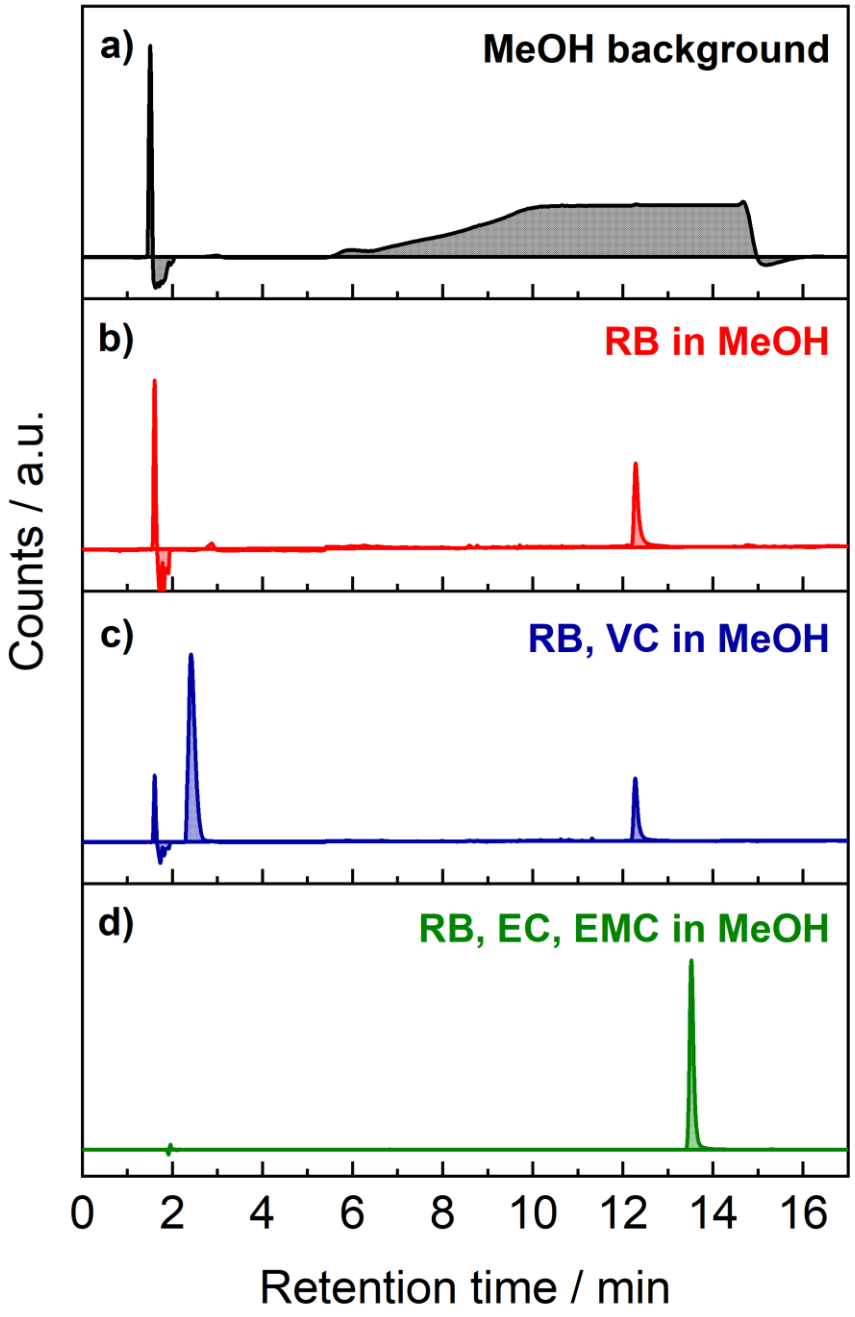


Figure 4.16. *HPLC chromatograms for injections of a) pristine MeOH, and MeOH doped with b) RB, c) RB and VC, d) RB, EC, and EMC. A MeOH background was subtracted from b, c, and d to smooth the baseline.*

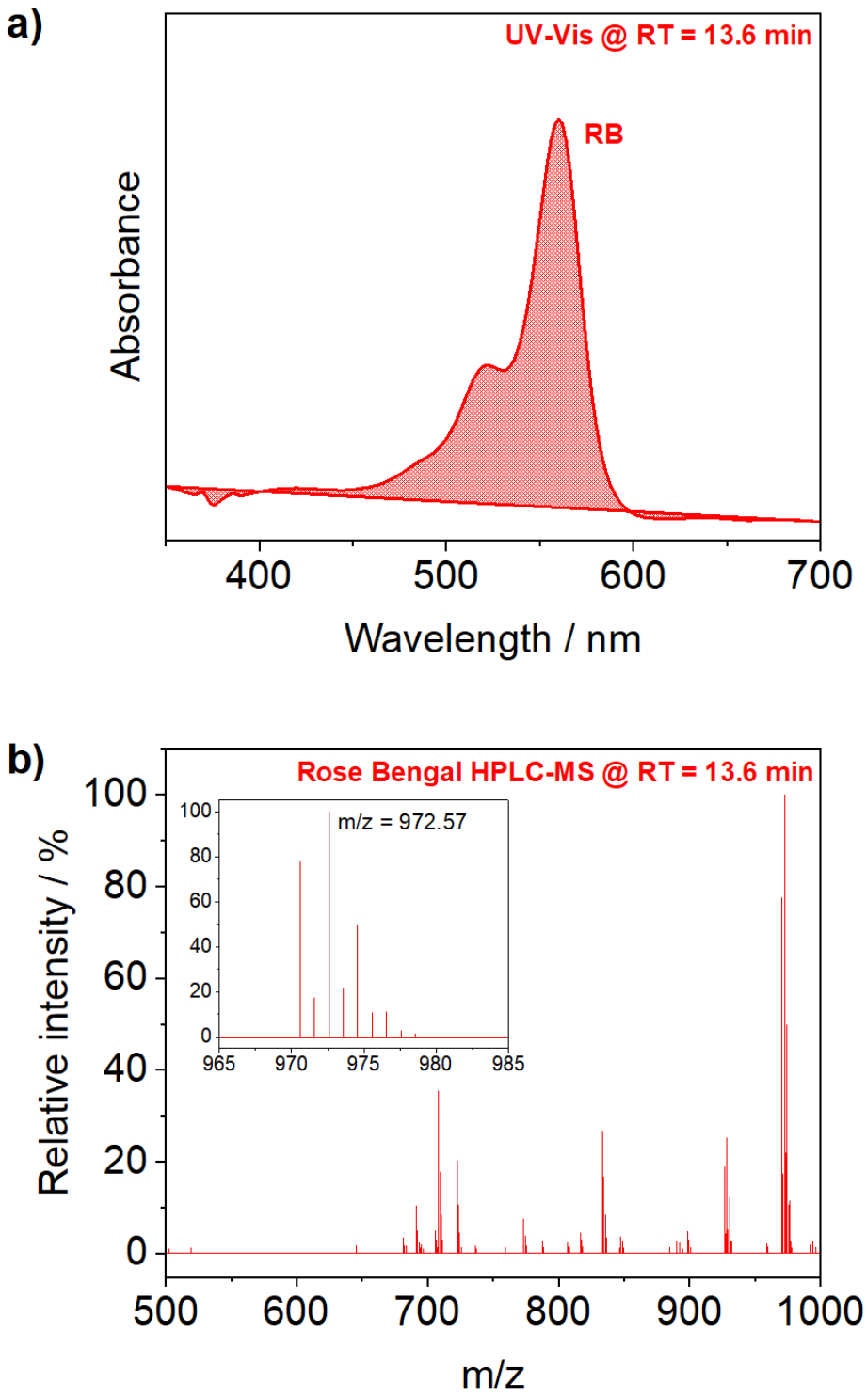


Figure 4.17. *a) UV-Vis and b) MS evidence confirming the identity of the HPLC chromatogram peak at 13.6 minutes as RB.*

is observed, indicative of the hydrogen adduct of RB ($[(C_{20}H_2Cl_4I_4O_5) + H]^+$, expected m/z = 972.49, **Figure 4.17**b).

The rate of discolouration of the RB solutions was evidently faster in the presence of VC. Therefore, a RB-containing sample of VC was saturated with $^3O_2$ and irradiated for 12 hours, before being analysed using the HPLC-MS method. **Figure 4.18** shows the resultant chromatogram of this solution extracted before and after 12 hours of irradiation. The high concentration of VC and RB in the samples are described by the intense peaks at ca. 2.4 and 13.6 minutes, respectively, in the initial sample (**Figure 4.18**a). After irradiation, no chromatogram peak is observed for the RB photosensitizer, indicating degradation, and an additional region of activity is observed between a retention time of 9.5 – 14.5 minutes (**Figure 4.18**b). This region is not well resolved, and likely contains several similar molecules that are formed through the degradation of RB with $^1O_2$, VC, or both. The inset shows the new region of activity in greater detail (**Figure 4.18**b). **Figure 4.19** shows the recorded mass spectrum across this new region of activity. Notably, no significant mass peak is observed at an m/z of ca. 972.49, confirming that RB is no longer present in the solution.

Analogous experiments were performed with 500 µM RB in a mixture of EC and EMC, again saturated with $^3O_2$, where the irradiation time was extended to 120 hours, until an observable colour change had occurred. **Figure 4.20** shows the results of these experiments where, comparable to the VC system, no significant RB peak is identified after irradiation and an additional region of activity is observed between retention times of 8.5 – 14.0 minutes (**Figure 4.20**b), with the inset showing the new activity in greater detail. **Figure 4.21** shows the recorded MS across this new region of activity. In good agreement with the VC system, no significant mass peak is observed at a m/z of ca. 972.49, confirming that RB is no longer present in the solution.

Control experiments were performed to understand the reactivity of VC in the presence of $^3O_2$ with no irradiation, and when irradiated without $^3O_2$ saturation. No colour change was observed in solutions of 500 µM RB in VC saturated with

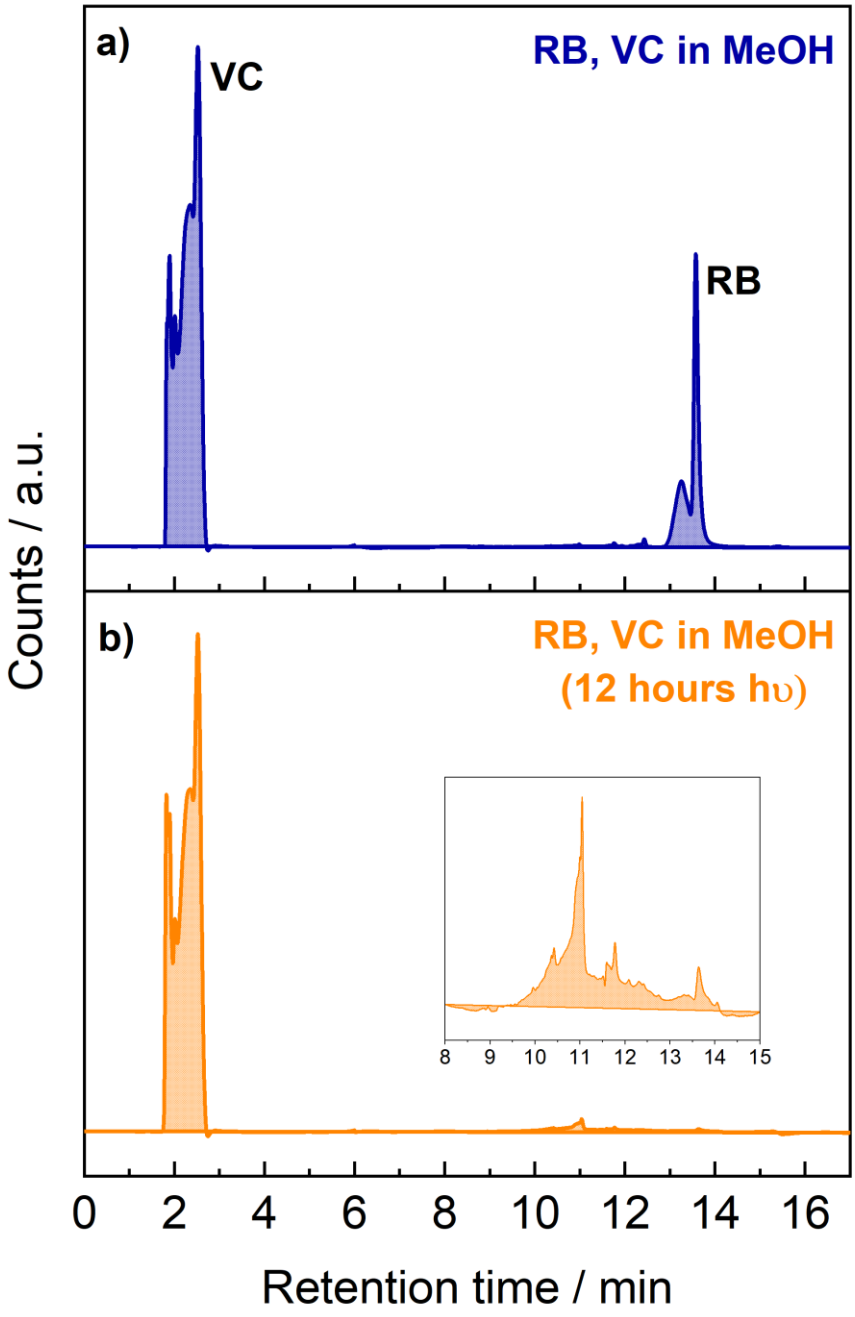


Figure 4.18. *HPLC chromatograms of solutions of MeOH doped with RB in VC. An aliquot was taken a) before saturation with $^3O_2$ and b) after saturation with $^3O_2$ and irradiation for 12 hours with green light (i.e. generating $^1O_2$). A MeOH background was subtracted to smooth the baselines. Inset shows magnified region of the irradiated sample between 8 – 15 minutes where new activity is present.*

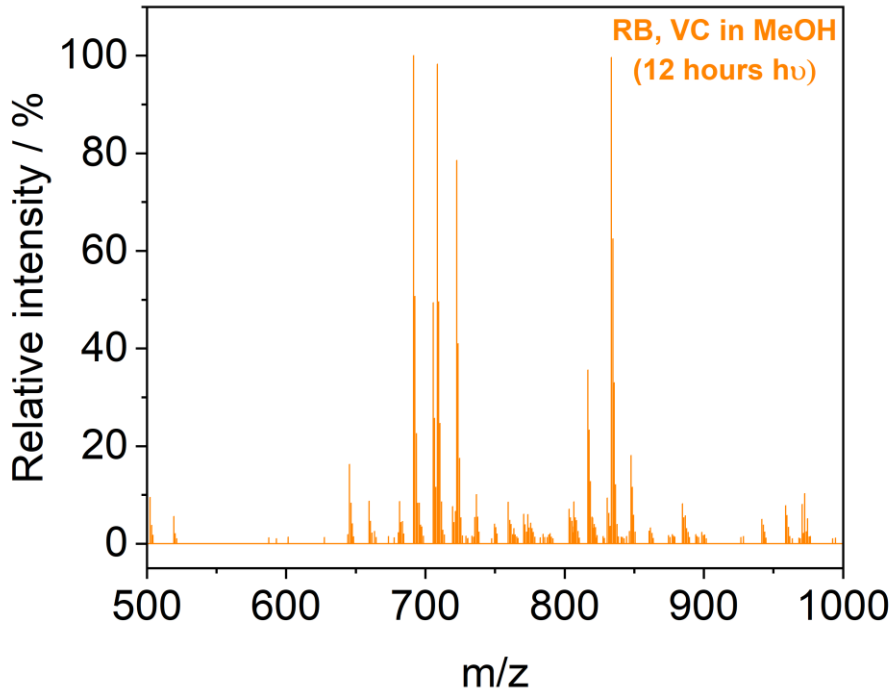


Figure 4.19. *MS of a $^1O_2$ degraded solution of RB in VC, recorded through HPLC-MS of the solution in MeOH over a retention time window of 8 – 15 minutes, showing no significant RB peak (expected m/z = 972.49).*

$^3O_2$ when stored under dark conditions for 120 hours, indicating that the discolouration reaction does not occur without photoinitiation. Furthermore, no colour change was observed when a 500 µM RB in VC solution was irradiated for 48 hours without the presence of $^3O_2$, indicating that irradiation and VC alone is not sufficient to degradation of the RB photosensitizer.

These data indicate that RB does not degrade as quickly as reported by Rinkel *et al.*,[4] but does undergo degradation in the presence of $^1O_2$ and each of the carbonate solvents over time. The interaction of RB with the solvent species, specifically VC, brings into question the validity of the $^1O_2$ studies carried out by Rinkel and Freiberg,[4,6] and further the applicability of RB as a method for studying the reaction of $^1O_2$ with the organic carbonates used as electrolyte solvents. With the homogenous use of RB being proven to be unsuitable for characterisation of the $^1O_2$ induced degradation of EC, a method for heterogenous $^1O_2$ generation was explored.

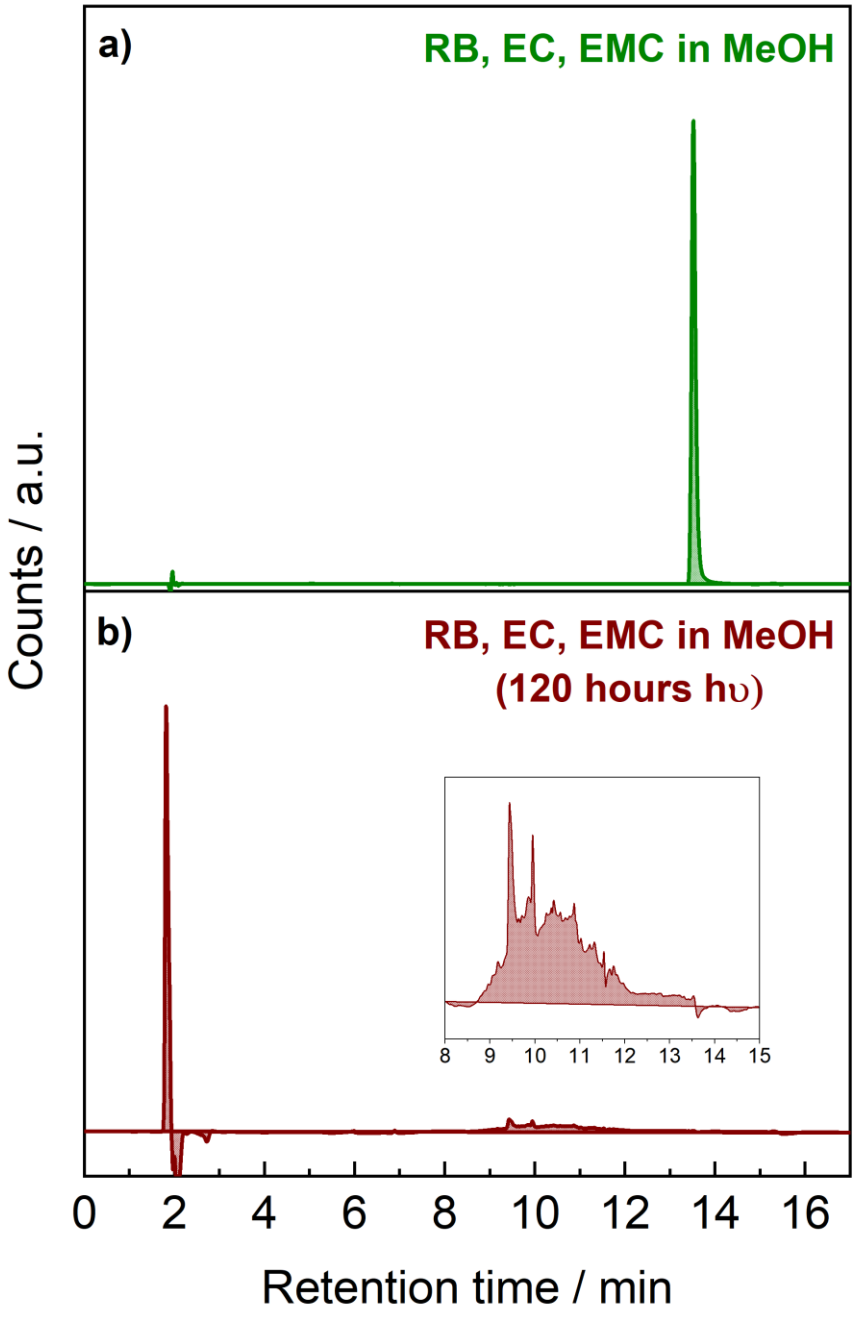


Figure 4.20. *HPLC chromatograms of solutions of MeOH doped with RB in EC and EMC. An aliquot was taken a) before saturation with $^3O_2$ and b) after saturation with $^3O_2$ and irradiation for 120 hours with green light (i.e. generating $^1O_2$). A MeOH background was subtracted to smooth the baselines. Inset shows magnified region of the irradiated sample between 8 – 15 minutes where new activity is present.*

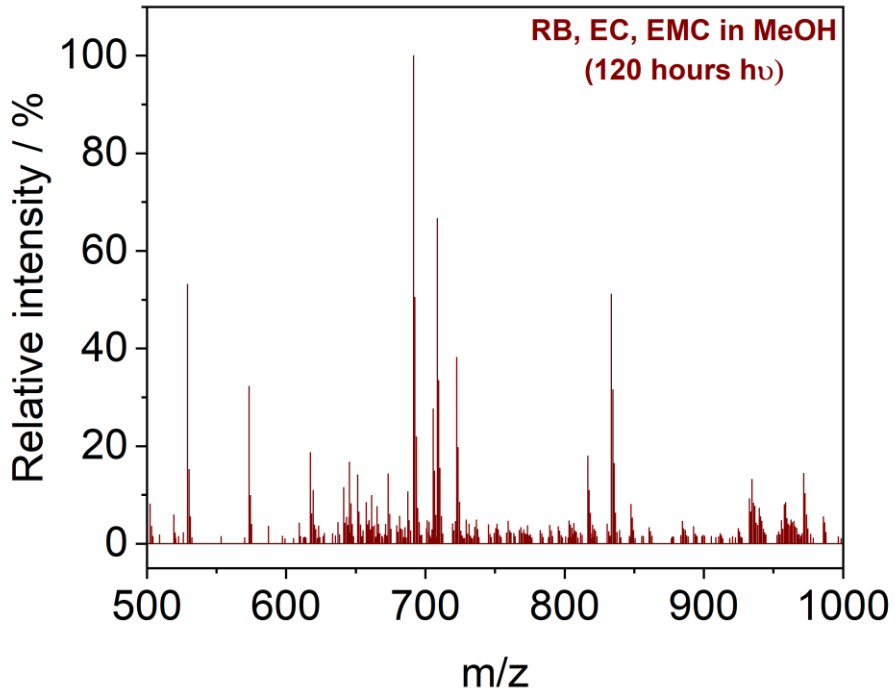


Figure 4.21. *MS of a $^1O_2$ degraded solution of RB in EC and EMC, recorded through HPLC-MS of the solution in MeOH over a retention time window of 8 – 15 minutes, showing no significant RB peak (expected m/z = 972.49).*

4.7 Synthesis and application of a $^1O_2$ selective single atom catalyst

In April 2022, Ma *et al.* published an article describing the synthesis and characterisation of a highly selective $^1O_2$ generating Fe-based single atom catalyst (Fe-SAC).[9] This work reports $^1O_2$ generation without the prerequisite of thermal- or photo-initiation, relying on the chemisorption of O_2 to atomically dispersed catalytic sites which facilitates the generation of $^1O_2$, through a spin-flip process intrinsic to the interaction of Fe and O_2, at room temperature and under dark conditions. These results present a promising system for heterogeneous $^1O_2$ generation. However, the activity of the catalyst was assessed in H_2O-based buffer solutions. Therefore, the ability of the Fe-SAC to produce $^1O_2$ in the EC:EMC mixture employed in this chapter needs to be assessed.

To ensure no Fe nanoparticles remained after synthesis, XRD was used to examine the Fe-SAC. **Figure 4.22** shows the XRD pattern, where no significant peaks are observed, and a background response comparable to that presented by Ma *et al.* is attained, with the broad activity being representative of the HNC support.[9] Critically, the peak positions of Fe, Fe_2O_3 and Fe_3O_4 are shown for reference, with no activity being observed in these regions, indicating well dispersed Fe sites and confirming that no large Fe nanoparticles are present. Moreover, the Fe content of the SAC was characterised by ICP-OES to be 0.5 wt.% Fe, confirming Fe-content.

Figure 4.23 shows the molecular structure of the $^1O_2$ trapping molecule 9,10-dimethyl anthracene (DMA), alongside its endoperoxide, DMA-O_2, which forms via reaction with $^1O_2$.[38,39] Due to the high degree of conjugation present in DMA, it absorbs strongly in the UV-vis region, and HPLC can be applied to track the conversion of DMA to DMA-O_2. **Figure 4.24** shows HPLC chromatograms of a reference solution of MeCN doped with EC, EMC and DMA (**Figure 4.24**a), and

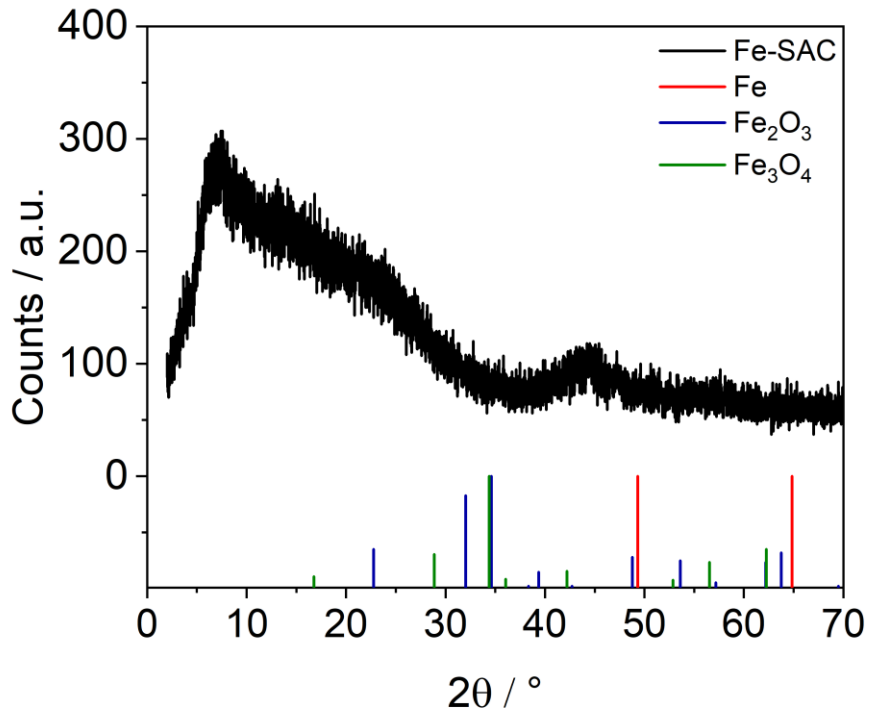


Figure 4.22. *XRD pattern of Fe-SAC confirming the absence of Fe nanoparticles. Reference Fe, Fe_2O_3 and Fe_3O_4 peak positions from the NIST ICSD database are shown for reference.*[37]

a solution of DMA-O_2, synthesised through direct photooxygenation, in MeCN (**Figure 4.24**b). MeCN was employed as the carrier solvent and HPLC eluent due to the poor solubility of both DMA and DMA-O_2 in MeOH, necessitating a change in eluent to avoid precipitation. A clear difference in the retention times of DMA and DMA-O_2 is observed, with the former eluting at ca. 2.2 minutes, and the latter at ca. 1.4 minutes, making analysis possible.

To assess the ability of the Fe-SAC to generate $^1O_2$ in the EC:EMC mixture employed in this chapter, DMA was doped into a solution of EC:EMC containing 5 mg of the Fe-SAC and saturated with $^3O_2$. If the Fe-SAC is capable of converting $^3O_2$ to $^1O_2$ in EC:EMC, then the conversion of DMA to DMA-O_2 will proceed over time and be observed in the HPLC chromatograms of extracted solutions. **Figure 4.25** shows HPLC chromatograms of an aliquot extracted from the reaction mixture after initial $^3O_2$ saturation and extracted 16 and 90 hours after saturating with $^3O_2$. The EC, EMC and DMA peaks identified in **Figure 4.25** are all present in the sample taken immediately after mixing. 16 hours after $^3O_2$ saturation a new, albeit small, peak at a retention time of ca. 1.4 minutes is observed, indicative of DMA-O_2 formation. After 90 hours, this new peak is now the dominant peak in the chromatogram, and the intensity of the DMA peak at ca. 2.2 minutes has decreased considerably, demonstrating that $^1O_2$ is formed by the Fe-SAC in EC:EMC mixtures and that this route for $^1O_2$ formation is viable for probing its reactivity with organic carbonates.

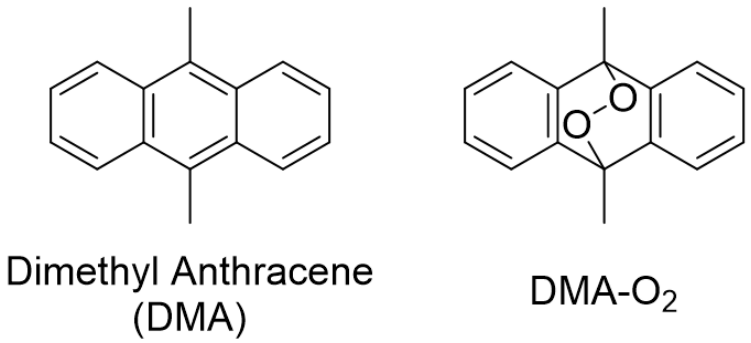


***Figure 4.23**. Molecular structure of DMA and the endoperoxide DMA-O_2 that is formed in the presence of $^1O_2$.*

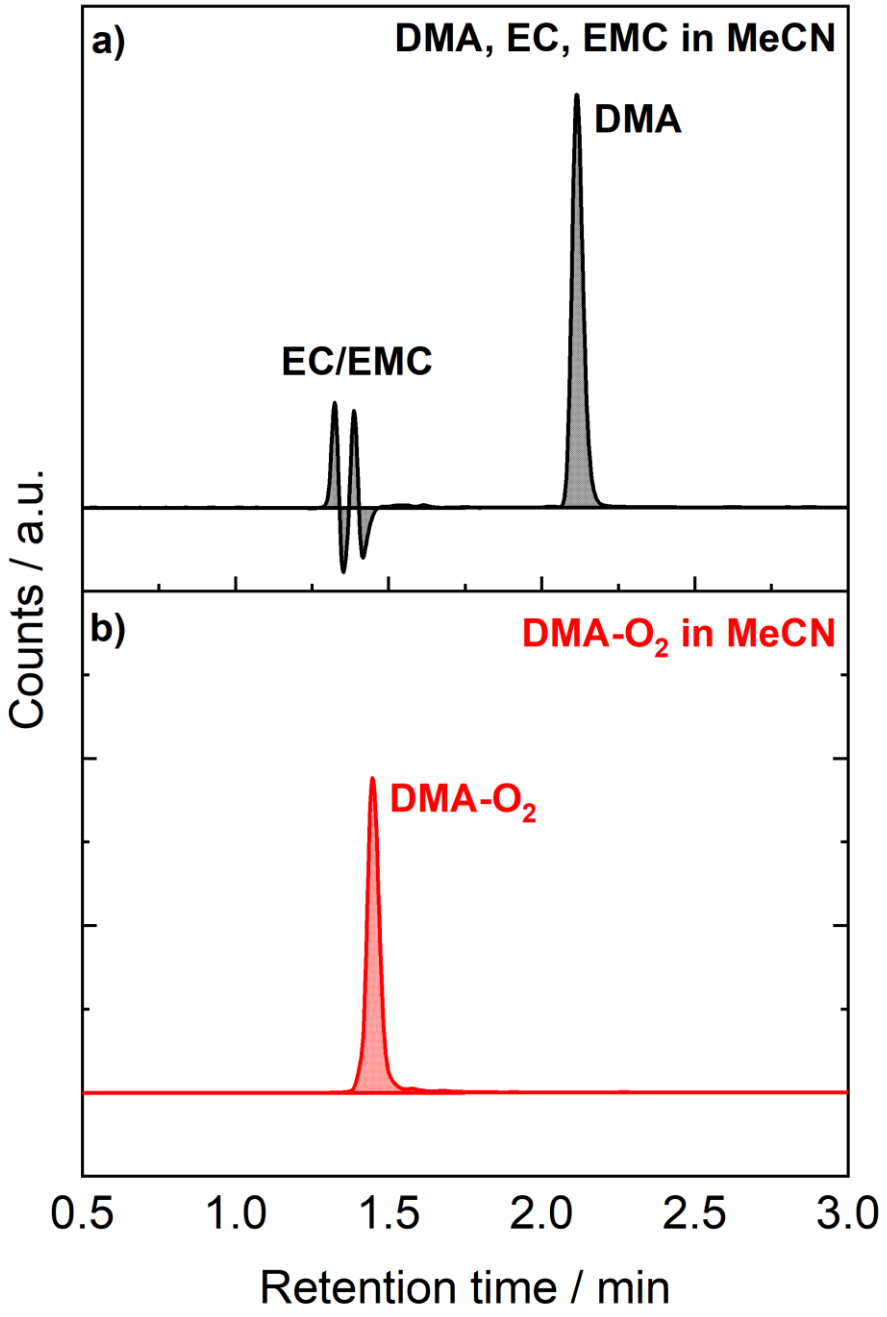


Figure 4.24. *HPLC chromatograms showing the peak retention times of EC, EMC, DMA and DMA-O_2 in MeCN.*

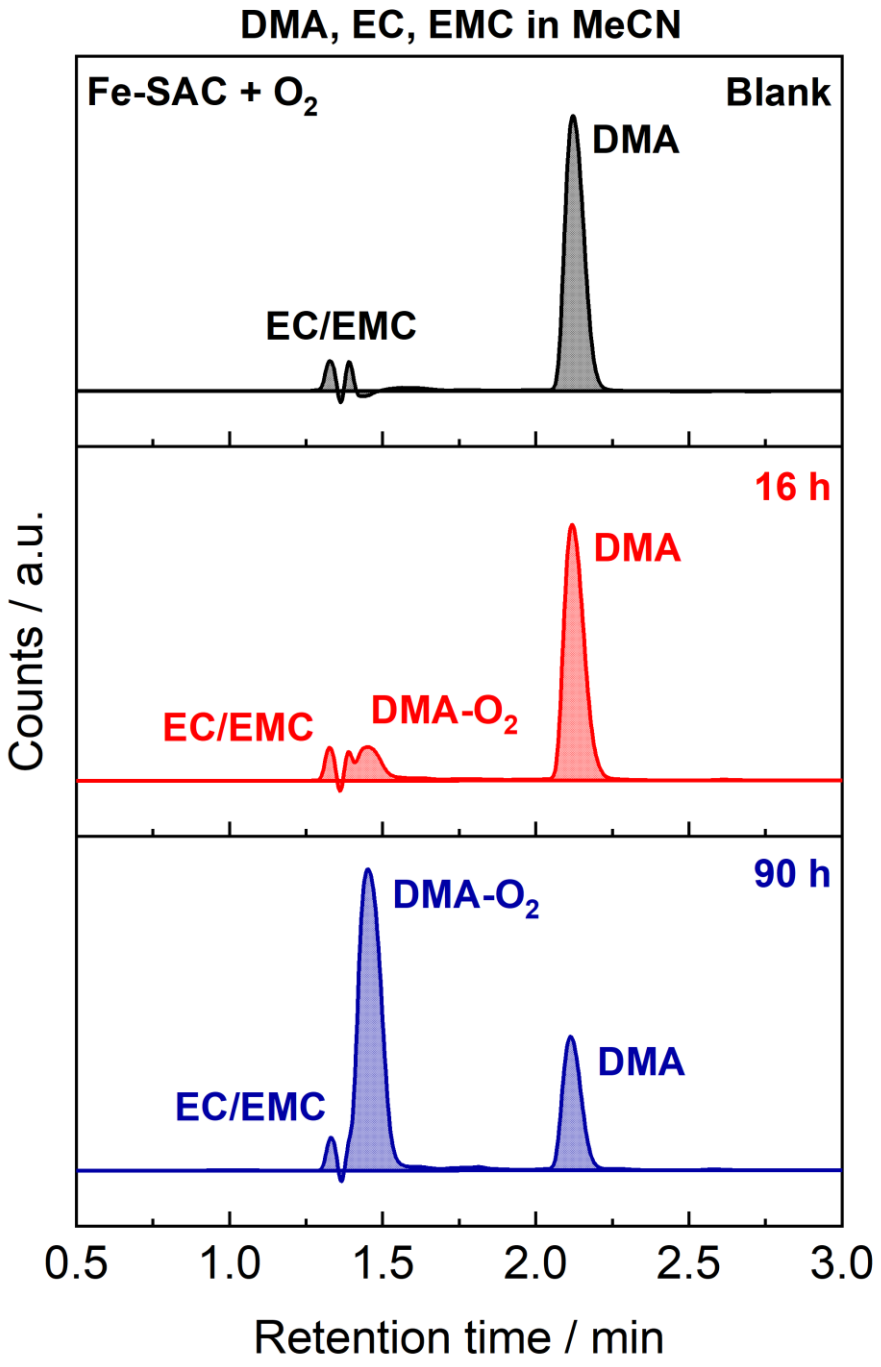


Figure 4.25. *HPLC chromatograms showing the conversion of DMA to DMA-O_2 in a $^3O_2$ saturated solution of EC:EMC containing a Fe-SAC, proving the generation of $^1O_2$ in these systems without heating or irradiation. An aliquot of solution was taken after saturating with $^3O_2$ (black line), 16 hours (red line) and 90 hours after saturation (blue line).*

To confirm that DMA would not convert to DMA-O_2 in EC:EMC without the Fe-SAC and $^3O_2$, two analogous systems were examined: 1) containing ca. 5 mg Fe-SAC and no $^3O_2$; 2) containing no Fe-SAC and no $^3O_2$. **Figure 4.26** shows the results of these experiments, where no change in the chromatogram is observed across the full 90-hour observation period, confirming that the combination of the Fe-SAC and O_2 is required to convert DMA to DMA-O_2.

With the production of $^1O_2$ by the Fe-SAC being confirmed in EC:EMC mixtures, an analogous experiment was run without the presence of the DMA molecule, to assess whether the reaction of the generated $^1O_2$ with EC results in VC formation. The GC-MS method employed earlier for low ppb detection of VC was used to study the mixture composition of the Fe-SAC containing solution 72 and 240 hours after saturation with $^3O_2$. **Figure 4.27** shows the resultant GC-MS chromatograms in the retention time region of VC. No activity is seen in any of the chromatograms, confirming that no VC accumulation occurs through the degradation of EC with $^1O_2$ in the presence of the Fe-SAC. Furthermore, no significant new peaks were observed in a broader scan of the chromatogram, indicating that no detectable soluble products are formed through this reaction. This leaves three options: 1) EC degrades into gaseous products; 2) EC does not significantly react with $^1O_2$ without the presence of the homogenous RB photosensitizer; or 3) no reaction occurs between $^1O_2$ and EC.

To explore the formation of H_2O, the only solution phase degradation product proposed by Rinkel *at al.*,[4] ^{1}H NMR analysis of this solution was performed after the 240-hour experimental period. **Figure 4.28** shows the ^{1}H NMR of the solution immediately after saturating with O_2 compared to a spectrum recorded of the mixture after 240 hours. In good agreement with the GC-MS data, no new peaks were observed in the spectrum after 240 hours. However, a H_2O peak, which was present in the freshly saturated sample, had disappeared from the ^{1}H NMR trace after 240 hours. These data are contrary to the findings reported by Rinkel *et al.*,[4] indicating that H_2O is actually consumed by the mixture rather than being generated in significant quantities.

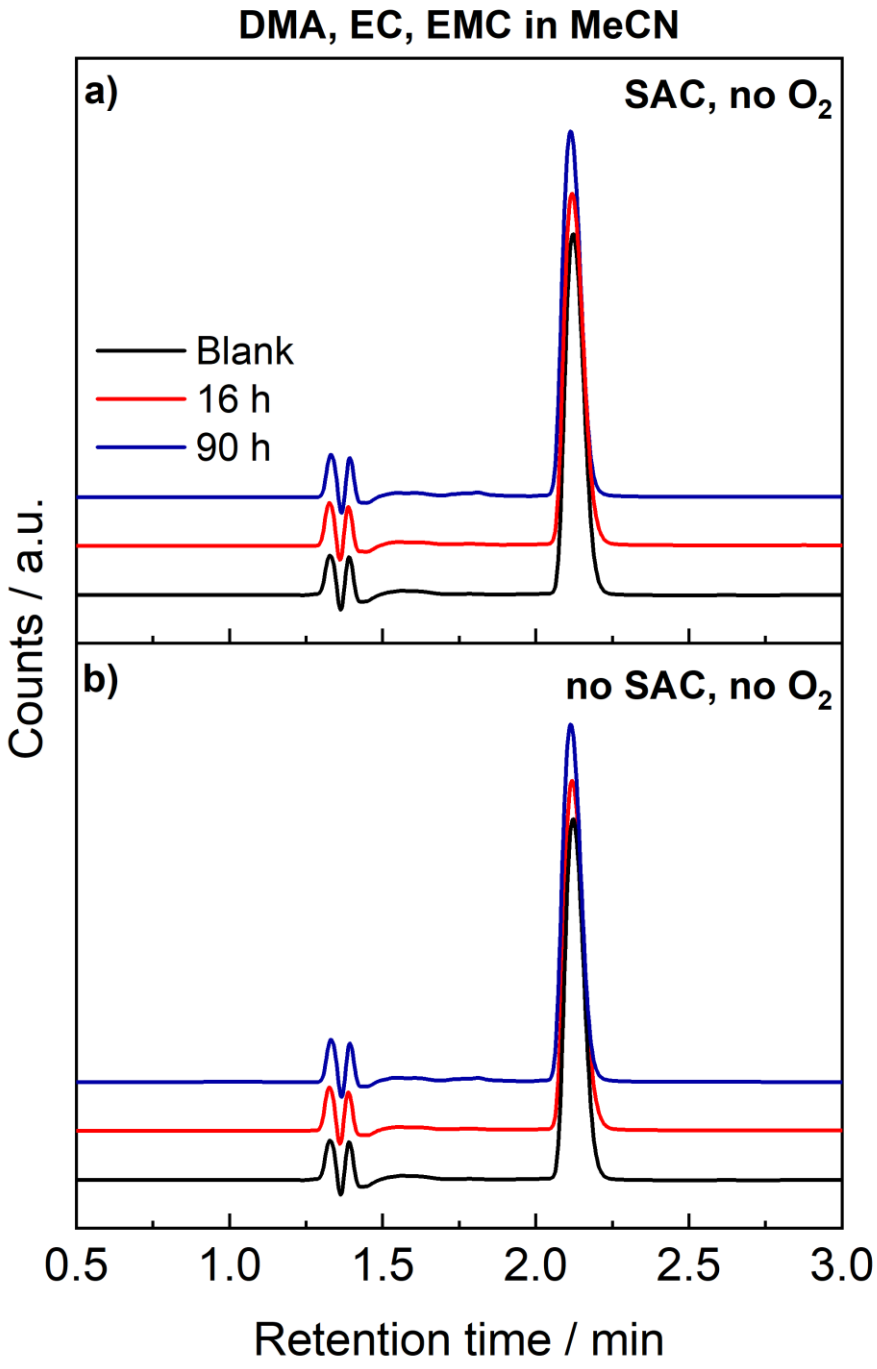


Figure 4.26. *Control HPLC chromatograms showing DMA does not convert to DMA-O_2 in an EC:EMC solution with a) no additional components and b) in the presence of a Fe-SAC with no $^3O_2$ saturation. Chromatograms were recorded when DMA was first added (black lines), and 16 (red lines) and 90 (blue lines) hours after DMA was added to the solution with a MeCN carrier solvent.*

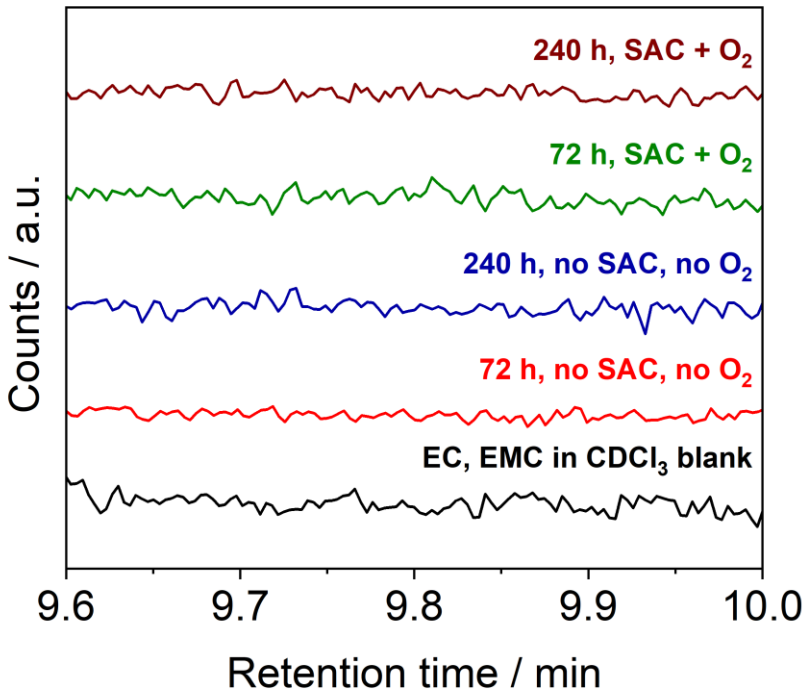


***Figure 4.27**. VC region of the GC-MS chromatograms confirming that VC does not form through the reaction of $^1O_2$ with EC. GC-MS chromatograms of a $^3O_2$ saturated EC:EMC solution containing a Fe-SAC (i.e. $^1O_2$ generating) are shown 72 (green line) and 240 (dark red line) after $^3O_2$ saturation. Blank chromatograms of a EC:EMC solution in $CDCl_3$ and EC:EMC solutions rested for 72 (red line) and 240 (blue line) are shown for reference.*

Taken together, these data demonstrate that Fe-SAC generated $^1O_2$ does not react with EC to produce soluble degradation products, nor degrades through the pathway proposed by Rinkel *et al.* to produce H_2O,[4] instead indicating that EC does not readily react with $^1O_2$. Furthermore, the participation of RB in degradation reactions renders it unsuitable for analysis of the reactivity of $^1O_2$ with the organic carbonates employed as lithium-ion battery electrolyte solvents. Moreover, it is possible that both the H_2O_2 and the H_2O detected by Freiberg *et al.* and Rinkel *et al.*, respectively, were in fact the result of RB-mediated degradation, rather than degradation of EC through interaction with $^1O_2$.[4,6] The distinct lack of VC formation through the reaction of $^1O_2$ with EC and EMC demonstrates that this reaction pathway cannot be the cause of VC accumulation in Gr-NMC811 half-cells. Instead, it is likely that, as proposed by Zhang *et al.*,[8] VC formation is the result of the dehydrogenation of EC through

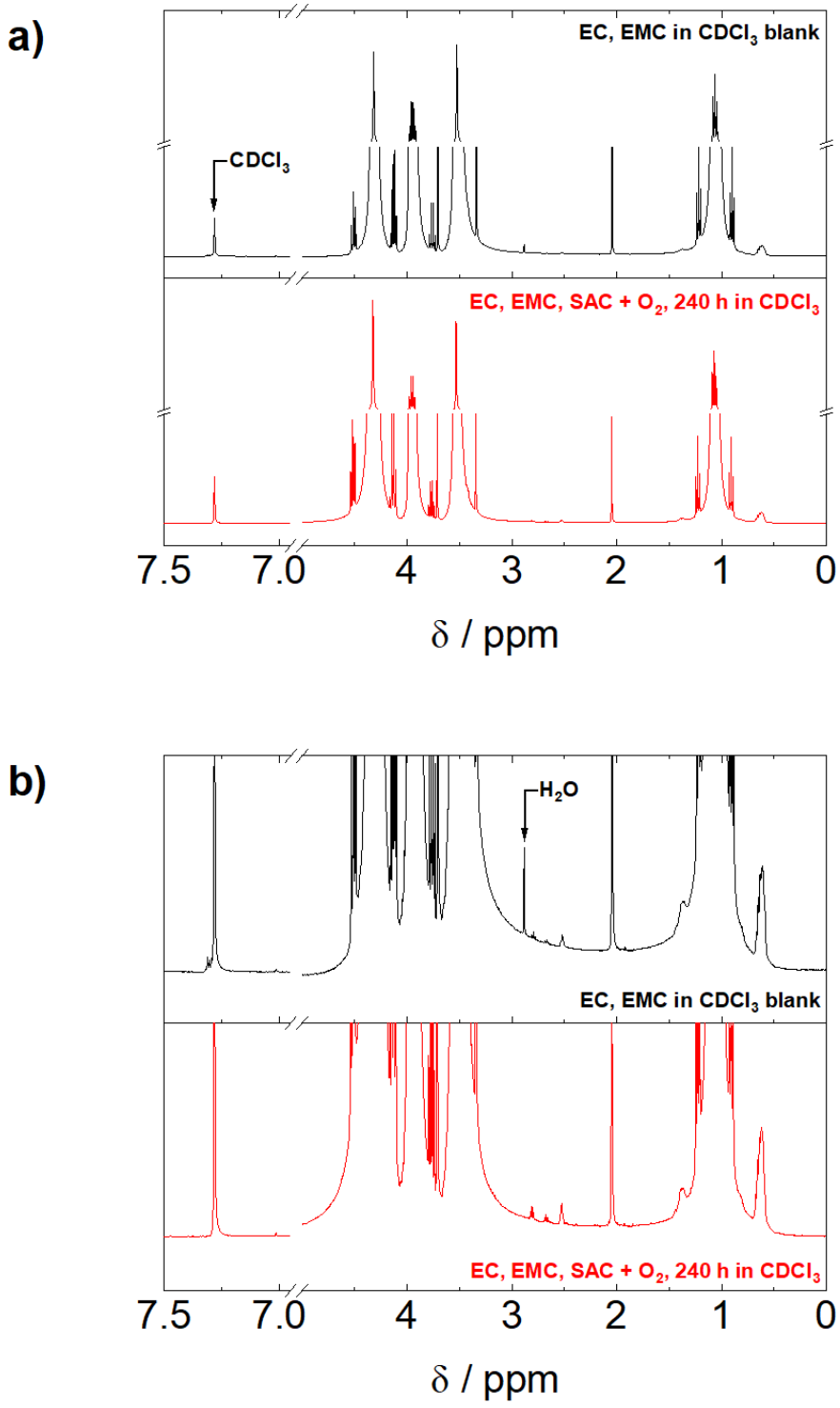


Figure 4.28. *a) ^{1}H NMR and b) magnified ^{1}H NMR spectra of a $^{3}O_2$ saturated solution of EC:EMC containing a Fe-SAC (i.e. $^{1}O_2$ generating) taken immediately after (black lines) and 240 hours after (red lines) $^{3}O_2$ saturation. No new significant peaks are observed, and a H_2O peak that is present in the blank is not present in the sample taken after 240 hours.*

Interaction with surface oxygen, the activity of which is defined by the composition of the metal oxide positive electrode material.

4.8 Conclusions

In this chapter, I explored the long-term cycling performance of Gr-NMC811 full-cells revealing that, contrary to current literature understanding, cells cycled with a VC-free electrolyte perform comparable to, or better than, cells containing a LP57 electrolyte with 2 wt.% VC over 500 cycles at C/2. OEMS measurements were performed on a Li-NMC811 half-cell to understand the onset potential of gas releasing oxidation reactions at the surface of NMC811 positive electrodes, where an earliest onset of ca. 4.32 V vs Li^+/Li was observed for O_2 and CO_2 evolution. This is above the standard potential limits of operation, indicating that any oxidation reactions occurring in the long-term cycling experiments would occur without the evolution of significant quantities of gaseous products.

I propose that the cycle stability seen in the cells cycled with a VC-free electrolyte is not the result of stability of the NMC811 positive electrode, but instead a phenomenon of crosstalk between the electrodes, wherein VC is formed through the dehydrogenation of EC at the surface of the NMC811 electrode in early-stage cycling, which can subsequently be reduced on the surface of the Gr electrode during formation cycling, generating a stable SEI. The feasibility of this was explored using GC-MS analysis, where statistically relevant quantities of VC were detected in electrolytes extracted from cells cycled for three C/20 formation cycles and cells cycled for an additional ten C/2 cycles, within standard operational conditions (UCV ≤4.2 V). Critically, these data confirm the formation of VC in early-stage cycling of Gr-NMC811 cells. Furthermore, considerable accumulation of VC was observed in the electrolytes where UCVs ≥4.3 V were employed, with the electrolytes extracted from cells cycled to an UCV of 4.5 V containing VC concentrations above the LOQ (135+ ppb). These data demonstrate that VC is continually formed and, once a stable Gr SEI has been established, is accumulated in the electrolyte, evidenced by more pronounced trends in the electrolytes extracted from cells cycled for ten

C/2 cycles. Although this study indicates that the formation of VC is beneficial for the performance of full-cells containing initially VC-free electrolytes, it highlights an oxidative degradation reaction that occurs at the surface of NMC811 electrodes throughout cycling. If electrolyte solutions are to be optimised, it is critical that these degradation reactions are assessed and prevented where possible.

With *in situ* VC formation being confirmed, the feasibility of $^1O_2$ driven VC formation was explored using a RB photosensitizer to generate $^1O_2$, in line with procedures applied in previous reports. Although these reports acknowledge the degradation of RB with irradiation, it is not discussed in detail. My work here confirms the degradation of RB in EC, EMC, VC or a mixture of these solvents, demonstrating that RB rapidly degrades in the presence of VC, and over a longer period in the presence of EC, bringing into question the validity of this system for carbonate degradation studies.

An Fe-SAC was synthesised and its $^1O_2$-generating ability was assessed through the formation of DMA endoperoxide, before long term degradation experiments were performed in an EC:EMC solvent mixture. No VC was identified in the solvent after 10 days of exposure to $^1O_2$, deeming this route improbable, and no significant degradation products are observed through either GC-MS or ^{1}H NMR analysis of the solution. These data indicate that EC may not be sufficiently reactive with $^1O_2$ to degrade through the mechanisms proposed previously, but instead these studies may be tracking the degradation of a complex reaction between RB, $^1O_2$ and the carbonate solvents.

This work highlights the importance of tracking all species when performing degradation analysis and presents a new heterogenous $^1O_2$ generation technique where no thermal- or photo-initiation is required for the generation of $^1O_2$. This provides a new avenue for heterogenous $^1O_2$ degradation studies, both in the field of battery electrolyte research and more broadly, wherein the reactivity of potential solvents can be probed in a bias-free and efficient manner.

4.9 References

1. Jiang, M., Danilov, D. L., Eichel, R.-A. & Notten, P. H. L. A Review of Degradation Mechanisms and Recent Achievements for Ni-Rich Cathode-Based Li-Ion Batteries. *Adv. Energy Mater.* **11**, 2103005 (2021).
2. Harris, O. C., Lee, S. E., Lees, C. & Tang, M. Review: mechanisms and consequences of chemical cross-talk in advanced Li-ion batteries. *J. Phys. Energy* **2**, 032002 (2020).
3. Ruff, Z., Xu, C. & Grey, C. P. Transition Metal Dissolution and Degradation in NMC811-Graphite Electrochemical Cells. *J. Electrochem. Soc.* **168**, 060518 (2021).
4. D. Rinkel, B. L., Padmanabhan Vivek, J., Garcia-Araez, N. & P. Grey, C. Two electrolyte decomposition pathways at nickel-rich cathode surfaces in lithium-ion batteries. *Energy Environ. Sci.* **15**, 3416–3438 (2022).
5. Günter, F. J. & Wassiliadis, N. State of the Art of Lithium-Ion Pouch Cells in Automotive Applications: Cell Teardown and Characterization. *J. Electrochem. Soc.* **169**, 030515 (2022).
6. Freiberg, A. T. S., Roos, M. K., Wandt, J., de Vivie-Riedle, R. & Gasteiger, H. A. Singlet Oxygen Reactivity with Carbonate Solvents Used for Li-Ion Battery Electrolytes. *J. Phys. Chem. A* **122**, 8828–8839 (2018).
7. Haregewoin, A. M., Wotango, A. S. & Hwang, B.-J. Electrolyte additives for lithium ion battery electrodes: progress and perspectives. *Energy Env. Sci* **9**, 1955–1988 (2016).

8. Zhang, Y. *et al.* Revealing electrolyte oxidation via carbonate dehydrogenation on Ni-based oxides in Li-ion batteries by in situ Fourier transform infrared spectroscopy. *Energy Environ. Sci.* **13**, 183–199 (2020).

9. Ma, W. *et al.* Highly selective generation of singlet oxygen from dioxygen with atomically dispersed catalysts. *Chem. Sci.* **13**, 5606–5615 (2022).

10. Mahne, N. *et al.* Singlet oxygen generation as a major cause for parasitic reactions during cycling of aprotic lithium–oxygen batteries. *Nat. Energy* **2**, 1–9 (2017).

11. Thompson, L. M. *et al.* Quantifying Changes to the Electrolyte and Negative Electrode in Aged NMC532/Graphite Lithium-Ion Cells. *J. Electrochem. Soc.* **165**, A2732 (2018).

12. NIST Mass Spectrometry Data Centre. https://chemdata.nist.gov/dokuwiki/doku.php?id=chemdata:start.

13. Heiskanen, S. K., Kim, J. & Lucht, B. L. Generation and Evolution of the Solid Electrolyte Interphase of Lithium-Ion Batteries. *Joule* **3**, 2322–2333 (2019).

14. Li, W., Erickson, E. M. & Manthiram, A. High-nickel layered oxide cathodes for lithium-based automotive batteries. *Nat. Energy* **5**, 26–34 (2020).

15. Li, W. *et al.* Long-Term Cyclability of NCM-811 at High Voltages in Lithium-Ion Batteries: an In-Depth Diagnostic Study. *Chem. Mater.* **32**, 7796–7804 (2020).

16. Beltrop, K. *et al.* Triphenylphosphine Oxide as Highly Effective Electrolyte Additive for Graphite/NMC811 Lithium Ion Cells. *Chem. Mater.* **30**, 2726–2741 (2018).

17. Xu, D. *et al.* Exploring synergetic effects of vinylene carbonate and 1,3-propane sultone on $LiNi_{0.6}Mn_{0.2}Co_{0.2}O_2$/graphite cells with excellent high-temperature performance. *J. Power Sources* **437**, 226929 (2019).

18. Burns, J. C. *et al.* The Impact of Varying the Concentration of Vinylene Carbonate Electrolyte Additive in Wound Li-Ion Cells. *J. Electrochem. Soc.* **159**, A85 (2011).

19. Xu, K. Electrolytes and Interphases in Li-Ion Batteries and Beyond. *Chem. Rev.* **114**, 11503–11618 (2014).

20. Peled, E. & Menkin, S. Review—SEI: Past, Present and Future. *J. Electrochem. Soc.* **164**, A1703 (2017).

21. Metzger, M., Strehle, B., Solchenbach, S. & Gasteiger, H. A. Origin of H_2 Evolution in LIBs: H_2O Reduction vs. Electrolyte Oxidation. *J. Electrochem. Soc.* **163**, A798 (2016).

22. Rinkel, B. L. D., Hall, D. S., Temprano, I. & Grey, C. P. Electrolyte Oxidation Pathways in Lithium-Ion Batteries. *J. Am. Chem. Soc.* **142**, 15058–15074 (2020).

23. Wandt, J., Freiberg, A. T. S., Ogrodnik, A. & Gasteiger, H. A. Singlet oxygen evolution from layered transition metal oxide cathode materials and its implications for lithium-ion batteries. *Mater. Today* **21**, 825–833 (2018).

24. Leanza, D., Mirolo, M., Vaz, C. A. F., Novák, P. & El Kazzi, M. Surface Degradation and Chemical Electrolyte Oxidation Induced by the Oxygen Released from Layered Oxide Cathodes in Li–Ion Batteries. *Batter. Supercaps* **2**, 482–492 (2019).

25. Jung, R., Metzger, M., Maglia, F., Stinner, C. & Gasteiger, H. A. Oxygen Release and Its Effect on the Cycling Stability of $LiNi_xMn_yCo_zO_2$ (NMC) Cathode Materials for Li-Ion Batteries. *J. Electrochem. Soc.* **164**, A1361 (2017).

26. Weber, F. M., Kohlhaas, I. & Figgemeier, E. Tuning the Reactivity of Electrolyte Solvents on Lithium Metal by Vinylene Carbonate. *J. Electrochem. Soc.* **167**, 140523 (2020).

27. Zhuang, G., Chen, Y. & Ross, P. N. The Reaction of Lithium with Dimethyl Carbonate and Diethyl Carbonate in Ultrahigh Vacuum Studied by X-ray Photoemission Spectroscopy. *Langmuir* **15**, 1470–1479 (1999).

28. Li, J. *et al.* The Impact of Electrolyte Additives and Upper Cut-off Voltage on the Formation of a Rocksalt Surface Layer in $LiNi_{0.8}Mn_{0.1}Co_{0.1}O_2$ Electrodes. *J. Electrochem. Soc.* **164**, A655 (2017).

29. Dose, W. M., Xu, C., Grey, C. P. & De Volder, M. F. L. Effect of Anode Slippage on Cathode Cutoff Potential and Degradation Mechanisms in Ni-Rich Li-Ion Batteries. *Cell Rep. Phys. Sci.* **1**, 100253 (2020).

30. Ruff, Z., Xu, C. & Grey, C. P. Transition Metal Dissolution and Degradation in NMC811-Graphite Electrochemical Cells. *J. Electrochem. Soc.* **168**, 060518 (2021).

31. Li, C. *et al.* Towards Higher Sensitivity of Mass Spectrometry: A Perspective From the Mass Analyzers. *Front. Chem.* **9**, 813359 (2021).

32. Belarbi, S. *et al.* Comparison of new approach of GC-HRMS (Q-Orbitrap) to GC–MS/MS (triple-quadrupole) in analyzing the pesticide residues and contaminants in complex food matrices. *Food Chem.* **359**, 129932 (2021).

33. Armbruster, D. A., Tillman, M. D. & Hubbs, L. M. Limit of detection (LQD)/limit of quantitation (LOQ): comparison of the empirical and the statistical methods exemplified with GC-MS assays of abused drugs. *Clin. Chem.* **40**, 1233–1238 (1994).

34. DeRosa, M. Photosensitized singlet oxygen and its applications. *Coord. Chem. Rev.* **233–234**, 351–371 (2002).

35. Bonnett, R. Photosensitizers of the porphyrin and phthalocyanine series for photodynamic therapy. *Chem. Soc. Rev.* **24**, 19–33 (1995).

36. Gianotti, E. *et al.* An Efficient Rose Bengal Based Nanoplatform for Photodynamic Therapy. *Chem. – Eur. J.* **20**, 10921–10925 (2014).

37. Levin, I. NIST Inorganic Crystal Structure Database (ICSD). (2020) doi:10.18434/M32147.

38. Córdoba, D., Rodríguez, H. B. & Calvo, E. J. Singlet Oxygen Formation during the Oxygen Reduction Reaction in DMSO LiTFSI on Lithium Air Battery Carbon Electrodes. *ChemistrySelect* **4**, 12304–12307 (2019).

39. Gross, E., Ehrenberg, B. & Johnson, F. M. Singlet oxygen generation by porphyrins and the kinetics of 9,10-dimethylanthracene

photosensitization in liposomes. *Photochem. Photobiol.* **57**, 808–813 (1993).

Chapter 5. Progress towards a next-generation Li-air battery

5.1 Meeting the energy demands of next-generation applications

The lithium-ion battery has revolutionised the way the world thinks about energy, transforming the consumer electronics markets and enabling the global electrification of transport. However, the practical energy density offered by lithium-ion batteries, even when fully developed (ca. 350 Wh kg^{-1}), is insufficient to meet the long-term demands of new and emerging transportation markets (i.e. long-range EVs, aviation).[1–4]

Developing commercially viable beyond lithium-ion batteries is non-trivial, however, a variety of potential candidates have emerged that explore alternative cell (electro)chemistries and materials to meet the requirements of next-generation applications. Among these, the use of a metallic Li negative electrode is one of the most prolific innovations, with solid-state, lithium-sulphur (Li-S), and lithium-air (Li-air) technologies leading the charge.[5–11] While each of these technologies has demonstrated higher capacity performance, improved safety and/or lower cost than current state-of-the-art lithium-ion, this often comes at the expense of long-term cycling performance (**Figure 5.1**).

Metallic Li intrinsically possesses the highest possible theoretical capacity and the lowest electrochemical potential of any proposed negative electrode candidate for advanced lithium batteries. However, its high reactivity with the traditional carbonate solvents, explored in detail in Chapters 1 and 3, render it incompatible with current generation lithium-ion battery chemistries. Solid-state batteries (SSBs), wherein the traditional organic liquid electrolyte is replaced with a solid inorganic or polymeric membrane, presents an exciting opportunity for the incorporation of a metallic Li negative electrode, without the performance and safety concerns associated with liquid electrolyte degradation.[12–15] Early solid electrolytes (SEs) suffered from poor ionic conductivity, dendritic growth at, and reactivity with, the metallic Li negative electrode, and incompatibility with the transition metal oxide positive electrode chemistries employed in application (**Figure 5.2**).[16–21]

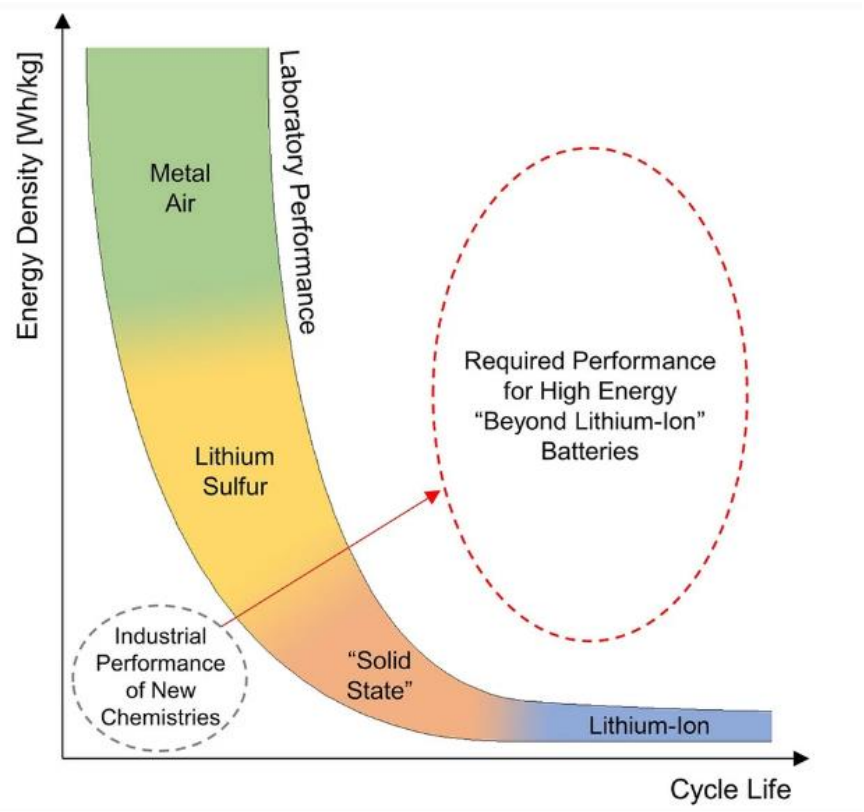


Figure 5.1. *General performance of lithium-ion, solid-state, Li-S and Li-air batteries compared to the performance requirements of future applications. Reproduced from Gao et al.*[6]

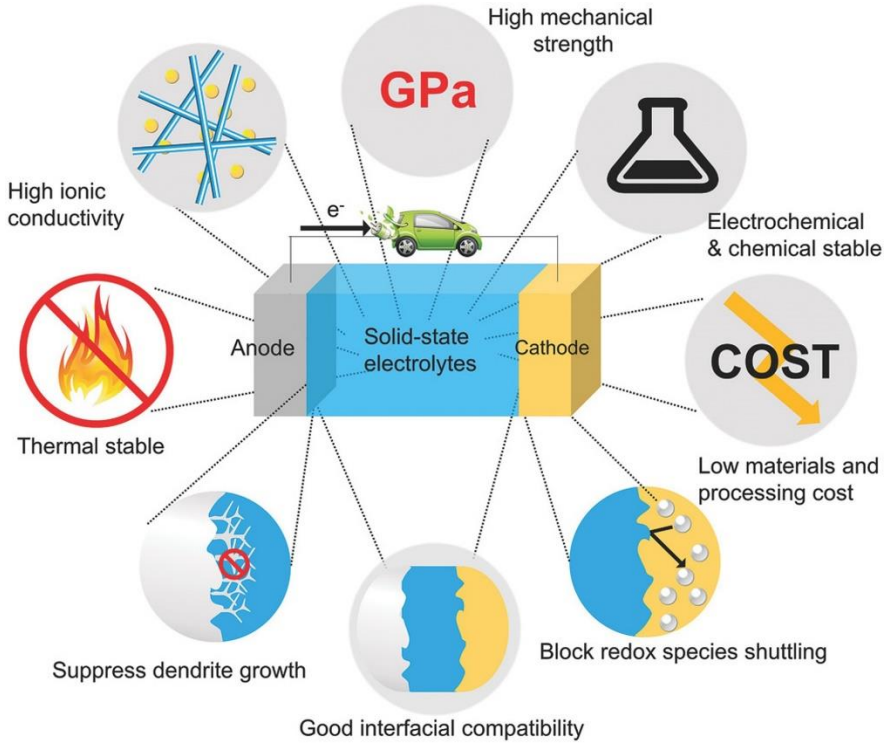


Figure 5.2. *Requirements for solid-state electrolytes to address the challenges of high-energy metal-based batteries. Reproduced from Fan et al.*[13]

However, over the past decade major advances have been made in SE chemistry that has enabled considerable progress to be made towards addressing these technological challenges. Current state-of-the-art sulfide-based SEs boast ionic conductivity comparable to, or exceeding, that of traditional liquid electrolytes.[15,16,22–24] Furthermore, advanced electrolyte design has improved SE (electro)chemical compatibility with electrode materials, enabling SSBs to achieve high performance while limiting interfacial degradation reactions and mitigating dendritic Li growth.[25–29] Although these innovations provide a promising outlook for SSBs, they also offer critical technological advancement towards the advent of an artificial metallic Li solid electrolyte interphase (SEI) that could enable development of even higher energy density technologies.[20]

The step-increase in theoretical energy density proposed by Li-S and Li-air batteries (ca. 2600 and 3500 Wh kg^{-1}, respectively) is anchored upon the incorporation of a metallic Li negative electrode.[1,6,8,30] However, the high (electro)chemical reactivity and dendritic Li growth still present fundamental barriers to the realisation of these technologies. Various strategies have been explored to enhance the stability of metallic Li in liquid electrolytes, including exploration of ether- or ionic liquid-based electrolyte solvents and substitution of electrolyte salts and additives.[9,20,31–37] Although effective at improving the long-term performance of metallic Li, identifying an electrolyte composition that is both optimised for metallic Li stabilisation and overall cell performance is non-trivial and remains a major challenge to realising long-term cycle stability.[9,34,38,39] With prolific innovations in metallic Li stabilisation being made throughout next-generation battery research, addressing the challenges of the positive electrode chemistry remains a critical barrier to commercialisation of Li-S and Li-air batteries (**Figure 5.3**).[7,9,40–42] Therefore, Chapters 6 and 7 explore a Li-air battery where metallic Li is substituted for a lithium iron phosphate negative electrode, to isolate and understand cell chemistry with respect to the positive electrode performance, appreciating that artificial protection of an essential metallic Li negative electrode is being explored in tandem.

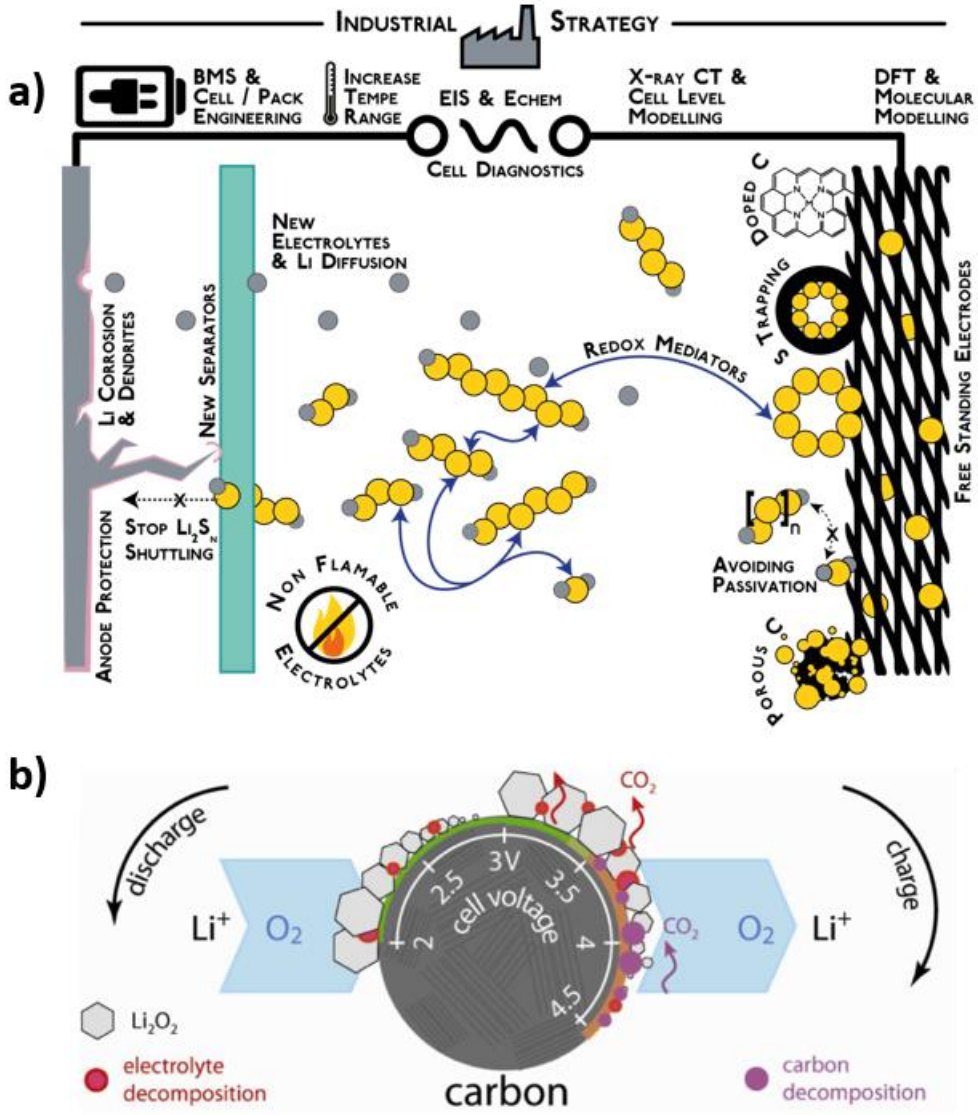


Figure 5.3. *Schematic representations of a) degradation mechanisms in the Li-S battery and b) positive electrode and electrolyte decomposition in the Li-air battery. Reproduced from a) LiSTAR.ac.uk,[43] and b) Jung et al.[10]*

5.2 Li-air battery (electro)chemistries

The theoretical energy density of the Li-air battery, which will be the focus of Chapters 6 and 7, is ca. 3500 Wh kg^{-1} based on the mass of the proposed discharge product, lithium peroxide (Li_2O_2).[9,44–47] This marks more than a 10-fold increase in performance compared to current state-of-the-art lithium-ion battery chemistries and would provide sufficiently energy-dense batteries to support the demands of next-generation applications.

Li-air batteries are defined by their electrolyte composition which, in turn, defines the electrochemistry exhibited by the system. In an aqueous Li-air battery, O_2 reduction proceeds via a $4e^-$ pathway (equation 5.1), whereas in non-aqueous, aprotic electrolytes O_2 reduction proceeds via a $2e^-$ process (equation 5.2). Although it is possible to achieve $4e^-$ O_2 reduction in non-aqueous aprotic electrolytes, forming lithium oxide (Li_2O) where metal catalysts are employed (equation 5.3), low potentials (<2.0 V vs Li^+/Li) are required, often inducing electrolyte reduction.

$$4Li^+_{(sol)} + O_{2\,(sol)} + 2H_2O_{(sol)} + 4e^- \rightarrow 4LiOH_{(sol)} \quad (5.1)$$

$$2Li^+_{(sol)} + O_{2\,(sol)} + 2e^- \rightarrow Li_2O_{2\,(s)} \quad (5.2)$$

$$4Li^+_{(sol)} + O_{2\,(sol)} + 4e^- \rightarrow 2Li_2O_{(s)} \quad (5.3)$$

In non-aqueous systems, LiOH and Li_2O formation are considered chemically irreversible due to the required cleavage of the exceptionally strong O=O bond (498 kJ mol^{-1}), when compared to Li_2O_2 formation, where an O-O bond is preserved.[48–52] It has been shown that, in the presence of catalysts, O_2 can be cycled via the $4e^-$ reaction, offering the intriguing possibility of reversible LiOH- and Li_2O-based batteries.[53–55] However, the heterogenous catalysts that are required for operation of LiOH-forming cell chemistries have been shown to be detrimental to long-term performance, causing considerable electrolyte degradation,[56–58] and the poor solubility of Li_2O in liquid electrolytes results in rapid passivation of the electrode surface, limiting the attainable discharge capacity. In 2023, Kondori *et al.* published an article in *Science* that reported a room-temperature rechargeable Li_2O-based Li-air battery that was capable of 1000 cycles with 100% coulombic efficiency.[59] However, the reported long-term cycling is performed at ca. C/100 and is normalised to the mass of the loaded trimolybdenum phosphide catalyst, resulting in the reported cycling capacity of 1000 mAh g^{-1}_{cat} being equivalent to an areal capacity of just 0.1 mAh cm^{-2}.[59] Upon discharge of the cell to its potential limit under analogous conditions, a capacity of 10.4 mAh cm^{-2} is achieved,[59] demonstrating that, even under extremely low power conditions, capacity performance is limited.

Although this report highlights that the use of a SE can enable cycling of Li_2O, closer inspection of the data confirms that considerable challenges still remain to enable Li_2O cell chemistries under practical conditions.

Given the challenges associated with charging LiOH and Li_2O chemistries, Chapters 6 and 7 explore the $2e^-$ O_2 reduction process to form Li_2O_2. Understanding the electrochemical reactions that occur throughout cycling is imperative for the successful development of any battery technology. In non-aqueous aprotic electrolytes, Li_2O_2 forms through an intermediate lithium superoxide (LiO_2) species that is generated via $1e^-$ O_2 reduction (equation 5.4 and 5.5).[60,61]

$$Li^+_{(sol)} + O_{2\,(sol)} + e^- \rightarrow LiO_{2\,(s)} \quad (5.4)$$

$$LiO_{2\,(s)} + Li^+_{(sol)} + e^- \rightarrow Li_2O_{2\,(s)} \quad (5.5)$$

Trahan *et al.* used RRDE to confirm the formation of LiO_2 in a dimethyl sulfoxide (DMSO)-based electrolyte, where a cyclic voltage sweep was performed on a carbon working electrode while a gold ring disk was simultaneously held at 2.93 V (i.e. below the equilibrium potential of Li_2O_2 = 2.96 V vs Li^+/Li) to selectively oxidise LiO_2 where present.[62] Analogous experiments in different electrolytes did not provide the same clarity of results as in the DMSO electrolyte, leading Trahan *et al.* to theorise that the high basicity of DMSO, evidenced by its high donor number (DN, 29.8), improved the stability of oxygen reduction intermediate species.[62] In fact, LiO_2 is thermodynamically unstable and chemically disproportionates to from Li_2O_2 (equation 5.6).[62,63]

$$2LiO_{2\,(s)/(sol)} \rightarrow Li_2O_{2\,(s)} + O_{2\,(sol)} \quad (5.6)$$

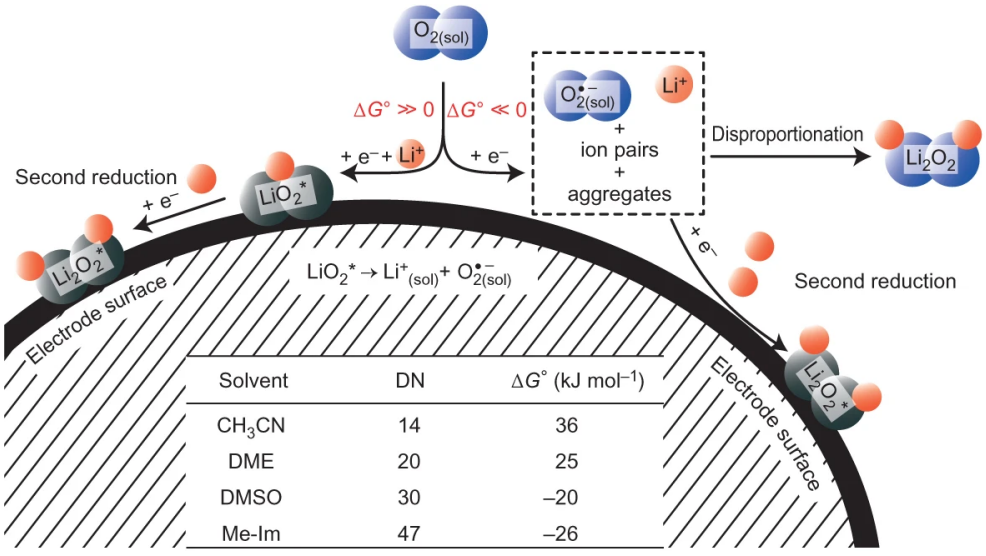
Pearson's hard-soft acid-base theory can be used to rationalise this observation where, if only ionic interactions are considered, O_2^- is a soft-base and Li^+ is a hard-acid, thus their interaction will be poor.[63,64] The disproportionation of LiO_2 results in the formation of one neutral O_2 molecule, alleviating the incompatibility, and one O_2^{2-} molecule, a harder-base which interacts more favourably with the hard-acid Li^+, resulting in the formation of the stable Li_2O_2.

Therefore, the critical driving force for LiO_2 disproportionation is the incompatibility of Li^+ and O_2^-.

Johnson *et al.* developed a theory that it is the solubility of LiO_2 or, more precisely, the free energy of the reaction of LiO_2 dissociation that dictates the extent of which Li_2O_2 will form through a solution or surface reaction mechanism (equation 5.7, **Figure 5.4**).[63]

$$LiO_{2\,(s)} \rightleftharpoons Li^+_{(sol)} + O_{2\,(sol)} \qquad (5.7)$$

The free energy of this reaction depends predominantly on the solvent-ion interactions and follows the trend that a high solvent basicity (i.e. high DN) results in a favourable environment for LiO_2 dissociation.[60,62,63] Johnson *et al.* highlight that this trend is critically concerned with the solvation of the cation (i.e. Li^+) and that the acceptor number (AN) of a given solvent would influence the solvation of O_2^-. Aetukuri *et al.* confirmed this hypothesis,[65] reporting the same mechanism where the high AN of H_2O was used as an O_2^- stabilising additive (**Figure 5.5**). Nevertheless, these studies identified that where solvent DN is low, LiO_2 exhibits poor solubility and its high thermodynamic instability



Solvent	DN	ΔG° (kJ mol^{-1})
CH_3CN	14	36
DME	20	25
DMSO	30	–20
Me-Im	47	–26

Figure 5.4. *Schematic of the O_2 reduction mechanism in non-aqueous aprotic solvents containing Li^+ showing the surface pathway followed when the free energy of LiO_2 dissociation is >>0 (i.e. low DN) and the solution pathway followed when the free energy of LiO_2 dissociation is <<0 (i.e. high DN). Reproduced from Johnson et al.*[63]

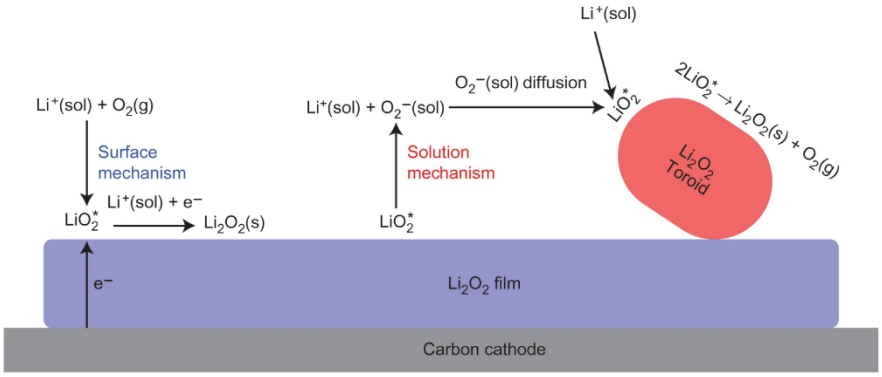


Figure 5.5. *Schematic of the deposition of Li_2O_2 in toroidal particles through the electrochemical formation of LiO_2 on the electrode surface and subsequent solvation by H_2O (i.e. high AN) which allows bulk Li_2O_2 formation. Reproduced from Aetukuri et al.*[65]

results in rapid conversion to Li_2O_2. The surface confined nature of this reaction leads to the generation of a passivating Li_2O_2 film that limits the discharge capacity of Li-air cells. Where high DN solvents are used, as in the case of DMSO, the solubility of the LiO_2 intermediate results in increased kinetic stability, enabling a chemical solution phase Li_2O_2 formation pathway that acts to somewhat mediate the growth of Li_2O_2 particles and improve the discharge capacity of cells.

Early studies indicated that the charge reaction of Li_2O_2 proceeded by a direct $2e^-$ oxidation to release Li^+ and O_2 (equation 5.8), demonstrated by the lack of electrochemical, spectroscopic or reactive evidence for LiO_2 presence.[60,61]

$$Li_2O_{2\,(s)} \rightarrow 2Li^+_{\,(sol)} + O_{2\,(sol)} + 2e^- \qquad (5.8)$$

However, Lu and Shao-Horn disputed this claim, using potentiostatic intermittent titration (PITT) and galvanostatic intermittent titration to probe the kinetics of Li_2O_2 oxidation, thus proposing a three-stage mechanism for Li_2O_2 oxidation.[66] The first stage is attributed to the delithiation of the outer part of the Li_2O_2 particle, resulting in the formation of lithium deficient $Li_{2-x}O_2$. The second concerns the chemical disproportionation of $Li_{2-x}O_2$ to release O_2. Finally, at high potentials, the bulk Li_2O_2 can be oxidised, either directly or through electrolyte degradation mediated oxidation.[66] Gallant *et al.* further built upon this mechanism, demonstrating that the charging behaviour was also

dependent on discharge product morphology, where larger particles exhibited less capacity in the sloping region of the charge profile as a result of the lower surface area to volume fraction compared to smaller particles (**Figure 5.6**).[67] To summarise, these reports demonstrated that the first stage of Li_2O_2 oxidation is the surface-related delithiation of Li_2O_2 to form $Li_{2-x}O_2$ (equation 5.9).

$$Li_2O_{2\,(s)} + xe^- \rightarrow Li_{2-x}O_2{}^{x-}{}_{(s)} + xLi^+{}_{(sol)} \qquad (5.8)$$

Given that small particles are majority 'surface-like', this sloped region makes up a large capacity contribution to the overall charging process (**Figure 5.6**). However, with larger Li_2O_2 morphologies, where a clear distinction can be made between surface and bulk Li_2O_2, the capacity contribution of this surface process is considerably reduced, and a stable charge plateau is rapidly reached.[67] Following the complete delithiation and removal of the surface Li_2O_2, the interior bulk Li_2O_2 is exposed which can then be oxidised through a two-phase process, wherein Li_2O_2 and O-rich LiO_2 species coexist and the latter can disproportionate to generate the required O_2.

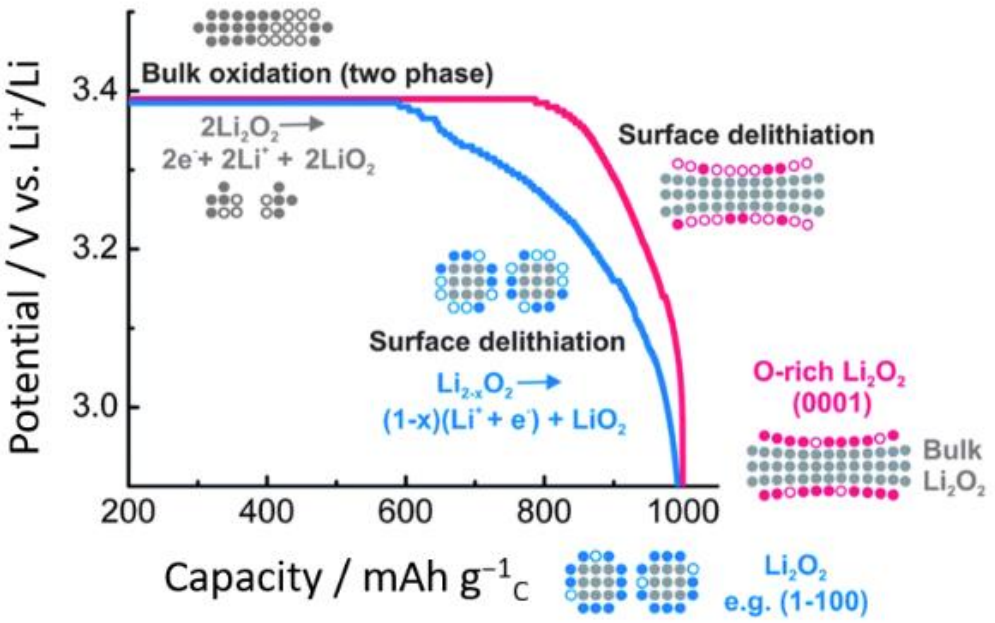


Figure 5.6. *Proposed charging process of Li_2O_2 with disk (grey/red, typical dimensions ~50 – 200 nm) or particle (grey/blue, typical dimensions <20 nm) morphologies overlaid on PITT data showing cell charging. Reproduced from Gallant et al.*[67]

In 2018, Wang *et al.* used a combination of thin-film rotating ring disk electrochemistry and synchrotron-based X-ray absorption near-edge structure spectroscopy to report the first direct evidence of soluble LiO_2 formation when oxidising Li_2O_2.[68] These data built upon the previously proposed charging mechanisms, revealing that in high DN solvents, where LiO_2 has increased solubility, the oxidation of Li_2O_2 results in preferential formation of LiO_2. However, in low DN solvents, where LiO_2 solubility is poor, no LiO_2 is detected, and the mechanisms previously proposed by Lu and Gallant are valid (**Figure 5.7**).[66,67] These findings are in good agreement with the improved solubility of the LiO_2 intermediate reported during discharge in high DN solvents, which provide a favourable free energy for LiO_2 dissociation when compared to low DN solvents.[63] The high reactivity of LiO_2 with electrolyte solvents, carbon electrode materials, and binders could rationalise the poor cycling performance of high DN solvents, where LiO_2 can act as a solution-phase nucleophile.[68] Identifying and understanding these degradation processes is critical to designing long-life Li-air batteries.[44,68–71]

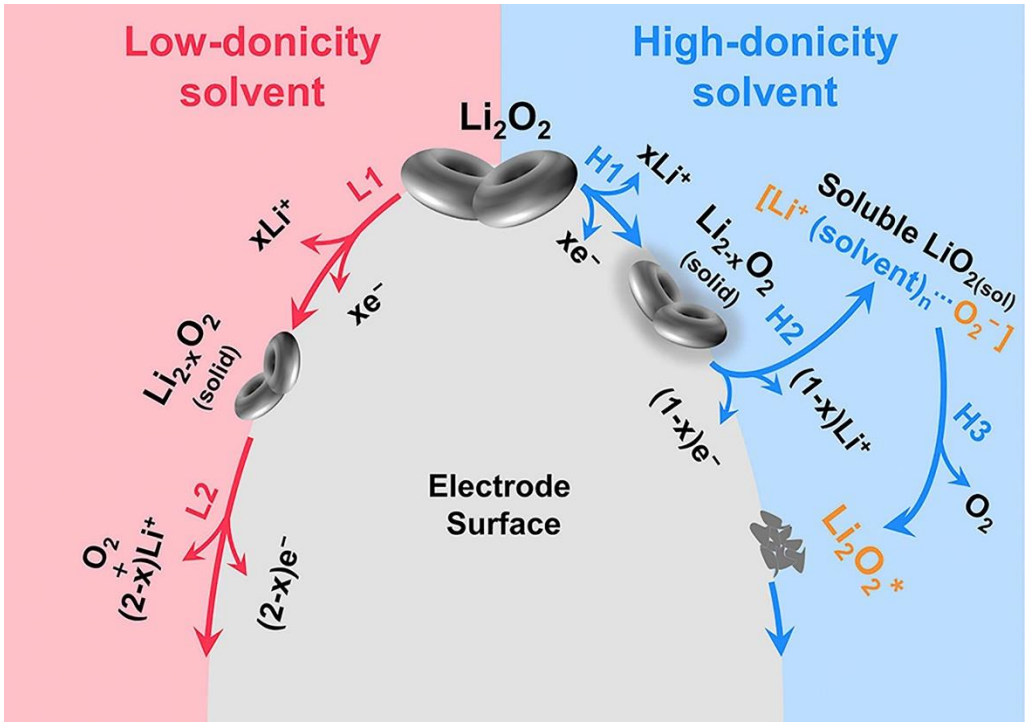


Figure 5.7. *Proposed solvent-controlled Li_2O_2 oxidation mechanism in which the solvent DN determines whether LiO_2 will form as a distinct species during the charging process. Reproduced from Wang et al.*[68]

5.3 Electrolyte solution degradation

Several antagonistic species including LiO_2,[69,72] Li_2O_2,[73,74] polyoxides,[75] and singlet oxygen ($^1O_2$),[76,77] have been identified. Consequently, extensive efforts have been applied to understand electrolyte solution degradation mechanisms in the Li-air battery, where several degradation pathways involving reactive oxygen species have been proposed (**Figure 5.8**).

Due to their broad success in application as lithium-ion battery electrolyte solvents, early Li-air cells used organic carbonates, most commonly propylene carbonate (PC), as the electrolyte solvent.[34,78–80] PC possesses many properties that deem it suitable for Li-air batteries, namely a wide electrochemical stability window, (electro)chemical stability to metallic Li, a high dielectric constant which results in good Li^+ solvation, and low volatility.[81] However, carbonate solvents were later found to be susceptible to nucleophilic attack by the LiO_2 intermediate, rendering them unsuitable for purpose.[79,82–85] Similarly, the DMSO-based electrolytes that were subsequently proposed were also found to suffer from nucleophilic attack by LiO_2.[86–91] Quantum-chemical calculations performed by Bryantsev *et al.* indicated that sulfone-derived solvents would be

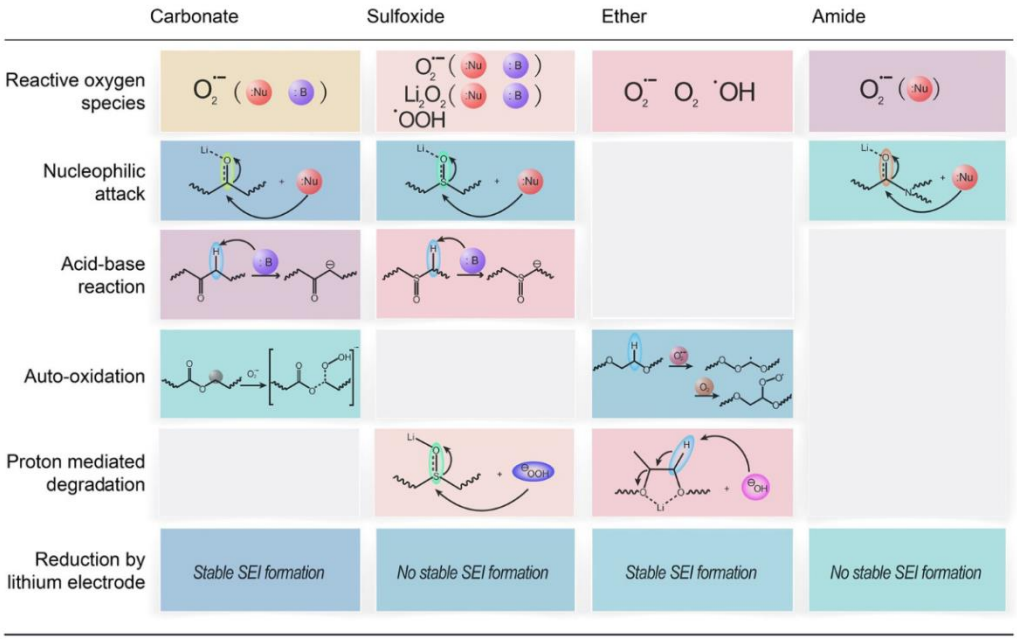


Figure 5.8. *Five decomposition pathways of Li-air electrolyte solvents and related reactive O_2 species. Reproduced from Lai et al.*[34]

stable to LiO_2,[70] which was subsequently confirmed experimentally.[92,93] However, this class of materials are often solid at room temperature, thus posing considerable technical challenges for incorporation into a practical Li-air cell.[79]

Amide-based solvents, namely dimethyl formamide (DMF), *N,N*-dimethyl acetamide and *N*-methyl-2-pyrrolidone (NMP) were then explored as potential electrolyte solvents.[34,47,78,94–97] Mixed results were obtained with this electrolyte class, where initial research indicated that amides had good stability to reactive oxygen species, with Chen *et al.* showing that the first cycle of a DMF-based Li-air cell was dominated by Li_2O_2 formation and decomposition.[78,98] Subsequent ^1H nuclear magnetic resonance, Fourier transform infra-red, and on-line electrochemical mass spectrometry measurements indicated that the decomposition of DMF accelerates with extent of cycling and results in poor long-term cycle life.[98,99] However, computational calculations did not support the hypothesis of DMF reactivity with reactive oxygen species, instead suggesting that the amides may undergo oxidative degradation at the surface of the cathode during the charge process.[47,98] Nevertheless, amides were deemed unsuitable candidates for use as Li-air battery electrolyte solvents.

Glyme ethers such as tetra ethylene glycol dimethyl ether (TEGDME) and 1,2-dimethoxyethane (DME) are the current state-of-the-art electrolyte solvents used in literature as a result of their oxidative robustness towards nucleophiles.[34,100–102] However, these too have been proposed to undergo proton extraction in the presence of LiO_2 and/or Li_2O_2, especially in the solution phase, which results in Li_2O_2 discharge yields <95% (**Figure 5.9**).[100,102–105] Shorter glyme ethers (i.e. diglyme, DME) are highly volatile, making them sub-optimal for a practical Li-air battery, where a flowing gas stream would be applied. However, as glyme chain length increases (i.e. TEGDME), and thus volatility decreases, the long-term cycling stability of cells has been shown to reduce considerably.[34,78,106]

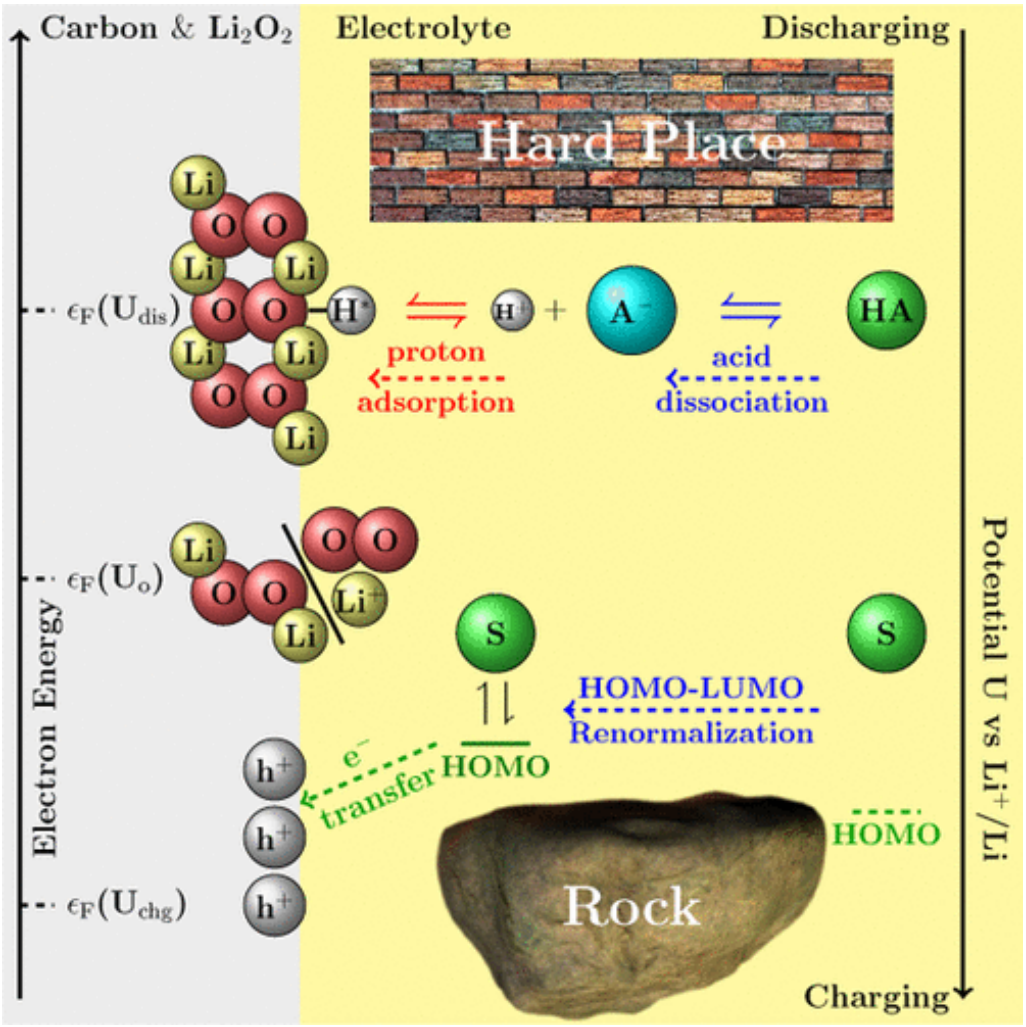


Figure 5.9. *Schematic showing the balance between solvent highest occupied molecular orbital (HOMO), which must be sufficiently low to ensure solvent molecules (green circles, S) are electrochemically stable to the cathode interface, and solvent pK_a value, which must be adequately low to prevent H-abstraction by the Li_2O_2/carbon cathode interface, that must be found to identify a stable Li-air electrolyte solvent. Solvent molecules are also shown as a weak acid, HA, which is in equilibrium with its conjugate base, A^-, and proton, H^+. Reproduced from Khetan et al.*[105]

Computational studies indicated that acetonitrile (MeCN) would be stable to the oxidative conditions of a Li-air cell suggesting that, although the adsorption of MeCN to Li_2O_2 surfaces weakens the nitrile bond and exposes it to nucleophilic attack, the poor solubility of peroxide species in MeCN result in no accessible geometry for degradation to proceed.[70] Early experimental studies confirmed the stability of MeCN and subsequent X-ray photoelectron spectroscopic analysis demonstrated that no degradation of MeCN occurs upon prolonged exposure to Li_2O_2 surfaces.[60,61,107] MeCN-based electrolytes have

oxygen solubility and diffusivity similar to glyme ethers, and the high dielectric constant of nitriles results in high ionic conductivity.[60] McCloskey *et al.* reported that a MeCN-based electrolyte achieved a ratio of electrons passed per molecule of oxygen consumed (e^-/O_2) of 2.05, close to the ideal 2 e^-/O_2 ratio of the desired Li_2O_2 formation, and the highest oxygen reduction/oxygen evolution reaction efficiency (ca. 0.9) of the electrolytes explored (i.e. DME, triglyme, DMSO, NMP, tetrahydrofuran, tri(ethylene glycol)-substituted trimethyl silane, *N*-methyl-*N*-propylpiperidinium).[108,109] However, the poor solubility of reactive oxygen species, which enables the stability of MeCN, is also a limitation due to the formation of thin-film Li_2O_2 which restricts the practical discharge capacity of MeCN-based cells. Moreover, the high volatility of MeCN and its reactivity with metallic Li deemed it impractical for operation in an ambient atmosphere Li-air cell using a metallic Li negative electrode.

In the pursuit of identifying solvents with sufficient oxidative stability, Bryantsev *et al.* performed a combination of computational and experimental degradation analysis on several prospective electrolyte solvents, including lower volatility aromatic and aliphatic nitrile and dinitriles.[47] This study identified trimethylacetonitrile (TMA) as the most stable nitrile solvent, with MeCN being identified as the second most stable.[47] TMA was the only aliphatic nitrile identified that passed the (electro)chemical degradation experiments, with the degradation of the other nitriles being associated with OH^- contamination that is present in the potassium dioxide disproportionation experiments used to simulate LiO_2 reactivity. Recent publications by Hase and co-workers have re-assessed MeCN as an electrolyte solvent, demonstrating that nitrile-based electrolytes can achieve a much greater discharge capacity than initially proposed where an appropriate operating potential is applied.[110,111] However, the thin-film nature of Li_2O_2 formation is still a critical factor limiting delivery of high power, high energy density Li-air batteries.

Clearly, the electrochemical (dis)charge processes of the aprotic Li-air battery, and the intermediate species (especially LiO_2) that form as a result of them, generate a harsh oxidising environment that any prospective electrolyte

composition must be able to tolerate. However, finding an electrolyte composition that is both stable to these harsh oxidising conditions and can deliver on the proposed power and energy density benefits of a Li-air battery, avoiding rapid passivation through thin-film Li_2O_2 formation, is non-trivial.

5.4 Redox-mediators

In 2016, Gao *et al.* proposed the use of 2,5-ditert-butyl-1,4-benzoquinone (DBBQ) to mediate the discharge process by providing an alternative pathway for Li_2O_2 formation that enables a discharge potential above that required for electrochemical LiO_2 formation.[112] On discharge, DBBQ is reduced on the surface of the cathode (equation 5.10), where it then binds to Li^+ and reduces O_2 to O_2^-, forming a $LiDBBQO_2$ complex in solution (equation 5.11). This complex is thermodynamically unstable and can go on to disproportionate, forming Li_2O_2 and regenerating DBBQ, allowing the cycle to continue, without passing through free LiO_2 (**Figure 5.10**, equation 5.12).[112]

$$DBBQ_{(sol)} + e^- \rightarrow DBBQ^-_{(sol)} \quad (5.10)$$

$$DBBQ^-_{(sol)} + Li^+_{(sol)} + O_{2\,(sol)} \rightarrow LiDBBQO_{2\,(sol)} \quad (5.11)$$

$$2LiDBBQO_{2\,(sol)} \rightarrow 2DBBQ_{(sol)} + Li_2O_{2\,(s)} + O_{2\,(sol)} \quad (5.12)$$

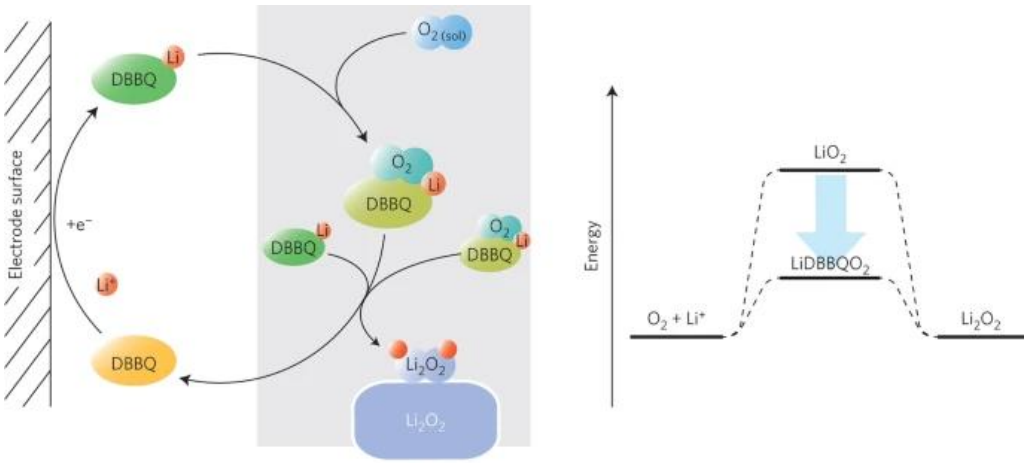


Figure 5.10. *Schematics of reaction on discharge (left) and the effect of DBBQ on the potential determining step (right). DBBQ is reduced at the electrode surface forming LiDBBQ, and then LiDBBQ reacts with O_2, producing Li_2O_2 and itself being regenerated to DBBQ. Schematic of free energy plot is at E^0 for O_2/Li_2O_2. Reproduced from Gao et al.*[112]

The use of discharge redox mediators marked a critical breakthrough for the Li-air battery, enabling solution-phase formation of Li_2O_2 in solvents that were previously confined to surface passivating Li_2O_2 formation, while simultaneously reducing the impact of the highly reactive LiO_2 intermediate, evidenced by increased Li_2O_2 yields where DBBQ is used.[112] However, the use of discharge mediators in such systems has the unintended consequence of isolating the discharge product from the electrode surface and limiting the attainable charge capacity.

Several charge mediators were proposed to address this challenge.[113–117] In 2017, Gao *et al.* designed a dual-mediator system, wherein DBBQ and 2,2,6,6-Tetramethylpiperidinyl-1-oxyl (TEMPO) were employed in tandem as discharge and charge mediators, respectively (**Figure 5.11**).[103] Here, TEMPO is oxidised at ca. 3.6 V vs Li^+/Li, to form $TEMPO^+$ (equation 5.13), a potential above the equilibrium potential of Li_2O_2 (2.96 V vs Li^+/Li). This thermodynamic driving force enables charge transfer between the $TEMPO^+$ and bulk Li_2O_2 particles in a solution-phase mechanism, providing a favourable route for Li_2O_2 oxidation

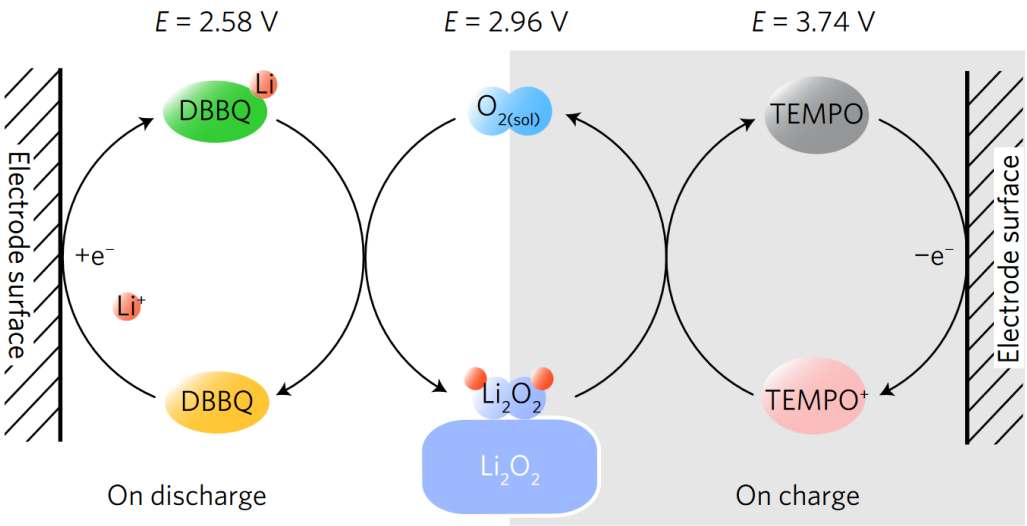


Figure 5.11. *Schematic of positive electrode reactions on discharge and charge in the presence of DBBQ and TEMPO which act as discharge and charge mediators of Li_2O_2 redox, respectively. Reproduced from Gao et al.*[103]

and facilitating oxidation of Li_2O_2 that is otherwise isolated from the electrode surface (equation 5.14).[44,103]

$$TEMPO_{(sol)} \rightarrow TEMPO^{+}_{(sol)} + e^{-} \quad (5.13)$$

$$2TEMPO^{+}_{(sol)} + Li_2O_{2\,(s)} \rightarrow 2TEMPO_{(sol)} + 2Li^{+}_{(sol)} + O_{2\,(sol)} \quad (5.14)$$

Electrochemical (dis)charge mediators are now the standard in state-of-the-art Li-air battery research, which is almost exclusively performed under a pure O_2 atmosphere to avoid parasitic chemical reactions that can be introduced by the presence of gas stream impurities such as H_2O and CO_2.[9,118–121] The role of H_2O in the Li-air battery is still hotly debated, with some early studies concluding that any H_2O is detrimental to the operation of Li-air cells, while others report that small quantities of H_2O improve discharge capacity by providing a chemical route for phase transfer catalysis of the Li_2O_2 discharge product morphology (equation 5.15).[65,91,119,122–124] The role of CO_2 is well-established, either driving direct electrochemical Li_2CO_3 formation or chemically converting Li_2O_2 to Li_2CO_3 (equations 5.16 and 5.17, respectively).[120,121,125]

$$Li_2O_{2\,(s)} + 2H_2O_{(sol)} \rightleftharpoons H_2O_{2\,(sol)} + 2LiOH_{(s)} \quad (5.15)$$

$$4Li^{+}_{(sol)} + O_{2\,(sol)} + 2CO_{2\,(sol)} + 4e^{-} \rightarrow 2Li_2CO_{3\,(s)} \quad (5.16)$$

$$2Li_2O_{2\,(s)} + 2CO_{2\,(sol)} \rightarrow O_{2\,(sol)} + 2Li_2CO_{3\,(s)} \quad (5.17)$$

Understanding that atmospheric CO_2 must be addressed for a transition to a true Li-air battery to be feasible, the remainder of this chapter will focus on the role of H_2O as a chemical Li_2O_2 mediator, with the aim of understanding the current state-of-the-art rhetoric on the feasibility of H_2O inclusion in the Li-air battery.

5.5 H_2O in the Li-air battery

In 2014, Gallagher *et al.* performed a techno-economic analysis intended to quantify the promise of non-aqueous lithium-air batteries using an atmospheric O_2 supply.[118] Various scenarios of prerequisite gas stream purification were explored, addressing the penalties that a practical 'air' battery would need to accept for real-world application. This material-to-system analysis looks to

deconvolute theoretical energy density by predicting the practical energy density of Li-air cells under a set of scenarios that take into account the requirements of cell design, battery cooling and packaging, and the equipment that is required to purify and deliver the gaseous O_2 reactant. The study is centred around the delivery of a 100-kWh battery pack, which anchors to optimistic material, design, and manufacturing targets for an automotive Li-air energy storage system and thus should be taken as a best-case scenario.

Figure 5.12, shows the additional system requirements of an open-architecture Li-air battery, wherein O_2 from the ambient atmosphere is used for operation.[118] Additional components include a compressor, separation processes to remove H_2O and CO_2, flow channels within the cell to enable convective air transport, and a solvent management system to prevent emission that could occur due to the volatility of electrolyte solvent components.[118] Of these components, the largest variance is introduced by the extent of H_2O and CO_2 exclusion required for cell operation, with the most restrictive case removing these contaminants to the 1 – 10 ppm level. In this case, a 33% energy density penalty would be realised through the mass of the

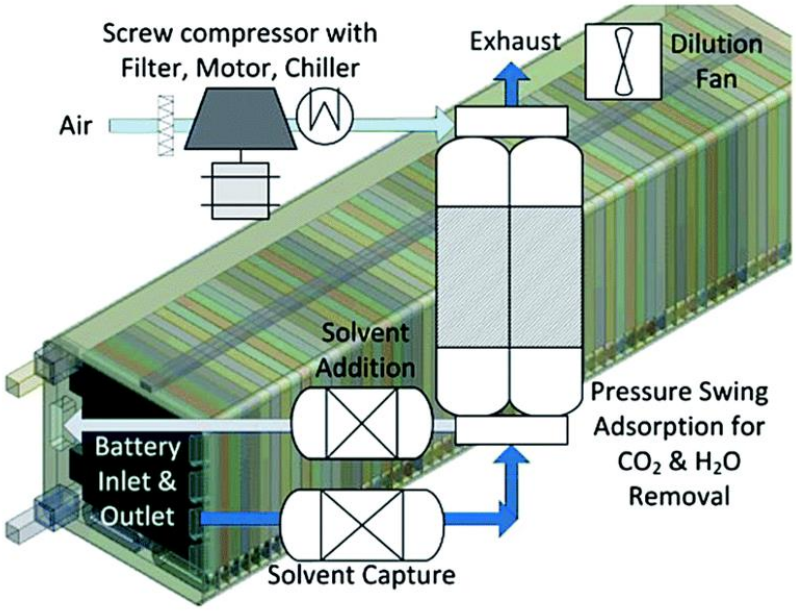


Figure 5.12. *Required components for open-architecture Li-air battery. Reproduced from Gallagher et al.*[118]

gas handling unit alone, greatly reducing the practical energy density of a Li-air system (i.e. gravimetric and volumetric energy density = 386 Wh kg^{-1} and 384 Wh L^{-1}, respectively, **Figure 5.13**). In fact, Gallagher *et al.* concluded that, where this level of pre-treatment was required, the Li-air battery offered no performance benefits over advanced lithium-ion technologies.[118] Therefore, if the promise of high energy density Li-air batteries is to be delivered, either technical advances in gas handling and purification are required, or strategies for inhibiting the antagonistic effects of gas stream impurities must be developed.

In line with the meticulous gas stream purification proposed by Gallagher *et al.*, early literature assumed that the presence of any H_2O would be detrimental to the performance of the Li-air battery, due to the spontaneous reaction of Li_2O_2 with H_2O that forms LiOH.[118,122,126,127] This was largely driven by the understanding that the aqueous Li-air battery operates through $4e^-$ O_2 reduction to form LiOH, wherein H_2O acts as a proton donor, enabling the electrochemical formation of intermediate protonated species including H_2O_2, HO_2^- and OH^-.[45,65,90,119,122,124] However, as discussed in section 5.2, where LiOH forms in non-aqueous electrolytes the cleavage of the O-O bond results in its

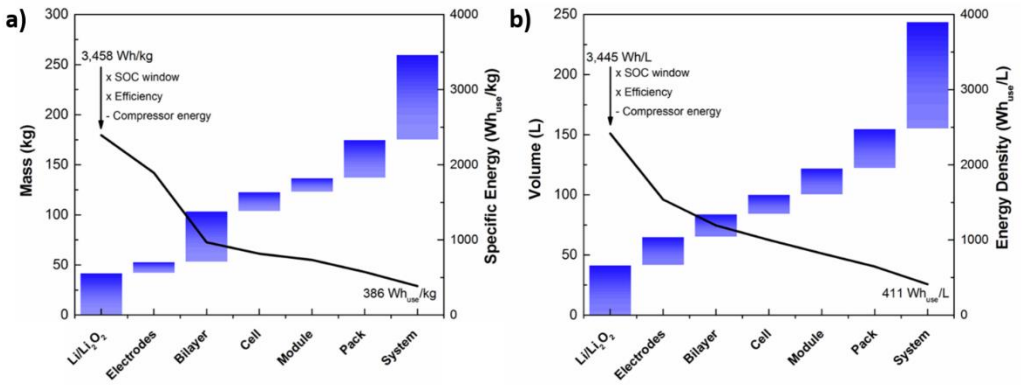


Figure 5.13. *a) Mass and b) volume breakdown for a Li-air open-architecture energy-storage system with a 100-kWh capacity and 80 kW net power at a nominal voltage of 360 V. Distribution of mass and volume penalties are detailed as increasing functionality is added to the active materials (left to right). Reproduced from Gallagher et al.*[118]

formation being considered chemically irreversible.[48–52] The resultant large overpotential that is required to drive its oxidation push the cathode into a region of high oxidative reactivity with the electrolyte solvent, thus LiOH is broadly considered a parasitic product.[56–58]

However, several studies have since reported that small quantities of H_2O can be present in a variety of Li-air electrolytes while still maintaining Li_2O_2 as the dominant electrochemical discharge product.[65,91,122,123,128] Moreover, many of these studies reported an improved discharge capacity relative to the dry electrolyte, indicating that the presence of H_2O delayed the passivation of the cathode with thin-film Li_2O_2.[65,91,119,122,123,129,130] The most dramatic performance enhancements were seen in electrolytes with poor solubility of the Li_2O_2 discharge product, wherein surface-confined electrochemical Li_2O_2 formation is the dominant pathway, resulting in rapid surface passivation and a low discharge capacity in dry electrolytes. Schwenke *et al.* reported that the inclusion of just 1000 ppm H_2O in a diglyme electrolyte could considerably increase the attainable discharge capacity, resulting in a distinctive toroidal morphology which has since become characteristic of H_2O-mediated discharge (**Figure 5.14**).[119,122–124] These findings were not uniform across solvents, with significant onset of LiOH formation observed in some solvent systems, clearly indicating a solvent dependence on H_2O activity.[9,53,91,120,131]

These findings raised mechanistic questions regarding the role of H_2O in these mixed H_2O-solvent systems, which several studies have attempted to solve. Aetukuri *et al.* proposed that it was the Lewis acidity of H_2O that results in the stabilisation of O_2^-, in line with the theories discussed in section 5.2.[65] It was suggested that the enhanced stabilisation of the LiO_2 intermediate enables a solution-phase mechanism for Li_2O_2 formation, delaying the passivation of the cathode surface and supporting the formation of the observed bulk toroidal morphology.[65] This theory rationalised the dramatic increase in particle size and complexity observed in glyme ether based solvents, where thin-film Li_2O_2 passivation is prevalent with dry electrolyte.[65,122]

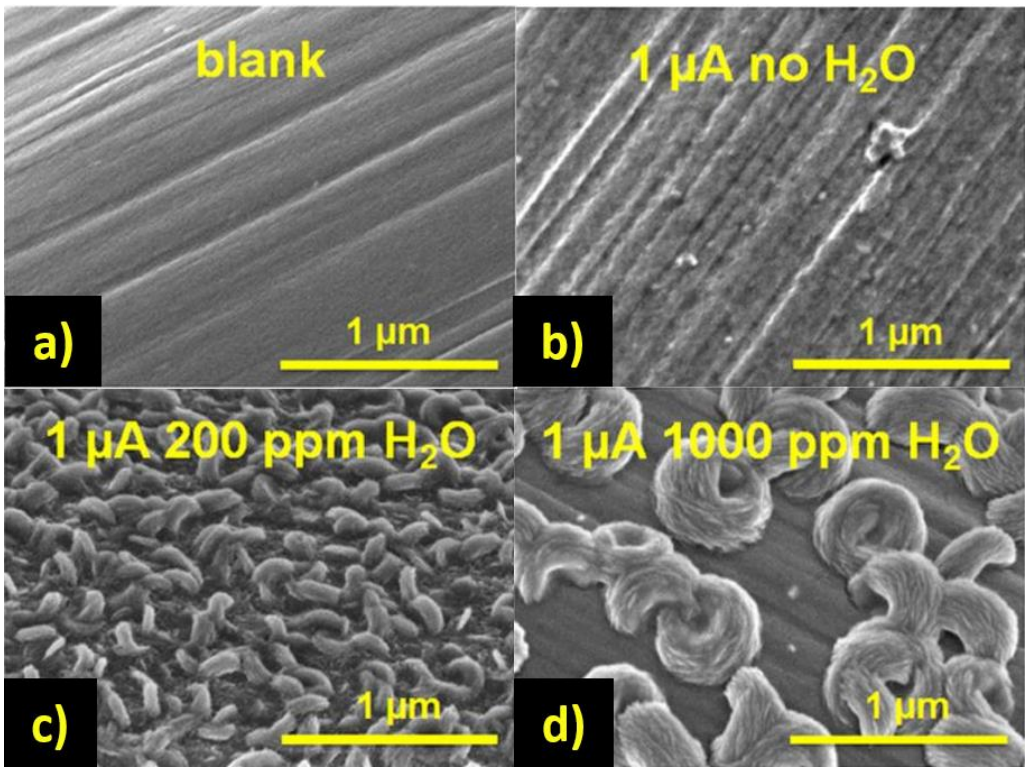


Figure 5.14. *SEM images of carbon paper electrodes after washing and drying of a a) blank electrode (pristine), b,c,d) discharged electrode extracted from a cell cycled at 1 µA containing a diglyme-based electrolyte doped with b) no H_2O, c) 200 ppm H_2O or d) 1000 ppm H_2O showing the change in Li_2O_2 particle morphology with H_2O concentration. Reproduced from Schwenke et al.*[122]

In parallel, Schwenke *et al.* proposed that trace quantities of H_2O, where activity is insufficient for electrochemical LiOH formation, establish chemical equilibria in which Li_2O_2 can be reversibly converted to H_2O_2 as described in equation 5.15, which can be further broken down into two distinct H_2O-mediated equilibria (equations 5.18 and 5.19).[122]

$$Li_2O_{2\,(s)} + H_2O_{\,(sol)} \rightleftharpoons LiOOH_{\,(sol)} + LiOH_{\,(s)} \qquad (5.18)$$

$$LiOOH_{\,(sol)} + H_2O_{\,(sol)} \rightleftharpoons H_2O_{2\,(sol)} + LiOH_{\,(s)} \qquad (5.19)$$

A distinction must be made between LiOH that is formed through these chemical equilibria and that which is formed through electrochemical O_2 reduction. In the former, the LiOH is formed through the deprotonation of H_2O and the consequent generation of lithium hydroperoxide (LiOOH) as described in equation 5.18. Where H_2O activity is sufficient, a further H_2O molecule can be deprotonated, generating another LiOH molecule and converting the LiOOH

to H_2O_2 as described in equation 5.19. Critically, the source of OH^- in both of these chemical reactions is the H_2O molecule, with the backwards reaction requiring only the exchange of Li^+ and H^+. Contrastingly, where LiOH is formed electrochemically through $4e^-$ O_2 reduction, the OH^- is produced through the cleavage of the O-O bond, thus the reversibility is determined by the thermodynamic requirements of O-O bond reformation, deeming it chemically irreversible.[48–52] Therefore, where H_2O activity is sufficiently low, the presence of some LiOH is indicative of a favourable equilibrium that can enhance discharge capacity, while where H_2O activity is sufficiently high, the accumulation of LiOH indicates an irreversible parasitic reaction pathway that will ultimately result in the passivation of the cathode surface.

Qiao *et al.* presented the first experimental evidence of hydroperoxide (HO_2^-), which is proposed to form through the deprotonation of H_2O by O_2^-.[123] The study observed that as H_2O content increases, the intensity of the LiO_2 Raman peak (O-O stretch) gradually decreases, in line with an increase in the intensity of the Raman peak associated with HO_2^- (O-O stretch, **Figure 5.15**). Furthermore, where H_2O content was above 0.75%, the LiO_2 species is no longer detectable through Raman spectroscopic analysis of the discharged cathode surface. In the concentration range that both LiO_2 and HO_2^- are

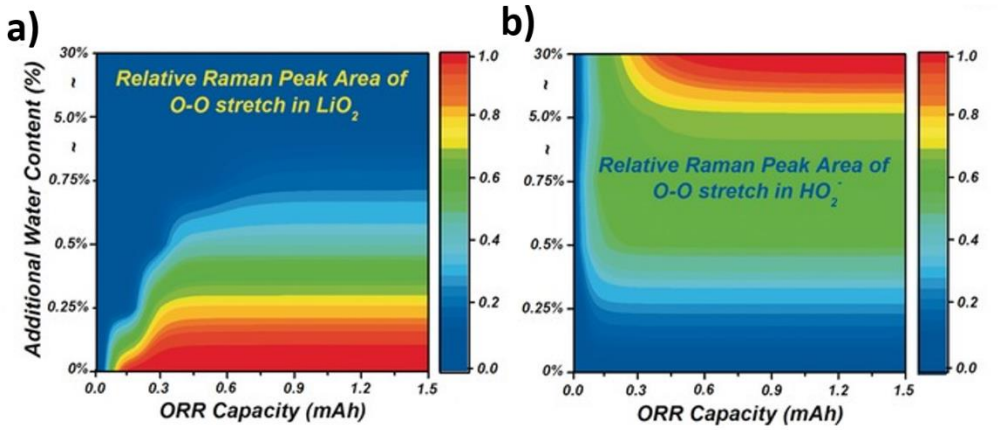


Figure 5.15. *Plots showing the relative peak area ratio of the Raman O-O stretch of a) LiO_2 and b) HO_2^-, normalised relative to the maximum value and shown as a function of oxygen reduction reaction capacity (x-axis) and doped H_2O content (y-axis). Cells contained a TEGDME-based electrolyte and were discharged to 1.5 mAh at a rate of 100 mA g^{-1}. Reproduced from Qiao et al.[123]*

detectable (i.e. 0.25 – 0.75% H_2O), no LiO_2 signal is observed until the saturation of the HO_2^- signal, demonstrating that HO_2^- is preferentially formed over LiO_2, which can only form in significant quantities once HO_2^- formation has reached its maximum rate.[123] Compared to the highly reactive LiO_2 species, HO_2^- is a relatively stable species, evidenced by the reduction in the observed degradation of the electrolyte solvent where H_2O was doped into the electrolyte.[123] Furthermore, these data confirmed the solution-phase transfer proposed by Schwenke *et al.* and further proposed an electrochemical pathway for $2e^-$ O_2 reduction to form Li_2O_2 that does not pass through the reactive LiO_2 intermediate species (equations 5.20 – 5.22).[122,123,132] Note that equation 5.22 is the reverse of equation 5.15, proposed by Schwenke *et al.* and is chemically driven by Le Chatelier's principle, wherein accumulation of H_2O_2 and the depletion of H_2O acts to drive the chemical equilibria towards replenishing H_2O, re-initiating the pathway.

$$O_{2\,(sol)} + H_2O_{\,(sol)} + 2e^- \rightarrow HO_2^-{}_{(sol)} + OH^-{}_{(sol)} \qquad (5.20)$$

$$HO_2^-{}_{(sol)} + H_2O_{\,(sol)} \rightarrow H_2O_{2\,(sol)} + OH^-{}_{(sol)} \qquad (5.21)$$

$$2LiOH_{\,(s)} + H_2O_{2\,(sol)} \rightleftharpoons Li_2O_{2\,(s)} + H_2O_{\,(sol)} \qquad (5.22)$$

To summarise, Qiao *et al.* proposed that the presence of trace quantities of H_2O in glyme ether electrolytes provided a pathway for $2e^-$ O_2 reduction to form Li_2O_2 without passing through the reactive LiO_2 intermediate, simultaneously reducing the amount of electrolyte solution degradation observed and enabling the formation of bulk Li_2O_2 through H_2O-mediated chemical equilibria, thus improving discharge capacity.

Although these reports focussed on the use of glyme ethers, the current state-of-the-art Li-air electrolytes solvent, Kwabi *et al.* reported that trace quantities of H_2O were not universally beneficial to discharge performance, suggesting that electrochemical LiOH formation was induced when a MeCN-based electrolyte was used.[91] The authors proposed that proton-induced disproportionation of O_2^- is the primary driver for LiOH formation, citing organic literature that examines the kinetics of HO_2^- formation in DMSO, DMF

and MeCN, wherein it is demonstrated that it is much more favourable for the H^+ to come from H_2O than the solvent molecule.[133–135] Thus, the proton availability (i.e. pK_a) of H_2O in a given H_2O-solvent mixture was rationalised as the key factor that determined whether Li_2O_2 or LiOH would be the primary discharge product in a given electrolyte.[91] The pK_a of 1 M H_2O in MeCN and DME was calculated to be 35.2 and >47.0, respectively, demonstrating that it is much more favourable for H_2O to be deprotonated in MeCN-based electrolytes than in DME-based electrolytes. These data were used to rationalise the ability of DME to tolerate some H_2O while maintaining Li_2O_2 as the only discharge product detectable with post-cycling X-ray diffraction (XRD) analysis.[65,91] Unlike in the DME-based electrolyte, it is suggested that the lower pK_a of H_2O in MeCN drives the electrochemical formation of LiOH and results in the formation of a mixture of Li_2O_2 and LiOH.[91]

In 2019, Holc published his thesis titled "The effect of H_2O on O_2 reduction in Li-O_2 batteries", in which he conducted a systematic study on the electrochemical reactions that occur in H_2O-containing electrolytes with the aim of developing a unifying mechanism to understand H_2O tolerance.[136] DMSO, TEGDME and MeCN were used as the electrolyte solvents of study, where electrochemical measurements using a TBA^+-containing electrolyte were used to understand the onset of $4e^-$ O_2 reduction in each H_2O-solvent mixture. The outcome of these experiments was subsequently confirmed through analogous measurements using Li^+-containing electrolytes. These studies established that the onset of electrochemical LiOH formation was decided by a combination of intrinsic solvent properties and H_2O concentration, demonstrating through the use of pressure cells that, although MeCN showed poor H_2O toleration, some solvents were capable of performing near ideal $2e^-$ O_2 reduction to form Li_2O_2 with H_2O content ≤1 M.[136] Holc theorised that it is not the pK_a of H_2O, but the stability of OH^- that is the critical factor that determines whether $4e^-$ O_2 reduction will proceed, suggesting that strong Lewis acids (i.e. H_2O-solvent mixtures with a high AN) would stabilise OH^- where formed and provide a favourable environment for LiOH formation.[136]

Furthermore, Holc proposed that solvent DN plays a critical role in determining the effect of H_2O on the overall H_2O-solvent mixture AN, where solvents with a low DN poorly interact with H_2O and result in a rapid increase in mixture AN, whereas solvents with a high DN interact strongly with H_2O, thus limiting its contribution to overall mixture AN.[136]

In summary, Holc proposed that a combination of a high DN, to complex H_2O and limit the effect it has on H_2O-solvent mixture AN, and a low dry solvent AN are the optimal combination when identifying a H_2O tolerant electrolyte solvent.[136] This H_2O-solvent mixture AN theory is the current state-of-the-art understanding of the role of H_2O in Li-air electrolytes.

5.6 Aims and objectives

Although several attempts have been made to understand the role of H_2O in Li-air cells, and Holc's thesis proposed a unifying H_2O-solvent mixture AN theory to predict the extent of H_2O tolerance exhibited by a given electrolyte solvent, the mechanism of electrochemical LiOH formation is still not understood.[65,91,122,123,136] It is broadly accepted that the chemical equilibria proposed by Schwenke *et al.* enable solution-mediated growth of toroidal Li_2O_2 through intermediate hydroperoxide species (i.e. LiOOH or H_2O_2), and further that H_2O can enable the conversion of O_2^- to HO_2^- which acts to limit the reactivity of O_2^-.[9,119,122,123] However, these equilibria generate LiOH chemically, through the deprotonation of H_2O, which cannot account for the increase in e^-/O_2 ratio, but could enable a situation where LiOH may be detected despite not being electrochemically formed.

Kwabi *et al.* reported that MeCN has an extremely poor tolerance to H_2O, suggesting electrochemical LiOH formation with ≤5000 ppm H_2O.[91] However, XRD was the only technique used to characterise this product, and does not categorically confirm electrochemical formation of LiOH, as the possibility of chemical formation is not explored. Although Holc's findings agree that MeCN-based electrolytes will show poor tolerance to H_2O concentration before the onset of $4e^-$ O_2 reduction, it is possible that some H_2O toleration, albeit small,

may be exhibited.[136] Furthermore, studies by McCloskey *et al.* reported that a dry MeCN-based electrolyte achieved an e^-/O_2 ratio of 2.05 and an oxygen reduction/oxygen evolution reaction efficiency of ca. 0.9, indicating that degradation processes may be occurring which are not currently reported.[108] Therefore, I will first study the effects of H_2O on the performance of Li-air cells containing an MeCN-based electrolyte, with the aim of deconvoluting the source of LiOH in previous studies and understanding the H_2O concentration at which cells deviate from the ideal $2e^-/O_2$ ratio.

Once a mechanism for LiOH accumulation in MeCN-based electrolytes has been established, the final chapter of this thesis will focus on understanding the mechanism of electrochemical LiOH formation. First Holc's H_2O-solvent mixture AN theory will be explored over a conclusive H_2O concentration range, using a combination of flooded cell electrochemical measurements, *in situ* pressure cells, and spectroscopic analyses of discharge product to enable the proposal of a mixture AN limit, over which the onset of $4e^-$ O_2 reduction will occur.[136] Subsequently, the feasibility of each possible chemical and electrochemical route of LiOH formation that could result in a deviation from the ideal $2e^-/O_2$ ratio will then be explored, with the aim of systematically ruling out formation pathways, to achieve mechanistic clarity. These findings will be used to propose high-performance Li-air cells that can operate under state-of-the-art conditions with H_2O concentration pushed to the limits identified through these analyses.

In coherence with Holc's mixture AN theory,[136] I hope to provide a unified mechanism for electrochemical LiOH formation in the Li-air battery and decisively prove that understanding the mechanism that underpins LiOH formation can enable operation of a Li-air cell with significant quantities of H_2O while maintaining $2e^-$ O_2 reduction.

5.7 References

1. Bruce, P. G., Freunberger, S. A., Hardwick, L. J. & Tarascon, J.-M. Li–O_2 and Li–S batteries with high energy storage. *Nat. Mater.* **11**, 19–29 (2012).
2. Christophersen, J. P. *Battery Test Manual For Electric Vehicles, Revision 3*. https://www.osti.gov/biblio/1186745 (2015) doi:10.2172/1186745.
3. Kim, S. *et al.* Projecting Recent Advancements in Battery Technology to Next-Generation Electric Vehicles. *Energy Technol.* **10**, 2200303 (2022).
4. Adu-Gyamfi, B. A. & Good, C. Electric aviation: A review of concepts and enabling technologies. *Transp. Eng.* **9**, 100134 (2022).
5. Lin, D., Liu, Y. & Cui, Y. Reviving the lithium metal anode for high-energy batteries. *Nat. Nanotechnol.* **12**, 194–206 (2017).
6. Gao, Y., Pan, Z., Sun, J., Liu, Z. & Wang, J. High-Energy Batteries: Beyond Lithium-Ion and Their Long Road to Commercialisation. *Nano-Micro Lett.* **14**, 94 (2022).
7. Liu, J. *et al.* Pathways for practical high-energy long-cycling lithium metal batteries. *Nat. Energy* **4**, 180–186 (2019).
8. Robinson, J. B. *et al.* 2021 roadmap on lithium sulfur batteries. *J. Phys. Energy* **3**, 031501 (2021).
9. Liu, T. *et al.* Current Challenges and Routes Forward for Nonaqueous Lithium–Air Batteries. *Chem. Rev.* **120**, 6558–6625 (2020).
10. Jung, J.-W., Cho, S.-H., Nam, J. S. & Kim, I.-D. Current and future cathode materials for non-aqueous Li-air (O_2) battery technology – A focused review. *Energy Storage Mater.* **24**, 512–528 (2020).

11. Wang, Z. *et al.* Toward safer solid-state lithium metal batteries: a review. *Nanoscale Adv.* **2**, 1828–1836 (2020).

12. Janek, J. & Zeier, W. G. A solid future for battery development. *Nat. Energy* **1**, 1–4 (2016).

13. Fan, L., Wei, S., Li, S., Li, Q. & Lu, Y. Recent Progress of the Solid-State Electrolytes for High-Energy Metal-Based Batteries. *Adv. Energy Mater.* **8**, 1702657 (2018).

14. Gao, Z. *et al.* Promises, Challenges, and Recent Progress of Inorganic Solid-State Electrolytes for All-Solid-State Lithium Batteries. *Adv. Mater.* **30**, 1705702 (2018).

15. Wang, Y. *et al.* Design principles for solid-state lithium superionic conductors. *Nat. Mater.* **14**, 1026–1031 (2015).

16. Sheng, O. *et al.* A Decade of Progress on Solid-State Electrolytes for Secondary Batteries: Advances and Contributions. *Adv. Funct. Mater.* **31**, 2100891 (2021).

17. Zhang, W., Nie, J., Li, F., Wang, Z. L. & Sun, C. A durable and safe solid-state lithium battery with a hybrid electrolyte membrane. *Nano Energy* **45**, 413–419 (2018).

18. Ma, Q. *et al.* Novel Li[(CF_3SO_2)(n-$C_4F_9SO_2$)N]-Based Polymer Electrolytes for Solid-State Lithium Batteries with Superior Electrochemical Performance. *ACS Appl. Mater. Interfaces* **8**, 29705–29712 (2016).

19. Liu, W. *et al.* LLZO@EmimFSI@PEO derived hybrid solid electrolyte for high-energy lithium metal batteries. *Mater. Technol.* **35**, 618–624 (2020).

20. Yang, C., Fu, K., Zhang, Y., Hitz, E. & Hu, L. Protected Lithium-Metal Anodes in Batteries: From Liquid to Solid. *Adv. Mater.* **29**, 1701169 (2017).

21. Yu, C. *et al.* Accessing the bottleneck in all-solid state batteries, lithium-ion transport over the solid-electrolyte-electrode interface. *Nat. Commun.* **8**, 1086 (2017).

22. Kamaya, N. *et al.* A lithium superionic conductor. *Nat. Mater.* **10**, 682–686 (2011).

23. Duan, Y. *et al.* Research progress and prospect in typical sulfide solid-state electrolytes. *J. Energy Storage* **55**, 105382 (2022).

24. Kato, Y. *et al.* High-power all-solid-state batteries using sulfide superionic conductors. *Nat. Energy* **1**, 1–7 (2016).

25. Ye, L. & Li, X. A dynamic stability design strategy for lithium metal solid state batteries. *Nature* **593**, 218–222 (2021).

26. Zahiri, B. *et al.* Revealing the role of the cathode–electrolyte interface on solid-state batteries. *Nat. Mater.* **20**, 1392–1400 (2021).

27. Xiao, Y. *et al.* Understanding interface stability in solid-state batteries. *Nat. Rev. Mater.* **5**, 105–126 (2020).

28. Zhang, X. *et al.* Self-Suppression of Lithium Dendrite in All-Solid-State Lithium Metal Batteries with Poly(vinylidene difluoride)-Based Solid Electrolytes. *Adv. Mater.* **31**, 1806082 (2019).

29. Zhou, L. *et al.* High areal capacity, long cycle life 4 V ceramic all-solid-state Li-ion batteries enabled by chloride solid electrolytes. *Nat. Energy* **7**, 83–93 (2022).

30. Aurbach, D., McCloskey, B. D., Nazar, L. F. & Bruce, P. G. Advances in understanding mechanisms underpinning lithium–air batteries. *Nat. Energy* **1**, 16128 (2016).

31. Aurbach, D., Zinigrad, E., Teller, H. & Dan, P. Factors Which Limit the Cycle Life of Rechargeable Lithium (Metal) Batteries. *J. Electrochem. Soc.* **147**, 1274 (2000).

32. J. Hu, J., K. Long, G., Liu, S., R. Li, G. & P. Gao, X. A LiFSI–LiTFSI binary-salt electrolyte to achieve high capacity and cycle stability for a Li–S battery. *Chem. Commun.* **50**, 14647–14650 (2014).

33. Liao, K. *et al.* Developing a "Water-Defendable" and "Dendrite-Free" Lithium-Metal Anode Using a Simple and Promising $GeCl_4$ Pretreatment Method. *Adv. Mater.* **30**, 1705711 (2018).

34. Lai, J. *et al.* Electrolytes for Rechargeable Lithium–Air Batteries. *Angew. Chem. Int. Ed.* **59**, 2974–2997 (2020).

35. Fu, J. *et al.* Lithium Nitrate Regulated Sulfone Electrolytes for Lithium Metal Batteries. *Angew. Chem.* **132**, 22378–22385 (2020).

36. Li, N.-W., Yin, Y.-X., Li, J.-Y., Zhang, C.-H. & Guo, Y.-G. Passivation of Lithium Metal Anode via Hybrid Ionic Liquid Electrolyte toward Stable Li Plating/Stripping. *Adv. Sci.* **4**, 1600400 (2017).

37. Zhang, Q.-K., Zhang, X.-Q., Yuan, H. & Huang, J.-Q. Thermally Stable and Nonflammable Electrolytes for Lithium Metal Batteries: Progress and Perspectives. *Small Sci.* **1**, 2100058 (2021).

38. Wang, Y., Sahadeo, E., Rubloff, G., Lin, C.-F. & Lee, S. B. High-capacity lithium sulfur battery and beyond: a review of metal anode protection

layers and perspective of solid-state electrolytes. *J. Mater. Sci.* **54**, 3671–3693 (2019).

39. Pang, Q., Liang, X., Kwok, C. Y. & Nazar, L. F. Advances in lithium–sulfur batteries based on multifunctional cathodes and electrolytes. *Nat. Energy* **1**, 1–11 (2016).

40. Liu, G., Sun, Q., Li, Q., Zhang, J. & Ming, J. Electrolyte Issues in Lithium–Sulfur Batteries: Development, Prospect, and Challenges. *Energy Fuels* **35**, 10405–10427 (2021).

41. Albertus, P., Babinec, S., Litzelman, S. & Newman, A. Status and challenges in enabling the lithium metal electrode for high-energy and low-cost rechargeable batteries. *Nat. Energy* **3**, 16–21 (2018).

42. Hong, H., Mohamad, N. A. R. C., Chae, K., Mota, F. M. & Kim, D. H. The lithium metal anode in Li–S batteries: challenges and recent progress. *J. Mater. Chem. A* **9**, 10012–10038 (2021).

43. LiSTAR - About the Project. *LiSTAR* https://www.listar.ac.uk/about.

44. Aurbach, D., McCloskey, B. D., Nazar, L. F. & Bruce, P. G. Advances in understanding mechanisms underpinning lithium–air batteries. *Nat. Energy* **1**, 1–11 (2016).

45. Qiao, Y. & Ye, S. Spectroscopic Investigation for Oxygen Reduction and Evolution Reactions on Carbon Electrodes in Li–O_2 Battery. *J. Phys. Chem. C* **120**, 8033–8047 (2016).

46. Xia, C. *et al.* Evolution of Li_2O_2 Growth and Its Effect on Kinetics of Li–O_2 Batteries. *ACS Appl. Mater. Interfaces* **6**, 12083–12092 (2014).

47. Bryantsev, V. S. *et al.* The Identification of Stable Solvents for Nonaqueous Rechargeable Li-Air Batteries. *J. Electrochem. Soc.* **160**, A160–A171 (2013).

48. Kwak, W.-J. *et al.* Lithium–Oxygen Batteries and Related Systems: Potential, Status, and Future. *Chem. Rev.* **120**, 6626–6683 (2020).

49. Thackeray, M. M., Wolverton, C. & Isaacs, E. D. Electrical energy storage for transportation—approaching the limits of, and going beyond, lithium-ion batteries. *Energy Environ. Sci.* **5**, 7854–7863 (2012).

50. McCloskey, B. D. *et al.* Combining Accurate O_2 and Li_2O_2 Assays to Separate Discharge and Charge Stability Limitations in Nonaqueous Li–O_2 Batteries. *J. Phys. Chem. Lett.* **4**, 2989–2993 (2013).

51. Liu, Z., De Jesus, L. R., Banerjee, S. & Mukherjee, P. P. Mechanistic Evaluation of Li_xO_y Formation on δ-MnO_2 in Nonaqueous Li–Air Batteries. *ACS Appl. Mater. Interfaces* **8**, 23028–23036 (2016).

52. McCloskey, B. D., Scheffler, R., Speidel, A., Girishkumar, G. & Luntz, A. C. On the Mechanism of Nonaqueous Li–O_2 Electrochemistry on C and Its Kinetic Overpotentials: Some Implications for Li–Air Batteries. *J. Phys. Chem. C* **116**, 23897–23905 (2012).

53. Gao, Z. *et al.* Recent Progress in Developing a LiOH-Based Reversible Nonaqueous Lithium–Air Battery. *Adv. Mater.* **35**, 2201384 (2023).

54. Lim, H.-D. *et al.* Superior Rechargeability and Efficiency of Lithium–Oxygen Batteries: Hierarchical Air Electrode Architecture Combined with a Soluble Catalyst. *Angew. Chem.* **126**, 4007–4012 (2014).

55. Temprano, I. *et al.* Toward Reversible and Moisture-Tolerant Aprotic Lithium-Air Batteries. *Joule* **4**, 2501–2520 (2020).

56. Lu, J. *et al.* Co_3O_4-Catalyzed LiOH Chemistry in Li–O_2 Batteries. *ACS Energy Lett.* **5**, 3681–3691 (2020).

57. Liu, T. *et al.* Cycling Li-O_2 batteries via LiOH formation and decomposition. *Science* **350**, 530–533 (2015).

58. Zhang, X., Dong, P. & Song, M.-K. Advances in Lithium–Oxygen Batteries Based on Lithium Hydroxide Formation and Decomposition. *Front. Chem.* **10**, (2022).

59. Kondori, A. *et al.* A room temperature rechargeable Li_2O-based lithium-air battery enabled by a solid electrolyte. *Science* **379**, 499–505 (2023).

60. Laoire, C. O., Mukerjee, S., Abraham, K. M., Plichta, E. J. & Hendrickson, M. A. Influence of Nonaqueous Solvents on the Electrochemistry of Oxygen in the Rechargeable Lithium−Air Battery. *J. Phys. Chem. C* **114**, 9178–9186 (2010).

61. Peng, Z. *et al.* Oxygen reactions in a non-aqueous Li^+ electrolyte. *Angew. Chem. Int. Ed.* **50**, 6351–6355 (2011).

62. Trahan, M. J., Mukerjee, S., Plichta, E. J., Hendrickson, M. A. & Abraham, K. M. Studies of Li-Air Cells Utilizing Dimethyl Sulfoxide-Based Electrolyte. *J. Electrochem. Soc.* **160**, A259 (2012).

63. Johnson, L. *et al.* The role of LiO_2 solubility in O_2 reduction in aprotic solvents and its consequences for Li–O_2 batteries. *Nat. Chem.* **6**, 1091–1099 (2014).

64. Pearson, R. G. Hard and Soft Acids and Bases. *J. Am. Chem. Soc.* **85**, 3533–3539 (1963).

65. Aetukuri, N. B. *et al.* Solvating additives drive solution-mediated electrochemistry and enhance toroid growth in non-aqueous Li–O_2 batteries. *Nat. Chem.* **7**, 50–56 (2015).

66. Lu, Y.-C. & Shao-Horn, Y. Probing the Reaction Kinetics of the Charge Reactions of Nonaqueous Li–O_2 Batteries. *J. Phys. Chem. Lett.* **4**, 93–99 (2012).

67. Gallant, B. M. *et al.* Influence of Li_2O_2 morphology on oxygen reduction and evolution kinetics in Li–O_2 batteries. *Energy Environ. Sci.* **6**, 2518–2528 (2013).

68. Wang, Y. *et al.* A Solvent-Controlled Oxidation Mechanism of Li_2O_2 in Lithium-Oxygen Batteries. *Joule* **2**, 2364–2380 (2018).

69. Black, R. *et al.* Screening for superoxide reactivity in Li-O_2 batteries: effect on Li_2O_2/LiOH crystallization. *J. Am. Chem. Soc.* **134**, 2902–2905 (2012).

70. Bryantsev, V. S. *et al.* Predicting Solvent Stability in Aprotic Electrolyte Li–Air Batteries: Nucleophilic Substitution by the Superoxide Anion Radical ($O_2^{\bullet-}$). *J. Phys. Chem. A* **115**, 12399–12409 (2011).

71. Lau, K. C., Lu, J., Luo, X., Curtiss, L. A. & Amine, K. Implications of the unpaired spins in Li-O_2 battery chemistry and electrochemistry: A minireview. *ChemPlusChem* **80**, 336–343 (2015).

72. Chau, V. K. C., Chen, Z., Hu, H. & Chan, K.-Y. Exploring Solvent Stability against Nucleophilic Attack by Solvated LiO_2^- in an Aprotic Li-O_2 Battery. *J. Electrochem. Soc.* **164**, A284 (2016).

73. Younesi, R., Hahlin, M., Björefors, F., Johansson, P. & Edström, K. Li–O_2 Battery Degradation by Lithium Peroxide (Li_2O_2): A Model Study. *Chem. Mater.* **25**, 77–84 (2012).

74. Laino, T. & Curioni, A. Chemical reactivity of aprotic electrolytes on a solid Li_2O_2 surface: screening solvents for Li–air batteries. *New J. Phys.* **15**, 095009 (2013).

75. Bryantsev, V. S., Blanco, M. & Faglioni, F. Stability of Lithium Superoxide LiO_2 in the Gas Phase: Computational Study of Dimerization and Disproportionation Reactions. *J. Phys. Chem. A* **114**, 8165–8169 (2010).

76. Dong, S. *et al.* Singlet oxygen and dioxygen bond cleavage in the aprotic lithium-oxygen battery. *Joule* **6**, 185–192 (2022).

77. Mahne, N. *et al.* Singlet oxygen generation as a major cause for parasitic reactions during cycling of aprotic lithium–oxygen batteries. *Nat. Energy* **2**, 17036 (2017).

78. Li, Y., Wang, X., Dong, S., Chen, X. & Cui, G. Recent Advances in Non-Aqueous Electrolyte for Rechargeable Li–O_2 Batteries. *Adv. Energy Mater.* **6**, 1600751 (2016).

79. Balaish, M., Kraytsberg, A. & Ein-Eli, Y. A critical review on lithium–air battery electrolytes. *Phys. Chem. Chem. Phys.* **16**, 2801 (2014).

80. Ogasawara, T., Debart, A., Holzapfel, M., Novak, P. & Bruce, P. G. Rechargeable Li_2O_2 electrode for lithium batteries. *J. Am. Chem. Soc.* **128**, 1390–1393 (2006).

81. Jiang, H. *et al.* Li-Ion solvation in propylene carbonate electrolytes determined by molecular rotational measurements. *Phys. Chem. Chem. Phys.* **21**, 10417–10422 (2019).

82. Sharon, D. *et al.* Oxidation of Dimethyl Sulfoxide Solutions by Electrochemical Reduction of Oxygen. *J. Phys. Chem. Lett.* **4**, 3115–3119 (2013).

83. Freunberger, S. A. *et al.* Reactions in the rechargeable lithium-O_2 battery with alkyl carbonate electrolytes. *J. Am. Chem. Soc.* **133**, 8040–8047 (2011).

84. Freunberger, S. A. *et al.* Reactions in the Rechargeable Lithium–O_2 Battery with Alkyl Carbonate Electrolytes. *J. Am. Chem. Soc.* **133**, 8040–8047 (2011).

85. Bryantsev, V. S. & Blanco, M. Computational Study of the Mechanisms of Superoxide-Induced Decomposition of Organic Carbonate-Based Electrolytes. *J. Phys. Chem. Lett.* **2**, 379–383 (2011).

86. Peng, Z., Freunberger, S. A., Chen, Y. & Bruce, P. G. A reversible and higher-rate Li-O_2 battery. *Science* **337**, 563–566 (2012).

87. Bardé, F. *et al.* Sulfone-Based Electrolytes for Nonaqueous Li–O_2 Batteries. *J. Phys. Chem. C* **118**, 18892–18898 (2014).

88. Mozhzhukhina, N., Méndez De Leo, L. P. & Calvo, E. J. Infrared Spectroscopy Studies on Stability of Dimethyl Sulfoxide for Application in a Li–Air Battery. *J. Phys. Chem. C* **117**, 18375–18380 (2013).

89. Mozhzhukhina, N. *et al.* Insights into dimethyl sulfoxide decomposition in Li-O_2 battery: Understanding carbon dioxide evolution. *Electrochem. Commun.* **80**, 16–19 (2017).

90. Kwabi, D. G. *et al.* Chemical Instability of Dimethyl Sulfoxide in Lithium–Air Batteries. *J. Phys. Chem. Lett.* **5**, 2850–2856 (2014).

91. G. Kwabi, D. *et al.* The effect of water on discharge product growth and chemistry in Li–O_2 batteries. *Phys. Chem. Chem. Phys.* **18**, 24944–24953 (2016).

92. Liang, C. *et al.* A stable electrolyte makes a nonaqueous Li–O_2 battery truly rechargeable. *New J. Chem.* **37**, 2568–2572 (2013).

93. Xu, D. *et al.* A stable sulfone based electrolyte for high performance rechargeable Li–O_2 batteries. *Chem. Commun.* **48**, 11674–11676 (2012).

94. Chen, Y., Freunberger, S. A., Peng, Z., Bardé, F. & Bruce, P. G. Li–O_2 Battery with a Dimethylformamide Electrolyte. *J. Am. Chem. Soc.* **134**, 7952–7957 (2012).

95. Walker, W. *et al.* A Rechargeable Li–O_2 Battery Using a Lithium Nitrate/N,N-Dimethylacetamide Electrolyte. *J. Am. Chem. Soc.* **135**, 2076–2079 (2013).

96. Bryantsev, V. S. *et al.* Investigation of Fluorinated Amides for Solid–Electrolyte Interphase Stabilization in Li–O_2 Batteries Using Amide-Based Electrolytes. *J. Phys. Chem. C* **117**, 11977–11988 (2013).

97. McCloskey, B. D. *et al.* Limitations in Rechargeability of Li-O_2 Batteries and Possible Origins. *J. Phys. Chem. Lett.* **3**, 3043–3047 (2012).

98. Chen, Y., Freunberger, S. A., Peng, Z., Bardé, F. & Bruce, P. G. Li–O_2 Battery with a Dimethylformamide Electrolyte. *J. Am. Chem. Soc.* **134**, 7952–7957 (2012).

99. Sharon, D. *et al.* Reactivity of Amide Based Solutions in Lithium–Oxygen Cells. *J. Phys. Chem. C* **118**, 15207–15213 (2014).

100. Sharon, D. *et al.* On the Challenge of Electrolyte Solutions for Li–Air Batteries: Monitoring Oxygen Reduction and Related Reactions in Polyether Solutions by Spectroscopy and EQCM. *J. Phys. Chem. Lett.* **4**, 127–131 (2012).

101. Jung, H.-G., Hassoun, J., Park, J.-B., Sun, Y.-K. & Scrosati, B. An improved high-performance lithium–air battery. *Nat. Chem.* **4**, 579–585 (2012).

102. Freunberger, S. A. *et al.* The lithium-oxygen battery with ether-based electrolytes. *Angew. Chem. Int. Ed.* **50**, 8609–8613 (2011).

103. Gao, X., Chen, Y., Johnson, L. R., Jovanov, Z. P. & Bruce, P. G. A rechargeable lithium–oxygen battery with dual mediators stabilizing the carbon cathode. *Nat. Energy* **2**, 17118 (2017).

104. Adams, B. D. *et al.* Towards a stable organic electrolyte for the Lithium oxygen battery. *Adv. Energy Mater.* **5**, 1400867 (2015).

105. Khetan, A., Pitsch, H. & Viswanathan, V. Solvent Degradation in Nonaqueous Li-O_2 Batteries: Oxidative Stability versus H-Abstraction. *J. Phys. Chem. Lett.* **5**, 2419–2424 (2014).

106. Sharon, D., Hirshberg, D., Afri, M., Frimer, A. A. & Aurbach, D. The importance of solvent selection in Li–O_2 cells. *Chem. Commun.* **53**, 3269–3272 (2017).

107. Younesi, R., Norby, P. & Vegge, T. A New Look at the Stability of Dimethyl Sulfoxide and Acetonitrile in Li-O_2 Batteries. *ECS Electrochem. Lett.* **3**, A15–A18 (2014).

108. McCloskey, B. D. *et al.* Limitations in Rechargeability of Li-O_2 Batteries and Possible Origins. *J. Phys. Chem. Lett.* **3**, 3043–3047 (2012).

109. McCloskey, B. D., Burke, C. M., Nichols, J. E. & Renfrew, S. E. Mechanistic insights for the development of Li-O_2 battery materials: addressing Li_2O_2 conductivity limitations and electrolyte and cathode instabilities. *Chem Commun Camb* **51**, 12701–12715 (2015).

110. Hase, Y. *et al.* Negative differential resistance as a critical indicator for the discharge capacity of lithium-oxygen batteries. *Nat. Commun.* **10**, 596 (2019).

111. Hase, Y. *et al.* Synergistic Effect of Binary Electrolyte on Enhancement of the Energy Density in Li–O_2 Batteries. *J. Phys. Chem. Lett.* **11**, 7657–7663 (2020).

112. Gao, X., Chen, Y., Johnson, L. & Bruce, P. G. Promoting solution phase discharge in Li-O_2 batteries containing weakly solvating electrolyte solutions. *Nat. Mater.* **15**, 882–888 (2016).

113. Chen, Y., Freunberger, S. A., Peng, Z., Fontaine, O. & Bruce, P. G. Charging a Li–O_2 battery using a redox mediator. *Nat. Chem.* **5**, 489–494 (2013).

114. Kundu, D., Black, R., Adams, B. & Nazar, L. F. A Highly Active Low Voltage Redox Mediator for Enhanced Rechargeability of Lithium–Oxygen Batteries. *ACS Cent. Sci.* **1**, 510–515 (2015).

115. Bergner, B. J., Schürmann, A., Peppler, K., Garsuch, A. & Janek, J. TEMPO: A Mobile Catalyst for Rechargeable Li-O_2 Batteries. *J. Am. Chem. Soc.* **136**, 15054–15064 (2014).

116. Bergner, B. J. *et al.* Understanding the fundamentals of redox mediators in Li–O_2 batteries: a case study on nitroxides. *Phys. Chem. Chem. Phys.* **17**, 31769–31779 (2015).

117. Liu, J. *et al.* An Organic Catalyst for Li-O_2 Batteries: Dilithium Quinone-1,4-Dicarboxylate. *ChemSusChem* **8**, 2198–2203 (2015).

118. Gallagher, K. G. *et al.* Quantifying the promise of lithium–air batteries for electric vehicles. *Energy Environ. Sci.* **7**, 1555 (2014).

119. Dai, A., Li, Q., Liu, T., Amine, K. & Lu, J. Fundamental Understanding of Water-Induced Mechanisms in Li–O_2 Batteries: Recent Developments and Perspectives. *Adv. Mater.* **31**, 1805602 (2019).

120. Geng, D. *et al.* From Lithium-Oxygen to Lithium-Air Batteries: Challenges and Opportunities. *Adv. Energy Mater.* **6**, 1502164 (2016).

121. Christensen, J. *et al.* A Critical Review of Li/Air Batteries. *J. Electrochem. Soc.* **159**, R1 (2011).

122. Schwenke, K. U., Metzger, M., Restle, T., Piana, M. & Gasteiger, H. A. The Influence of Water and Protons on Li_2O_2 Crystal Growth in Aprotic Li-O_2 Cells. *J. Electrochem. Soc.* **162**, A573–A584 (2015).

123. Qiao, Y. *et al.* From O_2^- to HO_2^-: Reducing By-Products and Overpotential in Li-O_2 Batteries by Water Addition. *Angew. Chem.* **129**, 5042–5046 (2017).

124. Policano, M. C., Anchieta, C. G., Nepel, T. C. M., Filho, R. M. & Doubek, G. Water in Aprotic Li-O_2 Batteries: A Critical Review. *ACS Appl. Energy Mater.* **5**, 9228–9240 (2022).

125. Meini, S. *et al.* Rechargeability of Li–air cathodes pre-filled with discharge products using an ether-based electrolyte solution: implications for cycle-life of Li–air cells. *Phys. Chem. Chem. Phys.* **15**, 11478–11493 (2013).

126. Guo, Z., Dong, X., Yuan, S., Wang, Y. & Xia, Y. Humidity effect on electrochemical performance of Li–O_2 batteries. *J. Power Sources* **264**, 1–7 (2014).

127. Zhang, T. & Zhou, H. A reversible long-life lithium–air battery in ambient air. *Nat. Commun.* **4**, 1817 (2013).

128. Li, F. *et al.* The water catalysis at oxygen cathodes of lithium–oxygen cells. *Nat. Commun.* **6**, 7843 (2015).

129. Ma, S., Wang, J., Huang, J., Zhou, Z. & Peng, Z. Unveiling the Complex Effects of H_2O on Discharge–Recharge Behaviors of Aprotic Lithium–O_2 Batteries. *J. Phys. Chem. Lett.* **9**, 3333–3339 (2018).

130. Shen, Z.-Z., Lang, S.-Y., Zhou, C., Wen, R. & Wan, L.-J. In Situ Realization of Water-Mediated Interfacial Processes at Nanoscale in Aprotic Li–O_2 Batteries. *Adv. Energy Mater.* **10**, 2002339 (2020).

131. Liu, T. *et al.* Understanding LiOH Chemistry in a Ruthenium-Catalyzed Li–O_2 Battery. *Angew. Chem. Int. Ed.* **56**, 16057–16062 (2017).

132. Matsui, M. *et al.* A novel aqueous lithium–oxygen cell based on the oxygen-peroxide redox couple. *Chem. Commun.* **51**, 3189–3192 (2015).

133. Andrieux, C. P., Hapiot, P. & Saveant, J. M. Mechanism of superoxide ion disproportionation in aprotic solvents. *J. Am. Chem. Soc.* **109**, 3768–3775 (1987).

134. Chin, D. H., Chiericato, G., Nanni, E. J. & Sawyer, D. T. Proton-induced disproportionation of superoxide ion in aprotic media. *J. Am. Chem. Soc.* **104**, 1296–1299 (1982).

135. Che, Y. *et al.* Water-Induced Disproportionation of Superoxide Ion in Aprotic Solvents. *J. Phys. Chem.* **100**, 20134–20137 (1996).

136. Holc, C. The effect of H_2O on O_2 reduction in Li-O_2 batteries. (University of Oxford, 2019).

Chapter 6. Hydroperoxide mediated degradation of acetonitrile in the lithium-air battery

6.1 Introduction

O_2 reduction in lithiated aqueous and non-aqueous solvents has been well explored.[1–3] In summary, O_2 reduction in Li^+-containing aprotic solutions proceeds via a $2e^-$ reduction to form lithium peroxide (Li_2O_2) and in aqueous systems proceeds via $4e^-$ reduction to form lithium hydroxide (LiOH) (equations 6.1 and 6.2).

$$2Li^+_{(sol)} + O_{2\,(sol)} + 2e^- \rightarrow Li_2O_{2\,(s)} \quad (6.1)$$

$$4Li^+_{(sol)} + O_{2\,(sol)} + 2H_2O_{(sol)} + 4e^- \rightarrow 4LiOH_{(sol)} \quad (6.2)$$

Although the majority of lithium-air (Li-air) research uses pure O_2 gas streams, it is widely accepted that some H_2O will inevitably be present in a practical Li-air battery, with even carefully assembled cells often containing 100-1000s of ppm H_2O.[4,5] The effect of introducing trace quantities of H_2O to aprotic Li-air electrolytes has attracted considerable research efforts due to the challenges associated with reducing H_2O concentration in ambient gas streams to levels representative of dry O_2 (H_2O <10 ppm).[4,6] Gallagher *et al.* reported that the weight penalty associated with such gas handling would reduce energy density by 33% at the system level.[4]

Early research suggested that the presence of H_2O in aprotic electrolytes introduces electrochemical LiOH formation, the oxidation of which requires high charge potentials (>4 V vs Li^+/Li), that induce electrochemical degradation of the carbon-based electrode, and generates hydroxyl free radicals that cause electrolyte decomposition.[7–9] However, more recent studies indicate that many solvents benefit from the presence of low concentrations of H_2O, which acts to facilitate solution phase growth of Li_2O_2 by establishing chemical equilibria that produce soluble hydroperoxide species (equations 6.3 and 6.4).[10–12]

$$Li_2O_{2\,(s)} + H_2O_{\,(sol)} \rightleftharpoons LiOOH_{\,(sol)} + LiOH_{\,(s)} \quad (6.3)$$

$$LiOOH_{\,(sol)} + H_2O_{\,(sol)} \rightleftharpoons H_2O_{2\,(sol)} + LiOH_{\,(s)} \quad (6.4)$$

In 2019, Holc demonstrated that the overall acceptor number of a H_2O-solvent mixture determines its ability to tolerate H_2O without initiating electrochemical LiOH formation, concluding that some Li-air electrolytes could in-fact tolerate ≥1 M H_2O while maintaining a 2 electron per molecule of oxygen (e^-/O_2) ratio, and exhibiting high Li_2O_2 yields, comparable to those of the analogous dry systems.[13]

Extensive efforts have been applied to understand electrolyte solution degradation mechanisms in the Li-air battery, and a number of antagonistic intermediates including lithium superoxide (LiO_2),[14,15] Li_2O_2,[16] polyoxides,[17,18] and singlet oxygen ($^1O_2$),[19] have been identified.[20,21] However, their specific roles remain an area of active debate. Early Li-air cells used organic carbonates and dimethyl sulfoxide,[22,23] but these were shown to be susceptible to degradation by the LiO_2 intermediate formed during discharge.[24,25] Amide and sulfone derived solvents were similarly shown to undergo oxidative degradation.[26–28] Glyme ether solvents are widely used in the literature due to their oxidative robustness, however they are proposed to undergo proton abstraction with LiO_2 and/or Li_2O_2,[29,30] and exhibit Li_2O_2 discharge yields <95%.[31,32]

Early studies showed that acetonitrile (MeCN) is stable towards Li_2O_2 with a relatively high activation barrier for nucleophilic attack and proton abstraction by O_2^-.[33–35] It has an oxygen solubility and diffusivity similar to glyme ethers, and its dielectric constant results in high ionic conductivity.[36] Furthermore, McCloskey *et al.* reported an e^-/O_2 ratio of 2.05 and the highest oxygen reduction/oxygen evolution reaction efficiency (ca. 0.9) of the electrolytes explored.[37,38] While promising, these results indicate that MeCN suffers from degradation reactions that are yet to be identified. Moreover, the capacity of MeCN electrolytes are limited by low LiO_2 solubility, which results in surface passivation at the positive electrode, and poor compatibility with metallic Li.

However, the use of redox mediators, which are routinely employed to facilitate solution-phase catalytic O_2 reduction,[39,40] and the advent of an artificial metallic Li solid electrolyte interphase,[41,42] have alleviated the requirements of high LiO_2 solubility and metallic Li compatibility.[6,31,43,44] Some recent studies have shown that MeCN-based cells can support significantly higher capacities than initially reported,[45,46] clearly justifying reassessment of MeCN as a potential Li-air electrolyte solvent.

In this chapter, I study the effect that H_2O has on the stability of Li-air cells containing MeCN-based electrolyte. I show that at high current density (250 μA cm^{-2}), often employed in literature to attain high power density,[31,47,48] MeCN performs comparably to the current state-of-the-art glyme ethers with ≤500 mM (9000 ppm) H_2O. Contrary to the findings reported by Kwabi *et al.*,[10] I show that electrochemical Li_2O_2 formation dominates at these H_2O concentrations, confirmed by high Li_2O_2 yields. However, at reduced current densities (50 μA cm^{-2}) deviation from the ideal $2e^-/O_2$ ratio and a simultaneous drop in the Li_2O_2 yield is observed. I identify a relationship between H_2O concentration and e^-/O_2, that indicates H_2O-mediated MeCN degradation. Model chemical systems are employed to replicate conditions within the cell, and chemical acetamide formation is confirmed as a degradation pathway. A reaction mechanism is proposed to account for the electrolyte degradation which identifies lithium hydroperoxide (LiOOH) as an antagonistic species in a Li-air cell for the first time. Critically, this degradation mechanism will be present in any Li-air cell containing MeCN where gas streams are not meticulously dried.

6.2 Experimental

6.2.1 Materials

MeCN (99.999%, Aldrich) was dried for several days over freshly activated molecular sieves (type 4 Å, Aldrich) before use. Lithium perchlorate ($LiClO_4$, 99.99%, Aldrich) was used as supplied without further purification. All electrolytes were prepared in an N_2-filled glovebox (MBRAUN, H_2O ≤0.1 ppm,

O_2 ≤0.1 ppm). H_2O content of the dry electrolyte was 4 ppm, determined by Karl-Fischer titration. Wet electrolyte solutions were prepared using deionised H_2O (18.2 MΩ cm, MilliQ). All cell components were dried at elevated temperature under vacuum and transferred to a N_2-filled glovebox without exposure to air. Further information regarding drying temperatures can be found in Chapter 2**.** All materials were prepared and stored in an N_2-filled glovebox prior to use.

Model chemical systems were prepared by mixing Li_2O_2 (10.7 mg, 95%, Acros) with deuterated acetonitrile (d_3-MeCN, ≥99.8 atom%D, Aldrich) and deionised H_2O to achieve a total mixture volume of 5 mL. This ratio of Li_2O_2 to solvent replicates the ratio of a 2 mAh discharge of a pressure cell containing 800 µL of electrolyte.

6.2.2 Pressure cell measurements

24 mm diameter Swagelok-type cells incorporating a pressure transducer (Omega Engineering) were used for *in situ* pressure analysis. Further details on cell design can be found in Chapter 2. Porous carbonaceous cathodes (H23, QuinTech) were paired with freestanding Li_xFePO_4 anodes (pre-oxidised to ca. 20% of total capacity) that were prepared by combining $LiFePO_4$ (MTI) with conductive carbon additive (Super P, Alfa Aesar) and 10 wt.% polytetrafluoroethylene in H_2O (Aldrich) in an 8:1:1 weight ratio. Two glass fibre separators (GF/F, Whatman) were used to separate the electrodes. Stainless steel mesh (316 grade, Advent) was placed on top of the cathode to ensure good electrical contact. The electrolyte volume was 800 µL. Prior to discharge, the cell headspace was sparged with O_2 (N5.5, BOC) for a total time of 3 minutes, alternating bypass and through cell to mitigate MeCN evaporation. The cell was discharged in an incubator at 20 °C. The cell volume was determined post-discharge for each measurement, further information on methodology can be found in Chapter 2. The H_2O concentration of dry MeCN cells was determined to be ca. 151 ppm through Karl-Fischer titration. 1600 µL of electrolyte was used in cells prepared for H_2O determination experiments.

The cells were allowed to rest at 20 °C for 72 hours before the excess electrolyte was extracted and analysed.

6.2.3 Li_2O_2 yield measurements

The quantity of Li_2O_2 formed was determined by UV-Vis spectrometry using a titration method reported previously, and described in detail in Chapter 2.[49,50] The cathode and separator were extracted from a discharged cell and added to a vial containing a known quantity of deionised H_2O. A known volume of this solution was then mixed in a 1:1 ratio with 2% titanium(IV) oxysulfate ($TiOSO_4$, Aldrich) in 1 M H_2SO_4 to achieve an optimum concentration of the coloured complex $[Ti(O_2)]^{2+}$ (λ_{max} = 405 nm) that is formed in the presence of H_2O_2. The UV-Vis absorption spectrum was measured and compared to a calibration fit. Further details can be found in Chapter 2.

6.2.4 NMR measurements

A syringe filter (0.2 µm, Fisher) was used to extract ca. 1 mL of mixture from model chemical systems into an airtight NMR tube fitted with a Young's tap (GPE Scientific). Time-resolved ^{1}H NMR was recorded on a Bruker Ascend 400 MHz spectrometer with 128 scans. The analyte was re-incorporated into the mixture after analysis. Model system acetamide and pure acetamide reference ^{1}H and ^{13}C NMR data were recorded on a Bruker AV(III)400 HD fitted with a 5mm BBFO probe. ^{1}H NMR were recorded at 400 MHz with 128 scans and ^{13}C NMR were recorded at 126 MHz with 16384 scans. Chemical shifts in ^{1}H and ^{13}C spectra were referenced to the residual (partially) non-deuterated solvent according to Fulmer *et al.*[51] Data was analysed on Bruker TopSpin software.

6.2.5 HPLC-MS measurements

Reference samples were prepared by mixing a small quantity of analyte with deionised H_2O. Where the analyte contained a liquid component, 200 µL of analyte was mixed with 800 µL of H_2O. Samples from the model chemical systems were prepared by extracting 200 µL of mixture using a syringe filter. For the sample prepared from an electrochemical cell, a cell discharged to 3.25 mAh cm^{-2} was disassembled in an N_2-filled glovebox and the cathode and

separator were extracted. The MeCN was allowed to evaporate before the components were mixed with 2 mL of deionised H_2O. The resultant suspension was extracted using a syringe filter. HPLC measurements were carried out on a Thermo Ultimate 3000 HPLC, equipped with a diode array detector capable of recording UV-Visible spectra from 190 – 800 nm. For HPLC-MS measurements, a Bruker microTOF II spectrometer with an electrospray ionisation source was connected to the HPLC outlet. 10 µL of sample was injected into an Accucore aQ (150 mm x 4.6 mm, 5 µm) column using MilliQ H_2O with 0.1% formic acid eluent at a constant flow rate of 0.5 mL min^{-1}. MS data was collected in positive mode between 3.4 – 5.0 minutes.

6.3 Determining the effect of H_2O on O_2 reduction

Parasitic (electro)chemical reactions typically reduce the consumption of O_2, leading to a higher e^-/O_2 ratio, e.g. 4 in the case of LiOH formation. The e^-/O_2 ratio can be determined *in-situ* using pressure cells, which I employ here over a range of H_2O concentrations up to 1 M. **Figure 6.1** shows a representative dataset from the first discharge of a pressure cell containing a dry MeCN-based electrolyte over the first mAh of capacity passed. An open circuit voltage (OCV) of 3.31 V vs Li^+/Li is observed for the cell at rest. Upon the application of current, rapid polarisation of the potential is observed as O_2 is reduced at the surface of the cathode, forming Li_2O_2. The potential stabilises between 2.51 – 2.44 V vs Li^+/Li, representing an ca. 0.50 V overpotential compared to the equilibrium potential for Li_2O_2 formation (2.96 V vs Li^+/Li). As solvated O_2 molecules are reduced, the electrolyte O_2 concentration drops below saturation. To account for this, O_2 molecules in the headspace of the cell are dissolved into the electrolyte, reducing the pressure of the headspace in accordance with the number of O_2 molecules reduced. These data taken together, enable a ratio of the number of electrons passed per molecule of O_2 consumed to be calculated.

Figure 6.2 shows the average e^-/O_2 and Li_2O_2 yields recorded for cells containing a MeCN-based electrolyte from dry to doped with 1 M H_2O, discharged to a capacity of 2 mAh at a current density of 250 µA cm^{-2}.

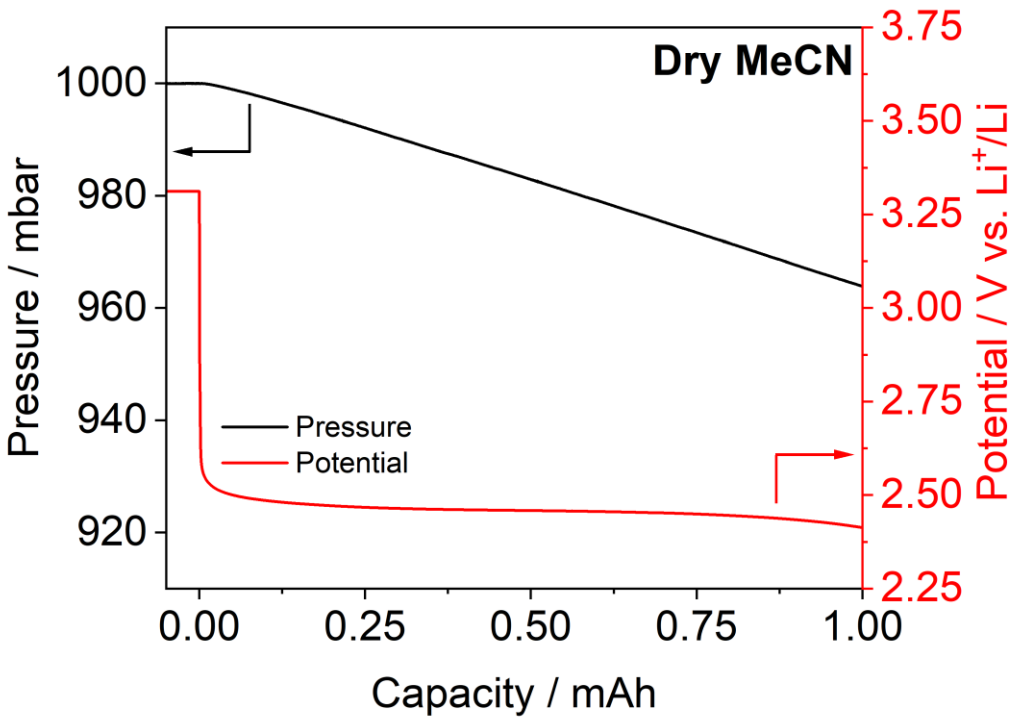


Figure 6.1. *Pressure decay (black line) and potential (red line) recorded during the discharge of a Li-air pressure cell at 250 µA cm^{-2} containing a 0.25 M $LiClO_4$ in dry MeCN electrolyte.*

Albeit limited by a discharge capacity of 1.19 mAh cm^{-2}, an e^-/O_2 ratio of 2.04 and a Li_2O_2 yield of 89.6% were recorded for the dry (151 ppm H_2O) electrolyte, in good agreement with previous reports.[37]

Shao-Horn and co-workers reported *ex situ* XRD analysis of discharged cathodes which indicated that LiOH is formed, as opposed to Li_2O_2, in an MeCN-based electrolyte doped with 275 mM (5000 ppm) H_2O,[10] proposing that this LiOH is formed electrochemically. Contrary to their findings, close to ideal e^-/O_2 ratios and high Li_2O_2 yields were recorded for all H_2O concentrations ≤500 mM, with average e^-/O_2 ratios of 2.04, 2.07, and 2.10 and Li_2O_2 yields of 89.2, 91.1, and 91.3% being recorded for doped H_2O concentration of 55 mM, 250 mM and 500 mM, respectively (**Figure 6.2**). Although the chemical equilibria described in equations 6.3 and 6.4 rationalise the detection of LiOH in *ex situ* analysis, the observed e^-/O_2 ratios and high Li_2O_2 yields obtained at H_2O concentrations ≤500 mM indicate that Li_2O_2 remains the dominant electrochemical product.

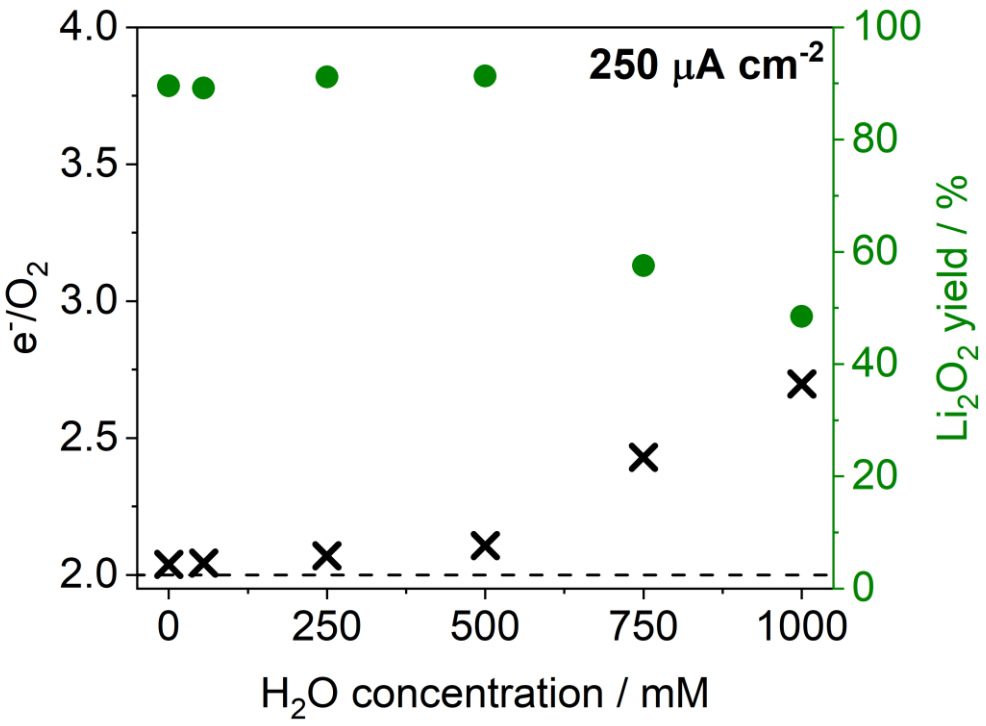


Figure 6.2. *Plot showing the effect of electrolyte H_2O concentration on e^-/O_2 ratio (black crosses) and Li_2O_2 yield (green circles) of Li-air cells. Cells were discharged at 250 μA cm^{-2} containing a 0.25 M $LiClO_4$ in MeCN electrolyte doped with the relevant H_2O concentration.*

Significant deviation from the ideal $2e^-/O_2$ ratio is observed above 500 mM H_2O, with average e^-/O_2 ratios of 2.43 and 2.70 being recorded for doped H_2O concentrations of 750 mM and 1000 mM, respectively (**Figure 6.2**). This sharp increase in e^-/O_2 ratio is indicative of the onset of parasitic electrochemical reactions that either reduce the quantity of O_2 consumed, i.e. $4e^-$ O_2 reduction to form LiOH, or result in the release of gaseous products, i.e. electrolyte degradation. In the case that electrochemical formation of both Li_2O_2 and LiOH are favourable, an e^-/O_2 ratio between 2 and 4 will be observed. At these H_2O concentrations, it is likely that the electrochemical formation of LiOH is the primary contributor. A simultaneous drop in Li_2O_2 yield, to 55.4 and 48.0% at 750 mM and 1000 mM, respectively, supports this conclusion (**Figure 6.2**). These data indicate that, contrary to previous reports, at high rates MeCN-based electrolytes can tolerate ≤500 mM H_2O (ca. 9000 ppm) while maintaining Li_2O_2 as the primary electrochemical product.

The high discharge rate employed in **Figure 6.2** results in a total experimental time of ca. 106 minutes. Although such rates are required to deliver high power output, a short experimental time carries the risk of masking underlying degradation pathways that are slow over this timescale but cumulative in nature, thus becoming significant over the lifetime of a practical Li-air cell. To explore the effect of rate on the performance of these cells, a cell containing dry electrolyte was discharged under analogous conditions to those described in **Figure 6.2**, with a reduced current density of 50 μA cm^{-2}. **Figure 6.3** compares the voltage profile and pressure decay gradients of cells discharged at 250 μA cm^{-2} and 50 μA cm^{-2} with dry electrolyte. These data clearly show the difference between the rate of O_2 consumption in the dry cells, with the cell discharged at 250 μA cm^{-2} adhering closely to the 2.0e^-/O_2 reference line and the analogous cell discharged at 50 μA cm^{-2} deviating marginally from it.

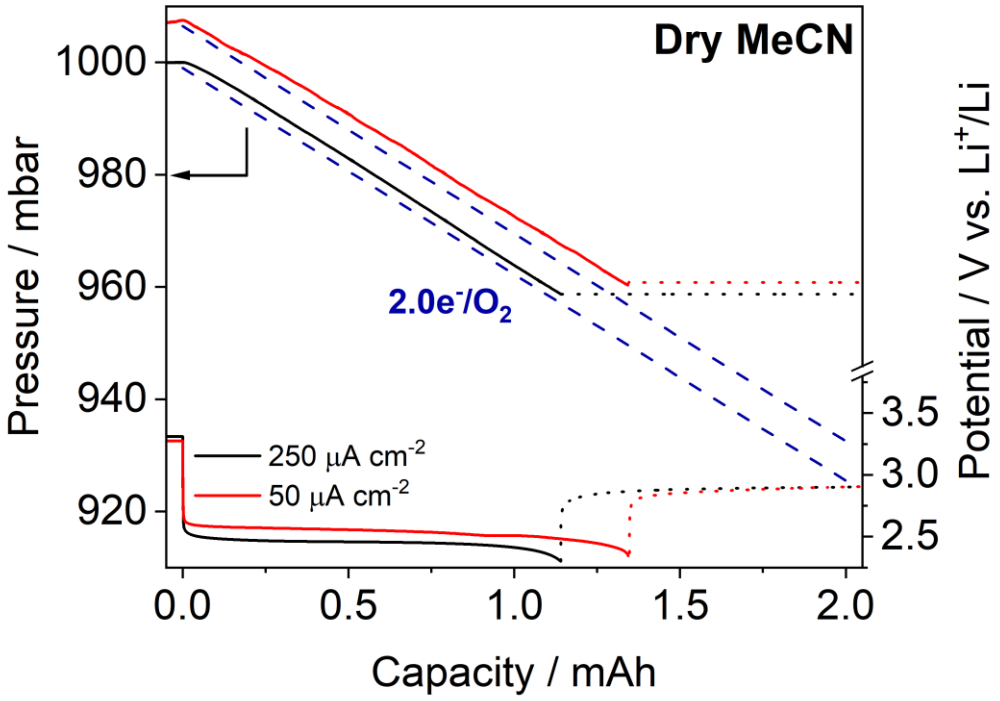


Figure 6.3. *Plot comparing the O_2 consumption of dry Li-air pressure cells when discharged at 250 (black lines) or 50 μA cm^{-2} (red lines). Cells were discharged containing a 0.25 M $LiClO_4$ in dry MeCN electrolyte to a potential limit of 2.3 V vs Li^+/Li. Ideal 2.0e^-/O_2 reference lines (blue dashed lines) are shown for clarity. Dotted lines indicate OCV after the potential limit is reached.*

It is evident that high discharge rates mask degradation processes that are revealed when discharge rate is reduced. To fully understand the effect of H_2O in MeCN-based electrolytes, the average e^-/O_2 and Li_2O_2 yields were recorded for cells discharged under analogous conditions to those described in **Figure 6.2**, with the applied current density reduced to 50 μA cm^{-2} (**Figure 6.4**). The cell containing dry electrolyte attained average e^-/O_2 and Li_2O_2 yield values of 2.14 and 85.9%, respectively. At H_2O concentrations >500 mM a sharp increase in e^-/O_2 is observed, with cells containing 750 mM and 1000 mM H_2O achieving average e^-/O_2 ratios of 2.75 and 3.16, respectively, accompanied by a significant drop in Li_2O_2 yields. This distinct region of increasing e^-/O_2 ratio is seen in cells discharged at both 250 μA cm^{-2} and 50 μA cm^{-2} and is often attributed in literature to the onset of electrochemical LiOH formation.

However, the e^-/O_2 trend with ≤500 mM H_2O differs from that seen in the cells discharged at high rate (**Figure 6.4**). A correlation between increasing H_2O

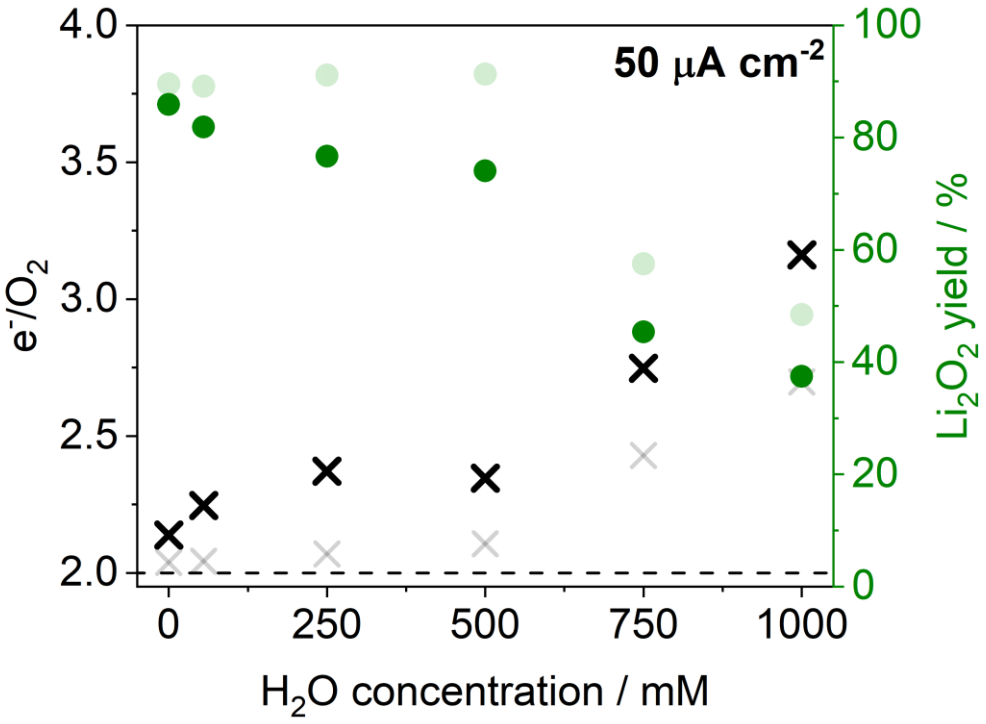


Figure 6.4. *Plot comparing the effect of electrolyte H_2O concentration on e^-/O_2 ratio (black crosses) and Li_2O_2 yield (green circles) of Li-air cells when discharged at either 250 (faded shapes) or 50 μA cm^{-2} (filled shapes). Cells contained a 0.25 M $LiClO_4$ in MeCN electrolyte, doped with the relevant H_2O concentration.*

concentration and increase in e^-/O_2 ratio is observed, with doped H_2O concentrations of 55 mM, 250 mM and 500 mM achieving e^-/O_2 ratios of 2.25, 2.37, and 2.35, respectively. Below 500 mM H_2O, electrochemical Li_2O_2 formation should be dominant, thus these results indicate that the presence of H_2O induces parasitic reactions that are masked at high discharge rates. Although the magnitude of this increase is non-linear, the relationship between H_2O concentration and e^-/O_2 ratio is especially clear at low (<250 mM) concentrations.

Since these results indicate that H_2O may induce electrolyte degradation reactions below the H_2O concentration necessary for significant electrochemical LiOH formation, I sought to understand whether these reactions would occur under conditions representative of a practical Li-air cell. Given that carefully assembled Li-air cells are known to contain some H_2O, a doped H_2O concentration of 1000 ppm (55 mM) was chosen to represent a practical Li-air cell.[4,5]

Figure 6.5 compares the voltage profile and pressure decay gradients of cells discharged at 250 μA cm^{-2} and 50 μA cm^{-2} containing electrolyte doped with 1000 ppm (55 mM) H_2O. In good agreement with the dry electrolyte, the pressure decay observed in the cell discharged at 250 μA cm^{-2} was comparable to the $2.0e^-/O_2$ reference line which, if taken in isolation, would indicate that no degradation is occurring at this H_2O concentration. However, the pressure decay gradient of the cell discharged at 50 μA cm^{-2} has increased compared to the cell containing dry electrolyte, from 2.18 to 2.25 e^-/O_2 (**Figure 6.3** and **Figure 6.5**). These data show a correlation between increasing H_2O concentration and deviation from ideal $2e^-/O_2$ Li_2O_2 formation.

To rule out electrochemical LiOH formation as the exclusive cause of this deviation, and explore the formation of soluble degradation species, a cell doped with 1000 ppm H_2O was discharged at 50 μA cm^{-2} to an extended capacity of 14.7 mAh (**Figure 6.6**). Electrochemical O_2 reduction to form LiOH in the presence of H_2O proceeds via a $4e^-$ O_2 reduction pathway as shown in equation 6.2. However, due to low solubility of LiOH in organic solvents, the

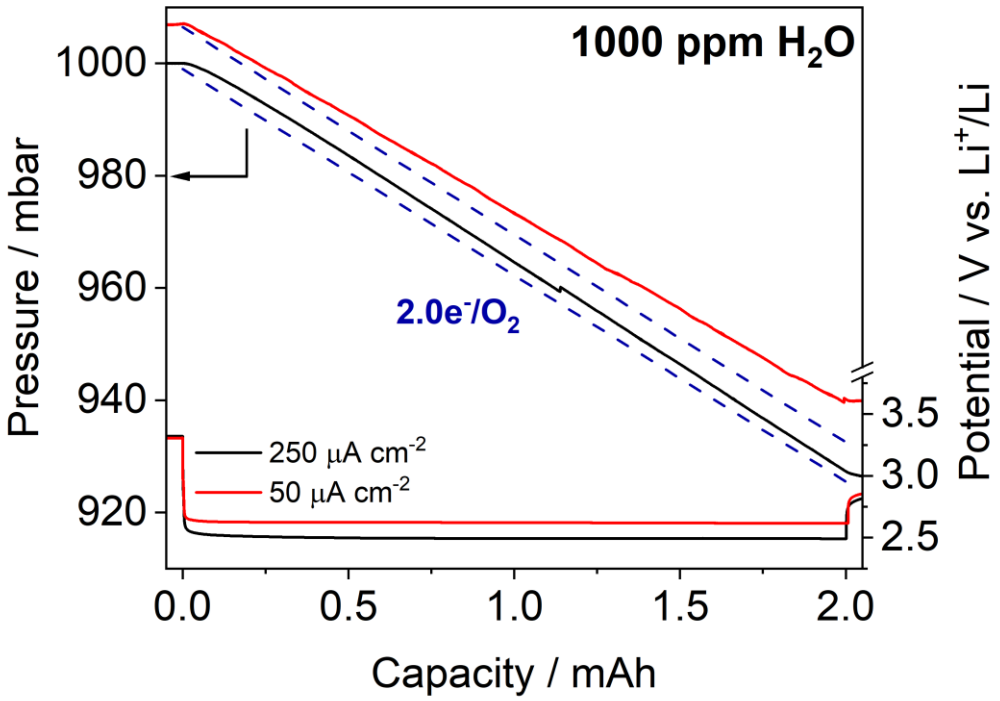


Figure 6.5. *Plot comparing the O_2 consumption in H_2O-doped Li-air pressure cells when discharged at 250 (black lines) or 50 μA cm^{-2} (red lines). Cells were discharged containing a 0.25 M $LiClO_4$ in MeCN electrolyte doped with 1000 ppm H_2O. Ideal 2.0e^-/O_2 reference lines (blue dashed lines) are shown for clarity.*

product may precipitate on the surface of the electrode as a monohydrate salt ($LiOH.H_2O$).[6,52] Therefore, if H_2O was consumed in the formation of LiOH, then the gradient of the pressure decay should vary throughout the experiment as H_2O decreases, eventually returning to the ideal 2e^-/O_2 gradient once all of the H_2O has been consumed. In reality, a constant discharge gradient of 2.22e^-/O_2 is observed, confirming that the deviation from the ideal pressure gradient cannot exclusively be the result of H_2O induced LiOH formation.

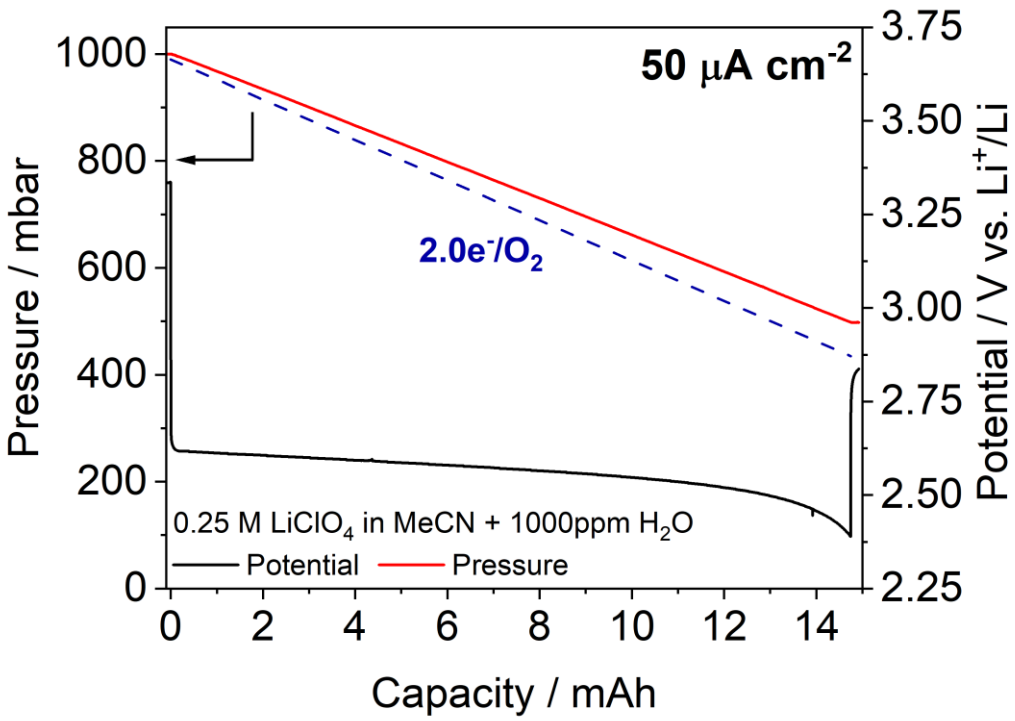


Figure 6.6. *Plot showing the non-ideal O_2 consumption of a H_2O-doped Li-air pressure cell discharged for 14.7 mAh (3.25 mAh cm^{-2}) at a rate of 50 μA cm^{-2}. The cell was discharged containing a 0.25 M $LiClO_4$ in MeCN electrolyte doped with 1000 ppm H_2O. An ideal 2.0e^-/O_2 reference line (blue dashed line) is shown for clarity.*

6.4 HPLC-MS study of electrolyte composition

The deviation from the 2e^-/O_2 gradient coincides with low Li_2O_2 yield, indicating that Li_2O_2 is involved in a degradation reaction. Although Li_2O_2 has negligible solubility, and has been shown to be stable in the presence of MeCN,[33] H_2O can introduce hydroperoxide species (equations 6.3 and 6.4) that could act as a solution phase nucleophile. The hydrolysis of molecules containing nitrile groups under hydroperoxide conditions have been previously reported in organic literature.[53–56] In these reactions, nucleophilic addition of hydroperoxide to the nitrile group results in the formation of an amide, with the release of O_2 and H_2O (equation 6.5).

$$RCN_{(l)} + 2H_2O_{2\,(sol)} \rightarrow RCONH_{2\,(l)} + O_{2\,(sol)} + H_2O_{(sol)} \qquad (6.5)$$

Thus the chemical hydroperoxide equilibria present in H_2O-containing Li-air cells represent conditions for solution degradation of MeCN to produce

acetamide. A HPLC method was developed to ascertain whether acetamide, or any other soluble degradation products, form in the electrolyte when Li_2O_2, MeCN and H_2O are all present. **Figure 6.7** shows the chromatograms produced by injecting 10 µL from a variety of reference samples with an eluent of H_2O doped with 0.1 vol.% formic acid. When pure H_2O was analysed, a minor peak with a retention time of 2.65 minutes and two negative regions of absorbance at retention times of 3.15 and 3.28 minutes were observed (**Figure 6.7**a). A reference UV-Vis spectrum is recorded at the start of each measurement, which is used as a baseline to determine regions of analyte activity. The peaks observed in the H_2O reference sample are the result of a dilution of the formic acid concentration as the injected H_2O passes through the system. These peaks should be considered to contribute to all further chromatograms recorded.

Figure 6.7b and c show the chromatograms produced when samples of H_2O doped with MeCN and $LiClO_4$ were injected, respectively. The same peak seen in the pure H_2O sample at 3.28 minutes is observed in each of these chromatograms, confirming that this is an artifact of the H_2O carrier solvent. Two additional peaks are observed in the MeCN doped samples (**Figure 6.7**b). The first comes before the H_2O peak and has a retention time of 3.14 minutes. The second comes after the H_2O peak, with a small peak observed at 3.56 minutes and a subsequent broad region of negative activity after 3.95 minutes. It is worth noting that the peak position and profile of the MeCN peaks varied considerably depending on injection volume. The sample doped with $LiClO_4$ absorbed strongly before the H_2O peak, with a distinct peak observed at a retention time of 2.61 minutes and broad activity between 2.69 – 3.21 minutes (**Figure 6.7**c). The perchlorate anion absorbs low wavelength UV, and the lithium cation may interact with H_2O resulting in a complex chromatogram.[57] No activity was observed after the H_2O peak, indicating that all of the $LiClO_4$ has been passed through the column.

Figure 6.7d shows the chromatogram recorded when H_2O doped with the dry electrolyte was injected into the column. The distinctive peaks of $LiClO_4$, MeCN

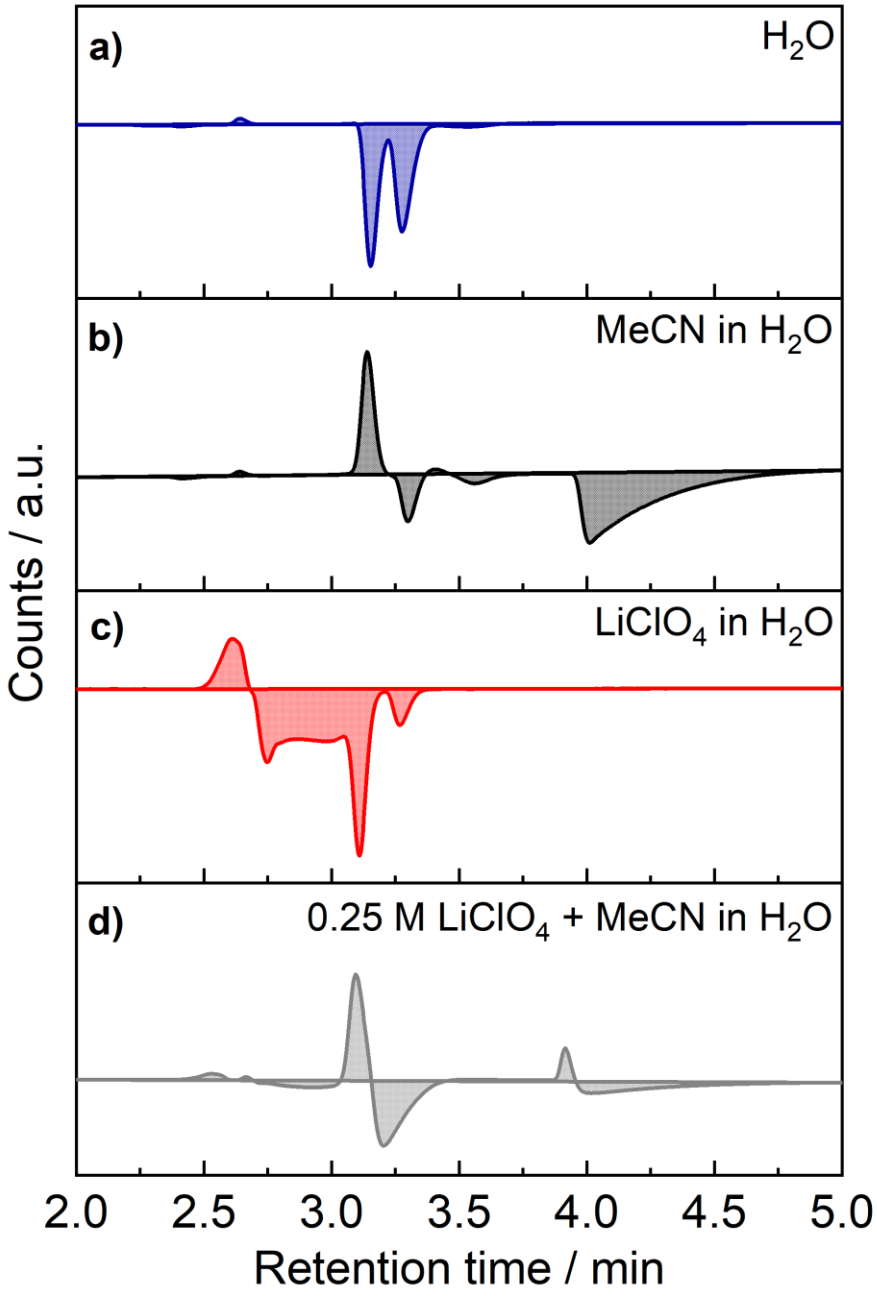


Figure 6.7. *Reference HPLC chromatograms of solutions of H_2O doped with a) no dopant, b) MeCN, c) $LiClO_4$, or d) 0.25 M $LiClO_4$ in MeCN.*

and H_2O can be seen before 3.5 minutes, with a new peak at a retention time of 3.92 minutes and subsequent broad region of baseline diversion being attributed to MeCN. To determine whether HPLC would be a suitable technique for the detection of amides, a sample of H_2O doped with MeCN, $LiClO_4$ and acetamide was injected into the HPLC column (**Figure 6.8**). This chromatogram revealed an additional peak at 3.52 minutes, a retention time where no other components have activity. The adequate separation of acetamide from the electrolyte components indicated that development of a HPLC-MS technique was possible.

A HPLC-MS method was developed to analyse species with retention times between 3.4 – 5.0 minutes using a mass spectrometer to confirm the identity of any degradation product. The reference solution containing acetamide was analysed and a mass spectrum consistent the m/z regions of the hydrogen adduct of the acetamide molecule and dimerised acetamide was attained at a retention time of 3.5 minutes (**Figure 6.9**). Acetamide is known to dimerise, or cluster, under mass spectrometer conditions as a result of the strong

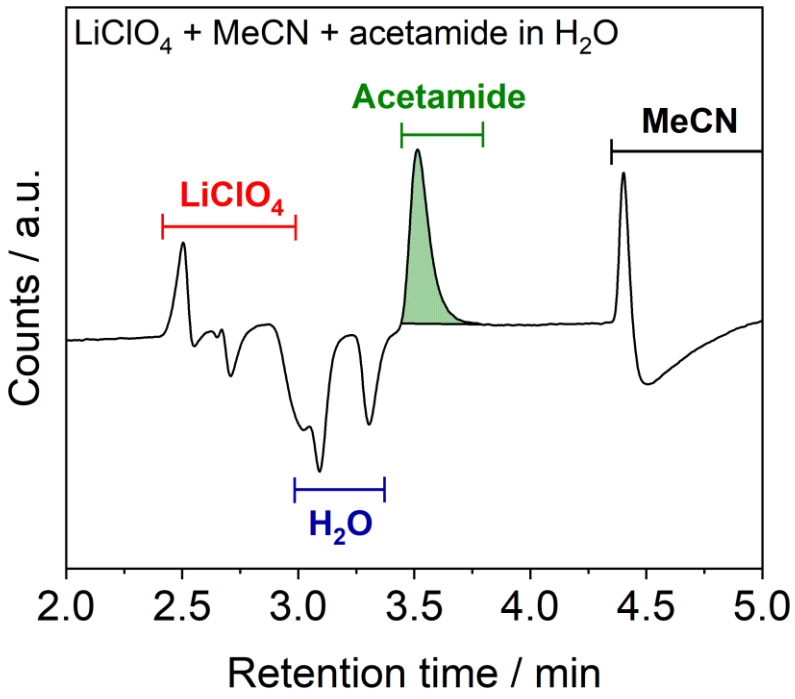


Figure 6.8. *Reference HPLC chromatogram of a solution of H_2O doped with MeCN, $LiClO_4$, and acetamide.*

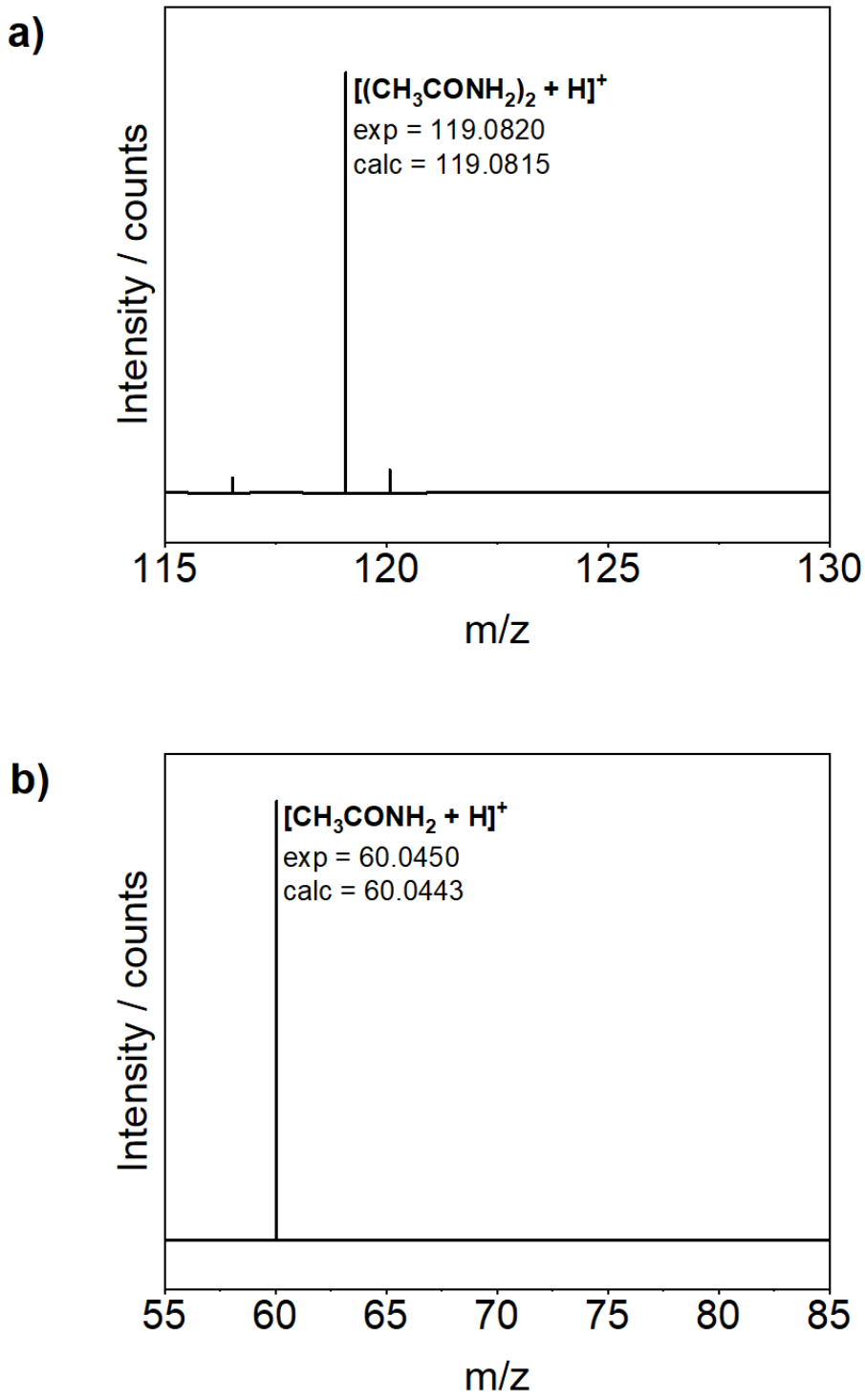


Figure 6.9. *Identification of the hydrogen adduct of an a) acetamide dimer and b) acetamide molecule through HPLC-MS analysis of a solution of H_2O doped with MeCN, $LiClO_4$, and acetamide. The spectrum was recorded at a retention time of 3.5 minutes to isolate the chromatogram peak of acetamide.*

hydrogen bonding environment of the amide group.[58] This was confirmed in the sample, where the primary mass peak was the hydrogen adduct of the acetamide dimer, observed at 119.1 m/z (**Figure 6.9**a). Although the hydrogen adduct of the acetamide molecule was also observed, at 60.0 m/z, the relative peak intensity was significantly lower, with ca. 200 counts recorded for this peak (**Figure 6.9**b). The low intensity of this signal explains the absence of an isotope pattern, which would be below the limit of detection.

To check the discharged electrolyte for soluble degradation products, the developed HPLC-MS method was conducted on the electrolyte extracted from the pressure cell shown in **Figure 6.6**, which was discharged to 14.7 mAh containing 1000 ppm H_2O to allow the accumulation of soluble degradation species. **Figure 6.10**a shows the HPLC chromatogram of the extracted electrolyte, where regions representative of $LiClO_4$, H_2O and MeCN can all be identified. A peak at a retention time of 3.41 minutes was also observed, which matches well with the retention time of the doped acetamide reference sample. The identity of this peak was confirmed to be acetamide through analysis of the mass spectrum recorded at 3.5 minutes, which revealed the hydrogen adduct and the lithium adduct of the acetamide dimer as the primary mass peaks (**Figure 6.10**b). These data confirm that acetamide is formed during the discharge of a Li-air cell containing an MeCN-based electrolyte doped with 1000 ppm H_2O. However, whether the formation pathway is chemical or electrochemical is yet to be determined.

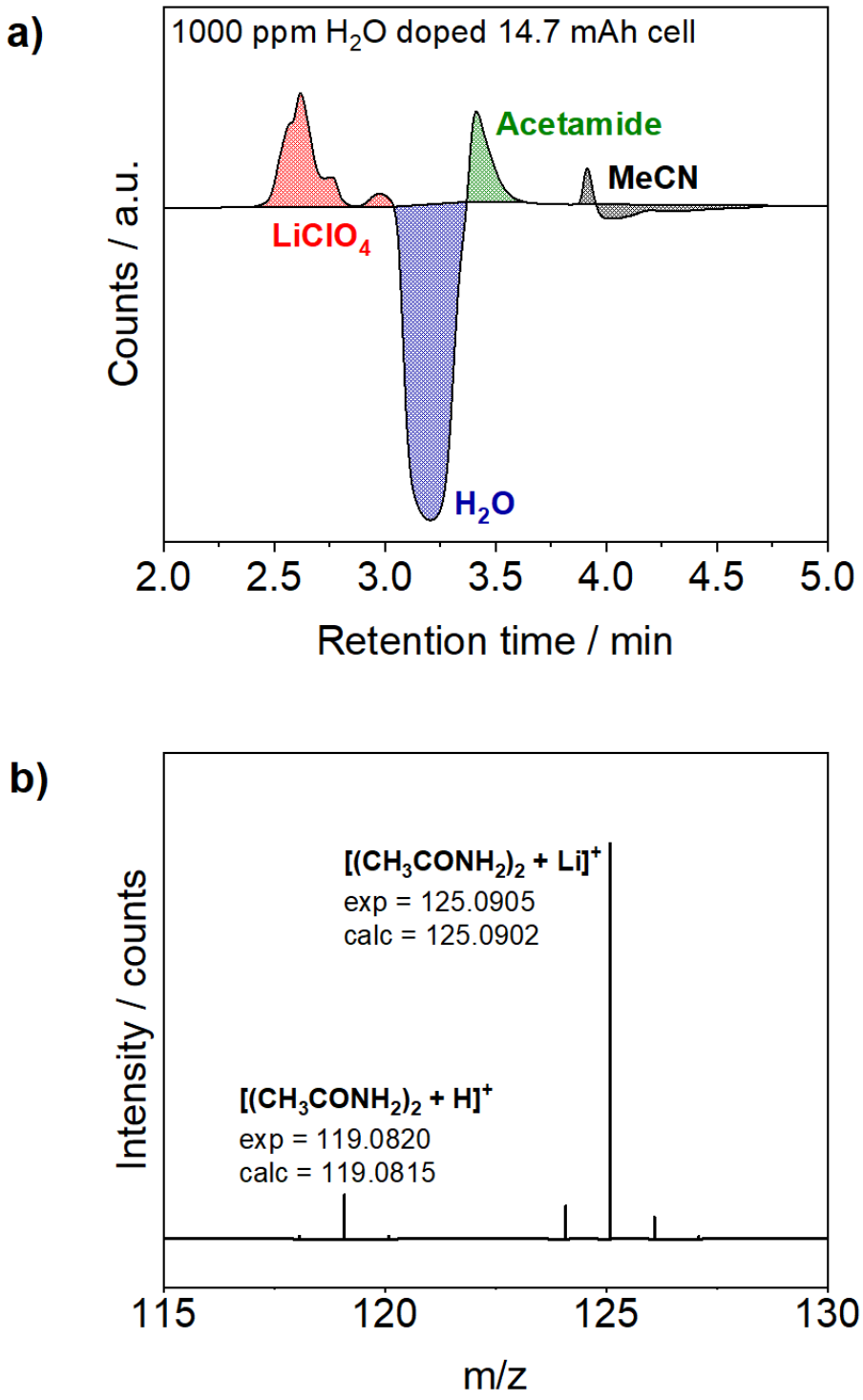


Figure 6.10. *a) HPLC chromatogram and b) MS recorded at a retention time of 3.5 minutes of a solution of electrolyte extracted from a H_2O-containing Li-air cell discharged to 14.7 mAh at a rate of 50 μA cm^{-2}. These data confirm acetamide formation under operational conditions in a Li-air cell.*

6.5 Spectroscopic exploration of model chemical systems

To determine whether acetamide forms chemically under the conditions present in a discharged Li-air cell, model chemical systems were developed to simulate the cell environment without any electrochemical bias. A heterogeneous mixture containing the mass equivalent ratio of 2 mAh of Li_2O_2 in d_3-MeCN was doped with 1000 ppm H_2O. Time-resolved ^1H NMR spectra were obtained over the course of the first 24 hours after mixing, wherein an extreme loss of intensity of the H_2O peak is observed in the first hour, and the signal is almost completely quenched after 24 hours (**Figure 6.11**), demonstrating that H_2O reacts in the model system without an applied bias.

If the presence of H_2O is the key determinant of chemical acetamide formation, increasing the concentration of H_2O will increase the quantity of acetamide formed in the model chemical system. An analogous mixture doped with 1 M H_2O was used to test this hypothesis, with time-resolved ^1H NMR being recorded over the first 72 hours after mixing (**Figure 6.12**). In agreement with

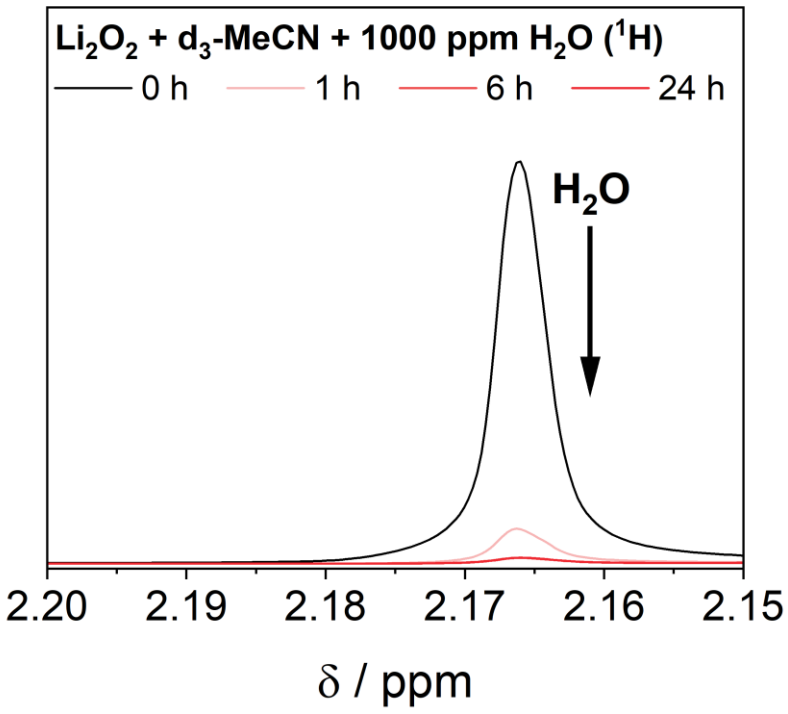


Figure 6.11. *Time-resolved ^1H NMR spectra showing the change in the H_2O peak intensity over the first 24 hours after doping a heterogeneous mixture of Li_2O_2 in d_3-MeCN with 1000 ppm H_2O.*

the 1000 ppm system, a drop in the ^{1}H signal for H_2O is observed across the timeframe of these measurements (**Figure 6.12**a). 1 hour after mixing, a new ^{1}H environment is observed in the form of two low intensity singlets at 5.74 and 6.35 ppm (**Figure 6.12**b), consistent with an amide (NH_2) group. The intensity of these signals continues to increase over the timeframe of the experiment, indicating that the concentration of the contributing species is increasing.

To confirm that this signal is the result of acetamide formation, reference ^{1}H and ^{13}C NMR consisting of acetamide dissolved in d_3-MeCN were prepared. **Figure 6.13** shows the acetamide reference spectra alongside data collected by extracting the analyte from the doped 1 M H_2O model system 72 hours after mixing. For ^{13}C NMR, the solution was concentrated through evaporation of excess MeCN before analysis. Broadening of the NH_2 signal is observed as the result of the presence of H_2O in the analyte sample (**Figure 6.13**a). Both the carbonyl (C=O) and NH_2 groups can participate in hydrogen bonding with H_2O molecules, with the downfield shift experienced here being the result of H_2O hydrogen-bonding with the NH_2 protons, thus deshielding them.

^{13}C NMR of the sample showed a singlet at 173.8 ppm, indicative of a sp^2 hybridised carbon, and a septet at 21.6 ppm, assigned to the methyl carbon of d_3-acetamide (**Figure 6.13**b). Although the spectra were run proton decoupled, deuterium decoupling is non-trivial, resulting in the latter signal being split into a septet through deuterium coupling. Splitting is determined by the 2n + 1 rule, where n is the spin state of the coupling atom in question. Deuterium possesses a nuclear spin of 1, double that of a proton, causing a splitting of 6 + 1, resulting in a septet. The downfield shift experienced by this ^{13}C peak is the result of hydrogen bonding between H_2O molecules and the C=O group, drawing electron density from the oxygen atom, which consequently draws electron density from the bonded carbon atom, deshielding it. An aliquot from both model systems was extracted and analysed through HPLC-MS 72 hours after mixing (**Figure 6.14**). Although the acetamide peak was absent in the chromatogram of the system doped with 1000 ppm H_2O, the superior sensitivity of mass spectrometry enabled identification of acetamide at

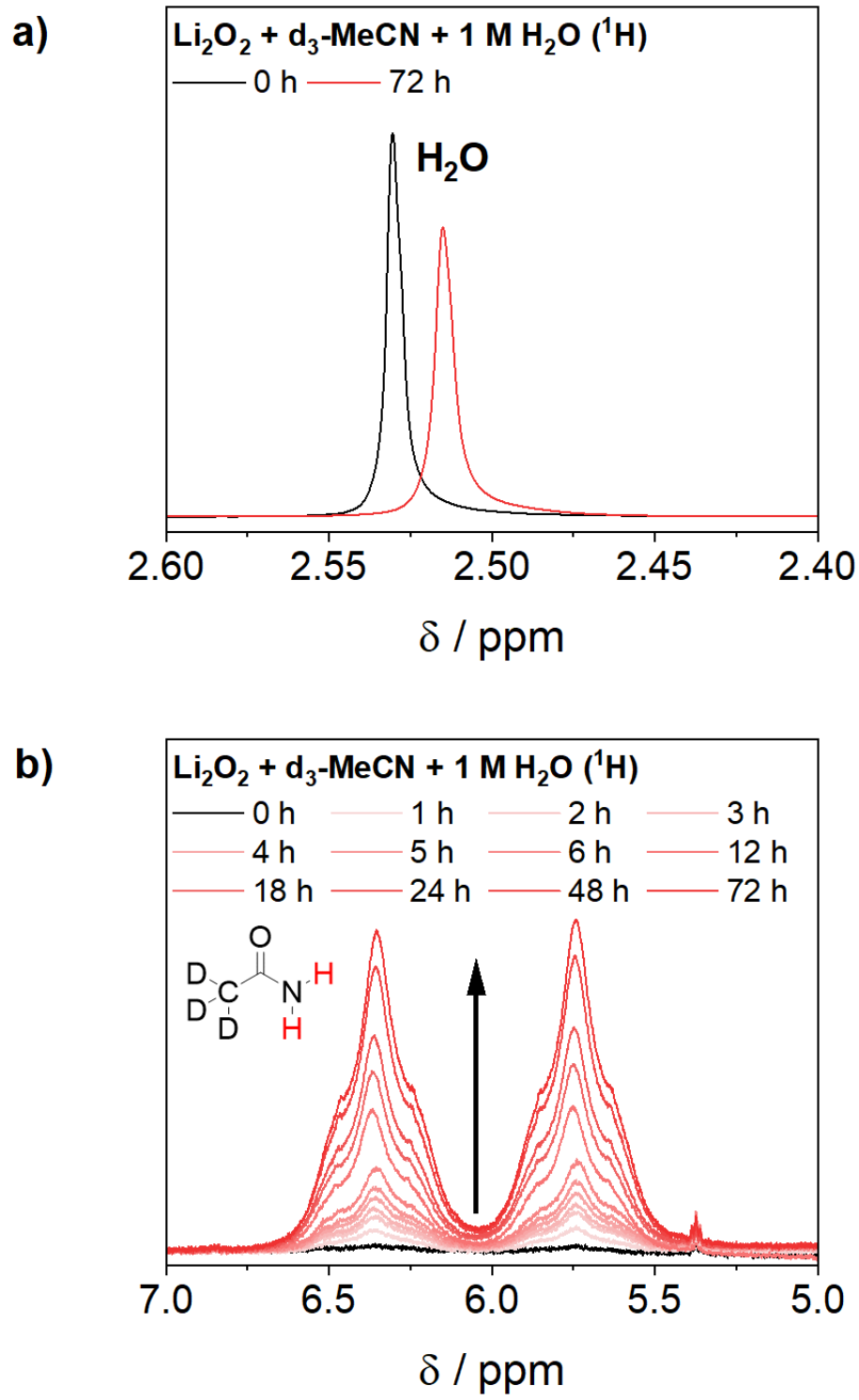


Figure 6.12. *a) H_2O and b) acetamide N-H regions of ^1H NMR spectra taken of a heterogeneous mixture of Li_2O_2 in d_3-MeCN doped with 1 M H_2O over the first 72 hours after mixing. Consumption of H_2O and formation of acetamide are shown.*

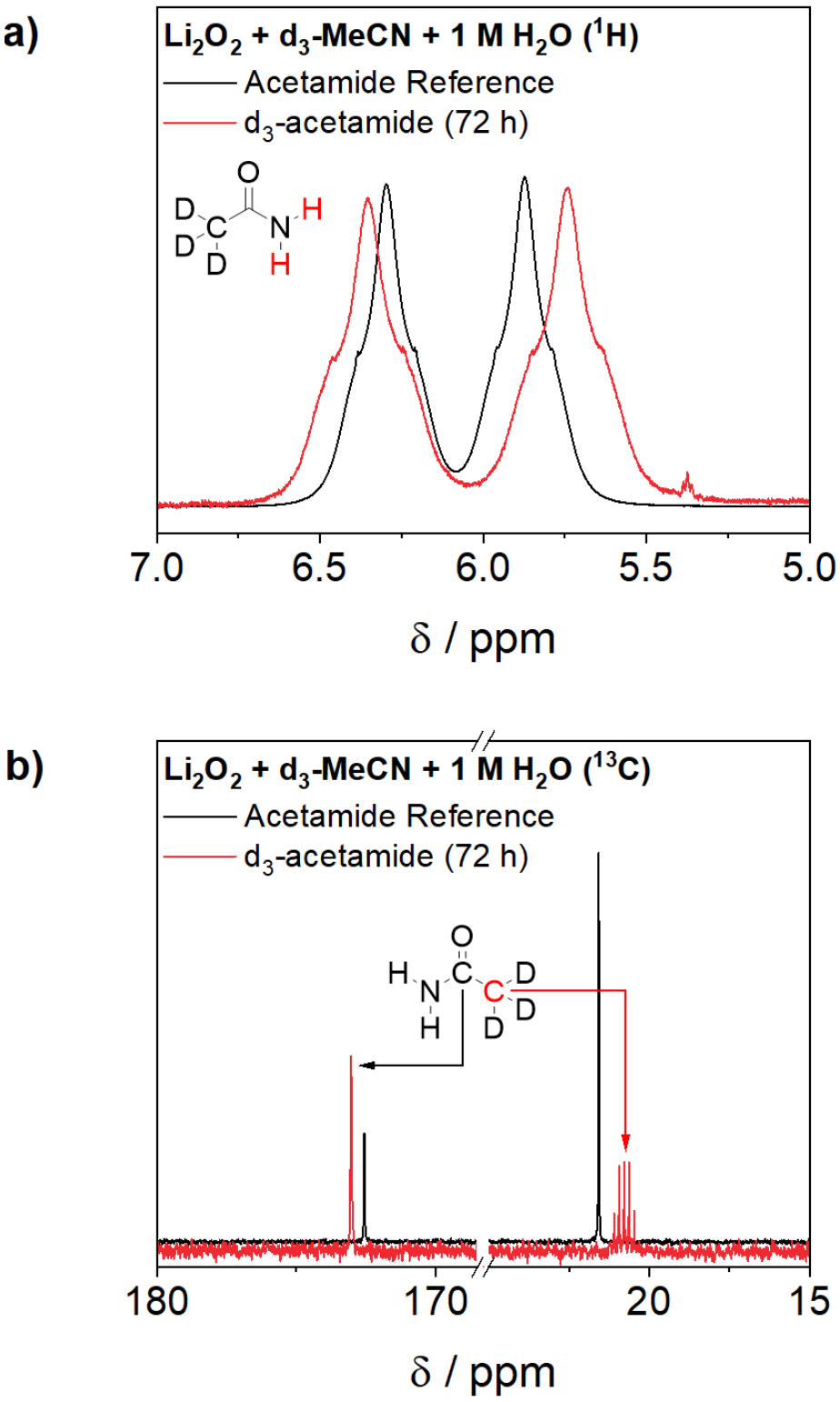


Figure 6.13. *Plot comparing the a) ^{1}H and b) ^{13}C NMR spectra of an acetamide reference (black lines) to a heterogeneous mixture of Li_2O_2 in d_3-MeCN doped with 1 M H_2O 72 hours after mixing (red lines) confirming the degradation product as acetamide.*

3.5 minutes with m/z values of 119.1 and 122.1, corresponding to the hydrogen adduct acetamide dimer ($[CH_3CONH_2 + H]^+$) and a dimer of one deuterated acetamide molecule and one protonated acetamide molecule ($[(CH_3CONH_2)(CD_3CONH_2) + H]^+$), respectively (**Figure 6.14**b). The presence of H_2O in the electrolyte will enable proton-deuteron exchange between the H_2O and the d_3-MeCN and acetamide.

In the system doped with 1 M H_2O, and in good agreement with the ^1H NMR data presented in **Figure 6.12**b, a distinct peak with a retention time of 3.48 minutes was observed and assigned to acetamide (**Figure 6.14**a). This is further confirmed by the presence of all molecular and dimer hydrogen adducts in the mass spectrum recorded at 3.5 minutes (**Figure 6.15**).

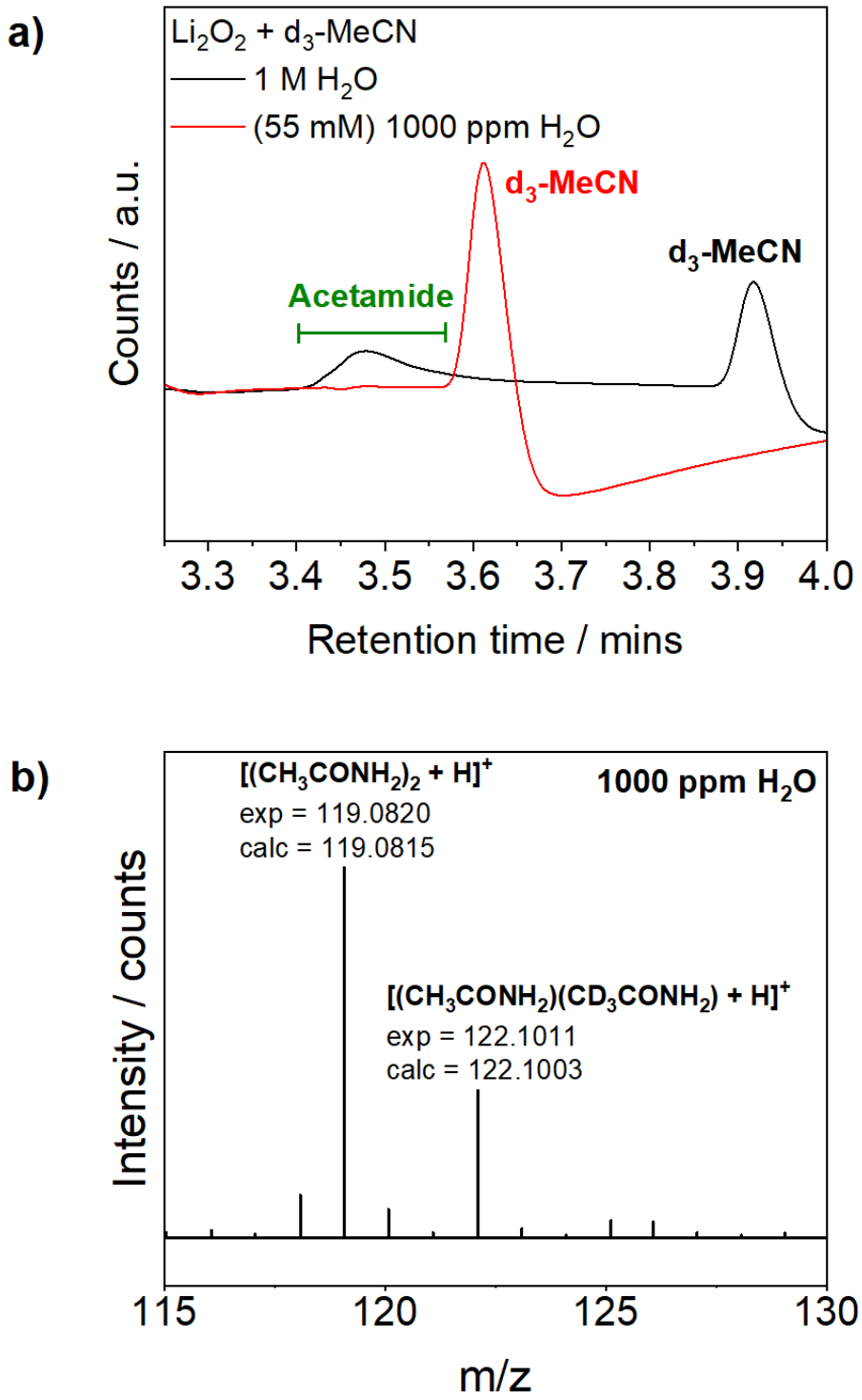


Figure 6.14. *a) HPLC chromatograms and b) MS recorded at a retention time of 3.5 minutes of heterogenous mixtures of Li_2O_2 in d_3-MeCN doped with either 1 M (black line) or 55 mM (red line) H_2O. The presence of the hydrogen and deuterium adducts of an acetamide dimer confirm chemical acetamide formation even when beyond the limit of detection of HPLC.*

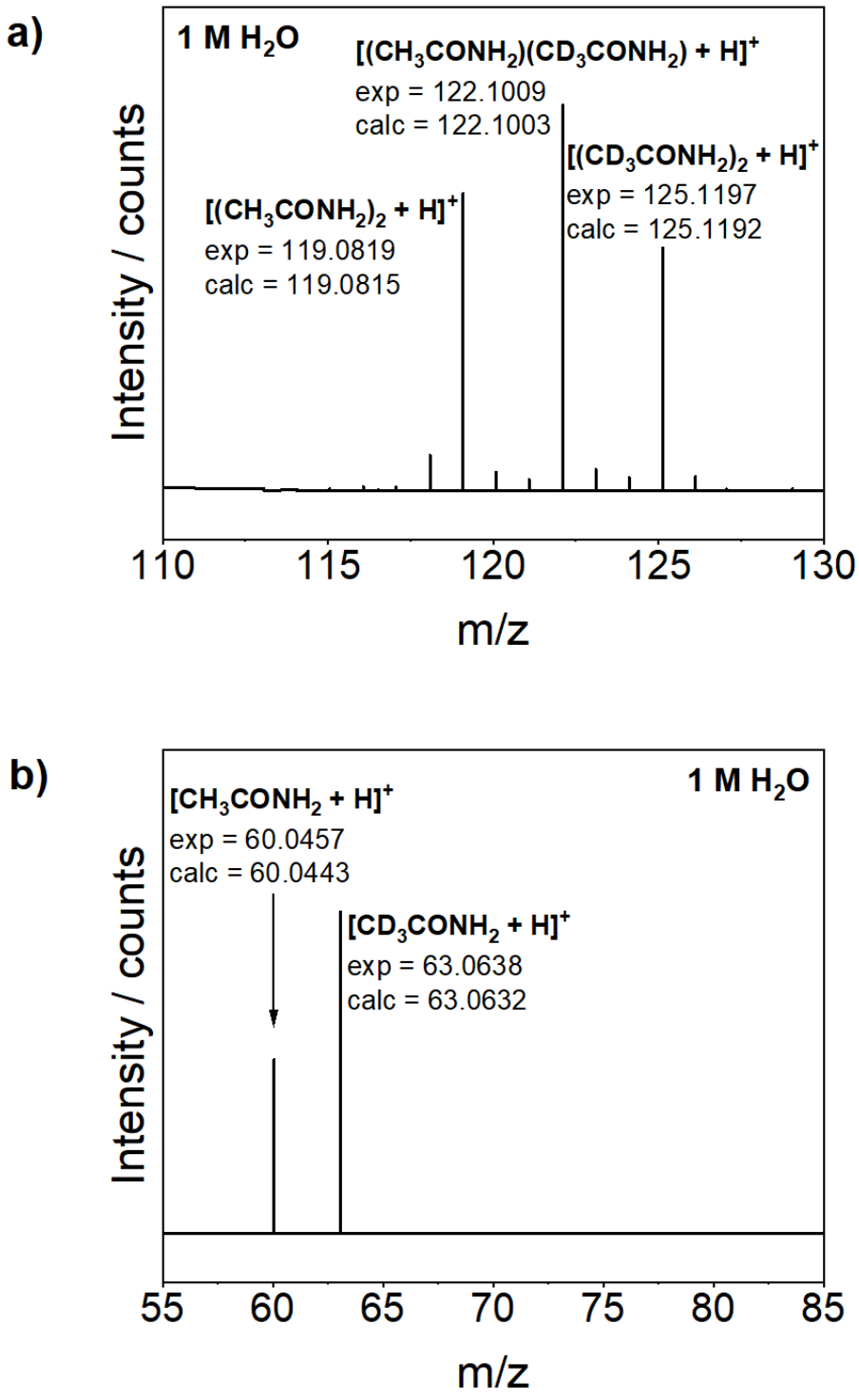


Figure 6.15. *Identification of hydrogen and deuterium adducts of an a) acetamide dimer and b) acetamide molecule through HPLC-MS analysis recorded at a retention time of 3.5 minutes of heterogenous mixtures of Li_2O_2 in d_3-MeCN doped with 1 M H_2O.*

6.6 Proposed hydroperoxide mediated MeCN degradation pathway

The detection of acetamide in both model systems and electrochemical cells supports my hypothesis that MeCN hydrolysis occurs under the conditions present during discharge. Previous computational studies have shown that the nitrile group can interact strongly with exposed lithium ions on the Li_2O_2 surface, or solvated lithium cations, resulting in activation of the nitrile bond.[59,60] Despite this, these studies conclude that no substantial degradation of aliphatic nitriles will occur from peroxide nucleophilic addition due to the mild nature of the nucleophilic interaction between the carbon of the nitrile group and the oxygen of the solid peroxide, confirming the stability reported in literature.[33,61]

However, these models consider an anhydrous system wherein all Li_2O_2 exists as a solid and no soluble nucleophiles are present. This assumption does not apply where gas stream purification is imperfect and trace H_2O is present, resulting in the formation of soluble hydroperoxide species via the chemical equilibria established in equations 6.3 (lithium hydroperoxide, LiOOH) and, if the H_2O concentration is sufficient, 6.4 (hydrogen peroxide, H_2O_2). As previously discussed, these soluble nucleophiles represent alkaline hydroperoxide conditions reported for the conversion of nitriles to amides in organic solvents,[53–56] but this has never been reported as a degradation mechanism in Li-air cell chemistries. I now propose a MeCN degradation pathway (**Figure 6.16**), which requires Li_2O_2, H_2O and MeCN to be simultaneously present for the reaction to occur. First, H_2O chemically reacts with Li_2O_2 generating LiOOH, which can be considered as a distinct Li^+ cation and hydroperoxyl (HOO^-) anion. Interaction between an MeCN molecule and the surface of a Li_2O_2 particle results in activation of the sp-hybridised carbon,[59,60] facilitating nucleophilic addition of HOO^- to the weakened nitrile bond generating an intermediate adsorbed amide **1**. Although this reaction will be in equilibrium, protonation of the adsorbed amide, likely by H_2O, and consequent desorption from the surface as imidoperoxic acid **2** will drive the equilibrium in favour of the amide product. Subsequent reaction with a second

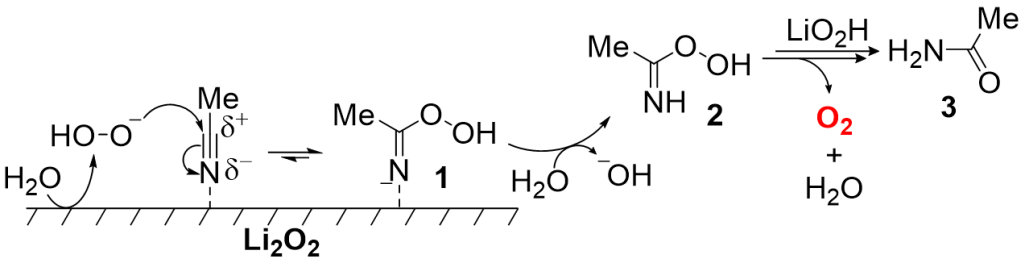


Figure 6.16. *Proposed degradation pathway of MeCN by LiOOH in a H_2O-containing Li-air system, mediated by solid phase Li_2O_2.*

HOO^- nucleophile generates acetamide (**3**), releasing H_2O and O_2 as the by-products. The release of O_2 in this degradation pathway rationalises the observed deviation from the ideal $2e^-/O_2$ gradient observed in the pressure cells.

While this degradation mechanism has been considered with respect to MeCN in this study, I highlight the fact that the mechanism is general and thus will operate with any electrolyte composition containing nitrile groups or particularly electrophilic functionalisation, as described in the general reaction scheme reported in literature (**Figure 6.17**).[54–56] Which places a fundamental restriction on the design of cells using nitriles.

Where trace H_2O is present in the electrolyte of a closed system it will be consumed in the degradation of MeCN until the electrolyte is effectively dry. However, in a practical Li-air battery, with continuous flow of a H_2O-containing gas stream, continual replenishment of H_2O would result in the unabating hydrolysis of MeCN. This result rules out nitrile containing molecules for use in Li-air batteries unless gas streams are meticulously dried.

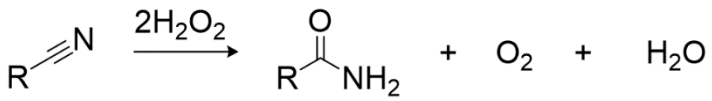


Figure 6.17. *General reaction scheme for nitrile hydrolysis under hydrogen peroxide conditions.*[54–56]

6.7 Conclusions

In this chapter, I evaluated the electrochemical discharge products of MeCN cells at high rates (250 μA cm^{-2}) commonly employed in literature. I revealed that, contrary to previous reports, MeCN-based electrolytes can maintain dominant electrochemical formation of Li_2O_2 with H_2O concentration as high as 500 mM, supported by an e^-/O_2 ratio close to 2 and high Li_2O_2 yields. When cells were discharged with more than 500 mM H_2O, significant deviation from the ideal $2e^-/O_2$ ratio and simultaneous reduction in Li_2O_2 yield were observed, indicating the onset of electrochemical LiOH formation.

To search for further degradation reactions that could be masked by the short experimental times of high-rate discharge (ca. 106 minutes), the discharge rate of cells was reduced to 50 μA cm^{-2}. Although the same sharp increase in e^-/O_2 ratio and drop in Li_2O_2 was revealed above 500 mM H_2O, a new region of degradation was revealed with H_2O concentration ≤500 mM that indicated a relationship between H_2O concentration and increased e^-/O_2 ratio and indicated a parasitic reaction involving H_2O.

To search the electrolyte for soluble degradation products, a HPLC-MS method was developed. A cell containing MeCN-based electrolyte doped with 1000 ppm H_2O was discharged to a capacity of 14.7 mAh (55 mM) H_2O before the electrolyte was extracted and analysed, revealing the formation of acetamide. To determine if acetamide formation was chemical or electrochemical, model chemical systems were prepared by mixing Li_2O_2 with d_3-MeCN and either 1000 ppm or 1 M H_2O. NMR and HPLC-MS analysis of these model systems confirmed the chemical formation of acetamide without an applied electrochemical bias.

I propose a new degradation pathway for MeCN by nucleophilic addition of the soluble LiOOH antagonistic intermediate species, introduced by H_2O-mediated chemical equilibria. This species will inevitably be present in a practical Li-air battery unless gas streams are meticulously dried and the 33% system level weight penalty as a result of this is accepted. The hydroperoxide conditions that

I propose represent reaction conditions for the hydrolysis of nitriles reported in organic literature and are applicable to a wide variety of nitrile containing molecules.

This work highlights the antagonistic role of hydroperoxide species that will inevitably be introduced by H_2O-containing Li-air gas streams. If suitable electrolytes are to be designed for practical Li-air batteries, the presence of hydroperoxide species should be recognised, and their reactivity with potential molecular electrolyte candidates (solvents, redox mediators, solid electrolytes) must be carefully considered.

6.8 References

1. Imanishi, N. & Yamamoto, O. Rechargeable lithium–air batteries: characteristics and prospects. *Mater. Today* **17**, 24–30 (2014).

2. Laoire, C. O., Mukerjee, S., Abraham, K. M., Plichta, E. J. & Hendrickson, M. A. Elucidating the mechanism of oxygen reduction for Lithium-air battery applications. *J. Phys. Chem. C* **113**, 20127–20134 (2009).

3. Laoire, C. O., Mukerjee, S., Abraham, K. M., Plichta, E. J. & Hendrickson, M. A. Influence of nonaqueous solvents on the electrochemistry of oxygen in the rechargeable lithium-air battery. *J. Phys. Chem. C* **114**, 9178–9186 (2010).

4. Gallagher, K. G. *et al.* Quantifying the promise of lithium–air batteries for electric vehicles. *Energy Environ. Sci.* **7**, 1555–1563 (2014).

5. Kang, J.-H. *et al.* Lithium–Air Batteries: Air-Breathing Challenges and Perspective. *ACS Nano* **14**, 14549–14578 (2020).

6. Liu, T. *et al.* Current Challenges and Routes Forward for Nonaqueous Lithium–Air Batteries. *Chem. Rev.* **120**, 6558–6625 (2020).

7. Ottakam Thotiyl, M. M., Freunberger, S. A., Peng, Z. & Bruce, P. G. The Carbon Electrode in Nonaqueous Li–O_2 Cells. *J. Am. Chem. Soc.* **135**, 494–500 (2013).

8. Liu, T. *et al.* Cycling Li-O_2 batteries via LiOH formation and decomposition. *Science* **350**, 530–533 (2015).

9. Zhang, X. *et al.* Unravelling the Complex LiOH-Based Cathode Chemistry in Lithium–Oxygen Batteries. *Angew. Chem. Int. Ed.* **62**, e202212942.

10. Kwabi, D. G. *et al.* The effect of water on discharge product growth and chemistry in Li–O_2 batteries. *Phys Chem Chem Phys* **18**, 24944–24953 (2016).

11. Qiao, Y. *et al.* From O_2^- to HO_2^-: Reducing By-Products and Overpotential in Li-O_2 Batteries by Water Addition. *Angew. Chem. - Int. Ed.* **56**, 4960–4964 (2017).

12. Gasteiger, H. A., Piana, M., Restle, T., Metzger, M. & Schwenke, K. U. The Influence of Water and Protons on Li_2O_2 Crystal Growth in Aprotic Li-O_2 Cells. *J. Electrochem. Soc.* **162**, A573–A584 (2015).

13. Holc, C. The effect of H_2O on O_2 reduction in Li-O_2 batteries. (University of Oxford, 2019).

14. Black, R. *et al.* Screening for superoxide reactivity in Li-O_2 batteries: effect on Li_2O_2/LiOH crystallization. *J. Am. Chem. Soc.* **134**, 2902–2905 (2012).

15. Zhang, X. *et al.* LiO_2: Cryosynthesis and Chemical/Electrochemical Reactivities. *J. Phys. Chem. Lett.* **8**, 2334–2338 (2017).

16. Younesi, R., Hahlin, M., Björefors, F., Johansson, P. & Edström, K. Li–O_2 Battery Degradation by Lithium Peroxide (Li_2O_2): A Model Study. *Chem. Mater.* **25**, 77–84 (2012).

17. Bryantsev, V. S., Blanco, M. & Faglioni, F. Stability of Lithium Superoxide LiO_2 in the Gas Phase: Computational Study of Dimerization and Disproportionation Reactions. *J. Phys. Chem. A* **114**, 8165–8169 (2010).

18. Dong, S. *et al.* Singlet oxygen and dioxygen bond cleavage in the aprotic lithium-oxygen battery. *Joule* **6**, 185–192 (2022).

19. Mahne, N. *et al.* Singlet oxygen generation as a major cause for parasitic reactions during cycling of aprotic lithium–oxygen batteries. *Nat. Energy* **2**, 17036 (2017).

20. Peng, Z. *et al.* Oxygen reactions in a non-aqueous Li^+ electrolyte. *Angew. Chem. Int. Ed.* **50**, 6351–6355 (2011).

21. Lau, K. C., Lu, J., Luo, X., Curtiss, L. A. & Amine, K. Implications of the unpaired spins in Li-O_2 battery chemistry and electrochemistry: A minireview. *ChemPlusChem* **80**, 336–343 (2015).

22. Ogasawara, T., Debart, A., Holzapfel, M., Novak, P. & Bruce, P. G. Rechargeable Li_2O_2 electrode for lithium batteries. *J. Am. Chem. Soc.* **128**, 1390–1393 (2006).

23. Peng, Z., Freunberger, S. A., Chen, Y. & Bruce, P. G. A reversible and higher-rate Li-O_2 battery. *Science* **337**, 563–566 (2012).

24. Sharon, D. *et al.* Oxidation of Dimethyl Sulfoxide Solutions by Electrochemical Reduction of Oxygen. *J. Phys. Chem. Lett.* **4**, 3115–3119 (2013).

25. Freunberger, S. A. *et al.* Reactions in the rechargeable lithium-O_2 battery with alkyl carbonate electrolytes. *J. Am. Chem. Soc.* **133**, 8040–8047 (2011).

26. Chen, Y., Freunberger, S. A., Peng, Z., Bardé, F. & Bruce, P. G. Li–O_2 Battery with a Dimethylformamide Electrolyte. *J. Am. Chem. Soc.* **134**, 7952–7957 (2012).

27. Bardé, F. *et al.* Sulfone-Based Electrolytes for Nonaqueous Li–O_2 Batteries. *J. Phys. Chem. C* **118**, 18892–18898 (2014).

28. Sharon, D. *et al.* Reactivity of Amide Based Solutions in Lithium–Oxygen Cells. *J. Phys. Chem. C* **118**, 15207–15213 (2014).

29. Sharon, D. *et al.* On the Challenge of Electrolyte Solutions for Li–Air Batteries: Monitoring Oxygen Reduction and Related Reactions in Polyether Solutions by Spectroscopy and EQCM. *J. Phys. Chem. Lett.* **4**, 127–131 (2012).

30. Freunberger, S. A. *et al.* The lithium-oxygen battery with ether-based electrolytes. *Angew. Chem. Int. Ed.* **50**, 8609–8613 (2011).

31. Gao, X., Chen, Y., Johnson, L. R., Jovanov, Z. P. & Bruce, P. G. A rechargeable lithium–oxygen battery with dual mediators stabilizing the carbon cathode. *Nat. Energy* **2**, 17118 (2017).

32. Adams, B. D. *et al.* Towards a stable organic electrolyte for the Lithium oxygen battery. *Adv. Energy Mater.* **5**, 1400867 (2015).

33. Younesi, R., Norby, P. & Vegge, T. A New Look at the Stability of Dimethyl Sulfoxide and Acetonitrile in Li-O_2 Batteries. *ECS Electrochem. Lett.* **3**, A15–A18 (2014).

34. Khetan, A., Luntz, A. & Viswanathan, V. Trade-offs in capacity and rechargeability in nonaqueous Li–O_2 batteries: Solution-driven growth versus nucleophilic stability. *J. Phys. Chem. Lett.* **6**, 1254–1259 (2015).

35. Bryantsev, V. S. *et al.* Predicting solvent stability in aprotic electrolyte Li-air batteries: Nucleophilic substitution by the superoxide anion radical ($O_2^{\bullet -}$). *J. Phys. Chem. A* **115**, 12399–12409 (2011).

36. Laoire, C. O., Mukerjee, S., Abraham, K. M., Plichta, E. J. & Hendrickson, M. A. Influence of nonaqueous solvents on the electrochemistry of oxygen in the rechargeable lithium-air battery. *J. Phys. Chem. C* **114**, 9178–9186 (2010).

37. McCloskey, B. D. *et al.* Limitations in Rechargeability of Li-O_2 Batteries and Possible Origins. *J. Phys. Chem. Lett.* **3**, 3043–3047 (2012).

38. McCloskey, B. D., Burke, C. M., Nichols, J. E. & Renfrew, S. E. Mechanistic insights for the development of Li-O_2 battery materials: addressing Li_2O_2

conductivity limitations and electrolyte and cathode instabilities. *Chem Commun Camb* **51**, 12701–12715 (2015).

39. Gao, X., Chen, Y., Johnson, L. & Bruce, P. G. Promoting solution phase discharge in Li–O_2 batteries containing weakly solvating electrolyte solutions. *Nat. Mater.* **15**, 882–888 (2016).

40. Cameron, J. M. *et al.* Molecular redox species for next-generation batteries. *Chem. Soc. Rev.* **50**, 5863–5883 (2021).

41. Trinh, N. D. *et al.* An Artificial Lithium Protective Layer that Enables the Use of Acetonitrile-Based Electrolytes in Lithium Metal Batteries. *Angew. Chem. Int. Ed.* **57**, 5072–5075 (2018).

42. Chi, X. *et al.* A highly stable and flexible zeolite electrolyte solid-state Li–air battery. *Nature* **592**, 551–557 (2021).

43. Wang, J., Zheng, J. & Liu, X. The key to improving the performance of Li–air batteries: recent progress and challenges of the catalysts. *Phys Chem Chem Phys* **24**, 17920–17940 (2022).

44. Kwak, W.-J. *et al.* Lithium–Oxygen Batteries and Related Systems: Potential, Status, and Future. *Chem. Rev.* **120**, 6626–6683 (2020).

45. Hase, Y. *et al.* Negative differential resistance as a critical indicator for the discharge capacity of lithium-oxygen batteries. *Nat. Commun.* **10**, 596 (2019).

46. Hase, Y. *et al.* Synergistic Effect of Binary Electrolyte on Enhancement of the Energy Density in Li–O_2 Batteries. *J. Phys. Chem. Lett.* **11**, 7657–7663 (2020).

47. Imanishi, N. & Yamamoto, O. Perspectives and challenges of rechargeable lithium–air batteries. *Mater. Today Adv.* **4**, 100031 (2019).

48. Jung, H. G., Hassoun, J., Park, J. B., Sun, Y. K. & Scrosati, B. An improved high-performance lithium-air battery. *Nat. Chem.* **4**, 579–585 (2012).

49. O'Sullivan, D. W. & Tyree, M. The kinetics of complex formation between Ti(IV) and hydrogen peroxide. *Int. J. Chem. Kinet.* **39**, 457–461 (2007).

50. Hartmann, P. *et al.* A comprehensive study on the cell chemistry of the sodium superoxide (NaO_2) battery. *Phys. Chem. Chem. Phys.* **15**, 11661–11672 (2013).

51. Fulmer, G. R. *et al.* NMR Chemical Shifts of Trace Impurities: Common Laboratory Solvents, Organics, and Gases in Deuterated Solvents Relevant to the Organometallic Chemist. *Organometallics* **29**, 2176–2179 (2010).

52. Lai, J. *et al.* Electrolytes for Rechargeable Lithium–Air Batteries. *Angew. Chem. Int. Ed.* **59**, 2974–2997 (2020).

53. Canterbury, D. P. *et al.* Asymmetric Synthesis of a Potent CXCR7 Modulator Featuring a Hindered Tertiary β-Amino Amide Stereocenter. *Org. Lett.* **20**, 5336–5339 (2018).

54. Yadav, G. D. & Ceasar, J. L. Kinetics of Selective Formation of Ibuprofenamide by Phase Transfer Catalyzed Oxidation of 2-(4-Isobutylphenyl)propionitrile with Basic Hydrogen Peroxide. *Org. Process Res. Dev.* **12**, 740–747 (2008).

55. Wiberg, K. B. The Mechanisms of Hydrogen Peroxide Reactions. I. The Conversion of Benzonitrile to Benzamide. *J. Am. Chem. Soc.* **75**, 3961–3964 (1953).

56. McIsaac, J. E., Ball, R. E. & Behrman, E. J. Mechanism of the base-catalyzed conversion of nitriles to amides by hydrogen peroxide. *J. Org. Chem.* **36**, 3048–3050 (1971).

57. Zhao, C. *et al.* Effect of soluble sulfur species on the electrochemical behavior of lithium–sulfur batteries with dual-phase electrolytes. *Sustain. Energy Fuels* **3**, 1966–1970 (2019).

58. Berholts, M. *et al.* Photofragmentation of gas-phase acetic acid and acetamide clusters in the vacuum ultraviolet region. *J. Chem. Phys.* **147**, 194302 (2017).

59. Chau, V. K. C., Chen, Z., Hu, H. & Chan, K.-Y. Exploring Solvent Stability against Nucleophilic Attack by Solvated LiO_2^- in an Aprotic Li-O_2 Battery. *J. Electrochem. Soc.* **164**, A284–A289 (2017).

60. Laino, T. & Curioni, A. Chemical reactivity of aprotic electrolytes on a solid Li_2O_2 surface: screening solvents for Li–air batteries. *New J. Phys.* **15**, 095009 (2013).

61. Bryantsev, V. S. *et al.* The Identification of Stable Solvents for Nonaqueous Rechargeable Li-Air Batteries. *J. Electrochem. Soc.* **160**, A160–A171 (2013).

Chapter 7. Understanding the requirements for and mechanism of $4e^-$ O_2 reduction in the lithium-air battery

7.1 Introduction

The $4e^-$ reduction of O_2 in H_2O is one of the most widely studied reactions in chemistry.[1,2] It is chemically irreversible when compared with $2e^-$ O_2 reduction in aprotic solvents, largely due to the preservation of the O-O bond in the latter.[3–5] As a result, the $2e^-$ reduction of O_2 to form Li_2O_2 is the basis of the cathodic reaction in the rechargeable lithium-air (Li-air) battery (Equation 7.1), and the $4e^-$ reduction of O_2 to form LiOH is broadly considered a parasitic reaction (Equation 7.2).[6–10]

$$2Li^+_{(sol)} + O_{2\,(sol)} + 2e^- \rightarrow Li_2O_{2\,(s)} \quad (7.1)$$

$$4Li^+_{(sol)} + O_{2\,(sol)} + 2H_2O_{\,(sol)} + 4e^- \rightarrow 4LiOH_{\,(sol)} \quad (7.2)$$

It has been shown that in the presence of a LiI catalyst, O_2 can be cycled via the $4e^-$ reaction, offering the intriguing possibility of reversible LiOH-based batteries.[11–13] However, such a reaction is detrimental to the aprotic battery due to the presence of the proposed heterogenous catalysts that enable the reverse reaction, which have been shown to cause considerable electrolyte degradation.[14–16]

It was originally reported that to avoid $4e^-$ O_2 reduction in the Li-air battery, the H_2O content would have to be reduced to extremely low levels (H_2O <10 ppm).[17] To achieve this, a 33% system level weight penalty would be required to facilitate adequate gas handling of a 100-kWh battery pack, greatly diminishing the attainable specific energy of a practical Li-air battery. However, more recent studies indicate that many Li-air electrolyte solvents benefit from the presence of small quantities of H_2O (<5000 ppm), which enables greater discharge capacities through solution-mediated growth of a toroidal Li_2O_2 morphology, delaying electrode passivation by otherwise surface-confined thin film Li_2O_2.[18–22] Aetukuri *et al.* proposed that this was the result of the high

acceptor number (AN) of H_2O improving the solubility of the superoxide (O_2^-) intermediate species, which enables O_2^- to promote solution-phase chemical Li_2O_2 formation, attaining a toroidal Li_2O_2 morphology where low current densities are employed.[21] Concurrently, Schwenke *et al.* proposed H_2O-mediated Li_2O_2 growth as a result of chemical equilibria that are established by the presence of H_2O, wherein hydroperoxide-mediated Li_2O_2 solubilisation delays passivation of the cathode surface (Equations 7.3 and 7.4).[18]

$$Li_2O_{2\,(s)} + H_2O_{\,(sol)} \rightleftharpoons LiOOH_{\,(sol)} + LiOH_{\,(s)} \quad (7.3)$$

$$LiOOH_{\,(sol)} + H_2O_{\,(sol)} \rightleftharpoons H_2O_{2\,(sol)} + LiOH_{\,(s)} \quad (7.4)$$

Kwabi *et al.* subsequently suggested that the pK_a of H_2O in a given H_2O-solvent mixture, and therefore the proton availability, was the determining factor underpinning the favourability of the $4e^-$ O_2 reduction process.[20] However, in 2019 Holc outlined a theory that the AN of a given H_2O-solvent mixture, rather than the pK_a of H_2O, was the critical indicator of whether O_2 reduction would proceed via a $2e^-$ or $4e^-$ pathway in H_2O-containing Li-air cells.[23] This work revealed that tetraethylene glycol dimethyl ether (TEGDME)-based electrolytes could tolerate ≥1 M H_2O while maintaining Li_2O_2 formation, with the ratio of electrons passed per molecule of O_2 (e^-/O_2) being close to the ideal value of 2. Although this marks a critical discovery in the field of Li-air batteries, the pathway of $4e^-$ O_2 reduction was not conclusively identified in this work. Understanding the mechanism of $4e^-$ O_2 reduction in H_2O-solvent mixtures is both of fundamental interest and is essential to enable the development of adequate methods that suppress irreversible $4e^-$ O_2 reduction where H_2O is present.

Ultimately, a practical Li-air battery must operate in ambient air, if the technology is to deliver on the proposed performance benefits, introducing both H_2O and CO_2 as gas stream contaminants.[17] Critically, establishing the amount of H_2O which an electrolyte can contain while preserving reversible $2e^-$ O_2 reduction and deconvoluting the mechanism of $4e^-$ O_2 reduction are vital milestones that are yet to be overcome. Consequently, this chapter focusses on

H_2O while recognising that addressing CO_2 in the gas stream is also essential.[18–21,24,25]

In this chapter, I present a systematic study of the effect of H_2O concentration on the AN of H_2O-solvent mixtures, confirming the AN theory proposed by Holc through a combination of *in situ* pressure analysis and *ex situ* characterisation of discharge product(s) across a broad range of H_2O concentrations. For each H_2O-solvent combination, the critical H_2O concentration at which the e^-/O_2 ratio deviates from the ideal $2e^-/O_2$ value is identified and these results are correlated to intrinsic solvent properties. These findings can be applied to any electrochemical process involving OH^- in mixed organic-aqueous electrolytes. To identify the pathway of $4e^-$ O_2 reduction to form LiOH, chemical and electrochemical routes are thoroughly explored using a combination of gas analysis, spectroscopic and electrochemical techniques. Contrary to current literature understanding, it is determined that $4e^-$ O_2 reduction in Li-air batteries proceeds via a 2+2 reaction mechanism, facilitated by the reduction of hydroperoxide species on the electrochemically active stainless steel (SS) current collector, rather than by direct $4e^-$ reduction on the carbon electrode. A high-performance Li-air cell containing 1 M H_2O is analysed, demonstrating the importance of understanding H_2O-solvent mixture AN when assessing H_2O tolerance. Furthermore, the absence of $4e^-$ O_2 reduction on carbon electrodes is validated by the cycling of a SS-free cell under conditions representative of a gas stream with a 100% relative humidity, where a high Li_2O_2 yield is recorded and efficient charging of Li_2O_2/LiOOH/H_2O_2 is achieved. This work shows that, with careful design, a practical Li-air cell that uses ambient air as the O_2 source will not require any drying, significantly reducing the complexity of the gas handling system and the associated system overheads.

7.2 Experimental

7.2.1 Materials

All electrolyte preparation and cell assembly were carried out in a N_2-filled glovebox without components being exposed to air. Acetonitrile (MeCN,

99.999%, Aldrich), dimethyl sulfoxide (DMSO, ≥99.5%, Aldrich), TEGDME (≥99%, Aldrich), and dimethoxyethane (DME, ≥99.5%, Aldrich) were dried for several days over freshly activated molecular sieves (type 4 Å, Aldrich) before use. Lithium perchlorate ($LiClO_4$, 99.99%, Aldrich), tetrabutylammonium perchlorate ($TBAClO_4$, ≥99%, Aldrich) potassium dioxide (KO_2, 97%, Aldrich), 2,5-di-tert-butl-1,4-benzoquinone (DBBQ, 99%, Aldrich), ferrocene methanol (FcMeOH, 97%, Aldrich), and 2,2,6,6-tetramethylpiperidinyl-1-oxyl (TEMPO, 98%, Aldrich) were used as supplied without further purification. The final H_2O content of dry electrolytes was ≤10 ppm, determined by Karl-Fischer titration. H_2O-solvent electrolytes were prepared using deionised H_2O (18.2 MΩ cm, MilliQ). H_2O_2 (30% wt. in H_2O, Fisher) was used fresh and as provided. All cell components were dried at elevated temperature under vacuum and transferred to a N_2-filled glovebox (MBRAUN, O_2 ≤0.1 ppm, H_2O ≤0.1 ppm) without exposure to air. Further information regarding drying temperatures can be found in Chapter 2**.**

7.2.2 Pressure cell measurements

24 mm diameter Swagelok-type cells incorporating a pressure transducer (Omega Engineering) were used for *in situ* pressure analysis. Further details on cell design can be found in Chapter 2. Porous carbonaceous cathodes (H23, QuinTech) were paired with freestanding Li_xFePO_4 anodes (pre-oxidised to ca. 20% of total capacity, i.e. $x \leq 0.8$) that were prepared by combining $LiFePO_4$ (MTI) with conductive carbon additive (Super P, Alfa Aesar) and 10% wt. polytetrafluoroethylene in H_2O (Aldrich) in an 8:1:1 weight ratio. Two glass fibre separators (GF/F, Whatman) were used to separate the electrodes. SS mesh (316 grade, Advent) was placed on top of the cathode to ensure good electrical contact. The electrolyte volume was 800 µL. Prior to discharge, the cell headspace was purged with O_2 (N5.5, BOC) for a total time of 3 minutes. A constant purge was employed for cells containing DMSO- and TEGDME-based electrolytes. An alternating flow on bypass and through cell was employed for cells containing a DME-based electrolyte to mitigate DME evaporation. Cells were discharged in an incubator at 20 °C. The cell volume was determined post-

discharge for each measurement. Further information on methodology can be found in Chapter 2.

7.2.3 Li_2O_2 yield measurements

The quantity of Li_2O_2 formed through discharge was determined by UV-Vis spectrometry using a titration method reported previously, and described in detail in Chapter 2.[26,27] The cathode and separator were extracted from a discharged cell and added to a vial containing a known quantity of deionised H_2O. A known volume of this solution was then mixed in a 1:1 ratio with a solution of 2 wt.% titanium(IV) oxysulfate ($TiOSO_4$, Aldrich) in 1 M H_2SO_4 to achieve an optimum concentration of the coloured complex $[Ti(O_2)]^{2+}$ (λ_{max} = 405 nm), which is formed in the presence of H_2O_2. The UV-Vis absorption spectrum was measured and compared to a calibration fit. Further details can be found in Chapter 2.

7.2.4 Characterisation of discharged cathodes

For all spectroscopic characterisation, cells were discharged to a capacity of 2 mAh cm^{-2} in a 12 mm Swagelok rifle-cell format, described in detail in Chapter 2. After discharge, cells were disassembled inside a N_2-filled glovebox, taking care to extract the top carbonaceous cathode. The electrode was thoroughly rinsed with dry DME, before being transferred to the glovebox antechamber under N_2 and dried under dynamic vacuum. The dried electrodes were then stored in sealed containment inside a N_2-filled glovebox prior to characterisation.

X-ray diffraction (XRD) measurements were performed using a Malvern PANalytical X'Pert MPD operating in capillary spinner transmission mode equipped with a PIXcel area detector and a sealed tube Cu source operating at a tube voltage and current of 40 kV and 40 mA, respectively. A PW3152/63 focussing mirror was attached to eliminate *K*β wavelength radiation, resulting in a beam height of 0.7 mm at the sample position. The incident beam and diffracted beam pass through a pair of 0.04 rad Soller slits to reduce axial beam divergence. A fixed mask matching the prepared sample width and a fixed 1°

anti-scatter slit were used in the incident beam path. Scans were performed from 30-70° in capillary spinning mode. Each spectrum was recorded over 30 minutes. A total measurement time of 1 hour (2 × 30-minute) was used to characterise the discharge product of cells that contained no redox mediators. A total measurement time of 12 hours (24 × 30-minute) was used to characterise the discharge product of cells that contained DBBQ and TEMPO. Samples were prepared for XRD analysis by slicing the electrode into thin strips and inserting them into a glass capillary (SGCT 1.5 mm, Capillary Tube Suppliers Ltd.), ensuring that the sample was located in the path of the X-ray beam when mounted on the capillary spinner. The capillaries were sealed using Torr seal (Agilent) which was allowed to set for ≥12 hours before the capillary was removed from a N_2-atmosphere. Samples were aligned with the X-ray beam prior to analysis using a microscope attachment. The capillaries were spun throughout the entire measurement to enhance signal resolution, enabling more crystallites to satisfy the Bragg conditions required for diffraction.

Fourier transform infra-red (FTIR) spectra were recorded on a Bruker Alpha II spectrometer with a Pt ATR module in a N_2-filled glovebox, without further manipulation of the dried electrode.

7.2.5 Electrochemical measurements

Electrolyte solutions were prepared in an N_2-filled glovebox. Stock solutions consisted of 0.25 M $TBAClO_4$ or $LiClO_4$ dissolved in DMSO, TEGDME, or DME. The desired H_2O concentration was achieved by doping the solutions with the relevant volume of H_2O required for a 10 mL stock solution volume.

For O_2 reduction experiments, saturation was achieved by bubbling O_2 through the electrolyte and monitoring the peak current ($i_{p,red}$) as a function of bubbling time. Once no increase in $i_{p,red}$ was observed with further bubbling, the solution was considered saturated. This time was taken as the minimum limit of O_2 bubbling to ensure saturation. 3 minutes of continuous O_2 bubbling was sufficient to saturate all electrolytes studied. When recording background CVs, N_2 was bubbled for at least 5 minutes to ensure purging of dissolved O_2.

RDE measurements were recorded using a three-electrode configuration consisting of either a 5 mm glassy carbon (GC) or SS working disk electrode (ChangeDisk, Pine Instruments), a fritted LFP reference electrode, and a Pt counter electrode. The disk electrodes were polished separately to prevent cross-contamination. The GC and SS disk electrodes were mechanically polished by hand using 0.1 μm alumina powder (Buehler) on a neoprene polishing pad. The electrode was then briefly sonicated in H_2O to remove any residual alumina on the surface, before being dried under vacuum at 70 °C and transferred to a N_2-filled glovebox for cooling. A bespoke five-neck flask, built by the University of Nottingham School of Chemistry glassblowing workshop was also dried at 70 °C under vacuum and transferred to a N_2-glovebox for cooling. Once the electrodes were cool, the RDE was assembled before being transferred into a N_2-filled glovebox. 10 mL of electrolyte was used for each measurement. As the electrode was rotating, it was not possible to make the five-neck flask gas tight. Saturation was achieved in this system through constant sparging of O_2 while the linear sweep voltammograms (LSVs) were recorded. A scan rate of 20 mV s^{-1} and a rotation speed of 1000 rpm was used for all measurements. Between measurements, the RDE electrode and flask were removed from the glovebox and cleaned prior to the next measurement. H_2O_2 measurements were carried out under an N_2-atmosphere, with no O_2 sparging of the electrolytes. A 5 mM H_2O_2 concentration was obtained by doping dry electrolyte with a 30 wt.% H_2O_2 solution and H_2O in the required ratio to achieve the desired H_2O concentration. After addition, the solution was stirred prior to recording a LSV. The RDE electrode and five-neck flask were then removed from the glovebox, cleaned, and dried between measurements.

SS flag measurements were recorded in a five-neck flask with a three-electrode configuration consisting of a SS flag working electrode, a fritted LFP reference electrode, and a Pt counter electrode. 5 × 5 mm (0.5 cm^2) SS flags were cut from mesh (316 grade, Advent) with a thin tail left to facilitate electrical connection. Care was taken to ensure only the square portion of the electrode was submerged in the electrolyte solution, to allow for normalisation to geometric

electrode area. Electrochemical measurements were referenced to FcMeOH by recording cyclic voltammograms in pristine, O_2-free electrolyte, with a three-electrode configuration consisting of a GC working electrode, a fritted LFP reference electrode, and a Pt counter electrode. A scan rate of 20 mV s^{-1} was used for all LSVs.

7.2.6 Raman spectroscopy measurements

A Horiba-Yvon LabRAM HR spectrometer was used for Raman spectroscopy measurements. Spectra were recorded using a 660 nm laser at 25 mW, at 10× objective. To scan a range of Raman shifts simultaneously, 600 lines mm^{-1} rotatable diffraction grating along a path length of 800 mm was employed. Spectra were detected by a Synapse CCS detector (1024 pixels), thermoelectrically cooled to −60 °C. Before measurements, the instrument was calibrated using the Rayleigh line at 0 cm^{-1} and a standard Si(100) reference band at 520.7 cm^{-1}. A spectrum was recorded by averaging 5 acquisitions of 120 seconds duration for the OH peak.

7.2.7 SEM imaging

Extracted cathodes were sputter coated with Pt prior to imaging to improve conductivity and increase resolution. Air-sensitive transfer and loading was achieved using a Quorum Technologies PP3010T Cryo-SEM Preparation System. SEM images were collected at 5 kV using an FEI Quanta200 3D DualBeam SEM housed at the University of Nottingham Nanoscale and Microscale Research Centre.

7.2.8 OEMS measurements

OEMS measurements were recorded on an instrument built in-house by the University of Nottingham Mechanical Workshop coupled to a quadrupole mass spectrometer (Hiden Analytical). Further information on the instrumentation and calibration can be found in Chapter 2. For chemical disproportionation experiments, a MS vial was filled with a known quantity of KO_2 (ca. 5 mg) in an Ar-filled glovebox and capped with a rubber bung. The vial was then transferred onto an isolated section of the flow line before the line was opened, allowing

Ar (99.999%, CK Isotopes) to flow through the headspace of the vial. The MS signals were allowed to reach equilibrium before the disproportionation reaction was initiated by the addition of the desired electrolyte mixture. Electrolyte mixtures were prepared as described in section 7.2.5. The addition of the lithiated electrolyte results in disproportionation of KO_2 and the release of O_2 gas, the quantity of which was normalised to the mass of KO_2 to calculate the ratio of the number of moles of O_2 evolved per mole of KO_2 consumed. Blank injections, where the vial contained no KO_2, were recorded to ensure that the injection of the electrolyte did not introduce additional O_2 contamination.

Differential electrochemical mass spectrometry (DEMS) measurements were recorded on the same on-line mass spectrometer described above, using a separate isolated loop which housed a bespoke DEMS cell manufactured by the University of Nottingham Mechanical workshop. Further information on the instrumentation and calibration can be found in Chapter 2. The cell housed a 24 mm freestanding LFP anode and a porous carbonaceous cathode, electrically isolated by two 26 mm glass fibre separators. SS mesh was placed on top of the cathode to ensure good electrical contact. The electrolyte volume used in these measurements was 600 µL. Prior to discharge, the cell was assembled in a N_2-filled glovebox and transferred to the isolated loop with minimal exposure to air. The headspace was then purged with a 20% O_2, 80% Ar gas mixture (99.999%, CK Isotopes) for at least 24 hours, or until the mass signals had reached equilibrium, ensuring that any air contamination had been purged and the electrolyte has reached equilibrium concentration with the headspace. Where humid gas streams were required, humidifying solutions were attached upstream of the DEMS cell to bubble the carrier gas through. Where 100% relative humidity was required, gas was diverted through a solution of H_2O, and where a 13% relative humidity was desired, gas was diverted through a solution of saturated LiCl in H_2O.[28] The DEMS cell and mass spectrometer were housed in insulated containment at 20 °C throughout the measurement.

7.2.9 NMR measurements

NMR samples were prepared in a N_2-filled glovebox and measurements were performed using air-tight NMR tubes fitted with Young's taps (GPE Scientific). The AN of solvent-H_2O mixtures were determined using a deuterated phosphoric acid (D_3PO_4 85% in D_2O, Aldrich) reference capillary and a triethylphosphine oxide (Et_3PO, 97%, Aldrich) molecular probe. Et_3PO was dried thoroughly by dissolution in freshly distilled dichloromethane (DCM) to which freshly activated molecular sieves were added for several days, before allowing the DCM to evaporate in a N_2-filled glovebox. Further information about the theory of AN determination can be found in Chapter 2. NMR spectra were recorded on a Bruker Ascend 400 MHz spectrometer and analysed using Bruker TopSpin software.

7.3 Understanding the role of solvent AN and DN on the overall AN of H_2O-solvent mixtures

Holc reported in 2019 that the ability of H_2O-solvent mixtures to stabilise hydroxide anions (OH^-), and therefore the Lewis acidity of a H_2O-solvent mixture, predominantly determines whether LiOH will form in a given H_2O-containing electrolyte.[23] AN is a measure of the Lewis acidity of a solution, with high AN solutions being good Lewis acids, thus providing a thermodynamically favourable environment for OH^- formation. Conversely, low AN solutions are poor Lewis acids and result in a high energy barrier for OH^- formation. Therefore, it is desirable for an electrolyte solvent to have a low AN to improve H_2O tolerance while maintaining a $2e^-/O_2$ discharge ratio. Furthermore, it is beneficial for an electrolyte solvent to be a good Lewis base, i.e. have a high donor number (DN). Solvents with a high DN will interact strongly with H_2O and restrict the rate of increase of overall H_2O-solvent AN as H_2O concentration increases.

To understand the role of solvent AN and DN on the overall AN of H_2O-solvent mixtures, four solvents with a range of ANs and DNs were chosen for analysis. DMSO, with a high DN (29.8) and moderate AN (19.3), is expected to show good

tolerance to H_2O before a major increase in H_2O-solvent AN is experienced, due to its high DN which facilitates strong intermolecular bonding interactions with H_2O molecules.[29–32] The interaction between DMSO and H_2O is well studied; the solvents are known to be fully miscible and readily interact through hydrogen-bonding.[30,31] DME and TEGDME were selected due to their low ANs (10.2 and 10.5, respectively) and moderate to low DNs (20.0 and 16.6, respectively). Both of these solvents have intrinsically low ANs, but should experience a greater increase in AN when mixed with H_2O than H_2O-DMSO mixtures due to their lower DNs.[33,34] Finally MeCN was chosen due to its moderate AN (19.3) and low DN (14.1) which provides a scenario where the initial high dry solvent AN should increase rapidly when doped with greater proportions of H_2O.[29]

Figure 7.1a shows the AN of each H_2O-solvent mixture as a function of H_2O concentration from dry solvent to 20 M H_2O. The AN was recorded using the method first described by Mayer *et al*,[35] wherein the ^{31}P chemical shift of triethylphosphine oxide is used to ascertain the AN of the analyte solution. A D_3PO_4 capillary was used as an internal reference without interacting with the analyte solution. More information on the experimental procedure and methodology can be found in Chapter 2. The experimentally measured dry solvent ANs are in good agreement with literature values, with solvent AN from high to low being MeCN (19.36) = DMSO (19.35) > TEGDME (11.21) > DME (9.75), confirming the validity of this experimental procedure (**Figure 7.1**, **Table 7.1**). Although the AN of DMSO begins as the joint highest, H_2O-DMSO mixture AN shows good toleration to the addition of H_2O, and by 2 M H_2O has the lowest H_2O-solvent AN of the systems studied. Contrastingly, the moderate to low DNs of DME, TEGDME and MeCN result in a rapid increase in H_2O-solvent AN with respect to H_2O concentration. The AN values of the H_2O-solvent mixtures begin to converge by 20 M H_2O concentration, likely as the contribution of H_2O-H_2O interaction becomes increasingly dominant.

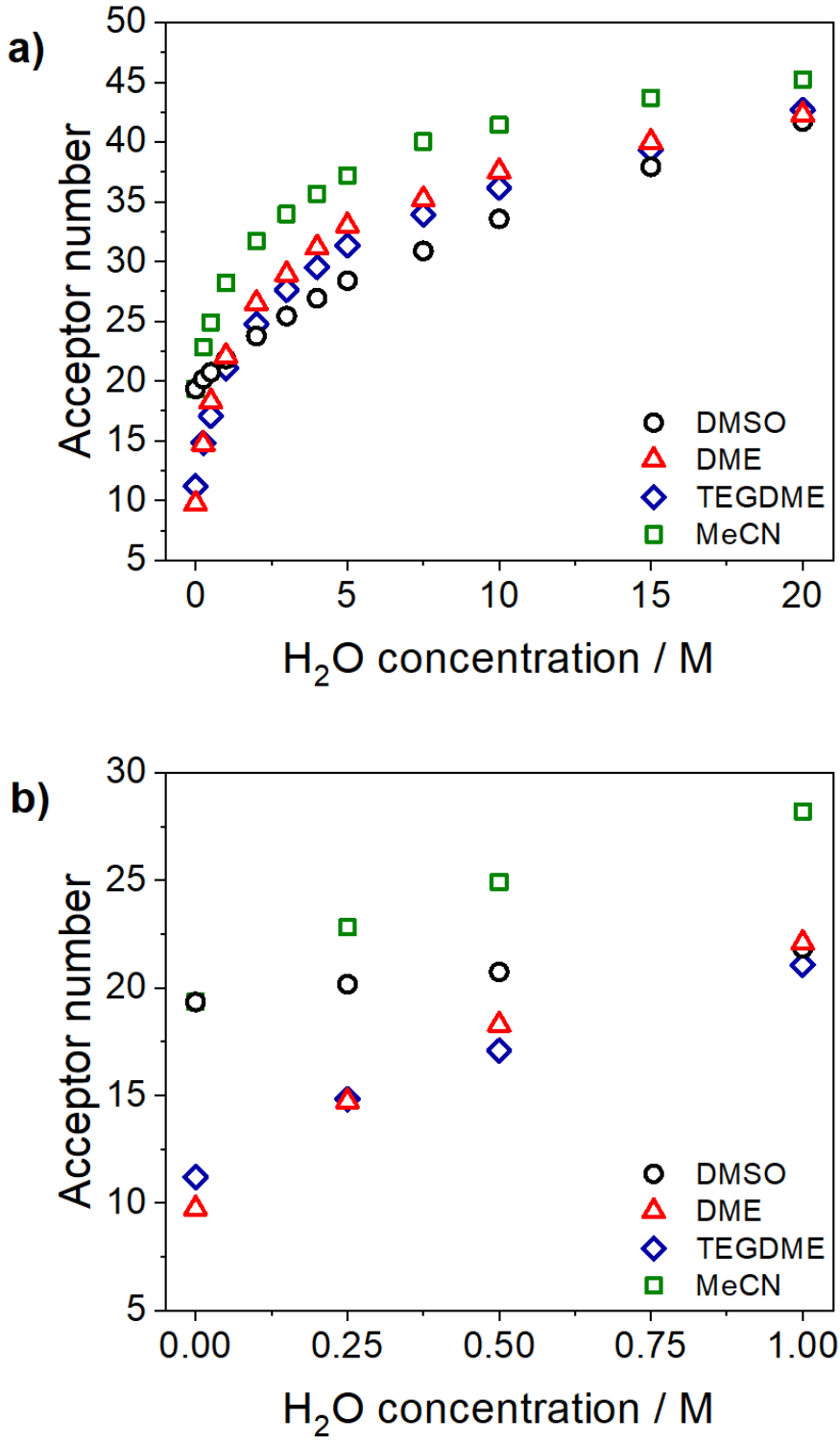


Figure 7.1. *Plot comparing H_2O-solvent mixture AN between dry solvent and a) 20 M or b) 1 M doped H_2O concentration for four common Li-air battery electrolyte solvents. ANs were obtained through NMR spectroscopic analysis as described previously by Mayer et al.*[35]

Table 7.1. *Comparison of the literature reported and experimentally observed ANs for the solvents studied in this chapter.*[35]

Solvent	Literature AN	Experimental AN
DMSO	19.3	19.35
DME	10.2	9.75
TEGDME	10.5	11.21
MeCN	18.9	19.36
H_2O	54.8	54.23

Figure 7.1b shows the H_2O-solvent mixture AN trend between dry solvent to 1 M H_2O, where greater clarity is presented for the initial trends. It is clear that DMSO has the greatest tolerance to H_2O with respect to increasing mixture AN, with H_2O-DMSO mixture ANs of 20.2, 20.7, and 21.8 being recorded for H_2O concentrations of 0.25, 0.50 and 1 M, respectively. This indicates that the hydrogen-bonding between DMSO and H_2O (due to the high DN of DMSO) limits the ability of H_2O to increase the overall mixture AN. In the case of DME, TEGDME and MeCN, the moderate to low DN of these solvents results in a rapid increase in H_2O-solvent AN, with mixture ANs of 22.1, 21.0, and 28.2 being reported at 1 M H_2O concentration, respectively (**Figure 7.1**b). Due to the high ANs of H_2O-MeCN mixtures even as low as 1 M H_2O, and given the results presented in Chapter 6, MeCN is deemed an unsuitable solvent for Li-air batteries and therefore is not explored further in this chapter. With these trends in mind, it is expected that DMSO will show the greatest tolerance to H_2O while maintaining $2e^-/O_2$ reduction. DME and TEGDME should also retain $2e^-/O_2$ reduction up to 1 M H_2O concentration, where performance may then deviate from that observed in H_2O-DMSO mixtures as the result of their H_2O-solvent ANs now exceeding those of H_2O-DMSO mixtures.

The effect of H_2O concentration on H_2O-solvent mixture AN can be rationalised by considering the solvation of H_2O by the solvent. This can be probed using Raman spectroscopy, where an O-H stretch peak below or above 3500 cm^{-1} indicates the presence or lack of hydrogen-bonding, respectively.[36] **Figure 7.2** shows the region of the Raman spectra associated with the O-H stretch peak for solutions of DMSO, DME and TEGDME, doped with 1 M H_2O. The spectra

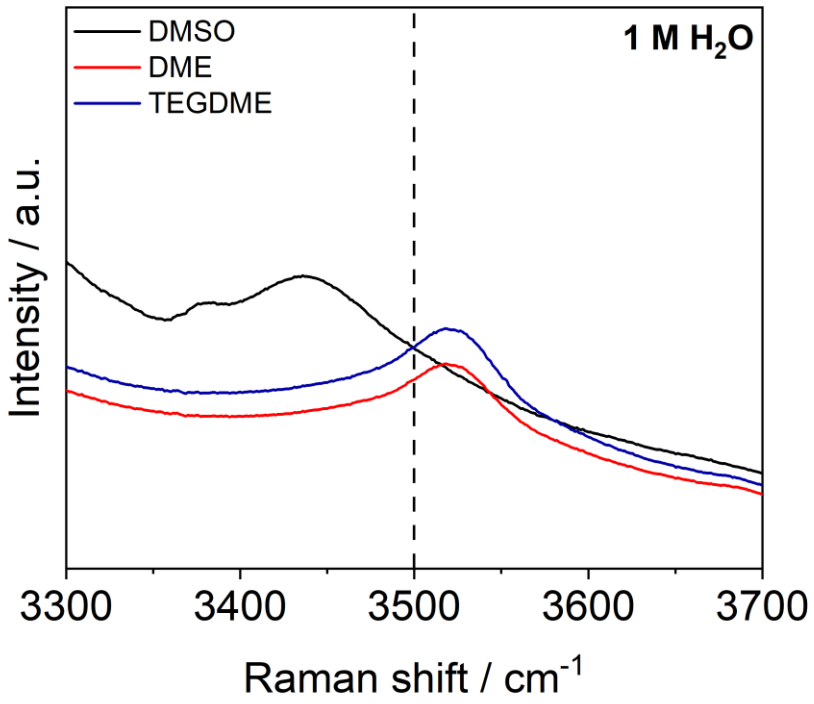


Figure 7.2. *Raman spectra examining the O-H stretch region of 1 M H_2O-containing solvents showing the presence of hydrogen-bonding in DMSO (Raman shift <3500 cm^{-1}), but not in either glyme ether.*

recorded for DME and TEGDME show peaks above 3500 cm^{-1}, indicating a lack of hydrogen-bonding and are therefore dispersed (not clustered) throughout the ether solvents. Consequently, H_2O in both solvents is readily available to complex anions (i.e. OH^-) and the addition of H_2O rapidly increases the mixture AN, in good agreement with the NMR data. Noting that the first solvent shell around OH^- will contain both H_2O and solvent molecules, the difference in the absolute AN between H_2O-DME and H_2O-TEGDME mixtures is due to the AN of the isolated solvents. In contrast to both DME and TEGDME, the observation of an O-H stretch below 3500 cm^{-1} in DMSO indicates that H_2O is strongly hydrogen-bonded to DMSO. Consequently, where other species are present (i.e. OH^-), they must compete against the strong H_2O-DMSO hydrogen-bonding interactions. Therefore, in good agreement with the NMR data, adding H_2O to DMSO will not impact the AN of the H_2O-DMSO mixture as dramatically as in the case of DME and TEGDME, thus providing a poor environment for OH^- solvation. In summary, it follows that the best solvents for tolerating high H_2O

concentrations would both strongly solvate H_2O and have an intrinsically low dry solvent AN.

7.4 The impact of H_2O concentration on the O_2 reduction pathway in Li-air cells

The presence of H_2O in a Li-air electrolyte introduces new electrochemical O_2 reduction pathways and chemical equilibria, which can result in a mixture of discharge products. In addition to the ideal $2e^-$ reduction of O_2 to form Li_2O_2, both LiOOH and H_2O_2 can be formed either electrochemically, through a $2e^-$ reduction process, or through H_2O-mediated chemical equilibria. Moreover, where H_2O activity is sufficiently high, LiOH can be electrochemically formed through a $4e^-$ O_2 reduction pathway. Equations 7.1 – 7.6, show the current literature understanding of the route to each of these discharge products and the requirements for established equilibria between them.[7,37,38]

$$2Li^+_{(sol)} + O_{2\,(sol)} + 2e^- \rightarrow Li_2O_{2\,(s)} \quad (7.1)$$

$$4Li^+_{(sol)} + O_{2\,(sol)} + 2H_2O_{(sol)} + 4e^- \rightarrow 4LiOH_{(sol)} \quad (7.2)$$

$$Li_2O_{2\,(s)} + H_2O_{(sol)} \rightleftharpoons LiOOH_{(sol)} + LiOH_{(s)} \quad (7.3)$$

$$LiOOH_{(sol)} + H_2O_{(sol)} \rightleftharpoons H_2O_{2\,(sol)} + LiOH_{(s)} \quad (7.4)$$

$$2Li^+_{(sol)} + O_{2\,(sol)} + H_2O_{(sol)} + 2e^- \rightarrow LiOOH_{(sol)} + LiOH_{(sol)} \quad (7.5)$$

$$2Li^+_{(sol)} + O_{2\,(sol)} + 2H_2O_{(sol)} + 2e^- \rightarrow H_2O_{2\,(sol)} + 2LiOH_{(sol)} \quad (7.6)$$

Provided that peroxo species, namely Li_2O_2, LiOOH or H_2O_2, are formed during cell discharge, the charging of a cell requires a much lower overpotential than where LiOH is electrochemically formed as a result of their intrinsic equilibrium potentials (3.32 V for LiOH compared to 2.96 V vs Li^+/Li for Li_2O_2).[16] Where LiOH is the primary discharge product, a high overpotential and/or catalysts are required to facilitate cell charging, both of which induce parasitic reactions.[14–16] Therefore, to understand the performance of Li-air electrolytes, it is critical to first determine which reactions occur in cells containing H_2O.

In this chapter, the primary metric used to assess cell performance is whether

overall O_2 reduction proceeds via a 2 or 4e^- pathway. To determine the extent of O_2 reduction occurring in cells, *in situ* pressure cells, which allow changes in pressure to be monitored as a function of charge passed, are employed to calculate the e^-/O_2 ratio. As shown in equations 7.1 – 7.6, and discussed in Chapter 6, relying solely on *ex situ* analysis can be misleading due to the Li_2O_2/LiOOH/H_2O_2 equilibria that are initiated by the presence of H_2O which reversibly forms LiOH. Therefore, it is possible for 2e^- O_2 reduction to occur in a cell and result in the electrochemical formation of peroxo species, while LiOH is also detected as a reversible by-product. **Figure 7.3** shows a representative dataset from the first discharge of a pressure cell containing a dry DMSO electrolyte over the first mAh of discharge capacity passed. An open circuit voltage (OCV) of 3.42 V vs Li^+/Li is observed for the cell at rest. Upon the application of current, O_2 is reduced at the surface of the cathode to form Li_2O_2, resulting in a stable plateau voltage between 2.68 – 2.70 V vs Li^+/Li, representing a ca. 0.30 V overpotential compared to the equilibrium potential

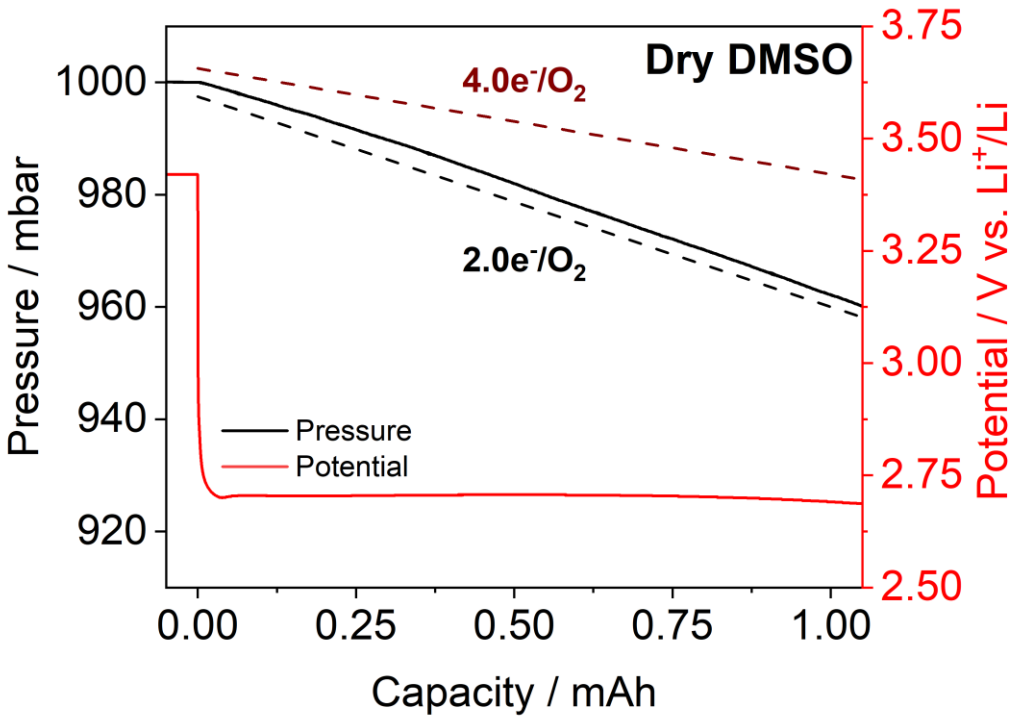


Figure 7.3. *Pressure decay (black line) and potential (red line) recorded during the discharge of a Li-air pressure cell at 50 µA cm^{-2} containing a 0.25 M $LiClO_4$ in dry DMSO electrolyte. Dashed reference lines show the ideal pressure decay gradients for a 2.0e^-/O_2 (black) and 4.0e^-/O_2 (red) process.*

for Li_2O_2 formation (2.96 V vs Li^+/Li). As solvated O_2 molecules are reduced, the electrolyte O_2 concentration drops below saturation. To account for this, O_2 molecules in the headspace of the cell are dissolved into the electrolyte, reducing the pressure of the headspace in accordance with the number of O_2 molecules reduced. These data taken together, enable an e^-/O_2 ratio to be calculated.

To understand the impact of H_2O on the discharge product of Li-air cells, *in situ* pressure analysis was used in conjunction with *ex situ* characterisation to monitor the e^-/O_2 ratio while confirming the nature of the dominant discharge product(s) in DMSO, DME and TEGDME H_2O-solvent mixtures. **Figure 7.4**a shows the average e^-/O_2 ratio and Li_2O_2 yield recorded for multiple cells containing DMSO-based electrolytes from dry to 10 M H_2O. The e^-/O_2 ratio in cells containing ≤5 M H_2O remains consistently around $2e^-/O_2$, showing H_2O does not disrupt $2e^-$ O_2 reduction in this range. The Li_2O_2 yield with ≤5 M H_2O also remains consistent between 55-60%. This low Li_2O_2 yield is indicative of the parasitic degradation of DMSO by both O_2^- and Li_2O_2, which has been previously reported and results in the formation of LiOH as a by-product.[39,40] Nevertheless, the stable yield indicates that the addition of ≤5 M H_2O does not result in further (electro)chemical degradation than that which occurs in the dry electrolyte. >5 M H_2O, both the e^-/O_2 ratio and the Li_2O_2 yield deviate significantly, with e^-/O_2 ratios of 2.34 and 2.73 and Li_2O_2 yields of 49.4 and 32.8% being recorded for cells doped with 7.5 and 10 M H_2O, respectively (**Figure 7.4**a).

Figure 7.4b shows the performance of representative pressure cells containing dry electrolyte compared to cells doped with 5, 7.5, and 10 M H_2O. The cells doped with 5 and 7.5 M H_2O are shown here to represent the highest H_2O concentration before the e^-/O_2 ratio deviated from 2 and the first observation point after this deviation, respectively. The discharge pressure decay gradient in both the cell containing dry electrolyte and the cell doped with 5 M H_2O follow the ideal $2e^-/O_2$ gradient, achieving average e^-/O_2 ratios of 1.95 and 2.01, respectively. The gradient of the pressure decay deviates from the ideal

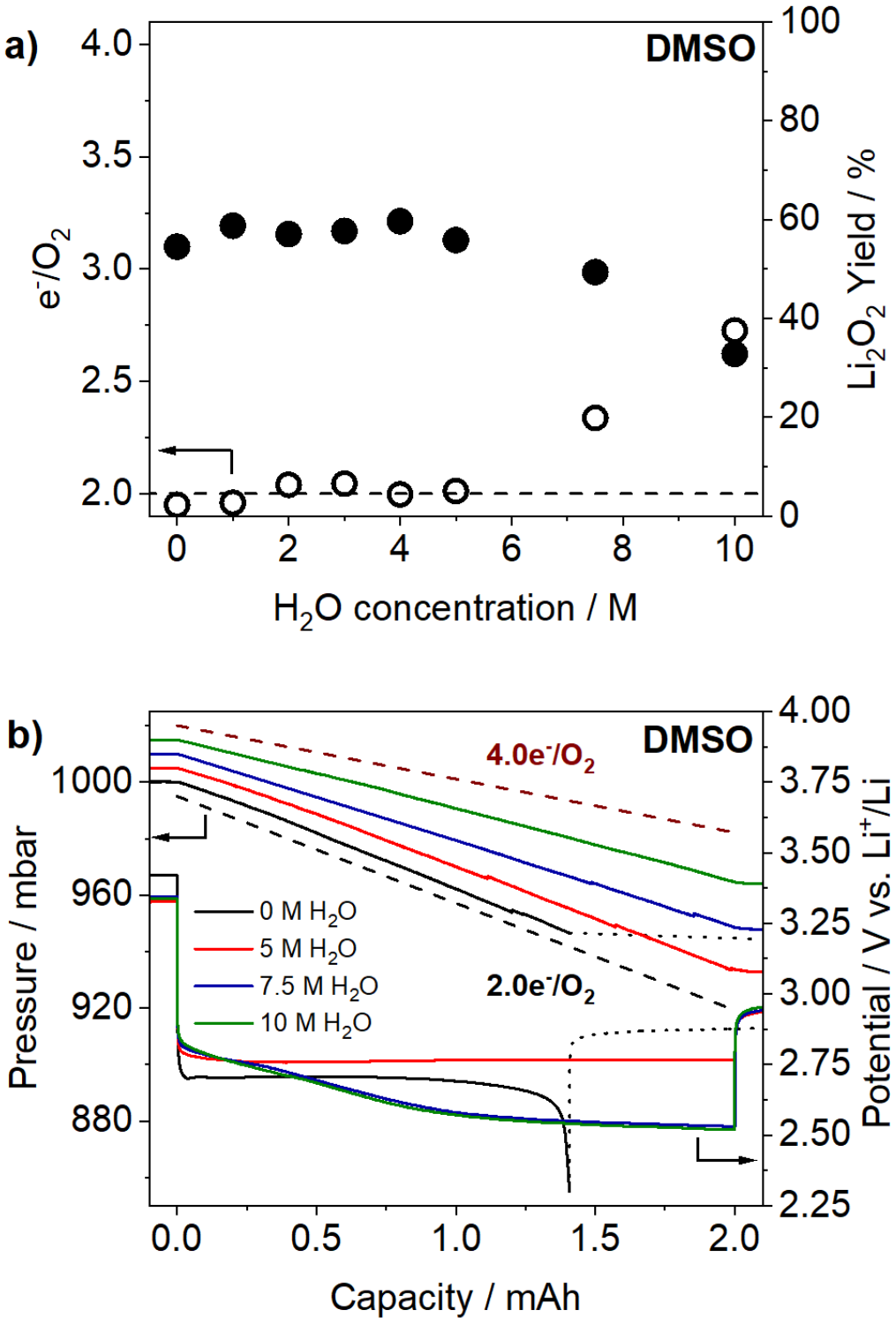


Figure 7.4. *Plots showing the effect of H_2O concentration on the a) e^-/O_2 ratio and Li_2O_2 yield and b) O_2 consumption and potential profiles of Li-air pressure cells containing DMSO-based electrolytes. Dashed reference lines show the ideal pressure decay gradients for a 2.0e^-/O_2 (black) and 4.0e^-/O_2 (red) process. Dotted lines indicate OCV after the potential limit is reached.*

$2e^-/O_2$ ratio in both cells containing electrolyte doped with 7.5 and 10 M H_2O.

To confirm the nature of the discharge products, the cathode was extracted from the cells containing DMSO-based electrolytes after discharge and analysed using XRD and FTIR spectroscopy (**Figure 7.5**). In good agreement with the e^-/O_2 and Li_2O_2 yield data, Li_2O_2 was identified as a primary discharge product in the diffraction patterns of both the cell discharged with dry electrolyte and the cell doped with 5 M H_2O (**Figure 7.5**a). Although some LiOH was found in all cells, this is the result of the previously discussed degradation of DMSO, known to occur in the presence of O_2^- and Li_2O_2 which produce LiOH.[39,40] In the samples where H_2O concentration is >5 M, the LiOH diffraction peaks become increasingly dominant, indicating proportionally greater amounts of LiOH formation. The FTIR spectra are in good agreement with the XRD data, confirming the presence of some LiOH at all H_2O concentrations (**Figure 7.5**b). Taken together, these data indicate that for DMSO electrolytes where H_2O concentration is ≤5 M, O_2 reduction proceeds via a $2e^-$ process to form Li_2O_2. Where H_2O concentration is >5 M, O_2 reduction proceeds via and mixture of $2e^-$ reduction to form Li_2O_2 and $4e^-$ reduction to form LiOH which results in a concurrent deviation in the observed e^-/O_2 ratio and a drop in the Li_2O_2 yield.

In the glyme ethers, using a dry electrolyte (<10 ppm H_2O) resulted in a low discharge capacity, which introduced significant error to the attained e^-/O_2 ratios and deemed the cathodes prepared for *ex situ* characterisation unsuitable to meet the limit of detection of either XRD or FTIR. To maintain consistency throughout *in situ* pressure cells analysis and *ex situ* characterisation, cells containing 'dry' glyme ethers were doped with 50 mM H_2O. This low H_2O concentration was sufficient to enable some solution phase transfer of Li_2O_2, highlighting the benefits of low H_2O concentrations and delaying electrode passivation for long enough to accumulate an acceptable quantity of discharge product for spectroscopic analysis.

Figure 7.6 shows the average e^-/O_2 ratio and Li_2O_2 yield recorded for cells containing a TEGDME-based electrolytes with H_2O concentrations ranging from

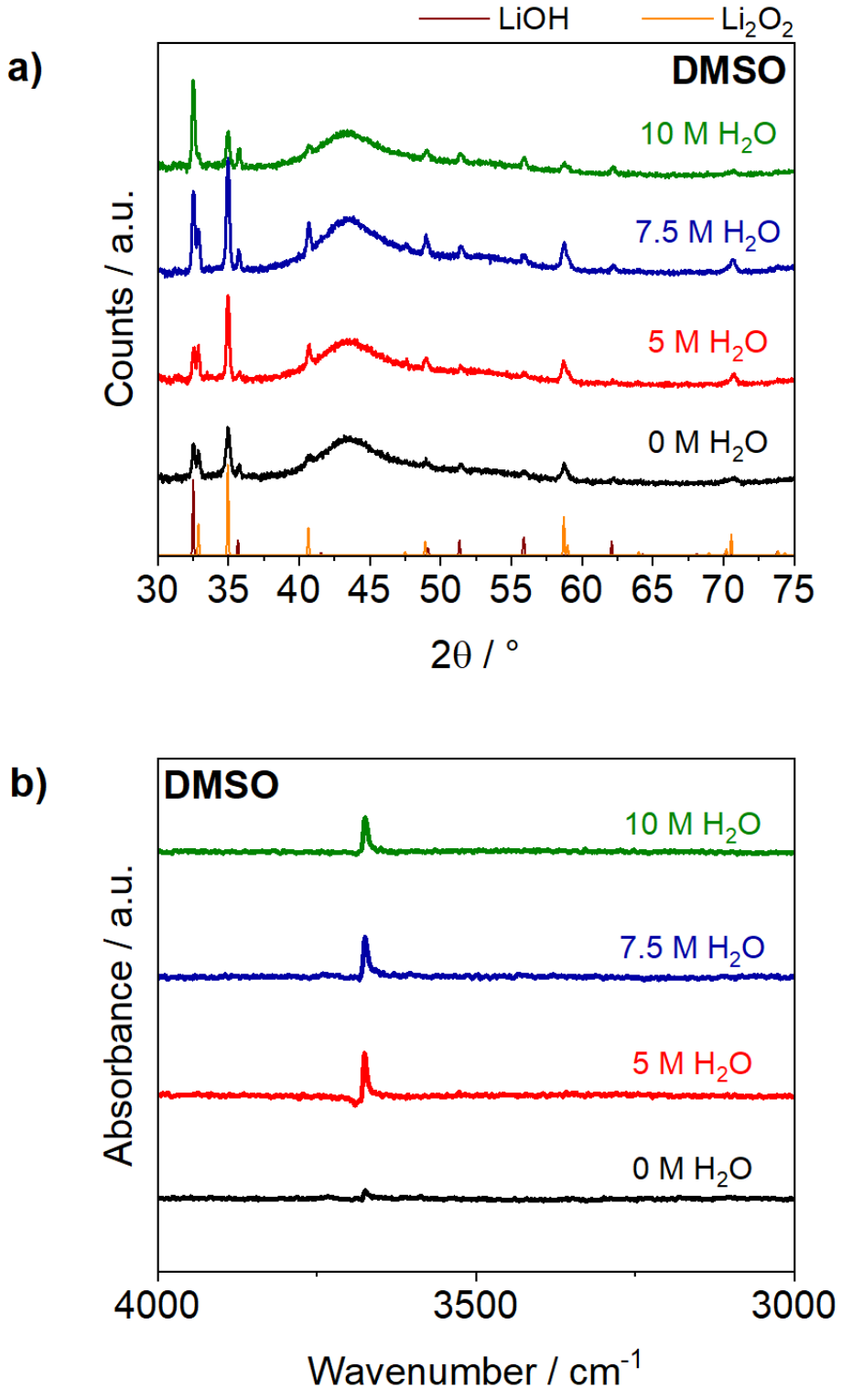


Figure 7.5. *Plots showing the change in discharge product as a function of electrolyte H_2O concentration examined through a) XRD and b) FTIR analysis of cathodes extracted from cells containing DMSO-based electrolytes. Cells were discharged to 2 mAh cm^{-2} prior to analysis. The driest (black) and wettest (green) sample are shown alongside the highest H_2O concentration before (red) and lowest after (blue) the onset of electrochemical LiOH formation. Reference Li_2O_2 and LiOH XRD patterns were recorded experimentally.*

50 mM to 10 M H_2O. An average e^-/O_2 ratio of 2.00 and Li_2O_2 yield of 78.6% were recorded for the cell containing 50 mM H_2O, indicating that Li_2O_2 is the primary discharge product (**Figure 7.6**a). The e^-/O_2 ratio remains consistent up to 1 M H_2O concentration, with average ratios of 2.06, 2.04, and 2.04 being recorded for electrolyte H_2O concentrations of 0.25, 0.50 and 1 M H_2O, respectively. Over this range an increase in the Li_2O_2 yield is observed, likely due to enhanced solution mediated growth of Li_2O_2 enabled by the presence of increasing quantities of H_2O, limiting the total surface area of Li_2O_2 that is exposed to the electrolyte (**Figure 7.6**a). Although an increase in the e^-/O_2 ratio to 2.13 is observed when the H_2O concentration is increased to 2 M, the high Li_2O_2 yield of 90.5% recorded with 2 M H_2O indicates that Li_2O_2 is still the primary electrochemical discharge product. Further deviation from the ideal $2e^-/O_2$ ratio, and a concurrent drop in Li_2O_2 yield, is observed where H_2O concentration is >2 M, with the average e^-/O_2 ratio increasing steadily to 2.26, 2.37, and 2.54 with doped H_2O concentrations of 3, 4, and 5 M, respectively (**Figure 7.6**a). Over this same region, the Li_2O_2 yield steadily drops to 60.9% at 5 M H_2O. When the electrolyte H_2O concentration is 10 M, the e^-/O_2 ratio is 2.87 and the Li_2O_2 yield has dropped to 22.3%, indicating that Li_2O_2 is no longer the primary discharge product.

Figure 7.6b shows the discharge pressure decays in representative cells discharged containing TEGDME-based electrolytes doped with 50 mM H_2O compared to cells doped with 2, 3, and 10 M H_2O. These cells represent 'dry' TEGDME, the highest H_2O concentration before and the first observation point after deviation from high Li_2O_2 yield (2 and 3 M H_2O, respectively), and a scenario where LiOH formation is a significant contributor to the overall e^-/O_2 ratio (10 M H_2O). The discharge pressure decay gradient in the cell with electrolyte doped with 50 mM H_2O follows the gradient of the ideal $2e^-/O_2$ process closely (**Figure 7.6**b). A small deviation from this gradient is observed when the electrolyte is doped with 2 M H_2O, which exacerbates further as H_2O concentration increases.

Figure 7.7 shows selected XRD patterns and FTIR spectra of cathodes extracted

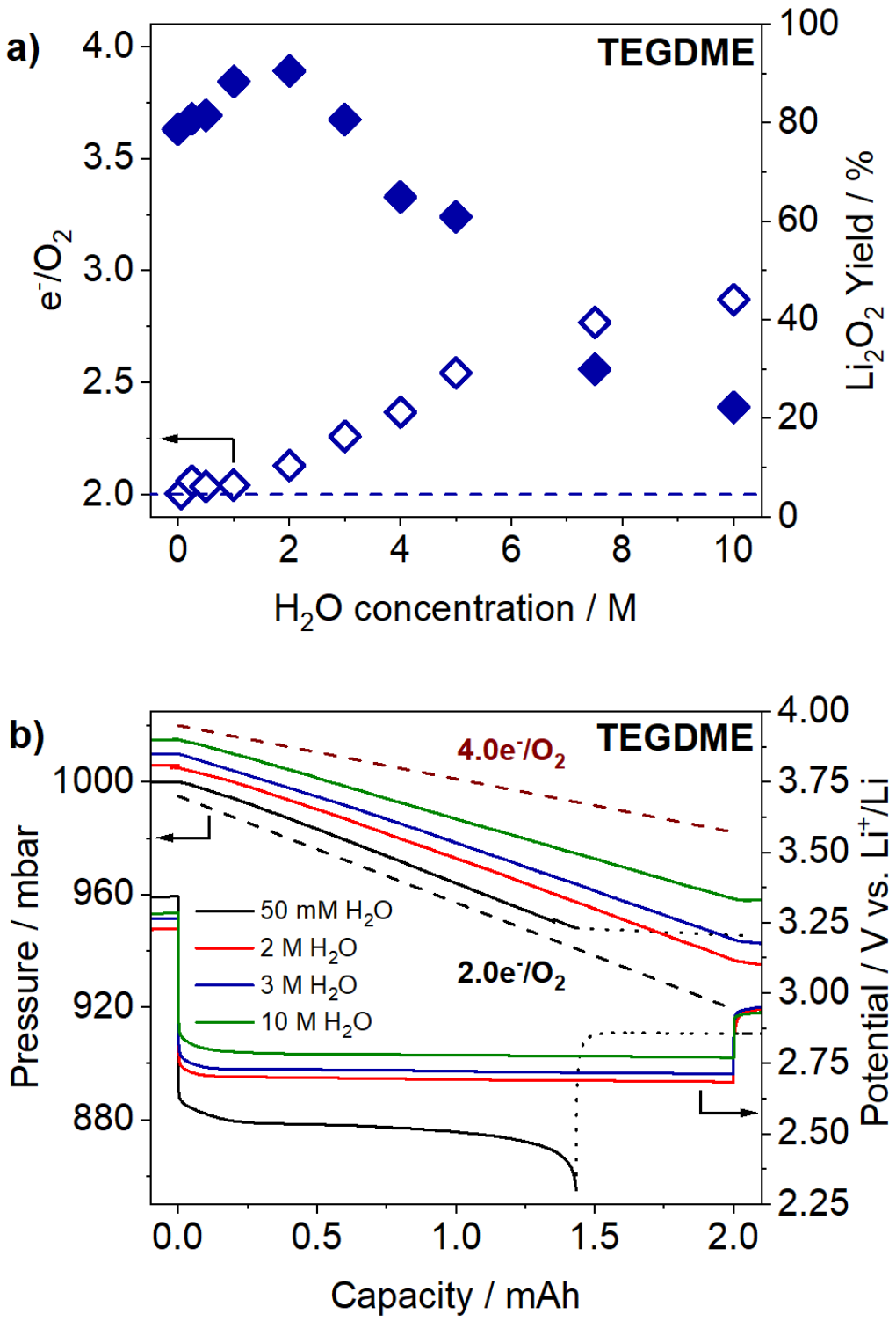


Figure 7.6. *Plots showing the effect of H_2O concentration on the a) e^-/O_2 ratio and Li_2O_2 yield and b) O_2 consumption and potential profiles of Li-air pressure cells containing TEGDME-based electrolytes. Dashed reference lines show the ideal pressure decay gradients for a $2.0e^-/O_2$ (black) and $4.0e^-/O_2$ (red) process. Dotted lines indicate OCV after the potential limit is reached.*

from cells containing TEGDME-based electrolytes after discharge. H_2O concentrations of 2 and 3 M were chosen to represent before and after deviation from electrochemical Li_2O_2 formation, evidenced by the significant drop in Li_2O_2 yield (**Figure 7.6**a). In good agreement with the pressure cell and Li_2O_2 yield data, Li_2O_2 was identified as the primary discharge product in the diffraction patterns of both the cell discharged containing an electrolyte doped with 50 mM H_2O and 2 M H_2O (**Figure 7.7**a). Although the e^-/O_2 ratio has increased to 2.26 when the electrolyte H_2O concentration was 3 M, the Li_2O_2 yield was 80.6%, comparable with the cell containing 50 mM H_2O (**Figure 7.6**a). Therefore, it is not surprising that the XRD pattern for the electrolyte containing 3 M H_2O does not show any LiOH peaks, as it is likely that the relative proportion of LiOH present is low (**Figure 7.7**a). However, due to the sensitivity of FTIR to the detection of the O-H stretching frequency, a LiOH peak is observed in the FTIR spectrum of the 3 M H_2O sample, confirming the presence of LiOH (**Figure 7.7**b). Small peaks are also observed in the 50 mM and 2 M H_2O spectra, indicating some LiOH presence at all H_2O concentrations. By 10 M H_2O, both Li_2O_2 and LiOH peaks are observed in the XRD pattern, and a clear LiOH peak is present in the FTIR spectrum. In good agreement with the mixture AN theory, TEGDME-based electrolytes show less tolerance to H_2O before deviating from the ideal $2e^-/O_2$ ratio than DMSO-based electrolytes. An electrolyte H_2O concentration of 1 M is sufficient to optimise Li_2O_2 yield, while avoiding the onset of LiOH formation through $4e^-$ O_2 reduction.

Figure 7.8 shows the average e^-/O_2 ratio and Li_2O_2 yield recorded for a range of cells containing DME-based electrolytes doped with between 50 mM and 5 M H_2O. An average e^-/O_2 ratio of 3.57 and Li_2O_2 yield of 37.4% were obtained at 5 M H_2O concentration. Above this concentration, the e^-/O_2 ratio exceeded $4e^-/O_2$, indicating parasitic reactions the nature of which are beyond the scope of this chapter, so were not investigated (**Figure 7.8**a). A stable e^-/O_2 ratio was observed between electrolyte doped with 50 mM – 2 M H_2O, with average e^-/O_2 ratios of 2.29, 2.30, 2.28, and 2.26 being achieved for cells doped with 50 mM, 0.25 M, 0.50 M, and 2 M H_2O, respectively. Although these values

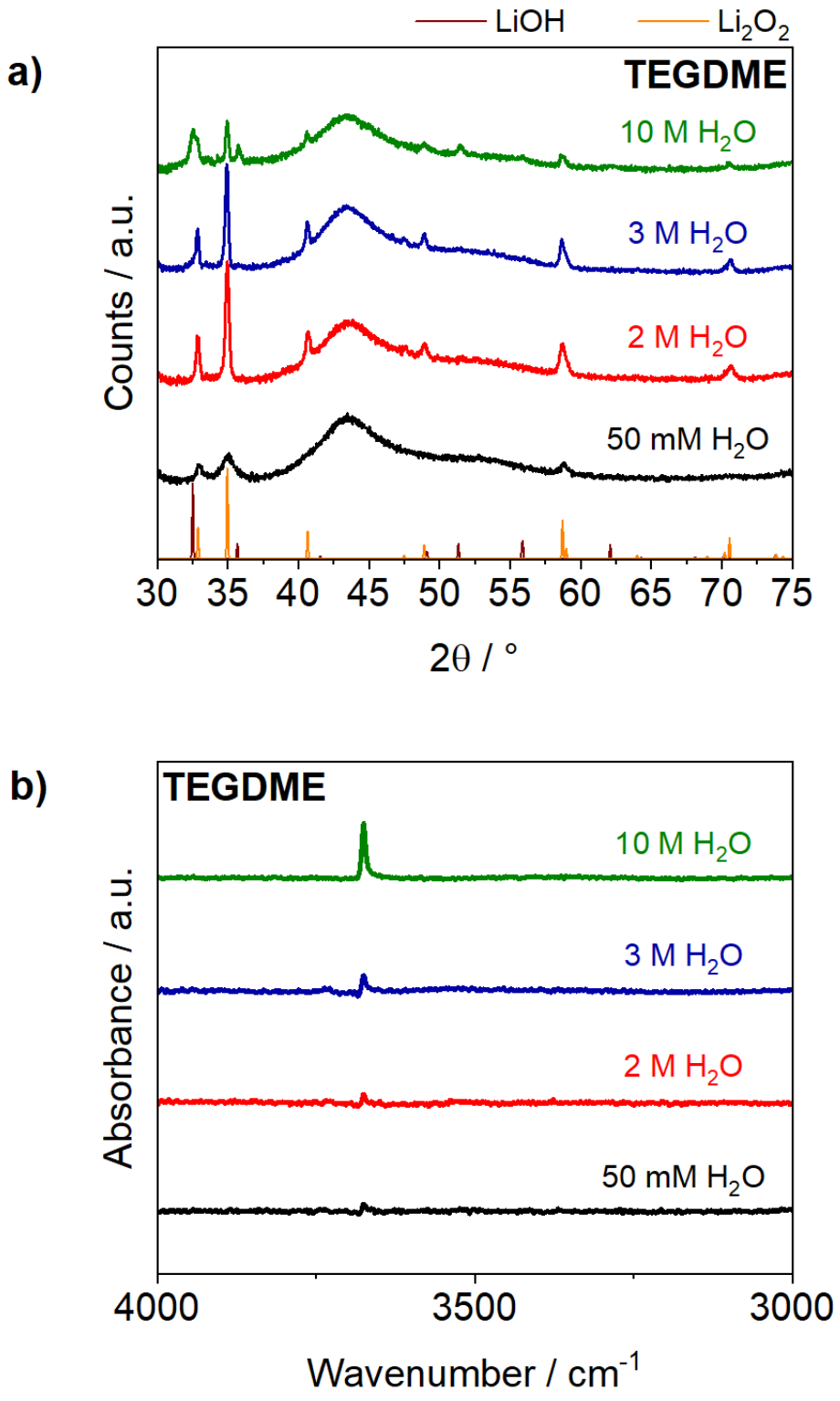


Figure 7.7. *Plots showing the change in discharge product as a function of electrolyte H_2O concentration examined through a) XRD and b) FTIR analysis of cathodes extracted from cells containing TEGDME-based electrolytes. Cells were discharged to 2 mAh cm^{-2} prior to analysis. The driest (black) and wettest (green) sample are shown alongside the highest H_2O concentration before (red) and lowest after (blue) the onset of electrochemical LiOH formation. Reference Li_2O_2 and LiOH XRD patterns were recorded experimentally.*

deviate from the ideal $2e^-/O_2$ ratio, they are consistent with those previously reported in the literature,[41] and achieve high Li_2O_2 yields of 84.2, 95.5, 91.3, and 81.6% at H_2O concentrations of 50 mM, 0.25 M, 0.5 M, and 2 M, respectively (**Figure 7.8**a), indicating that the primary discharge product is Li_2O_2. Constant gassing was observed in DME cells, which accounts for this deviation from the ideal $2e^-/O_2$ ratio. However, the consistently high Li_2O_2 yield indicates that this deviation is not the result of a change in discharge product. When the DME-based electrolyte was doped with 3 M H_2O, a significant deviation from the ideal $2e^-/O_2$ ratio and concurrent decrease in Li_2O_2 yield were observed, indicating deviation from electrochemical Li_2O_2 formation.

Figure 7.8b shows the discharge pressure decays in representative cells containing DME-based electrolyte doped with 50 mM H_2O compared to cells doped with 2, 3, and 5 M H_2O. Consistent pressure decay gradients for the cells doped with 50 mM H_2O and 2 M H_2O were observed, indicating that no significant change in rate of O_2 consumption occurred. A significant deviation in pressure decay gradient was observed between the cells containing 2 and 3 M H_2O, with the e^-/O_2 ratio approaching 4 when the electrolyte was doped with 5 M H_2O.

Figure 7.9 shows selected XRD patterns and FTIR spectra of cathodes extracted from cells containing DME-based electrolytes after discharge. H_2O concentrations of 2 and 3 M were chosen to represent before and after the onset of electrochemical LiOH formation, evidenced by the significant increase in average e^-/O_2 ratio and concurrent drop in Li_2O_2 yield that is observed between electrolytes doped with 2 and 3 M H_2O (**Figure 7.8**a). In good agreement with the pressure cell and Li_2O_2 yield data, Li_2O_2 was identified as the primary discharge product in the diffraction patterns of both cathodes extracted from cells discharged containing 50 mM and 2 M H_2O (**Figure 7.9**a). The absence of LiOH at these concentrations is further confirmed by the absence of LiOH peaks in both the XRD patterns (**Figure 7.9**a) and the FTIR spectra (**Figure 7.9**b). At 3 M H_2O, small LiOH peaks are observed in the XRD pattern, and a clear LiOH peak is observed in the FTIR spectrum, indicating the

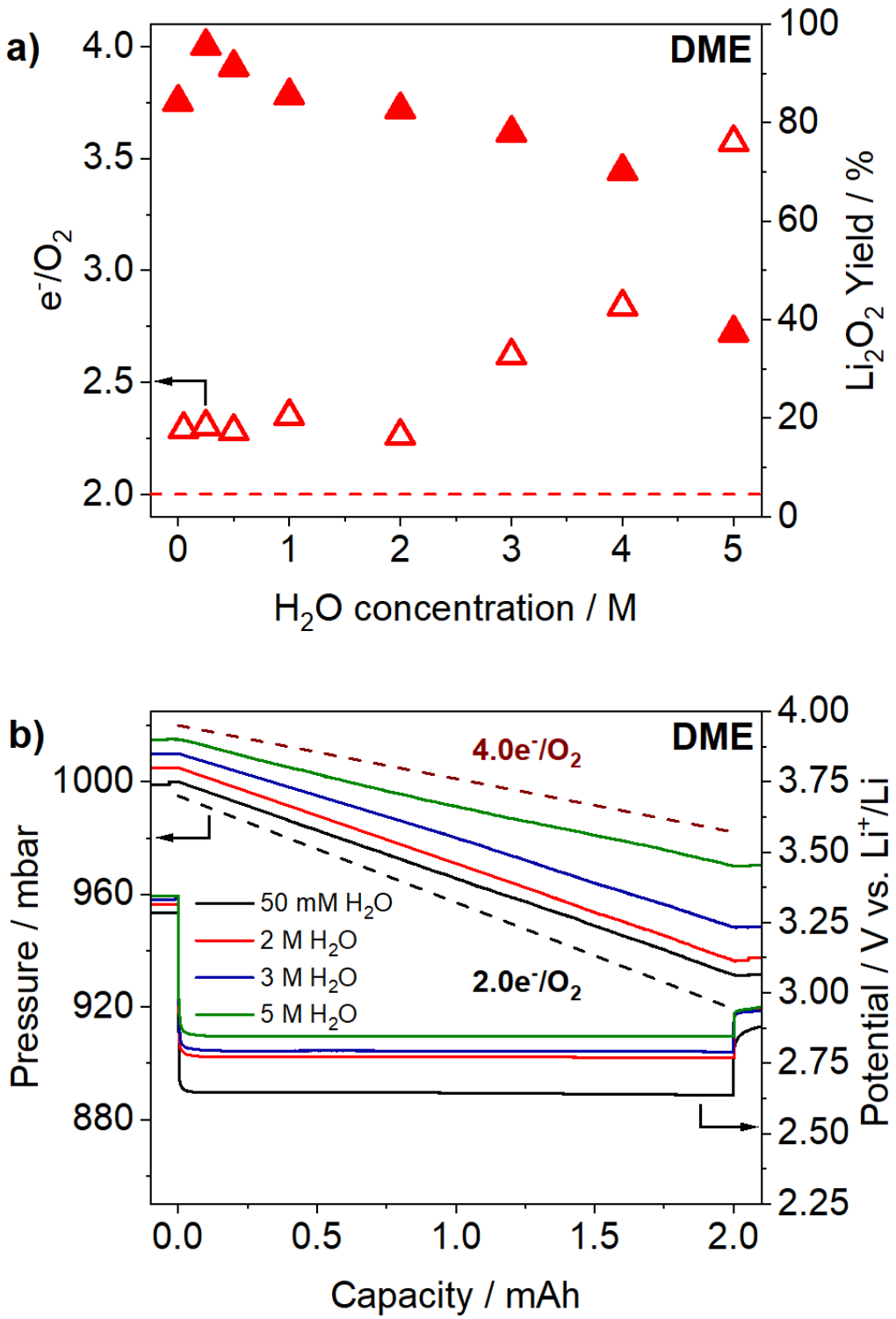


Figure 7.8. *Plots showing the effect of H_2O concentration on the a) e^-/O_2 ratio and Li_2O_2 yield and b) O_2 consumption and potential profiles of Li-air pressure cells containing DME-based electrolytes. Dashed reference lines show the ideal pressure decay gradients for a $2.0e^-/O_2$ (black) and $4.0e^-/O_2$ (red) process.*

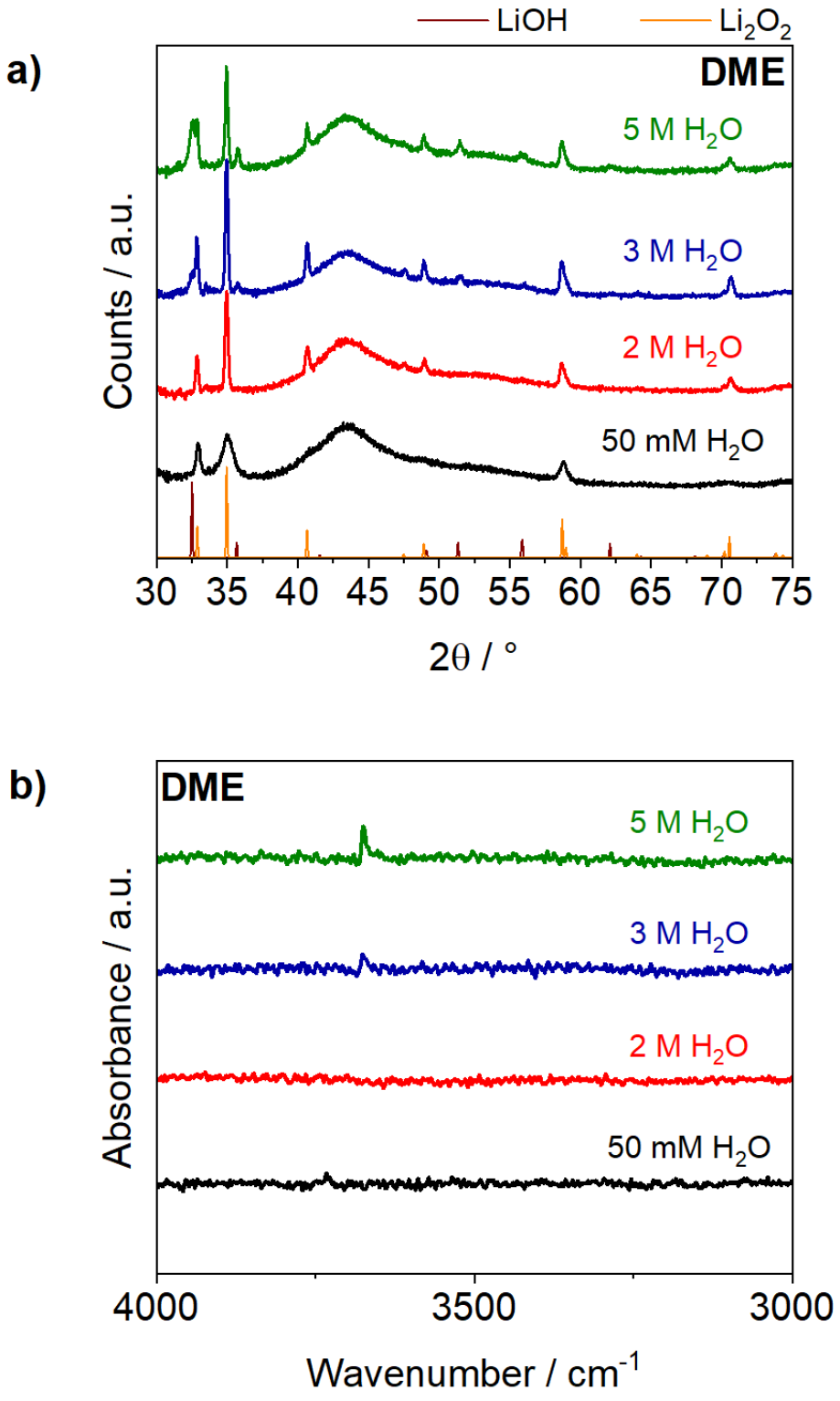


Figure 7.9. *Plots showing the change in discharge product as a function of electrolyte H_2O concentration examined through a) XRD and b) FTIR analysis of cathodes extracted from cells containing DME-based electrolytes. Cells were discharged to 2 mAh cm^{-2} prior to analysis. The driest (black) and wettest (green) sample are shown alongside the highest H_2O concentration before (red) and lowest after (blue) the onset of electrochemical LiOH formation. Reference Li_2O_2 and LiOH XRD patterns were recorded experimentally.*

onset of considerable amounts of electrochemical LiOH formation, in good agreement with the pressure cell and Li_2O_2 yield data. By 5 M H_2O, LiOH is a major discharge product.

To summarise these data, the addition of H_2O induces $4e^-$ O_2 reduction in all three electrolyte systems. However, the threshold concentration differs depending on the solvent, with DMSO requiring >5 M H_2O and glyme ethers requiring ≥2 M H_2O. These data are in good agreement with the mixture AN theory, which predicted that the hydrogen-bonding in DMSO would enable greater H_2O tolerance before formation of OH^- becomes thermodynamically favourable enough to initiate $4e^-$ O_2 reduction. In the glyme ethers, despite their lower dry solvent ANs, their inability to sufficiently interact with H_2O molecules results in a rapid increase in H_2O-solvent mixture AN, establishing a favourable environment for OH^- formation with lower H_2O concentrations. Thus, I propose a mixture AN threshold of ca. 25, below which Li_2O_2 will be the primary discharge product of a given H_2O-solvent mixture (**Figure 7.10**). Any

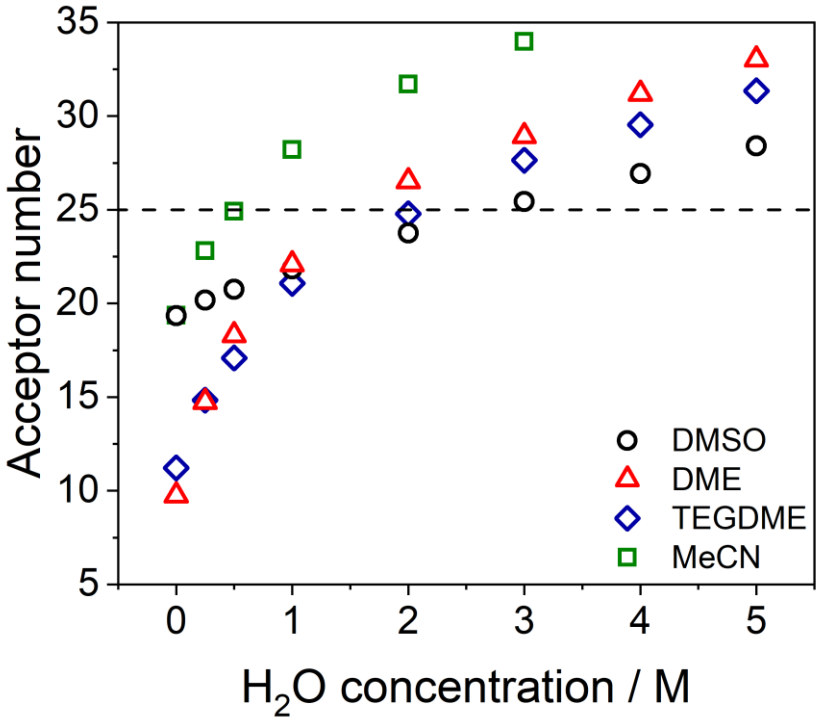


Figure 7.10. *Plot comparing H_2O-solvent mixture AN from 0 – 20 M H_2O, highlighting a H_2O-solvent mixture AN threshold of ca. 25 under which $2e^-$ O_2 reduction to form Li_2O_2 will be the primary electrochemical pathway.*

H_2O-solvent mixture that lies below this threshold will exhibit a higher discharge capacity relative to the dry solvent system, due to the solution phase transfer of Li_2O_2 enabled by the presence of H_2O, while maintaining $2e^-$ O_2 reduction as its primary electrochemical pathway. It is worth noting that MeCN also fits this trend, where significant deviation from the $2e^-/O_2$ ratio and a concurrent drop in Li_2O_2 yield are observed above 0.50 M H_2O, as explored in Chapter 6. Clearly, the solvent plays a crucial role in determining the onset of $4e^-$ O_2 reduction. The remainder of this chapter will address my understanding of the mechanistic pathway of this process.

7.5 Exploring the feasibility of chemical LiOH formation

The formation of LiOH in H_2O-containing electrolytes could occur via chemical and/or electrochemical routes. I first explore the feasibility of chemical LiOH formation in each of the H_2O-solvent mixtures. When mixed with a Li^+-containing electrolyte, KO_2 disproportionates to form Li_2O_2 with the release of O_2 (equation 7.7).[23,42]

$$2KO_{2\,(sol)} + 2Li^+_{\,(sol)} \rightarrow 2K^+_{\,(sol)} + Li_2O_{2\,(s)} + O_{2\,(g)} \qquad (7.7)$$

In this reaction, one O_2^- is reduced to form O_2^{2-}, i.e. Li_2O_2, while the other is oxidised to form O_2 which is evolved as a gaseous product. This results in the release of 1 mole of O_2 for every 2 moles of KO_2 consumed. Where H_2O is present in the electrolyte, pathways for both chemical peroxide and hydroxide formation become viable (equations 7.8 and 7.9).

$$2KO_{2\,(sol)} + 2H_2O_{\,(sol)} \rightarrow 2KOH_{\,(sol)} + H_2O_{2\,(sol)} + O_{2\,(g)} \qquad (7.8)$$

$$4KO_{2\,(sol)} + 2H_2O_{\,(sol)} \rightarrow 4KOH_{\,(sol)} + 3O_{2\,(g)} \qquad (7.9)$$

In the former, as in the dry electrolyte, 1 mole of O_2 is released for every 2 moles of KO_2 consumed. However, where chemical hydroxide formation is thermodynamically favourable, 3 moles of O_2 are released for every 4 moles of KO_2 consumed. Equations 7.10 and 7.11 show the overall reaction schemes for chemical peroxide and hydroxide formation, respectively, where charges are balanced by available cations in solution.

$$2O_2^{-}{}_{(sol)} + 2H_2O_{(sol)} \rightarrow 2OH^{-}{}_{(sol)} + H_2O_2{}_{(sol)} + O_{2\,(g)} \quad (7.10)$$

$$4O_2^{-}{}_{(sol)} + 2H_2O_{(sol)} \rightarrow 4OH^{-}{}_{(sol)} + 3O_{2\,(g)} \quad (7.12)$$

Therefore, the quantity of O_2 evolution resulting from the disproportionation of KO_2 when mixed with Li^+ and/or H_2O can be used to establish the chemical product formed in a given electrolyte mixture.

Figure 7.11 shows examples of on-line mass spectrometry (OEMS) responses recorded when KO_2 is mixed with either a dry TEGDME electrolyte or a TEGDME electrolyte doped with 5 M H_2O. The integrated area of the O_2 flux vs time plot enables quantification of the volume of O_2 released in the disproportionation reaction, which can be used to determine the chemical product that is formed, thus establishing the feasibility of chemical LiOH formation. It is clear that the rate of initial O_2 evolution is greater when KO_2 is mixed with a TEGDME electrolyte containing 5 M H_2O compared to when mixed with the dry

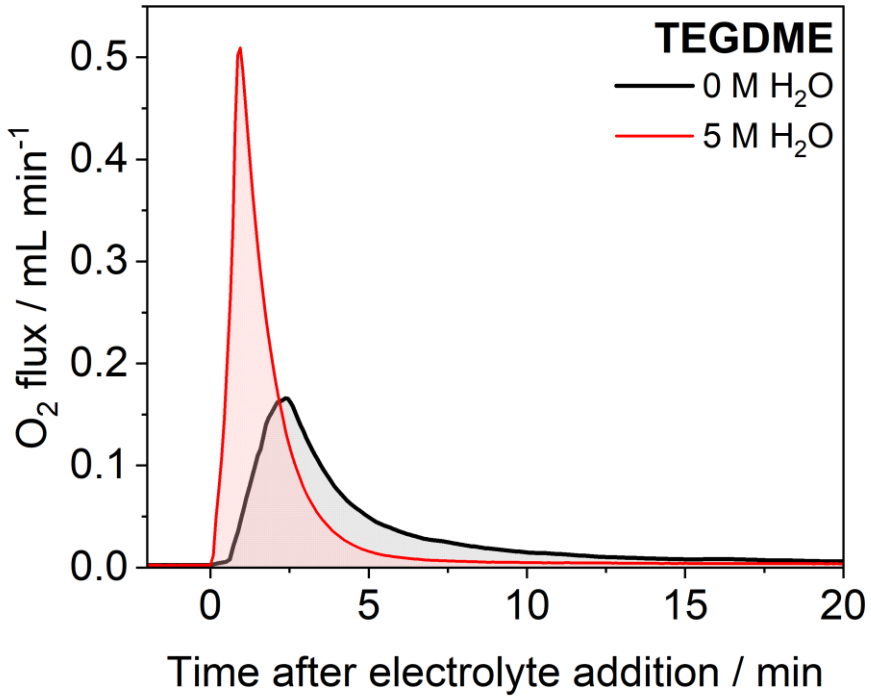


Figure 7.11. *Plot showing the rate of O_2 formation upon mixing KO_2 with a Li^+-containing dry (black) or 5 M H_2O doped (red) TEGDME-based electrolyte. The area under the curve can be used to calculate the molar ratio of O_2 evolution:KO_2 consumption to derive the chemical reaction pathway.*

electrolyte. This is due to the poor solubility of KO_2 in TEGDME, which limits the rate of the disproportionation reaction. The presence of H_2O enables both an additional pathway of KO_2 disproportionation and, where Li_2O_2 is formed, improves the solubility of the product, exposing fresh KO_2 surfaces which may otherwise be temporarily passivated by Li_2O_2. The area under both curves is equivalent to ca. 0.5 moles of O_2 per mole of KO_2 consumed, confirming that peroxide species are the primary chemical product in both the dry TEGDME electrolyte, and the electrolyte doped with 5 M H_2O. This rules out chemical formation of LiOH in TEGDME-based electrolytes with ≤5 M H_2O.

Figure 7.12 shows the ratio of the number of moles of O_2 evolved per mole of KO_2 consumed in equivalent disproportionation experiments with DMSO-, DME-, and TEGDME-based electrolytes both in their dry form and when doped with 5 M H_2O. These experiments were also run in the presence of a small strip (ca. 0.5 cm^2) of SS mesh to determine whether the surface of the mesh could

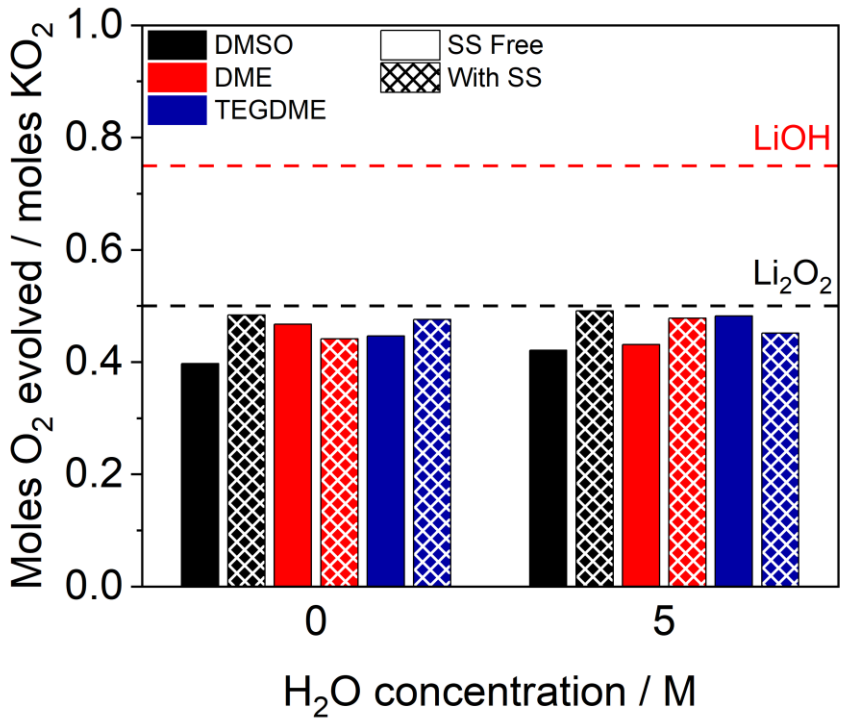


Figure 7.12. *Plot showing the molar ratio of O_2 evolved:KO_2 consumed through the disproportionation of KO_2 in a Li^+-containing dry (LHS) or 5 M H_2O doped (RHS) TEGDME-based electrolyte. Each electrolyte is shown with (hatched) and without (solid) SS present. Dashed lines show the expected ratio values for chemical Li_2O_2 (black) and LiOH (red) formation.*

act as a heterogenous catalyst and facilitate chemical LiOH formation. A ratio close to, and critically not above, 0.5 moles of O_2 was evolved per mole of KO_2 consumed in all dry electrolytes, consistent with the chemical formation of peroxide species. A comparable molar ratio was observed when H_2O concentration was increased to 5 M and when SS was present in any of the electrolytes, demonstrating that SS does not act as a chemical catalyst and there is no chemical route to LiOH formation in any of the H_2O-solvent mixtures where H_2O concentration is ≤5 M (**Figure 7.12**). These data mark a critical discovery in Li-air battery research. If the chemical pathway of LiOH formation was possible, LiOH accumulation in the presence of H_2O would be inevitable unless the O_2 supply was meticulously dried, accepting the ca. 33% specific energy penalty that is required to facilitate this.[17] With chemical formation ruled out, electrochemical pathways to LiOH are now explored.

7.6 The impact of H_2O on electrochemical O_2 reduction

O_2 reduction on carbon electrodes has been extensively studied in aqueous systems and it is widely accepted that the formation of H_2O_2 via a $2e^-$ O_2 reduction pathway is favourable compared to forming OH^- via $4e^-$ O_2 reduction, as a result of the exceptionally strong O=O bond (498 kJ mol^{-1}) that would need to be cleaved to form OH^-.[43–45] To understand if this same selectivity is exhibited in H_2O-solvent mixtures, RDE using a GC disk electrode was employed to study the O_2 reduction process. $TBAClO_4$ was used as the electrolyte salt to ensure sufficient solubility of the O_2 reduction products to allow for Levich analysis. If the kinematic viscosity (υ) of the electrolyte and the diffusion coefficient (D_O) and saturation concentration (C_O) of the redox active species are known, equation 7.13 can be applied to calculate the number of electrons (n) transferred in a faradaic process recorded at a RDE of known surface area (A) and rotational velocity (ω) by recording the limiting current (i_L), where F is the Faraday constant.[46]

$$i_L = 0.620nFAC_OD_O^{2/3}\upsilon^{-1/6}\omega^{1/2} \quad (7.13)$$

Literature values for dry solvent D_O and C_O were obtained (9.75 ×10^{-6} cm^2 s^{-1} and 2.10 mM, respectively, for DMSO and 3.88 ×10^{-6} cm^2 s^{-1} and 9.57 mM, respectively, for DME).[34] D_O was approximated using the Stokes-Einstein equation to account for H_2O concentration, resulting in final applied values of 1.04 ×10^{-5} cm^2 s^{-1} and 7.48 ×10^{-6} cm^2 s^{-1} for DMSO and DME, respectively (equation 7.14).

$$D_O = \frac{k_B T}{6\pi\eta r} \qquad (7.14)$$

Where k_B is the Botlzmann constant, T is the absolute temperature, r is the molecular radii of O_2 and η is the dynamic viscosity which was measured experimentally (SVM 3000, Anton Paar) and converted between η and *υ* as required by assuming a linear relationship between solvent concentration and contribution to overall mixture density. **Figure 7.13** shows RDE LSVs recorded with a GC electrode in DMSO- and DME-based electrolytes doped with

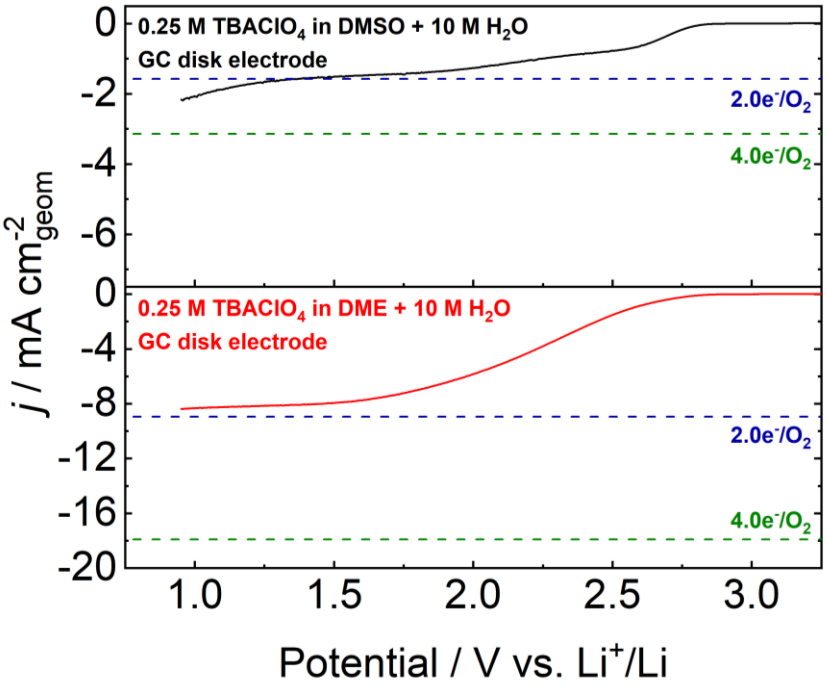


Figure 7.13. *RDE (1000 rpm) LSVs showing O_2 reduction on GC in TBA^+-containing DMSO- (black) and DME-based (red) electrolytes doped with 10 M H_2O. A GC disk working electrode, fritted LFP reference electrode and Pt counter electrode were used. Dashed lines show 2.0 (blue) and 4.0 (green) e^-/O_2 values calculated through Levich analysis and normalised to geometric electrode area.*

10 M H_2O, at which concentration the pressure cell measurements indicate that significant quantities of $4e^-$ O_2 reduction will be occurring. Levich analysis of these LSVs indicates that in both systems O_2 reduction proceeds via a $2e^-$ process, matching the observed behaviour in fully aqueous systems and indicating that $4e^-$ O_2 reduction does not occur at carbon electrodes, even with a high H_2O concentration. Equivalent analysis with TEGDME was not possible due to insufficient solubility of $TBAClO_4$ in 10 M H_2O-TEGDME electrolyte.

With $4e^-$ O_2 reduction at the carbon electrode ruled out, the only other electroactive material that is in contact with the electrolyte at the positive electrode surface is the SS mesh, which is commonly employed as a current collector. To explore the possibility of SS being the source of $4e^-$ O_2 reduction, analogous RDE LSVs were performed using a SS disk electrode (**Figure 7.14**). The current density recorded for O_2 reduction with a SS electrode was approximately double that observed for the GC electrode in both systems,

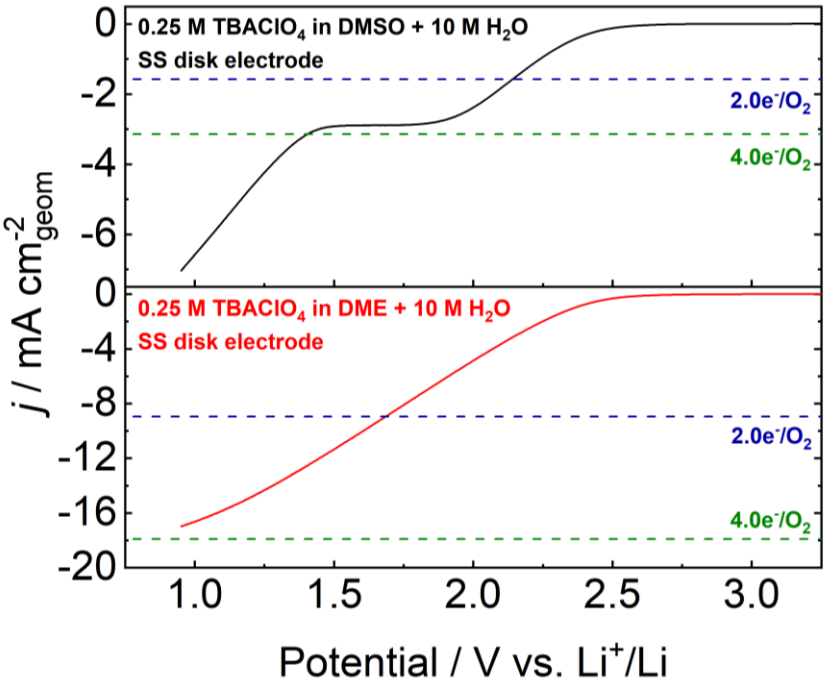


Figure 7.14. *RDE (1000 rpm) LSVs showing O_2 reduction on SS in TBA^+-containing DMSO- (black) and DME-based (red) electrolytes doped with 10 M H_2O. A SS disk working electrode, fritted LFP reference electrode and Pt counter electrode were used. Dashed lines show 2.0 (blue) and 4.0 (green) e^-/O_2 values calculated through Levich analysis and normalised to geometric electrode area.*

showing good agreement with the Levich analysis and demonstrating that $4e^-$ O_2 reduction is possible on SS. These data indicate that carbon electrodes are not capable of $4e^-$ O_2 reduction and it is instead likely that $4e^-$ O_2 reduction occurs at the electroactive SS mesh current collector where H_2O concentration is sufficient.

These RDE data demonstrate that O_2 reduction is substrate sensitive. However, the measurements required for an idealised system may not be representative of the conditions in the pressure cell measurements described in section 7.4. To confirm that $4e^-$ reduction occurs on the SS surface in the pressure cells, LSVs using SS mesh flags as working electrodes in a Li^+-containing electrolyte were recorded in DMSO-, DME-, and TEGDME-based electrolytes doped with 1 – 5 M H_2O. This range coincides with the region in which the pressure cell data suggests deviation from the ideal $2e^-$ O_2 reduction should occur in the glyme electrolytes, and the threshold of H_2O-DMSO mixtures will be reached. To ensure direct comparability between electrolyte H_2O concentrations, FcMeOH was used as an internal reference. **Figure 7.15** shows the LSVs recorded in DMSO-based electrolytes, where a clear relationship between increasing peak current and increasing H_2O concentration is observed, demonstrating that the addition of H_2O facilitates O_2 reduction by improving the solubility of the discharge products, preventing passivation of the SS mesh. No major shift in the onset potential of O_2 reduction is observed across this H_2O concentration range, indicating that there is little change in the thermodynamic favourability of O_2 reduction in H_2O-DMSO electrolytes across this range.

Figure 7.16 shows equivalent LSVs carried out in DME- and TEGDME-based electrolytes doped with 1 – 5 M H_2O. As seen in the H_2O-DMSO mixtures, a clear relationship between increasing H_2O concentration and increasing peak current is observed, confirming that the presence of H_2O improves the solubility of the discharge product in each of the solvents studied. However, the magnitude of this change is not uniform across solvents, with O_2 reduction in DME exhibiting a greater dependence on H_2O concentration than either TEGDME or DMSO. This demonstrates that the electrolyte solvent also has an influence on the

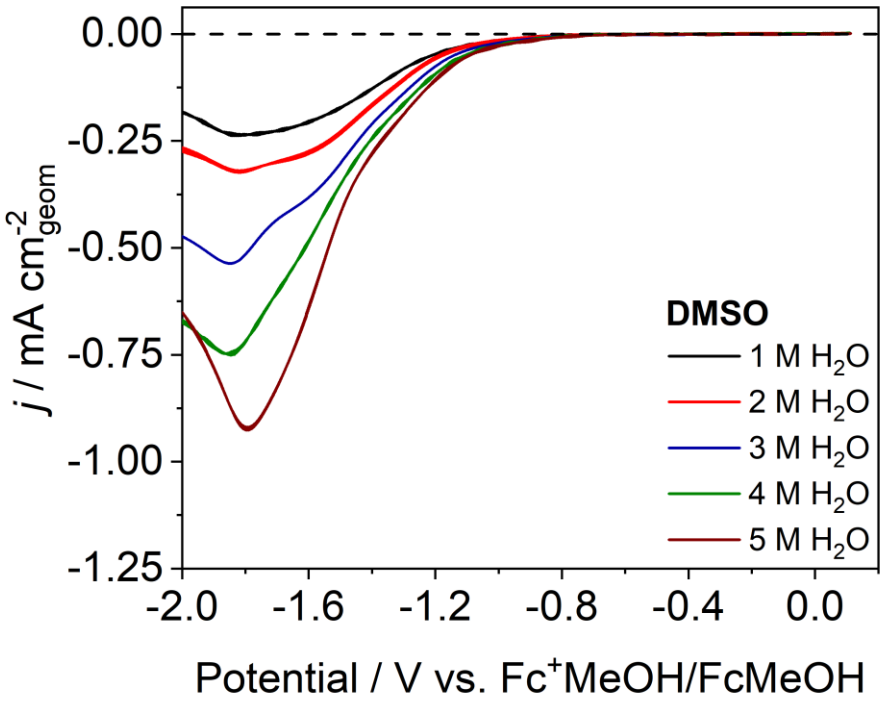


Figure 7.15. *LSVs showing O_2 reduction on a SS flag electrode in Li^+-containing DMSO-based electrolyte doped with between 1 – 5 M H_2O. A SS mesh working electrode, fritted LFP reference electrode and Pt counter electrode were used. The current was normalised to the geometric surface area of the submerged SS mesh (0.5 cm^2). The dashed line tracks a value of 0 for clarity.*

thermodynamic favourability of O_2 reduction. Moreover, the onset potential of O_2 reduction in both glyme electrolytes shifts positively with respect to increasing H_2O concentration, with ca. 0.14 and 0.18 V shifts in onset potential observed for DME- and TEGDME-based electrolytes between doped H_2O concentrations of 1 – 5 M, respectively, indicating that O_2 reduction becomes more thermodynamically favourable as H_2O increases.

In summary, SS can facilitate $4e^-$ O_2 reduction in all H_2O-solvent mixtures. Although in DMSO-based electrolytes little-to-no change in the onset potential of O_2 reduction is observed where H_2O concentration is ≤5 M, in both DME- and TEGDME-based electrolytes increasing H_2O concentration improves the thermodynamic favourability of O_2 reduction. However, the potentials required for O_2 reduction on SS mesh are outside of the operational potentials of the pressure cells, with the lowest discharge potential measured across these

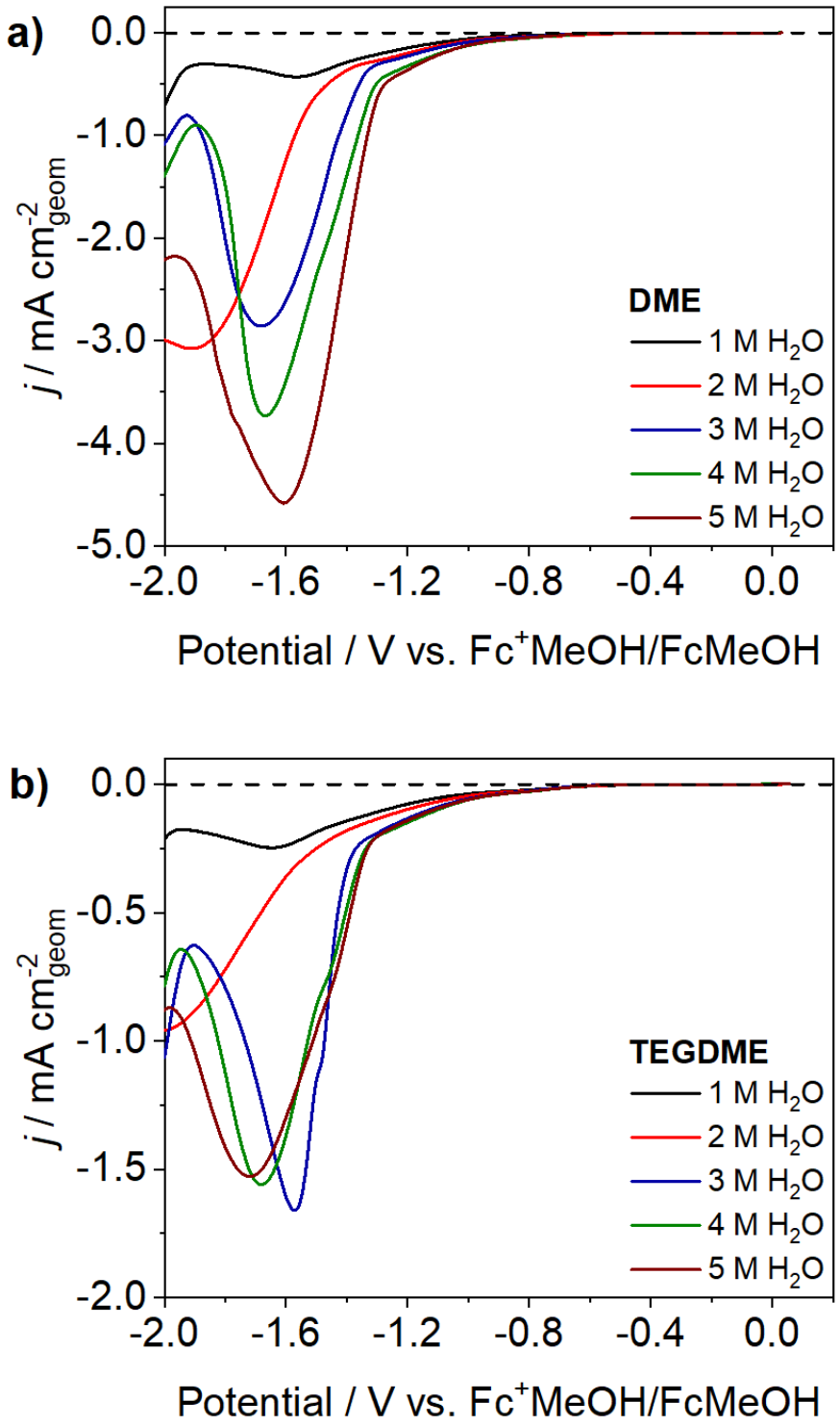


Figure 7.16. *LSVs showing O_2 reduction on a SS flag electrode in Li^+-containing a) DME- and b) TEGDME-based electrolyte doped with between 1 – 5 M H_2O. A SS mesh working electrode, fritted LFP reference electrode and Pt counter electrode were used. The current was normalised to the geometric surface area of the submerged SS mesh (0.5 cm^2). The dashed line tracks a value of 0 for clarity.*

H_2O-solvent mixtures being equivalent to −1.07 V vs Fc^+MeOH/FcMeOH. This indicates that, although SS can facilitate $4e^-$ O_2 reduction, this electrochemical pathway is not accessible under the conditions present in pressure cell measurements, ruling out this as the route to electrochemical LiOH formation under operational conditions. This raises the question as to how $4e^-$ O_2 reduction can be observed in the pressure cells and suggests that another reaction may be involved.

7.7 The fate of hydroperoxide species in Li-air cells

With no direct electrochemical route from O_2 to OH^- possible with carbon or SS electrodes, another species must be involved that facilitates electrochemical LiOH formation. Where H_2O is present in an electrolyte, hydroperoxide species are formed either through H_2O-mediated chemical equilibria, that enable solution phase transfer of Li_2O_2, or through direct electrochemical formation (equations 7.3-7.6).

$$Li_2O_{2\,(s)} + H_2O_{(sol)} \rightleftharpoons LiOOH_{(sol)} + LiOH_{(s)} \quad (7.3)$$

$$LiOOH_{(sol)} + H_2O_{(sol)} \rightleftharpoons H_2O_{2\,(sol)} + LiOH_{(s)} \quad (7.4)$$

$$2Li^+_{(sol)} + O_{2\,(sol)} + H_2O_{(sol)} + 2e^- \rightarrow LiOOH_{(sol)} + LiOH_{(sol)} \quad (7.5)$$

$$2Li^+_{(sol)} + O_{2\,(sol)} + 2H_2O_{(sol)} + 2e^- \rightarrow H_2O_{2\,(sol)} + 2LiOH_{(sol)} \quad (7.6)$$

Where the H_2O concentration is low, it is unlikely that any H_2O_2 will form, and any LiOOH that does form will be short lived due to the poor environment for OH^- stabilisation offered by a low mixture AN, thus these equilibria strongly favour Li_2O_2. As the H_2O concentration increases, consequently increasing the overall H_2O-solvent mixture AN, a more favourable environment for OH^- formation will be presented. This will in turn increase the activity of LiOOH in solution and, where H_2O concentration is sufficient, allow H_2O_2 formation. With the presence of these hydroperoxide species being intrinsically tied to the stabilisation of OH^- in solution, it is possible that either LiOOH or H_2O_2 could be reduced on a GC or SS electrode.

To assess the feasibility of hydroperoxide reduction on GC and SS electrodes, RDE LSVs were recorded in 10 M H_2O-solvent mixtures doped with 5 mM H_2O_2. **Figure 7.17** shows the results of these experiments in a DMSO-based electrolyte, where little-to-no electrochemical activity is seen with a GC electrode in both the background sample with no H_2O_2, and where electrolyte contained 5 mM H_2O_2, demonstrating that hydroperoxide reduction is not possible on carbon electrodes. A similar response is seen in the background LSV with a SS electrode, with the onset of some electrolyte degradation, likely H_2 evolution, occurring earlier than in the analogous GC LSV. However, when the electrolyte is doped with 5 mM H_2O_2, it is immediately clear that a reduction process occurs on the SS electrode, with an onset potential (i.e. deviation from the measured background) of ca. −0.5 V vs Fc^+MeOH/FcMeOH, indicating that hydroperoxide species can be electrochemically reduced at SS surfaces in a DMSO-based electrolyte doped with 10 M H_2O.

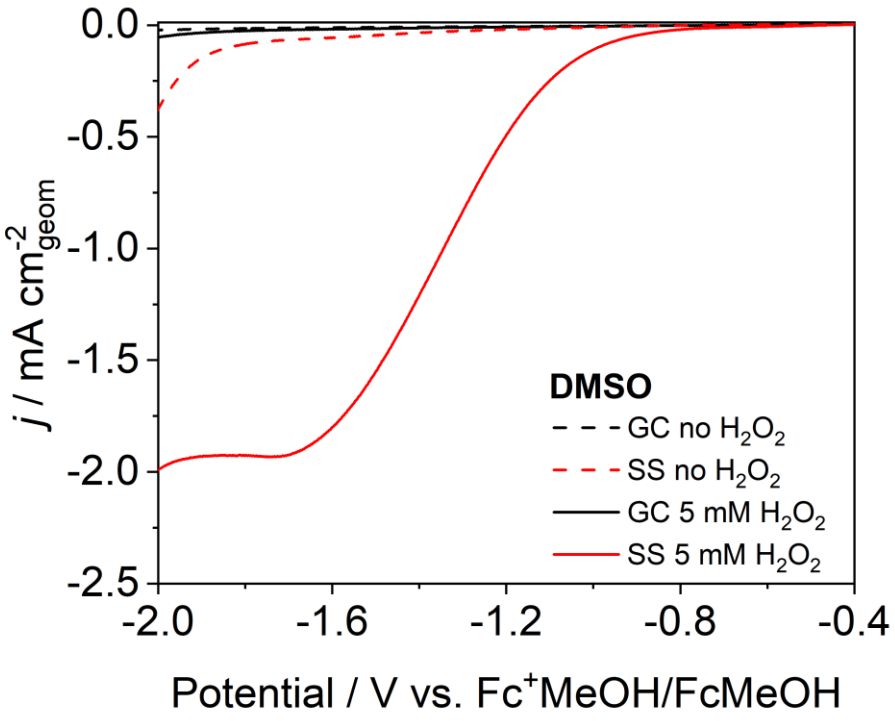


Figure 7.17. *RDE (1000 rpm) LSVs showing H_2O_2 reduction (solid lines) on GC (black) and SS (red) electrodes in Li^+-containing DMSO-based electrolytes doped with 10 M H_2O. A GC or SS disk working electrode, fritted LFP reference electrode and Pt counter electrode were used. Dashed lines show background LSVs under an N_2-atmosphere, demonstrating the onset of solvent reduction.*

Figure 7.18 shows the results of equivalent experiments carried out with DME- and TEGDME-based electrolytes doped with 10 M H_2O. The same observations translate to these systems, with no electrochemical activity towards H_2O_2 being seen with a GC electrode, but a significant new reduction process being observed with a SS electrode. To summarise, it is immediately clear that H_2O_2 is readily reduced at SS electrodes, while GC electrodes are incapable of doing so. These data strongly suggest that the reduction of hydroperoxide species on the surface of SS mesh could be the source of electrochemical LiOH formation.

To assess the feasibility of hydroperoxide reduction being the source of the $4e^-$ O_2 reduction process, a standard $Fc^+MeOH/FcMeOH$ reference scale is applied to enable comparison across flooded cell and pressure cell analyses. **Figure 7.19**a shows the discharge voltage plateaus for the first electrochemical discharge of cells containing DMSO electrolytes doped with 1 – 5 M H_2O. It is clear that increasing the H_2O content of DMSO-based electrolytes changes the observed voltage plateau, with a range of −1.07 to −0.97 V vs $Fc^+MeOH/FcMeOH$ being recorded across the full range of doped H_2O concentrations. **Figure 7.19**b and c show the discharge potential profiles of equivalent DME- and TEGDME-based electrolytes, respectively. A comparable relationship between H_2O concentration and discharge voltage plateau to that seen in the H_2O-DMSO system is observed. Discharge voltage plateau ranges of −0.77 to −0.74 and −0.86 to −0.81 V vs $Fc^+MeOH/FcMeOH$ were recorded for H_2O-DME and H_2O-TEGDME mixtures, respectively.

These voltage ranges lie on the threshold of reduction onset in the RDE LSVs of each of the 10 M H_2O-solvent mixtures. It is important to note that the catalytic activity of the SS RDE disk electrode may be different to the SS mesh current collector used in the pressure cells. To ascertain whether hydroperoxide reduction occurs under conditions representative of a pressure cell discharge, SS flag LSVs were recorded in DMSO-, DME- and TEGDME-based electrolytes doped with 1 – 5 M H_2O and 5 mM H_2O_2. **Figure 7.20** shows the LSVs recorded in DMSO-based electrolytes, where the onset of H_2O_2 reduction is >100 mV positive of the onset of O_2 reduction (dashed line), comfortably within the

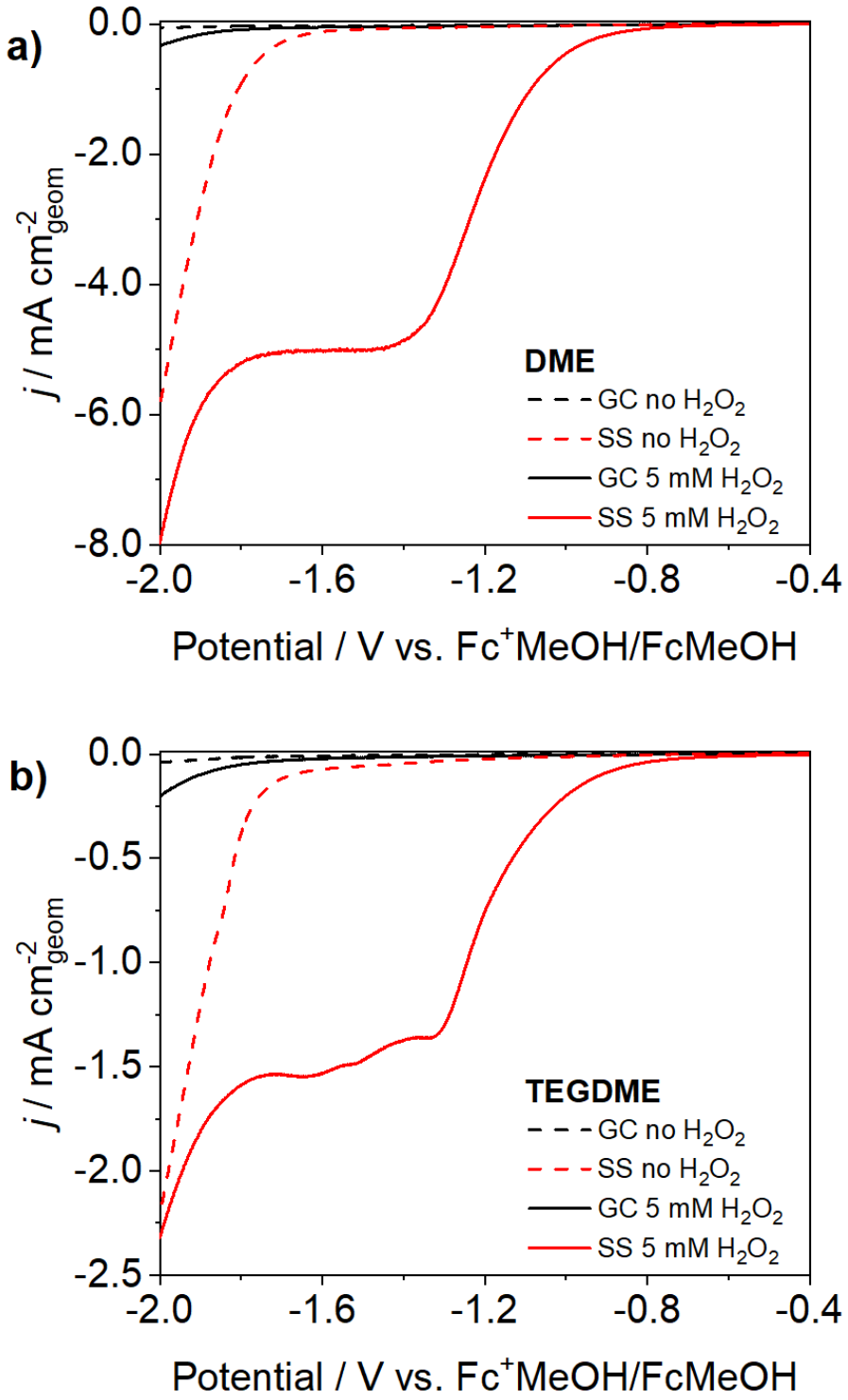


Figure 7.18. *RDE (1000 rpm) LSVs showing H_2O_2 reduction (solid lines) on GC (black) and SS (red) electrodes in Li^+-containing a) DME- and b) TEGDME-based electrolytes doped with 10 M H_2O. A GC or SS disk working electrode, fritted LFP reference electrode and Pt counter electrode were used. Dashed lines show background LSVs under an N_2-atmosphere, demonstrating the onset of solvent reduction.*

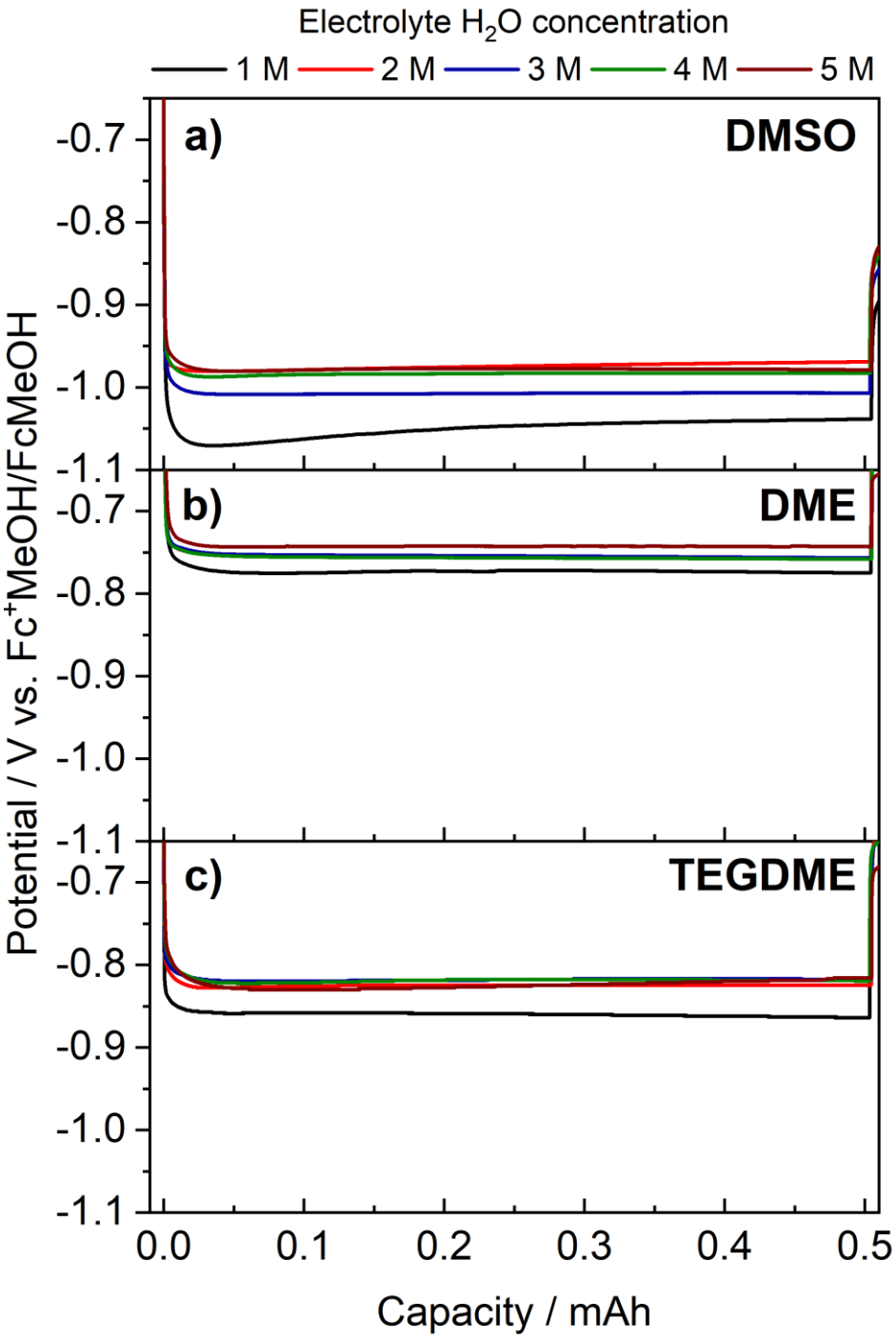


Figure 7.19. *Discharge voltage profiles of H_2O-containing a) DMSO-, b) DME- and c) TEGDME-based electrolytes. A 0.5 mAh discharge is shown across a H_2O concentration range of 1 – 5 M. Measured potential has been referenced to the Fc^+MeOH/FcMeOH redox couple to allow direct comparison between data.*

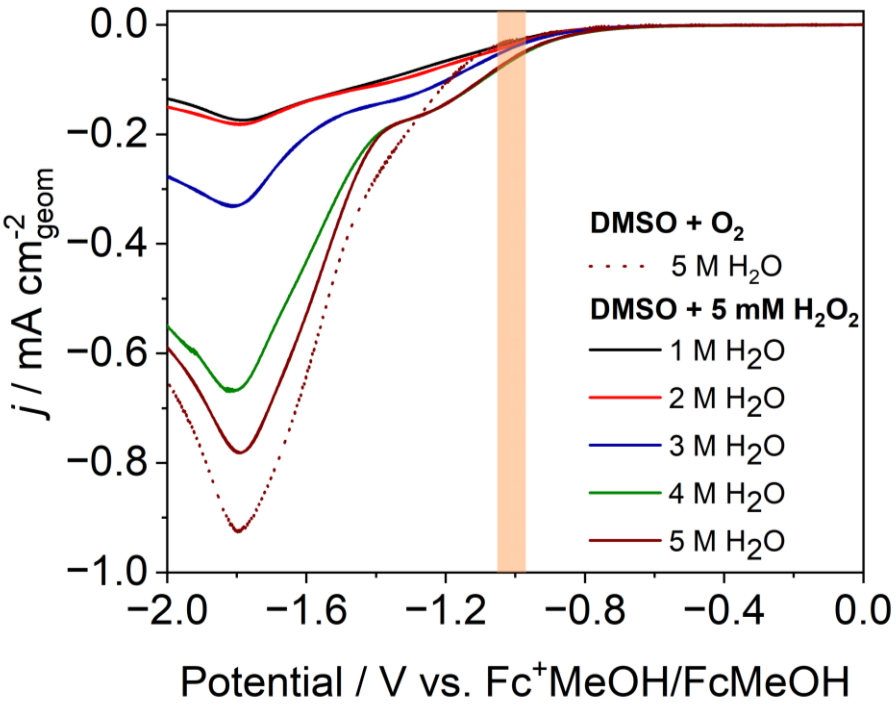


Figure 7.20. *LSVs showing H_2O_2 reduction on a SS flag electrode in a Li^+-containing DMSO-based electrolyte doped with between 1 – 5 M H_2O. A SS mesh working electrode, fritted LFP reference electrode and Pt counter electrode were used. A LSV of O_2 reduction on a SS flag electrode in Li^+-containing DMSO-based electrolyte doped with 5 M H_2O (dotted line) and the spread of the recorded discharge voltage plateaus (orange box, data shown in Figure 7.19a) are shown for comparison.*

plateau region of cell discharge (indicated by the orange box). **Figure 7.21** shows the analogous LSVs recorded in DME- and TEGDME-based electrolytes wherein H_2O_2 reduction is shifted positive of O_2 reduction to a greater extent (>400 mV).

These data indicate that the 4e⁻ O_2 reduction likely proceeds via a two-step mechanism, wherein O_2 is electrochemically reduced by 2e⁻ on a carbon surface forming peroxide species (Li_2O_2/LiOOH/H_2O_2). A dynamic equilibrium is formed between solid Li_2O_2 and hydroperoxide species (LiOOH and/or H_2O_2), mediated by the presence of H_2O. These hydroperoxide species can then be reduced by a further 2e⁻ on the surface of the electroactive SS mesh current collector, forming LiOH and removing hydroperoxide species from the equilibrium, driving the forward reaction as per Le Chatelier's principle. **Figure 7.22** brings

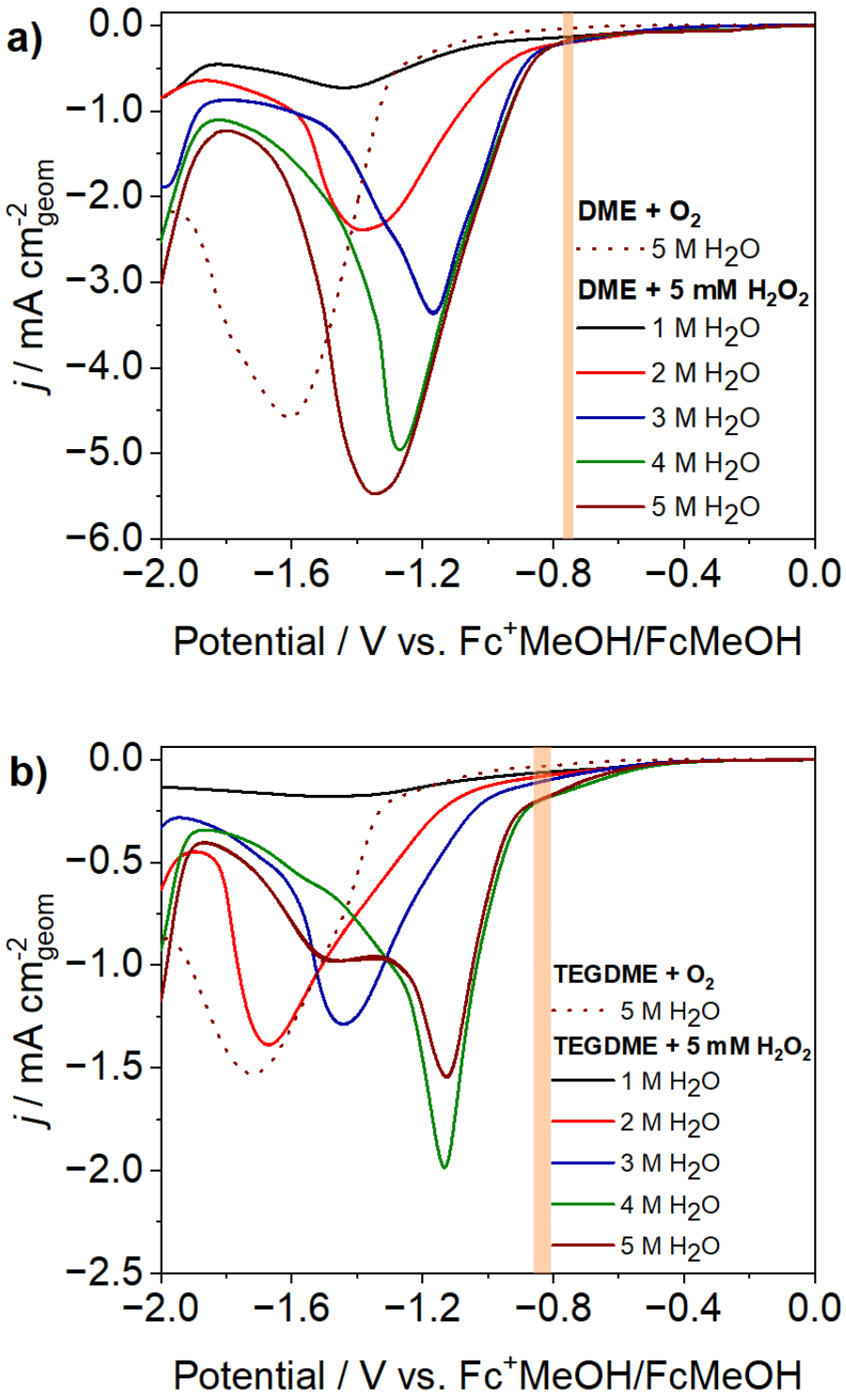


Figure 7.21. *LSVs showing H_2O_2 reduction on a SS flag electrode in a Li^+-containing a) DME- and b) TEGDME-based electrolyte doped with between 1 – 5 M H_2O. A SS mesh working electrode, fritted LFP reference electrode and Pt counter electrode were used. A LSV of O_2 reduction on a SS flag electrode in Li^+-containing electrolyte doped with 5 M H_2O (dotted line) and the spread of the recorded discharge voltage plateaus (orange box, data shown in Figure 7.19) are shown for comparison.*

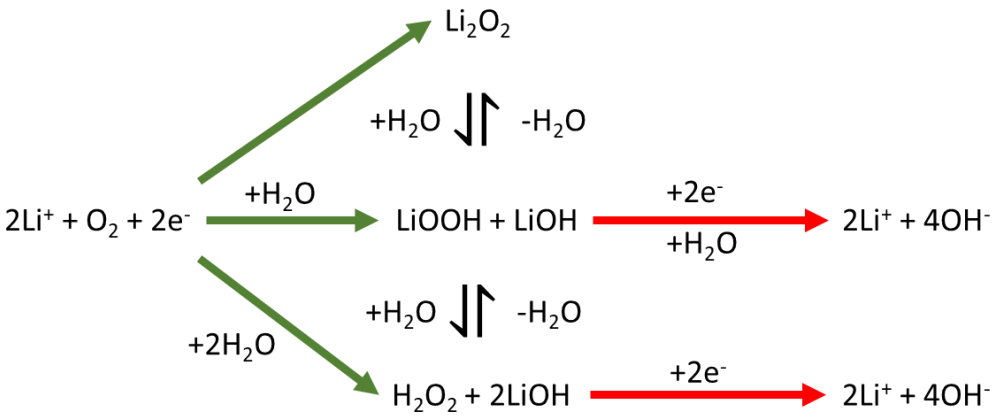


Figure 7.22. *Schematic representation of the possible electrochemical discharge pathways in a Li-air cell on a carbon (green arrows) and SS (red arrows) electrode in a Li^+-containing electrolyte. Black arrows describe the chemical equilibria established between peroxide species where H_2O is present.*

together these observations, demonstrating that $4e^-$ O_2 involves several reactions: chemical and/or electrochemical formation of LiOOH or H_2O_2 on carbon, followed by an additional $2e^-$ reduction on SS to form LiOH. The identification of this 2+2 reaction mechanism marks a critical discovery in the field of Li-air batteries.

With the second stage of the 2+2 mechanism that has been identified for $4e^-$ O_2 reduction being reliant on the presence of hydroperoxide species, the amount of H_2O that a given electrolyte solvent can tolerate before switching to $4e^-$ O_2 reduction can be described by the mixture AN theory. Where H_2O-solvent mixture AN is low, there will be a high thermodynamic barrier for OH^- formation and the hydroperoxide forming chemical equilibria will strongly favour Li_2O_2. As H_2O concentration increases, so will the mixture AN until a favourable environment for OH^- stabilisation is established, thus providing a stable environment for hydroperoxide species. Where these hydroperoxide species are present in the electrolyte, and the conditions are sufficient that the reaction is favourable, the electrochemically active SS mesh can induce $2e^-$ reduction of these hydroperoxide species to form LiOH, driving the chemical equilibrium away from Li_2O_2 and increasing the observed e^-/O_2 ratio.

7.8 High-performance Li-air batteries with 13% and 100% humidity

The results presented in this chapter thus far have identified two prerequisites for $4e^-$ O_2 reduction to occur, namely, (electro)chemical formation of hydroperoxide species and the presence of a SS electroactive surface to reduce these hydroperoxide species to LiOH, the $4e^-$ reduction product. Either combatting the environment for hydroperoxide formation, through electrolyte solvent selection to maintain low H_2O-solvent mixture AN, or removal of SS electroactive surfaces should allow the presence of H_2O while maintaining $2e^-$ O_2 reduction. TEGDME was taken forward as the electrolyte solvent for these high-performance cell studies due to its low vapour pressure making it most suitable for analysis with a flowing gas stream.[38] To match state-of-the-art cell conditions, DBBQ and TEMPO were employed as discharge and charge redox mediators, respectively.[7,47,48] Where SS is present, a limit of 1 M H_2O was chosen to ensure that the H_2O-TEGDME mixture AN was below the identified deviation from $2e^-$ O_2 reduction (**Figure 7.6**). Where a SS-free cell design was applied, a H_2O concentration of 9.1 M was chosen, to reflect an environment with 100% relative humidity (20 °C), to understand the cell electrochemistry under the most extreme humidity conditions (no drying of a H_2O saturated gas stream). The saturation H_2O concentration of the TEGDME-based electrolyte at 20 °C was calculated by housing an open bottle of electrolyte beside an open bottle of H_2O in sealed containment, insulated at 20 °C with a humidity sensor, until the relative humidity had stabilised at 100% for more than 12 hours. The H_2O concentration of the electrolyte was then calculated through Karl-Fischer titration to be ca. 9.1 M. Previous work carried out by Holc determined that 13% relative humidity was approximately equivalent to 1 M H_2O in the TEGDME-based electrolyte used in this study.[23]

To attain a baseline performance for comparison of our H_2O-containing systems, the discharge performance of cells containing a dry TEGMDE electrolyte with 25 mM DBBQ and 25 mM TEMPO were discharged to a potential limit of 2.3 V vs Li^+/Li at various rates between 0.1 – 1 mA cm^{-2}. The inclusion of redox mediators is necessary to achieve high discharge and charge

rates.[49] DBBQ acts to mediate discharge, being reduced on the surface of the cathode and promoting solution phase O_2 reduction, delaying the passivation of the electrode surface and enabling both higher discharge rates and capacities to be achieved. Similarly, TEMPO mediates charge, being oxidised at the surface of the cathode and subsequently facilitating the oxidation of Li_2O_2 that may not be directly in contact with the electrode surface, thus providing a route for charge transfer to the toroidal Li_2O_2 that is formed on discharge. Although H_2O will enable some mediation of both discharge and charge, through solubilising species, this process is chemical rather than electrochemical and therefore does not provide a significant contribution to the charging performance or enable higher charge rates.

Figure 7.23a shows discharge voltage profiles for the first discharge of these cells, where a clear relationship between increasing discharge rate and decreasing capacity is observed. It is worth noting that the overpotential required for O_2 reduction also increases as a function of rate, due to a larger proportion of O_2 reduction occurring on the electrode surface, forming thin film Li_2O_2, rather than through DBBQ-mediated solution phase O_2 reduction. This results in a higher rate of electrode passivation per unit charge passed, reducing the active surface area and increasing the relative current density (i.e. causing electrode polarisation). Despite this, the Li_2O_2 yield remains consistently high across all discharge rates, demonstrating that the poor capacity performance is the result of electrode passivation, due to surface O_2 reduction outcompeting DBBQ, rather than parasitic degradation reactions (**Figure 7.23**b). At low rates, DBBQ will effectively mediate the discharge process, facilitating solution-phase O_2 reduction and delaying the passivation of the electrode surface with thin film Li_2O_2. As the discharge rate increases, direct O_2 reduction on the surface of the positive electrode becomes increasingly favourable and competes with DBBQ-mediated O_2 reduction, resulting in earlier passivation of the electrode surface and reducing discharge capacity. At high discharge rates surface O_2 reduction will dominate, outcompeting the effects of the redox mediator and resulting in rapid thin film Li_2O_2 formation.

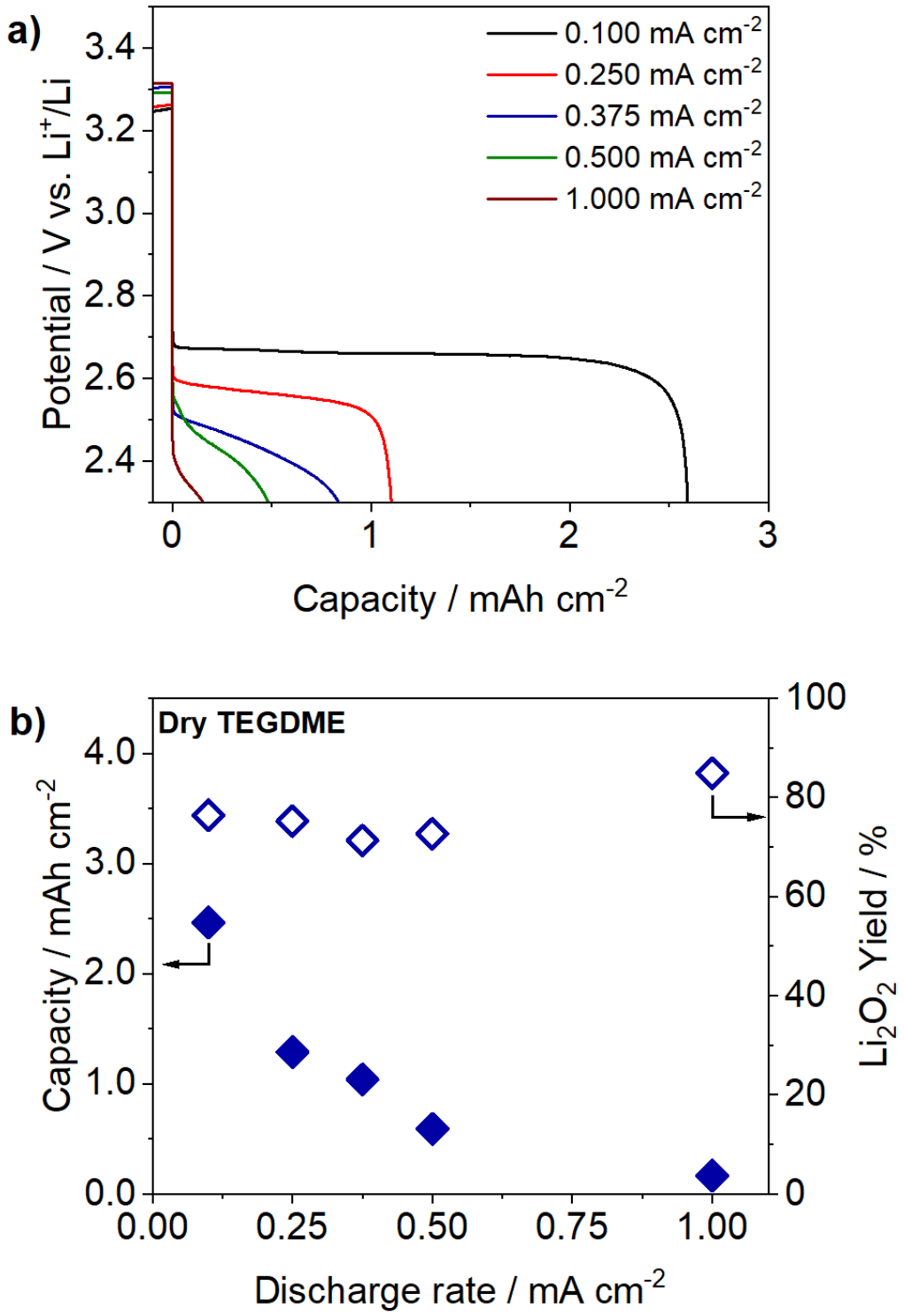


Figure 7.23. *Plots showing a) representative discharge voltage profiles and b) the average discharge capacity and Li_2O_2 yield as a function of discharge rate for Li-air cells containing a dry TEGDME-based electrolyte doped with 25 mM DBBQ and 25 mM TEMPO.*

To understand the effect of H_2O on discharge performance, equivalent experiments were carried out with cells containing a TEGDME-based electrolyte doped with 1 M H_2O, 25 mM DBBQ, and 25 mM TEMPO. **Figure 7.24**a shows the discharge voltage profiles of representative cells, where a clear increase in discharge capacity can be seen across all rates compared to the dry system (**Figure 7.23**a). **Figure 7.24**b shows the average discharge capacity and Li_2O_2 yields recorded across the full range of discharge rates, where a consistently high Li_2O_2 yield, comparable to the dry cells is observed (**Figure 7.23**b). The highest average discharge capacity is achieved at a rate of 250 μA cm^{-2}, which likely finds the best balance between the H_2O-mediated solution-phase transfer of Li_2O_2 and DBBQ-mediated solution-phase O_2 reduction. These data clearly indicate that the presence of 1 M H_2O has a positive impact on the discharge performance of cells containing a state-of-the-art TEGDME-based electrolyte. To maximise the performance of subsequent cells, 250 μA cm^{-2} was chosen as the cycling rate.

To understand the effect of H_2O on the charge process, cells containing a TEGDME electrolyte doped with 1 M H_2O, 25 mM DBBQ, and 25 mM TEMPO were cycled at a rate of 250 μA cm^{-2}. **Figure 7.25** shows a representative example of the first cycle hysteresis, where a coulombic efficiency (CE) of 95.1% is observed. The combination of a high Li_2O_2 yield and CE of >95% indicate that cells containing 1 M H_2O were comparable to state-of-the-art dry literature cells.[7,49] However, CE only measures the ratio of the number of electrons passed on charge relative to the number of electrons passed on discharge and thus could encompass degradation reactions.

To understand if these electrons are being used to form O_2 through the oxidation of peroxo species, gas analysis and post-cycling characterisation must be performed on the cell and cathode surface, respectively. DEMS is a technique that measures the changes in the composition of a flowing gas stream as the result of operation of an electrochemical device. By cycling a Li-air DEMS cell, the amount of O_2 consumed in the discharge process can be calculated, giving direct evidence of the e^-/O_2 ratio, and the amount of O_2

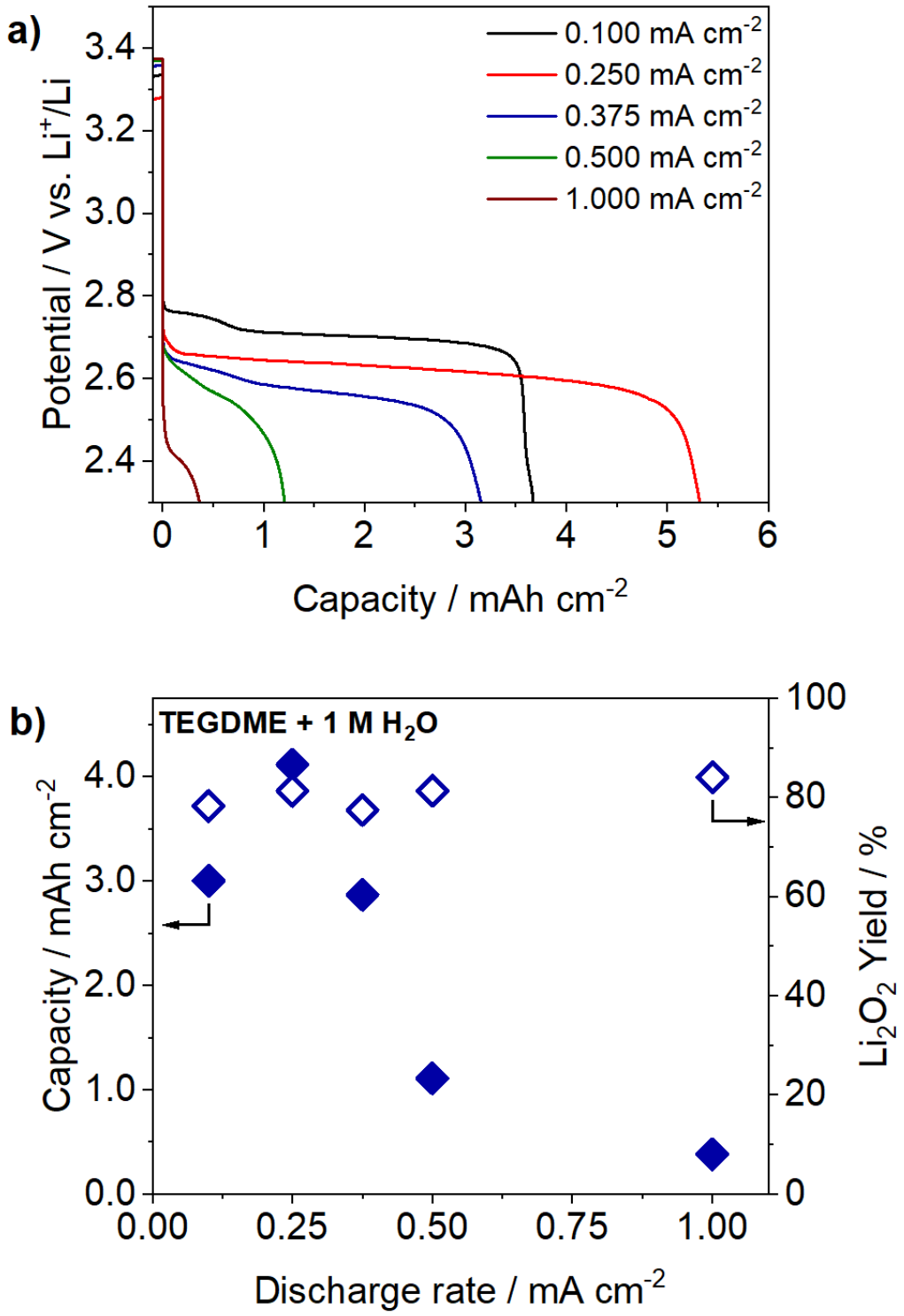


Figure 7.24. *Plots showing a) representative discharge voltage profiles and b) the average discharge capacity and Li_2O_2 yield for H_2O-containing Li-air cells as a function of discharge rate. A TEGDME-based electrolyte doped with 1 M H_2O, 25 mM DBBQ, and 25 mM TEMPO was used.*

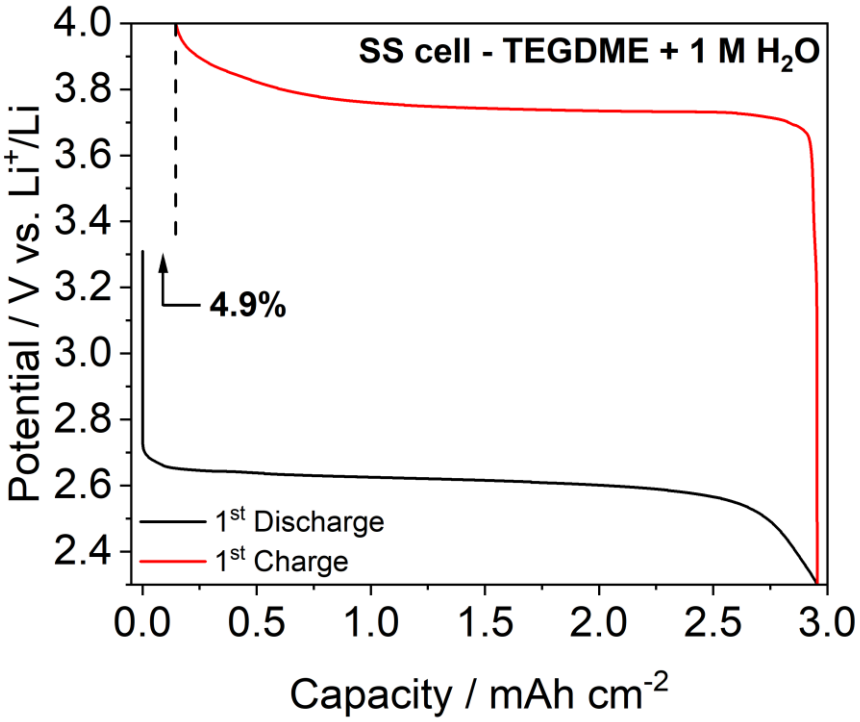


Figure 7.25. *Hysteresis plot of the first cycle of a Li-air cell containing a TEGDME-based electrolyte doped with 1 M H_2O, 25 mM DBBQ and 25 mM TEMPO, where a high CE of 95.1% is observed.*

released in the subsequent charge process can be calculated, enabling assessment of the overall O_2 round-trip efficiency during (dis)charge. **Figure 7.26** shows the results of the first cycle of a DEMS cell containing a dry TEGDME-based electrolyte doped with 25 mM DBBQ and 25 mM TEMPO, compared to the results from an analogous cell also doped with 1 M H_2O. Both cells successfully reach the desired discharge capacity limit of 2 mAh cm^{-2}, with the rate of O_2 consumption following the $2e^-/O_2$ ratio closely (**Figure 7.26**a). Upon charging, the dry cell does not produce enough O_2 to reach the predicted quantity required for a $2e^-/O_2$ process, indicating that not all of the electrons passed result in the $2e^-$ oxidation of Li_2O_2 to form O_2 (**Figure 7.26**b). The dry cell achieved an O_2 round-trip efficiency of 75%, accounting for the incomplete charge. The cell containing 1 M H_2O outperformed the dry cell, both in attainable charge capacity and O_2 round-trip efficiency, reaching and stabilising at the ideal $2e^-/O_2$ evolution rate for the majority of charge. An O_2 round-trip efficiency of 91% was achieved, both demonstrating the benefits of including

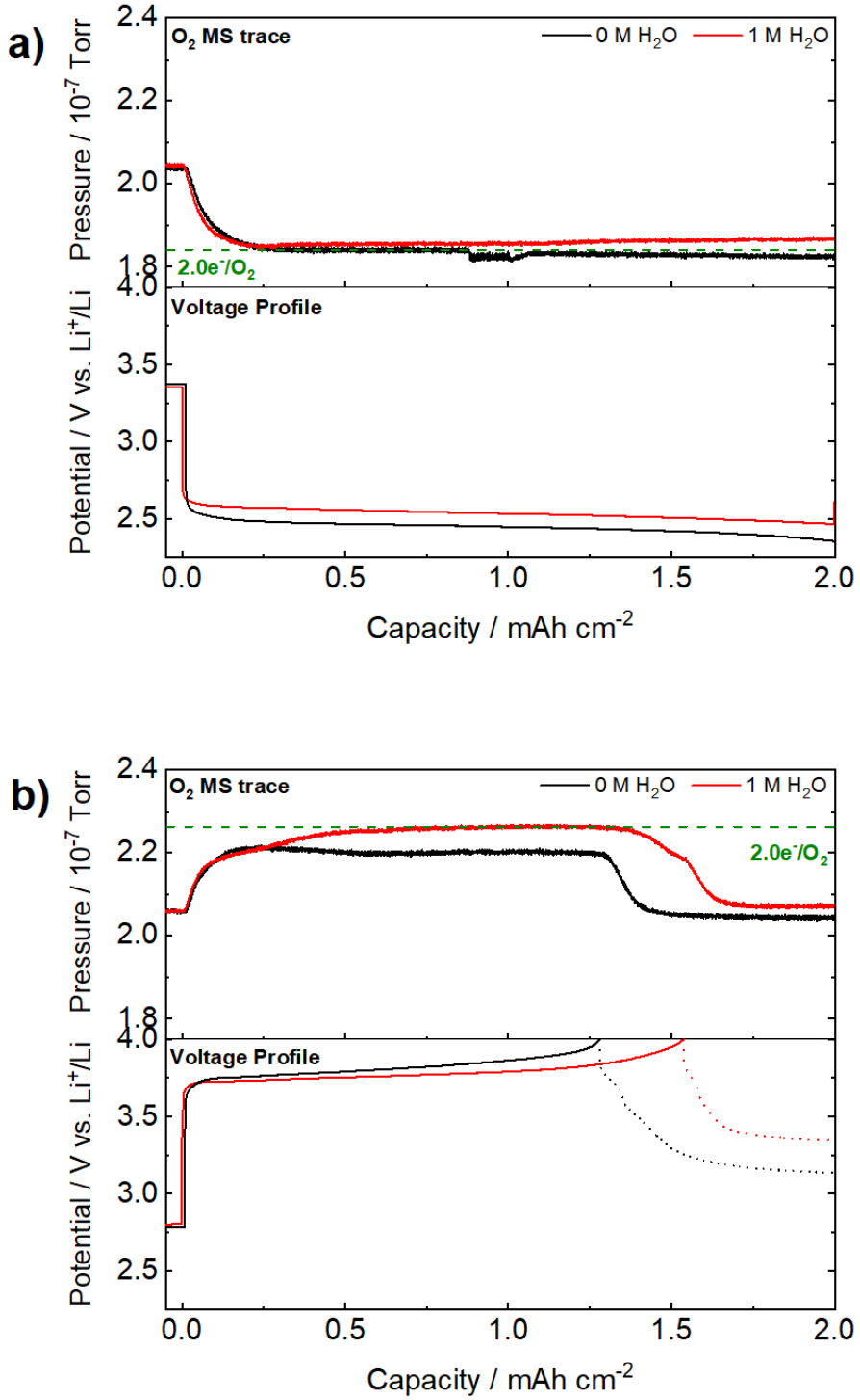


Figure 7.26. *Plots showing the change in measured O_2 pressure (top) and voltage profiles (bottom) of the first a) discharge and b) charge of a Li-air DEMS cell containing either a dry (black lines) or 1 M H_2O-containing (red lines) TEGDME-based electrolyte doped with 25 mM DBBQ and 25 mM TEMPO. The green dashed line indicates the ideal pressure change to achieve a 2.0e⁻/O_2 process. Dotted lines indicate OCV after the potential limit is reached.*

H_2O concentrations below the H_2O-solvent mixture AN threshold that was identified in section 7.4 and indicating that the presence of H_2O does not detrimentally impact the operation of either DBBQ or TEMPO (**Figure 7.10**).

To understand the effect of high H_2O concentration on the O_2 round-trip efficiency, a DEMS cell containing a TEGDME-based electrolyte doped with 12.5 mM DBBQ, 25 mM TEMPO, and 9.1 M H_2O was studied. The poor solubility of DBBQ in H_2O necessitated a reduction of DBBQ concentration in electrolytes that contained 9.1 M H_2O. However, it was expected that the combinatory effects of H_2O and DBBQ would sustain the discharge with the same conditions as the 1 M H_2O cell. **Figure 7.27** shows the first cycle DEMS results of the cell doped with 1 M H_2O compared to the cell doped with 9.1 M H_2O, where a reduced rate of O_2 consumption is observed during discharge of the cell containing 9.1 M H_2O, likely due to LiOH formation (**Figure 7.27**a). Although the inclusion of redox mediators may have an effect on the performance of these cells relative to the pressure cells reported in **Figure 7.6,** further studies are required to determine the precise impact. However, it is apparent that the same overall trend prevails, with a higher e^-/O_2 ratio being observed in the cell doped with 9.1 M H_2O. Considerable differences are also seen in the charging process where, although a capacity comparable to the dry cell is achieved with 9.1 M H_2O, the O_2 evolution is extremely poor (**Figure 7.27**b). An overall CE of 63.9% is observed and an O_2-round trip efficiency of 61% is achieved, accounting for the incomplete charge. This result demonstrates the importance of understanding the limits of H_2O concentration in Li-air electrolytes if a successful H_2O-tolerant Li-air battery is to be achieved.

A charge e^-/O_2 ratio greater than 2 indicates that charge is being passed in electrochemical processes that do not release O_2 in a $2e^-/O_2$ ratio, demonstrating deviation from the ideal Li_2O_2 oxidation process. If significant quantities of Li_2CO_3 were formed and could be oxidised in the 9.1 M H_2O cell, or electrolyte degradation was occurring, this may be reflected in the pressure recorded to track CO_2 evolution (i.e. m/z = 44). **Figure 7.28** shows the recorded pressure change of CO_2 as a function of cycle time for a cell containing a dry

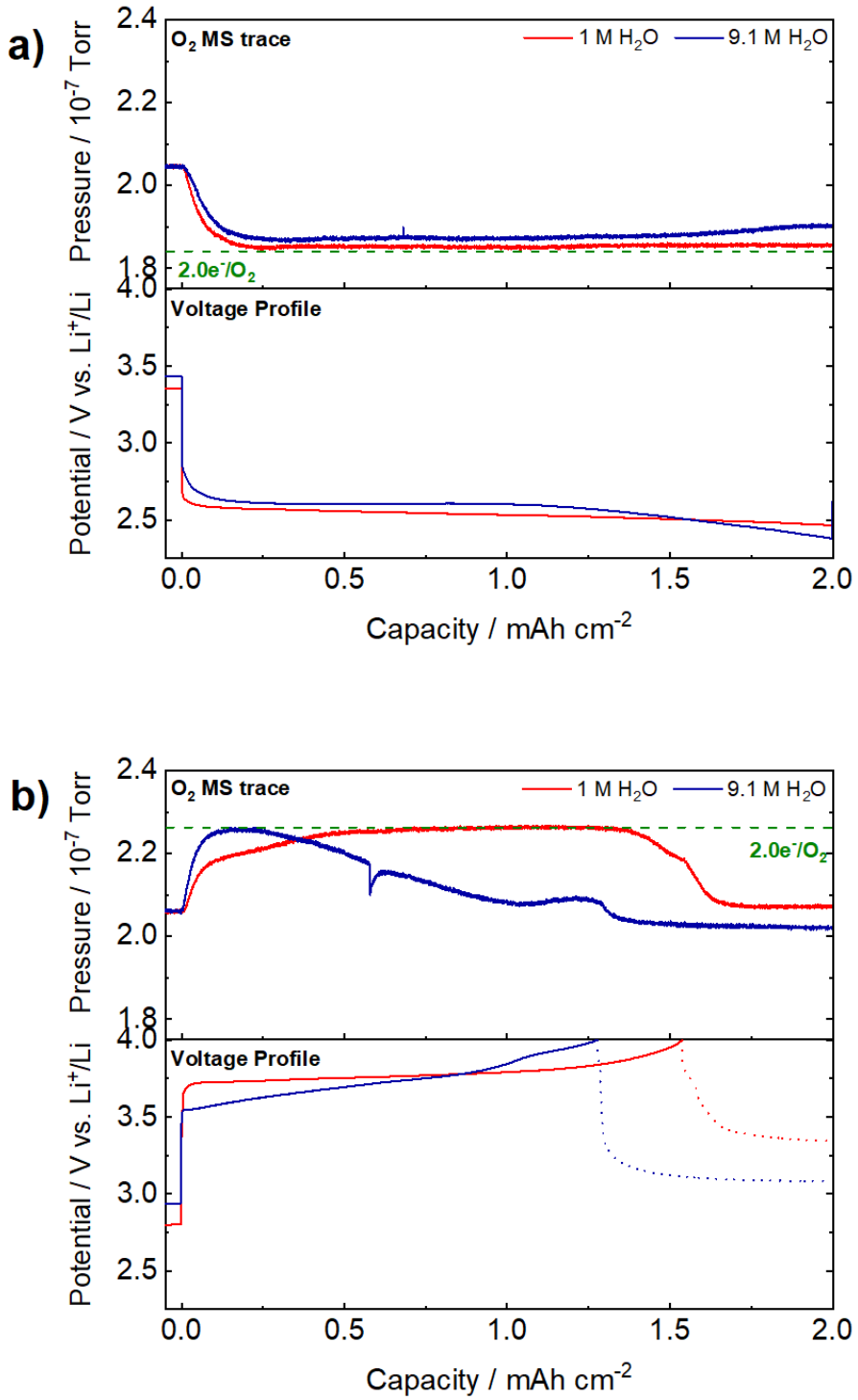


Figure 7.27. *Plots showing the change in measured O_2 pressure (top) and voltage profiles (bottom) of the first a) discharge and b) charge of a Li-air DEMS cell containing a TEGDME-based electrolyte doped with a) 1 M H_2O, 25 mM DBBQ and 25 mM TEMPO or b) 9.1 M H_2O, 12.5 mM DBBQ and 25 mM TEMPO. The green dashed line indicates the ideal pressure change to achieve a 2.0e$^-$/O_2 process. Dotted lines indicate OCV after the potential limit is reached.*

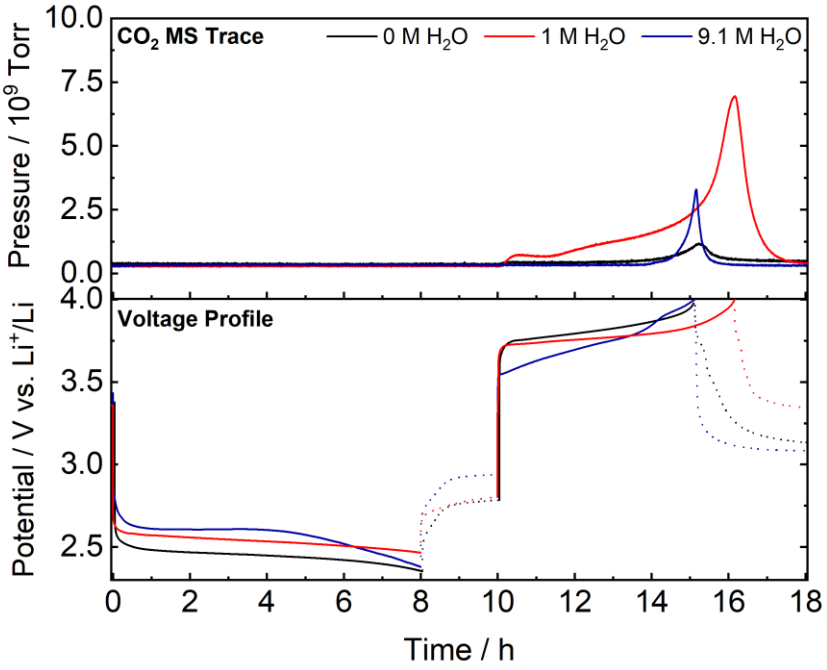


Figure 7.28. *Plot showing the change in measured CO_2 pressure (top) and voltage profiles (bottom) of the first cycle of a Li-air DEMS cell containing a a) dry, b) 1 M or c) 9.1 M H_2O-containing TEGDME-based electrolyte doped with DBBQ and TEMPO. Dotted lines indicate OCV after the potential limit is reached.*

TEGDME-based electrolyte compared to analogous cells doped with 1 M and 9.1 M H_2O. Surprisingly, in both the dry electrolyte and the electrolyte doped with 9.1 M H_2O, no major CO_2 evolution is observed until the potential reaches 3.85 V vs Li^+/Li. This indicates that parasitic electrochemical reactions occur above 3.85 V vs Li^+/Li that result in the release of CO_2 that are not possible below this potential.

In the cell containing 1 M H_2O, small quantities of CO_2 are evolved throughout the charge process, indicating that some degradation reactions are occurring throughout charge. In good agreement with the phenomenon observed in the cells containing the dry electrolyte and the electrolyte doped with 9.1 M H_2O, above 3.85 V vs Li^+/Li a significant increase in the CO_2 evolution is observed, which indicates the onset of parasitic reactions that release CO_2. It is important to note that the scale of the CO_2 intensity is ca. 100 times smaller than the O_2 signal intensity, indicating that this may only be one contributor to the

observed drop in O_2 evolution. Moreover, the high rate employed in this study pushes the cell charge voltage plateau to ca. 3.7 V vs Li^+/Li, which could be initiating degradation reactions that may not occur at lower rates. A reduction in the applied current density would enable TEMPO and H_2O to better mediate the charge, bringing the charge voltage plateau closer to the TEMPO oxidation potential of 3.55 V vs Li^+/Li. It has been previously reported that the oxidation of LiOH results in the release of no gaseous products, which could be a significant contributor to this lack of gaseous products detected in the 9.1 M H_2O system.[38,50]

To rule out Li_2CO_3 formation, the nature of the discharge product in cells containing 1 M and 9.1 M H_2O was determined through XRD and FTIR analysis of cathodes extracted from cells discharged at 250 µA cm^{-2} to a capacity of 2 mAh cm^{-2}. **Figure 7.29** shows representative XRD patterns and FTIR spectra of cathodes extracted both after discharge to 2 mAh cm^{-2} and after a subsequent charge to an upper cut-off voltage (UCV) of 4.0 V vs Li^+/Li. In both the 1 M H_2O discharged and charged samples, neither the XRD patterns nor the FTIR spectra show evidence of LiOH. Moreover, no Li_2O_2 was detected in the XRD pattern of the charged sample, indicating that the discharge product was effectively re-oxidised beyond the limit of detection of the technique. In the cells containing 9.1 M H_2O, both Li_2O_2 and LiOH peaks were seen in the XRD analysis of the discharged cathode, with LiOH also evident in the FTIR spectrum. Although the XRD pattern of the charged cathode from the cell containing 9.1 M H_2O did not contain any significant peaks, indicating that the majority of the discharge product was re-oxidised on charge, the FTIR spectrum identified some LiOH remaining in the charged sample.

With characterisation indicating that most of the discharge product is re-oxidised in both cells containing 1 and 9.1 M H_2O, SEM images were taken of the discharged and charged cathodes to understand the discharge product morphology and the nature of the electrode surface after charging. **Figure 7.30**a-d show representative images of the fibrous surface of the cathode extracted after a discharge to 2 mAh cm^{-2} with electrolyte doped with

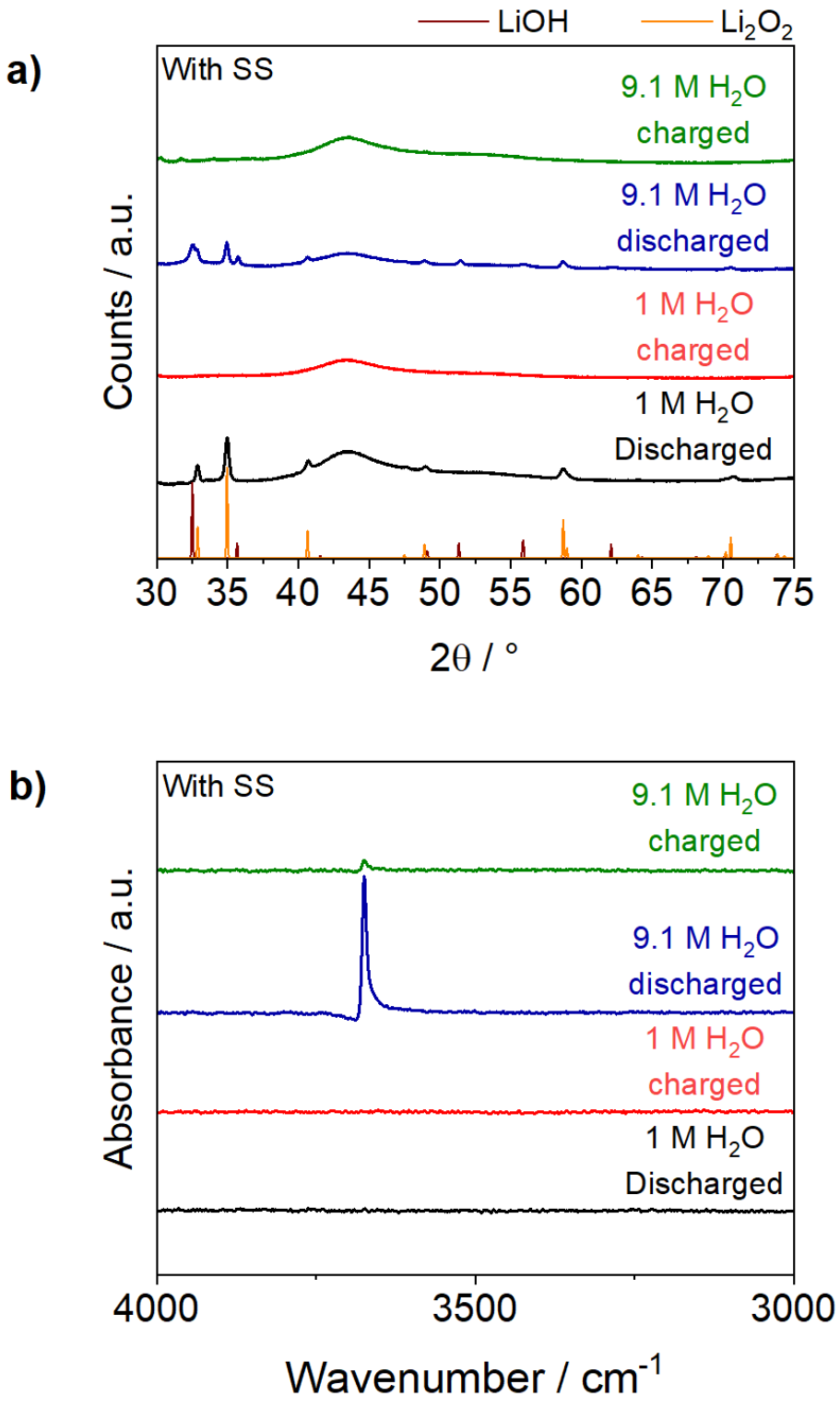


Figure 7.29. *a) XRD patterns and b) FTIR spectra identifying the nature of the discharge product formed on cathodes extracted after either the first discharge (black, blue) or charge (red, green) from cells containing either 1 M or 9.1 M H_2O-containing TEGDME-based electrolytes with DBBQ and TEMPO. Reference Li_2O_2 and LiOH XRD patterns were recorded experimentally.*

1 M H_2O. A distinctive toroidal morphology is seen, in good agreement with previous reports of electrolyte containing H_2O.[21] **Figure 7.30**e and f show the cathode surface after charging to a potential limit of 4.0 V vs Li^+/Li, where a near pristine electrode surface is observed. These images support the conclusion that in a state-of-the-art TEGDME electrolyte doped with 1 M H_2O, a high CE and O_2 round trip efficiency can be achieved through nearly complete oxidation of the discharge product.

Figure 7.31a-d show analogous images of a discharged cathode where the electrolyte was doped with 9.1 M H_2O. The discharge product morphology in these images is clearly different to that observed in the cell containing 1 M H_2O. A mixture of large sheet-like crystalline material interwoven between the fibres (**Figure 7.31**a and b) and small crystallites deposited on the surface of the fibres (**Figure 7.31**c and d) are observed. The fibres are largely clear of discharge product, indicating that where product is formed on the surface of the cathode, the solution mediation effects of H_2O allow the reorganisation of the discharge product away from the electroactive surface. **Figure 7.31**e and f show images of the charged cathode, wherein the majority of the large sheet-like particles are no longer present. Interestingly, the fibre surface is now completely covered with small crystallites, indicating that the charge process may result in surface passivation of the electrode. Images of a pristine cathode are shown in the Appendix for reference.

These data confirm that a cell containing a TEGDME-based electrolyte doped with 1 M H_2O, 25 mM DBBQ, and 25 mM TEMPO is capable of performance comparable to the current state-of-the-art, demonstrating the importance of understanding H_2O-solvent mixture AN when assessing H_2O tolerance.

Given the findings from the mechanistic studies identified SS as a prerequisite for the 2+2 reduction to form LiOH, a SS-free cell consisting of a PFA-cell housing with carbon paper current collectors was constructed to determine whether Li_2O_2 would be the exclusive electrochemical discharge product when discharged in a 100% relative humidity atmosphere (9.1 M H_2O equivalent). Further details of the cell design can be found in Chapter 2. To understand the

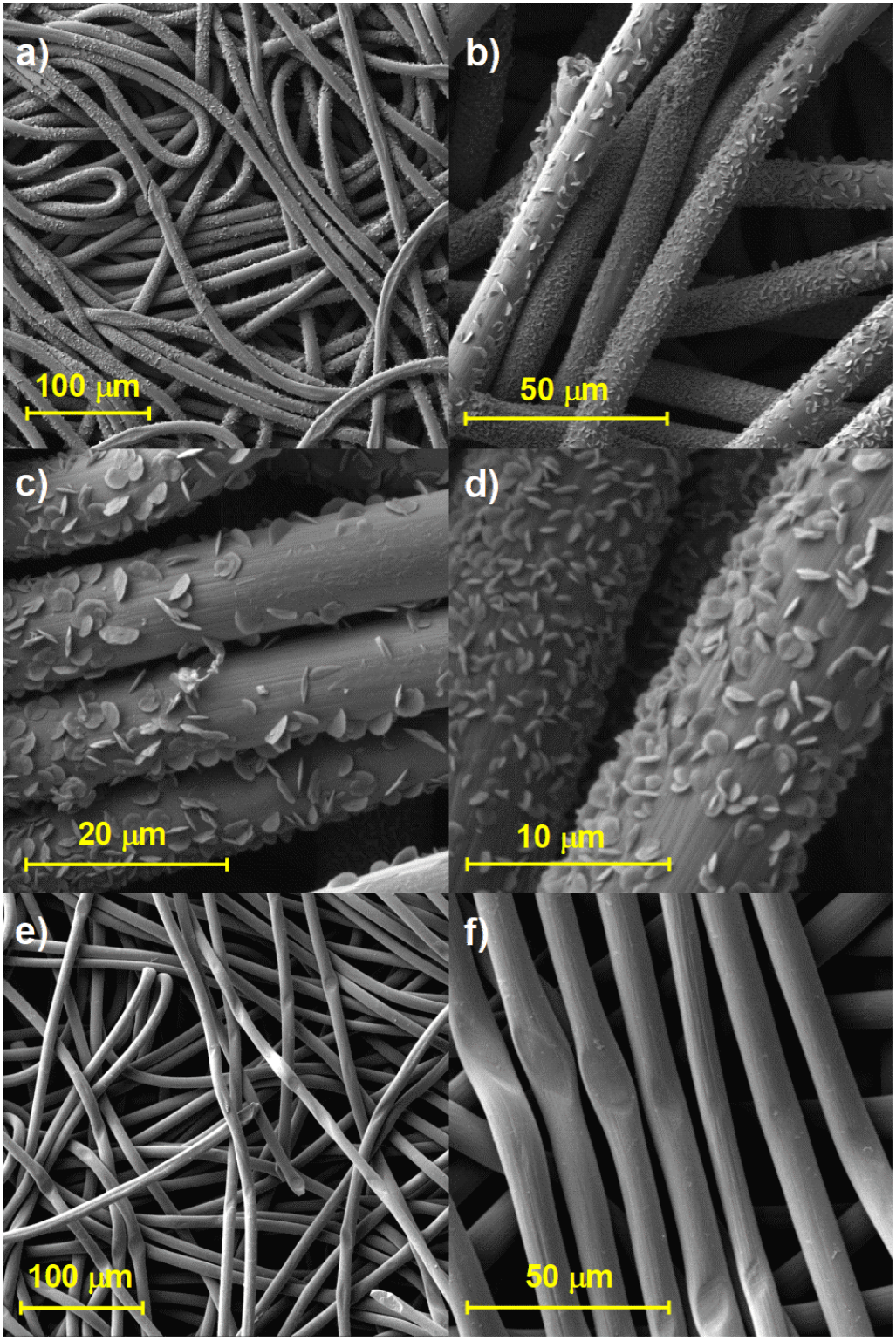


Figure 7.30. *Representative SEM images taken of the surface of a cathode extracted after the first a-d) discharge to 2 mAh cm^{-2} or e,f) charge of a Li-air cell to an UCV of 4.0 V vs Li^{+}/Li. Cells contained a TEGDME-based electrolyte doped with 1 M H_2O, 25 mM DBBQ and 25 mM TEMPO. Characteristic toroidal Li_2O_2 is seen in discharged samples, which is not seen on the electrode surface after charge.*

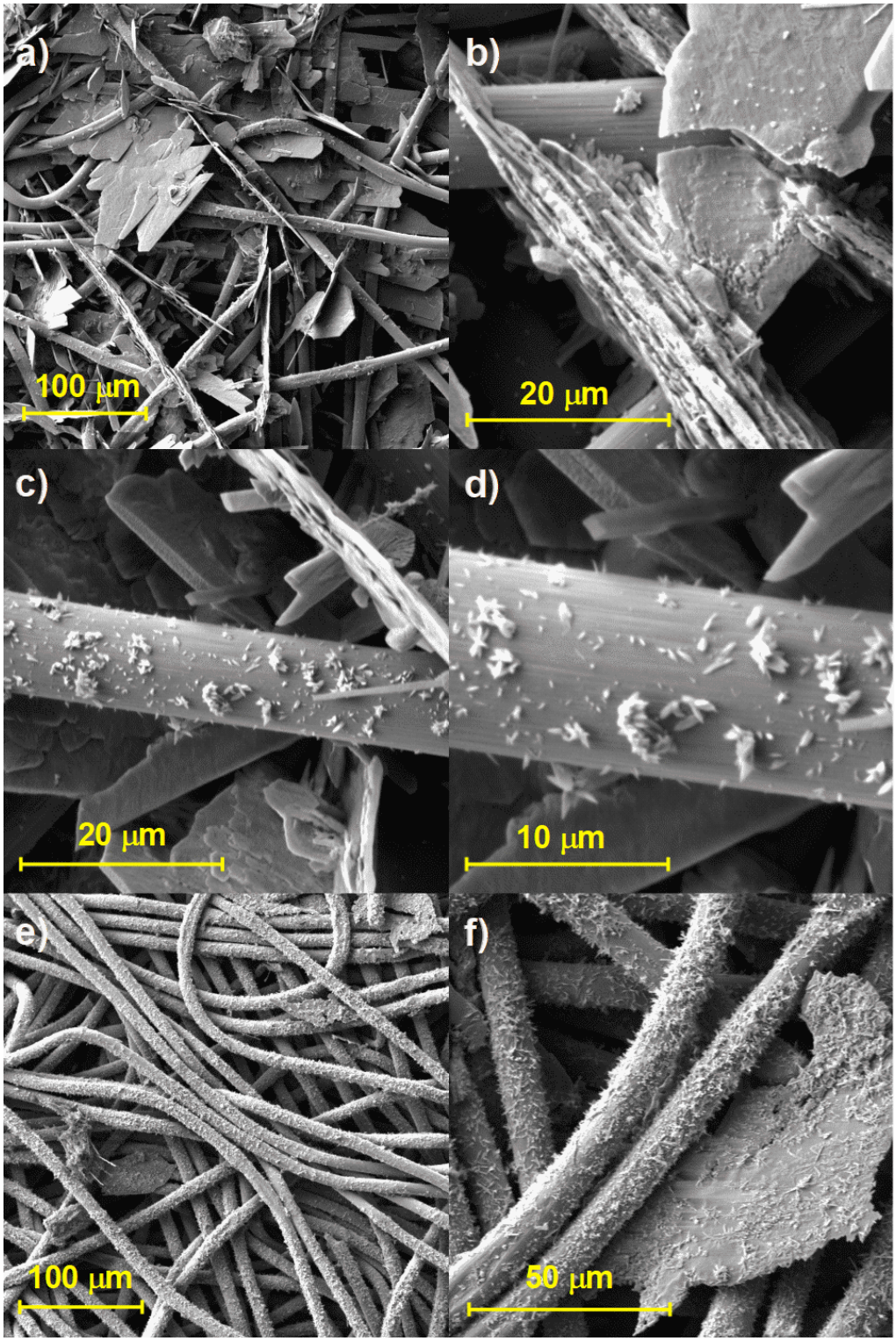


Figure 7.31. *Representative SEM images taken of the surface of a cathode extracted after the first a-d) discharge to 2 mAh cm^{-2} or e,f) charge of a Li-air cell to an UCV of 4.0 V vs Li$^+$/Li. Cells contained a TEGDME-based electrolyte doped with 9.1 M H_2O, 12.5 mM DBBQ and 25 mM TEMPO. Large crystalline discharge product morphologies are formed, indicative of LiOH formation rather than Li_2O_2 formation. After charging, the large morphologies are no longer present, but small crystallites are left on the fibrous electrode surface.*

cycling performance of the SS-free cells, cells containing a TEGDME-based electrolyte doped with 12.5 mM DBBQ, 25 mM TEMPO, and 9.1 M H_2O were discharged at a rate of 250 µA cm^{-2} to a potential limit of 2.3 V vs Li^+/Li. **Figure 7.32** shows a charge-discharge hysteresis plot, where a CE of 82.5% is achieved across the first cycle, demonstrating good electrochemical reversibility of a SS-free Li-air cell discharged with 100% relative humidity (20 °C). *Ex situ* characterisation was performed on cathodes extracted from cells discharged at 250 µA cm^{-2} to a capacity of 2 mAh cm^{-2} and from cells subsequently charged to an UCV of 4.0 V vs Li^+/Li. **Figure 7.33** shows the XRD patterns and FTIR spectra of these cathodes. Clear Li_2O_2 peaks are observed in the XRD pattern of the discharged electrode, with no LiOH being identified in either the XRD pattern or the FTIR spectrum, confirming that Li_2O_2 is the primary discharge product. This is further supported by an average Li_2O_2 yield of 87%. The XRD pattern of the charged electrode shows no significant peaks, cathode to beyond the limit of detection of this technique. These results are

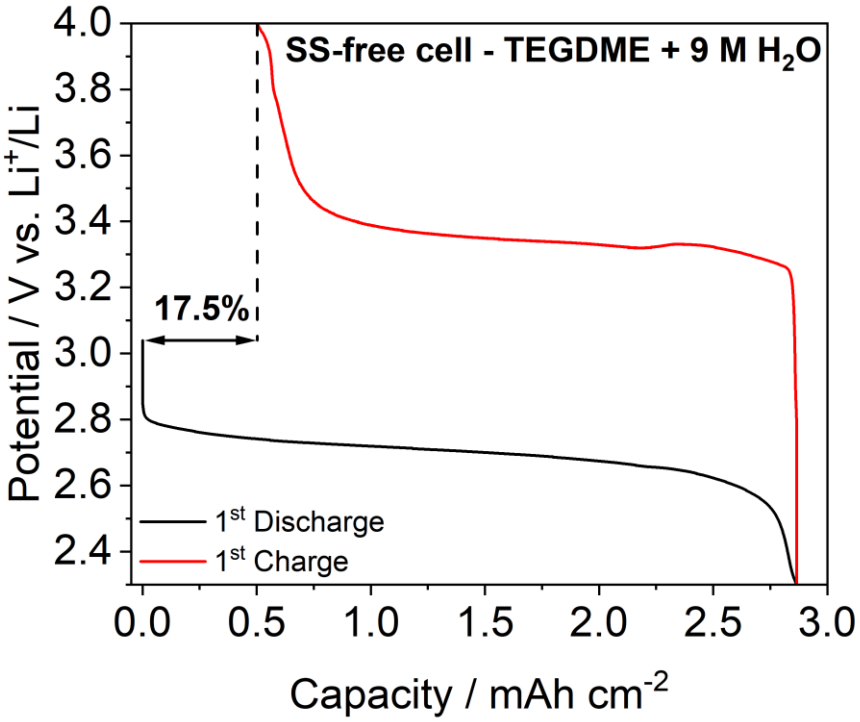


Figure 7.32. *Hysteresis plot of the first cycle of a SS-free Li-air cell containing a TEGDME-based electrolyte doped with 9.1 M H_2O, 12.5 mM DBBQ and 25 mM TEMPO, where a CE of 82.5% is observed.*

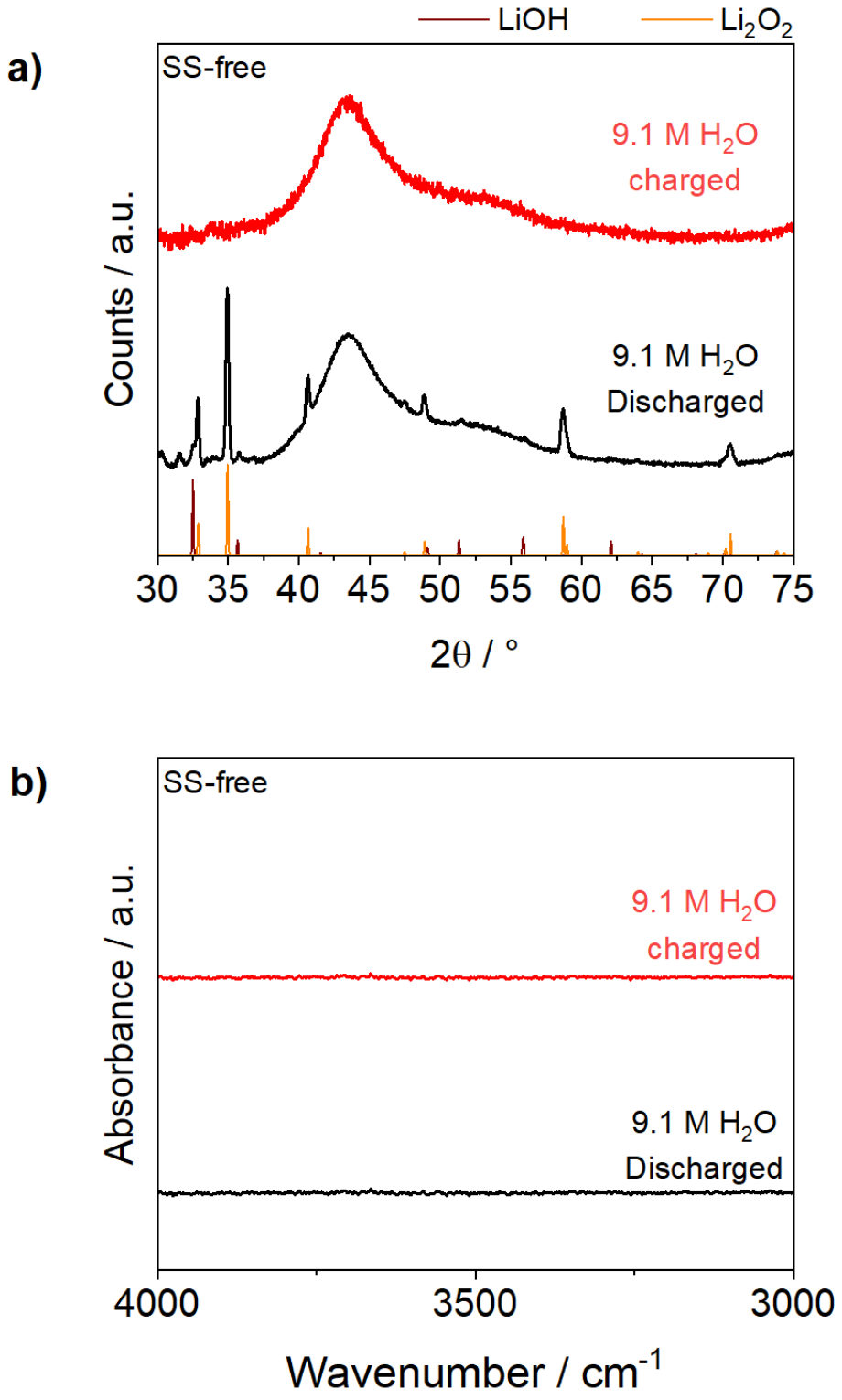


Figure 7.33. *a) XRD patterns and b) FTIR spectra identifying the nature of the discharge product formed on cathodes extracted from a SS-free Li-air cell after either the first discharge (black) or charge (red) containing a TEGDME-based electrolyte doped with 9.1 M H_2O, 12.5 mM DBBQ and 25 mM TEMPO. Reference Li_2O_2 and LiOH XRD patterns were recorded experimentally.*

indicating that the discharge product is removed from the surface of the comparable with the SS-containing 1 M H_2O system, demonstrating a high-performance cell operating in 100% relative humidity (20 °C) conditions.

To understand the morphology of the Li_2O_2 discharge product in these high H_2O cells, SEM images were taken of extracted cathodes after both the first discharge and the first charge. **Figure 7.34**a-d show representative images of a discharged cathode, where a novel discharge product morphology is identified. Large spherical particles and web-like structures are formed in these cells, likely the result of a combination of the many solution-phase chemical and electrochemical discharge pathways that are enabled by the presence of the H_2O, hydroperoxide species, and DBBQ, with the notable absence of a route for electrochemical LiOH formation. **Figure 7.34**e and f show the images of a cathode extracted from a SS-free cell after charge, where none of the large spherical particles remain, indicating that although these large particles contain a lot of material that is not directly attached to the electroactive surface, the combination of equilibrated species and mediated charge is sufficient to re-oxidise the majority of the discharge product. In good agreement with the SS cell discharged with 9.1 M H_2O, the electrode surface was covered in small crystallites after the charge process, although to a lesser extent. It is possible that due to the high concentration of H_2O, some peroxide species may be isolated from the electrode due to their stability in the electrolyte, which could result in a proportion of peroxide species being in solution and outside of the double-layer of the electrode surface. When the cathode is extracted and rinsed with dry DME, this may cause these species to precipitate on the surface of the electrode, resulting in visible product on the cathode surface that may be soluble in an operational cell.

These data confirm my hypothesis that the removal of SS from Li-air cells, even where humidity is 100%, results in electrochemically formed peroxides (Li_2O_2/LiOOH/H_2O_2) being the dominant discharge products. Taken together, these results demonstrate that, by either limiting the H_2O-solvent mixture AN or by removing SS, $2e^-$ O_2 reduction in the Li-air battery can be maintained with

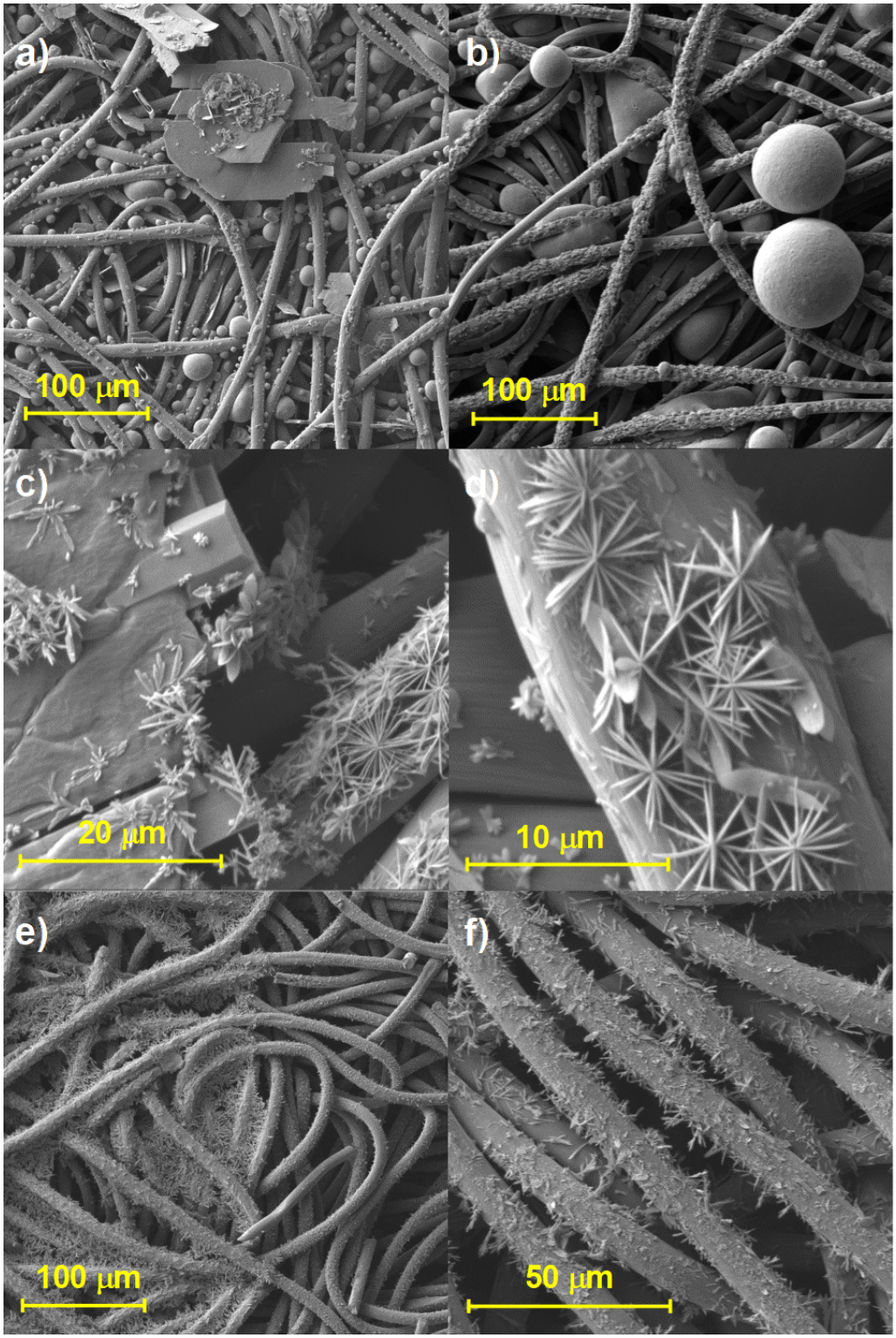


Figure 7.34. *Representative SEM images taken of the surface of a cathode extracted from a SS-free Li-air cell after the first a-d) discharge to 2 mAh* cm^{-2} *or e,f) charge to an UCV of 4.0 V vs* Li^{+}/Li*. Cells contained a TEGDME-based electrolyte doped with 9.1 M* H_2O*, 12.5 mM DBBQ and 25 mM TEMPO. Novel large spherical and web-like* Li_2O_2 *morphologies are observed in discharged samples. Small crystallites are left on the fibrous electrode surface after the charge process.*

high quantities of H_2O, eliminating the requirement of meticulous gas stream drying and providing rationale for future solvent and material selection.

7.9 Conclusions

In this chapter, I explored H_2O-solvent mixture AN as a function of H_2O concentration in DMSO-, DME-, and TEGDME-based electrolytes up to a H_2O concentration of 20 M. In good agreement with the H_2O-solvent mixture AN theory first proposed by Holc,[23] I have shown that solvents with a low DN experience a rapid increase in H_2O-solvent mixture AN with addition of H_2O, whereas solvents with a high DN experience good tolerance to the addition of H_2O with minimal increase in mixture AN. Raman spectral analysis of H_2O-solvent mixtures containing 1 M H_2O revealed that in H_2O-DMSO mixtures hydrogen-bonding was possible, evidence by a Raman shift <3500 cm^{-1}, which did not occur in DME- or TEGDME-based mixtures. The strong intermolecular interactions formed between H_2O and DMSO result in H_2O having a low activity which, in turn, presents an unfavourable environment for OH^- stabilisation. In DME- and TEGDME-based mixtures, the lack of strong intermolecular interactions between H_2O and solvent molecules results in increased H_2O activity, thus providing a more favourable environment for OH^- stabilisation at any given H_2O concentration. Critically, these findings can be applied to any electrochemical process involving OH^- in mixed organic-aqueous electrolytes.

In situ pressure analysis was performed using pressure cells containing H_2O-solvent mixture electrolytes to determine the H_2O tolerance of each solvent while maintaining ideal $2e^-$ O_2 reduction. In good agreement with the mixture AN theory, a DMSO-based electrolyte showed the highest tolerance to H_2O concentration, with a 2.01 e^-/O_2 ratio observed in a cell containing an electrolyte doped with 5 M H_2O, supported by a Li_2O_2 yield comparable to a cell discharged containing an analogous dry DMSO electrolyte. DME- and TEGDME-based electrolytes showed less tolerance to H_2O, however, both systems maintained a consistent e^-/O_2 ratio where the H_2O concentration was ≤1 M, supported by high Li_2O_2 yields. *Ex situ* XRD and FTIR characterisation of

discharged electrodes was used to confirm the nature of the discharge product, in good agreement with the pressure analysis.

Each of the possible chemical and electrochemical pathways for $4e^-$ O_2 reduction were explored through a combination of spectroscopic and electrochemical techniques. Chemical LiOH formation was ruled out by applying on-line mass spectrometry to observe the disproportionation reaction of KO_2 when mixed with dry and 5 M H_2O containing H_2O-solvent mixtures, where a ≤0.5 molar ratio of O_2 : KO_2 was observed, indicating formation of only peroxo species in all systems.

Levich analysis of O_2 reduction RDE LSVs performed in a TBA^+-containing electrolyte revealed that GC electrodes are not capable of $4e^-$ O_2 reduction, in good agreement with the behaviour reported in both fully aqueous and aprotic systems. However, analysis using a SS electrode revealed that $4e^-$ O_2 reduction on SS is possible and, moreover, the SS mesh used in the pressure cells is capable of O_2 reduction, determined through LSVs in flooded cells. Although $4e^-$ O_2 reduction was shown to be possible, the onset was beyond the operational discharge voltage plateau region of pressure cells, indicating that no direct pathway for $4e^-$ O_2 reduction was possible under operational conditions.

Instead, carbon and SS act in tandem, the former reducing O_2 to peroxide species (Li_2O_2/LiOOH/H_2O_2), which the latter can then further reduce to LiOH, in a 2+2 mechanism. The presence of H_2O in electrolytes establishes chemical equilibria that introduce hydroperoxide species, the active participation of which in the electrochemical discharge pathway of a Li-air battery has never been studied. The reduction of H_2O_2 on GC and SS was explored through RDE LSVs, where no activity was found on a GC electrode, but a major reduction process was identified on SS in all electrolyte systems, shifted positive of the O_2 reduction process. The viability of H_2O_2 reduction in Li-air cells was assessed through LSVs using SS flags, where a good agreement between the operational discharge voltage of Li-air cells and onset of H_2O_2 reduction is observed. These data identify that, contrary to the current literature understanding, $4e^-$ O_2

reduction in Li-air batteries proceeds via 2 individual $2e^-$ reduction processes, the former being $2e^-$ O_2 reduction on a carbon electrode to form peroxide species and the latter being the $2e^-$ reduction of H_2O-mediated hydroperoxide species on the surface of the SS current collector.

The practical implications of these findings were demonstrated in two ways using high-performance H_2O-containing cells: first, the electrolyte was designed to limit the formation of hydroperoxide species through application of the mixture AN theory; second, cells devoid of steel were constructed to prove that Li_2O_2 would be the dominant discharge product in 100% relative humidity (20 °C). The former was achieved through comprehensive analysis of a Li-air cell containing an electrolyte consisting of 0.25 M $LiClO_4$ in TEGDME doped with 25 mM DBBQ, 25 mM TEMPO, and 1 M H_2O, just below the H_2O concentration limit for the onset of $4e^-$ O_2 reduction. DEMS cell analysis revealed that the cell doped with 1 M H_2O outperformed a cell containing an analogous dry electrolyte, achieving a charge capacity normalised O_2-round trip efficiency of 91%, supported by an average cell CE and Li_2O_2 yield of 95.1 and >80%, respectively. In the latter, a SS-free cell doped with 9.1 M H_2O achieved an average CE and Li_2O_2 yield of 82.5 and 87%, respectively, with no LiOH being observed in *ex situ* characterisation. These data conclusively prove that the prerequisites for $4e^-$ O_2 reduction are the presence of hydroperoxide species, itself requiring a sufficiently high H_2O-solvent mixture AN, and a SS electroactive surface, where the $2e^-$ reduction of hydroperoxide species on SS is the source of an increasing e^-/O_2 ratio.

This work highlights the importance of understanding the mechanisms of the O_2 reduction processes in the Li-air battery and the role that solvents and electroactive surfaces play in them. If H_2O tolerant electrolytes are to be designed, a critical requirement for commercialisation of this technology, it is desirable for the electrolyte solvent to have either a low AN, a high DN, or ideally a combination of both. Furthermore, it is of critical importance that O_2 and hydroperoxide electrochemistry of any electroactive materials, particularly metals, in contact with the electrolyte are comprehensively understood.

7.10 References

1. Stamenkovic, V. R., Strmcnik, D., Lopes, P. P. & Markovic, N. M. Energy and fuels from electrochemical interfaces. *Nat. Mater.* **16**, 57–69 (2017).
2. Bruce, P. G., Freunberger, S. A., Hardwick, L. J. & Tarascon, J.-M. Li–O_2 and Li–S batteries with high energy storage. *Nat. Mater.* **11**, 19–29 (2012).
3. Kwak, W.-J. *et al.* Lithium–Oxygen Batteries and Related Systems: Potential, Status, and Future. *Chem. Rev.* **120**, 6626–6683 (2020).
4. Thackeray, M. M., Wolverton, C. & Isaacs, E. D. Electrical energy storage for transportation—approaching the limits of, and going beyond, lithium-ion batteries. *Energy Environ. Sci.* **5**, 7854–7863 (2012).
5. McCloskey, B. D. *et al.* Combining Accurate O_2 and Li_2O_2 Assays to Separate Discharge and Charge Stability Limitations in Nonaqueous Li–O_2 Batteries. *J. Phys. Chem. Lett.* **4**, 2989–2993 (2013).
6. Aurbach, D., McCloskey, B. D., Nazar, L. F. & Bruce, P. G. Advances in understanding mechanisms underpinning lithium–air batteries. *Nat. Energy* **1**, 1–11 (2016).
7. Liu, T. *et al.* Current Challenges and Routes Forward for Nonaqueous Lithium–Air Batteries. *Chem. Rev.* **120**, 6558–6625 (2020).
8. Qiao, Y. & Ye, S. Spectroscopic Investigation for Oxygen Reduction and Evolution Reactions on Carbon Electrodes in Li–O_2 Battery. *J. Phys. Chem. C* **120**, 8033–8047 (2016).
9. Xia, C. *et al.* Evolution of Li_2O_2 Growth and Its Effect on Kinetics of Li–O_2 Batteries. *ACS Appl. Mater. Interfaces* **6**, 12083–12092 (2014).

10. Bryantsev, V. S. *et al.* The Identification of Stable Solvents for Nonaqueous Rechargeable Li-Air Batteries. *J. Electrochem. Soc.* **160**, A160–A171 (2013).

11. Gao, Z. *et al.* Recent Progress in Developing a LiOH-Based Reversible Nonaqueous Lithium–Air Battery. *Adv. Mater.* **35**, 2201384 (2023).

12. Lim, H.-D. *et al.* Superior Rechargeability and Efficiency of Lithium–Oxygen Batteries: Hierarchical Air Electrode Architecture Combined with a Soluble Catalyst. *Angew. Chem.* **126**, 4007–4012 (2014).

13. Temprano, I. *et al.* Toward Reversible and Moisture-Tolerant Aprotic Lithium-Air Batteries. *Joule* **4**, 2501–2520 (2020).

14. Lu, J. *et al.* Co3O4-Catalyzed LiOH Chemistry in Li–O_2 Batteries. *ACS Energy Lett.* **5**, 3681–3691 (2020).

15. Liu, T. *et al.* Cycling Li-O_2 batteries via LiOH formation and decomposition. *Science* **350**, 530–533 (2015).

16. Zhang, X., Dong, P. & Song, M.-K. Advances in Lithium–Oxygen Batteries Based on Lithium Hydroxide Formation and Decomposition. *Front. Chem.* **10**, 923936 (2022).

17. Gallagher, K. G. *et al.* Quantifying the promise of lithium–air batteries for electric vehicles. *Energy Environ. Sci.* **7**, 1555 (2014).

18. Schwenke, K. U., Metzger, M., Restle, T., Piana, M. & Gasteiger, H. A. The Influence of Water and Protons on Li_2O_2 Crystal Growth in Aprotic Li-O_2 Cells. *J. Electrochem. Soc.* **162**, A573 (2015).

19. Qiao, Y. *et al.* From O_2^- to HO_2^-: Reducing By-Products and Overpotential in Li-O_2 Batteries by Water Addition. *Angew. Chem.* **129**, 5042–5046 (2017).

20. G. Kwabi, D. *et al.* The effect of water on discharge product growth and chemistry in Li–O_2 batteries. *Phys. Chem. Chem. Phys.* **18**, 24944–24953 (2016).

21. Aetukuri, N. B. *et al.* Solvating additives drive solution-mediated electrochemistry and enhance toroid growth in non-aqueous Li–O_2 batteries. *Nat. Chem.* **7**, 50–56 (2015).

22. Policano, M. C., Anchieta, C. G., Nepel, T. C. M., Filho, R. M. & Doubek, G. Water in Aprotic Li-O_2 Batteries: A Critical Review. *ACS Appl. Energy Mater.* **5**, 9228–9240 (2022).

23. Holc, C. The effect of H_2O on O_2 reduction in Li-O_2 batteries. (University of Oxford, 2019).

24. Lim, H.-K. *et al.* Toward a Lithium–"Air" Battery: The Effect of CO_2 on the Chemistry of a Lithium–Oxygen Cell. *J. Am. Chem. Soc.* **135**, 9733–9742 (2013).

25. Yin, W., Grimaud, A., Lepoivre, F., Yang, C. & Tarascon, J. M. Chemical vs Electrochemical Formation of Li_2CO_3 as a Discharge Product in Li–O_2/CO_2 Batteries by Controlling the Superoxide Intermediate. *J. Phys. Chem. Lett.* **8**, 214–222 (2017).

26. Hartmann, P. *et al.* A comprehensive study on the cell chemistry of the sodium superoxide (NaO_2) battery. *Phys. Chem. Chem. Phys.* **15**, 11661–11672 (2013).

27. O'Sullivan, D. W. & Tyree, M. The kinetics of complex formation between Ti(IV) and hydrogen peroxide. *Int. J. Chem. Kinet.* **39**, 457–461 (2007).

28. Greenspan, L. Humidity Fixed Points of Binary Saturated Aqueous Solutions. *J. Res. Natl. Bur. Stand. Sect. Phys. Chem.* **81A**, 89–96 (1977).

29. Gutmann, V. Empirical parameters for donor and acceptor properties of solvents. *Electrochimica Acta* **21**, 661–670 (1976).

30. Wong, D. B. *et al.* Water Dynamics in Water/DMSO Binary Mixtures. *J. Phys. Chem. B* **116**, 5479–5490 (2012).

31. Baker, E. S. & Jonas, J. Transport and relaxation properties of dimethyl sulfoxide-water mixtures at high pressure. *J. Phys. Chem.* **89**, 1730–1735 (1985).

32. Kirchner, B. & Reiher, M. The Secret of Dimethyl Sulfoxide−Water Mixtures. A Quantum Chemical Study of 1DMSO−nWater Clusters. *J. Am. Chem. Soc.* **124**, 6206–6215 (2002).

33. Cataldo, F. A revision of the Gutmann donor numbers of a series of phosphoramides including TEPA. *Eur. Chem. Bull.* **4**, 92–97 (2015).

34. Laoire, C. O., Mukerjee, S., Abraham, K. M., Plichta, E. J. & Hendrickson, M. A. Influence of Nonaqueous Solvents on the Electrochemistry of Oxygen in the Rechargeable Lithium−Air Battery. *J. Phys. Chem. C* **114**, 9178–9186 (2010).

35. Mayer, U., Gutmann, V. & Gerger, W. The acceptor number — A quantitative empirical parameter for the electrophilic properties of solvents. *Monatshefte Für Chem. Chem. Mon.* **106**, 1235–1257 (1975).

36. Singh, S. & Krueger, P. J. Raman spectral studies of aqueous solutions of non-electrolytes: Dimethylsulfoxide, acetone and acetonitrile. *J. Raman Spectrosc.* **13**, 178–188 (1982).

37. Chen, K., Yang, D.-Y., Huang, G. & Zhang, X.-B. Lithium–Air Batteries: Air-Electrochemistry and Anode Stabilization. *Acc. Chem. Res.* **54**, 632–641 (2021).

38. Kang, J.-H. *et al.* Lithium–Air Batteries: Air-Breathing Challenges and Perspective. *ACS Nano* **14**, 14549–14578 (2020).

39. Kwabi, D. G. *et al.* Chemical Instability of Dimethyl Sulfoxide in Lithium–Air Batteries. *J. Phys. Chem. Lett.* **5**, 2850–2856 (2014).

40. Mozhzhukhina, N., Méndez De Leo, L. P. & Calvo, E. J. Infrared Spectroscopy Studies on Stability of Dimethyl Sulfoxide for Application in a Li–Air Battery. *J. Phys. Chem. C* **117**, 18375–18380 (2013).

41. Lepoivre, F., Grimaud, A., Larcher, D. & Tarascon, J.-M. Long-time and reliable gas monitoring in Li-O_2 batteries via a Swagelok derived electrochemical cell. *J. Electrochem. Soc.* **163**, A923–A929 (2016).

42. Black, R. *et al.* Screening for Superoxide Reactivity in Li-O_2 Batteries: Effect on Li_2O_2/LiOH Crystallization. *J. Am. Chem. Soc.* **134**, 2902–2905 (2012).

43. Kulkarni, A., Siahrostami, S., Patel, A. & Nørskov, J. K. Understanding Catalytic Activity Trends in the Oxygen Reduction Reaction. *Chem. Rev.* **118**, 2302–2312 (2018).

44. Stacy, J., Regmi, Y. N., Leonard, B. & Fan, M. The recent progress and future of oxygen reduction reaction catalysis: A review. *Renew. Sustain. Energy Rev.* **69**, 401–414 (2017).

45. Ma, R. *et al.* A review of oxygen reduction mechanisms for metal-free carbon-based electrocatalysts. *Npj Comput. Mater.* **5**, 1–15 (2019).

46. Treimer, S., Tang, A. & Johnson, D. C. A Consideration of the Application of Koutecký-Levich Plots in the Diagnoses of Charge-Transfer Mechanisms at Rotated Disk Electrodes. *Electroanalysis* **14**, 165–171 (2002).

47. Lai, J. *et al.* Electrolytes for Rechargeable Lithium–Air Batteries. *Angew. Chem. Int. Ed.* **59**, 2974–2997 (2020).

48. Cao, D., Tan, C. & Chen, Y. Oxidative decomposition mechanisms of lithium carbonate on carbon substrates in lithium battery chemistries. *Nat. Commun.* **13**, 4908 (2022).

49. Gao, X., Chen, Y., Johnson, L. R., Jovanov, Z. P. & Bruce, P. G. A rechargeable lithium–oxygen battery with dual mediators stabilizing the carbon cathode. *Nat. Energy* **2**, 17118 (2017).

50. Meini, S. *et al.* Rechargeability of Li–air cathodes pre-filled with discharge products using an ether-based electrolyte solution: implications for cycle-life of Li–air cells. *Phys. Chem. Chem. Phys.* **15**, 11478–11493 (2013).

Chapter 8. Summary and Perspectives

The primary objective of this research was to understand degradation mechanisms in lithium-ion and lithium-air batteries. Chapters 3 and 4 were dedicated to the lithium-ion battery, where half-cell and full-cell formats were used to identify critical failure and degradation mechanisms. In Chapter 3, the failure mechanism of Li-NMC811 half-cells was conclusively identified, being attributed to a combination of indiscriminate electrolyte degradation at the surface of the metallic Li electrode and the consequent increase in the impedance of the NMC811 cathode electrolyte interphase. Although stabilisation of the metallic Li electrode was aided by the presence of a sacrificial additive (i.e. vinylene carbonate, VC), once this species was consumed, degradation species formed at the negative electrode crossed through the electrolyte and destabilised the positive electrode surface.

These data highlight the impracticality of metallic Li half-cells and their limitations to understanding the performance of prospective electrode chemistries. Lithium titanate was proposed as an alternative counter electrode for these studies, where 300 cycles of a LTO-NMC811 cell with no additive to an upper cut-off voltage of 4.4 V was achieved with limited capacity fade. The application of LTO as a counter electrode for the testing of prospective cathode chemistries and their long-term performance is an impactful finding which should be adopted more broadly throughout academic and industrial research.

With crosstalk being identified as the primary failure mechanism of half-cells, Chapter 4 explored the feasibility of a previously proposed crosstalk reaction, wherein gas chromatography mass spectrometry was used to detect trace quantities of VC being formed in the early-stage cycling of Gr-NMC811 cells. The data presented showed that, contrary to literature understanding, Gr-NMC811 full-cells with no VC additive showed comparable performance, or even exceeded the performance of, cells doped with VC. This confirmed the theory that VC is formed at the surface of NMC811 electrodes in the early-stages of cycling, with calibration of the mass spectroscopic method enabling

the identification of VC above the limit of detection, within standard operational potential limits, and at high upper cut-off-voltages, above the limit of quantification.

Although the theory of VC formation has been proposed before, direct quantification has never been achieved, marking a critical contribution to the field. The reactivity of an electrode surface with a given electrolyte is defined by its composition, with increasing nickel content being directly related to increased reactivity. Given this, it is likely that lower nickel NMC chemistries can also oxidise ethylene carbonate (EC) to form VC, albeit requiring a higher potential. The high sensitivity (10s – 100s ppb) of GC-MS for the detection of VC provides an ideal analytical system for the study of VC formation at the surface of positive electrode chemistries, which should be systematically explored to understand this phenomenon in detail.

Moreover, the work presented in Chapter 4 then set out to deconvolute the mechanism of VC formation, where it was shown that the Rose Bengal photosensitizer, that has previously been used for $^1O_2$ generation experiments, reacts with the organic carbonates in the presence of $^1O_2$, deeming these methods unsuitable for analysis. A heterogenous selective singlet O_2 generating single atom catalyst was synthesised and tested in an EC-containing solution, wherein it was proven that the catalyst could produce $^1O_2$. However, no reaction was seen with EC, indicating that $^1O_2$-driven VC formation is not feasible.

These data not only rule out $^1O_2$ release as the mechanism for VC formation in Gr-NMC811 cells, but also demonstrate that the Rose Bengal photosensitizer is not suitable for these experiments in the organic carbonates used as lithium-ion battery electrolyte solvents. To categorically confirm the findings of Chapter 4, further characterisation of the single atom catalyst, and its successful facilitation of organic $^1O_2$ reaction should be performed, alongside rigorous characterisation using X-ray absorption fine structure spectroscopy. When these results are confirmed, the single atom catalyst synthesised in Chapter 4 should be used in all experiments where the reactivity of $^1O_2$ with battery

electrolyte solvents is being assessed to avoid the potential for interference of photosensitizers in degradation processes.

Chapters 6 and 7 were dedicated to the lithium-air battery, where H_2O and the equilibrated species that it forms were studied in detail. In Chapter 6, the hydroperoxide intermediate was identified as an antagonistic species for the first time, revealing that the fast discharge rates, which are commonly employed in lithium-air battery research to demonstrate high power performance, can mask electrolyte degradation pathways that would otherwise become apparent. This finding marks a critical discovery in the field of lithium-air battery research, revealing a new antagonistic species that will inevitably be present if the field moves away from pure O_2 gas streams to an 'air' system, where H_2O will be present. Therefore, it is imperative that the reactivity of hydroperoxide species with prospective electrolyte solvent and salts, electrode materials, redox mediators, and any other cell components is screened with the same veracity as the lithium superoxide intermediate, if a truly 'air' system is to be achieved.

The aim of Chapter 7 was to bring together the acceptor number theory for H_2O tolerance in lithium-air battery electrolytes, proposed by Holc *et al.* in his 2019 thesis, and use this understanding to identify the mechanism of electrochemical LiOH formation in the Li-air battery in H_2O-solvent mixture electrolytes. A systematic study of H_2O-solvent mixture AN with respect to H_2O concentration was performed and correlated to *in situ* pressure analysis, which enabled the ratio of the number of electrons passed per molecule of O_2 at each H_2O concentration to be calculated. These data enabled the determination of an approximate H_2O-solvent mixture AN limit of 25, below which a given H_2O-solvent mixture will perform $2e^-$ O_2 reduction to form Li_2O_2, and above which some $4e^-$ O_2 reduction will proceed. This finding confirms that an ideal H_2O tolerant electrolyte solvent will have a high donor number (i.e. interact strongly with H_2O) and a low acceptor number (i.e. poorly stabilise OH^-) to enable high H_2O concentration while maintaining $2e^-$ O_2 reduction.

With the theory for H_2O tolerance confirmed, the mechanism for LiOH formation was systematically studied. First the feasibility of chemical LiOH formation was examined using the number of moles of O_2 produced in the disproportionation of potassium dioxide with dry and wet electrolytes to assess the chemical product. These experiments indicated that no LiOH formed in any of the systems studied, ruling out chemical formation. Glassy carbon rotating disk electrochemistry in O_2 saturated solutions revealed that, in good agreement with the pristine aqueous and pristine aprotic non-aqueous systems, glassy carbon was incapable of performing $4e^-$ reduction of O_2. Although analogous stainless steel rotating disk electrochemical measurements revealed that $4e^-$ O_2 reduction was possible, this too was outside of the electrochemical window of discharge of a lithium-air cell. These findings alone mark a critical discovery in the field of lithium-air research, demonstrating that direct $4e^-$ O_2 reduction is not possible on any of the electroactive surfaces present within the lithium-air battery within the potential window of the discharge process.

With direct O_2 reduction being ruled out, the search for soluble electroactive species revealed the same antagonistic intermediate that was identified in Chapter 6. It was theorised that, where lifetime is sufficient, the hydroperoxide species that are formed during solution-mediation of Li_2O_2 particle morphology could be electrochemically reduced on either a carbon or stainless steel electroactive surface. Rotating disk electrochemical measurements of electrolytes doped with H_2O_2 revealed that, the glassy carbon electrode was not capable of reducing H_2O_2 within the window of operation. However, the stainless steel electrode could reduce H_2O_2, identifying the pathway for lithium hydroxide formation. These findings revealed that, contrary to previous understanding, LiOH formation in H_2O-solvent mixtures proceeds via 2 step mechanism, the first of which is $2e^-$ O_2 reduction on the surface of the carbon electrode. Where H_2O concentration is sufficient, the formed Li_2O_2 can then be converted to hydroperoxide species, through H_2O-mediated chemical

equilibria, which can then be reduced by a further $2e^-$ at the surface of the stainless steel current collector to form LiOH.

Two high-performance H_2O-containing systems were used to substantiate these findings, the first where a TEGDME-based electrolyte with a H_2O concentration below the identified H_2O-solvent mixture AN was cycled in a stainless steel containing cell and demonstrated gas consumption and evolution representative of state-of-the-art performance, and the second where a stainless steel free design was created and Li_2O_2 was identified as the primary electrochemical discharge product with a H_2O concentration equivalent to 100% relative humidity. These finding mark a critical development towards a true lithium-air battery, outlining strict criteria for the development of H_2O tolerant electrolytes that would remove the necessity of meticulous drying of the gas stream.

With this in mind, two research streams naturally follow the findings outlined in Chapter 7, the first being the exploration and screening of current collector materials towards the reduction of hydroperoxide species, and the second being the identification of solvents that are suitably tolerant of H_2O. Both research streams would be aided by the use of computational analysis, which could in the former be used to assess the reactivity of several prospective materials and in the latter determine the activity of hydroxide ions in a given H_2O-solvent mixture. The findings from these analyses would be a monumental step towards a true lithium-air battery that performs exclusive $2e^-$ O_2, with the caveat that CO_2 scrubbing or an adequate method of Li_2CO_3 oxidation is still required.

Taking the findings from Chapters 6 and 7 together, the role of hydroperoxide species, both in potential chemical degradation processes and in their newly identified critical role in electrochemical lithium hydroxide formation, must be understood and their impact should be assessed whenever a new electrolyte component or electroactive material is proposed.

Appendix

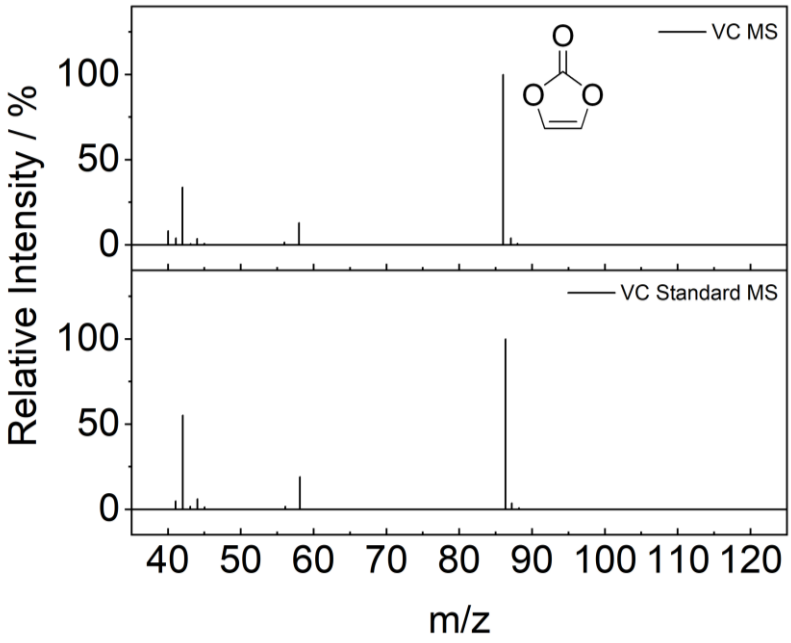


Figure A.1 *Comparison of the mass spectrum recorded during GC-MS analysis of a LP57 electrolyte doped with 2 wt.% VC at a retention time of 10 minutes to the NIST mass spectral library entry for VC, confirming the identity of this peak.*

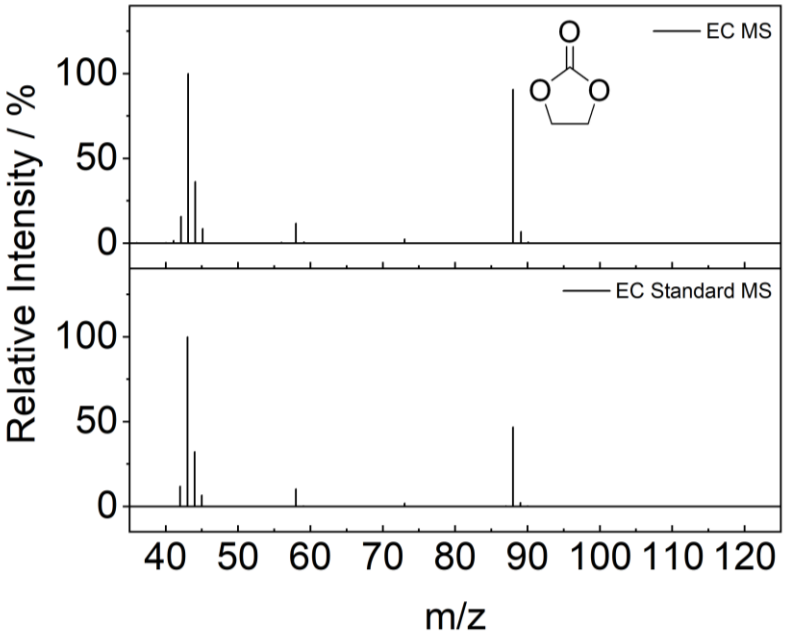


Figure A.2. *Comparison of the mass spectrum recorded during GC-MS analysis of a LP57 electrolyte doped with 2 wt.% VC at a retention time of 24 minutes to the NIST mass spectral library entry for EC, confirming the identity of this peak.*

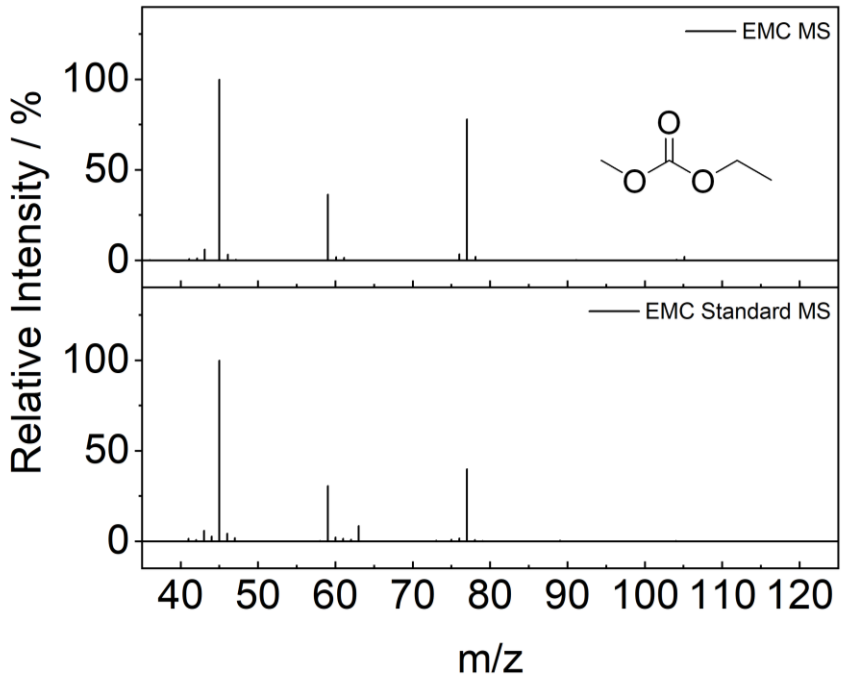


Figure A.3. *Comparison of the mass spectrum recorded during GC-MS analysis of a LP57 electrolyte doped with 2 wt.% VC at a retention time of 5.5 minutes to the NIST mass spectral library entry for EMC, confirming the identity of this peak.*

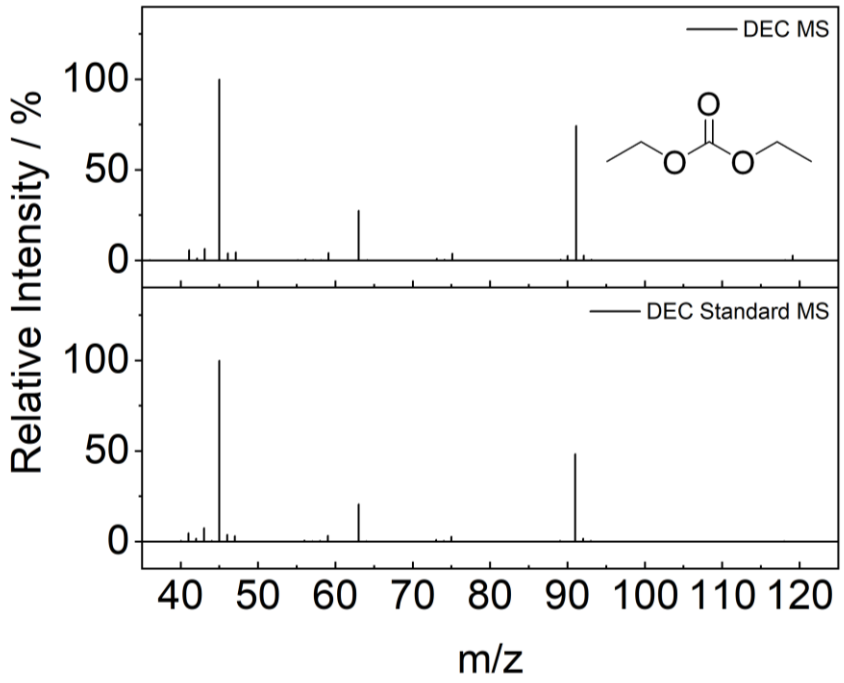


Figure A.4. *Comparison of the mass spectrum recorded during GC-MS analysis of a LP57 electrolyte doped with 2 wt.% VC at a retention time of 7.5 minutes to the NIST mass spectral library entry for DEC, confirming the identity of this peak.*

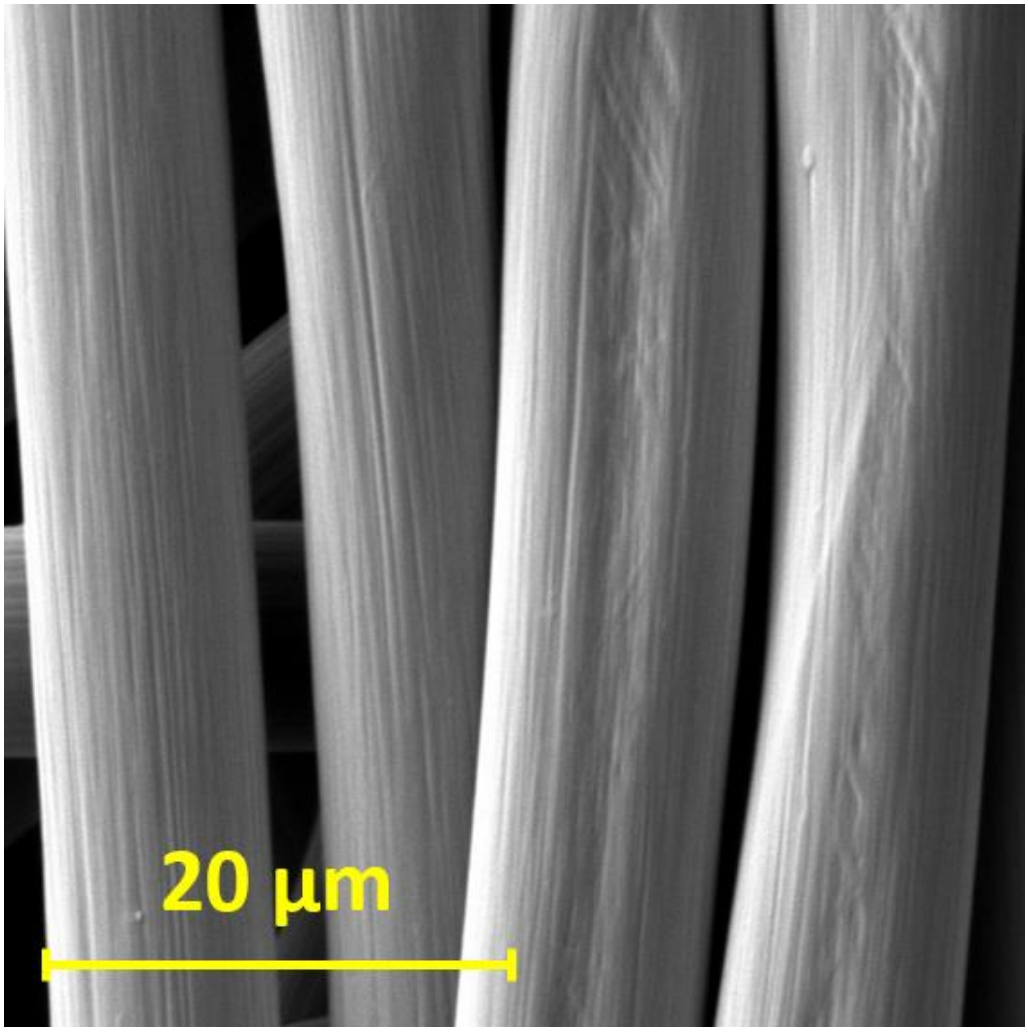


Figure A.5. *Representative SEM images taken of the surface of a pristine cathode used for electrochemical measurements in Chapter 7.*